Pressure and Saturation Estimation from PRM Time-Lapse Seismic data for a Compacting Reservoir

Wong Ming Yi

Thesis presented for the degree of Doctor of Philosophy.

Heriot-Watt Institute of Petroleum Engineering
School of Energy, Geoscience, Infrastructure and Society
Heriot-Watt University, Edinburgh, UK

May 2017

ABSTRACT

Observed 4D effects are influenced by a combination of changes in both pressure and saturation in the reservoir. Decomposition of pressure and saturation changes is crucial to explain the different physical variables that have contributed to the 4D seismic responses. This thesis addresses the challenges of pressure and saturation decomposition from such time-lapse seismic data in a compacting chalk reservoir. The technique employed integrates reservoir engineering concepts and geophysical knowledge. The innovation in this methodology is the ability to capture the complicated water weakening behaviour of the chalk as a non-linear proxy model controlled by only three constants. Thus, changes in pressure and saturation are estimated via a Bayesian inversion by employing compaction curves derived from the laboratory, constraints from the simulation model predictions, time strain information and the observed fractional change in V_P and V_S. The approach is tested on both synthetic and field data from the Ekofisk field in the North Sea. The results are in good agreement with well production data, and help explain strong localized anomalies in both the Ekofisk and Tor formations. These results also suggest updates to the reservoir simulation model.

The second part of the thesis focuses on the geomechanics of the overburden, and the opportunity to use time-lapse time-shifts to estimate pore pressure changes in the reservoir. To achieve this, a semi-analytical approach by Geertsma is used, which numerically integrates the displacements from a nucleus of strain. This model relates the overburden time-lapse time-shifts to reservoir pressure. The existing method by Hodgson (2009) is modified to estimate reservoir pressure change and also the average dilation factor or R-factor for both the reservoir and overburden. The R-factors can be quantified when prior constraints are available from a well history matched simulation model, and their uncertainty defined. The results indicate that the magnitude of R is a function of strain change polarity, and that this asymmetry is required to match the observed time-shifts. The recovered average R-factor is 16, using the permanent reservoir monitoring (PRM) data. The streamer data has recovered average R-factors in the range of 7.2 to 18.4. Despite the limiting assumptions of a homogeneous medium, the method is beneficial, as it treats arbitrary

subsurface geometries, and, in contrast to the complex numerical approaches, it is simple to parameterise and computationally fast.

Finally, the aim and objective of this research have been met predominantly by the use of PRM data. These applications could not have been achieved without such highly repeatable and short repeat period acquisitions. This points to the value in using these data in reservoir characterisation, inversion and history matching.

This thesis is dedicated to my late grandfather, 黄金源 *who taught me to be fearless and courageous, my grandmother,* 郭宝婵*, a woman of indomitable spirit,*

and to the rest of my family.

ACKNOWLEDGEMENTS

'That which does not kill us makes us stronger' – Friedrich Nietzsche (1844-1900)

I am very grateful to Prof. Colin MacBeth for taking a chance on a geologist for doing a PhD in Reservoir Geophysics. His knowledge, experience, and patience has been a great inspiration to me. I am extremely lucky to have a supervisor who cared so much about the work of his students and that no questions were ever too trivial or unimportant to him. I am also grateful to him for helping me to understand what makes relevant and important research. I would also like to thank Dr. Asghar Shams for being my second supervisor. The Edinburgh Time-Lapse Project is an exciting place to do research and to grow not only as a researcher but also as an individual. I am very proud to be part of it. This place has transformed me to be a stronger person. Acknowledgments go to all the ETLP sponsors for financial support, especially ConocoPhillips Skandinavia AS for the Ekofisk dataset. The Ekofisk partnership (Total E&P Norge AS, Eni Norge AS, Statoil Petroleum AS and Petoro AS) are acknowledged for permission to publish for journals and conferences. Working on the Ekofisk field high resolution Life of Field Seismic data has been quite a privilege. Thank you to ETLP sponsors Milana Ayzenberg, Andrew Wilson, Alex Bertrand, and Sean Ferris for all their advice and encouragement throughout the years.

In Edinburgh, I have made great friends: without their support and friendship, this could have been a very lonely and challenging journey. The members of ETLP and IPE have contributed immensely to my personal and professional time, many thanks to Angel Briceno, Mathieu Chamberfort, Ricardo Rangel, David Yin, Dennis Obidegwu, Sean Tian, Lu Ji, Danil Khakimov, Niki Obiwulu, Pollux Sii, Veronica Omofoma, Justin Geng, Phung Nguyen, Eric Alvarez, Lee Jean, Romain Chassagne, Miguel and Qi Zhang. My friends from across the globe, who always checked in on me and prayed for me, life is not the same without you. I thank Mark Ong and family for their kind words and support. I would like to acknowledge the help I received during the course of my PhD, especially: Hamed Amini, Ilya Fursov, and Maria Mangriotis for the many fruitful discussions and technical assistance. Thank you Ilya for proofreading the mathematical equations in my thesis. Many thanks to Mathieu and Hamed for helping me when I first started to learn programming. My heartfelt gratitude to IPE staff members Eric MacKay and Jim Sommerville for answering my questions related to reservoir simulation, and petroleum engineering. I also thank Schlumberger,

Ikon Science, and CGG for providing the software (Petrel, VISAGE, RokDoc and Hampson Russell software) and technical support.

I am very grateful for the internship opportunity in Stavanger, Norway provided by ConocoPhillips AS Scandinavia. This opportunity opened many doors for me. I really appreciate the encouragement, technical help and advice I received from my mentor Alex Bertrand. I would also like to thank Ole Eeg, Carlos Pacheco, Evgeny Tolstukhin, Jean De Lanlay, Reidar Midtun, Bjarne Lyngnes, and Per Gunnar Folstad for the technical support. In addition, I am also grateful for the Bayesian McMC collaborative effort with Arash JafarGandomi and Henning Hoeber from CGG. My internship with ExxonMobil Upstream Research Company in Houston was a unique experience. I would like to thank my mentor Kaushik Bandyopadhyay for his support, he had set an example of excellence as a both a researcher and mentor. I am also extremely grateful to David Johnston, Xin Zhan, Kevin Searles, Sekhar Gosavi, Rune Musum, David Abt, Xinyou Lu, Cody MacDonald, Eric Obrock, Tonya Brami and Brenda Roper. Thank you to Huang XiaoJun for acknowledging my contribution and giving me many opportunities to present my research.

As a recipient of the SEG/Leon Thomsen Scholarship, I would like to express my heartfelt thanks to the SEG Foundation Scholarship Program and to Dr. and Mrs. Thomsen for their kind contribution. I acknowledge the SEG/Chevron Student Leadership Symposium, and SEG/ExxonMobil Student Education who provided the funding to participate in their programmes and help me realise the joy in being a student again. In addition, many thanks to my examiners Olav Barkved, Mikael Luthje, and Maria-Daphne Mangriotis, for taking the time to read through this thesis and their constructive suggestions.

I want to thank my parents, Seng Yen and Louk My for all their support, love and encouragement throughout my years of study. Without them, I would not have had the courage to embark on this journey. My grandparents who always motivated me to be a better person. To my mischievous brothers, Meng Tze, Ming Jie and Ming Hui, life will be dull without the three of you! To my best friend, Hamed, no words are adequate to describe what an amazing partner you are. Your love, friendship and kindness has kept me going, even in my lowest moment. I am glad to be able to share life with you, *ajijam*. Finally, thank you God for His goodness and grace.

DECLARATION STATEMENT

ACADEMIC REGISTRY
Research Thesis Submission

Name*:*	Wong Ming Yi		
School:	School of Energy, Geoscience, Infrastructure and Society/ IPE		
Version: *(i.e. First, Resubmission, Final)*	Final	Degree Sought:	PhD

Declaration

In accordance with the appropriate regulations I hereby submit my thesis and I declare that:

1) the thesis embodies the results of my own work and has been composed by myself
2) where appropriate, I have made acknowledgement of the work of others and have made reference to work carried out in collaboration with other persons
3) the thesis is the correct version of the thesis for submission and is the same version as any electronic versions submitted*.
4) my thesis for the award referred to, deposited in the Heriot-Watt University Library, should be made available for loan or photocopying and be available via the Institutional Repository, subject to such conditions as the Librarian may require
5) I understand that as a student of the University I am required to abide by the Regulations of the University and to conform to its discipline.
6) I confirm that the thesis has been verified against plagiarism via an approved plagiarism detection application e.g. Turnitin.

* *Please note that it is the responsibility of the candidate to ensure that the correct version of the thesis is submitted.*

Signature of Candidate*:*		Date:	

Submission

Submitted By *(name in capitals):*	
Signature of Individual Submitting:	
Date Submitted:	

For Completion in the Student Service Centre (SSC)

Received in the SSC by *(name in capitals):*			
Chapter 1Method of Submission (Handed in to SSC; posted through internal/external mail):			
Chapter 2*E-thesis Submitted* ***(mandatory for final theses)***			
Signature:		Date:	

TABLE OF CONTENTS

LIST OF FIGURES

LIST OF TABLES

CHAPTER ONE

INTRODUCTION

This chapter lays the foundation and sets out the framework of this thesis. First, the importance of integrating 4D seismic data and production data in resolving the challenges of complex reservoir characterization is demonstrated, using examples from the literature. Geomechanically active reservoirs and the associated challenges in seismic interpretation and analysis are also discussed. I also explore the literature on pressure-saturation estimation on chalk reservoirs and the proxy model solution. Finally, I provide an overview of the content of this thesis.

1.1 Preamble

Time-lapse seismic or 4D seismic is the investigation of seismic attribute changes by acquiring seismic data through different time periods during the production period of a field. The first repeated 3D seismic surveys were acquired in North Texas in 1982/1983 to monitor a combustion process around an injection well (Mohamed and Samsudin, 2011). Since this seismic study was performed as the first is sui generis, and it was ahead of its time, the results did not prove it to be an economic method. However, now, nearly forty years after its first beginnings, 4D seismic has become commonplace in oil and gas field development as a proven technology. For example, nearly 75% of today's Statoil's field had acquired 4D seismic surveys by the year 2009 (Sandø et al., 2009). Traditionally, time-lapse seismic was used to discover the "low hanging fruits", such as identifying un-swept areas and by-passed oil, to target infill drilling wells and to improve our knowledge of the geological framework.

In recent years, combined with reservoir modelling, time-lapse seismic monitoring enables reservoir engineers to improve reservoir characterization and reduce uncertainty in production forecasts (Roggero et al., 2012). Pressure and saturation monitoring is key in field development, such as assessment of field connectivity, monitoring well performance, drilling infill wells, understanding injection and aquifer support and evaluating the average pressure state of the field (Corzo et al., 2013). The decomposition of pressure and saturation changes is also crucial to explain different physical variables that contributed to similar 4D seismic differences. The oil and gas industry is constantly pushing the boundaries of technology and ideas. Figure 1.1 shows the value chain of 4D seismic, demonstrating the vast contributions of 4D in different reservoir management and operations domains.

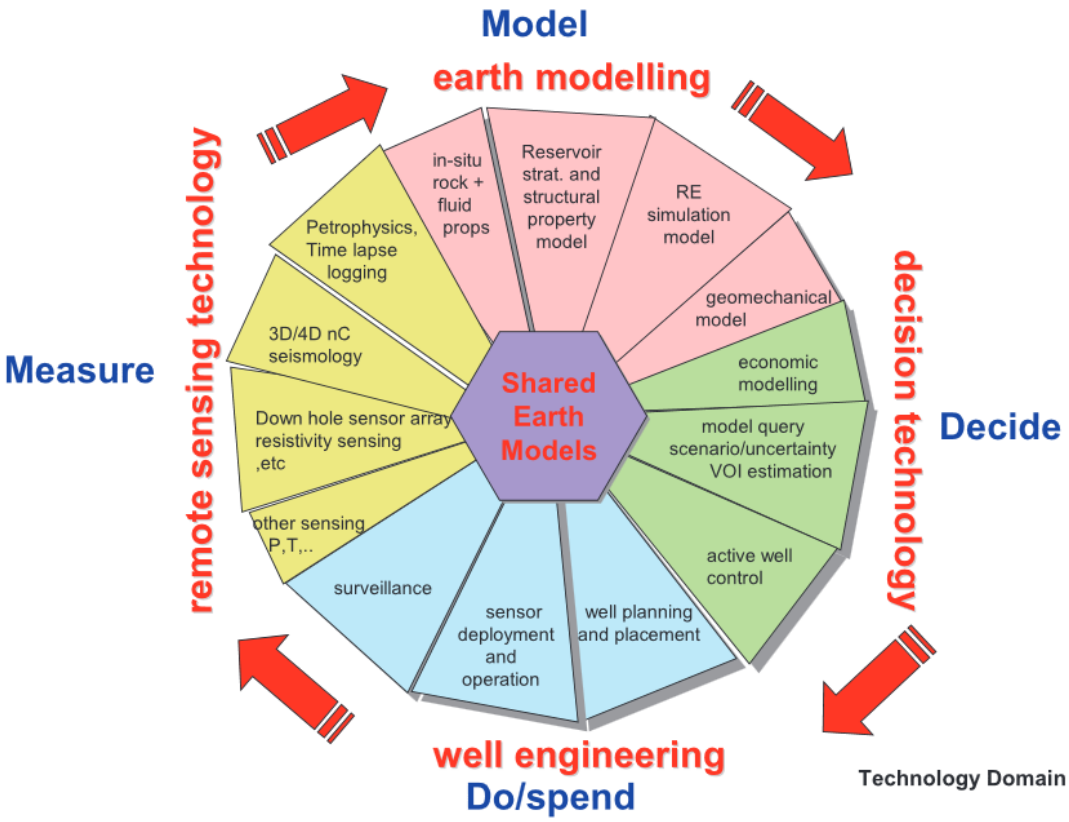

Figure 1.1: The 4D 'Value Loop' (de Waal and Calvert 2003).

An emerging technology known as the seismic permanent reservoir monitoring (PRM) system, is paving the way to delivering better quality and higher repeatability seismic data. In the past, the majority (in the range of 95%) of offshore seismic time-lapse surveys were acquired using towed streamer, but this is now changing. The PRM system has improved repeatability so much that the technology has claimed changes in travel time as small as a few hundred microseconds, and 2-3% changes in amplitude are detectable above noise level (Bertrand et al., 2014). Figure 1.2 illustrates the growth in offshore PRM use since the Foinaven installation, we can see an increase in the number of kilometers of installed seismic sensor cables versus the year of installation. The forecast does not specify field names. Higher detectability in time-lapse seismic change means better operational efficiency, lower reservoir management costs, reduction of overburden drilling risk, better monitoring of cap rock integrity and higher success rate in unravelling reservoir dynamic changes such as pressure and saturation (Caldwell et al., 2015).

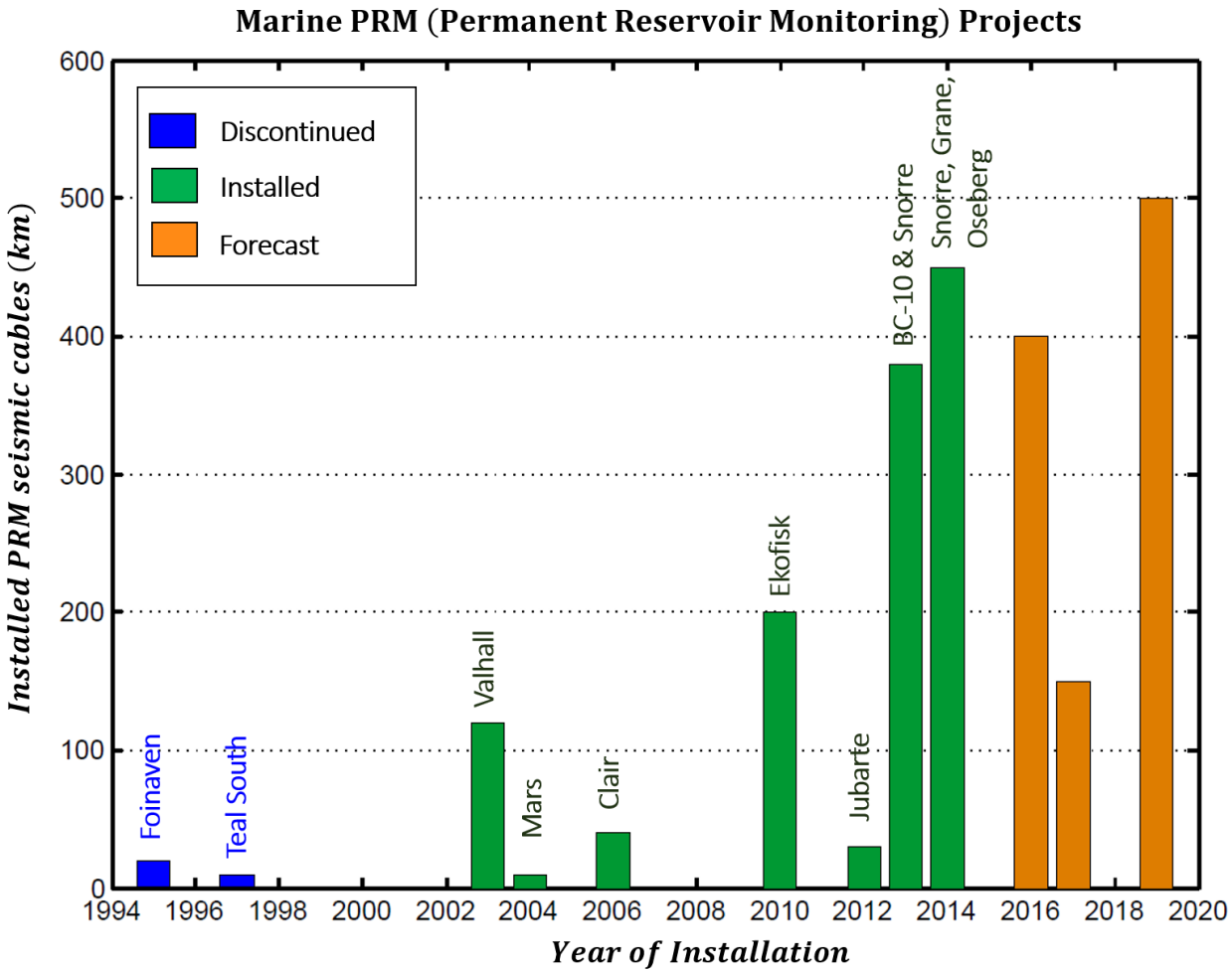

Figure 1.2: Summary of seabed PRM projects over the last 20 years and those forecasted for the future (Reproduced after Caldwell et al., 2015).

1.2 Integration of Time-lapse Seismic and Engineering data

The integration of seismic and engineering data has been mainly qualitative, such that anomalies are often inferred to be changes in oil, water, or gas saturation (Sønneland et al., 1996; Anderson et al., 1997; He et al., 1998), or semi-quantitative, in which the interpretation of reservoir performance has been aided by the visual comparison of maps and plots of seismic attributes with areal plots of the reservoir simulator output. As a result, the reservoir model can often be improved by updating the model in areas of misfit. Semi-quantitative integration of time-lapse seismic and production data can be found in Al-Najjar et al. (1999), Waggoner (2001), Staples et al. (2002),

Marsh et al. (2003), Landa and Kumar (2011), Ayzenberg et al. (2013), Alerini et al. (2014), Ayzenberg and Liu (2014) and Tian et al. (2014). A review of these articles shows that the comparison of the 4D signature with the predicted output from a simulation model has been successful in locating dynamic barriers, varying fault transmissibility multipliers, altering aquifer connectivity, identifying injected water slumping, STOIIP adjustment, well planning and changes in production strategies.

To move towards more quantitative solutions, one would need to merge flow simulation and 4D seismic in an attempt to provide vastly improved forecasts of reservoir behaviour and make major improvements in geological reservoir models. These developments hold significant impact on the future of 4D within the industry. Other examples are from the "global inversion" scheme by El Ouair and Stronen (2006) and Lafet et al. (2009); constraining 4D inversion results to the stratigraphy constraints, which honours the reservoir zonation, expected production effects and rock-physics trends (Figure 1.3). Seismic inversion is by its nature ill-posed and there are non-unique solutions. In addition, the inherent errors in the 4D data, as well as the imperfect modelling process, will make the inversion unstable. Therefore, the key for a successful 4D inversion lies in collaboration among the disciplines.

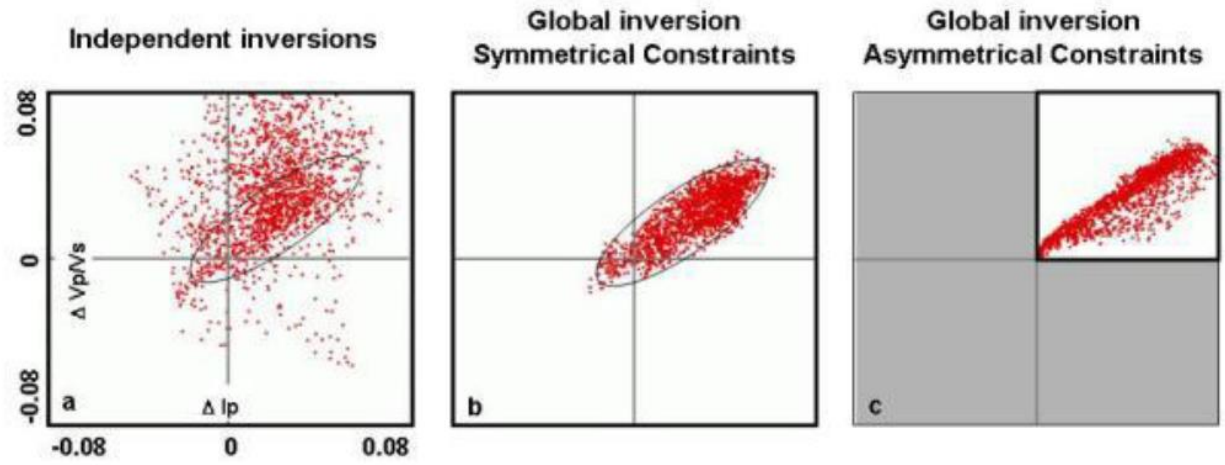

Figure 1.3: Inverted elastic attributes for a water flooded area by (a) independent inversion of baseline and monitor seismic data, (b) a global 4D inversion with a symmetrical searching window and (b) a non-symmetrical searching window as constraints (Lafet et al., 2009).

Quantitative examples such as that of Yin et al. (2015) have involved using well2seis attributes in seismic-assisted history matching to honour data from both seismic and engineering domains, and remaining consistent with fault interpretation. The well2seis attribute determines the correlation between production and seismic data across time. This promoted a 90% reduction in the misfit errors and 89% lowering of the corresponding uncertainty bounds after history matching with the well2seis attribute (Yin et al., 2015). Figure 1.4 shows that area 'I' shows a hardening signal due to pressure depletion, and this is not predicted in the simulation model in Figure 1.4 (b).

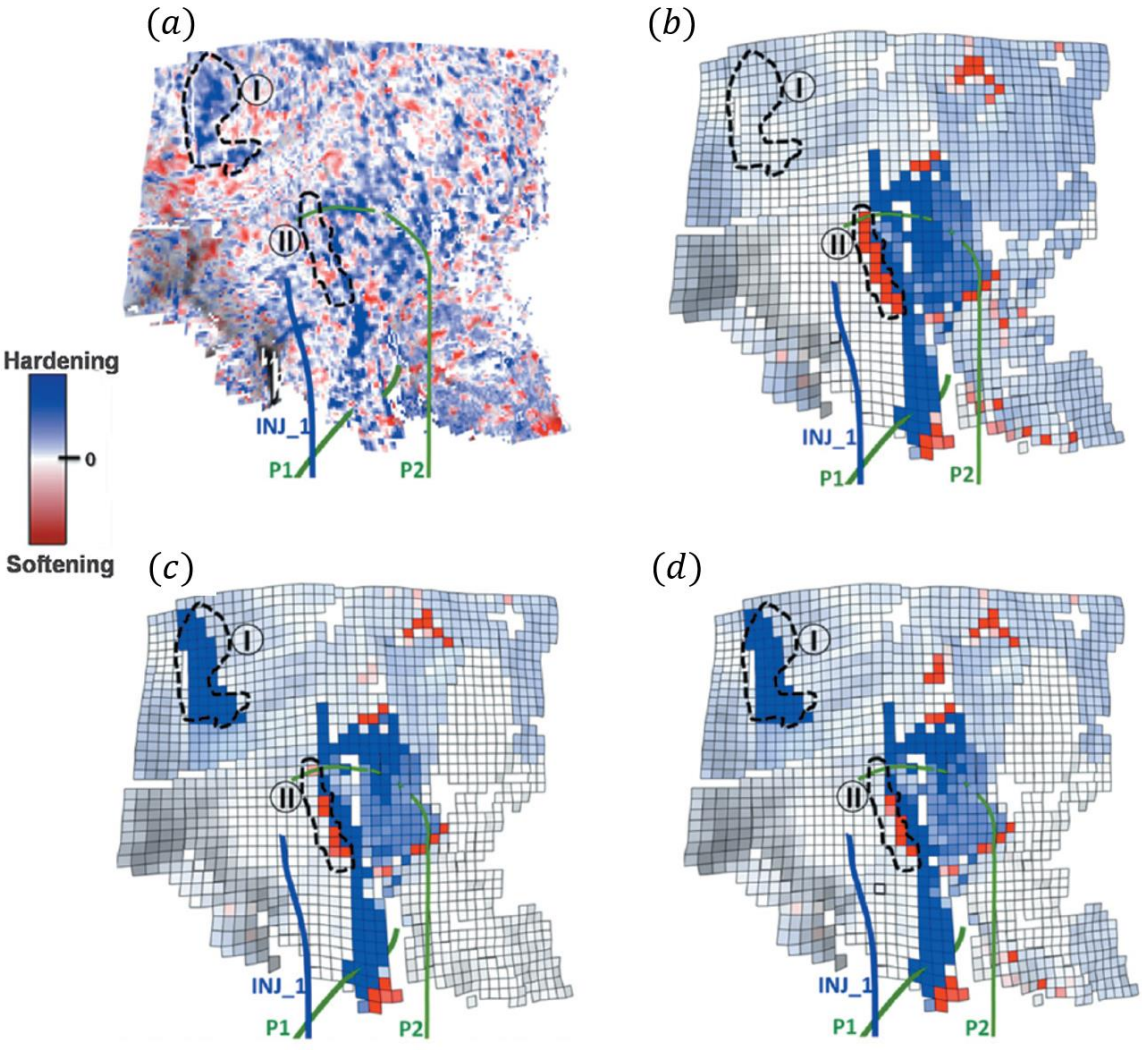

Figure 1.4: (a) Observed 4D seismic difference between baseline and monitor, (b) simulated 4D seismic difference from simulation model using traditional history matching without well2seis attribute, (c) simulated 4D seismic difference after direct updating and (d) the 4D difference after assisted history matching using well2seis (Yin et al., 2015).

1.3 Geomechanically Active Reservoirs

Reservoir compaction, subsidence and potential fault reactivation are notorious in depleting, weak, unconsolidated sandstone and chalk reservoirs. Reservoir compaction has been observed in a wide range of geographical locations and reservoir types, such as the North Sea, the Gulf of Mexico, California, Canada, South America and Southeast Asia (Bruno, 2002). It can be a positive phenomenon, because the compaction mechanism can provide significant energy to drive production, analogous to squeezing water from a sponge (Setarri, 2002). The value of the added production outweighs the negative effects of compaction, which are chalk production, well failures and damage on infrastructure (Barkved, 2012). The geomechanical challenges associated with a compacting reservoir are shown in Figure 1.5. Some of these challenges include slip planes in the overburden, well failure due to buckling-induced casing damage, a high shear zone in the overburden and a risk in seal integrity (Dusseault et al., 2001).

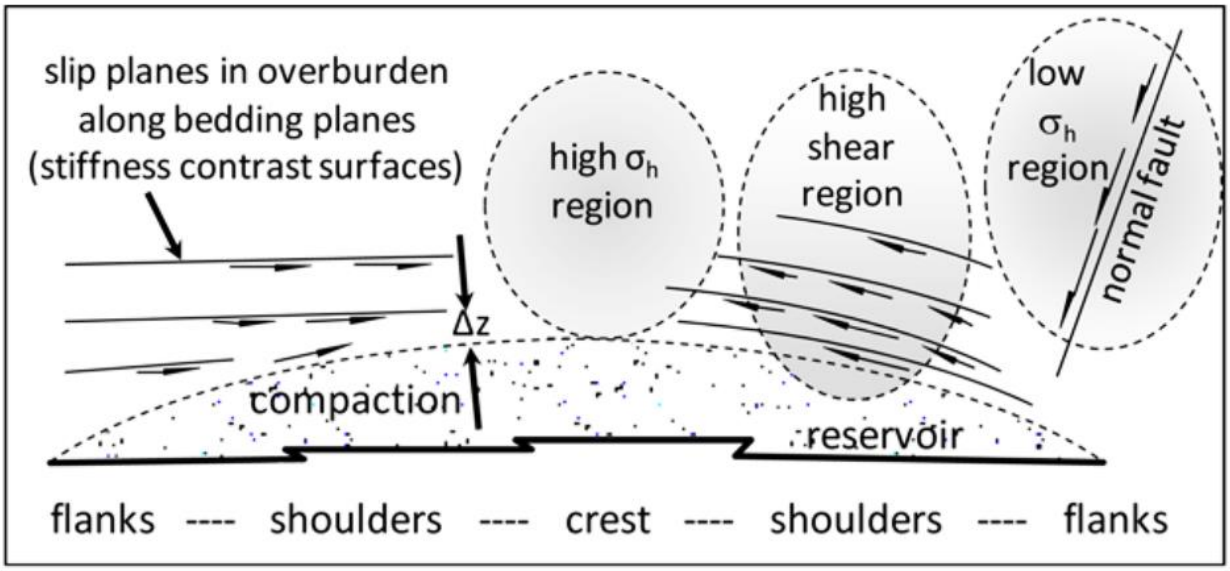

Figure 1.5: Geomechanical challenges both inside and outside the reservoir induced by production (Dusseault et al., 2001).

1.3.1 Challenges for time-lapse seismic analysis of a compacting reservoir

There are many challenges to interpret time lapse seismic signals from a compacting reservoir, due to the additional component of porosity reduction making interpretation more ambiguous. This is

demonstrated in Figure 1.6: in the event of an injection event at high effective stress in a chalk reservoir, we have an interplay of (1) increase of water saturation, (2) pressure build up at injection point and (3) compaction due to weakening of the chalk. This results in complex behaviour such as cancellation in signals in the relative change of elastic properties and consequently amplitude changes and time-shifts.

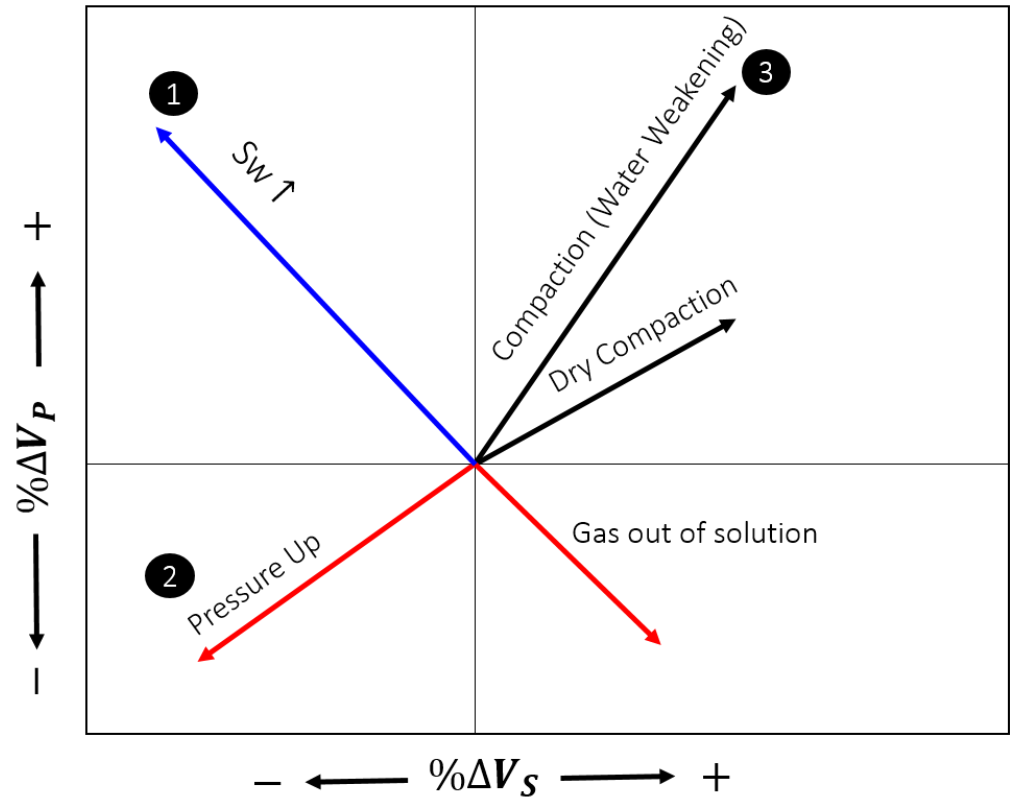

Figure 1.6: The behaviour of the relative change in P and S-wave velocity in an isolated event with different dynamic changes.

As the reservoir compacts, the immediate overburden stretches in response. Often the seabed produces subsidence, which means the seismic signal becomes time variant and cannot be exploited to match time-lapsed seismic surveys with each other. In the Valhall field, time-shifts up to 48ms have been measured from streamer 4D seismic data (Barkved et al., 2003). In order to discriminate between subsidence effects, and image subtle time-lapse effects in the reservoir, high repeatability is required in the data. This can be achieved by having the locations of both the source

and receivers repeated as closely as possible in each survey. This is one of the reasons why many compacting reservoirs such as the North Sea chalk fields have a PRM system installed.

Time-shifts, or travel time differences measured between baseline and monitor, are now transformed as an important reservoir characterisation tool especially for compacting reservoirs. The very first published 4D seismic example of reservoirs inducing changes in the overburden was by Guilbot and Smith (2002). This work provided a detailed interpretation of the towed streamer surveys of 1989 and 1999, with strong correlation between time-lapse time-shifts data and reservoir compaction. However, this was not always the case in the past, small time-shifts between baseline and monitor were often corrected for, instead of being preserved for interpretation, in order to improve repeatability. This small time misalignment could be due to acquisition, geometry, processing algorithms, velocity models and parameterisation (Johnston, 2013).

In the Valhall field, challenges in tying wells to seismic using VSP and check shot data from older wells were also reported. The mismatch could be 20-30ms, using legacy data. An improvement was found when using wells that were newly drilled, with a mismatch of only 2ms. The most likely explanation was due to lateral variation in gas charges across a fault, commonly found in many compacting chalk fields with gas charges in the overburden (Barkved, 2012).

Monitoring of stress and strain in compacting reservoirs is also key in making reservoir management decisions. This requires accurate prediction of changes in stress and strain due to various operations, including production, injection and fracturing, via a geomechanical model. The main challenge of geomechanical modelling and prediction is the availability of input data – primarily rock strength and in situ stresses. To acquire these data, expensive core logging and laboratory tests are required, which also is time consuming. These data are, however, sparse in the overburden to characterise the surrounding medium of the reservoir. There are also constitutive models which are difficult to parameterise. In Chapter 6 and 7, I will discuss in more depth analytical models such as Geertsma's model (1963, 1977), to characterise stresses and strain in the overburden. An analytical or semi-analytical model like Geertsma's can also be formulated in an inversion scheme, to estimate change in pore pressure.

1.3.2 Chalk reservoir inversion

Acoustic impedance inversion can significantly improve data interpretation, since the interpretation is now carried out on rock layers and not interfaces. It is also beneficial, in the sense that comparison to the simulation model can be made on a cell-by-cell basis instead of using map-based methods. There are many examples documented in the literature on impedance inversion for compacting or slightly compacting chalk reservoirs. The examples here will be focused on North Sea chalk reservoirs. In South Arne, both 3D and 4D AVO inversions were carried out. The inverted products were the baseline and the ratio of changes of baseline over monitor for acoustic impedance and Poisson's ratio. Then, using a calibrated rock physics model allows translation of the changes of acoustic impedance and Poisson's ratio into reservoir properties, such as changes in saturation for water and gas, and allows the changes in porosity to be quantified (Herwanger et al., 2010). This example is further elaborated in Section 1.4.

In Halfdan, the reservoir is relatively thinner than Ekofisk (average thickness of 75m) and relies on implementation of long horizontal multilateral wells for completion. The chalk has little or no compaction if initial porosity is less than 35%, therefore compaction is expected to have less impact on 4D response in most areas of the field (Dons et al., 2007). In Halfdan, an integrated 4D inversion, showing time strain was used as a prior model, while inverting for 4D impedance changes. The role of time strain is twofold: it was first used to time-align the amplitude in TWT and also included as a prior model to estimate the low frequencies of the 4D impedance changes, giving a broadband estimation and also to reduce the side-lobes above and below the real 4D signal. The inverted relative change in impedance with a prior model looks cleaner, with more distinctive signals (Micksch et al. 2014), and is more intuitive to interpret compared to amplitude differences. From the inverted impedance difference, hardening signals were observed surrounding the injectors representing flood front progression, and softening in the upper part of Ekofisk, due to gas exsolution (Calvert et al, 2013, 2014), as shown in Figure 1.7 (a) and (b). This observation is not necessarily obvious by looking at changes in 4D seismic amplitude due to tuning and interference.

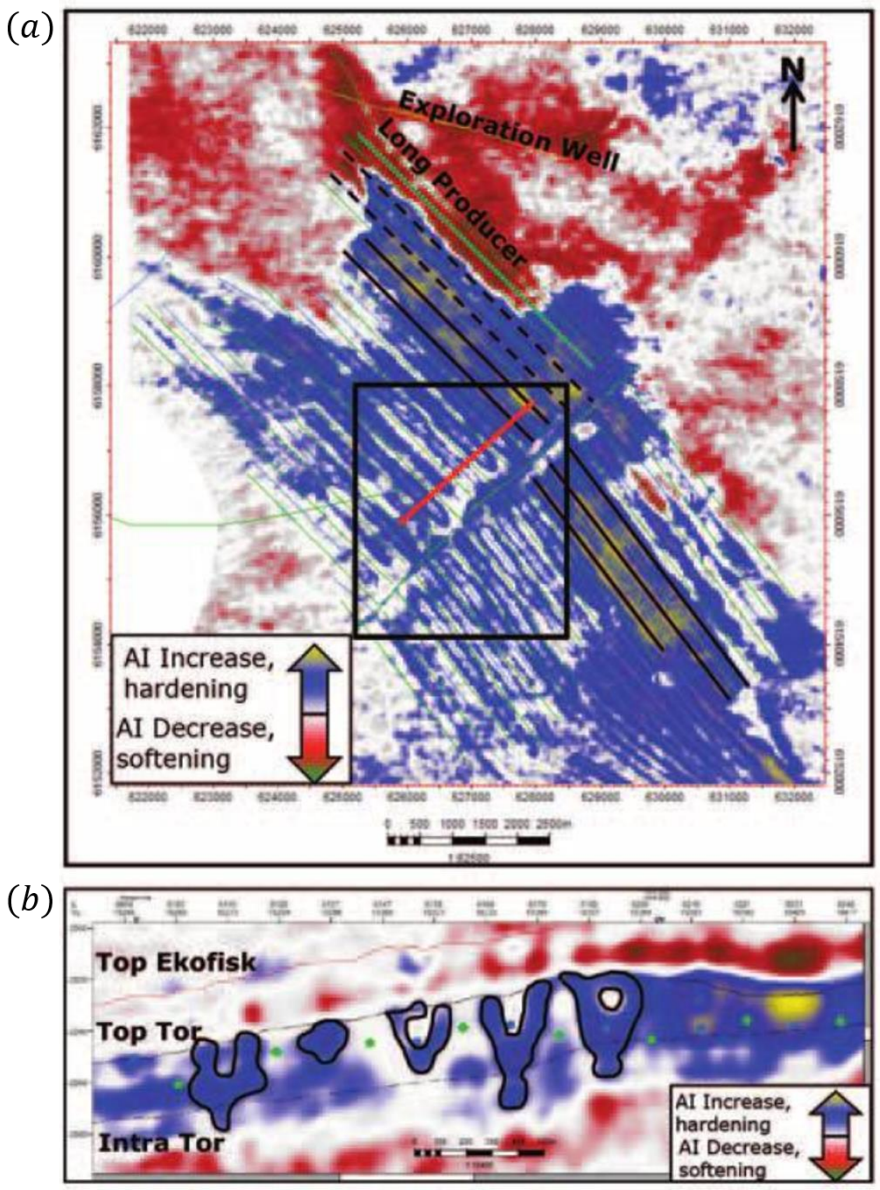

Figure 1.7: (a) Map view of inverted acoustic impedance, blue colour corresponding to AI increase/hardening and red colour representing AI decrease/softening, (b) section view showing Tor formation: blue halo shows water sweep patterns (Calvert et al., 2014).

In Valhall, the coloured inversion on the data shows the clear signal for pressure increase (a reduction in acoustic impedance) due to re-pressurization from a newly-installed injector (shown in Corzo et al., 2009). This effect is less apparent from the 4D amplitude anomaly overlaid, as this

decrease could be attributed to side lobe interference. In Ekofisk, seismic impedance inversion was used as a powerful technique in detailed reservoir characterization. It was used mainly for porosity mapping and to understand reservoir layering and diagenesis. The impedance inversion results shown in Figure 1.8 reveal detailed stratigraphic facies (EL3 facies, SEE, SED2 facies, tight layer and porous layers) in Ekofisk, based on the strength of impedance (Guilbot et al., 2002).

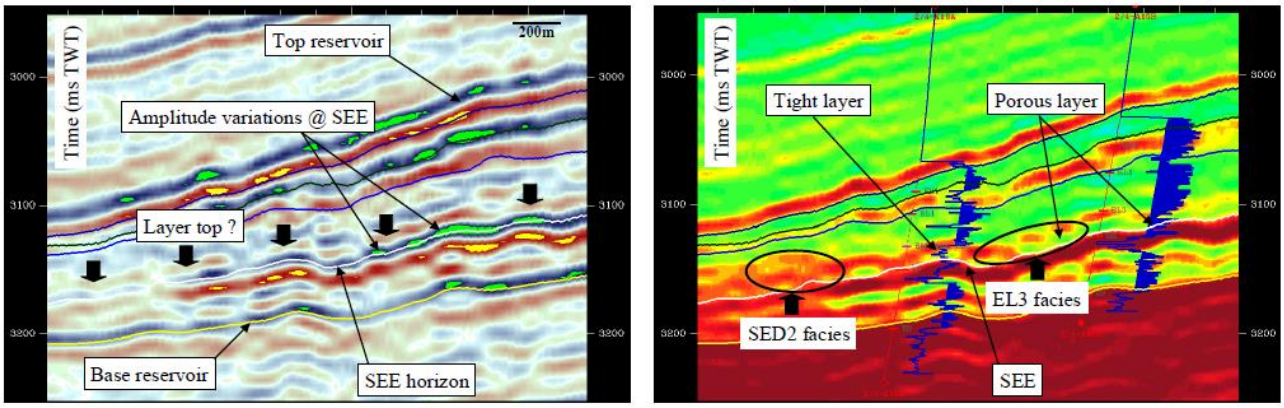

Figure 1.8: (left) Cross-section of amplitude and (right) acoustic impedance inverted from post-stack inversion - good agreement was found with log data (Guilbot et al., 2002).

In the Dan field, impedance inversion was carried out using Bayesian classification constrained by well data and rock physics analysis to define lithological boundaries and fluid distribution. The inverted products shown in Figure 1.9 illustrate the gas cap and tilted fluid contact are highlighted, where the both I_P, and V_P/V_S are low. This process also helps in updating the interpretation of the top structure (Herbet et al., 2013).

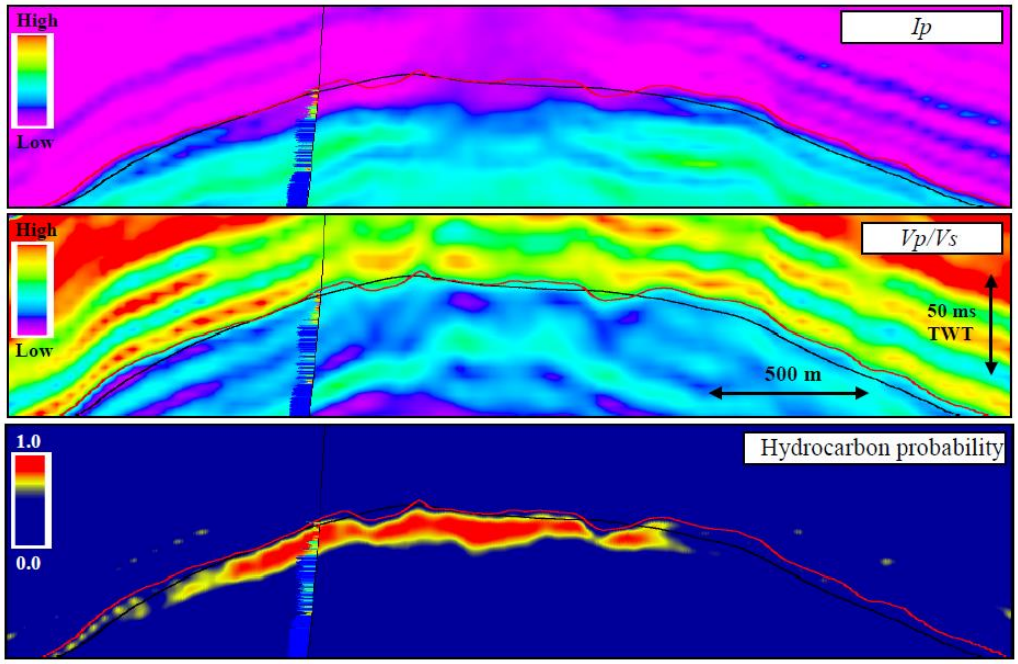

Figure 1.9: (top) Inverted acoustic impedance, (middle) inverted V_P/V_S ratio and (c) hydrocarbon probability for the Dan field (Herbet et al., 2013).

1.4 Pressure-Saturation Estimation using 4D Seismic on Chalk reservoirs

The quantification of pressure and saturation distribution is an important improvement in the interpretation and applicability of time-lapse seismic analysis. The Holy Grail of the 4D seismic technology is the ability to separate time-lapse seismic response into pressure and saturation changes. In the case of a compacting reservoir, estimation of porosity and stress changes is also top on the list of deliverables from 4D seismic. Saturation changes supply information on fluid movement and barriers, while pressure changes provide data on the position of barriers and compartments, fault sealing and non-sealing, and general connectivity. An accurate estimation of pressure and saturation requires a careful time-lapse analysis and a more quantitative integration between the engineering and seismic domains. This can be carried out by relating the changes in the seismic to corresponding changes in fluid pressure and/or saturation. The workflow presented in Figure 1.10 shows how seismic is incorporated into reservoir models: information can be compared in three key domains: seismic amplitude trace, impedance or elastic properties and the dynamic properties domain.

Different studies have shown that the matching in the seismic domain is very difficult (Gosselin et al., 2003, and Roggero et al., 2007). This is related to the nature of seismic data, which are very different from production data. Furthermore, seismic modelling is often a time intensive process. Due to CPU time constraints, reservoir simulation often requires upscaling. Thus the resolution of the simulated seismic attributes can be very low in comparison to the resolution of the observed seismic. This creates unfavourable comparisons.

Matching in the impedance or elastic property domain has its pluses and minuses. The drawbacks are that acoustic impedances are derived from a preliminary inversion process of the seismic data which is generally noisy. In addition, the result of the inversion process is largely dependent on the choice of the prior model, and thus is uncertain. However, if the seismic data is of reasonable quality, the inverted acoustic impedance, which is an interval property, proves to be an attribute that can be compared to the predicted ones more effectively. The petro-elastic model, which is key in this process, requires many calibrations from well logs and laboratory stress sensitivity coefficients and assumptions (Landrø, 2001, Gosselin et al., 2003, Stephen et al., 2005, Floricich, 2006, Wen et al., 2006, Amini, 2014).

The third domain is to compare maps or volumes of the dynamic properties such as pressure and saturation changes, inverted from seismic, which can be directly compared to the outputs of the simulation model prediction; this helps to reduce ambiguity in interpretation. However, these inverted products carry more uncertainties than elastic changes, as the uncertainties associated with inverted products from 4D seismic such as elastic properties and time-shifts are used as inputs. If pressure and saturation changes can be accurately and effectively extracted from time-lapse seismic data, a direct comparison can be made with predictions from the engineering domain. There have been other methods that circumvent the complex seismic modelling process to arrive at these dynamic properties, which will be provided in Section 1.5.

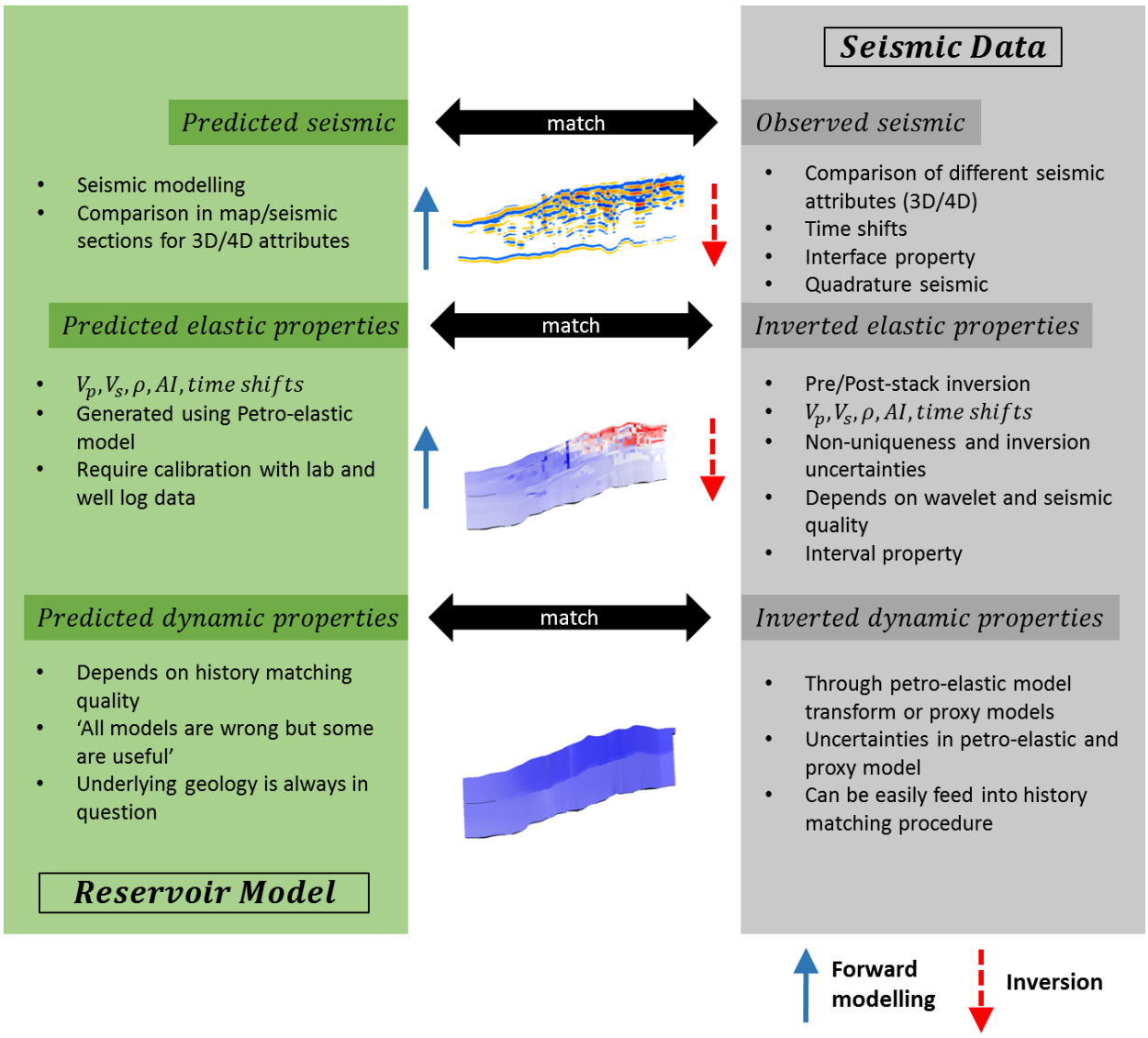

Figure 1.10: A workflow showing how to make a comparison of the seismic data to the reservoir model (engineering domain). Comparisons can be carried out in the domains of seismic, elastic properties and dynamic properties

The majority of pressure -saturation inversion work reported in the literature is mainly focused on the development and application of model driven approaches. In these methods, dynamic properties are inverted using AVO inversion which is based on the physical principles of seismic wave propagation. It is often a two-step procedure, where seismic amplitudes are inverted into various elastic properties and, subsequently, using a rock physics transform, these elastic properties are translated into pressure and saturation changes. In the work of Herwanger et al. (2010), angle-band stacks of baseline and monitor surveys are used as inputs to invert for acoustic impedance and Poisson's ratio and the ratio changes of these parameters. A calibrated rock physics model then allows translation of these elastic properties into pressure, water saturation and porosity changes. The results from this deterministic 4D AVO inversion work are reported in Figure 1.11. In general, model-driven approaches are computation-intensive and could be hard to parameterise.

Data-driven methods, on the other hand, use production and seismic data at well locations to compute some correlations. The correlations established at these sample points are then used to estimate pressure and saturation changes from 4D seismic at the un-sampled locations between wells. In data-driven approaches, pressure-saturation estimation is driven by what is learned from field data, and thus sometimes does not require a rock-physics model. Further examples will be given in Section 1.5. In the current literature, most data-driven 4D seismic inversion commonly results in 2D maps displaying changes in reservoir pressure and saturation. This represents a major shortcoming of the approach when compared to model-driven methods that generate 3D volumetric changes in reservoir pressure and saturation. Extending the data-driven method into volumetric or into 3D space is one of the goals of this thesis. I will also discuss the rationale of breaking way from 2D maps for the Ekofisk field in Section 1.5.

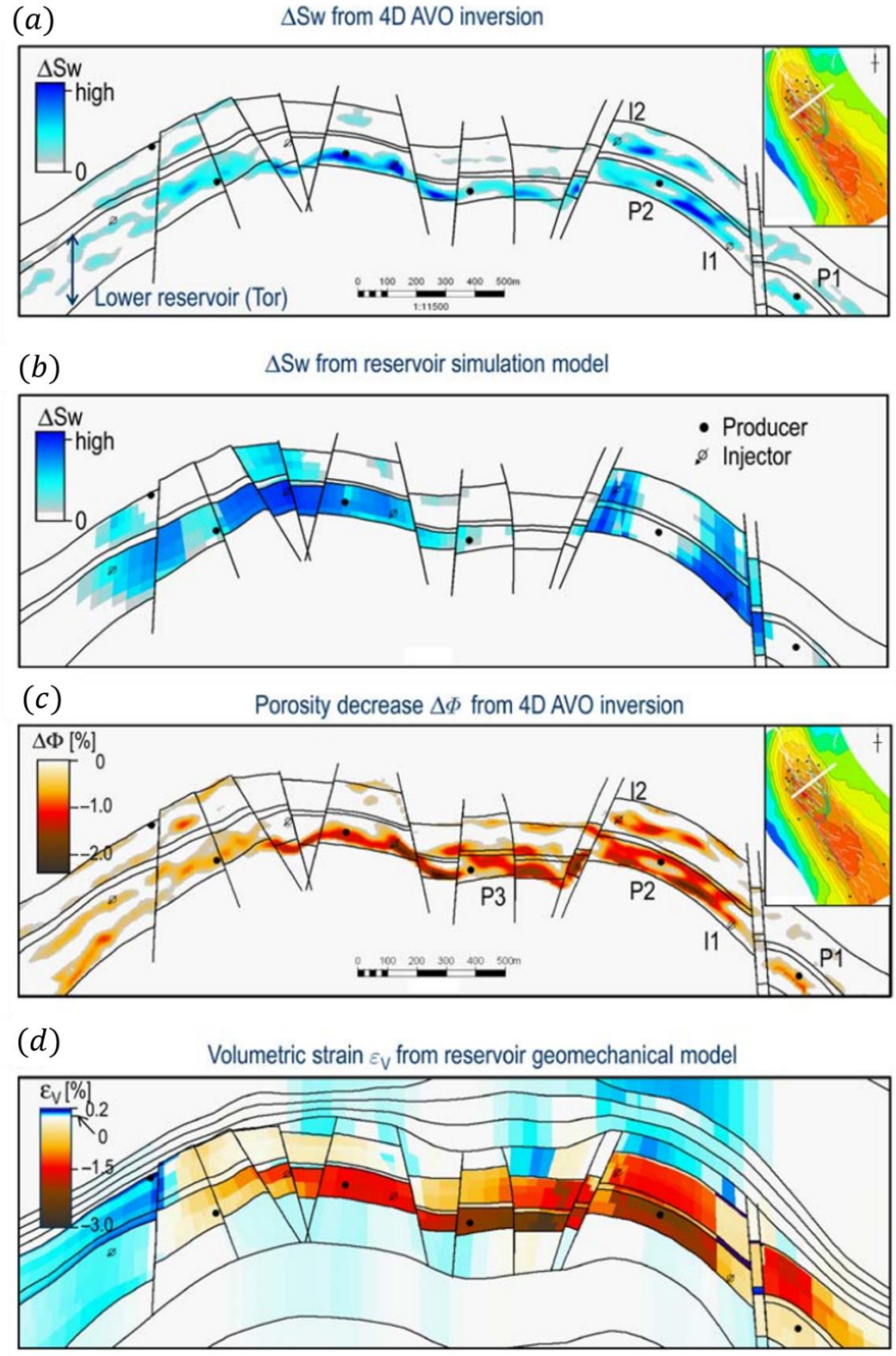

Figure 1.11: (a) Water saturation change inverted from 4D AVO inversion compared to (b) water saturation predicted from reservoir simulation model. (c) and (d) show comparisons for porosity changes from an inversion result and volumetric strain from a geomechanical model (Herwanger et al, 2010).

1.4.1 Taking advantage of multiple repeated surveys

The move towards more quantitative interpretation requires analysis of multiple 4D seismic attributes to estimate the engineering measures of reservoir change. According to Watts (2011), the use of seabed mounted four-component receiver technology will bring 4D seismic data to whole new level of data quality, with an unprecedented level of repeatability and multi-azimuth sampling of seismic wave field. Therefore, dedicated permanent reservoir monitoring (PRM) data could provide an important contribution in this area of development. Well engineers in the Valhall Field have been some of the most enthusiastic customers of PRM data (Caldwell et al., 2015). The current state of the industry, as highlighted in the red box in Figure 1.12, shows how seabed systems have provided a significant step-change in reservoir monitoring. Field operation and management decisions are taken on a monthly to weekly basis, where PRM data can effectively provide new snapshots of the reservoir in that time frame.

There are many examples showing the benefits of repeated surveys and a PRM system. One of such examples is the Clair field, as illustrated in Figure 1.13, showing a towed streamer data in 1992, a sparse OBC in 2002 and lastly the high-density OBC from 2006 to present day. What is being demonstrated is a significant improvement in data quality from a narrow azimuth acquisition to full, coarsely-sampled data, to well-sampled full azimuth data (Davies et al., 2011). It can be seen that there is a step change in improving the structural imaging and low frequency of the data.

Hypothetically, if changes in the dynamic properties of the reservoir can be easily and effectively inverted from multiple seismic data across different time periods, this could ultimately replace the concept of a simulation model. Building an up-scaled geological model (simulation model) requires a tremendous amount of time, effort and data. Moreover, the constrained reservoir models obtained by history matching with well production data often yield solutions that are not unique, and data is sparse and local. In the Ekofisk field, with dedicated PRM surveys, seismic data are acquired and processed as often as every six months (Bertrand et al., 2014). This provides a unique opportunity to monitor these reservoirs and retrieve information from the subsurface at an unprecedented pace, often surpassing the time required to history match the entire simulation model from start to finish.

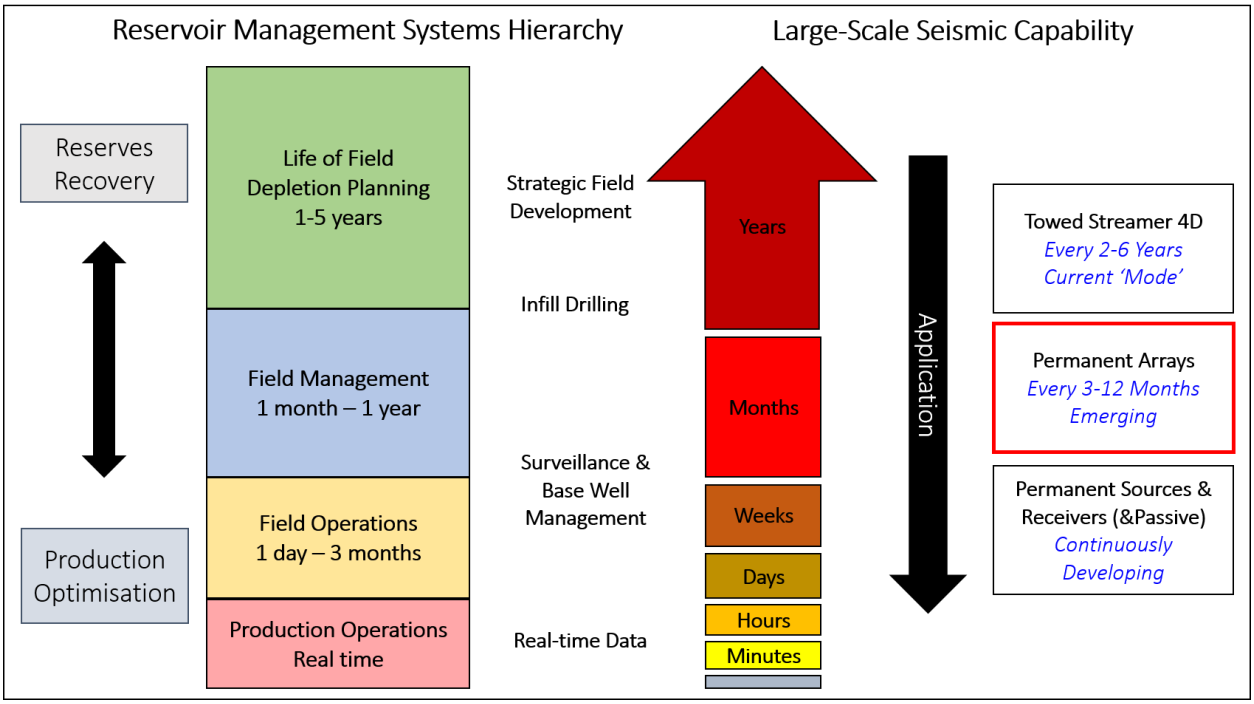

Figure 1.12: Many oil management decisions and interventions are made on a monthly basis. This could benefit from input from more frequently acquired seismic data (highlighted in red box) than is the current norm (Reproduced after Caldwell et al., 2015).

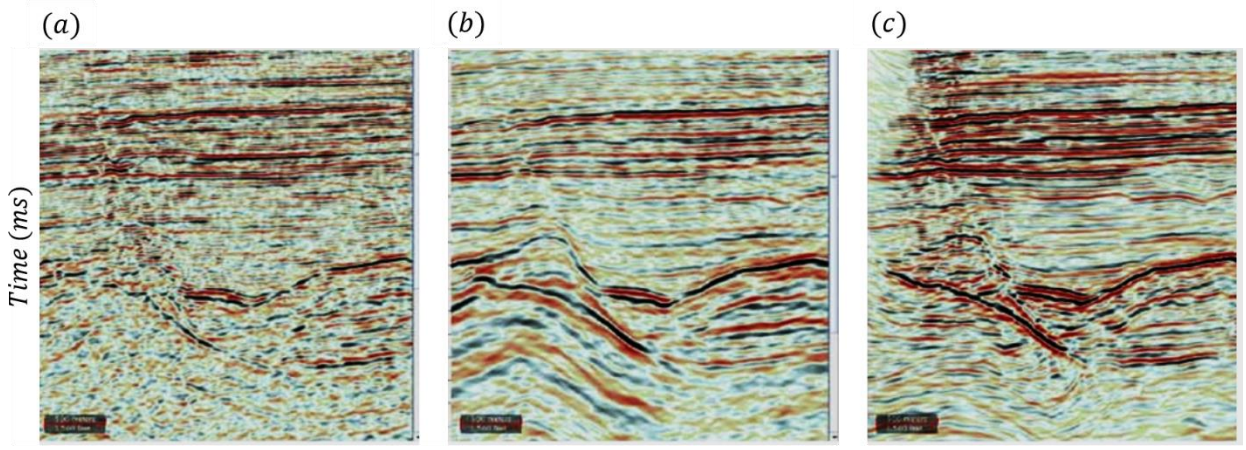

Figure 1.13: A comparison of seismic quality for (a) a towed streamer, (b) sparse OBC, and (c) high-density OBC (taken from Davies et al., 2011).

1.5 A Proxy Model Solution

One branch of active research is the determination of quantitative estimates of pressure and saturation changes from observed 4D seismic signals. Myriad techniques have been developed over the years, and these fall between two end-members - those based on rock-physics models, such as Tura and Lumley (1999), Cole et al. (2002), Landrø et al. (2003), Davolio et al. (2011) and Trani et al. (2011), and those relying on statistical calibration against the well or field wide production data, such as Landrø (2001), MacBeth et al. (2004), Floricich et al. (2006), Chu and Gist (2010), and Falahat et al. (2013). The major challenge with all these methods is that one needs to ensure that a forward model can adequately describe time-lapse elastic properties as a function of the dynamic reservoir parameters, and that the inverted dynamic properties are realistic and engineering consistent (EC).

1.5.1 Rationale of a Proxy Model approach

The use of a proxy model for inversion, modelling and production optimization is becoming more popular. For example, MacBeth et al. (2004, 2006) proposed an approach for inversion of pressure and saturation changes, where the linear relationship in Equation 1.1 describes the change of pressure and oil saturation with time-lapse seismic attributes.

$$\frac{\Delta A(x,y)}{\bar{A}_b} \approx C_s \Delta S_o(x,y) + C_p \Delta P(x,y) \tag{1.1}$$

where the constants C_s and C_p can be determined by calibration against production data for wells or the simulation model. $\Delta A(x,y)$ represents the changes in amplitude at each spatial location, $\bar{A}_b$ is the baseline amplitude, $\Delta S_o(x,y)$ and $\Delta P(x,y)$ are the changes in oil saturation and pressure at each spatial location. The change in time-lapse amplitude difference is normalized by the amplitude computed in the baseline survey. Multiple seismic attributes can be used and the above linear system is to be solved in the least-squares sense, to invert for pressure changes and saturation changes (Floricich et al., 2006). Such a linear relationship is said to be generally valid for a petroleum reservoir under production. Work from Alvarez and MacBeth (2013) shows that Equation 1.1 can also be written as Equation 1.2:

$$\Delta A = C_s \Delta S_w - C_p \Delta P \quad (1.2)$$

where the controlling parameters C_s and C_p provide the balance between the relative contribution of saturation and pressure change to the overall time-lapsed seismic signature. The negative sign in Equation 1.2 shows that an increase in water saturation (hardening of impedance) has an opposing physical effect on the reservoir, to an increase in pore pressure (softening of impedance), when C_s and C_p are both positive values.

The key trends that shape my proposed equation come from Floricich et al. (2006) and Corzo et al. (2013), where 4D seismic attributes are directly calibrated against field production data, and with the latter, a linear relationship was found between porosity, pressure changes and 4D amplitude changes in the compacting Valhall field. Linearity is not a necessary condition for this type of approach, as in the presence of complicated rock deformation mechanisms like water weakening, non-linear compaction trends can also be captured in the forward modelling procedure and subsequently used for inversion. In the work of Corzo et al. (2013), initial porosity was included to solve for pressure changes, specifically pressure depletion:

$$\Delta A = (C_1 \varphi_i + C_2) \Delta P \quad (1.3)$$

where C_1 and C_2 are fixed constants to be determined for a particular reservoir. Initial porosity, φ_i was considered as an important factor in inverting for pressure depletion in the Valhall field, a different mechanical stress sensitivity characteristics, depending on whether the initial porosity is above or below 35%. A higher initial porosity gives rise to stronger stress sensitivity, whilst lower porosity rocks are less stress sensitive for similar pressure ranges. This is similarly to the case of Ekofisk, where different mechanical stress sensitivity is found above and below 28% of initial porosity. The relationship between the time-lapse attribute (speed-up) versus pressure depletion as a function of initial porosity is shown in Figure 1.14 (a) and (b). The results of the inversion applied on the Valhall field are shown in Figure 1.15. The general conclusion from this work is that the estimation of pressure depletion from time-lapse seismic differs from the simulation model in some areas and the approach is easily implemented and data-driven.

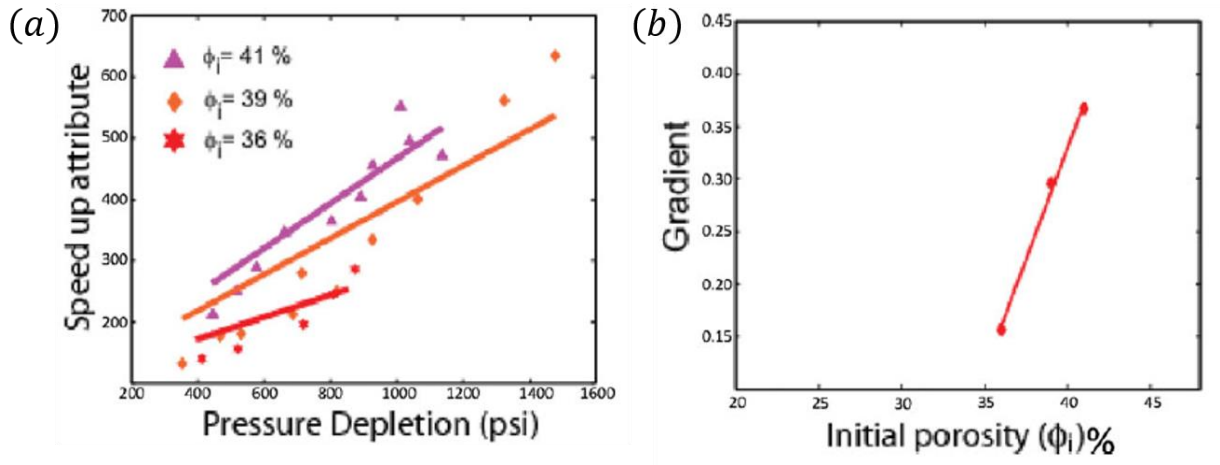

Figure 1.14: (a) Correlation between speed-up attribute from 4D seismic and pressure depletion from pressure change predicted from simulation model at well perforations and (b) the variation of the resultant gradient term (C_1) with initial porosity (Corzo et al., 2013).

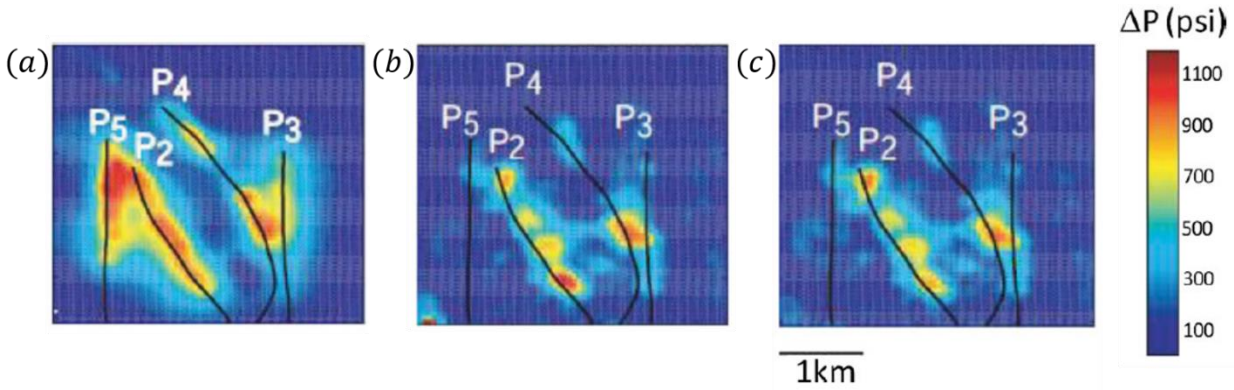

Figure 1.15: Estimated pressure change from (a) a coupled geomechanical-fluid flow simulator, (b) inverted using 4D seismic amplitude attribute – Largest Positive Value (LPV) with initial porosity averaged from certain layers in the reservoir and (c) inverted from LPV using initial porosity of one zone only (Corzo et al., 2013).

This technique is also employed by Landa et al. (2015), where the correlation between 4D seismic and pressure-saturation information is obtained by calibrating with well data. Uncertainty or probabilistic analysis in the map-based estimation of reservoir pressure and saturation changes is performed in the calibration process in order to bring forward the uncertainty in this process to the final estimation of pressure and saturation changes. These uncertainties include seismic noise, location of top and bottom surfaces to compute seismic attributes, and the production data. The

pressure and saturation changes estimated for a clastic turbidite reservoir are presented in Figure 1.16.

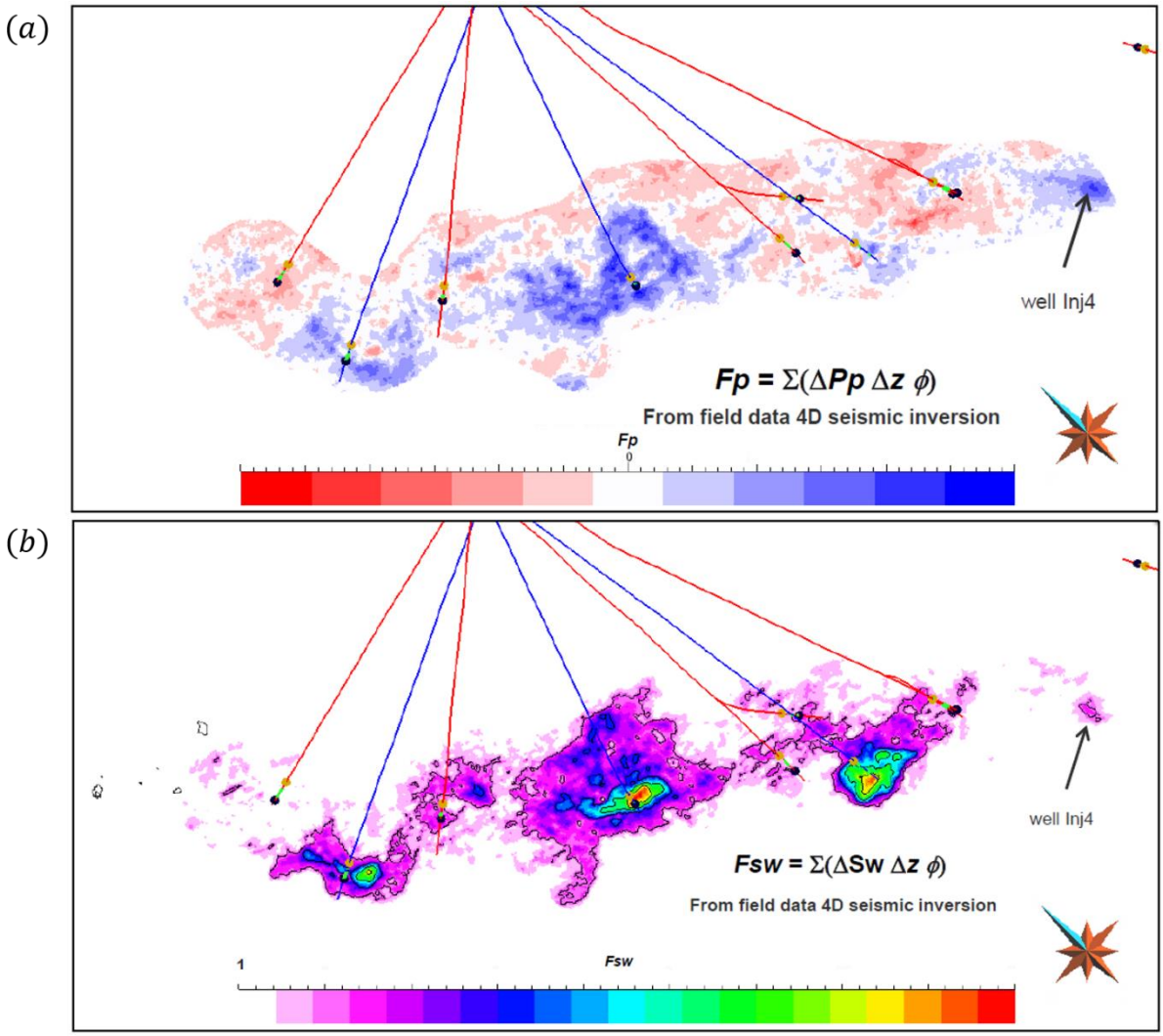

Figure 1.16: (a) Maps of inverted pressure change and (b) water saturation change from Landa et al., (2015) using a data-driven inversion approach.

I am inspired to break away from the map-based approach into something more suitable for the thick, multi-cycle, compacting chalk reservoir of the Ekofisk field. Equation 1.3 applied in the Valhall field is not totally applicable to Ekofisk, due to their different production history and the nature of the reservoirs, such as their heterogeneity and thickness. Ekofisk had twenty-nine years of water injection between 1987 and 2015, whereas the water flooding in Valhall has only been

operating for nine years, to date, and full scale water injection only started in 2007. This implies the water weakening signal is less dominant in the Valhall field in comparison to Ekofisk. The map-based approach of Equation 1.3 works effectively in Valhall, since the main producing Tor formation is only 30m thick, which translates to half a cycle on the seismic data (Jack et al., 2010). A comparative study between Valhall and Ekofisk is provided in Table 1.1, highlighting the main differences between the two neighbouring chalk fields:

	Ekofisk	**Valhall**
Thickness	Ekofisk formation (100 to 168 metres), Tight Zone (20m on average), Tor formation (76 to 152 metres) Multicycles	Tor is on average 30m, Hod is thicker but only contributes 8% to production Half cycle
Burial depth	2896 – 3261 m	2400 m
Water weakening behaviour	• More substantial in Ekofisk, since the thermo-chemical aspect of the water weakening is different, with a higher reservoir temperature at 130 ^{o}C • Do not have seismic information on pressure depletion alone as seismic acquisition started after water injection, as opposed to Valhall. • Study shows seawater is able to change enhance wettability of the chalk towards more water-wet at high temperature >100^{o}C (Puntervold et al., 2009)	• Reservoir temperature is 93 ^{o}C
Production history	Production in 1971 Full field water injection In 1987 (after 17 years of primary depletion)	Production in 1982 Water injection in 2007 (after 26 years) 20 years on primary depletion

Table 1.1: Showing a comparison between Valhall and Ekofisk in terms of reservoir thickness, burial depth, geomechanical behaviour and production history (Kristiansen and Plischke, 2010, Madland et al., 2010).

1.5.2 Proxy models in other applications

The concept of a proxy model is novel in the oil and gas related disciplines, but it has a long and pivotal history in the fields of optimisation, statistics and uncertainty quantification. A proxy model is used to provide a fast approximation to the actual function (Goodwin, 2015). Some of the proxy models used in the oil and gas industry include the surrogate model, the kriging model, neural networks, and the regression model. In history matching, response surface proxies are commonly used to approximate the functional relationship between the input parameters and the aggregated mismatch (Castellini et al., 2006, Friedmann et al., 2003, Landa and Güyagüler, 2003). The mismatch function in history matching is the misfit between the simulated data and observed data (Tarantola, 2005), which quantifies the degree of consistency of a reservoir model and the historical data. Each evaluation of the mismatch function requires a simulation run, making the history matching process laborious and computationally expensive. One way to reduce the computational cost is to construct a response surface proxy for the mismatch function, which is a parameterized mathematical expression that can be calibrated on a set of training data to approximate the input to output relations of the mismatch function. After calibration, the response surface proxy can be used to replace the simulator to evaluate the mismatch function.

Other uses of proxy include using an analytical expression to speed up the estimation of seismic data using outputs from the reservoir simulator instead of running a full simulator-to-seismic workflow. As successfully demonstrated by Fursov (2015), a linear relationship between seismic and reservoir dynamic properties: pressure, water and gas saturation change:

$$\Delta A = \left(a_p \Delta P + a_{Sw} \Delta S_w + a_{Sg} \Delta S_g\right) \cdot A_0 \tag{1.4}$$

was used to generate seismic attributes to speed up the history matching process. A_0 is the seismic attribute at baseline survey. The coefficients a_p, a_{Sw} and a_{Sg} in the equation are calculated from seismic data of the given reservoir from multiple monitors. The left hand side of the equation will include all the points of time-lapse attribute maps from all monitors; the right hand side will include the points of the reservoir dynamic property maps from the corresponding time steps, scaled by the baseline seismic attribute. According to the findings obtained by Fursov (2015), the fast-track procedures, conducted by applying a regression between 4D seismic attribute maps and the average

maps of the dynamic reservoir properties, are considerably faster than the full-fledged history matching. However, the fast track method is more applicable if noise is low, whereas the slower history matching workflows are more robust for the situation where there are noisier inputs.

Map vs. volume

Thin and thick reservoirs should be treated differently for interpretation. Because many of the sand thickness in clastic reservoirs are below tuning thickness, many case studies on 4D amplitude interpretation employ a quadrature-phase difference approach (Johnston, 2013). Moreover, for a thin reservoir, quadrature amplitude analysis is useful if the reservoir is a half cycle, such as in the North Sea clastic Schiehallion field. In that case, changes in amplitude are then directly related to the primary changes in impedance. Map-based methods will be sufficient, since averaging across a thin reservoir will not compromise the signal too much. In contrast, thick reservoirs will have a very different character at both top and base of the reservoir; thus, when looking at maps, this reservoir should be interpreted using top and base maps separately and with caution, instead of averaging the amplitude difference across the entire reservoir thickness.

The caveats of interpreting such reservoirs are interference, tuning and side lobe problems. The 4D signals will comprise of too many destructive and constructive events and will not truly reflect primary changes, such as in the case of the Ekofisk field. This is also one of the reasons that prompts us to look at volumes instead of maps. Moreover, this is particularly true for long wavelength spatial components such as pressure; averaging the time-lapse response across the entire reservoir will smear the signal significantly if there is a competing response between pressure and saturation. Imagine there is a positive to negative pressure gradient from top to base of the reservoir: computing a single map for the entire reservoir will significantly underestimate the actual magnitude and spatial distribution of the signal. Table 1.2 shows the common analysis carried out for both thin and thick reservoirs, the caveats are associated with the reservoir thickness, the effectiveness of the interpretation and the necessity of a volume based approach. In this thesis, I will demonstrate a new method to invert for changes in pressure and saturation for a thick and multicycle reservoir such as the Ekofisk field, in three dimensions.

Reservoir type	Analysis	Caveats	Interpretation	2D versus 3D
Thin	Quadrature amplitude analysis	• Effect of tuning	Reflects primary impedance changes	• Map-based application suffices
Thick	• Treat top and base reservoir separately • Require elastic inversion	• Interference • Tuning • Side lobes complications	Does not reflect primary reservoir dynamic changes	• Averaging smears signals • Long wavelength spatial component of pressure loses out • Map-based application less effective • Requires volumetric analysis

Table 1.2: Showing a compilation of the type of analysis, caveats of those analysis, methods of interpretation and 2D versus 3D interpretation on thin versus thick reservoirs.

1.6 Focus of this Thesis

1.6.1 Outline of the thesis

This thesis will develop the ideas of monitoring changes inside the reservoir, namely changes in dynamic properties, such as pressure and saturation changes, by utilizing time-lapse seismic observations from both inside and outside the reservoir. Chapters 4 and 5 focus on using time-lapse seismic attributes inside the reservoir, whereas Chapters 6 and 7 utilise overburden time-lapse anomalies induced by production changes.

Here are the contents of the remaining seven chapters of my thesis, in brief:

Chapter 2 provides an overview of the literature on the Ekofisk field, covering topics from geological setting to field production history and the challenges in geomechanics. I also evaluate various rock physics models to establish a suitable rock physics model for the Ekofisk field. This rock physics model is calibrated using data from rock mechanics, well logs and mineral moduli from the literature.

Chapter 3 shows how 4D seismic data are used for dynamic reservoir characterization in the Ekofisk field. A summary of the seismic data from both acquisition strategies, streamer and Life of Field Seismic (LoFS) is provided. An analysis is carried out to compare and contrast the reservoir time-shifts in both types of surveys and the correlation with different production mechanisms.

Chapter 4 presents the formulation of a new equation to invert for pressure and saturation changes in a thick, compacting chalk reservoir. A synthetic model is created to understand the impact of rock compaction and different dynamic changes on impedance changes. By employing backward engineering, the composite impedance change is decomposed to analyse its individual components and workings in detail, in order to recreate the same property using a proxy model. Physical phenomena such as water weakening and compaction, which are notorious in chalk reservoirs, are accounted for in the proxy model, and also described in this chapter.

Chapter 5 applies the proxy model set out in Chapter 4 to data from the Ekofisk field, in the Norwegian North Sea. A stochastic approach via Bayesian McMC is employed to invert for the changes in pressure and saturation and to capture uncertainties in the result.

Chapter 6 shows a different route to estimate pressure changes by using time-lapse information from the overburden. The Geertsma pressure inversion method from Hodgson (2009) provides the basis for a linear inversion scheme to estimate both pressure changes and also the Hatchell-Bourne-Røste R-factor. A synthetic example is provided to demonstrate the success of estimating the R-factor by constraining the inversion result with pressure information from a well-history matched simulation model.

Chapter 7 applies the inversion scheme introduced in Chapter 6 to the Ekofisk field. This chapter draws conclusions on the average R-factor recovered in the Ekofisk field. The chapter also discuss the R-factors calculated for different regions of pressure build-up and drawdown identified in the field, and the results confirm the current understanding determined by laboratory experiments and previous studies that the magnitude varies as a function of strain polarity, with the asymmetry being at most a factor of three.

Chapter 8 presents a summary of the thesis. In addition, recommendations are also made for further development of the ideas presented in this thesis.

1.6.2 Publications

Parts of this thesis have been independently presented in the following publication:

Wong, M. Y., MacBeth, C., JafarGandomi, A., Bertrand, A., and Amini, H. (2017). An Engineering-consistent approach for separating pressure and saturation changes in the Ekofisk field. *Petroleum Geoscience*. (Accepted with revision)

1.6.3 Conferences with extended abstracts

Wong M. Y., MacBeth, C., and Amini, H. (2017). Time-shifts Interpretation of legacy and frequent repeat seismic data in a compacting chalk reservoir. *79th EAGE Conference and Exhibition*.

Wong, M.Y., and MacBeth, C. (2016). R-factor Recovery via Geertsma's Pressure Inversion Assisted by Engineering Concepts. *EAGE Geophysics and Geomechanics, Jointly Applied to Subsurface Characterisation workshop.*

Wong, M.Y., JafarGandomi, A., MacBeth C., and Bertrand, A. (2015). Pressure and saturation change inversion using 4D seismic: Application to a chalk reservoir in North Sea, *SEG International Exposition and Annual Meeting.*

Wong, M.Y., MacBeth, C., and Bertrand, A. (2015). Engineering Consistent Constraints for the Inversion of Changes in Pressure and Saturation on Ekofisk. *77th EAGE Conference and Exhibition.*

Wong, M.Y., MacBeth, C., and Bertrand, A. (2015). Engineering Consistent Constraints for the Inversion of Changes in Pressure and Saturation on Ekofisk. *EAGE 4D Workshop: Getting the most out of 4D - from reservoir to surface.*

CHAPTER TWO

AN OVERVIEW: A SUITABLE ROCK PHYSICS MODEL FOR THE EKOFISK FIELD

This chapter provides an overview of the literature on the Ekofisk field, and includes the geological description, field production history and the associated geomechanical challenges. Specific attention is given to the deformations of the reservoir, the surrounding rock and how it affects reservoir performance. The success of 4D feasibility studies and inversion depends heavily on the robustness of the rock physics model. I will show the calibration of the parameters in the rock physics model using rock mechanics and data gathered from the literature. A full description of the rock physics model proposed in generating synthetic time-lapse attributes for the Ekofisk, along with a summary of different chalk rock physics models in the literature is provided.

2.1 Geological Description

The Ekofisk field is a naturally fractured chalk field situated in the central graben in the southern part of the Norwegian sector of North Sea. The location of the field is shown in Figure 2.1. It was the first commercial oil and gas field discovered on the Norwegian continental shelf. The chalk field is characterized by a four way dip anticline, elongated in a North-South direction. A seismic amplitude cross-section is displayed in Figure 2.3 (a) with the major horizons (Top Reservoir, Tight Zone and Tertiary Base Unconformity) highlighted. The two major formations in Ekofisk are the Ekofisk formation (Danian) and Tor formation (Maastrichtian). Both units separated by a relatively impermeable layer of argillaceous, siliceous, cherty chalk known as the tight zone. The reservoir has an average thickness of 175 - 300m, with greater thickness at the crest and a thinning towards the flank (Keszthelyi et al., 2016). Top reservoir is located around 3050m (10,000ft). A well-defined oil-water contact does not exist in the Ekofisk Field due to migration history of oil. This is commonly found in many other chalk reservoirs. The base of the hydrocarbon deposit appears domed, possibly due to post accumulation salt movement. The cap rock is the highly over-pressured Paleocene Balder shale (Feazel et al. 1985).

The porosity distribution in each formation varies both areally and vertically. The average porosity in the Ekofisk Formation is 32%. However, porosities of up to 48% have been also been encountered. The average porosity in the Tor Formation is 28%, and the maximum porosity encountered in this zone is 41%. Porosity is lost towards the flanks, and once the water zone is encountered porosity falls to about 15%. Figure 2.3 (b) shows the distribution of the chalk porosity in both formations. The reservoir permeability is low, ranging from 0.1 to 5 mD. From the porosity-matrix permeability correlations the maximum permeability expected in the Ekofisk Field is 8 mD. However, well-test results indicate effective permeabilities of up to 150 mD. This enhancement in permeability is due to fracturing of the formation.

The fluid flow characteristics of the reservoir are largely governed by the distribution, orientation and interconnectivity of the natural fracture system, forming primary conduits for produced and injected fluids (Hermansen, 2008). Three types of fractures, healed, tectonic and stylolite associated, have been identified from cores. The healed fractures are filled with a base material similar to the chalk and do not provide enhancement of the permeability. The tectonic fractures

are those most likely to enhance the effective permeability. It has been found from core studies that these fractures are predominantly sub-vertical (60^o-75^o dip). The intensity of fracturing varies both vertically and areally; fracture spacings as small as 10-15 cm have been observed. Stylolite-associated fractures form adjacent to stylolites. The usual length of such fractures is only 5 cm (Brown, 1987). This type of fracture does not have a great influence on the effective permeability.

The chalk primarily consists of the skeletal remains of coccolithophorid algae. These calcareous nannofossils are composed of individual calcareous plates (coccoliths) that form clay to silt-sized spherical bodies called coccospheres, shown in Figure 2.2. Complete coccospheres are sporadically present within the chalk but the majority are broken up into single coccolith plates or laths (Håkansson et al., 1974, Hancock, 1975, Scholle, 1977). Clays and shales with thin interlayered limestone or silt are the main composition of the overburden. A detailed description of the overburden lithology is provided in Table 2.1.

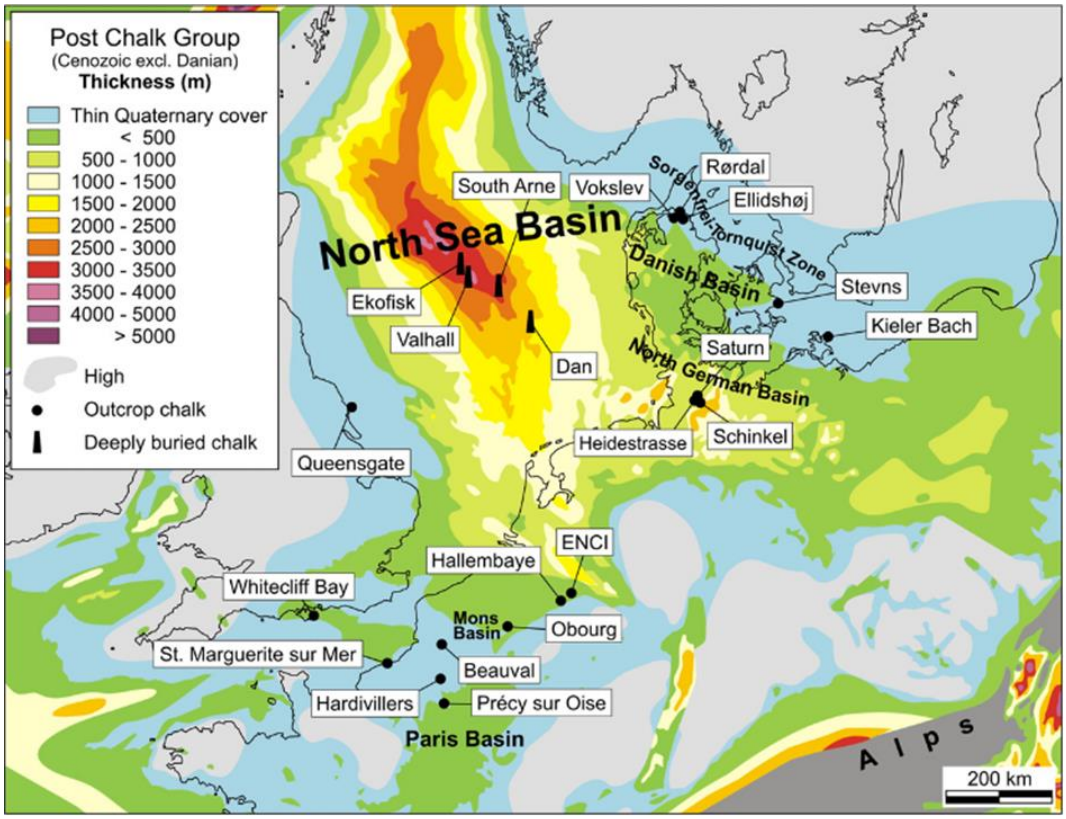

Figure 2.1: Map shows the distribution of various chalk fields and important outcrops in the North Sea with hot colours showing deeper burial depth (Hjuler, M. L., 2007).

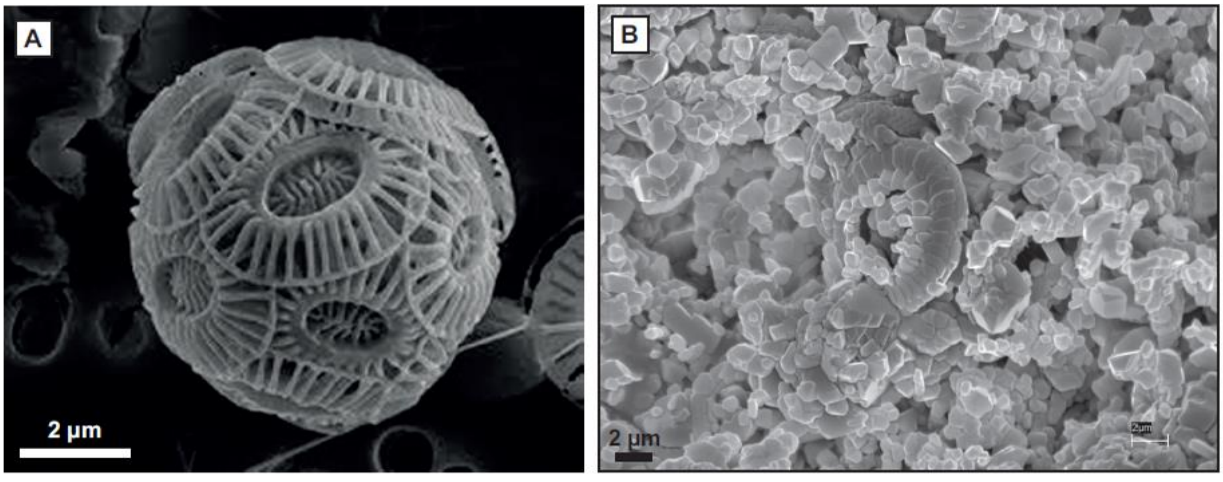

Figure 2.2: (a) a Scanning-electron micrograph (SEM) showing a coccolithophore (Tyrrel and Merico 2004); (b) an SEM photo of a rock sample from the Ekofisk formation (Gennaro 2011).

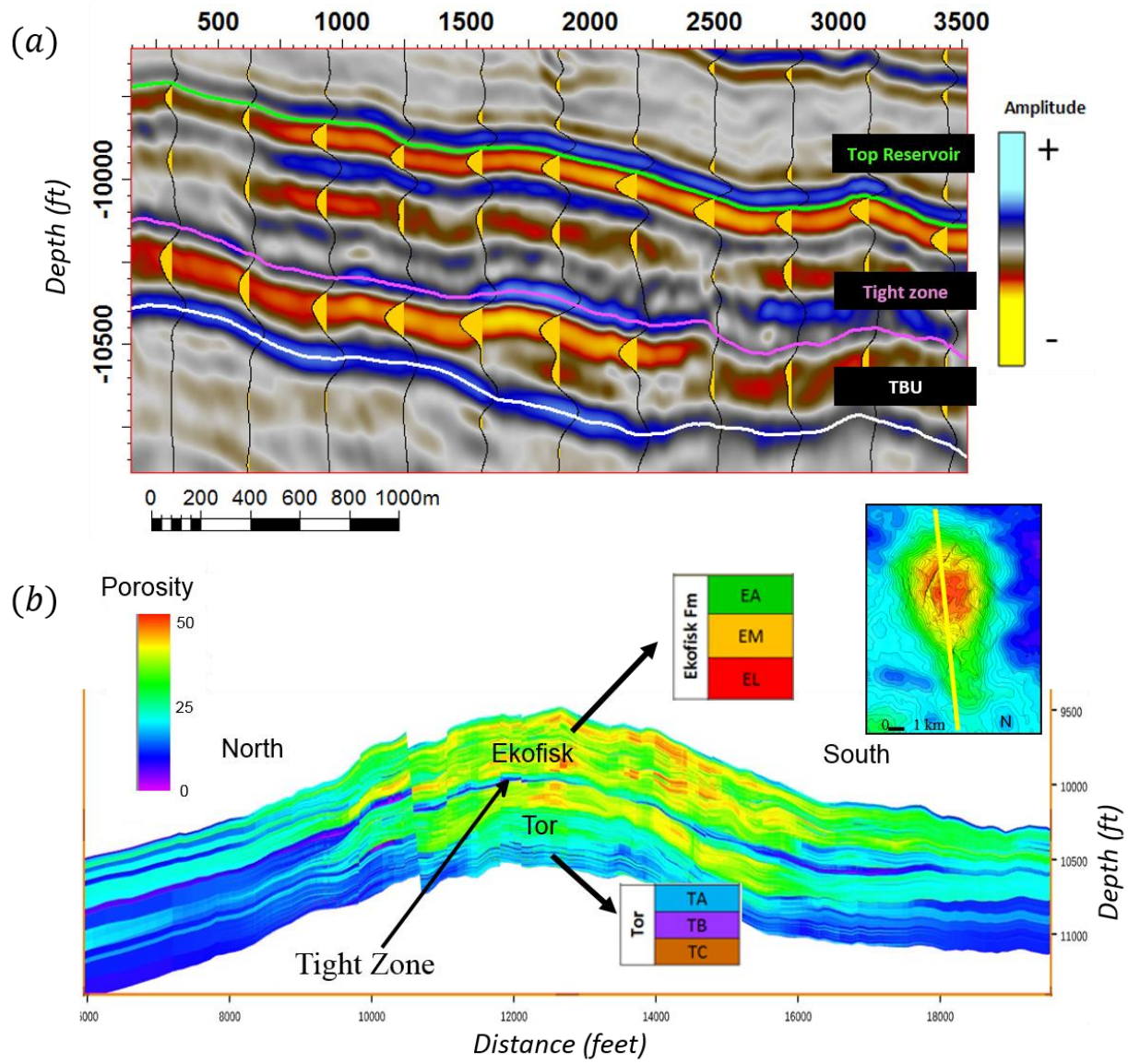

Figure 2.3: (a) Cross-section showing seismic amplitude of LoFS 2 data from the Ekofisk field. (b) A cross-section along the North-South direction of the field showing the porosity distribution of the field in both Ekofisk and Tor formation, separated by a relatively impermeable layer of argillaceous, siliceous and cherty chalk known as the tight zone. The sub-intervals of each formation is also provided.

Epoch		Lithology
Pleistocene	Nordland	Sand intervals interbedded with claystone
Pliocene		Claystone with traces of coarse sand, 98% clay, 2% sand
Miocene		Claystone with limestone intercalations, 95% clay, 2% sand, 3% limestone
Oligocene	Hordaland	Claystone/shale with dolomite interbeds and traces of sand, 97% clay, 1% sand, 2% limestone
Eocene		Shale with limestone interbeds and traces of sand/silt, 95% clay, 2% sand, 3% limestone
Paleocene	Rogaland	Balder: Volcanic tuff
		Sele: Claystone with limestone stringers
		Lista: Claystone with stringers
		Vale: Marl
		Ekofisk: Chalk

Table 2.1: Lithology of the Ekofisk field overburden (Nagel, 1998).

2.2 Production Setting

The estimated stock tank original oil in place (STOOIP) in Ekofisk field is 7.1 billion bbl. The prolific reservoir was discovered in 1969, it was initially overpressured and contained an undersaturated oil at 7129 psi and 268ºF at a datum elevation of 10,400ft subsea (Tolstukhin et al., 2012). The bubble point pressure was approximately 5545 psig (Agarwal et al., 1999). Figure 2.4 shows the Ekofisk field historical production and injection plot. Initial production started in 1971 from the discovery well and appraisal wells. The initial recovery mechanism was primary depletion with production supported from gas reinjection. In 1971, laboratory studies were carried out to examine the potential of water flooding. A water flood using seawater was piloted in 1981. A large scale water flood started in 1987 following favourable pilot results. The reservoir responded positively to secondary recovery operations such as a very efficient oil displacement and limited water breakthrough even after 10 years of waterflood operations.

The Ekofisk field's oil is 38°API, and has a viscosity of approximately 0.25 cp. Oil production increased from 70 MSTBO/D in 1987 to 300 MSTBO/D by mid-2000. A total of 1.5 billion barrels of water has been injected in the first ten years of the operation. However, the full field water injection program not only increased the oil production rate and stabilized field pressure, it also resulted in the water weakening of chalk. This phenomenon resulted in substantial seafloor subsidence. Reinjection of natural gas in excess of sales has been ongoing since 1975 with 1.3 Tcf of gas injected as of the year 2000 (Agarwal et al. 2000). This resulted in the decrease of the average field gas to oil ratio (GOR) during this period of time from approximately 8000 SCF/STB to 1150 SCF/STB (Tolstukhin et al. 2012).

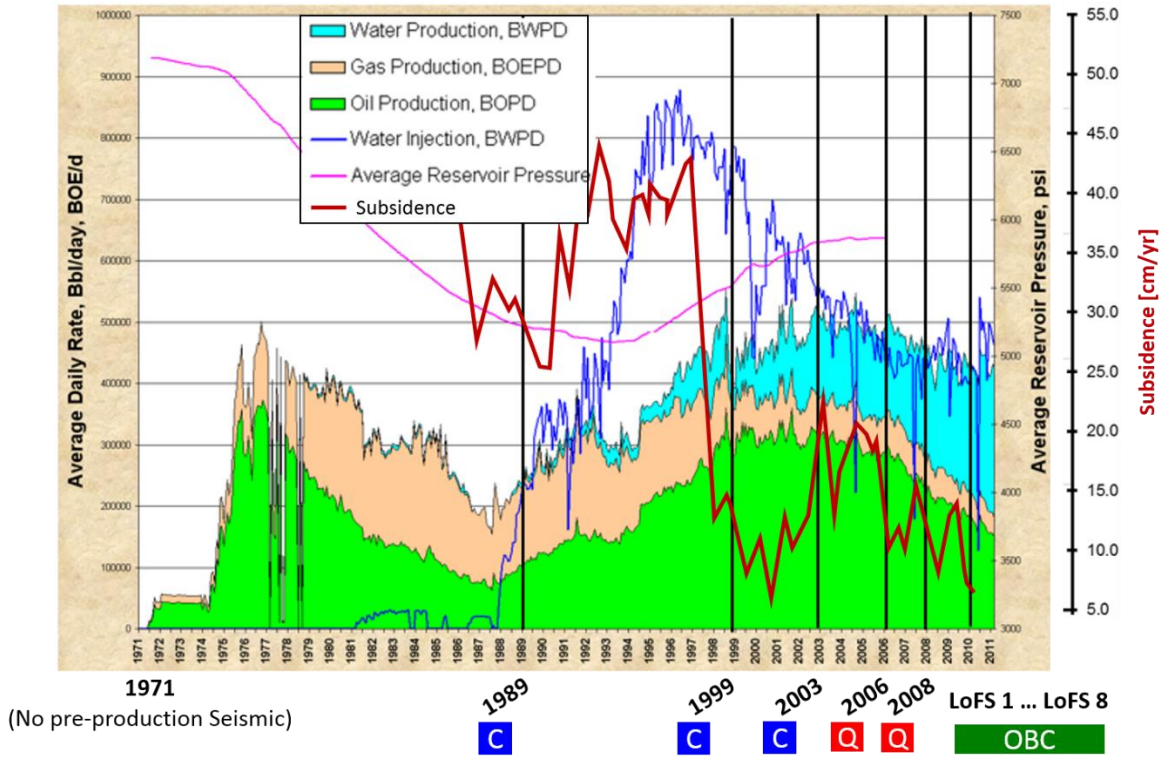

Figure 2.4: Ekofisk field historical production and injection data. Seismic coverage on the Ekofisk field with baseline shot in 1989, and streamer monitors on 1999, 2003, 2006 and 2008. The LoFS was put on stream in 2010. C, Q and OBC represent conventional, Q-marine and Ocean Bottom Cable.

2.3 Geomechanical Challenges in Ekofisk

Various geomechanical challenges were encountered in the Ekofisk field. These geomechanical occurrences affected the performance of the reservoir. Several aspects of the geomechanical challenges are listed below.

2.3.1 Seabed subsidence

Over 7.8 metres of seafloor subsidence has occurred at the Ekofisk Field since the start of production in 1971. Full water injection was initiated at Ekofisk on a limited scale in 1987. The surface subsidence is a result of reservoir compaction, which is considered primarily to be due to

pressure depletion until the early 1990's and water weakening thereafter. "This phenomenon was first noticed in 1984, where approximately three metres of seafloor subsidence has occurred at the crest of the field", according to Sylte et al., 1999. The measured subsidence rate averaged about 33cm/year. Several factors that contributed to the compaction are high porosity, overpressured reservoir, large areal extent of the field relative to its burial depth, large thickness of the production interval, and large reduction in pore pressure. The incremental efforts of water injection as a recovery mechanism and pressure maintenance was expected to slow and eventually arrest subsidence at the producing platforms. However, as the pressure began to stabilize in 1993 and early 1994, there was little impact on stopping the subsidence rate. The subsidence rate remained essentially unchanged through 1998. The continued subsidence after 1994 coupled with laboratory and field data indicated that a water weakening phenomenon is responsible for the compaction of the field (Sylte et al., 1999). The persistence of subsidence is observed throughout the entire field production, this is depicted in Figure 2.5.

Reservoir compaction and seabed subsidence continues to be a very important consideration in Ekofisk Field reservoir management strategies. Efforts to monitor early reservoir compaction and seabed subsidence include twice-a-year compaction logging in a monitoring well, daily GPS measurements at the platforms, and periodic bathymetry surveys with nine surveys span from the year 1970 to 1999 (Guilbot and Smith 2002). Figure 2.6 shows seismic data in time along the well 2/4-X-09 in an area with strong compaction. The seismic trace along this well shows changes in time and amplitude from 1989 (baseline survey) to 1999 (monitor survey) after a decade long of water injection activities.

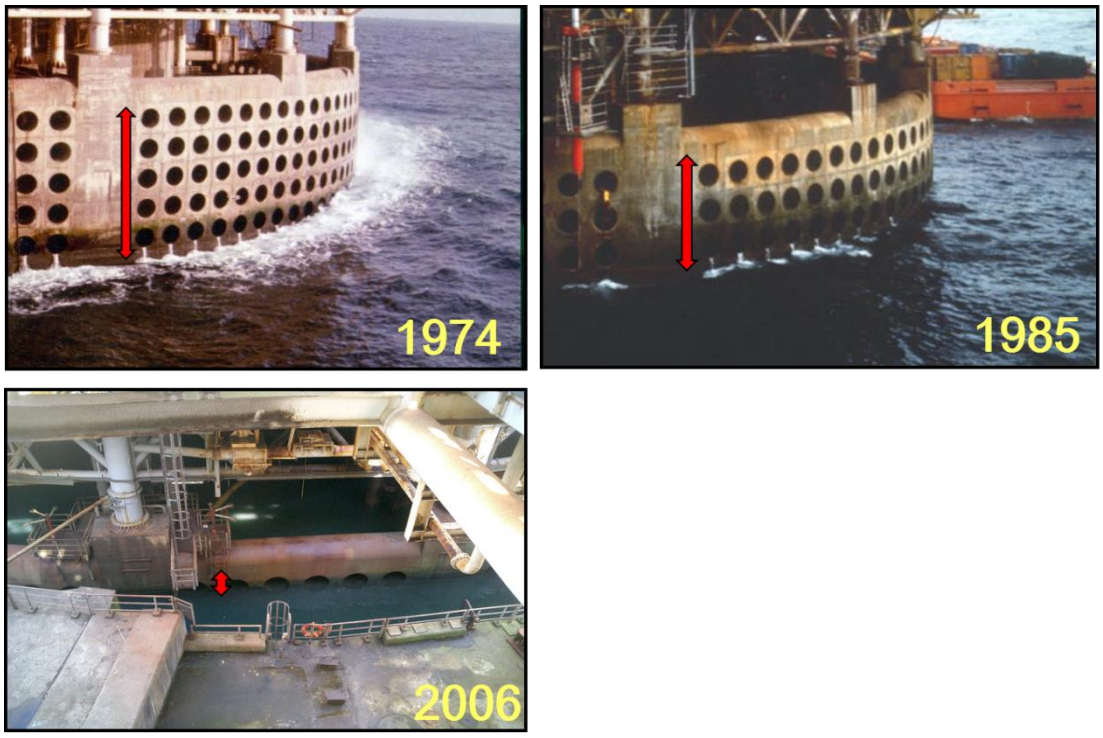

Figure 2.5: Seabed subsidence is evident from the progressive sinking of the Ekofisk platform, indicated by red up-down arrow (ConocoPhillips internal report).

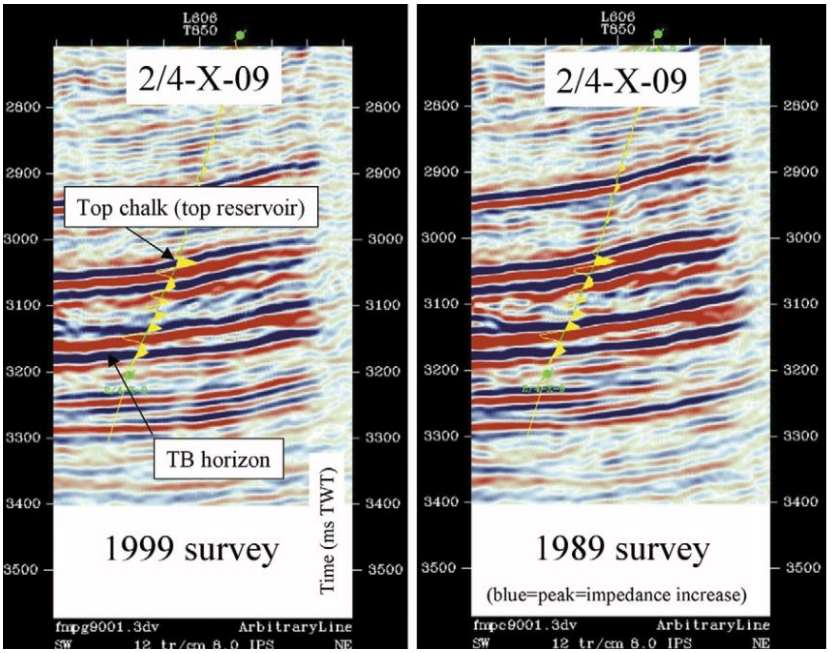

Figure 2.6: shows the time section along the well 2/4-X-09 at monitor (1999) and baseline (1989). The yellow seismic trace is calibrated to the 1999 survey. This is an area of strong compaction, a time subsidence effect is observed at top reservoir in 1999 (Guilbot and Smith, 2002).

2.3.2 Reservoir performance and productivity effects

Reservoir compaction and subsidence was recognised in late 1984, but loss in reservoir productivity was not observed. As of today, it has been widely recognised that compaction has aided reservoir productivity immensely. In a nearby field - Valhall, we see rock compaction as the main driver in contributing to the total cumulative oil contribution compared to other drive mechanisms such as oil expansion, aquifer, gas influx and water flooding (Cook et al, 1996). This is demonstrated in Figure 2.7.

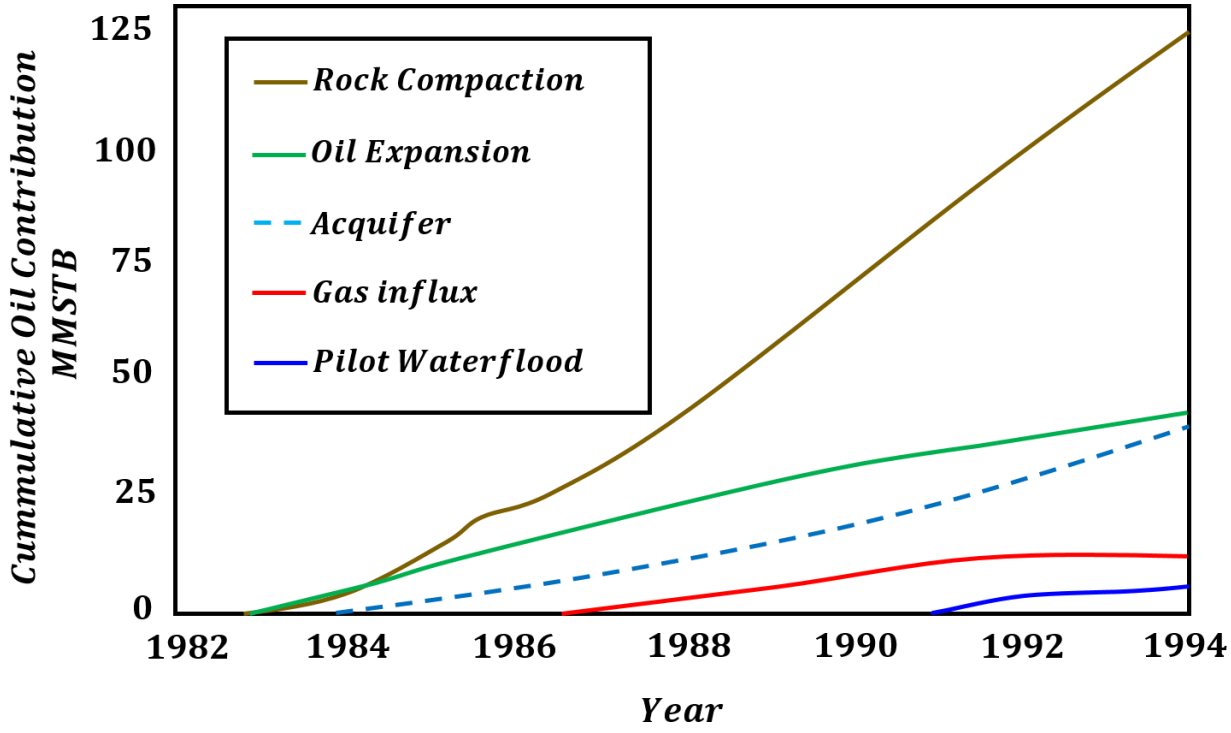

Figure 2.7: Cumulative oil contribution in MMSTB from various production mechanisms in the Valhall field (Redrawn after Cook et al., 1996).

In chalk reservoirs, the water flooding decreases the pore collapse strength, and rock compaction accelerates. The overpressure and the mechanically weak structure of the chalk are the elements that trigger the rapid reservoir compaction. The compaction has the positive effect of being the drive energy to produce fields like Valhall for more than 20 years without any other recovery mechanism. Approximately 50% of the drive mechanism has come from the rock compaction (Barkved et al., 2003). This compensates for the negative consequences such as chalk production, influx failures and casing collapse problems.

Waterflooding efforts in Ekofisk have generally been positive and visible. Early water injection shows individual wells experienced significant increase in oil rates, dramatic drops in GOR and limited water breakthrough (Hermansen et al., 1997). For strongly water-wet areas such as the Tor and Lower Ekofisk formations at Ekofisk, the bulk of waterflood displacement is a capillary dominated process and the rate of recovery is strongly dependent on the matrix block size and the amount of matrix surface area exposed to fractures, with ultimate recovery determined by the capillary, gravity, and viscous equilibrium. For less water-wet areas, such as the Upper Ekofisk formation at Ekofisk, viscous and gravity forces as well as capillary forces are important. Figure 2.8 shows an imbibition experiment where water invades a chalk core and displaces oil.

Apart from the positive hydrocarbon recovery from compaction drive, are there any detrimental effects on productivity? The Ekofisk chalk is relatively tight but is naturally fractured, these fractures vary in terms of spacing, inclination, length, and conductivity significantly, in both vertical and sub-horizontal directions. Increasing stress levels in the reservoir affects the closing and opening of fractures. For example, stress components perpendicular to a fracture face tend to close the fracture and reduce fracture conductivity. Shear stresses on the other hand may increase conductivity and even open new ones. In the work from Sulak and Danielsen (1989), they reported that no changes have been observed from productivity that might indicated changes in stress affecting the fracture system. Nearby field (West Ekofisk) has a similar depletion history and geology with a higher effective stress has also not reported negative productivity changes in the field.

Figure 2.8: Imbibition experiment was carried out on chalk cores in the Ekofisk field showing the water wet chalk shows absorption of water quite effectively at low in situ water saturation (ConocoPhillips internal report).

2.3.3 Casing deformation

One of the geomechanical challenges faced in the Ekofisk field is casing deformation, this was first discovered in 1978. Casing deformation was first noticed while routine workover and wireline operations were performed. By 1989, about two-thirds of Ekofisk well casings have reportedly failed. One of the hypothesis of casing failure was due to excessive matrix acidizing, resulting in lack of lateral support around the casing, and causing buckling as it is loaded in compression. Other possible failure modes are collapse due to radial stresses, tensile break due to axial tension and thread jump resulting from axial compression or tension. Several measures were taken to understand failure mechanisms such as running caliper logs through failure casing. Such measures were taken in well 2/4 B-10 in the overburden, where it shows ovaling or deformation in the overburden. The overburden section of the casing string, close to the top reservoir is under tension as a result of compaction inside the reservoir. Other methods of monitoring include using radioactive markers placed at various depths in the well and utilizing highly accurate casing collar logs to measure changes in the casing length (Yudovich and Morgan 1989).

2.3.4 Overburden Stretching

Reservoir compaction is balanced by changes in the stress state of the overburden. Above a compacting reservoir the overburden stress will decrease as the overburden expands to accommodate the reduction in reservoir volume. This is accompanied by a reduction in acoustic velocity of the overburden rock. An important publication from Guilbot and Smith (2002) on 4D constrained depth conversion for reservoir compaction estimation: Application to Ekofisk field, shows time-shifts at top reservoir could not be produced by the physical displacement of top reservoir alone, as this assumption would result in compaction estimates of 2-4 times greater than the reservoir model-based prediction. Guilbot and Smith (2002) shows that without taking into account of the changes in overburden interval velocity, there is a 75% error in the compaction prediction. More description will be provided in Chapter 6 on how the overburden signals are useful in characterizing reservoir dynamic changes. Stress changes in the overburden could also lead to redistribution of gas in the shallow overburden (Olav Barkved, personal communication).

2.3.5 Overburden Compaction

Stress arching in the overburden is also often associated with compacting reservoirs, this phenomenon was found in nearby chalk field, Valhall (Barkved, 2012). Since the reservoir undergoes significant compaction, a pressure gradient could form from the overpressured overburden into the reservoir. Additional compaction and subsidence can arise from this pressure gradient leading to depletion of the overburden. The overburden is mainly shales with low permeability in the matrix. Drainage of the low permeability overburden sediments would require an extensive fracture system or fractures caused by out of zone injection. There is currently no data suggesting the existence of such fracture network in the overburden nor is the stress level in the overburden suggesting the potential for creation of open fractures (Sulak and Danielsen 1988). Compaction monitoring efforts such as radioactive markers show that the overburden is not compacting. However, I show that localised time strain data in the overburden contains hardening signal on top of injection activities in the reservoir. This does not necessarily suggest physical changes in the overburden but re-orientation of stresses. We will evaluate this topic further in Appendix D, where some examples on overburden compaction is presented.

How can we understand these physical changes in seismic information?

One way to quantify and understand these phenomenon from seismic is to carry out rock physics modelling. A rock physics model is a set of equations and statistics capturing the relationships between physical properties for a particular rock type or formation. Essentially, the goal is to create synthetic seismic using multiple scenarios from a fluid flow simulator to match the observed seismic. It is therefore crucial to have an accurate rock physics model that captures the full physics between the reservoir rock and fluid properties and the elastic properties picked up by the seismic sound waves.

2.4 An Overview: Rock Physics Modelling

There are a growing number of publications studying and comparing rock physics models on carbonate rocks. Although carbonate reservoirs represent many of the major oil and gas reservoirs in the world, the experimental data on carbonate rocks (including chalk samples) have not been as thoroughly studied as silici-clastic sedimentary rocks. In some cases, the relations developed for sandstones are also applied in carbonates, which does not represent the full physics at best. A close examination of the current literature in the subsequent section provides some insights into which rock physics model is suitable for the purpose of estimating elastic properties of chalk in the present study. I first start with the validity of Gassmann relations in chalk reservoirs?

2.4.1 Validity of Gassmann relations in chalk

The Gassmann equations make several fundamental assumptions such as that the pore spaces between grains are well connected, and this assumption works well in monomineralic rocks. Gassmann also assumed no chemical interaction occurs between the rock frame and the pore fluid, and that the rock is isotropic (Gassmann 1951). These assumptions mean that these equations are most applicable to porous, clean sandstones rather than chalk or other hard carbonate rocks.

Chalk differs greatly in its composition and structure from clastic rocks. While clastic rocks have mainly inter-granular pores, chalk can have various pore types, such as inter-particle, intra-particle,

moldic and vuggy pores (Xu et al., 2007). Works from Walls et al. (1998), Borre (1998), Wang (2000), Borre and Fabricius (2001), Gommesen, Mavko, Murkerji (2002), Japsen et al. (2004), Røgen et al. (2005), Adam et al. (2006), Gommesen et al. (2007), Fabricius et al. (2007), Bhakta and Landrø (2013) and Das et al. (2016) have shown Gassmann's relationships are valid in both fluid substitution and estimation of elastic properties of the chalk. It is argued that, as a consequence of the relative homogeneity and high pore-connectivity of the chalk, combined with high porosity and permeability (Fabricius et al., 2007), the chalk interacts with sonic waves in a low frequency manner, hence Gassmann's relation can be applied.

From the work of Adam et al. (2006), it was demonstrated that at seismic frequencies, the brine-saturated bulk modulus for carbonates rocks (with round pores and vugs) with small differential pressure dependence is well estimated by Gassmann. However in his work it was also demonstrated that carbonates samples that are strongly influenced by compliant pores and micro cracks led to predictions that deviated from the observed ones. The samples that deviates from observed values studied by Adam et al. (2006) are less applicable to the present case, as they are mostly hard limestone, with some samples that have been dolomitized.

Another school of thought argues that instead of Gassmann's relation, inclusion based scattering theories would be more appropriate for modelling chalk samples. Reasons for disapproving the validity of Gassmann's relation on chalk include the heterogeneity and pore types of the chalk and the sensitivity of shear moduli to fluid (Adam et al., 2005). A full review on why Gassmann's model is not as valid in chalk reservoirs is presented in Misaghi et al. (2010). Different scattering models have been presented, such as Kuster-Toksöz implemented by Sørnes and Brevik (2000), self-consistent approximation (SCA), from Berryman (1980) implemented in Bhakta and Landrø (2013) and the differential effective medium (DEM) model and SCA in Misaghi et al. (2010).

The results from using inclusion based scattering theories interestingly enough, are only marginally better than or similar to those predicted by Gassmann's relations. Larger differences between the models with respect to Vs (S-wave velocity) estimation were found rather than discrepancies in predictions between Gassmann and scattering theories. A summary of the different rock physics models used for fluid substitution and elastic properties modelling in chalk reservoirs is provided in Table 2.2; the respective research objectives, conclusions and fields of

interest are also provided. Two publications that require special attention are those from Walls et al. (1998) and Das et al. (2016). These publications were published by the operator (ConocoPhillips) of my field of interest, using laboratory measurements for the Ekofisk chalk.

Paper	Research questions/Objectives	Conclusions/Outputs	Field
Walls et al. (1998)	To model seismic velocity of chalk reservoir as a function of its porosity and fluid saturations	First application of combined cementation theory and modified upper Hashin-Shtrikman model to chalk. The model slightly overestimates bulk modulus for low porosity chalk. Computed and modelled shear modulus are in good agreement. Applied Gassmann's relations.	Ekofisk, Norwegian Sea
Sørnes and Brevik (2000)	Challenged the suitability of Gassmann model for carbonate fluid substation. A workflow using Kuster-Toksöz to perform fluid substitution was carried out.	The scattering theory falsely let shear moduli be affected by the fluids' bulk moduli, when data suggested otherwise. The errors between Gassmann model and Kuster-Toksöz are small.	Confidential
Røgen et al. (2005)	Acquire acoustic properties of chalk and to test whether dry moduli can be predicted from measurements on water saturated chalk samples.	Presence of large grains of microfossils and smectite influences elastic properties of the chalk. The dry moduli calculated via inverse Gassmann's relations fits the measured dry moduli; but underestimates V_P and V_S. by 2% and 4% on average respectively.	Dan, South Arne, Gorm, Danish North Sea
Adam et al. (2006)	The applicability of Gassmann's theory on carbonate rocks in the context of shear and bulk modulus dispersion and rock frame sensitivity to saturation.	Rock shear modulus is sensitive to brine saturation at seismic frequencies, this is attributed to weakening of the matrix due to possible surface energy loss and/or subcritical crack growth at low differential pressure. No positive relation is found between weakening of rock shear modulus and failure of Gassmann's theory to predict saturated bulk modulus at seismic frequencies. In fact, Gassmann predicts quite accurately brine saturated bulk modulus with small differential pressure, possibly closing soft fractures and pores.	Confidential
Gommesen et al. (2007)	To compare the low-frequency Gassmann and high-frequency self-consistent approximation method on fluid substitution to well log data	Gassmann is applicable in the log frequency domain. Predictions from Gassmann and the self-consistent approximation method differs marginally.	Chalk field in Danish North Sea

Fabricius et al. (2007)	An iso-frame (IF) model with combination of petrographic data to generate elastic properties of impure chalk	Core sample studies provided mineralogical composition and fluid saturations of the rock. The IF parameter was found iteratively to fit the elastic modulus log. Paper also show how the iso-frame method can be extended to log data.	South Arne, Danish North Sea
Misaghi et al. (2010)	Investigated the effectiveness of the differential effective medium (DEM) model and self-consistent (SC) model to model elastic properties of carbonate samples	Both Gassmann and DEM models yield good agreement with measured saturated V_P, with the later having a better accuracy.	Carbonate and sandstone from south-west Iran
Bhakta and Landrø (2013)	Applicability of Gassmann's relations for chalk and how well shear wave velocities can be generated from empirical and rock physics models.	A universal rock physics model for chalk reservoir cannot be established. SC approximation and IF model are similar to Gassmann estimates for dry P-wave velocity. Larger differences between models with respect to Vs estimation in comparison to which fluid substitution model is most accurate.	Ekofisk, Norwegian Sea
Das et al. (2016), Das et al. (2013)	An integrated rock physics model based on an extended form of Nur's modified Voight's model, Hertz-Mindlin to model pressure change and Gassmann equation for fluid substitution is presented	The model predicts velocities and density fairly accurately for high porosity, low water saturation chalk, but underestimated for low porosity chalk. A set of parameters used for specific layers in the model.	Ekofisk, Norwegian Sea

Table 2.2: Summary of published rock physics models to compute various elastic properties in different chalk fields.

2.4.2 Proposed rock physics model

Following the selected successful application of Gassmann's in the petro-elastic model for elastic properties estimation, the proposed rock physics model in this study also takes the same approach. Unlike the DEM and the iso-frame models, which assume a fixed microstructure independent of pressure, the present rock physics model is pressure dependent. This approach is similar to that of Das et al. (2016), where the model takes into consideration the combined effect of porosity, pressure and fluid saturation on the effective elastic properties.

My rock physics model employs three main steps. Firstly the compaction-induced porosity change is calculated using a compaction model first proposed by Sylte et al. (1999), and also mentioned in Smith et al. (2002). The compaction model is illustrated in Figure 2.9 for dry compaction and water weakening. The compaction model has a few assumptions based on observations made from extensive geomechanical experiments performed in the laboratory. The assumptions of the compaction model are that compaction depends on the initial oil filled chalk porosity, and that chalk with porosity lower than 28% does not undergo compaction. Compaction also depends on the increase in water saturation, in which the compressibility of high porosity, water-weakened chalk is many times greater than that for the same chalk in its water-free state. Extensive rock test results also indicate that the relative amount of water-weakened chalk is a linear function of water saturation, from zero water saturation (i.e., water-free state) to the state with the maximum attainable water saturation, at 0.325, when the entire matrix is fully water-wetted and the chalk is fully water-weakened. After this point, no additional compaction is induced once the water saturation has reached 0.325 from a water-free state. Compaction also occurs when the effective stress is greater than 2000 psi (approximately 13.7MPa).

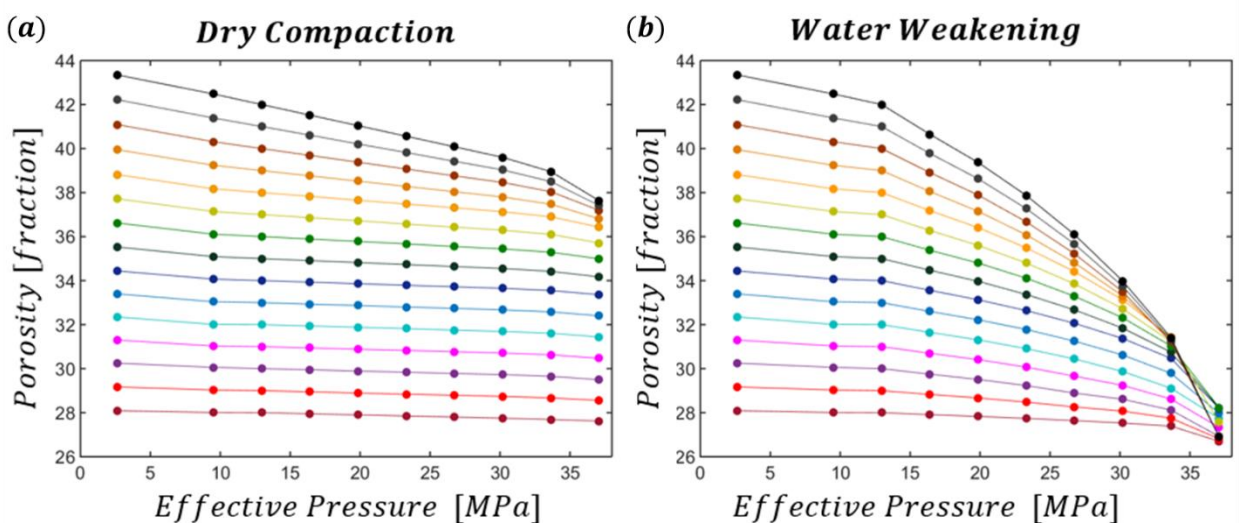

Figure 2.9: The compaction model for (a) dry compaction at 0% water saturation and (b) water weakening at water saturation of 33%. Below the initial porosity of 28%, the rock is insensitive to compaction. The curves in both (a) and (b) show fitting of the compaction measurements. The highest porosity rocks has the steepest compaction gradient.

The second step is to calculate the elastic moduli as a function of pressure effects on the dry rock frame. Stress sensitivity of reservoir rock remains a critical factor in understanding reservoir performance through seismic monitoring and feasibility studies. The effect of pore pressure change in fluid is easily calculated through the equations of Batzle and Wang (1992), and Han and Batzle (2000). To estimate the pressure compliance of the dry rock frame, I follow a pressure model from MacBeth (2004), shown in Equations (2.1) and (2.2), that describe the behaviour of the dry frame with increasing effective pressure.

$$K_{dry} = \frac{K_{inf}}{1+(E_k e^{-P_{eff}/P_k})} \tag{2.1}$$

$$\mu_{dry} = \frac{\mu_{inf}}{1+(E_\mu e^{-P_{eff}/P_\mu})} \tag{2.2}$$

where the coefficients K_{inf}, μ_{inf} are the bulk and shear infinity, which control the high pressure asymptotes, in which an empirical relation is derived as a function of initial porosity. P_k, P_μ are the

characteristic pressure constants and determine the rollover point beyond which the rock frame attains its state of relative insensitivity; in other words, they control the slope of the curve. The coefficients E_K, E_μ determine the intercept of the curves. For the pressure dependence, this model takes a form which assumes the compliances to be slowly varying functions of confining pressure. In this study, the coefficients of the pressure model proposed by MacBeth (2004) are optimized using input data from the rock mechanics tests.

In order to calculate the effective pressure, the equation from Terzaghi (1923) on the effective stress law is employed:

$$\sigma_{ij} = S_{ij} - \delta_{ij}\alpha P_p \tag{2.3}$$

where the effective pressure, σ_{ij} equals to the applied stress, S_{ij} minus the multiplication of the effective stress coefficient, α and the pore pressure P_p. The effective stress law requires the rock to be elastic, depends only on the state of stress, the pore pressure is uniform throughout the pore spaces and no hysteresis in the stress-strain cycles. Since no rock is absolutely elastic all effective-stress laws for rocks are approximations (Mavko et al., 2009). The α parameter is proposed as Biot's coefficient in Equation (2.3) by Nur and Byerlee, 1971, and is only valid for volumetric strain. Biot's theory of poroelastitcity (Biot 1941, Geertsma 1857) shows that the effective stress coefficient for bulk volumetric strain is a description of how strain is distributed in the porous media between the solid matrix and the pore volume. If Biot's coefficient equals to one means an elastically incompressible matrix, and zero corresponds to the case when the pore volume is incompressible. The determination of the Biot-coefficient of chalk has been carried out in several separate studies. While some of them claim a coefficient as low as 0.7–0.8 (Alam et al., 2012 and Kristiansen and Plischke 2010), other experiments indicated a Biot-coefficient of 0.9 (Warpinski and Teufel 1992). Since the Biot's coefficients measures the rock at static condition, there is no theoretical justification for extrapolating Biot's coefficient to elastic moduli and seismic velocities. However, a dynamic effective stress coefficient, α is calculated from sonic data shows not a constant value for chalk but ranges between 0.80 and 0.95 for the studied samples from the Valhall field (Alam et al., 2012). Since no laboratory measurements on the effective stress coefficent is available, I will assume the effective stress coefficient equal to to 1 for the Ekofisk chalk. The

effective stress coefficients for various properties of rocks composed of a number of mineral constituents, is summarised in Berryman (1992).

Since porosity is a dynamic parameter, depending on how the pore pressure changes in the reservoir, the porosity can be either reduced, due to pore pressure decrease, or remain constant if pore pressure increases. The porosity has a direct impact on the K_{inf}, μ_{inf} values and the dry frame, K_{dry}, μ_{dry} modelling of the rock. This relationship is given in Equations 2.1 and 2.2. As illustrated in Figure 2.10, as the rock compacts from point A to point B as a result of dry compaction or water weakening, the porosity reduces; in turn, the K_{inf}, μ_{inf} values will increase and the dry rock frame moduli, K_{dry}, μ_{dry} increase in stiffness. As the rock undergoes depletion without compaction, such as for rocks with less than 28% initial porosity, the dry frame of the rock takes the path from point B to point C. There is no change in $K_{inf}, \mu_{inf},$ but there is still an increase in the dry frame K_{dry}, μ_{dry} values, but this increase is much less than from point A to point B. Lastly, if there is an increase in pore pressure, hypothetically speaking from point C to point D, the K_{inf}, μ_{inf}stays the same as the porosity is constant, but the K_{dry}, μ_{dry} becomes smaller.

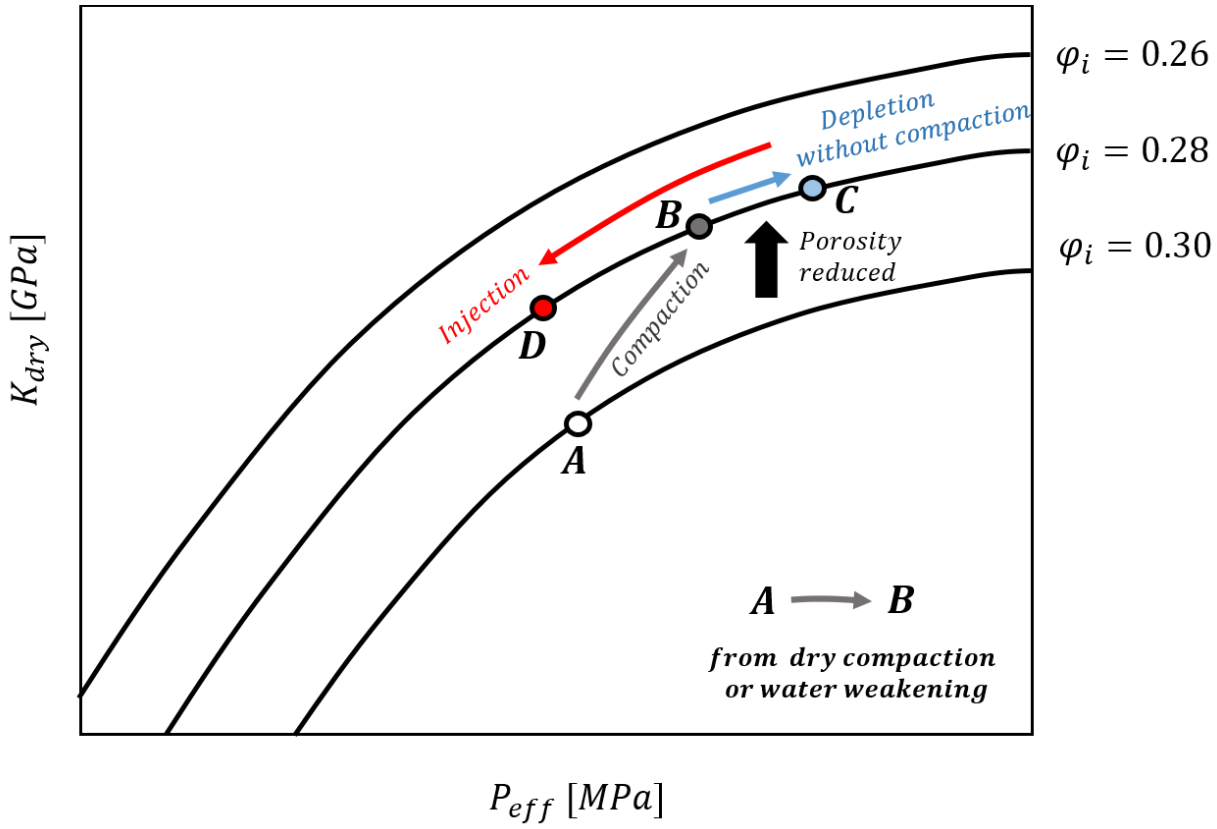

Figure 2.10: A schematic diagram showing how porosity changes K_{inf}, μ_{inf} values used in rock physics modelling.

Why is stress sensitivity calibration important?

Figure 2.11 shows the sensitivity of P-wave velocity as a function of stress. Depending on the rock properties, each field or rock type has very different stress sensitivity characteristics. For example, the Ekofisk chalk (North Sea chalk) is a lot more stress sensitive than the West of Shetland sandstone, and in comparison, the West of Shetland sandstone is relatively more stress sensitive than the Balder sands. The stress sensitivity is also dependent on loading and unloading mechanisms and the initial effective stress. The rock is usually more stress sensitive at low effective stress and also in unloading events, such as injection compared to depletion. By using these description, we can quantify how stress sensitive the rock is due to production changes and what percentage change will be manifested in P-wave or even S-wave velocities.

The calibration of the MacBeth law (2004) parameters ($K_{inf}, \mu_{inf}, P_k, P_{\mu,} E_K, E_\mu$) using data points from rock mechanics laboratory measurements provided from the field operator ConocoPhillips are shown in the Table 2.3. Each sample was fitted with its individual stress sensitivity parameters which are governed by the heterogeneity of the rock sample. In order to translate these parameters to describe a rock physics model that will be used for the simulation model, an averaged value or correlation with the initial porosity needs to be used. A correlation between (K_{inf}, μ_{inf}) and initial porosity was established from the data, showing a dependency on initial porosity, as shown in Figure 2.12. It was found that an exponential relationship between (K_{inf}, μ_{inf}) and porosity gives the best correlation, with a regression R-squared coefficient of 0.9211 and 0.907 for bulk and shear infinity respectively.

The curve fitting using individually optimised parameters ($K_{inf}, \mu_{inf}, P_k, P_{\mu,} E_K, E_\mu$) based on their respective initial porosity for both bulk and shear modulus is shown in Figure 2.13. No specific trends were found between $P_k, P_{\mu,} E_K, E_\mu$ and the initial porosity; hence the averaged $P_k, P_{\mu,} E_K, E_\mu$ were initially employed. However, the results shown in Figure 2.14 show considerable discrepancy between the data points and the fitting. I revised this approach by optimising the parameters $P_k, P_{\mu,} E_K, E_\mu$ globally, by using all the data points: essentially using all data points from all samples to generate a best fitting $P_k, P_{\mu,} E_K, E_\mu$ for the model. This has markedly improved the fitting for bulk modulus, but less so for shear modulus, as shown in Figure 2.15. The lack of improvement for shear modulus is most likely due to poor data quality. The data points for sample 20 has higher bulk modulus than sample 9, however, this is the opposite for shear modulus. This could be a measurement error in shear modulus for sample 20. The optimization using all data points and the goodness of fit for both bulk and shear modulus are illustrated in Figure 2.16. These parameters help to describe the stress sensitivity model to generate elastic properties in the simulation model.

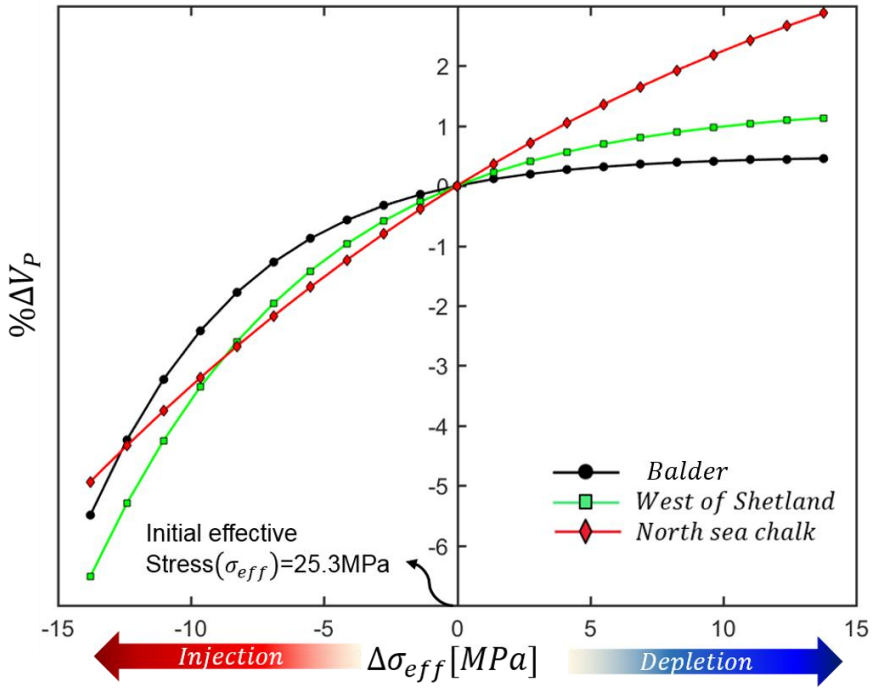

Figure 2.11: P-wave velocity percentage change as a function of effective stress for Ekofisk chalk, West of Shetland and Balder sandstone.

Sample Number	**Porosity**	**Res Unit**	K_{inf}	E_k	P_k	μ_{inf}	E_μ	P_μ
1	0.403	EA	4.61	1.45	8.02	4.03	0.18	15.64
32	0.375	ED1	6.39	0.94	15.06	4.10	0.79	23.98
3	0.339	EC	9.69	0.91	9.35	6.67	0.30	12.34
4	0.339	ED	9.43	0.91	9.35	6.53	0.30	12.9
20	0.261	EA	11.72	0.45	24.15	8.21	0.20	38.53
9	0.229	EE	16.54	0.31	25.36	9.32	0.07	12.53
			Averaged	0.83	15.22	Average	0.31	19.32
			Optimised	0.49	17.74	Optimised	0.19	21.5

Table 2.3: Stress sensitivity parameters ($K_{inf}, \mu_{inf}, P_k, P_{\mu,} E_K,$ and E_μ) calibrated from rock mechanic tests.

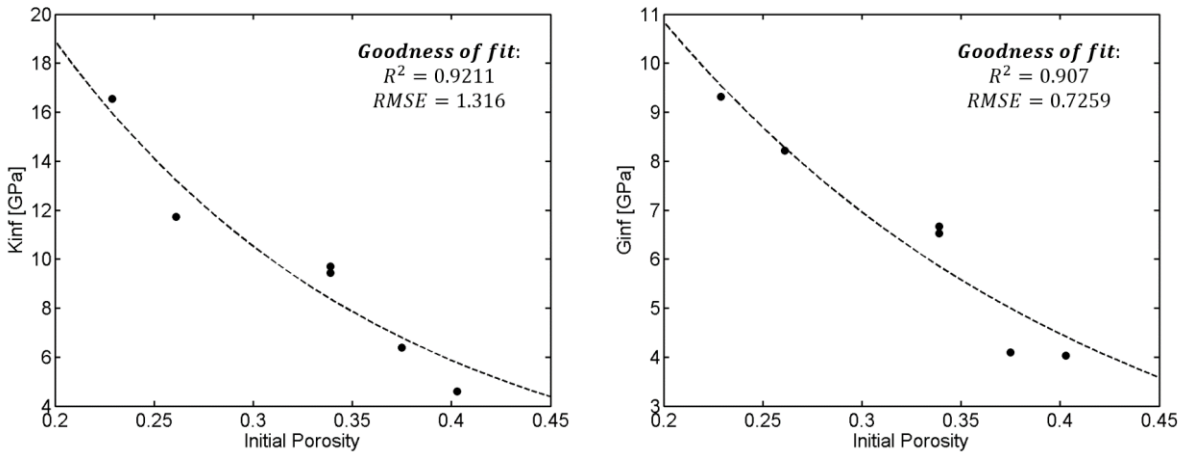

Figure 2.12: Correlation was found for (left) K_{inf} and (right) μ_{inf} with initial porosity from the data.

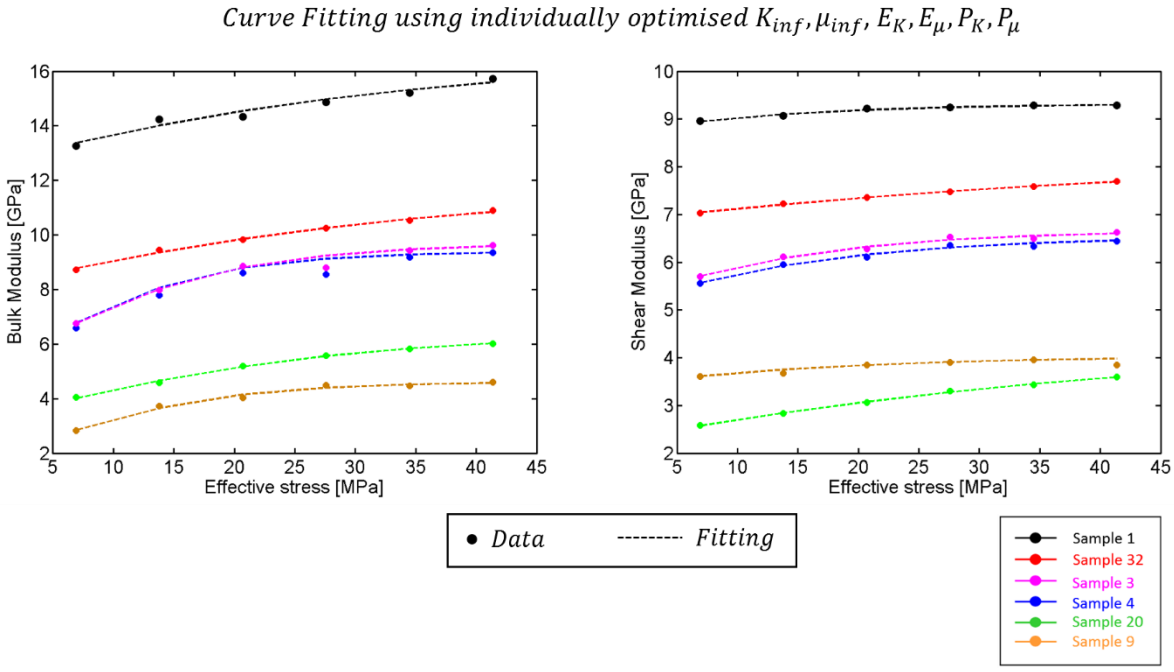

Figure 2.13: Curve fitting using individually optimised ($K_{inf}, \mu_{inf}, P_k, P_{\mu,} E_K, E_\mu$) based on their respective initial porosity for both (left) bulk and (right) shear modulus.

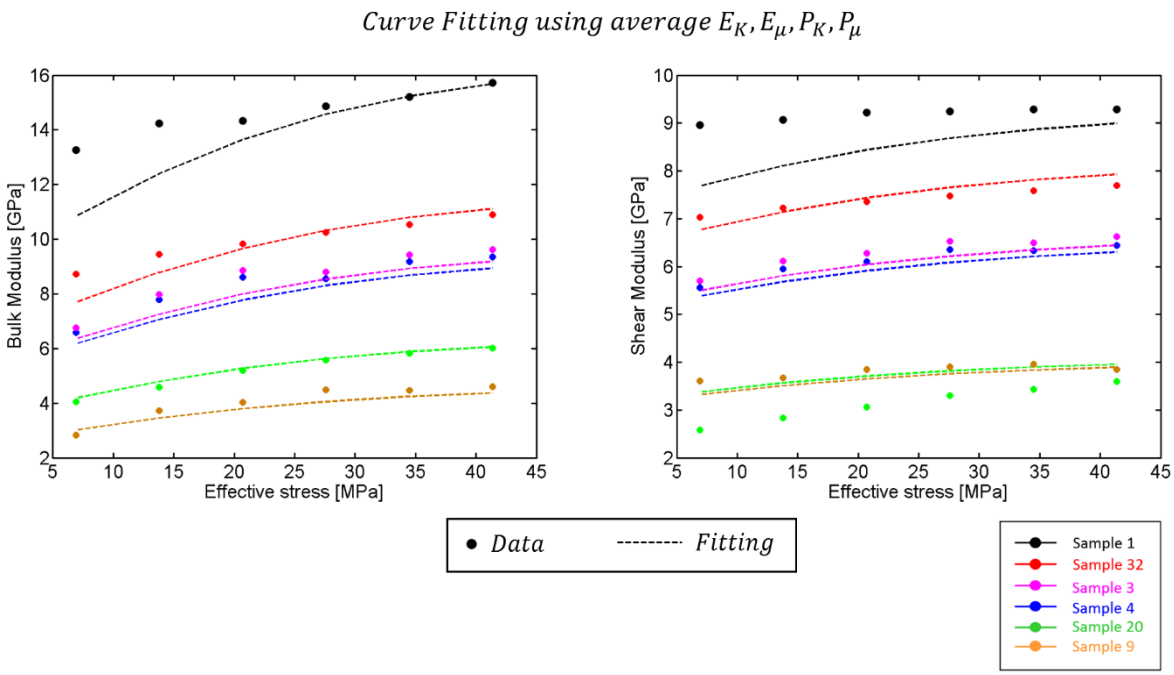

Figure 2.14: Curve fitting using averaged ($P_k, P_{\mu,} E_K, E_\mu$) for both (left) bulk and (right) shear modulus.

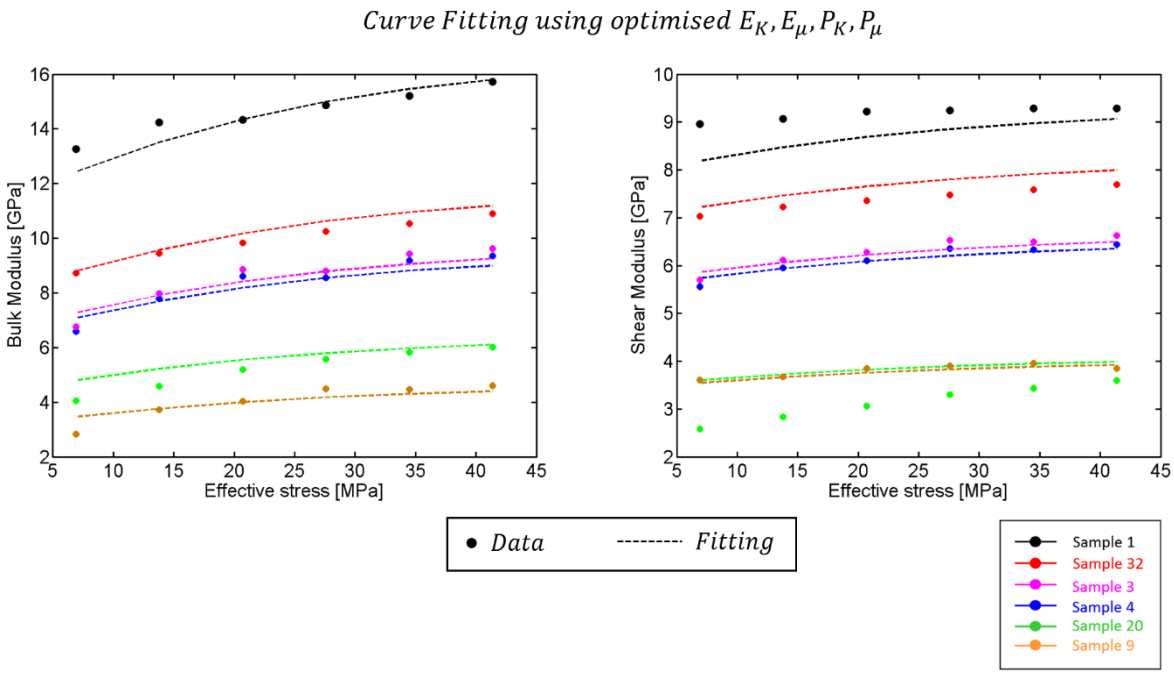

Figure 2.15: Curve fitting using newly optimised ($P_k, P_{\mu,} E_K, E_\mu$) for both (left) bulk and (right) shear modulus.

It is commonly known that cores taken from wells do not provide a statistically meaningful representation of the 3D heterogeneity of the reservoir, because samples, naturally, are taken from the most competent and productive rock. This may, for example, lead to pressure-sensitive mesoscale pockets of unconsolidated/consolidated sands, perhaps shales, or even fractures/faults being by-passed in the analysis. The samples used in the present rock physics model calibration ranged from 22-40% porosity in the Ekofisk formation and 24-37% in the Tor formation. This is a fair representation of the field, since the 4D seismic activities were mostly concentrated in these porosity regions and the fitting for this porosity range can also be extended to rocks with porosity lower than 22%.

Another argument contributing to the validity of calibrating elastic properties with core samples is that in our case, the core samples were taken from different sub-formations in the reservoir, hence representing a fair heterogeneity of the reservoir. Furthermore, a good trend was also found between the bulk and shear infinity modulus, with the initial porosity. Another issue with cores is that they are loaded back to their in-situ stress state do not recover their original velocities, and their stress dependence is usually larger than it was in situ (Fjær and Holt, 1999). Damage resulting from core unloading needs to be estimated and subtracted from the rock-frame measurements.

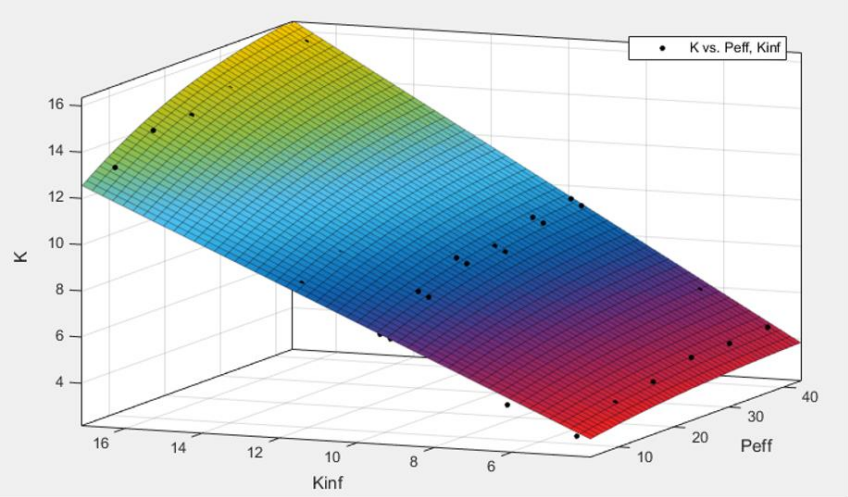

General model:
f(x,y) = y./(1+a.*exp(-x./b))
Coefficients (with 95% confidence bounds):
a = 0.4887 (0.3886, 0.5889)
b = 17.74 (14, 21.49)

Goodness of fit:
SSE: 5.059
R-square: 0.9886
Adjusted R-square: 0.9883
RMSE: 0.3857

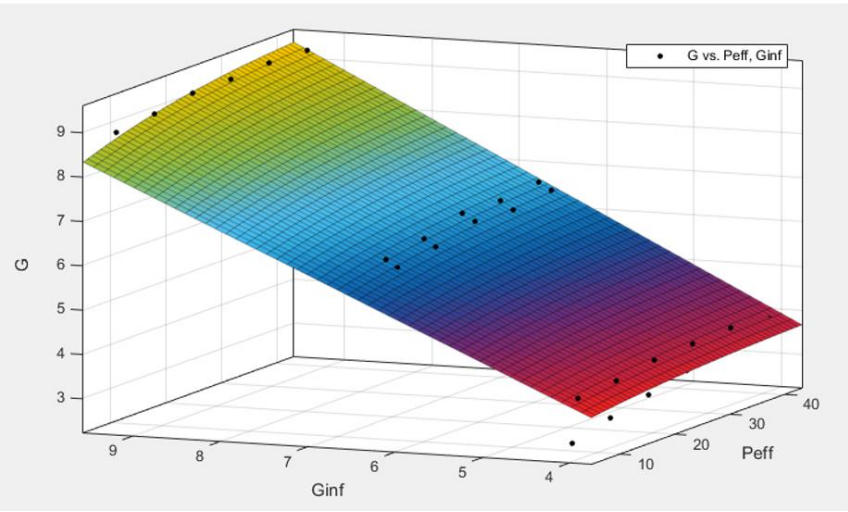

General model:
f(x,y) = y./(1+a.*exp(-x./b))
Coefficients (with 95% confidence bounds):
a = 0.1903 (0.08217, 0.2984)
b = 21.5 (6.364, 36.64)

Goodness of fit:
SSE: 5.336
R-square: 0.9651
Adjusted R-square: 0.9641
RMSE: 0.3962

Figure 2.16: Optimising the parameters $P_k, P_{\mu,} E_K, E_\mu$ globally by using all the data points, to generate best fitting $P_k, P_{\mu,} E_K, E_\mu$ for the model.

The fitting model for K_{inf} and μ_{inf} with initial porosity is given as Equations (2.4) and (2.5) as follows:

$$K_{inf} = 62.14e^{-5.915\varphi} \tag{2.4}$$

$$G_{inf} = 26.2e^{-4.402\varphi} \tag{2.5}$$

These equations represent the empirical correlation between the infinity bulk and shear modulus and initial porosity.

The third and final step is the fluid substitution to in situ saturations. The fluid properties were modelled using the laboratory derived equations from Batzle and Wang (1992) and Han and Batzle (2000). The equations from Gassmann's model (1951) are given as below:

$$K_{sat} = K_{dry} + \frac{(1-K_{dry}/K_m)^2}{\frac{\varphi}{K_{fl}}+\frac{1-\varphi}{K_m}-\frac{K_{dry}}{K_m^2}} \tag{2.6}$$

$$\mu_{sat} = \mu_{dry} \tag{2.7}$$

where K_{sat} and μ_{sat} are the saturated bulk and shear modulus, K_m and μ_m are mineral bulk and shear modulus, K_{dry} and μ_{dry} are dry-rock bulk and shear modulus, K_{fl} is the fluid bulk modulus and φ is the porosity. The difference here compared to a non-compacting reservoir is, that due to changes in porosity as a function of pressure depletion and water weakening, the porosity, the dry rock bulk and shear modulus are dynamic components that change with time for the same rock. The changes in dry rock bulk and shear modulus depends on mechanisms such as depletion-related pressure drop and re-pressurisation due to water injection. On the other hand, mineral moduli such as K_m and μ_m are constants, and the most commonly used values from the literature are listed in Table 2.4. In the present rock physics model, I employed values that are equal to those in Das et al. (2013) and Das et al. (2016). Since the clay distribution in both Ekofisk and Tor formation is less than 5%, the rock is assumed as monomineralic, with a composition of 100% calcite.

Figure 2.17 shows the P-wave velocity log reconstruction at a producer well. The match between measured and predicted P-wave velocity is in good agreement except at intervals with bad hole and the tight zone interval with higher quartz content. This is where the monomineralic assumption could break down.

	Walls et al. (1998)	Japsen et al. (2004)	Gommesen et al. (2007)	Das et al. (2013, 2016)
K chalk GPa)	65	71	71	72
K clay (GPa)	20.9	25	Not provided	n/a
μ chalk (GPa)	27.1	30	24	36
μ clay (GPa)	6.85	9	Not provided	n/a
ρ chalk (g/cc)	2.71	2.71	2.71	2.71
ρ clay (g/cc)	2.85	2.7	Not provided	n/a

Table 2.4: A summary of mineral bulk modulus, shear modulus and density used from other published works.

The modelling results are shown for application of the rock physics model to a reservoir simulation grid using pressure, temperature, saturation and compaction values at each cell to compute the changes in P-velocity, S-velocity, density and two-way time (time-shifts) for a time period of two and a half years a part (LoFS 2 – LoFS 6). In Figure 2.18 time-shift results from the present rock physics model, and results from the operator, employing a different rock physics model (Smith et al., 2003, Smith and Brown 2005, Das et al., 2016), are compared with field observation, where the former show a better agreement with field-measured reservoir time-shifts between LoFS 2 to LoFS 6. Areas highlighted in yellow demonstrate that my rock physics predictions more closely represent the field observations. The southern part of the field, shows hardening signals due to depletion and reservoir compaction, this is supported from the prediction from the reservoir simulation model. The western part of the field, shows pressure depletion and gas saturation increase; however, the gas signals are not conspicuous in the field, due to the masking effects of geomechanics. The masking of gas effect is more accurately portrayed in my rock physics predicted in Figure 2.18(b) than those predicted in Figure 2.18 (a) when compared to the observed reservoir time shifts in Figure 2.18(c). The forward predictions from both rock physics models are noise-free hence the overall time-shift values predicted are slightly higher than the observed

values. The proposed rock physics model more accurately modelled the overall 4D seismic reservoir time-shifts then the operator's rock physics model.

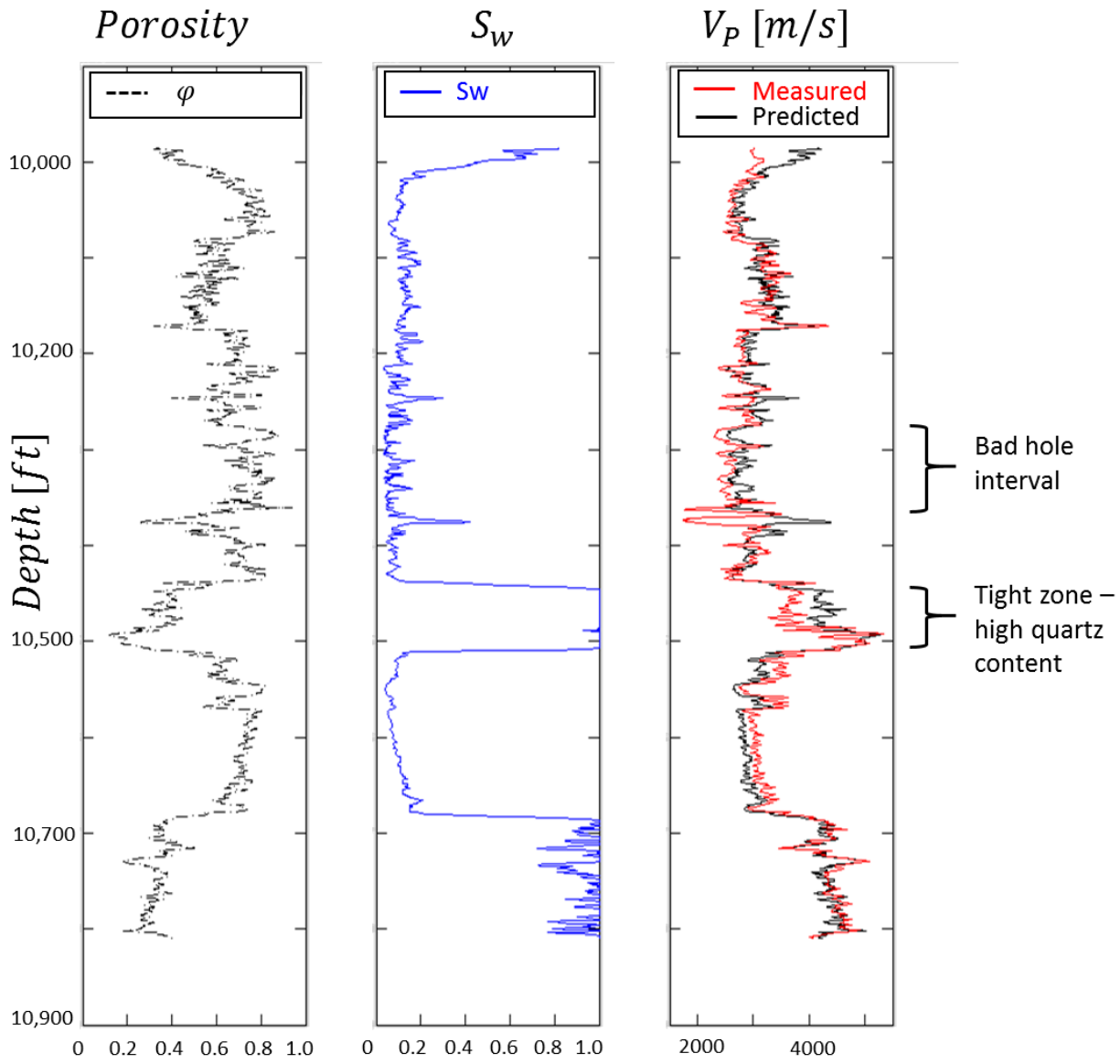

Figure 2.17: Porosity and water saturation logs interpreted from petrophysical evaluation, the rock physics model proposed in this chapter is then used to reconstruct the P-wave velocity log.

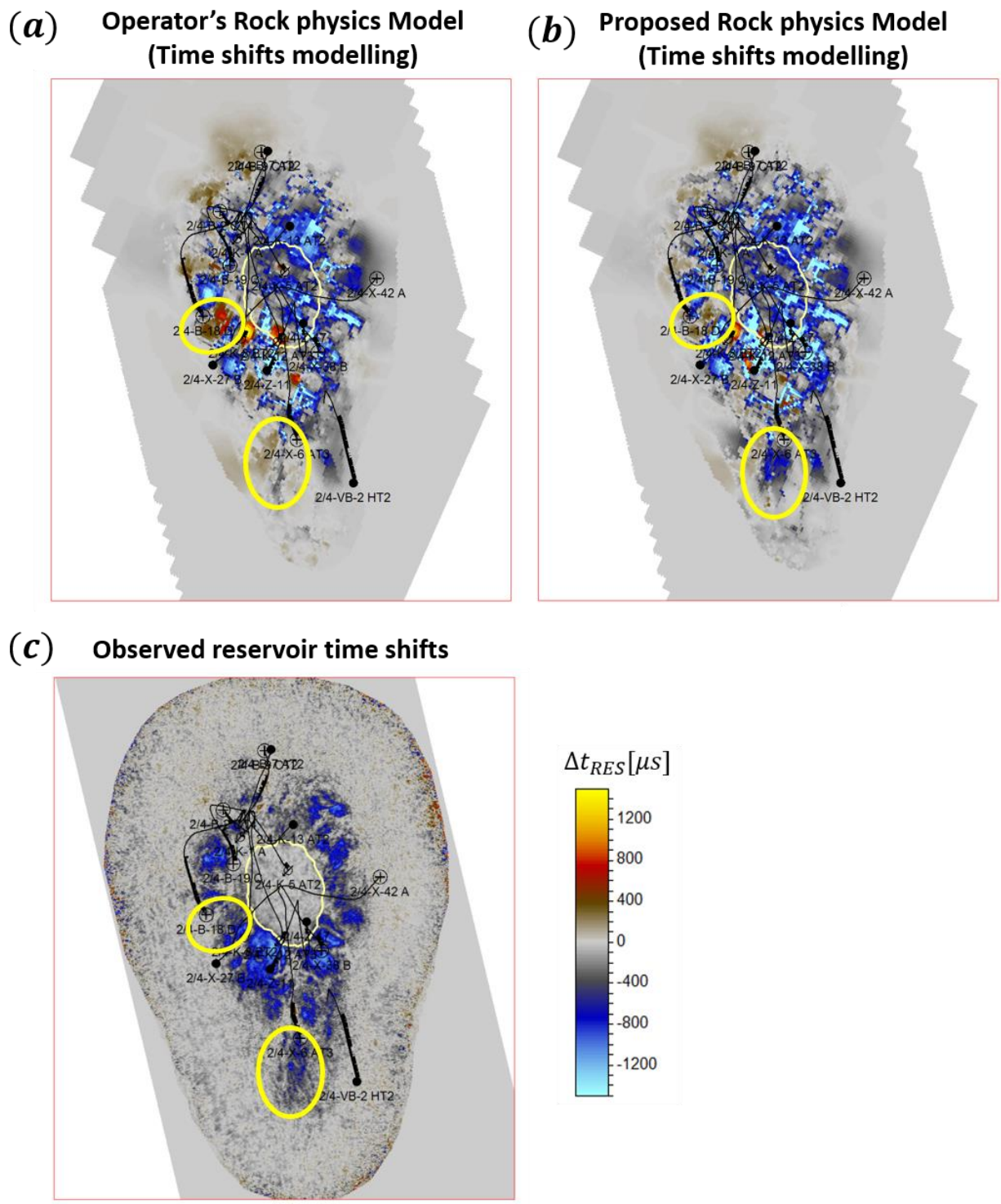

Figure 2.18: A comparison between the predicted reservoir time shifts from (a) operator's rock physics model, (b) proposed rock physics model and (c) the observed reservoir time-shifts.

2.5 Summary

This chapter has focused on establishing a rock physics model for the compacting chalk reservoir. In addition, a critical examination of different rock physics approaches in the literature is also provided. I explored the literature to determine the applicability of using Gassmann's fluid substitution theory to estimate the effects of fluids on bulk modulus in a chalk reservoir. The majority of the work from literature (Sørnes and Brevik 2000, Røgen et al., 2005, Gommesen et al., 2007, Misaghi et al., 2000 etc.) shows that this relation is a valid for chalk samples. Results from inclusion based scattering theories are marginally better or comparable to those predicted by Gassmann's relations.

I then presented a rock physics model for the Ekofisk field; calibrated with data from rock mechanics and the literature. The rock physics model proposed comprised of three main procedures. A dynamic compaction model calibrated to geomechanical data (Sylte et al., 1999) is used to model porosity change due to dry compaction or water weakening. The next step is to model the dry rock frame of bulk and shear modulus as a function of effective stress. This is carried out by calibrating stress sensitivity parameters from the MacBeth (2004) pressure model to rock mechanics data. This allows a field calibrated porosity-dependent pressure relationship for the baseline and monitor time, which is crucial for studying time-lapse seismic anomalies. Lastly, Gassmann's relations (1951) are employed to model fluid effects. This workflow was applied to model the reservoir time-shifts between LoFS 2 and LoFS 6, where this approach shows better agreement to the observed time-lapse time-shifts, compared to the model proposed by the field operator. In the next chapter, I will employ this rock physics model for dynamic reservoir characterization, primarily using it to model time-shifts measurements from both streamer and LoFS data.

CHAPTER THREE

DYNAMIC RESERVOIR CHARACTERISATION

This chapter provides an overview of the use of 4D seismic data in dynamic reservoir characterization in the Ekofisk field. A summary of the seismic data from both acquisition strategy for streamer and Life of Field Seismic (LoFS) is provided. A comparison is then made between streamer and LoFS data where a clear evolution of LoFS reservoir time-shifts as a function of pressure change was observed, whilst the streamer time-shifts portray signals that are dominated by an interplay of pressure and saturation changes. The rock physics model described in Chapter 2 is employed to compute reservoir elastic properties and time-shifts as a function of pressure and saturation changes. Lastly, I provide two separate examples on reconciling the observed and modelled reservoir time-shifts in streamer and LoFS surveys by taking into account hysteresis in the rock's stress sensitivity to effective stress.

3.1 Life of Field Seismic for Reservoir Monitoring

The production history of Ekofisk is provided in Chapter 2. Here, I will give a brief description on the seismic data acquired in the Ekofisk field. Two separate acquisition strategies were adapted through time: streamer and Life of field seismic (LoFS) using ocean bottom cables. There was no pre-production seismic data and the first baseline seismic survey was shot in the year 1989 followed by four streamer monitor surveys in the year 1999, 2003, 2006 and 2008. The first survey however coincides with the water injection programme started in 1987 hence it is a good baseline survey for monitoring water flooding (Guilbot and Smith 2002). The monitor surveys indicated significant time-shifts in the upper reservoir that were related to reservoir compaction. Despite the success of these surveys in showing reservoir compaction, the operator determined that this challenging field required more frequent surveys with higher repeatability. The acquisition configurations for marine streamer and LoFS time-lapse surveys in the Ekofisk field are provided in Table 3.1. The first three seismic surveys are conventional streamer, followed by two surveys using Q-marine, point-receiver marine seismic system. The result of using Q-marine technology shows lower source-receiver positioning error, with as low as 50m in most of the survey area (Haugvaldstad et al., 2011). This improvement is depicted in Figure 3.1. The repeatability (NRMSd) of the streamer data and the gas cloud in the overburden which prevents optimal imaging is depicted in Figure 3.2

A permanent seismic monitoring system was installed in 2010 as an effort to acquire more frequent and higher-repeatability 4D LoFS data. By 2010, with more than 1 billion STBO planned to be produced and more than 80 wells to be drilled during the next 15 years, a dedicated monitoring system is necessary to support the drilling programme (Bertrand et al. 2014). The LoFS data is used for the purpose of reservoir surveillance such as to optimize new well locations and trajectories, prioritize well interventions, update the reservoir model and monitor the geomechanical behaviour of the overburden (Bertrand et al. 2013a). High repeatability (5% NRMS) has been achieved (shown in Figure 3.3), resulting in detectable 4D time-shifts of less than 200μs and amplitude changes of the order 2 to 3%. Currently, the LoFS data are routinely used in well planning and reservoir management workflows by the field operator. Nine LoFS surveys have been acquired to date, the acquisition is carried out on average once every 6 months.

Acquisition parameters	1989, 1999, 2003	2006, 2008	LoFS (2010 – present)
Technology	Conventional	Q-Marine	OBC 4 components
Configurations	1-2 sources / 2-8 streamers	1 source / 8 streamers	
Source depth (m)	5 – 6	5	
Source separation (m)	50	50	
Streamer/cable separation (m)	100	50	300
Streamer depth (m)	6 – 8	6	
Streamer length (m)	3000, 3000, 3600	3600	
In-line bin size	12.5	12.5	12.5
Cross-line bin size	12.5	12.5	12.5
Number of sensor stations/sensor station separation (m)	N/A	N/A	4000 / 50
Acquisition interval	11 years, 5 years, 5 years	3 years	3 – 6 months

Table 3.1: Acquisition configurations for Ekofisk field seismic streamer and LoFS data (compiled from Haugvaldstad et al., 2011, Bertrand et al., 2014, personal comm. Alex Bertrand).

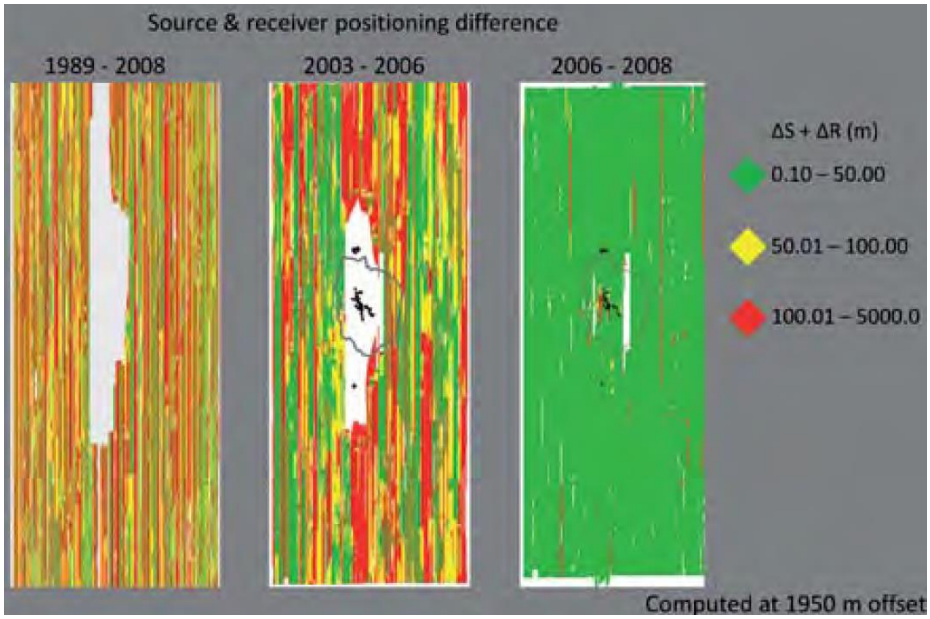

Figure 3.1: Source and receiver positioning difference maps showing significantly improvement with the employment of Q-marine technology (Haugvaldstad et al., 2011).

The acquisition periods and durations of the first six LoFS surveys at the Ekofisk field is shown in the Table 3.2.

Survey	Acquisition	Duration (days)
LoFS 1	Nov. 2010 – Jan 2011	71
LoFS 2	May – June 2011	33
LoFS 3	Sept – Nov 2011	43
LoFS 4	June – July 2012	38
LoFS 5	March – April 2013	36
LoFS 6	Sept – Nov 2013	56

Table 3.2: The acquisition period and duration of the first six LoFS surveys at the Ekofisk field (Bertrand et al., 2014).

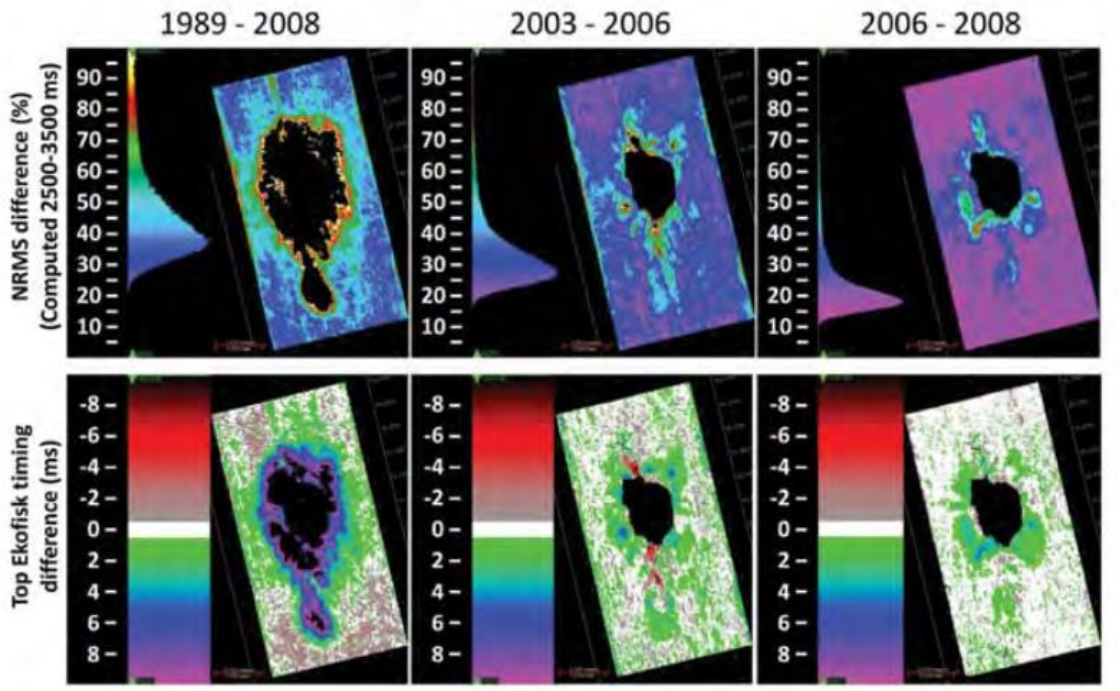

Figure 3.2: (top) NRMS difference maps computed at 2500-3500ms and (bottom) top Ekofisk time difference maps for 1989 – 2008, 2003 – 2006 and 2006 – 2008. The gas cloud is depicted as a black ellipse in the middle of the survey area (Haugvaldstad et al., 2011).

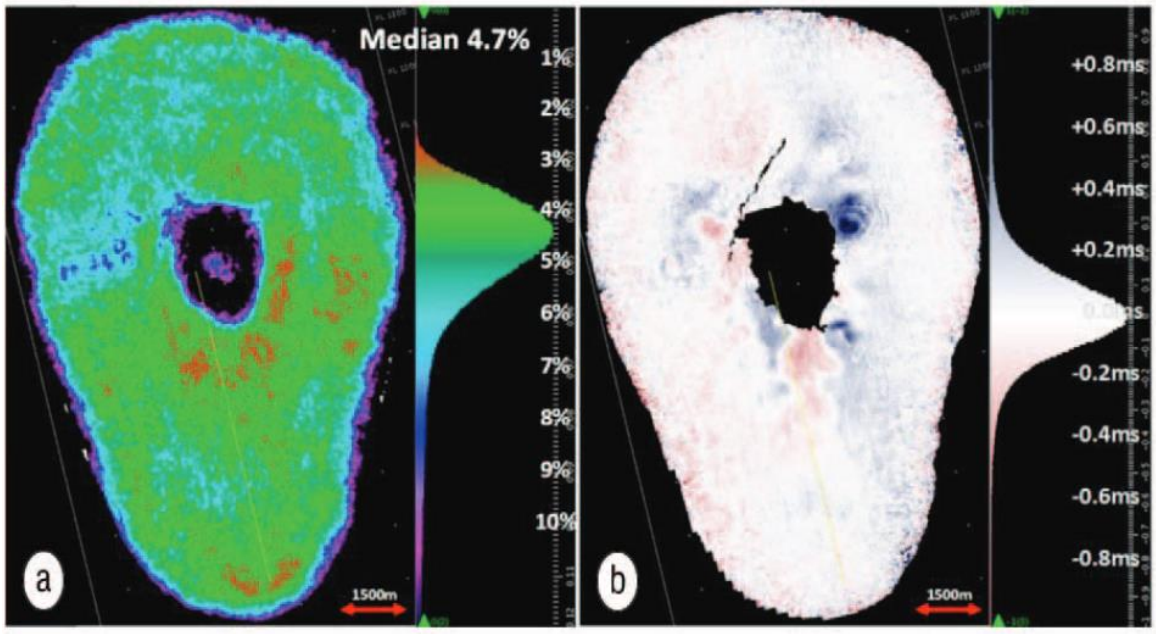

Figure 3.3: (a) NRMS map computed in a 2500 – 3500ms window for LoFS 2 – LoFS 3. (b) Time-shifts at top reservoir between LoFS 2 – LoFS 3 acquired 4.5 months apart (Bertrand et al., 2014).

3.2 Dynamic Reservoir Characterization

In this section, the proposed rock physics model from Chapter 2 is utilized to better understand the production mechanisms in the field under study from both periods of streamer and LoFS, in order to relate these dynamic changes to field observations. The accurate estimation of time-shifts and amplitude changes is important in the imaging and characterization of changes in reservoir properties. Historically in the Ekofisk field, the subtle amplitude changes are noisy and challenging to interpret reliably from streamer 4D seismic data; hence, more emphasis is given to time-shift measurements (Folstad 2011).

3.2.1 Time-shift methods

In the reservoir, where the rock is compacted and the path length is decreased, travel time will decrease through the reservoir zone. At the same time, compaction will increase the effective stress inside the reservoir, which generally increases velocity. The net effect is a decrease in the travel time through the reservoir. The opposite is true if the rock is dilated (stretched), as is the case in the overburden. The path length will increase, which will increase the travel time. Generally, dilation will cause the velocity to decrease, which will also have the effect of increasing the travel time. The schematic diagram in Figure 3.4 helps explain this. Of course, apart from geomechanical effects, time-shifts can be induced by changes in velocity alone, due to changes in pore pressure and saturation.

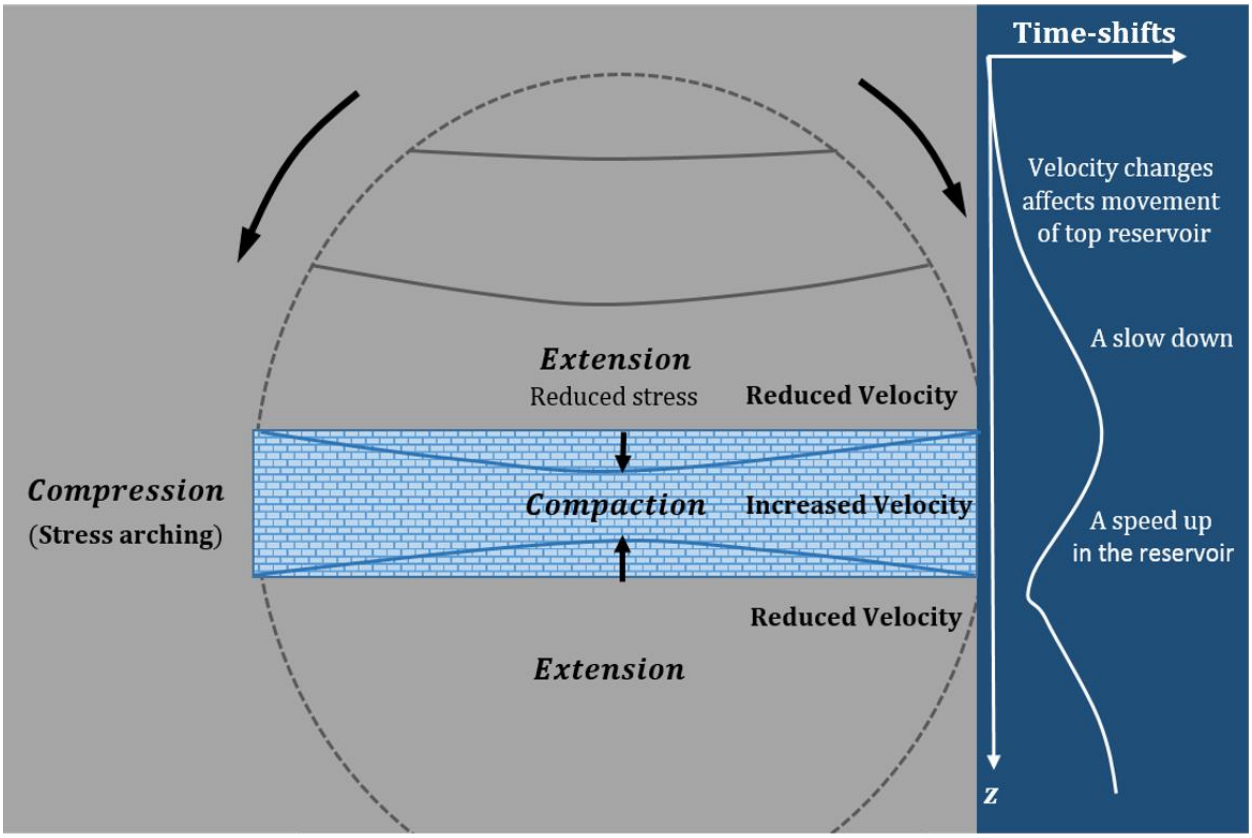

Figure 3.4: Changes in total time-shifts and velocity as a function of compaction and dilation.

Accurate characterization of the different dynamic changes, such as pressure, saturation and porosity, relies on signal matching of the 4D seismic data and accurate estimation of the shifts or warping function in the 4D data. The time-shift volume is the result of changes in velocity properties and from path-length changes both within and outside the reservoir. Many efforts were made to resolve the shift function between baseline and monitor surveys. These algorithms include cross correlation (Xcorr), nonlinear inversion (NLI) by Rickett et al. (2007), local cross correlation (Hale, 2006), the correlated-leakage method (CLM) proposed by Whitcombe et al. (2010), the dynamic-warping method (Dwarp) proposed by Hale (2013), and the Multi-Scale and Iterative Refinement Optical Flow (MSIROF) algorithm used by Zhang and Du (2016). A comprehensive review of the strengths and weaknesses of these different methods can be found in Kanu et al. (2016). The window based cross-correlation method has traditionally suffered from the trade-off between accuracy and the resolution of the estimated time-shifts. The Rickett et al. (2007) non-linear inversion method, which depends on a measure of misfit of the 4D signals between baseline and monitor trace, gives a more robust estimate of the time-shifts and is free from the trial and

error process of determining the optimum window size, since it calculates for the entire seismic trace.

The NLI method introduced in Rickett et al. (2007) shows that the inversion based approach to time-shift calculation yields superior estimates of time strain compared to local cross-correlation methods. The stability of the time-shifts derivative is included in the objective function, ensuring that the time-shift estimates also give a stable time strain, which is overall less noisy and more interpretive. The objective function is given as Equation (3.1):

$$E = |d - f(m)|^2 + \alpha|\nabla_t^2 m|^2 \tag{3.1}$$

where data vector, d contains the seismic data volume $x_1(x, y, t)$ and the model vector, m contains the time-shift volume $\tau(x, y, t)$ and the nonlinear function, $f(m)$ applies $\tau(x, y, t)$ to the second survey to give $x_2(x, y, t + \tau(x, y, t))$. The spatial constraints for the time direction is a Laplacian ∇_t^2 used as the vertical constraint operator, since we want the time strain (the first-derivative of the time-shifts) to be smooth (Rickett et al. 2007). The weighting coefficient, α represents the significance of the second term in the objective function; minizing the extra feature in the objective function increases the smoothness in the solution. This objective function is minimised using a descent-based Gauss-Newton algorithm. The Gauss-Newton algorithm works by linearizing the non-linear operator around the current model, solving the resulting linear problem, updating the model, and iterating.

Based on the work of Hodgson (2009), shown in Figure 3.5, it was demonstrated that the inversion approach also suffers from similar limitations to the cross-correlation method. There is a similar trade-off between the stability and the resolution of the solutions. If the weighting coefficient for the second derivative in the objective function is given more importance, the resultant time-shifts and time strains are more accurate away from the reservoir, at the expense of resolution inside the reservoir interval. This is evident in Figure 3.5, where accuracy outside the reservoir improves with a larger weighting coefficient, at the expense of less accurate time strain inside the reservoir. This is a result of the underlying assumption in the inversion that the time strain is varying slowly, whereas in reality the strain can have extreme changes due to large changes in velocity. If we are

only concerned with the time-shift measurements inside the reservoir, then a smaller weighting coefficient should be employed at the expense of poorer accuracy in time-shifts of the overburden and underburden. Hence, this method should be considered with caution when applied to reservoirs with larger time-shifts. The time-strain volume can be calculated by taking the vertical derivative of time-shifts. Time strains are more sensitive to noise than time-shifts, but their interpretation is more direct and intuitive, since it can be compared to changes in interval velocity. In all subsequent analysis, the reservoir time-shifts are calculated using the Rickett et al., (2007) NLI method.

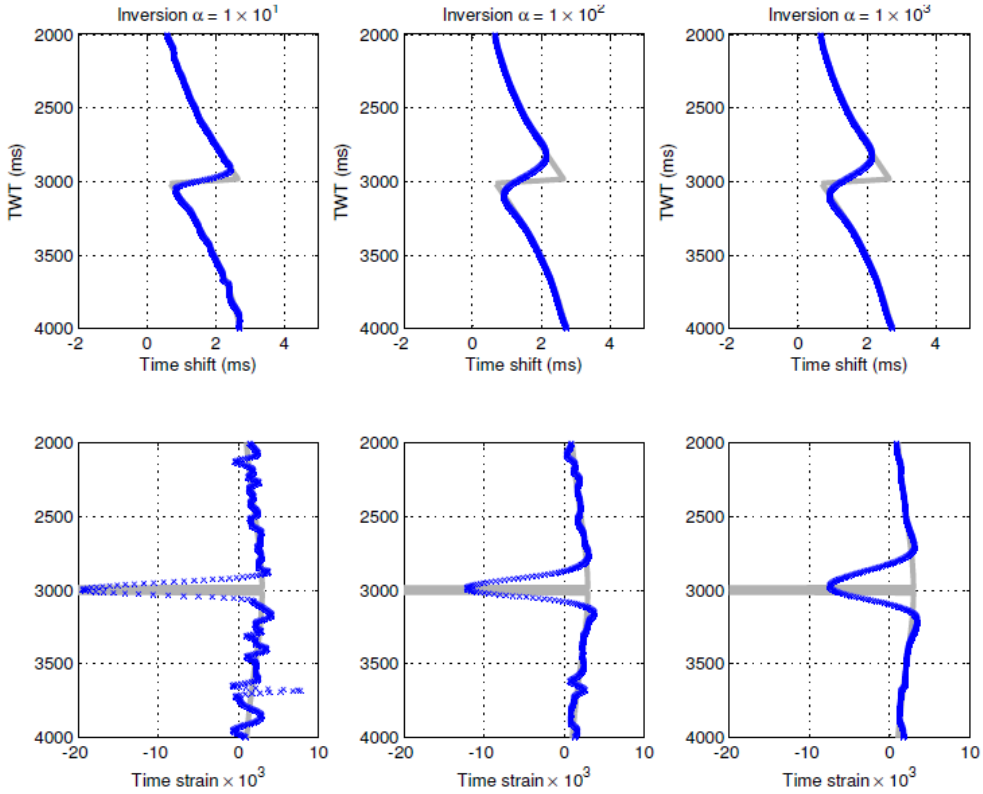

Figure 3.5: A synthetic test to recover time-shifts and time strain using the NLI method. The synthetic data is highlighted in grey and the inverted solutions are in blue; recovered using different weighting coefficients for the second derivative in the objective function (Hodgson 2009).

3.2.2 Reservoir time-shifts and production mechanisms

In this section, I will show the attribute I used in my time-shift analysis for both streamer and LoFS seismic data, and also compare and contrast the characteristics of the time-shifts estimated between two different types of surveys. The attribute known as the reservoir time-shifts is defined as the difference between the top and base reservoir time-shifts. This was first analysed in the Valhall field by Barkved (2012), with proven success. In a schematic diagram in Figure 3.6 (left), the reservoir time-shifts is given as the difference between point A and B. A positive reservoir time-shifts is a speed-up being attributed to compaction or impedance hardening. A negative reservoir time-shifts is a slow-down due to dilation or impedance softening. The time-shifts volume is calculated using Rickett et al., (2007) NLI method discussed in the previous section.

I computed the reservoir time-shifts attribute for the reservoir interval between 1989 –1999; the map in Figure 3.6 (right) shows speed-up or impedance hardening in most areas. One advantage of using this attribute is that the reservoir time-shifts has the same polarity convention as impedance changes. A speed-up (coloured in blue) corresponds to impedance hardening and a slow-down (in red) represents impedance softening. To carry out further analysis, all the data were gathered, in the form of seismic, well and production records across different acquisition periods for both streamer and LoFS. Seven wells are used in this analysis from the streamer data and ten wells from LoFS data. The selection criteria were prominent 4D signals observed around wells, large to moderate fluctuations in production data and observable changes from simulation model prediction that are also consistent with historic production data.

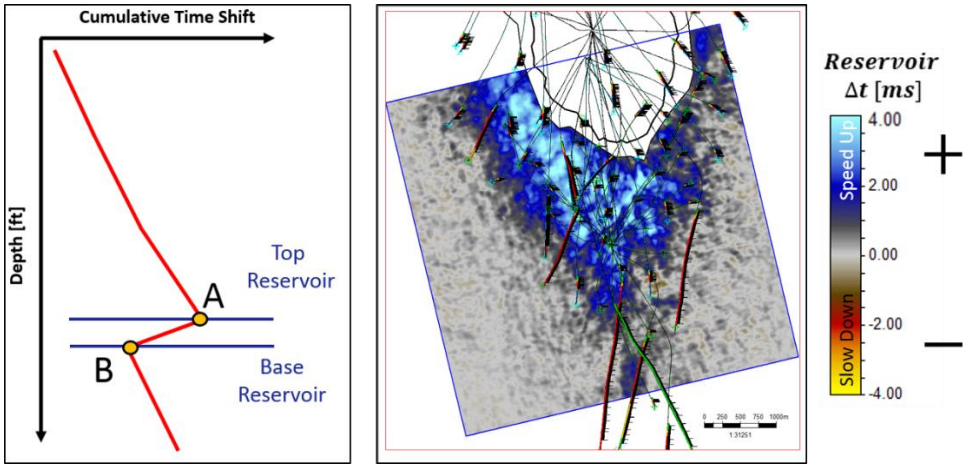

Figure 3.6: (left) Schematic diagram on how reservoir time-shifts are calculated by taking the difference between point A and B of the time-shifts of each trace. (Right) Reservoir time-shifts map between 1989 and 1999.

Before showing the differences in the time-shifts behaviour between streamer and LoFS data, the data quality of these two different surveys are shown. The seismic quality of the streamer data and LoFS, which is acquired using ocean bottom cables (OBC), is compared by looking at seismic cross-sections and maps for both reservoir and overburden, in Figure 3.7. The Q marine survey illustrates improvement in seismic resolution and more refined faults. This improvement is more apparent in the OBC, where we see clearer signals with significantly reduced side lobes above and below 3D signals. The fault located in the overburden is also more defined, highlighted by the yellow arrow. The bottom section in Figure 3.7 shows a map below the reservoir horizon created using a 45ms window, mapping the highest amplitude trough. As a consequence of new technology such as OBC, the main fault running along the northwest direction is more defined and, as a whole, the data are less noisy.

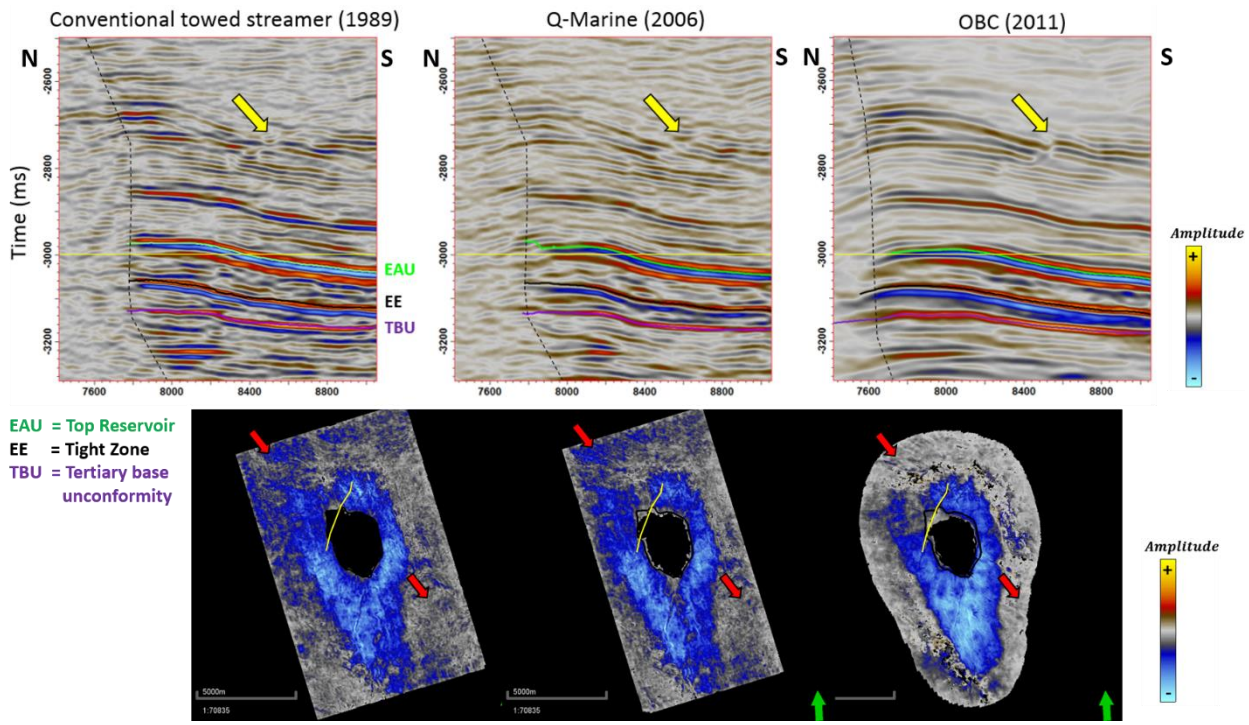

Figure 3.7: (top) Comparison of seismic quality between conventional towed streamer (1989), Q-marine (2006) and OBC (2011). (Bottom) maps generated below the reservoir horizon created using 45ms window tracking the highest amplitude trough.

To interpret these 4D reservoir time-shift signals in a meaningful way, we first need to understand the noise floor in these data. Figure 3.8 compares the noise floor for the streamer and LoFS data. The noise floor of both data types is computed by taking the average of the reservoir time-shifts across all surveys in an area (shown as small black box) which is relatively quiet from well activities. The noise floor of the streamer is expected to be higher, more than 3-fold, than the LoFS, due to high non-repeatability. The noise floor in the streamer data is calculated to be 0.3ms whilst in the LoFS it is 0.08ms (80µs). This means any reservoir time-shift values falling below 0.3ms in the streamer data and 0.08ms in the LoFS data will be treated as noise.

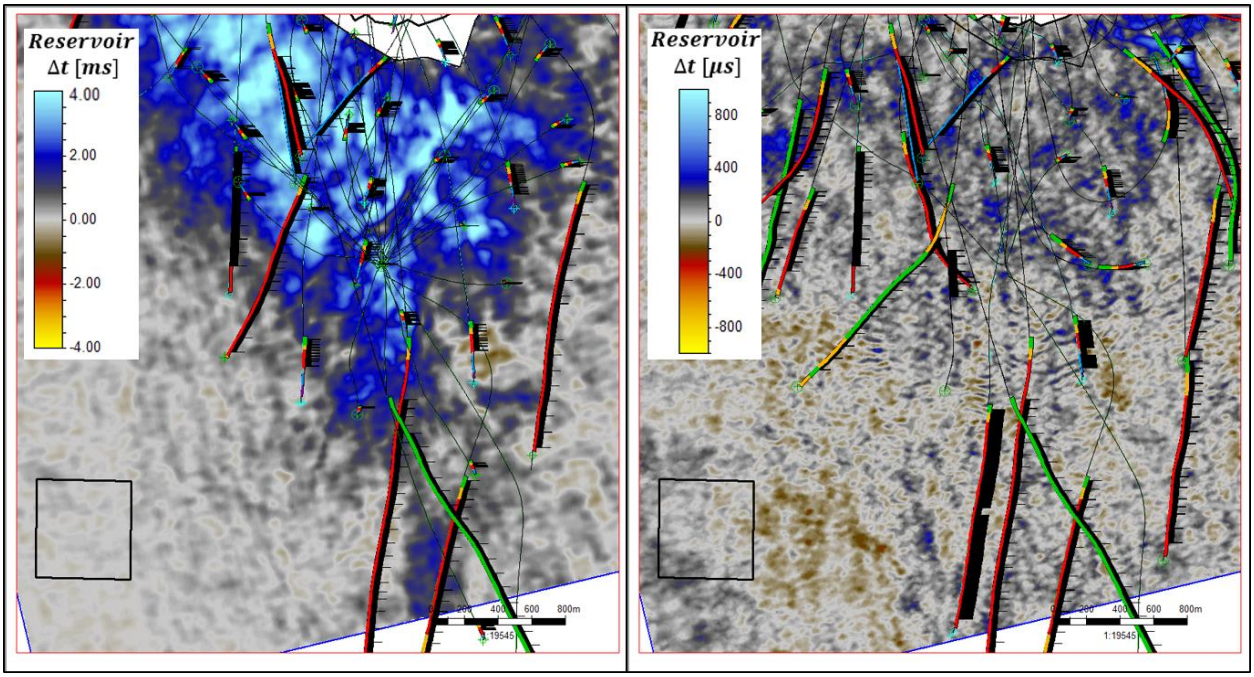

Figure 3.8: An area that is free from production changes is highlighted (in black rectangle) to compute the average background noise for streamer (left) and LoFS (right).

The relationship between reservoir time-shifts and production changes

Here, I will present a general understanding on the relationship of reservoir time-shifts and various production mechanisms in the Ekofisk field as a cross-plot, illustrated in Figure 3.9. In this cross-plot, the X-axis corresponds to the changes in pressure and the Y-axis shows the polarity of the reservoir time-shifts. In the second quadrant, the time-shift signal shows hardening corresponding to a decrease in pressure. This can be caused by one of the following scenarios: a pressure relaxation situation due to a reduction in injection activities or shutting in of an injector, or a pressure depletion such as that from extracting oil from the reservoir. This effect, coupled with water invasion, may lead to water weakening, which is known to result in further compaction of the chalk. The third quadrant shows an opposite polarity, due to pressure reduction, which is a result of pressure going below bubble point resulting in gas exsolution. Fluid replacement of an incompressible oil with highly compressible gas creates significant softening; however, in the case of this reservoir, which is also geomechanically active, this depends on the amount of gas saturation changes and the initial gas saturation, and the amount of pressure drawdown.

The fourth quadrant corresponds to injection into the water leg, which causes pressure increase and a softening signal on 4D seismic data. One way to create an impedance hardening with pressure increase is a change in saturation, such as water replacing oil or gas going back into solution or a combination of both - this is highlighted in the first quadrant. A creep effect takes place when the state of stress in the rock is kept constant but continual deformation is recorded. If 4D responses are expected but none are recorded, this is likely to be due to a cancellation between pressure and saturation changes. My analysis of the data will be based on these general conventions. The undetected 4D seismic signal can also indicate un-depleted regions, which provides infill well opportunities or an absence of reservoir hydrocarbon column or poor reservoir properties. Brain (2017) also discussed other possible explanations for weak or undetected signals such as poor processing workflow. He showed an acquisition consistent approach to statics in the Southern North Sea Rotliegend sandstone reservoir, by using a static solution for each source and receiver combination which slowly varied along sail lines. This reprocessing step has greatly improved the detectability of 4D time-shifts and improved the repeatability.

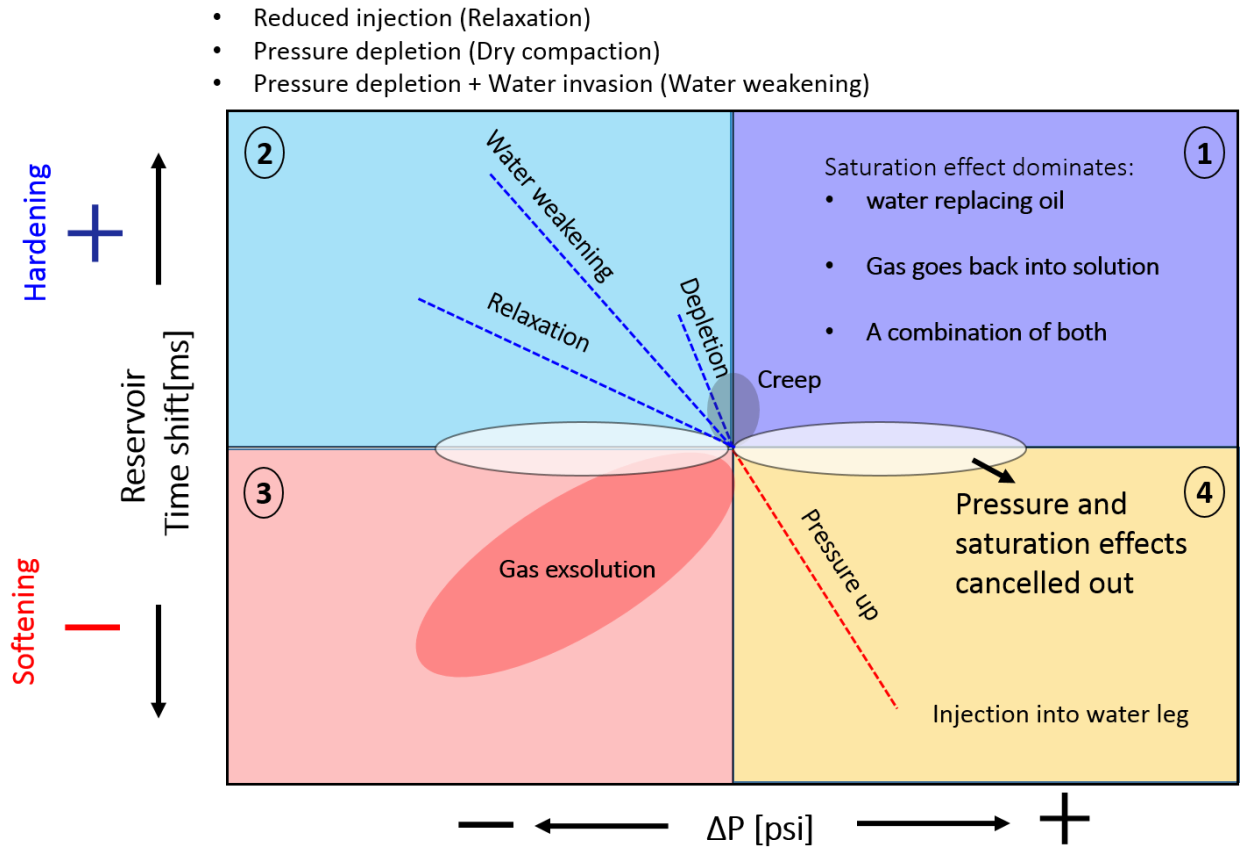

Figure 3.9: Inferred relationship of reservoir time-shifts and various production mechanisms in Ekofisk.

I first look at an injector well I3 across the streamer period in the 20 years from 1989 to 2008, shown in Figure 3.10. Like many other injectors or producers in the streamer period, wells are mostly located in the virgin areas that are pre-water-flood. The water saturation log shows in-situ water saturation of around 5%, hence the influence of saturation in the 4D time-shift signals will be strong once production starts. I created a polygon (shown in Figure 3.10 as yellow box) around the well to extract the average and the standard deviation of the reservoir time-shifts. I then compare the average reservoir time-shifts in the polygon to simulate pressure from the fluid flow simulator.

Recorded data such as the historic tubing head pressure (HTHP) is not used as comparison as it is not representative of the pressure changes in the reservoir. Figure 3.10 shows that as pressure

increases from 1989 to 1999, the reservoir time-shifts recorded a hardening signal of 1.7ms. Likewise from 1999-2003 a surge in pressure shows a reservoir time-shift value of 0.9ms. From 2003-2006 and 2006-2008, a slight drop in pressure resulted in hardening signals of 0.48ms and 0.3ms. We therefore see an anti-correlation between reservoir time-shifts and pressure data from 1989-1999 and 1999-2003. This informs us that during the streamer period, or at least from the period of 1989 to 2003, pressure increase is not the major contributor to the 4D seismic signal: instead the 4D seismic changes are dominated by saturation changes. This is also supported by the water saturation log interpreted at most injector wells, showing water saturation close to connate water saturation at 0.05.

To understand the 4D seismic signal in the LoFS data, I analysed a vertical injector well I8 from the LoFS period (2010 to 2014) where 4D seismic surveys were acquired on average every 6 months; this is shown in Figure 3.11. Similarly, I used a polygon (shown in Figure 3.11 as a black box) to extract the mean and standard deviation values of the reservoir time-shifts around the well of interest. The wells in the LoFS period are mostly water-flooded, hence the 4D seismic signal is interpreted to be pressure driven. The water saturation log of I8 shows that the water saturation is close to $1 - S_{or} - S_{wi}$. Comparing my 4D reservoir time-shifts and the simulated pressure, a good correlation can be observed between the two. As the pressure increases, the 4D reservoir time-shifts shows a softening signal, and between LoFS 5 –6, as the well is shut in, a hardening signal in the time-shifts reflects the pressure relaxation around the well. Between LoFS 3-4, and LoFS 4-5, although the increases in pressure are relatively similar, a much larger 4D response was recorded for the period LoFS 4-5. This is due to the shut-in of a producer well close by, highlighted in yellow. It can be observed that as the producer well is shut in the LoFS 4-5, the hardening signal around it also reduces, due to gradual pressure build up around the producer.

It is appropriate to compare the 4D time-shifts signals to the simulated pressure that has honoured material balance, if no recorded pressure is found at the well. This comparison between streamer and LoFS well activities and their 4D seismic signal signifies the pressure and saturation regimes in these different acquisition periods. The streamer 4D seismic signals are mostly a combination of both pressure and saturation, whereas in the LoFS period, due to wells positioned in post-water

swept areas, the 4D seismic signals are more pressure driven. I carried out the same procedures for all the wells selected for this analysis.

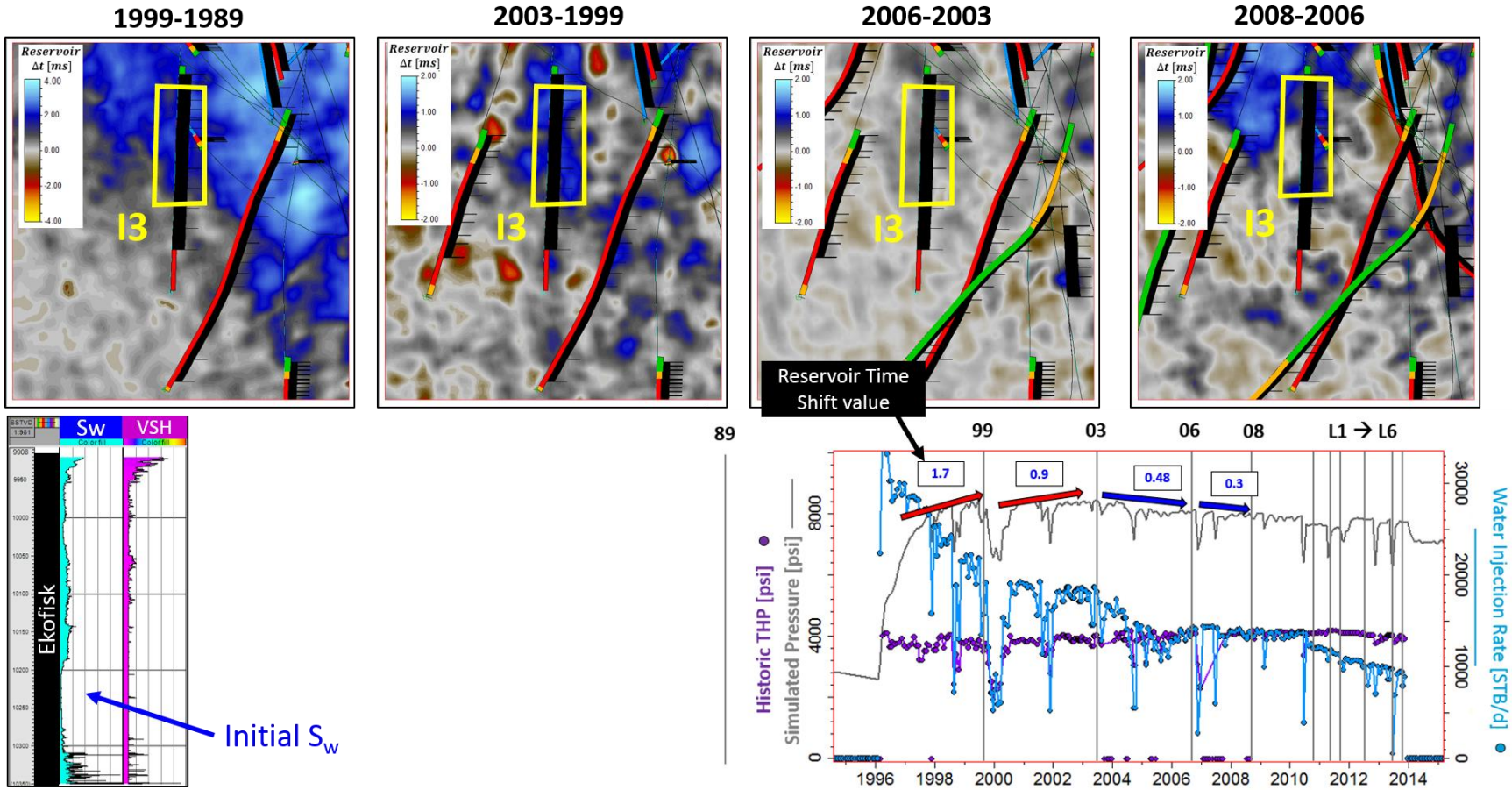

Figure 3.10: Progressive changes in 4D seismic reservoir time-shifts at well I3 as a function of time for streamer data. (Bottom left) Water saturation log of I3. (Bottom right) Historic and simulated production data overlain with reservoir time-shifts values for I3. Yellow box shows the polygon employed to extract time-shifts values from seismic, and water and pressure change values from simulation predictions.

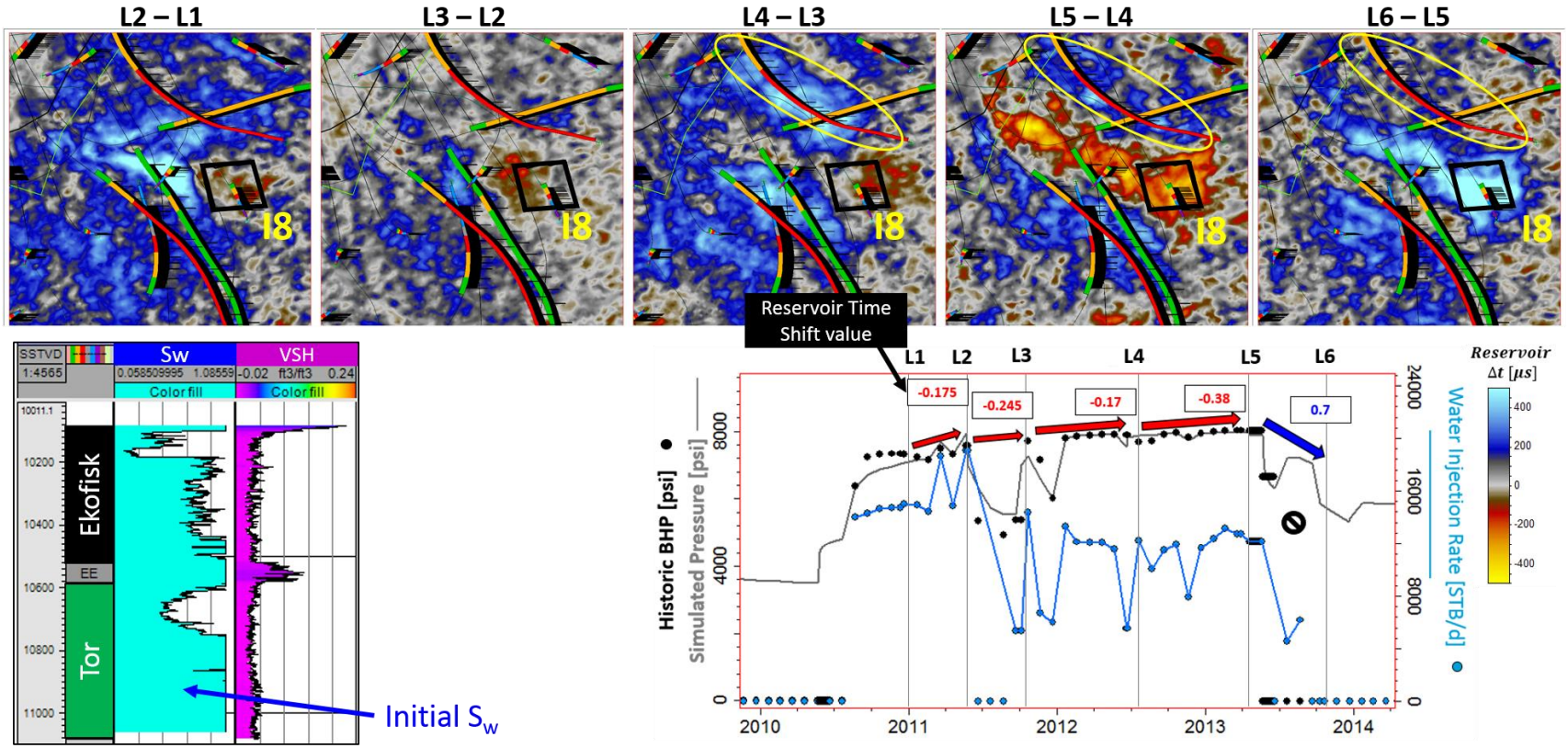

Figure 3.11: Progressive changes in 4D seismic reservoir time-shifts at well I8 as a function of time for LoFS data. (Bottom left) Water saturation log of I8. (Bottom right) Historic and simulated production data overlain with reservoir time-shifts values for I8. Black box shows the polygon employed to extract time-shifts values from seismic, and water and pressure change values from simulation predictions.

3.2.3 Streamer versus LoFS production scenarios

In this section the time-shift information in both the towed streamer and the life of field seismic (LoFS) data in the Ekofisk field are compared. Both data sets exhibit notable differences. Such differences are manifested as a range of different reservoir time-shift magnitudes, spread, repeatability, noise and resolution. By careful selection of the 4D anomalies around a set of producers and injectors, we see a clear evolution of LoFS reservoir time-shifts as a function of pressure change and these signals are more localised, whilst the streamer data reservoir time-shifts portray signals that are more of an intermixture of pressure and saturation changes and the signals are more spread out. This is expected as the seismic data was recorded after a long period of production in the streamer data. These signals are strongly correlated to production mechanisms and the timing of how pressure and saturation propagate in the reservoir. Polygons around the wells are used to extract not only reservoir time-shifts values from seismic data but also water, gas and pressure changes predicted from a well history matched simulation model and pressure values measured at bottom-hole pressure gauges (only available for the LoFS data). For the streamer data period, limited bottom-hole pressure values are available, therefore, only the prediction of the simulation model is employed. Due to the uncertainties in the simulation model predictions, error bars are calculated. Whereas in the LoFS data period, pressure measurements are available from bottom-hole pressure gauges, and no error bars are computed for the measured values. The standard deviation from the various extracted values (seismic and simulation predicted information) defines the error bars and are displayed in Figures 3.12 and 3.13. The noise floor calculated in Section 3.2.2 for both streamer and LoFS data are shown as grey rectangle boxes in both images.

Due to the strong saturation effects in the streamer data, water saturation change is plotted as the primary x-axis, as shown in Figures 3.12 (a) and (b). Two distinctive trends are observed in the cross-plot of reservoir time-shifts versus water saturation changes: the trends are also divided by well types. These trends are characterised by an increase in pressure and water saturation, and a reduction in gas saturation, as highlighted by the arrows along the x, y and coloured axes. The trend on the right is made up of injector wells and the trend on the left are producer wells. The former trend has a larger increase in both pressure and water saturation but the same amount of

gas going back into solution for the same reservoir time-shifts, compared to the producers, suggesting that the effects of pore pressure and water saturation increase cancel out. This interpretation is consistent with our observations since larger water influx is expected at the injector compared to the producer wells. The noise floor is highlighted as a grey box here, as ±0.3ms, any data points that fall within this range will not be treated as data and will be excluded in all analyses.

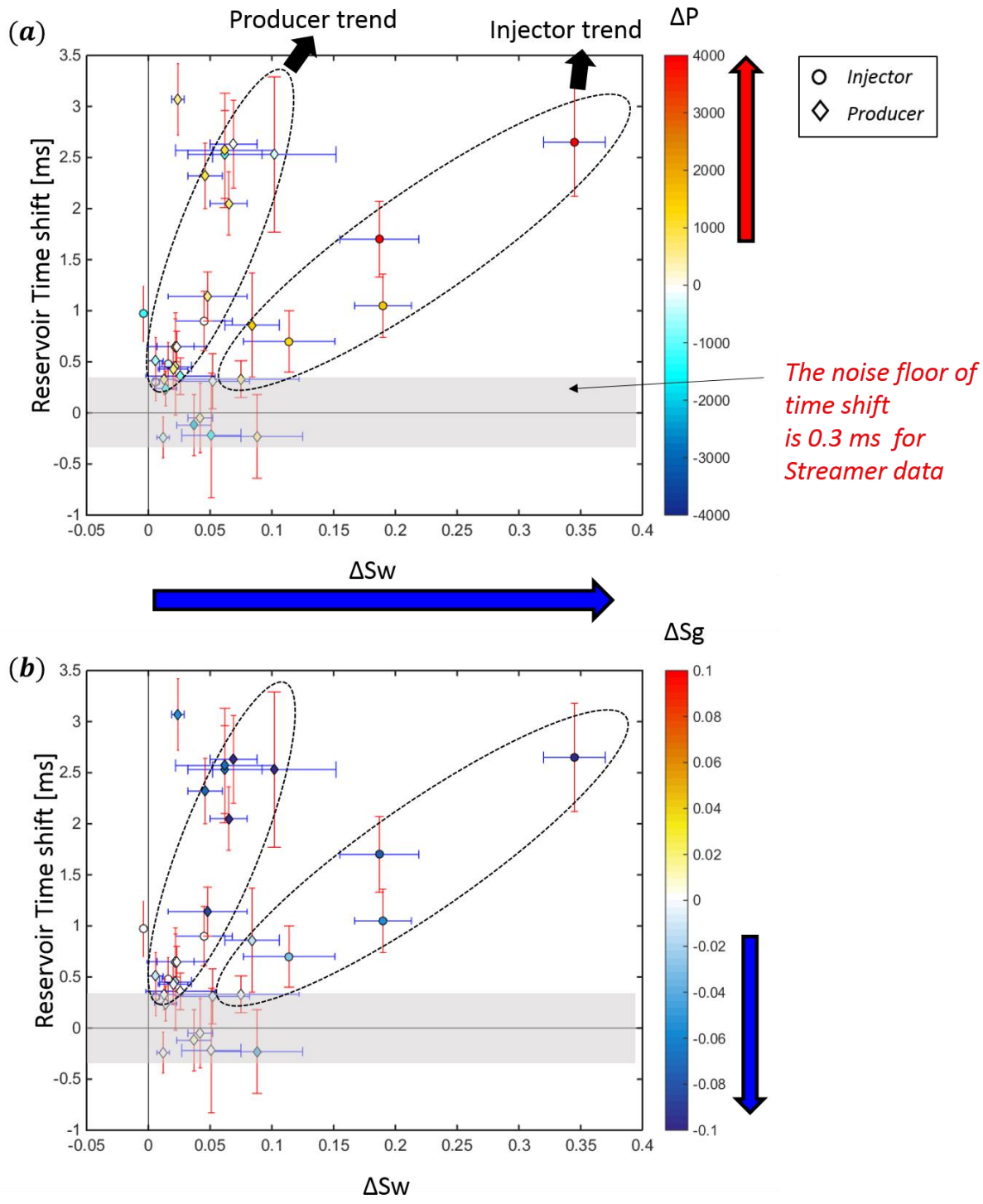

Figure 3.12: Cross-plots of streamer data reservoir time-shifts versus changes in water saturation coloured by (a) pressure change and (b) gas saturation change. Points in producer and injector trends are characterised by an increase in pressure and water saturation, and a reduction in gas saturation.

The LoFS reservoir time-shift data is more pressure driven and by cross-plotting pressure change as the primary X-axis with 4D reservoir time-shifts, in Figures 3.13 (a) and (b), two trends are observed, both from injector wells. The large pressure variation from the injectors shows a relaxation trend and a pressure build-up trend. A cluster of producers shows small hardening signals due to pressure depletion; this agrees with the general observation that a pressure depletion signal is often less observable compared to pressure build-up, and the complexity of interpreting the signal is more due to the interplay of other saturation or geomechanical effects. Pressure depletion below initial pore-pressure is much more difficult to detect, except when associated with reservoir compaction, or with gas breakout below bubble point. My goal here is also to reconcile these reservoir time-shifts using a rock physics modelling approach. These trends are asymmetric, showing that the rock undergoing re-pressurization yields a larger response compared to depletion. Work from Holt, Nes and Fjær (2005) has indicated that during loading the stress sensitivity is significantly less and harder to detect compared to unloading.

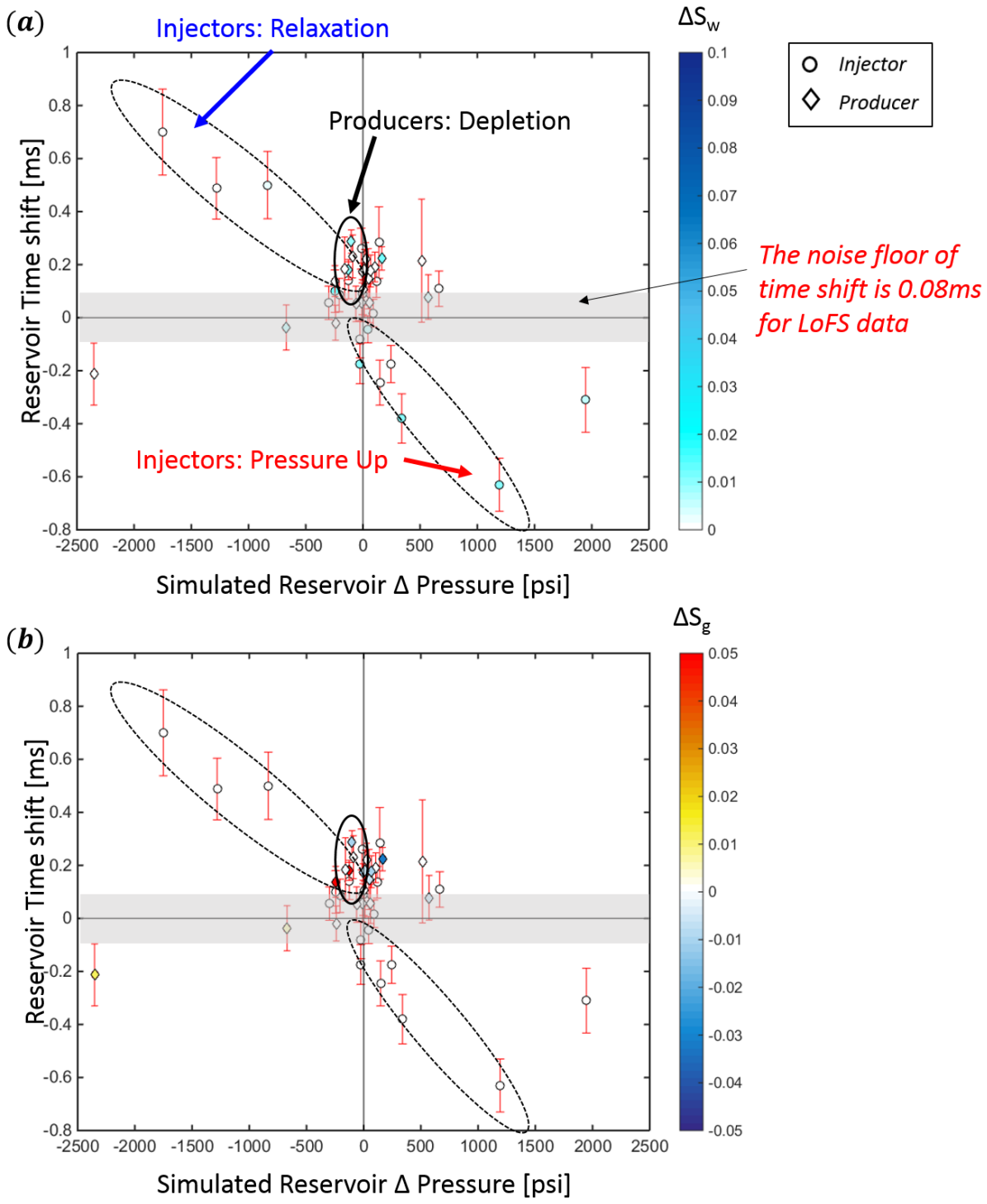

Figure 3.13: Cross-plots of LoFS data reservoir time-shifts versus changes in pore pressure with (a) water saturation change and (b) gas saturation change as the colour axis.

3.2.4 Reconcile observations with rock physics modelling

So far, I have addressed the difference between streamer and LoFS data in terms of the characteristics of reservoir time-shifts and its relations to production mechanisms; and established a working rock physics model for the field of interest. Next, I am interested in reconciling the 4D observed reservoir time-shifts with my modelled estimations using the proposed rock physics model. There appear to be discrepancies between the observed and modelled reservoir time-shift estimates for the streamer data, where the modelled reservoir time-shifts are lower than those observed in the field. In order to paint a full picture on the stress evolution of the rock at the monitor survey of 1999, I will firstly describe production history from the pre-production to the first monitor survey. Prior to the baseline shot in 1989, the reservoir underwent primary depletion without any pressure maintenance efforts which resulted in gas exsolution, high effective stress and compaction of the chalk. In the subsequent 10 years from 1989 to 1999, water flooding was continuously implemented to increase reservoir pressure resulting in large pressure increase, water invasion and gas going back into solution.

I will attempt to model these effects for both producers and injectors from this time period. Cross-sections of the fluid flow simulator with the corresponding pressure and saturation predictions in both 1989 and 1999 are also displayed in Figure 3.14. The location of the injector wells has been highlighted, showing a large pore pressure increase from 3500 psi to 8000 psi, 30% of gas going back into solution, and changes in water saturation as high as 40%, due to the water flooding efforts. Around the producer wells, compaction is expected if the effective stress is high; the compaction is aggravated if the wells are also cutting water, resulting in water-weakening.

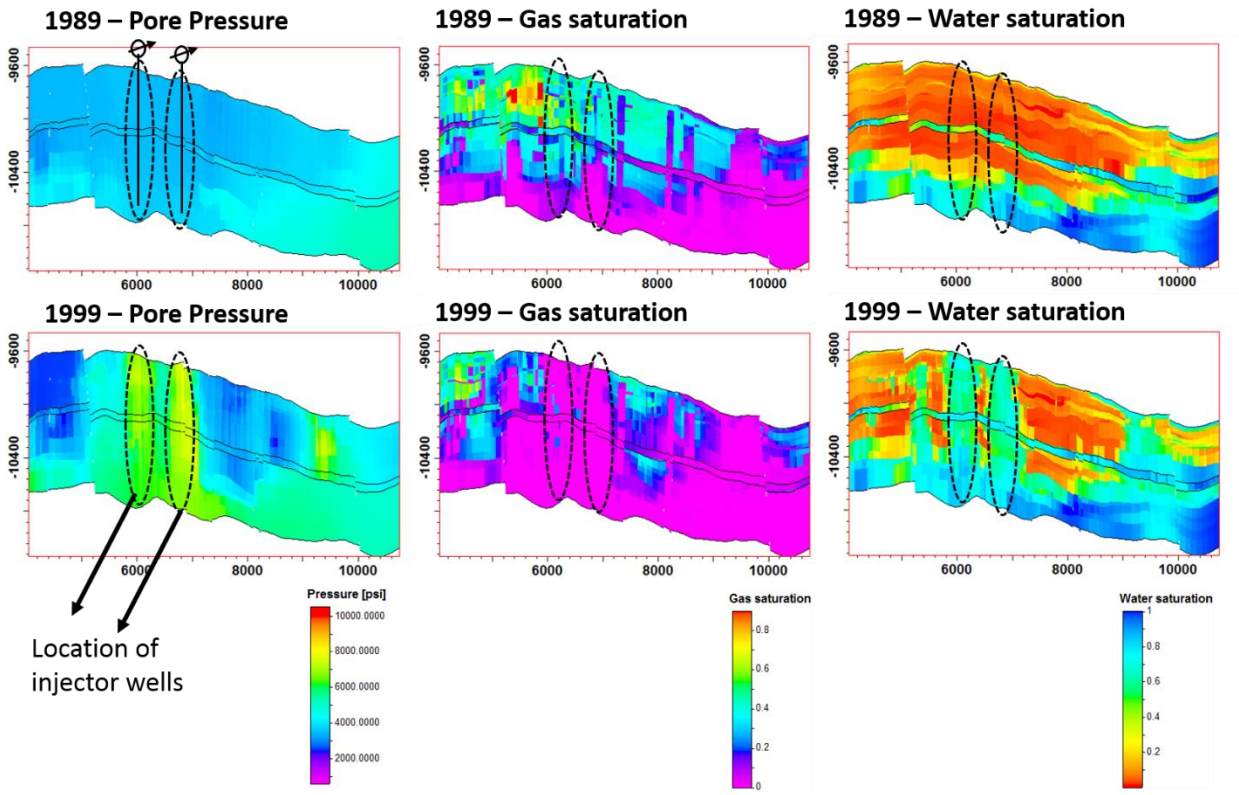

Figure 3.14: Cross-sections of the fluid flow simulator and the corresponding pressure and saturation prediction in both 1989 and 1999.

What happens to the rock as a result of this intermixture of pressure and saturation changes? We can look at this from the perspective of the stress-sensitivity of the rock due to the changes from effective stress. As shown in Figure 3.15, from 1971 (start of production) to 1989, there is 18 years of primary depletion strategy, which resulted in compaction of the chalk, essentially moving the stress sensitivity curve of the rock to a lower porosity curve ($\varphi_{71} > \varphi_{89}$), resulting in a stiffer bulk and shear modulus ($K_{71} < K_{89}$, $\mu_{71} < \mu_{89}$). The initial effective stress is 22.9 MPa in 1971 during pre-production and increased towards 53 MPa due to long period of depletion from 1971 to 1989. From 1989 to 1999, the re-pressurisation programme increased pore pressure in the reservoir to as high as 5000 psi or more. The stress sensitivity of the chalk tends towards a lower effective stress, around 28 MPa, but never return to its initial stress state.

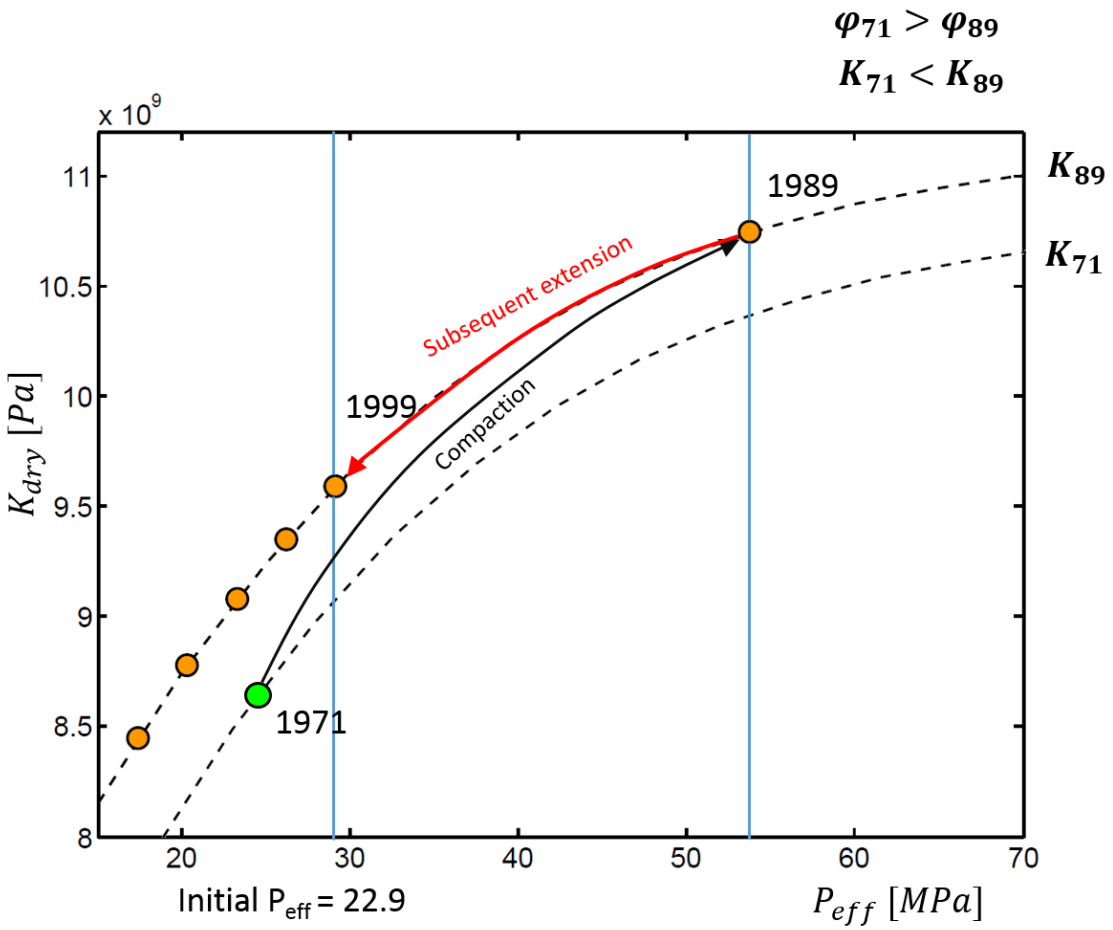

Figure 3.15: Evolution of the dry frame as a function time due to compaction and subsequent extension events. Numbers inside the plot represents the year (1971- pre-production, 1989 – baseline and 1999 – monitor).

3.2.5 Asymmetric relationship between injection and depletion

Figure 3.15 demonstrates an asymmetric relationship of the rock frame between compaction (depletion) and extension (injection). The nonlinear dependence of rocks on stress is generally attributed to the deformation of micro-cracks and pores, grain boundary contacts, and fractures with changing confining stress (e.g. Rutqvist, 1995, Herwanger and Horne 2009). Rock properties also display stress hysteresis (e.g. Helbig and Rasolofosaon 2000, Hueckel et al., 2001, Ferronato et al., 2013) and this hysteresis has been observed to occur not only at large strains but also small strains. The hysteresis behavior observed in the stress sensitivity behavior is also partly attributed to an irreversible compaction. Hatchell and Bourne (2005) shows the crack opening contributes to a much larger velocity-strain coupling coefficient outside the reservoir, this could be an important

rock characteristic in explaining the asymmetric behavior of 4D seismic observations of producing reservoirs. Sayers (2007) points out that the velocity changes depend on the ratio between the variations of horizontal and vertical stress, which are functions of reservoir properties and geometry, as well as of the surrounding formations. It has been suggested that this asymmetry may be due to the different stress-paths followed by the overburden and the underburden (e.g. Sayers, 2007, Scott Jr, 2007). In addition, if the rock fails and enters the plastic regime, as may occur in the reservoir (e.g. Kristiansen et al., 2005, Fjær et al., 2008) then post-failure velocity stress is not a phenomenon that is easily (or usually) measured in the laboratory, and therefore not well understood.

Laboratory experiments (Holt et al. 2008, Holt and Stenebråten, 2013) have shown that a rock that has gone through an initial cycle of depletion followed by re-pressurisation is different or less stress sensitive compared to the same rock undergoing only injection (as shown in Figure 3.16), suggesting possible excess deformation due to internal defects from the first process. The strain sensitivity for the vertical P-wave or dilation factor is shown to be larger in unloading segments than in loading, and also larger during first time unloading than during unloading subsequent to loading. This understanding will be tested in the current dataset, since the production mechanisms in my dataset demonstrate such behaviour. An unloading event subsequent to a loading event is the result of a long period of re-pressurisation from 1989 to 1999, which allows me to calibrate the stress sensitivity parameters using observed time-lapse seismic data, to examine if these parameters should stay constant.

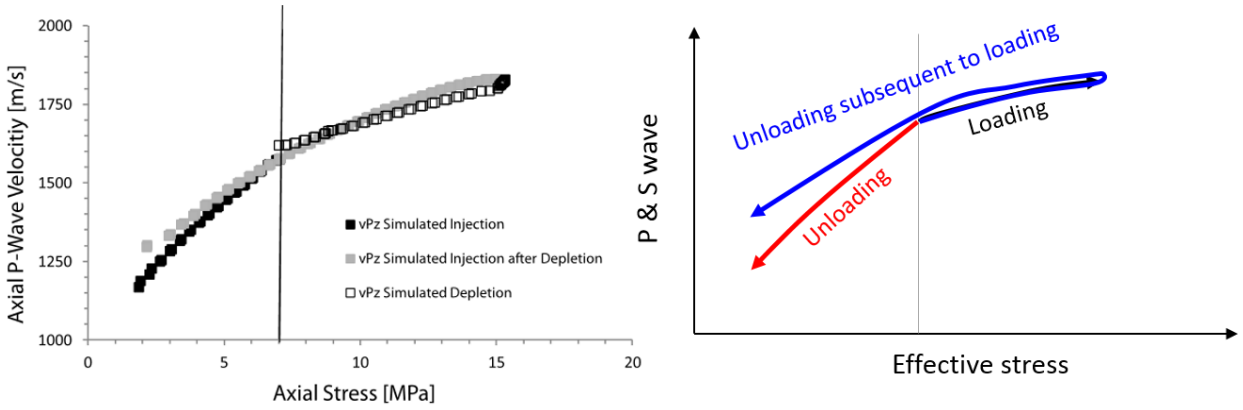

Figure 3.16: (left) Axial P-wave velocity versus axial stress in uniaxial strain test with synthetic sandstone sample for simulated injection and simulated depletion and injection (Holt et al., 2013). (Right) Modified diagram from Holt et al. (2013) showing changes in P and S-wave due to loading, unloading, and unloading subsequent to loading events.

3.3 Calibration of Rock Stress-sensitivity Parameters via 4D Seismic

I modelled the reservoir time-shifts using the initial stress sensitivity parameters calibrated from the laboratory measurements in Chapter 2, where both loading and unloading events employed the same stress sensitivity parameters. Figure 3.17(a-left) shows the stress path taken by the rock during the unloading event from 1989 to 1999, where a decrease in effective stress is shown. Figure 3.17 (a-right) showcases the increase of pressure, on the x-axis, and the changes in saturation, on the y-axis, whereby water increases from 0 to 40% and gas goes back into solution from 30% to 0%. The coloured bar shows red as softening and blue as hardening. The modelled reservoir time-shifts for the producer X is 2.12ms, whereas the recorded reservoir time-shifts is 2.5ms. For the injector W, the modelled time-shifts is considerably lower, at 1.34ms, compared to the recorded time-shifts at 2.65ms. Since this re-pressurisation (unloading) occurred after an event of large pressure depletion (loading), the rock could have undergone pore collapse or closing of internal cracks, and subsequently become less stress sensitive.

To test this, I implemented Holt's asymmetric stress sensitivity unloading parameters into the modelling. Using the 1989 data point and the modified E_k (parameter that controls the intercept) and P_k (describes curvature), we can back-calculate the new bulk and shear infinity (controlling

the curves' asymptote). The Holt's relation E_k and P_k values are 18.7% lower than the initial values calibrated using the rock mechanic tests. I applied these new E_k and P_k values for the unloading and observed an improvement in the modelled reservoir time-shifts, shown in Figure 3.17(b). Since Holt's experiments were carried out on synthetic high porosity sandstone (mechanically similar to shallow, poorly cemented high porosity reservoir sand), which is less relevant to the chalk. The stress sensitivity unloading parameters are further modified to match the observed reservoir time-shifts in Figure 3.17(c). I had to reduce the stress sensitivity by 40% via E_k and P_k values from its initial values in order to match the modelled and observed reservoir time-shifts at both well X and well W. This demonstrates that after taking into account hysteresis in the rock strain, it reduces the overestimation of the softening effect during injection event, and resulted in a better agreement between the observed and modelled reservoir time-shifts.

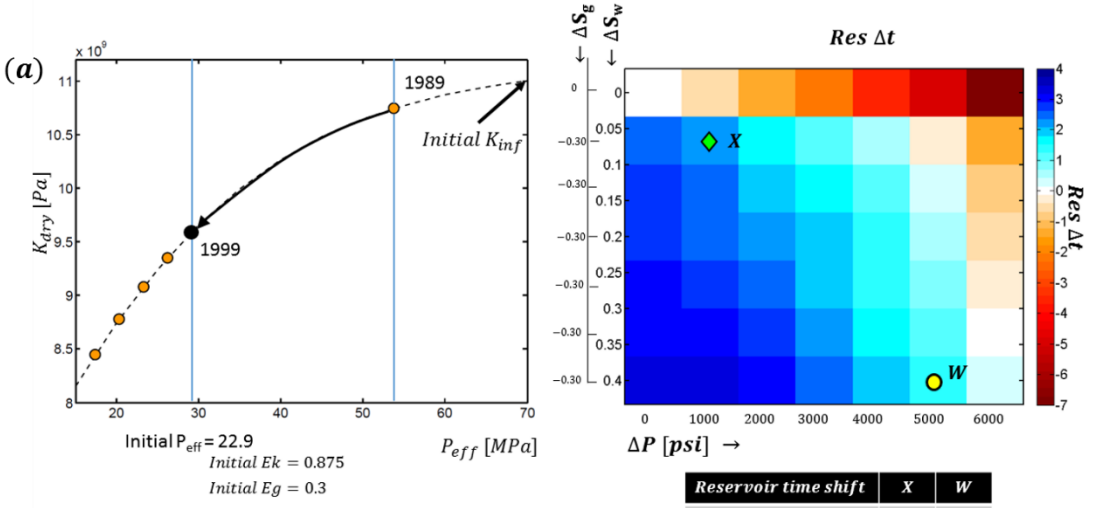

Reservoir time shift	X	W
Measured Δt (ms)	2.5	2.65
Modelled Δt (ms)	2.12	1.34

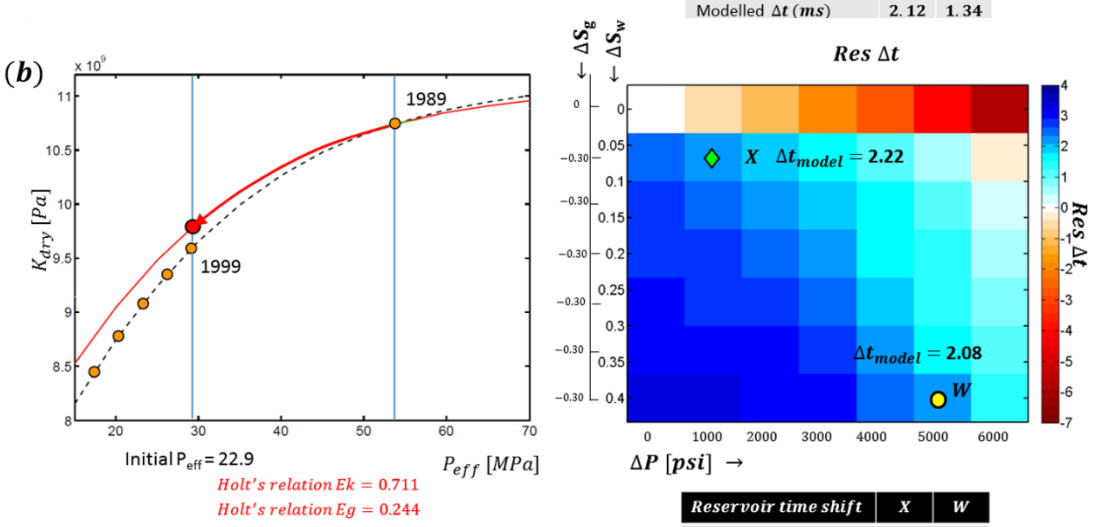

Reservoir time shift	X	W
Measured Δt (ms)	2.5	2.65
Modelled Δt (ms)	2.22	2.08

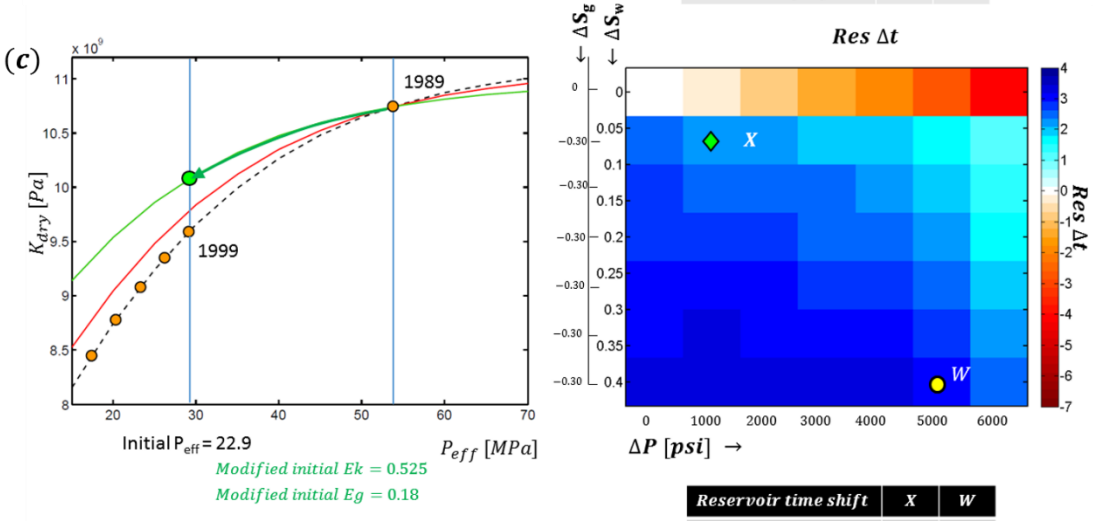

Reservoir time shift	X	W
Measured Δt (ms)	2.5	2.65
Modelled Δt (ms)	2.33	2.95

Figure 3.17: (a,b,c - left) Evolution of dry frame as a function of decrease in effective stress using original, Holt's and the modified stress sensitivity parameters. (a,b,c - right) shows the modelling of reservoir time-shifts for wells X and W using the original, Holt's and the modified parameters. The tables show comparison between observed and modelled reservoir time-shifts for wells X and W for each modelling exercise.

Having successfully reconciled the observed and modelled 4D seismic reservoir time-shifts for the streamer data in Figure 3.17, I carried out the same modelling exercise on the LoFS data. The 4D seismic signals are predominantly pressure driven with small saturation effects. The two pressure effects of interest in the modelling are pressure build up and pressure relaxation, such as those shown in the cross-plots (Figure 3.13 a and b). Two different trends are observed from the data gathered, injector wells show a trend of pressure relaxation, where the reservoir time-shifts indicates hardening when production data shows a drop in pressure. On the other hand, a pressure-up trend shows wells with a pressure increase coupled with reservoir time-shifts showing softening.

The modelling results for re-pressurisation and relaxation for the two selected injector wells are shown in Figure 3.18. My modelling results are consistent with the observed reservoir time-shifts recorded at the wells, in which the unloading (pressure increase) effect caused a stronger 4D reservoir time-shift signal compared to loading (pressure relaxation). Figure 3.18 (left) shows the scenarios of two injectors undergoing pressure increase due to water-leg injection and pressure relaxation due to shut-in of a well. The LoFS modelling result shows agreement with the common understanding that pressure build-up results in a stronger 4D signal than in pressure relaxation or pressure depletion (in the event of no gas exsolution). Some examples from the literature show pore pressure increases induced by water injection into hydraulically isolated compartments or channels (Alsos et al., 2009) with large 4D responses. In comparison to injection, the effects of pore pressure decrease due to primary depletion are less pronounced (MacBeth et al., 2006, Staples et al., 2006).

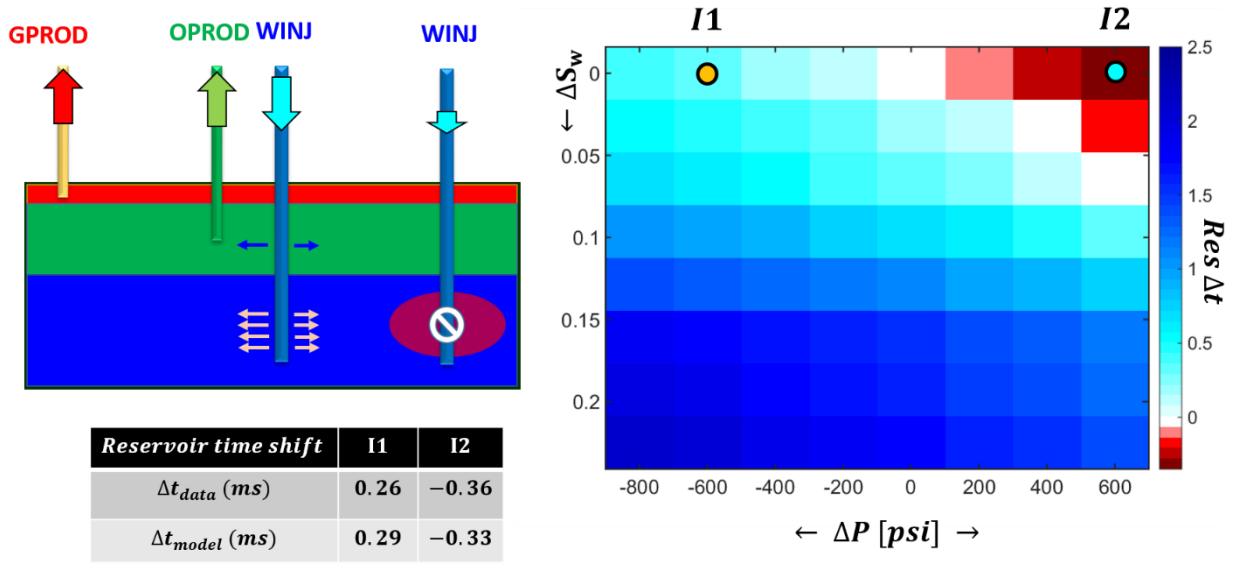

Reservoir time shift	I1	I2
$\Delta t_{data}\ (ms)$	0.26	−0.36
$\Delta t_{model}\ (ms)$	0.29	−0.33

Figure 3.18: (Left) production scenario observed in most wells in LoFS period. (Right) Prediction of reservoir time-shifts as a function of change in pressure and water saturation for injector wells I1 and I2. Table in bottom left shows comparison between modelled and observed values.

3.4 Summary

This chapter has been predominantly about how 4D seismic time-shifts are used for dynamic reservoir characterization, and showcasing in particular how the reservoir time-shifts change as a function of different acquisition strategy. The pursuit of understanding the reservoir level signature is an important one, and to do that, we need to have a good handle on the different parameters that can affect the predictions of the reservoir signals via a rock physics model. Of all the parameters of the petro-elastic model, the rock stress sensitivity is the one which carries the highest uncertainty: the main reason for this is the difficulty of measuring this parameter using core samples. Core damage, frequency dispersion, geomechanical effects and the selection of the effective stress coefficient could lead to underestimation of the rock stress sensitivity, whereas the rock drying processes, the presence of shales, imperfect stress recovery and stress asymmetry could lead to an overestimation. In this chapter, I have shown how hysteresis or imperfect stress recovery could lead to overestimation of the unloading behaviour of the rock, resulting in a lower speed-up estimation for the reservoir time-shift attribute.

I also compared the time-shift information in both the towed streamer and the LoFS data in the Ekofisk field. Due to the advances in technology, the frequency of acquiring seismic for reservoir monitoring and the interplay of different production mechanisms that had taken place across various time periods during field life, the two data sets exhibit notable differences. Such differences are manifested as a range of different reservoir time-shift magnitudes, repeatability, noise and the observable change due to specific petrophysical changes across time. A clear evolution of LoFS reservoir time-shifts as a function of pressure change is observed, whilst the streamer data reservoir time-shifts portray signals that are more of an intermix between pressure and saturation changes. These signals are strongly correlated to production mechanisms and the timing of how pressure and saturation propagate. This understanding is crucial for us to decompose pressure and saturation signals from 4D seismic data. I will describe my efforts to pull apart pressure and saturation changes using synthetic data in Chapter 3 and application on real data in Chapter 5.

CHAPTER FOUR

INVERSION FOR PRESSURE AND SATURATION CHANGES: A SYNTHETIC EXAMPLE

In this chapter, I formulate a new equation to invert for pressure and saturation changes in a thick, compacting, chalk reservoir. This is achieved via synthetic modelling of changes in different dynamic properties such as pressure, saturation and compaction, using the fluid flow simulator ECLIPSE and then translating them into elastic properties using a petro-elastic model. Subsequently, by employing backward engineering, I decompose the composite relative impedance to analyse its individual components and workings in detail in order to then recreate the composite relative impedance using a simpler approximation or a proxy model. Physical phenomena such as water weakening and compaction notorious in chalk reservoirs are accounted for in the proxy model, and also described in this chapter. The validation of the proxy model is carried out in both forward modelling and inversion, and the benefits of incorporating constraints such as engineering concepts and bounding values are also discussed at length.

4.1 Introduction

Chapter 1 introduced various quantitative approaches in estimating the reservoir dynamic properties such as pressure and saturation changes, specifically the use of data-driven proxy models (MacBeth et al., 2006, Floricich et al., 2006, Corzo et al., 2013, Alvarez and MacBeth, 2013). These models relate the changes of seismic amplitude to the changes in dynamic properties. The inspiration to break away from these map-based models arises from their complicated application on the Ekofisk field, which is a thick, multi-cycle, compacting chalk reservoir. This chapter describes the derivation of a more appropriate proxy model, through acoustic impedance and time-shifts.

4.2 Simulation Model Description

We can study fluid movements, pressure propagation rates and drainage patterns using a numerical reservoir model and simulations to evaluate changes in a reservoir during production. I will first describe in detail the characteristics of the Ekofisk reservoir simulation model which will be used to generate synthetic elastic properties to help us to better understand how pressure, saturation and compaction affect the elastic parameters. This model is unique in that it represents the complex dry compaction and water weakening mechanisms that greatly influence how reservoir fluids are produced, injected and affect the rock frame.

The simulation model has 128 x 155 x 22 (436480) grid cells, with an average cell size of 100 x 110 x 45 m corresponding to an area of approximately 11 km x 6 km. The model is built to be consistent with the geological features, flow units and fault planes; hence, the grid uses non-vertical pillars and irregular cells (corner-point geometry (CPG)). The reservoir model has an anticlinal structure. The reservoir is composed of chalk material. The initial porosity ranges between values of 0.02 to 0.48 and the horizontal permeability ranges between 0.0007 to 2000mD and in the vertical direction ranges between 0.00007 to 200mD. The static parameters are well constrained by the large amount of well data. Data from wells and an acoustic impedance background trend were used in the porosity modelling. There are 23 geological horizons and 22 geological layers in the model. The preferential fluid flow patterns and, therefore, the preferential

changes in seismic attributes are influenced by the rock types of the model. The simulation model with all 22 layers of initial porosity is illustrated in Figure 4.1. The fluid properties and initial reservoir conditions are shown in Table 4.1.

The Ekofisk field has a large variability in reservoir quality. The fracture network indicators are characterised deterministically by large amount of data using both static (e.g. fracture distribution) and dynamic observations (e.g. well tests, water breakthrough). The effective permeability model is a combination of two properties: fracture-enhanced matrix permeability and fracture network permeability based on 14 different indicators: interpreted fractures, flow path analysis, distinct water breakthrough, tracer, super tracer, temperature anomaly, pressure supported data, interference test, rapid gas-oil ratio (GOR) increase, mud loss, PLT kick, fracture, fracture cluster and observations from 4D seismic data. These fracture network indicators are mapped directly into the flow simulation grid. This deterministic 3D mapping forms the basis of a high-contrast single porosity and permeability model, which is used as input for dynamic simulation (Tolstukhin et al., 2012).

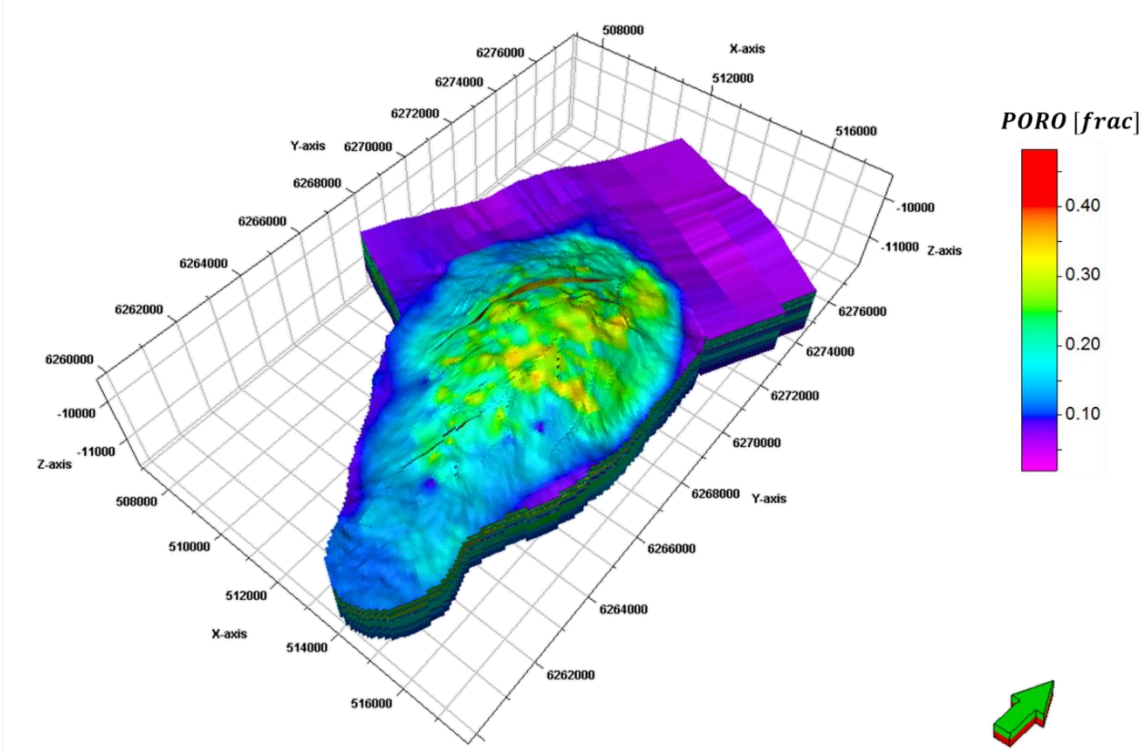

Figure 4.1: The fluid flow simulation for the Ekofisk field with 128x155x22 grid cells in total. High porosity regions are found in the crest of the reservoir.

Property	Description
System	Gas, oil, water, dissolved gas in live oil, vaporized oil in wet gas
Oil gravity (API)	38
Initial reservoir pressure (psia)	7150
Temperature (^{o}F)	268
Gas gravity	0.73
Salinity (ppm)	65,000
Gas density (lb/ft^3)	0.055
Oil density (lb/ft^3)	52.23
Water density (lb/ft^3)	62.37
Residual oil saturation (S_{orw})	0.275
Connate water (S_{wi})	0.05
Residual gas saturation (S_{org})	0.04
Critical gas saturation (S_{gc})	0.36

Table 4.1 Fluid reservoir properties and initial reservoir conditions used in the reservoir simulation.

4.2.1 Rock typing

The modelled porosity, effective permeability and fracture index are used to calculate the eight different rock types in the simulation model, where the function of rock typing is to allocate relative permeability and saturation region information for each of the cells in the model. The model is a single porosity model; hence the fracture or matrix exchange needs to be covered by pseudo relative permeability functions due to the approximation of physics (dual porosity model was not employed) and due to discrepancy in scale (as the reservoir simulation model grid cells are much larger than geological model cells and core samples) as reported in ConocoPhillips Internal Report. The absolute permeability is a property of the reservoir porosity and is a measure of the capacity of the rock to transmit fluids. When two or more fluids flow at the same time, the relative permeability of each phase at a specific saturation is the ratio of the effective permeability of the phase to the absolute permeability (Ahmed, 2010). The same rock type can have varying porosity and permeability but correspond to the same relative permeability curves. The mapping criteria for the eight different rock types are shown in Table 4.2 below:

Rock Type	Effective permeability		Porosity Description	
20	>100mD	Thief zone	No collapse	
18			Collapse	
16	>15mD	Fractures	>32%	High porosity
15			<32%	Low porosity
14	5mD> & <15mD	Intermediate	>32%	High porosity
13			<32%	Low porosity
12	<5mD	Matrix	>32%	High porosity
11			<32%	Low porosity

Table 4.2 Rock types in the Ekofisk field are divided based on the effective permeability and porosity.

Major fracture corridors along the faults with effective permeability greater than 15mD are categorised under rock types 15 and 16, whereas the background matrix is mostly described by rock types 11 and 12. Rock types 18 and 20 are thief zones, which are horizontal permeability conduits which contribute to early water breakthroughs in producer wells. The rock types are shown in Figure 4.2, where majority of the cells are described as matrix.

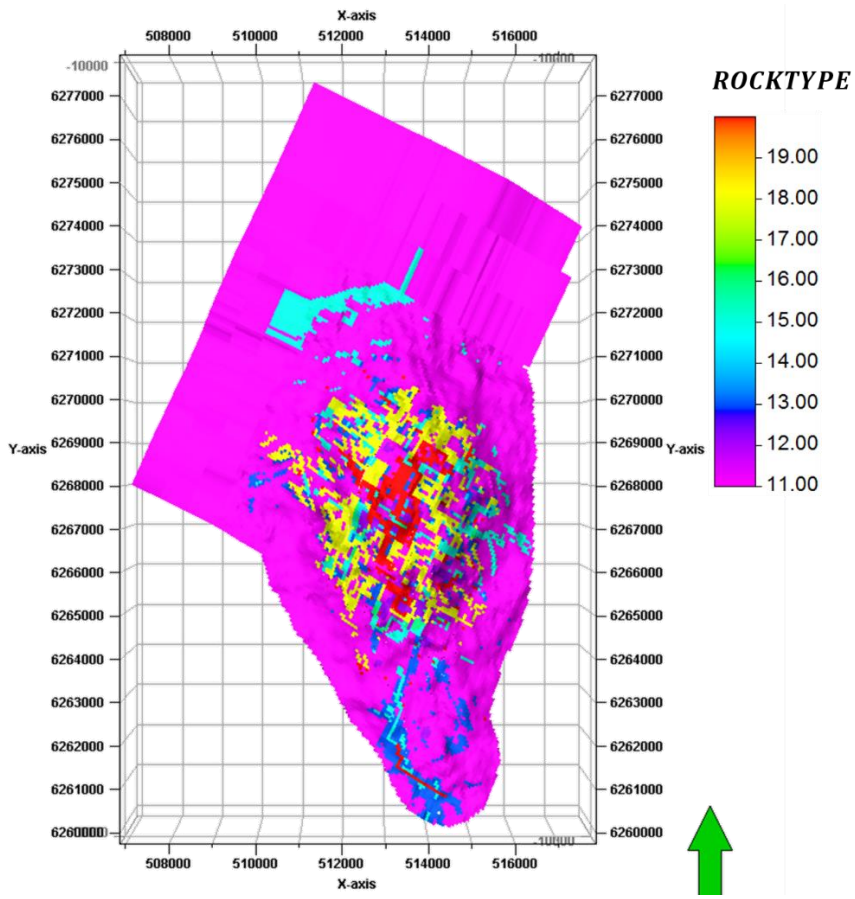

Figure 4.2: A map view of the Ekofisk simulation model (layer 11) coloured by rock types. Fractures are highlighted as cyan.

4.2.2 Geomechanical changes handled by reservoir simulation

The water weakening phenomenon was widely studied in the 90s, with many notable publications (Newman, 1983, Schroder and Shao, 1996, Delage et al., 1996, Risnes and Flaageng, et al., 2004, Risnes at al., 2005, Austad et al., 2008). The change in pore volume has been shown in laboratory experiments where the rock compacts as a function of increase in effective stress, rocks that are more porous also underwent more dramatic compaction gradient than less porous chalk. According to the compaction model (Sylte et al., 1999) provided by the operator (ConocoPhillips), porosity rebound does not occur due to unloading events. This means the rock behaves in an inelastic manner, even after pore pressure has increased to its initial condition. The same relations also apply to the relationship between permeability and stress: for less porous chalk, there is no change in fracture conductivity or matrix permeability as effective stress reduces in the reservoir. Porous

chalk will undergo a more severe reduction in permeability in the presence of water coupled with pressure depletion compared to only pressure depletion. The dry compaction and water weakening mechanisms are incorporated into the simulation by using the keyword 'ROCKCOMP' in ECLIPSE. The compaction tables are read into the simulator using the 'ROCKTAB' keyword.

4.3 Dry Compaction and Water Weakening

Dry compaction is where the rock reduces in pore volume when the fluid pressure falls or the effective stress increases. This behaviour can have both positive and adverse effects on the reservoir, such as adding significant energy to the reservoir but also causing massive compaction which translates into subsidence of the seafloor. However, some rocks, typically chalks, will exhibit additional compaction when the water meets oil bearing rock, even at constant stress. Laboratory work by Newman (1983) and Loe et al. (1992) on North Sea chalk showed immediate and dramatic weakening of water-free chalk when injected with sea water. From the work of Smith et al. (2002), based on an extensive database of chalk core measurements, it has been shown that the pressure drawdown mechanism or dry compaction creates a gentler compaction trend compared to water weakening, at the same effective stress. It also showed that both compaction mechanisms are weaker for chalk with lower initial porosity.

Laboratory tests also indicate that the relative amount of water weakened chalk is a linear function from zero water saturation to the critical water saturation, which is when the entire matrix is fully water wet and the chalk is fully water weakened. The critical water saturation or the maximum attainable water saturation (S_{wmax}) has been determined as 0.325 in the Ekofisk field (Smith et al., 2002), although it was initially reported to be 0.25 (Sylte et al., 1999). The rock is known to be 'fully-wetted' when the maximum water saturation is reached, as shown in Figure 4.3. The chalk does not need to be saturated at 1-S_{orw} (residual oil saturation) to be consider fully wetted. The fully wetted stage is when the chalk undergoes maximum compaction after water invasion from 0 to 33% at a given effective stress for a specific porosity. The maximum attainable water saturation (S_{wmax}) is unique to the water weakening phenomenon. The deformation mechanisms described here are paramount in capturing the changes of porosity as a function of effective stress and changes in fluid composition. The effects of water weakening are first visible in samples of

oil saturated chalk appear to be 2-3 times as strong as water saturated samples (Risnes and Flaageng, 1999), as illustrated in Figure 4.4. This further complicates the stress-strain behaviour of chalk, as samples with the same porosity, will display different curves for different water saturations (shown in Figure 4.5).

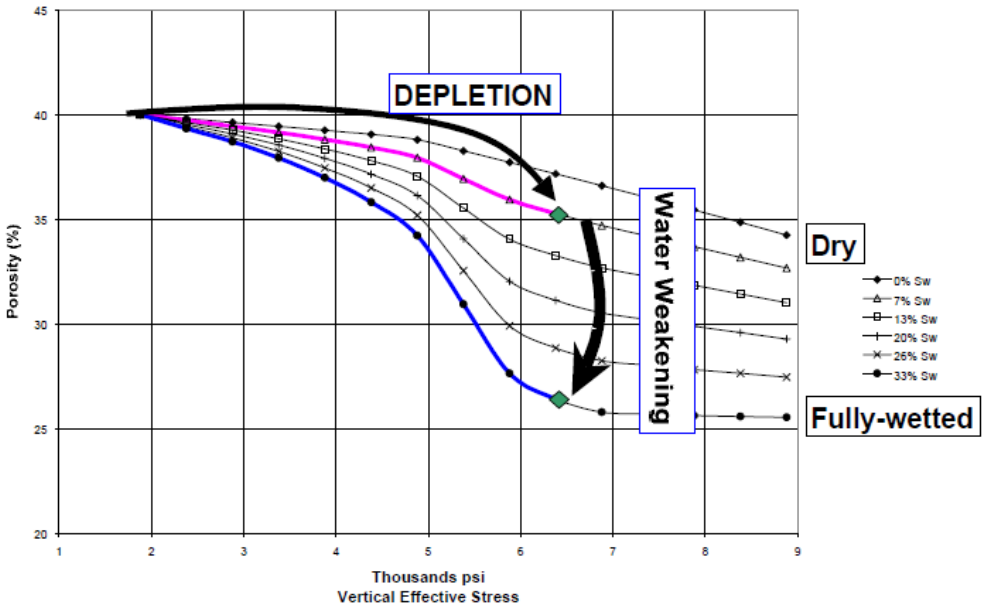

Figure 4.3: Porosity reduction is more dramatic in the event of water weakening compared to dry compaction (Smith et al., 2002).

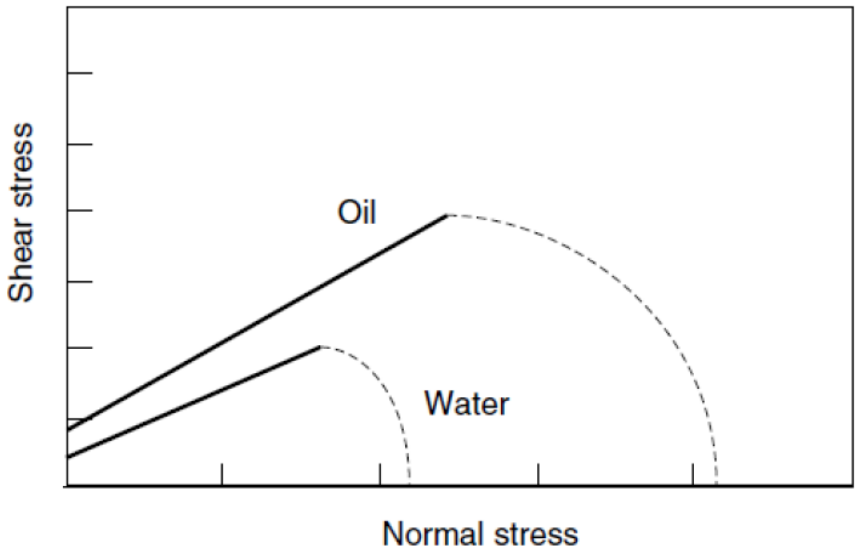

Figure 4.4: Illustrated in Risnes and Flaageng (1999), showing the Mohr-Coulomb failure diagram for both oil and water saturated chalk samples.

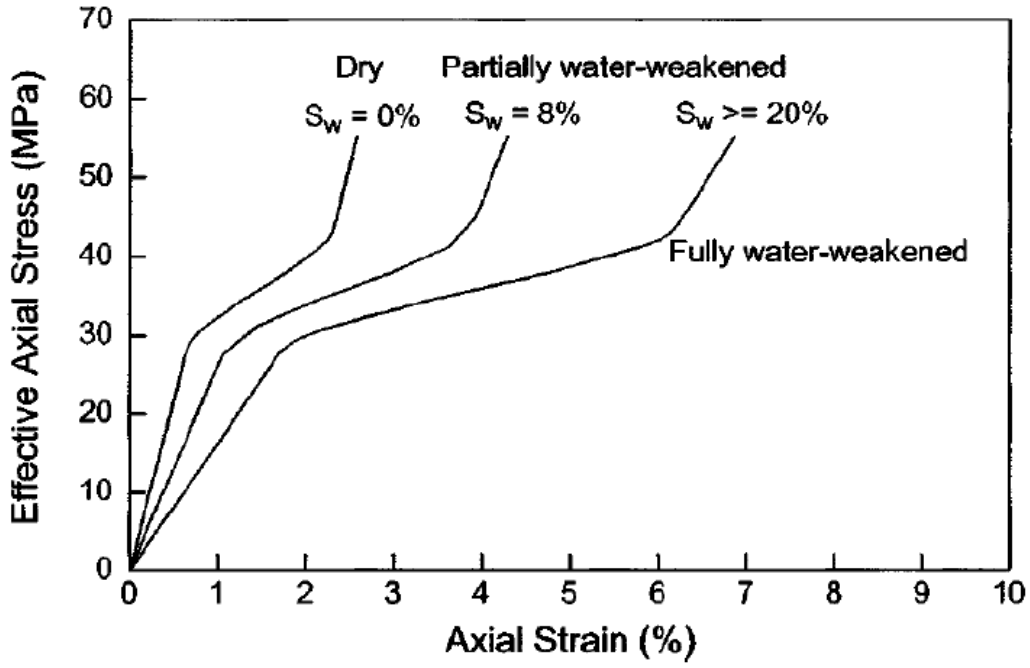

Figure 4.5: Stress and strain relationship as a function of water saturation for a sample with 36% initial porosity of a chalk sample. A fully water weakened chalk shows higher strain at the same stress level compared to a dry chalk (Chin and Nagel, 2004).

4.4 Separating Pressure and Saturation changes in a thick versus thin reservoir

In this section, I outline how the thickness and heterogeneity of the reservoir determine techniques carried out in 4D seismic data interpretation, and more importantly, in efforts to separate pressure and saturation changes. I will also explain some of the advantages of working in the impedance domain instead of the reflectivity domain. Figure 4.6 shows a spectrum of the different types of reservoir from ultra-thin to thick, heterogeneous, compacting reservoirs. My field of interest, Ekofisk is categorised under thick, heterogeneous and compacting reservoirs, similar to reservoirs such as Luconia, Sleipner and the Dan field. The reservoir thickness is determined by the tuning thickness, which is one-quarter wavelength. The limit of separability of bed thickness depends on the velocity at reservoir interval and dominant frequency.

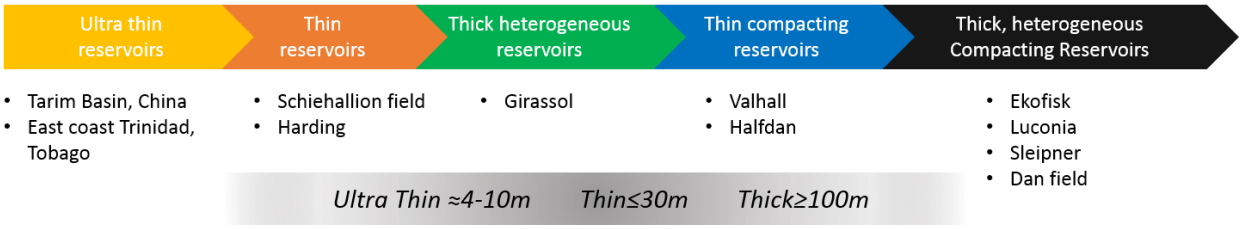

Figure 4.6: Different reservoirs categorised based on reservoir tuning thickness and heterogeneity.

Two synthetic examples are generated to demonstrate why impedance are the most suitable attributes to decompose pressure and saturation signals for a thick and heterogeneous reservoir as compared to seismic amplitude. In the first case, shown in Figure 4.7, I modelled a thin reservoir with an injector injecting water into an oil leg, and observed an intermixture of pressure and saturation changes in the compartment. The change in pressure is assumed to be 1000psi and the change in water saturation is 30%. The reservoir is thin; hence the gravitational effects of fluids are less apparent. As shown in Figure 4.7 (a) and (b), pressure diffuses across the entire reservoir and water slumps due to the gravitational effect. Assuming there is a producer up dip of the injector (a typical scenario), the pressure gradient is shown in Figure 4.7(b), and water is shown to have migrated towards the producer, potentially with water coning around the producer. The pressure effect is more dominant than saturation changes; therefore, an overall decrease in impedance of -3% is observed at the injector based on rock physics modelling.

The seismic profile in Figure 4.7(c) at the injector well shows the quadrature phase (-90^{o}) amplitude of the baseline (the blue trace) and of the monitor (the red trace). The dashed black line is the difference in amplitude of the quadrature phase before warping, and the solid black line is the time aligned quadrature phase difference in amplitude, which shows a negative value. In the case of any zero-phase data, the energy peaks at interfaces, which are at the top and bottom of the reservoir. The reason I convert seismic difference to quadrature phase (-90^{o}) is to display the energy difference within the reservoir interval, and it is also useful for facilitating volume-based interpretation techniques (Johnston, 2013).

From a map view of a seismic attribute such as the difference in root mean squared amplitude shown in Figure 4.7 (d), it can be seen that both top and base of the reservoir show a softening

response and it will not be possible to separate these changes easily. If the reservoir is thinner than tuning thickness, the base of the reservoir might not be resolved. If there is prior knowledge that the injection is in an oil leg and not the water leg, such that the depth of the original oil-water contact is known, it can be inferred that the softening is attributed to a combined effect of both pressure and saturation. Moreover, if the reservoir corresponds to a half cycle of the seismic amplitude, these softening responses can be mapped spatially. In the case in point, I cannot proceed further in terms of separating pressure and saturation solely by analysing the amplitude difference, unless I invert the amplitude difference to impedances and subsequently carry out a rock physics transform to separate the individual dynamic properties.

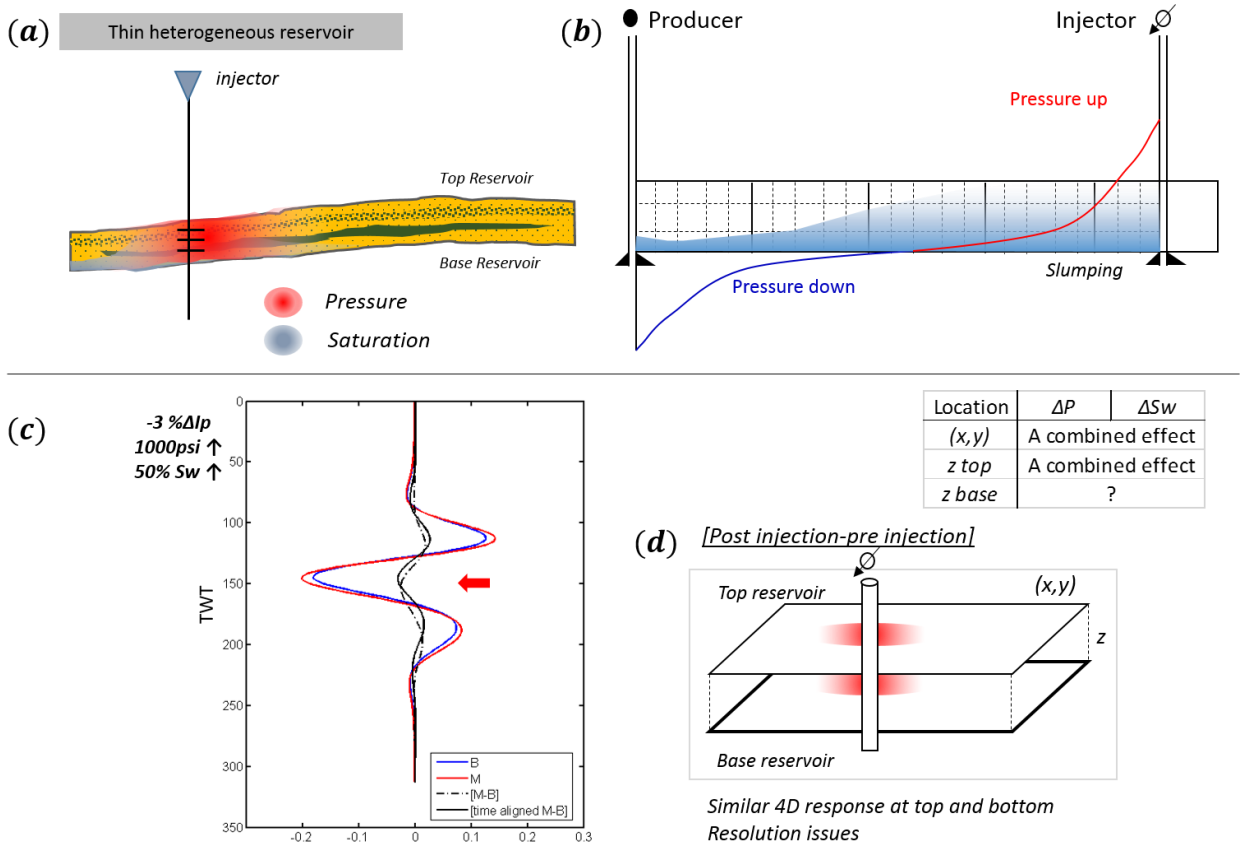

Figure 4.7: (a) A cross-section of a thin heterogeneous reservoir with an injector providing pressure maintenance into the oil leg. (b) Pressure profile from a producer (up dip) to the injector in (a). (c) Seismic trace profile at injector location. (d) Showing 4D response if a dRMS map of the reservoir is made between baseline and monitor.

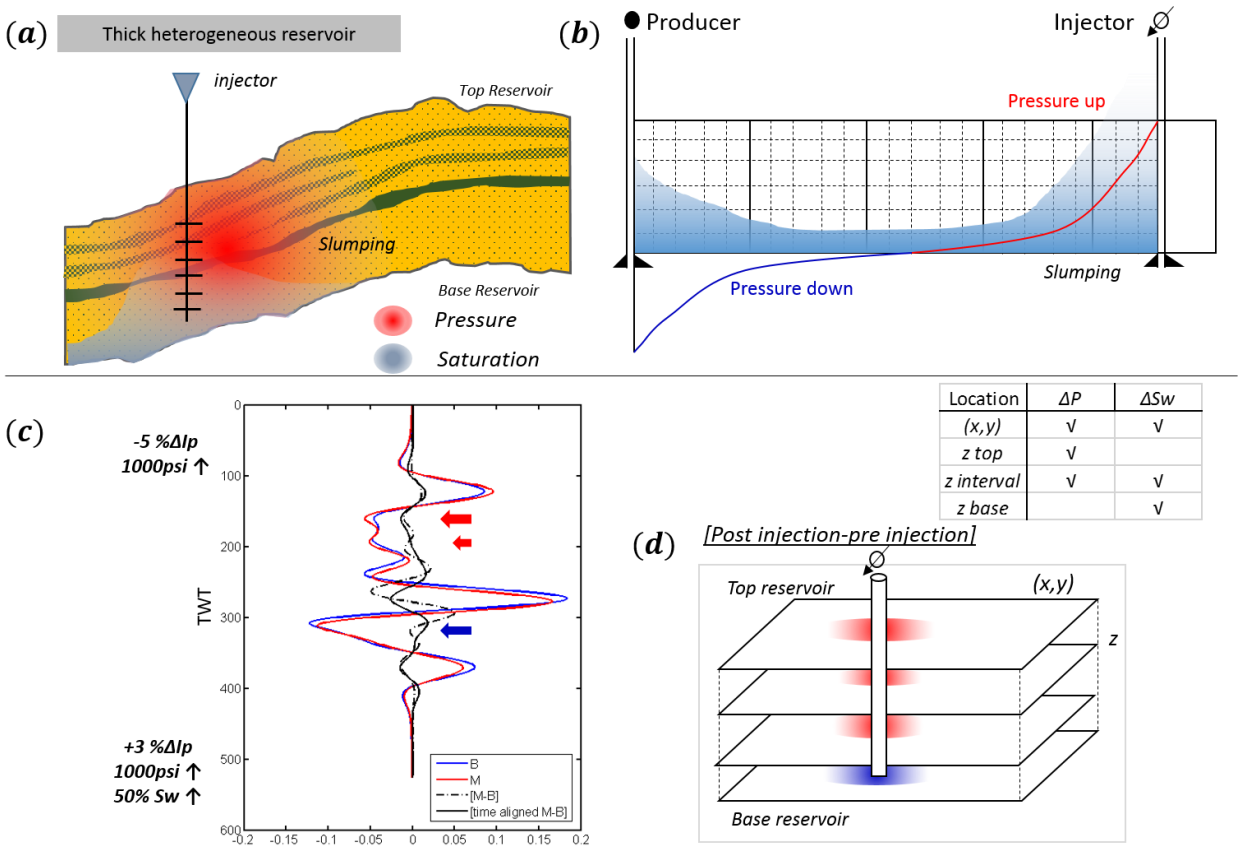

Figure 4.8: (a) A cross-section of a thick heterogeneous reservoir with an injector providing pressure maintenance into the oil leg. (b) Pressure profile from a producer (up dip) to the injector in (a); the slumping effect is more prominent compared to a thinner reservoir. (c) Seismic trace profile at injector location. (d) Showing 4D response if a dRMS map of the reservoir is generated at different intervals between baseline and monitor.

With a thick and heterogeneous reservoir, for which there is potentially a vast amount of information, it is apparently more complicated to interpret the seismic anomalies, and the same anomalies can be explained by many different production mechanisms. In Figure 4.8 (a), using the same example as the thin reservoir with an injection into the oil leg, a different anomaly is observed. I assumed a greater gravitational effect in the thick reservoir, where a longer transition zone exists between oil and water, as shown in Figure 4.8 (b). Again, assuming a producer up dip of the injector, we expect to see slumping of the heavier reservoir fluid (water) at the injector well, and water coning at the producer well. Of course, the coning is subjected to production rate at the well. On the other hand, we expect pressure to diffuse uniformly throughout the reservoir interval.

The top reservoir therefore will have a stronger pressure signal compared to the bottom of the reservoir, because the water coning effect is stronger at the base of the reservoir. In the thick, heterogeneous reservoir, I can observe both the changes in pressure and saturation, spatially, and also the vertical extent of the injection. This is due to the varying impedance contrast of the different chalk layers, which is an intrinsic property of the rock, like porosity and permeability. Figure 4.8 (c) shows the quadrature difference as a solid black line. A softening signal (negative amplitude difference) near the top of the reservoir is observed, whereas a hardening (positive amplitude difference) is observed at the base of the reservoir. Both of these signals are highlighted by the red and blue solid arrows. These are genuine signals caused by dynamic changes. The hardening and softening responses in the middle of the reservoir are due to side-lobe interference.

In multiple stacked reservoirs similarly to those demonstrated in this synthetic example, the side lobes can interfere with or be confused with the primary difference signal. The solution for such quadrature shortcomings is 4D model-based stochastic seismic inversion. Although I cannot accurately separate the pressure and saturation signals within the reservoir completely, it helps us to interpret the vertical extent of the water propagation, based on the polarity of the amplitude difference. More sophisticated methods, such as impedance inversion will be required to ultimately separate both of these effects. If I tackle this problem from a map-based method, as illustrated in Figure 4.8 (d), different responses will be seen at distinct interfaces of the reservoir. The separation of pressure and saturation is case-dependent with this type of reservoir, such that the top reservoir and perhaps the intra-reservoir layer will yield softening responses due to pressure and the base reservoir shows hardening due to water saturation. This interpretation strategy is also applied in the Andrew field. From the 4D difference cross-section in Figure 4.9(a), the extent of gas and water changes can be visually inferred from the polarity alone. 4D water and gas migration maps were computed by summing the positive and negative differences across the oil column (Trythall et al., 2003). The map generated for the top reservoir in Figure 4.9(c) shows gas saturation changes based on the softening signals and vice versa for the map generated from the base of the reservoir, shown in Figure 4.9(b), where hardening is correlated to water injected.

In the case of Sleipner, due to the nature of the reservoir with many intra-reservoir shales in the Utsira sandstone, the extensive propagation of gas was effectively revealed by the shales when the

gas was trapped beneath thin shale layers. Thus, the thick, intra-shale reservoir enabled the successful qualitative monitoring of the migration of carbon dioxide gases (Figure 4.10). Thus, there are also many advantages to a thick, heterogeneous reservoir and careful interpretation can help us to gain insights into the dynamic changes of the reservoir without impedance inversion, to a qualitative extent. However, due to the interference of side-lobes and without prior knowledge regarding the geology, it will be difficult to interpret the seismic anomalies, it is henceforth beneficial to use a layer property such as impedance instead of an interface property like amplitude.

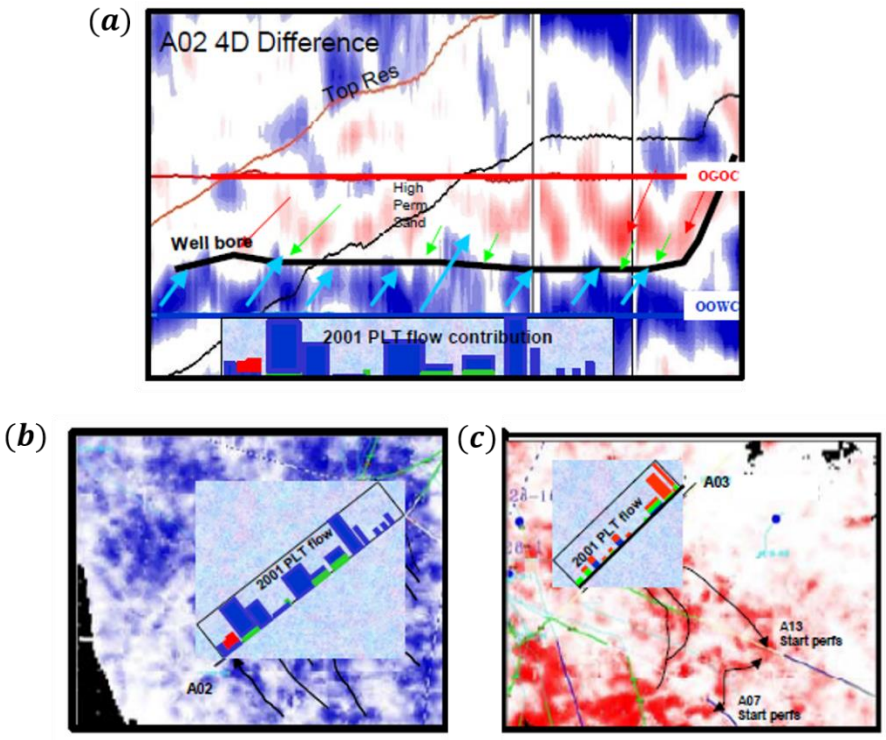

Figure 4.9: (a) Showing the 4D difference in the Andrew field, with good correlation with PLT flow; large scale increase in impedance (blue) from the OOWC shows water fingering. (b) and (c) are maps generated to map water and gas differences between baseline and monitor by summing the positive and negative differences across the oil column (Trythall et al., 2003)..

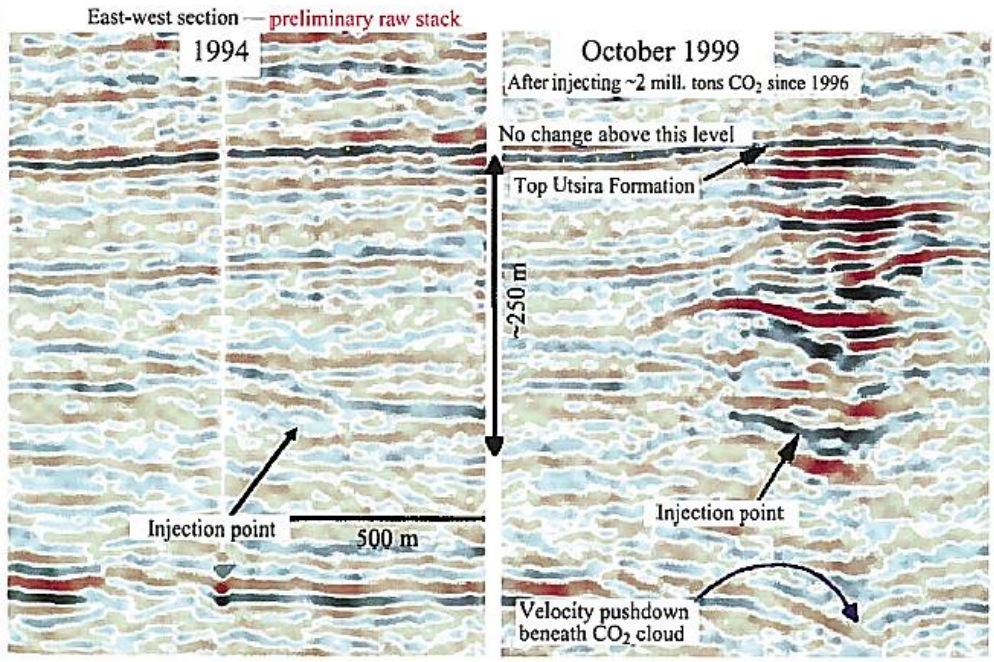

Figure 4.10 Left: showing raw stack seismic data of the Sleipner field in 1994. Right: showing the seismic event at monitor time in 1999, where velocity pushdown beneath the injection point can be seen, and many constructive and destructive events above the injection point, due to the shale intervals in the Utsira formation.

4.5 Pressure and Saturation Sensitivity on Elastic Properties

In this section, I will present the responses in various elastic properties influenced by primary production mechanisms in the Ekofisk field, modelled for the LoFS surveys. This sensitivity analysis was carried out to understand the different production mechanisms in isolation, particularly for pressure, saturation and porosity changes. The modelling was carried out for a chalk sample with an average porosity of 35%, with no shale content at a burial depth of 3100 metres (top reservoir). The synthetic time-lapse response in Figures 4.11 and 4.12 are generated using the calibrated rock physics model described in Chapter 2. Figure 4.11 shows that compaction resulting from water weakening and water flooding has the highest impact on P-wave and S-wave velocity changes. The water weakening behavior in Figures 4.11 and 4.12 are modelled by only considering porosity reduction due to changes in pore pressure, without taking into account of the changes in elastic properties due to water saturation changes. Smaller changes are observed due to dry compaction and pressure build-up. Unlike other clastic reservoirs, where pressure depletion in the oil leg is often not detectable above noise, in the Ekofisk field, the pressure depletion is coupled with porosity reduction; hence pressure depletion is often associated with a strong hardening signal. This, of course, depends on the pressure draw-down and the initial porosity of the rock. Figure 4.11 show how changes in P-wave velocity correlate well with compaction and saturation changes, whilst changes in S-wave velocity largely depend on pore pressure perturbation.

Similar observations are made for time-shifts, and the percentage change in P-impedance, compaction due to water weakening and sole water saturation changes plays a major role in increasing both of these attributes, as shown in Figure 4.12. Dry compaction, pressure build up and gas coming out of solutions present weaker signals in both the relative change of P-impedance and in time-shifts. In these plots, changes in time-shift and impedance due to gas saturation increases are not predicted to be as large as the changes induced by compaction or water saturation alone. This is because the initial gas saturation is already quite high (10%) in the LoFS surveys, therefore the non-linear portion of the property versus saturation behaviour curve is not accessed. Based on the prediction from the fluid flow simulator, the gas saturation increase is minimal in the LoFS period, around a fraction of 0.3. These plots are useful to help in understanding the time-lapse signals measured from the LoFS surveys.

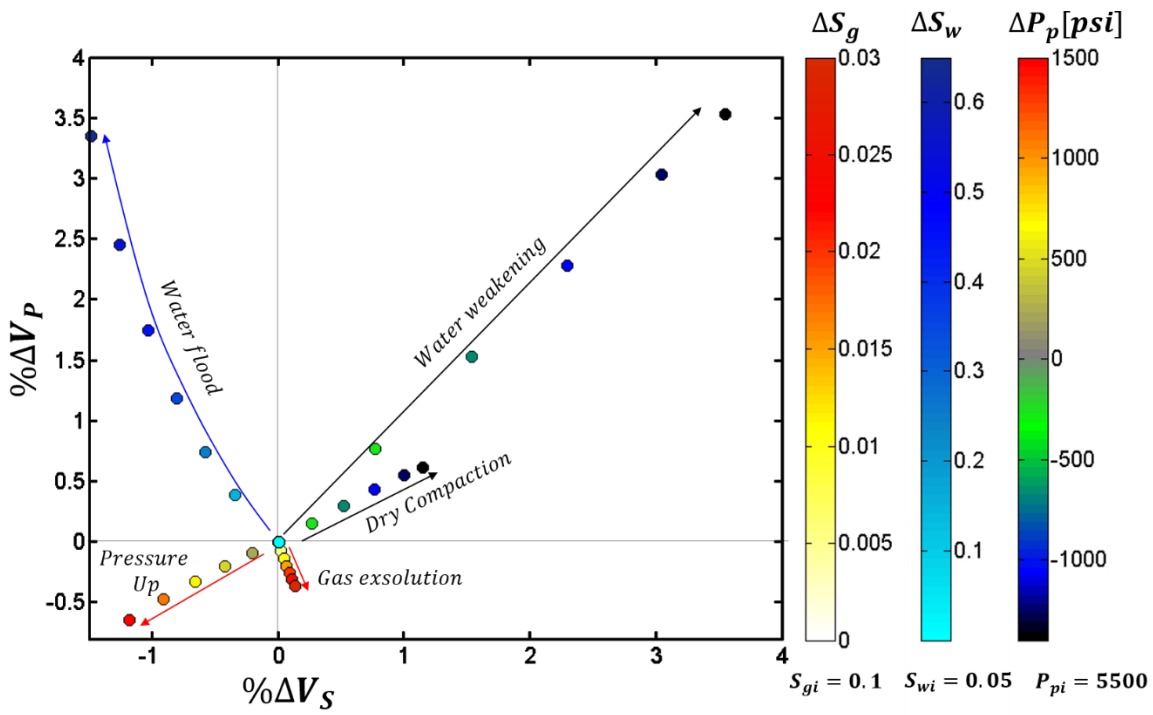

Figure 4.11: Showing the sensitivity of the percentage change of P-wave velocity and S-wave velocity to various production mechanisms that were modelled in isolation.

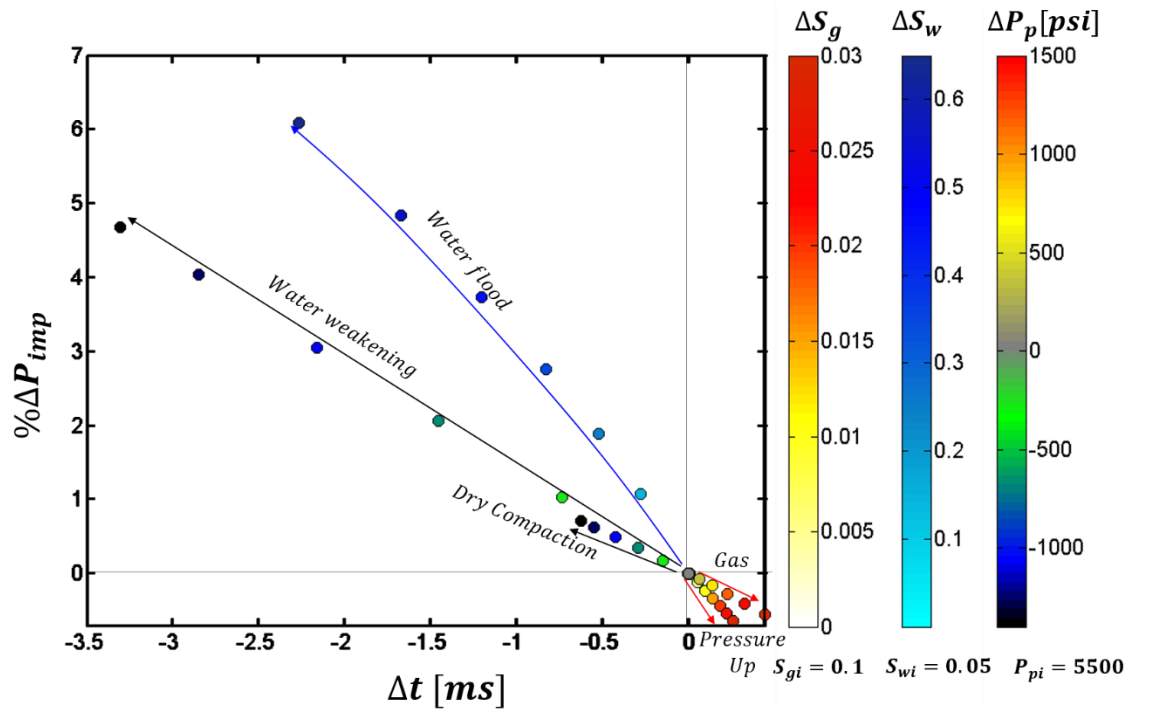

Figure 4.12: Shows the sensitivity of the percentage change of P-impedance and time-shifts to various production mechanisms that were modelled in isolation.

4.6 Derivation of a Proxy model via Synthetic Modelling

I have previously highlighted the rationale of a proxy model in various applications from reservoir characterization to seismic history matching. Most of this proxy model focuses on the relationship between the changes in dynamic properties and the difference in 4D seismic amplitude. Whilst the relation observed between dynamic properties and amplitude differences are encouraging, this particular approach is not the only one available, nor the most obvious choice for a thick, multi-cycle reservoir like Ekofisk. Another possibility is to relate dynamic changes to the relative change in impedances $\left(\frac{\Delta I_P}{I_P} \times 100\right)$ or other elastic properties which are interval properties. Impedances are usually modelled by a petro-elastic model to convert dynamic changes from the simulation model.

The relative change in impedance was chosen instead of seismic amplitudes, since it is also intuitive, and shows the relative strength of saturation or pressure changes in the 4D signals. The relative change in impedance is easier to interpret compared to the difference of impedance for baseline-monitor. It is more meaningful to look at this attribute than the difference in impedance, which is in the range of very large numbers. It is much more meaningful to quote that a 300psi change in pressure resulted in 1% change in impedance than 75000 m/s.kg/m^3 change in impedance between baseline and monitor. Seismic amplitude is an interface or contrast property, whilst impedance is a layer or rock interval property; thus the latter is more easily related to dynamic properties. In the following sections, I will demonstrate the formulation of this proxy model using a synthetic model.

4.6.1 Synthetic model description

To analyse the individual impact of pressure, saturation and porosity reduction, the relative changes in impedances are modelled for a sector model of the Ekofisk field simulation model. This is carried out using the simulation-to-impedance procedure of Amini et al. (2011), which from here on will be simply known as ‘sim2imp’. The sector model in Figure 4.13(a) has the same heterogeneity as the real data, and was simulated in a way that follows the production history of

the actual dataset by limiting the number of wells to six injectors and six producers. Figure 4.13(b) illustrates the production evolution of field pressure, field oil, gas production rate, water cut and water injection rate. During the first 18 years of production, due to the nature of the oil and the initial pressure being close to bubble point, the gas came out of solution rapidly with poor pressure maintenance. In parallel to the real data, a water injection programme was initiated later to maintain pressure, resulting in an increase in oil production rate and water cut. Having simulated the dynamic changes, such as pressure, gas, water and oil saturation at different time steps, I then put these results into the sim2imp workflow to generate impedances.

In order to study the impact of compaction (dry compaction and water weakening) on pressure and saturation and, in turn, on the impedances, I ran the fluid flow simulator in two separate scenarios: (1) no compaction, and (2) compaction; this workflow is shown in Figure 4.13(c). In this approach, petroelastic parameters were firstly calibrated from the wireline logs (P- and S -wave velocities, density, water saturation and gamma logs) and fluid properties obtained directly from PVT data. The dry frame properties for the chalk were derived from laboratory rock-mechanics tests and stress-sensitivity curves coefficients were also taken from the laboratory and put into the stress-sensitivity model of MacBeth (2004). Fluid acoustic properties are calculated using black-oil PVT data in combination with the Batzle and Wang (1992) equations and are then mixed using a harmonic average. Calibrated chalk parameters are then used to perform fluid substitution. The petroelastic model used in the sim2imp procedure has been thoroughly described in Chapter 2.

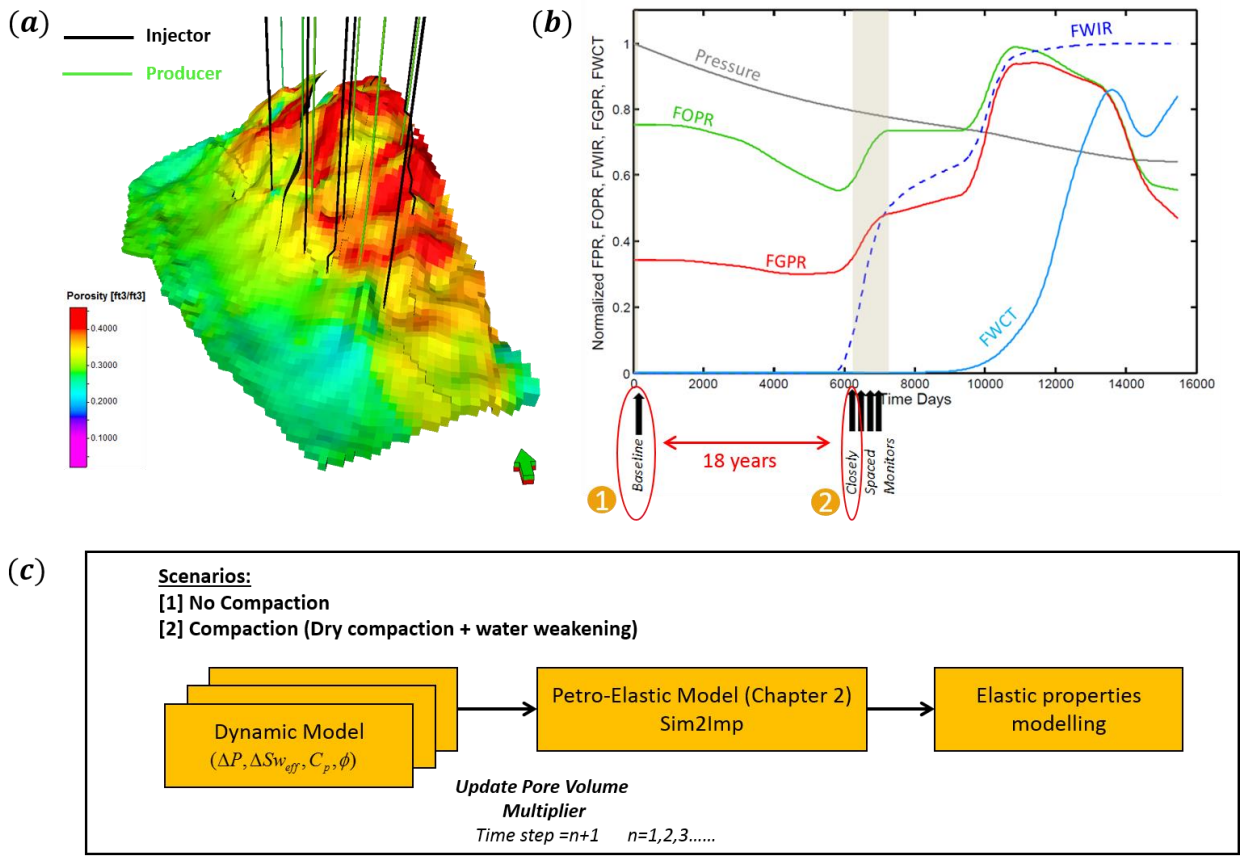

Figure 4.13: (a) A sector model of the Ekofisk full fluid flow with location of producer and injector wells. (b) Field production profile as a function of time. (c) The fluid flow simulation is carried out in three separate scenarios: no compaction, dry compaction and, lastly, water weakening.

Here, I demonstrate the results from my synthetic model for the individual contribution of pressure, saturation and compaction for case number 2, by including dry compaction and water weakening. Figure 4.14 (left panel) shows the dynamic changes such as gas, pressure and water by taking into account of compaction. Here, the term compaction encompasses physical changes such as dry compaction and water weakening. Figure 4.14 (right) shows the changes in P-impedance as percentages for the individual dynamic changes. Figure 4.14 (b – right, and c – right) depicts the effects of compaction due to pressure depletion and water invasion. The hardening signals in the relative change of impedance was amplified due to porosity reduction in those regions.

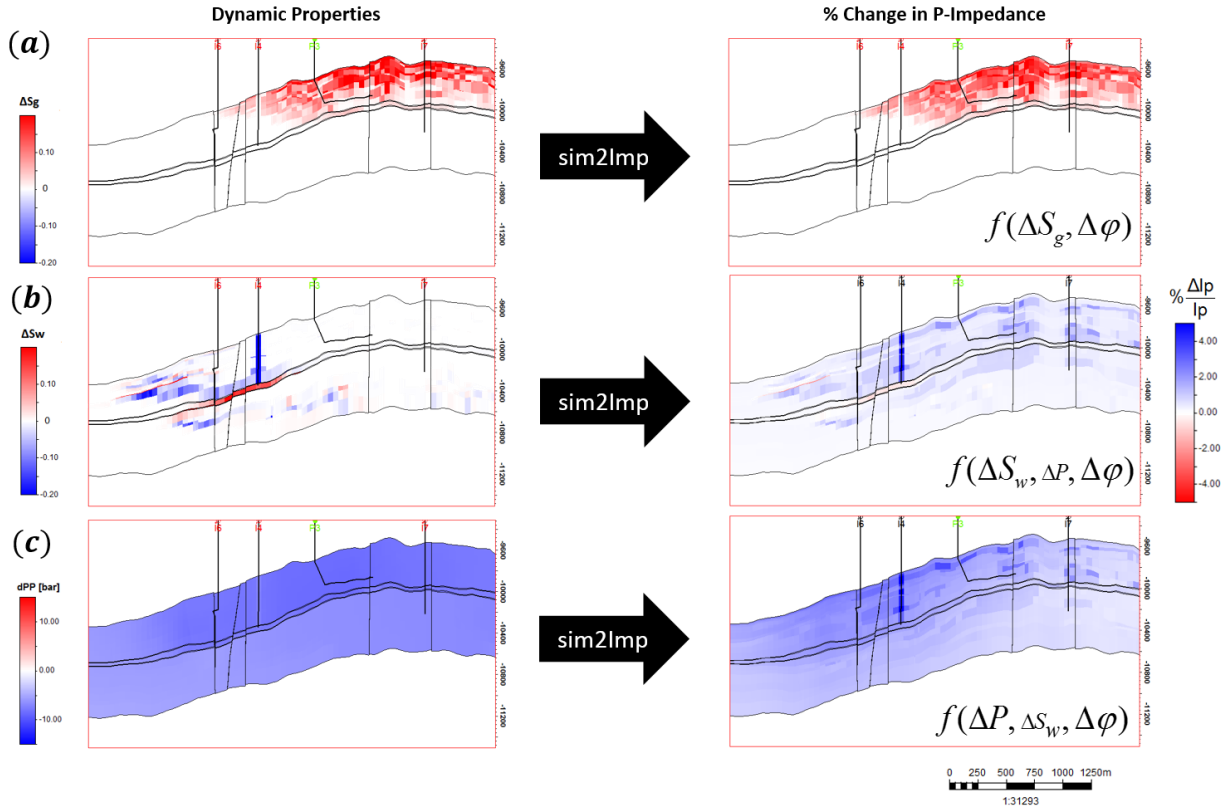

Figure 4.14: Cross-sections for the sector model showing (left) simulation model prediction and (right) percentage change of P-impedance from sim2imp for (a) gas, (b) water saturation and (c) pressure change. This is generated for the case of water weakening.

4.6.2 Reverse Engineering

Reverse engineering or backward engineering is, by definition, the process of extracting knowledge or design information and re-producing it based on that acquired information. In this case, I am trying to decompose the composite impedance from sim2imp to analyse its individual components and workings in detail, and recreate it using a simpler approximation. Modelling provides a way to examine the impact of pressure, gas, water saturation changes and geomechanical responses on the petroelastic parameters by independently isolating each of these controlling changes during the petroelastic modelling step, as shown in Figure 4.14. I can examine the effect of these different dynamic and geomechanical changes on the change of elastic properties, in the cases of no compaction, versus compaction. For simplicity the percentage change of any elastic properties are annotated in this chapter using the symbol 'δ':

$$\delta I_P = \frac{\Delta I_P}{I_P} \times (100) \tag{4.1}$$

In the case of no compaction, I anticipated the composite impedance response might be decomposed as a sum of individual responses:

$$\delta I_P(\Delta P, \Delta S_w, \Delta S_g) = \delta I_P(\Delta P, 0,0) + \delta I_P(0, \Delta S_w, 0) + \delta I_P(0,0, \Delta S_g) \tag{4.2}$$

where $\Delta P, \Delta S_w, \Delta S_g$ are changes in pressure and water and gas saturation respectively. By adding the independent δI_P due to gas, water and pressure changes, the end product predicts the very same changes as if one ran running the full petro-elastic model. This is found to be accurate in the model across a wide range of geological and fluid conditions to within an error of 2% for P-impedance. This suggests that, in the case of no compaction, the system is additive for simultaneous pressure and saturation changes, and these changes honour the principle of superposition. This linearly additive behaviour forms the initial framework of the proposed proxy model equation.

The principle of superposition states that in all linear systems, the net response caused by two or more stimuli is the sum of the response caused by each stimulus individually. The relationship between the composite δI_P from sim2imp is linearly related to the sum of the respective δI_P computed from different dynamic changes. This is clearly demonstrated in Figure 4.15, with the cross-plotting of $\delta I_P(\Delta P, \Delta S_w, \Delta S_g)$ versus $\delta I_P(\Delta P, 0,0) + \delta I_P(0, \Delta S_w, 0) + \delta I_P(0,0, \Delta S_g)$. The goodness of fit is reflected in a high coefficient of determination, R^2 of 0.91. R^2 indicates how well a model obtained by linear regression fits the data. Therefore, the equation can be written in the form:

$$\delta I_P = \alpha \Delta P + b \Delta S_w + c \Delta S_g \tag{4.3}$$

The coefficients of α, b and c are obtained via linear regression of the individual dynamic changes and their respective impedance changes, while they are modelled in isolation of gas, water and pressure.

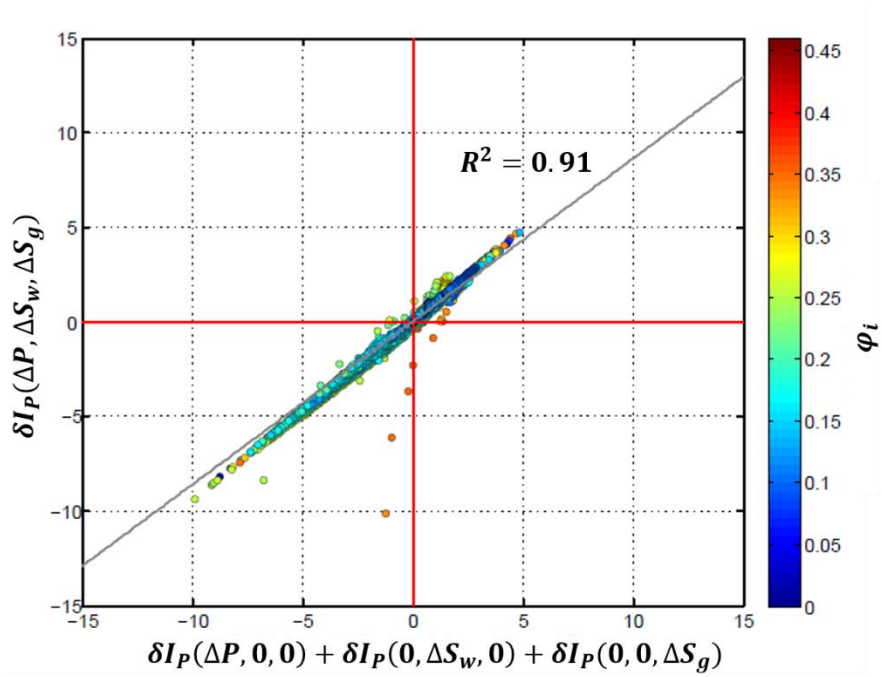

Figure 4.15: Showing the linear relationship between $I_P(\Delta P, \Delta S_w, \Delta S_g)$ *and* $\delta I_P(\Delta P, 0,0) + \delta I_P(0, \Delta S_w, 0) + \delta I_P(0,0, \Delta S_g)$ *for the case of no compaction.*

The actual system contains compaction due to both dry compaction and water weakening, therefore, the same procedure is carried out by running the full simulator, but this time taking account of these geomechanical effects. In the sim2imp procedure, I then isolate the effect of each controlling factor, such as pressure, water saturation, gas saturation and porosity changes on the elastic parameters. In the water weakening system, the composite relative change in impedance can be similarly decomposed as:

$$\delta I_P(\Delta P', \Delta S_w', \Delta S_g', \Delta\varphi) = \delta I_P(\Delta P', 0,0, \Delta\varphi) + \delta I_P(0, \Delta S_w', 0, \Delta\varphi) + \delta I_P(0,0, \Delta S_g', \Delta\varphi) \quad (4.4)$$

where $\Delta\varphi$ represents the change in porosity; this extra term is attributed to compaction.

Additionally, the impact of compaction on the changes of gas reflected as relative changes in P-impedance inside the reservoir can be studied by taking the difference of the functions derived from the compaction case and those from the no compaction case for gas: $\delta I_P(0,0, \Delta S_g', \Delta\varphi) -$

$\delta I_P(0,0,\Delta S_g,0)$. The difference between $\delta I_P(0,0,\Delta S_g{}',\Delta\varphi) - \delta I_P(0,0,\Delta S_g,0)$ in Figure 4.16(a) shows compaction results in less gas liberation and in turn an increase in the relative change of P-impedance. Likewise, for the impact of pressure on the relative change in P-impedance as a function of compaction, in Figure 4.16(b): $\delta I_P(\Delta P',0,0,\Delta\varphi\ ) - \delta I_P(\Delta P,0,0,0)$. Thus, as a result of pore collapse and higher compressibility, there is an increase in pore pressure and an increase in relative P-impedance. Moreover,$\delta I_P(0,\Delta S_w{}',0,\Delta\varphi\ ) - \delta I_P(0,\Delta S_w,0,0)$ in Figure 4.16(c) shows that the intrusion of water results in further pore collapse and reduction in permeability, which causes a greater overall relative change of P-impedance. Figure 4.16(d) shows the changes in porosity due to compaction. The change in porosity, $\Delta\varphi$ is given as the difference between initial porosity and the updated porosity (in the monitor survey). By comparing the effects of compaction on pressure, water and gas, I found the influence on pressure and water is much greater, with approximately 3% increase in relative impedance, while for gas it was slightly below 0.2%.

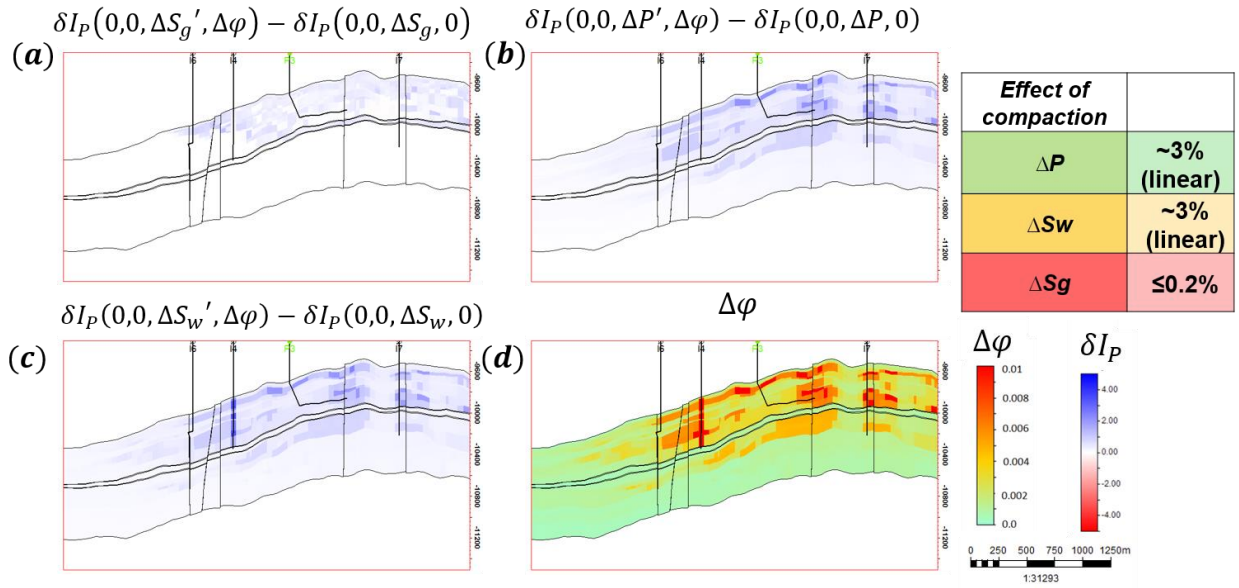

Figure 4.16: Cross-sections for the sector model, showing the δI_P between the cases of compaction and no compaction for (a) gas, (b) pressure (c) water saturation and (d) porosity change.

To assess if the composite impedance, $\delta I_P(\Delta P',\Delta S_w{}',\Delta S_g{}',\Delta\varphi)$ is indeed linearly correlated to the sum of the individual impedances from dynamic and porosity changes, $\delta I_P(\Delta P',0,0,\Delta\varphi) +$

$\delta I_P(0, \Delta S_w', 0, \Delta\varphi) + \delta I_P(0,0, \Delta S_g', \Delta\varphi)$, both terms are cross-plotted in Figure 4.17. The best fit, linear regression yields a goodness of fit, R^2 of 0.85, which shows that these terms are linearly related.

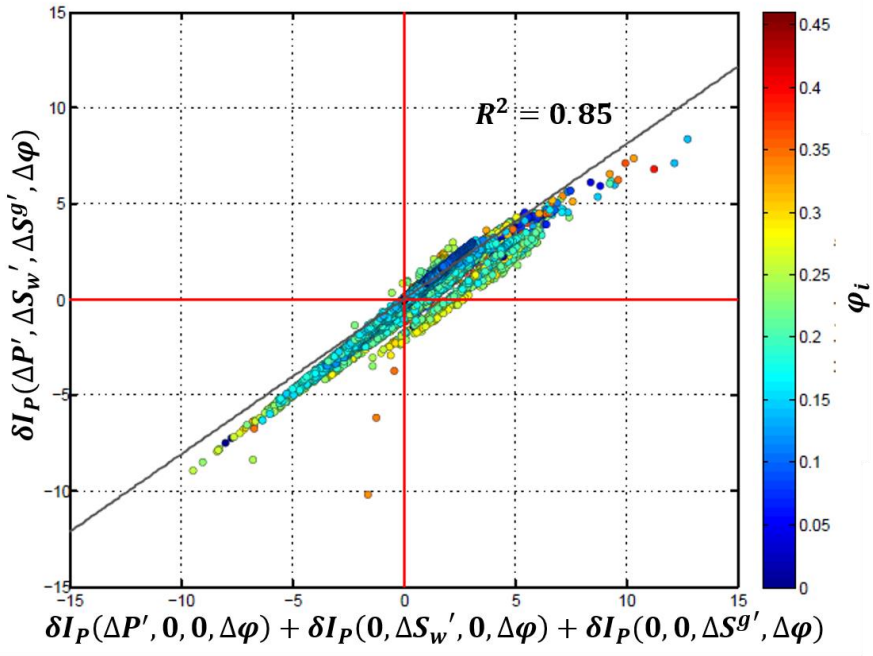

Figure 4.17: Showing the best fit, linear relationship between $\delta I_P(\Delta P', \Delta S_w', \Delta S_g', \Delta\varphi)$ and $\delta I_P(\Delta P', 0,0, \Delta\varphi) + \delta I_P(0, \Delta S_w', 0, \Delta\varphi) + \delta I_P(0,0, \Delta S_g', \Delta\varphi)$ for the case of compaction.

In addition, I assessed the linearity behaviour between compaction versus the change in impedance resulting from porosity reduction. This linear relation is depicted in Figure 4.18, by cross-plotting the effect of compaction on $\delta I_P(\Delta P', 0,0, \Delta\varphi)$ versus the changes in porosity, $\Delta\varphi$. The linear proxy function for the compaction case can be written as:

$$\delta I_P = \alpha\Delta P' + b\Delta\varphi + c\Delta {S_w}' + d\Delta {S_g}' \tag{4.5}$$

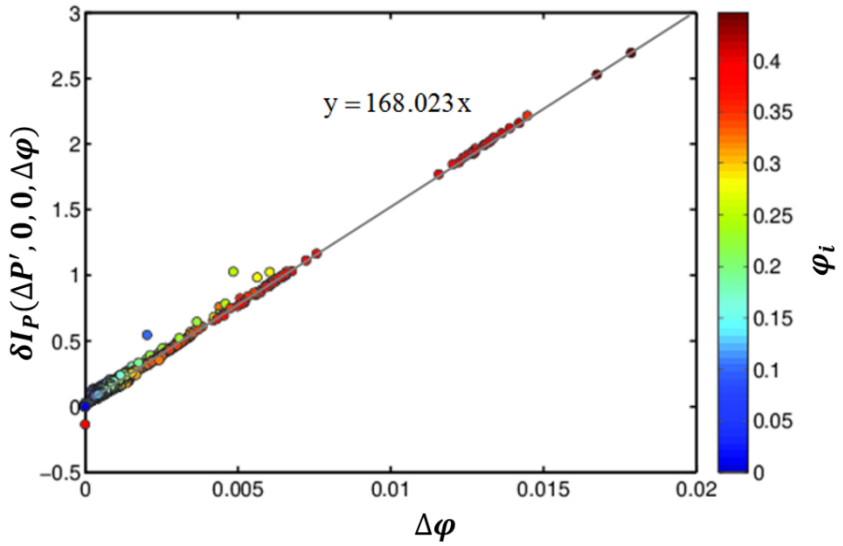

Figure 4.18: Cross-plotting of the change in porosity $\Delta\varphi$ versus the relative change in impedance due to compaction $\delta I_P(\Delta P', 0,0, \Delta\varphi)$ also yields a linear relationship.

In the case of compaction, by adding the independent relative impedance changes due to gas, water and pressure changes, as shown in Figure 4.19(b), the end product predicts the same change as through the full petro-elastic model, as illustrated in Figure 4.19(a). This shows that the principle of superposition is also applicable in the case of compaction, and that the approximation of the petro-elastic model as a single equation is valid for the modelling of relative change in P-impedance.

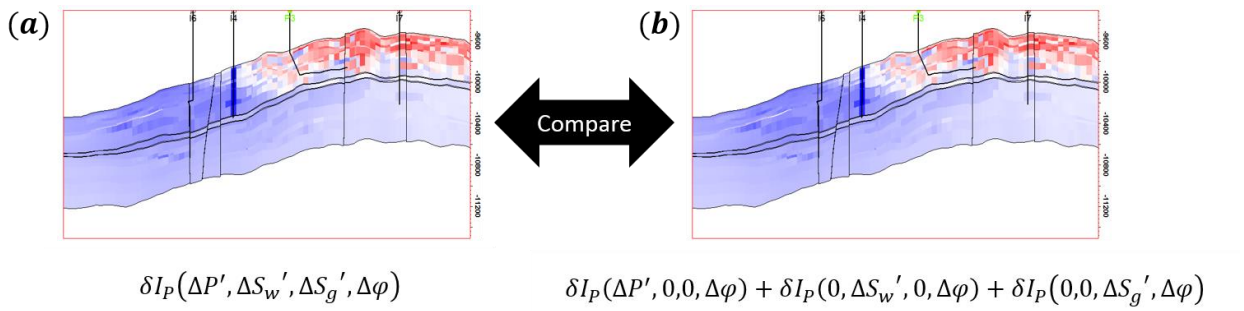

Figure 4.19: Comparison of the cross-sections for the composite impedance difference in percentages between baseline and monitor from sim2imp to the sum of individual difference in impedance, in percentages.

4.6.3 Linearisation of compaction curves

Apart from providing a faster way to compute the relative changes in elastic properties, the other objective of this proxy model is to estimate porosity reduction efficiently and intuitively. This is achieved by incorporating rock mechanics laboratory data as constraints into the proxy model equation. The crucial parameters that describe porosity reduction can be computed via a set of compaction curves for dry compaction and water weakening. These curves are similar to those used in the fluid flow simulation model. The changes in porosity can be described as the difference between porosity during the initial and subsequent time steps:

$$\Delta\varphi = \varphi_i - \varphi_{updated} \tag{4.6}$$

Here, φ_i represents the initial porosity and $\varphi_{updated}$ represents the porosity after simulation conditions, whereby $\varphi_{updated} < \varphi_i$, as the compaction process is irreversible. $\varphi_{updated}$ can also be expanded as the partial differentiation of porosity to changes in pressure:

$$\Delta\varphi = \varphi_i - \left[\frac{\partial\varphi}{\partial P} \cdot \Delta P + \varphi_i\right] \tag{4.7}$$

$$\Delta\varphi = -\frac{\partial\varphi}{\partial P} \cdot \Delta P \tag{4.8}$$

The compaction curves for both dry compaction and water weakening mechanisms provided by the field operator are displayed in Figure 4.20(a-left) and 4.20(a-right). These curves were calibrated using well data to interpolate the compaction gradient for each of the initial porosity classes. In work from Sylte et al. (1999) and Janssen, Smith and Byerley (2006) radioactive marker bullets were instrumented in wells and repeatedly logged to monitor strain and displacement in relation to reservoir compaction, and these data were used to calibrate the compaction model. I first linearized the compaction curve for each porosity curve in both dry compaction and water weakening behaviours, essentially replacing the gradient for each initial porosity member with a constant. Using a stepwise algorithm, I replaced $\frac{\partial \varphi}{\partial P}$ by two numerical functions called F_p and F_{ww}, each describing the gradient for initial porosity based on the amount of change in pressure; this captures the reduction of porosity for both dry compaction and water weakening. These functions are depicted in Figure 4.20(b).

$$F_p = -\frac{\partial \varphi|_{\Delta P}}{\partial P} \tag{4.9}$$

$$F_{ww} = -\frac{\partial \varphi|_{\Delta sw}}{\partial P} \tag{4.10}$$

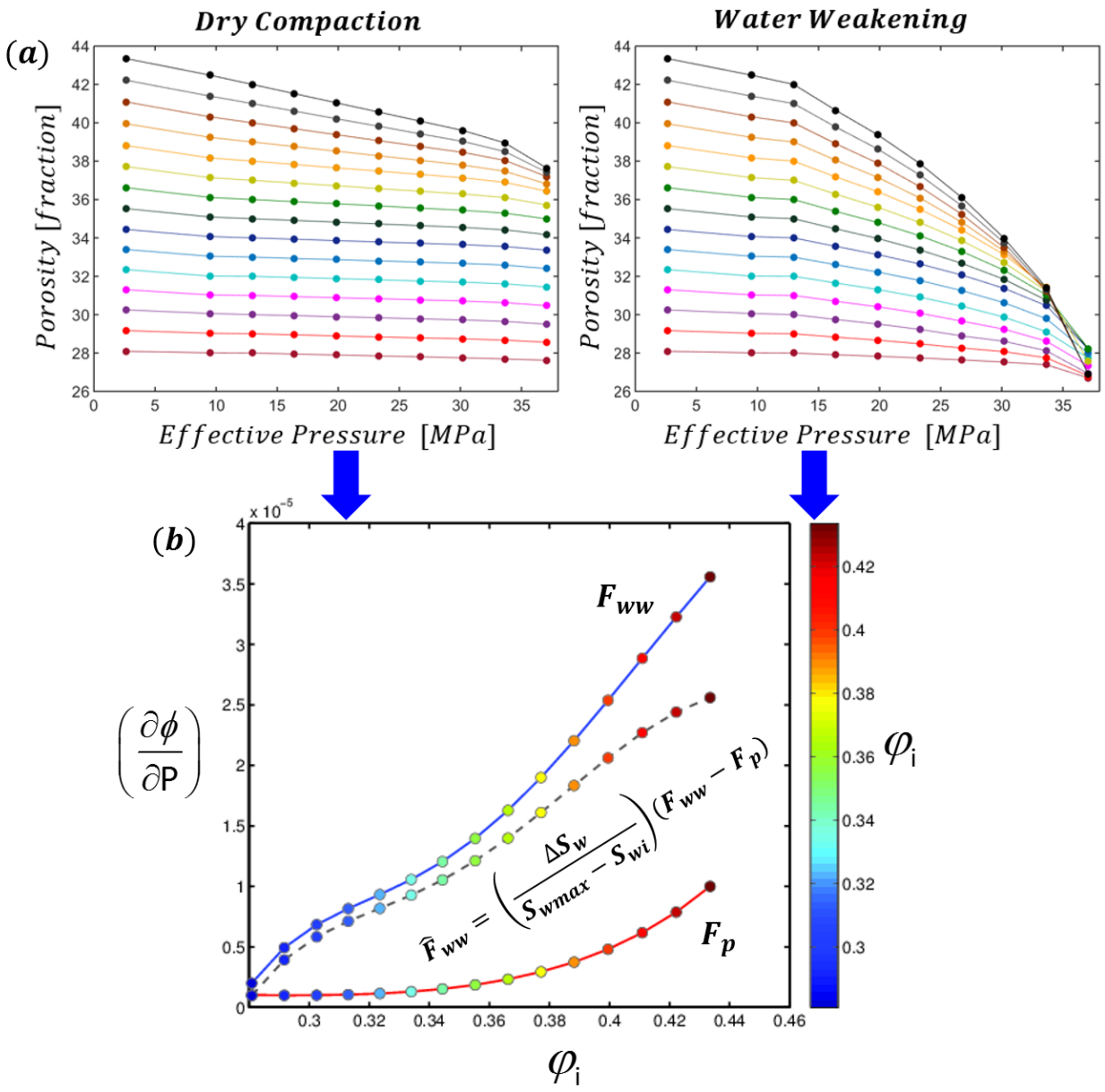

Figure 4.20: (a-left) Compaction curves derived from laboratory measurements of chalk cores under dry condition showing how compaction occurs when pressure is drawn down during production. (a-right) Compaction curves for cores under simulated water-flood conditions. (b) After linearizing the compaction gradient for curves in (a-left) and (a-right), two separate functions describing the compaction gradient (y-axis) for each porosity class (x-axis) for dry compaction (F_P) and water weakening (F_{WW}) are given.

The F_{ww} case occurs when the maximum attainable water saturation (S_{wmax}) is reached. The model was first put forward by Sylte et al. (1999), showing no additional compaction for S_w > 0.325 when water invasion occurs. Therefore, even when the water saturation exceeds the maximum attainable water saturation (S_w=0.33), there will be no additional compaction (Das et al. 2016). However, in many cases, the increase in water saturation does not exceed this value, and hence a new function is introduced to avoid overestimation of the relative change in impedance due to maximum water weakening. This pseudo function $\hat{F}_{ww}$ manipulates the correct amount of compaction of the two end members F_{ww} and F_p by weighting each one with the ratio of $\left(\frac{\Delta S_w}{S_{wmax}-S_{wi}}\right)$; this function is shown in Figure 4.20(b). The pseudo-function is described as:

$$\hat{F}_{ww} = \left(\frac{\Delta S_w}{S_{wmax}-S_{wi}}\right)\left(F_{ww} - F_p\right) \tag{4.11}$$

The equation can be re-written by including the pseudo function $\hat{F}_{ww}$ as:

$$\delta\Delta I_P = \alpha\Delta P' + b(F_p + \hat{F}_{ww})\Delta P' + c\Delta {S_w}' + d\Delta {S_g}' \tag{4.12}$$

If we expand on the pseudo function $\hat{F}_{ww}$:

$$\delta I_P = \alpha\Delta P' + b\left[F_p + \left(\frac{\Delta S_w}{S_{wmax}-S_{wi}}\right)\left(F_{ww} - F_p\right)\right]\Delta P' + c\Delta {S_w}' + d\Delta {S_g}' \tag{4.13}$$

Since the initial water saturation, S_{wi} in the Ekofisk field is low, at 0.05, it can be treated as negligible and the equation is further simplified as:

$$\delta I_P = \alpha\Delta P' + b\left[F_p + \left(\frac{\Delta S_w}{S_{wmax}}\right)\left(F_{ww} - F_p\right)\right]\Delta P' + c\Delta {S_w}' + d\Delta {S_g}' \tag{4.14}$$

A condition of $S_{wi} < S_{wmax}$ is also incorporated for the forward and backward modelling of the proxy model, so that the maximum compaction is not exceeded. In summary, the proposed proxy model is derived analytically through modelling and reverse engineering and a comprehensive synthetic modelling exercise. To predict the relative changes in impedance, the proxy model requires a set of calibrated coefficients (a, b, c and d) from the petro-elastic model, changes in

pressure (ΔP) and saturation (ΔS_w), and compaction curves from the laboratory, expressed as functions (F_{ww} and F_p) of initial porosity (φ_i). The procedure used to construct the proxy model for the relative change in P-impedance, δI_P is also carried out for S-impedance, δI_S, P-wave velocity, δV_P, S-wave velocity, δV_S, and density, $\delta \rho$. A different proxy model equation for each of the elastic parameters can be derived separately, where the general form is similar but coefficients a, b, c and d have different magnitudes.

4.6.4 Validating the proxy model

One way to cross-check the validity of the proxy model, is to compare the porosity reduction estimated from the fluid flow simulator with that calculated from the proxy model. The input parameters required in the proxy model are the changes in pressure and water saturation, and the initial porosity; these are readily available as outputs from the fluid-flow simulator. Figure 4.21 shows a comparison between the results from the simulator (left) and the linearised compaction functions (right). In general, I obtained a good agreement between both estimations, with marginal discrepancies, the maximum percentage difference is 2%. The unevenness of the porosity change generated from the fluid simulator is caused by rock typing in the model. As previously mentioned in Section 4.2.1, the different rock types are assigned with different relative permeability and rock compaction information although they can have the same porosity and permeability ranges. The compaction functions on the other hand, are irrespective of rock typing and the compaction gradients employed are only a function of the initial porosity.

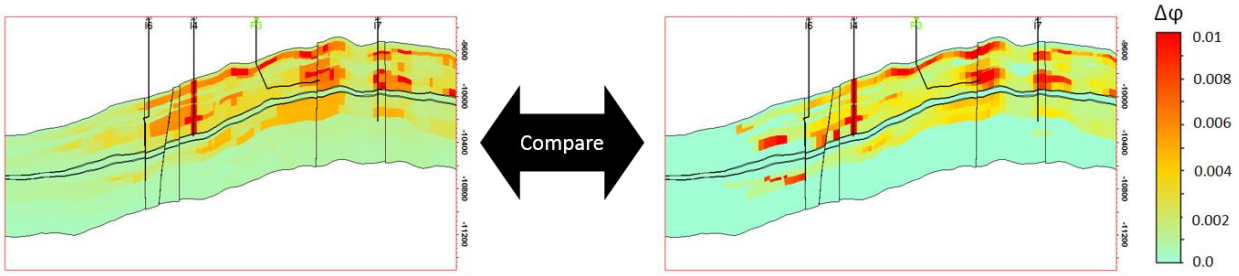

Figure 4.21: (Left) porosity reduction simulated from ECLIPSE compared to (right) porosity reduction calculated from F_P and F_{WW} functions.

Another way to gauge the accuracy of the estimation from the proxy model is to calculate the percentage error between the percentage change in P-impedance from the sim2imp procedure and the proxy model for the individual components of gas, water and pressure. The percentage error is described as:

$$\frac{(\delta I_P)_{sim2imp} - (\delta I_P)_{proxy}}{(\delta I_P)_{sim2imp}} \times (100) \tag{4.15}$$

The percentage error between the full sim2imp procedure and the proxy model is generally small, with errors less than ± 5%. The percentage error is shown in Figure 4.22 (a, b, and c) for the respective changes in P-impedance as a function of gas and water saturation and of pressure change.

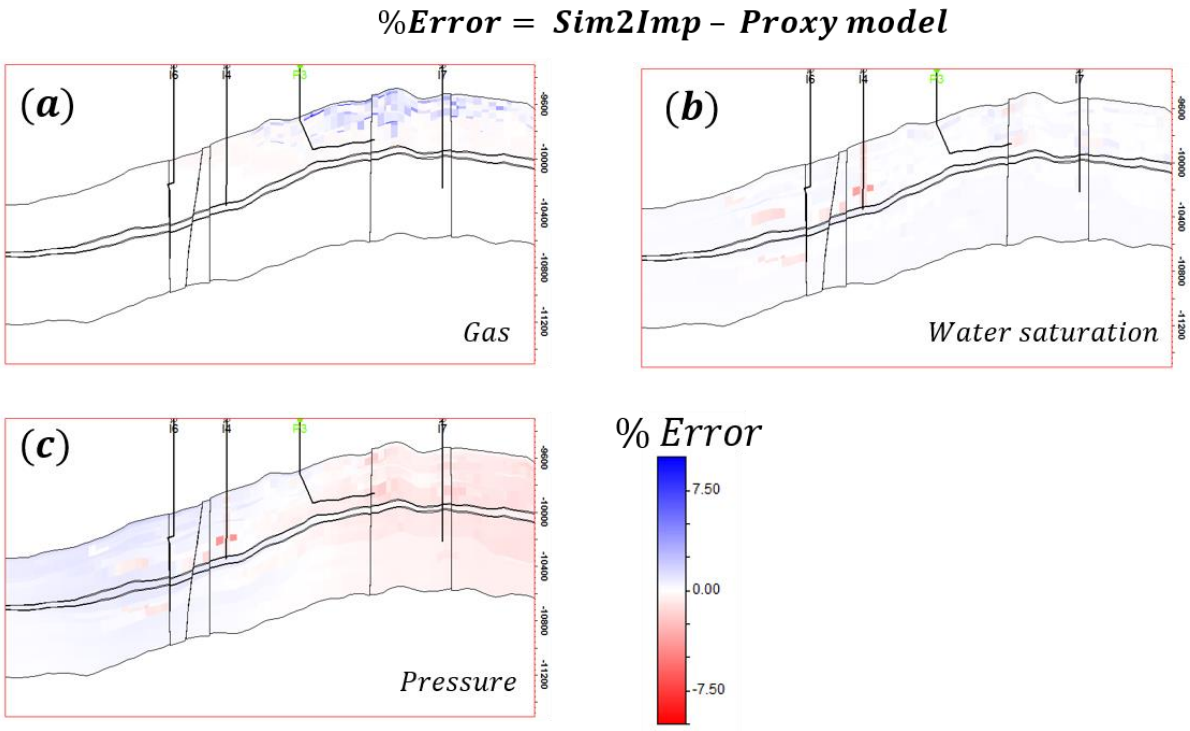

Figure 4.22: Showing percentage error of the percentage change of P-impedance estimated for (a) gas saturation, (b) water saturation and (c) pressure change between sim2imp and proxy model

4.7 Solving the Inversion Problem with a Proxy Model

I will next demonstrate how the proxy model is applied in inversion. Modelling and inversion are closely related: in modelling we seek to reproduce an observation (or measurement) by perturbing parameters that are somehow related to such observations. Inversion uses a series of observed measurements to calculate those parameters we are interested in, by calculating a series of predictions from an established model and comparing them to the observations (Menke, 1989). In both cases, the core of the process is to establish a model which relates the measurements with the parameters we wish to estimate and vice versa. In this section, I would like to demonstrate the following propositions:

1. The inversion scheme using the proposed proxy model produces realistic results for the synthetic data.
2. Constraints and prior information are crucial in narrowing the search space and subsequently provide us with better estimates of the model parameters.

4.7.1 The inverse problem and the optimisation solution

The inverse problem, as described by Menke (1989), can be mathematically defined as an integral function that relates the measurements d_i to the parameters we wish to estimate, m(x), through $G(x)$, which relates the two:

$$d_i = \int G(x)m(x)dx \tag{4.16}$$

where d is the data observation vector and m is given as the parameter vector and G is the data kernel matrix. Here, I attempt to solve the inverse problem on a sample by sample or cell by cell basis in the simulation model, the data epresents the synthetic elastic properties: the percentage changes in P-impedance, S-impedance, P-wave velocity, S-wave velocity and density generated using the sim2imp procedure. The model parameters are pressure and saturation changes and the data kernel matrix, G is the forward operator relating the two. Given the proposed proxy model equation takes a non-linear form, this inherently makes the inverse problem particularly difficult. There are two reasons: firstly that nonlinear error propagation is a difficult problem, and secondly, it introduces non-uniqueness in the solutions. If the forward problem is linear, and if a $L2$-norm is

used for the calculation of the misfit, the misfit function has a parabolic dependence on the model parameters, and therefore the misfit function has a single minimum. Any type of descent method will lead to this unique minimum. When the forward problem is non-linear, the misfit function can have multiple minima. The problem with these local minima is that search methods for the global minimum may misidentify a local minimum as the global minimum. In that case the estimated model is not the model that gives the best data fit.

The idea of an optimisation is to achieve the best possible result in acceptable conditions. Since the problem is described as non-linear, I cannot solve this via the linear least squares solution and need to tackle this deterministically, using other numerical optimization solutions. Typically, one seeks to recover the model parameter, m, based on observations, d, where both are related by a forward modelling operator G, as discussed earlier. The problem is to find m such that the misfit is less than a certain tolerance:

$$minimize\|G(m) - d\| \tag{4.17}$$

I start off by assuming that a local optimal solution exists for this problem, and a local search algorithm will suffice for my cause. I will talk more about using global algorithms in the subsequent section; this sort of algorithm is computationally expensive and is capable of looking at objective function values more exhaustively in the search space. The traditional local algorithms are subdivided into two main classes: direct (search) and gradient-based methods (Reklaitis et al., 1983, Deb,1995, 1998). In direct methods, only the objective function and constraints are used to guide the search strategy. The gradient-based methods use the first and/or second-order derivatives of the objective function and/or constraints to guide the search process. These algorithms can converge quickly to the solution. For quasi-linear problems, these algorithms are a good selection. I will be employing the Trust-Region Reflective algorithm available from the MATLAB optimisation toolbox, which is a subclass of the gradient-based methods. The Trust-Region Reflective algorithm used in the optimization is described in Coleman and Li (1994, 1996). Each iteration involves the approximate solution of a large linear system using the method of preconditioned conjugate gradients (PCG) (MATLAB documentation). A typical simple definition of the objective function is through the sum of squared differences:

$$f = \sum_{k=1}^{N_d} (d_k^{obs} - d_k^{mod})^2 \tag{4.18}$$

where the sum is taken over all available observed data, d_k^{obs}, and N_d is the total number of these data. The objective function of this problem is solved cell-by-cell, it can be written in the same format as:

$$minimize\ f(\Delta P, \Delta S_w, \Delta S_g)$$

where

$$f(\Delta P, \Delta S_w, \Delta S_g) = \left[\delta I_P - G_{Ip}(\Delta P, \Delta S_w, \Delta S_g)\right]^2 + \left[\delta I_S - G_{Is}(\Delta P, \Delta S_w, \Delta S_g)\right]^2 + \left[\delta V_P - G_{Vp}(\Delta P, \Delta S_w, \Delta S_g)\right]^2 + \left[\delta V_S - G_{Vs}(\Delta P, \Delta S_w, \Delta S_g)\right]^2 + \left[\delta \rho - G_{\rho}(\Delta P, \Delta S_w, \Delta S_g)\right]^2 \tag{4.19}$$

G is the forward operator and represents the proxy model equation, which is unique to generate different elastic properties such that the coefficients in the proxy model for P-impedance will be different from S-impedance, P-wave velocity, S-wave velocity and density. The inversion of various data sets was done jointly. Joint inversion is carried out in this case to produce mutually consistent estimates of the unknown parameters. As demonstrated in Equation 4.19, one objective function is to be optimized from the summation of individual objective functions representing various data sets. In this synthetic example, given that the data is generated and not measured from the field, the quality of the data is consistent. However, for the actual field data, the quality of the different types of measurement may differ, such as for time-shifts, amplitude and the inverted elastic properties. The component objective functions should therefore be multiplied by weight factors giving them the correct contribution for determining the model parameters (Drahos, 2008). This is discussed further in the next chapter when using actual field data. As previous researchers (Floricich, 2006; Alvarez, 2014) observed, in obtaining reliable estimations of ΔP and ΔS_w, especially with the highly correlated nature of the 4D signals, incorporating additional constraints into the inversion scheme is helpful. There will be several possible combinations of ΔSw and ΔP which will produce the same change in petro-elastic properties, for example, both a decrease in pore pressure and an increase in water saturation will generate a hardening signal. The implication of this is that the inversion problem is ill-posed and hence it is required to provide constraints in order to find a solution that falls within the expected ranges of change.

4.7.2 Constraints

To find a unique solution, one must add some constraints in the solution space. For example, in order to aid the convergence of the optimisation, a good initial guess or starting point in solving the optimisation problem is helpful. In this case, I used the mean value from the simulation model prediction for gas, water and pressure changes ($\overline{\Delta P}, \overline{\Delta S_W}, \ \overline{\Delta S_g}$) as the initial starting point.

Another way to ensure a better feasible solution is by setting boundaries for the parameter estimates. If one knows the bounds on the location of an optimum, one can obtain faster and more reliable solutions by explicitly including these bounds in the problem formulation. For example, the change in water and gas saturation cannot exceed 0 and 1, respectively, with further constraints in certain compartments of the reservoir, such that no water saturation changes should be expected in the water leg, since the water saturation is already unity or at its maximum. Moreover, it is unlikely for other types of reservoir fluid to replace water in the aquifer due to density variation, where water is denser than oil and gas. On rare occasions, the injectors could push oil into the aquifers, however this is not the norm and will not be considered in this modelling. In most parts of the reservoir, the water saturation change is constrained to: $0 \leq \Delta S_w \leq (1 - S_{or} - S_{wirr} \approx 0.675)$. In the Ekofisk field, the irreducible water saturation, S_{wirr} is given as 0.05 and the residual oil saturation, S_{or} has a value of 0.275. Below the oil-water contact, the change in water saturation is $\Delta S_w = 0$.

Based on the prediction of the simulation model for gas changes, the maximum value peaks at 0.6, and no gas was expected to go back into solution, due to a significant overall pressure depletion in the reservoir. Therefore, the expected gas saturation change is limited to $0 \leq \Delta S_g \leq 0.6$. On the other hand, the pore pressure change in the reservoir can also be constrained by studying the production history of the field. Based on the minimum and maximum estimates of the change in pressure predicted from the simulation model, the bounds set on pore pressure change is between: $-20 \leq \Delta P \ (bar) \leq 0$. These constraints can be incorporated into the optimisation problem in the form of an equation such as $Hm \geq h$:

$$\begin{bmatrix} 1 & 0 & 0 \\ -1 & 0 & 0 \\ 0 & 1 & 0 \\ 0 & -1 & 0 \\ 0 & 0 & 1 \\ 0 & 0 & -1 \end{bmatrix} \begin{bmatrix} \Delta S_w \\ \Delta S_g \\ \Delta P \end{bmatrix} \geq \begin{bmatrix} 0 \\ 0.675 \\ 0 \\ 0.6 \\ -20 \\ 0 \end{bmatrix} \tag{4.20}$$

Since I know the location of the original oil-water contact prior to production, the constraints in the water leg are given as the equations below. Below the oil-water contact, the water saturation will always be 1, and no change is assumed to occur; the model parameter for ΔS_w equals to 0. Below the oil water contact, the optimisation problem is solved subject to these conditions:

$$-20 \leq \Delta P\ (bar) \leq 0 \tag{4.21}$$

$$\Delta S_w = 0, \Delta S_g = 0 \tag{4.23}$$

4.8 Results and Discussion

The non-linear inversion solution is a non-unique one, given there are a multitude of models that explain the data equally well. My approach here is to reconstruct an estimated model (proxy model) that still captures the full physics as the true model, for the use of forward modelling and inversion. The proxy model is capable of forward modelling a series of different elastic properties with good agreement to the data estimated from the true model, which in this case is represented by the sim2imp procedure. Of course, one can also argue that a different rock physics model will give a different set of data. In this case, the true model is assumed as the rock physics model calibrated with well measurements in the sim2imp procedure, which is used as a benchmark for estimation of elastic properties. In this section, I will carry out two separate inversions, highlighted in two separate routes as '1' and '2' in Figure 4.23. The first route involves using the data from the proxy model to invert for the model parameters. The second route uses data estimated from the full physics model but inverted back to the respective model parameters using the proxy model.

Figure 4.24(a) shows the comparison between the dynamic changes predicted from the simulation model and Figure 4.24(b) shows the inverted dynamic changes using the proxy model from data

generated from the same proxy model in route 1. Route 1 is also known as 'inverse crime' (Wirgin, 2004), when the same (nearly same) theoretical ingredients are employed to synthesize as well as to invert data in an inverse problem. In general, route 1 managed to reproduce the pressure and saturation changes, even in places where these changes overlap (close to the crest of the reservoir, where gas accumulates and pore pressure reduces). The model data are uniquely resolved with very small residual errors. This is expected, as the same data kernel (G') is used in both forward and backward modelling. This procedure is useful to investigate the stability of the inversion solution in the presence of noise and to assess the effectiveness of the proxy model in an underdetermined problem. To truly assess the robustness of the proxy model, the inversion is carried out using data generated from the full physics model, as described in route 2.

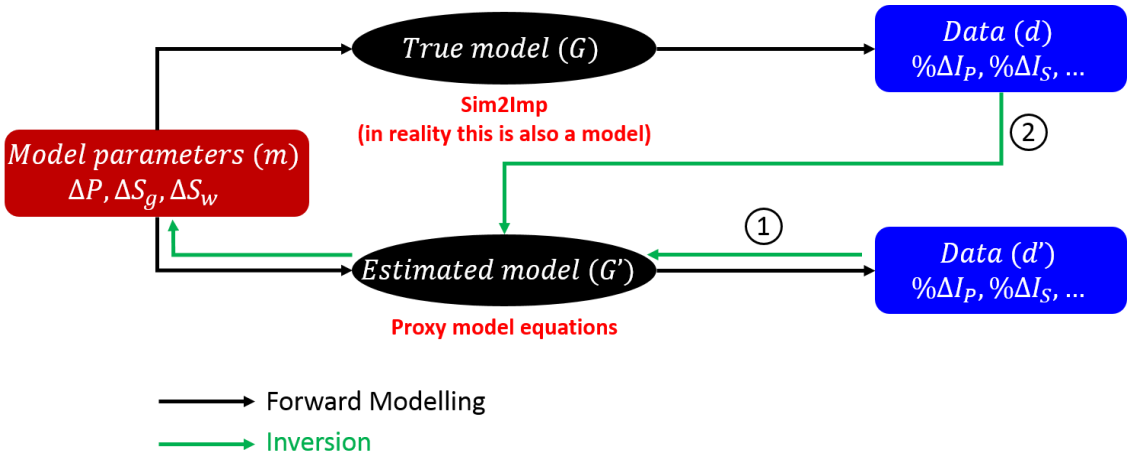

Figure 4.23: The workflow comprising the forward modelling and inversion routes using the full physics model (sim2imp) versus the proxy model.

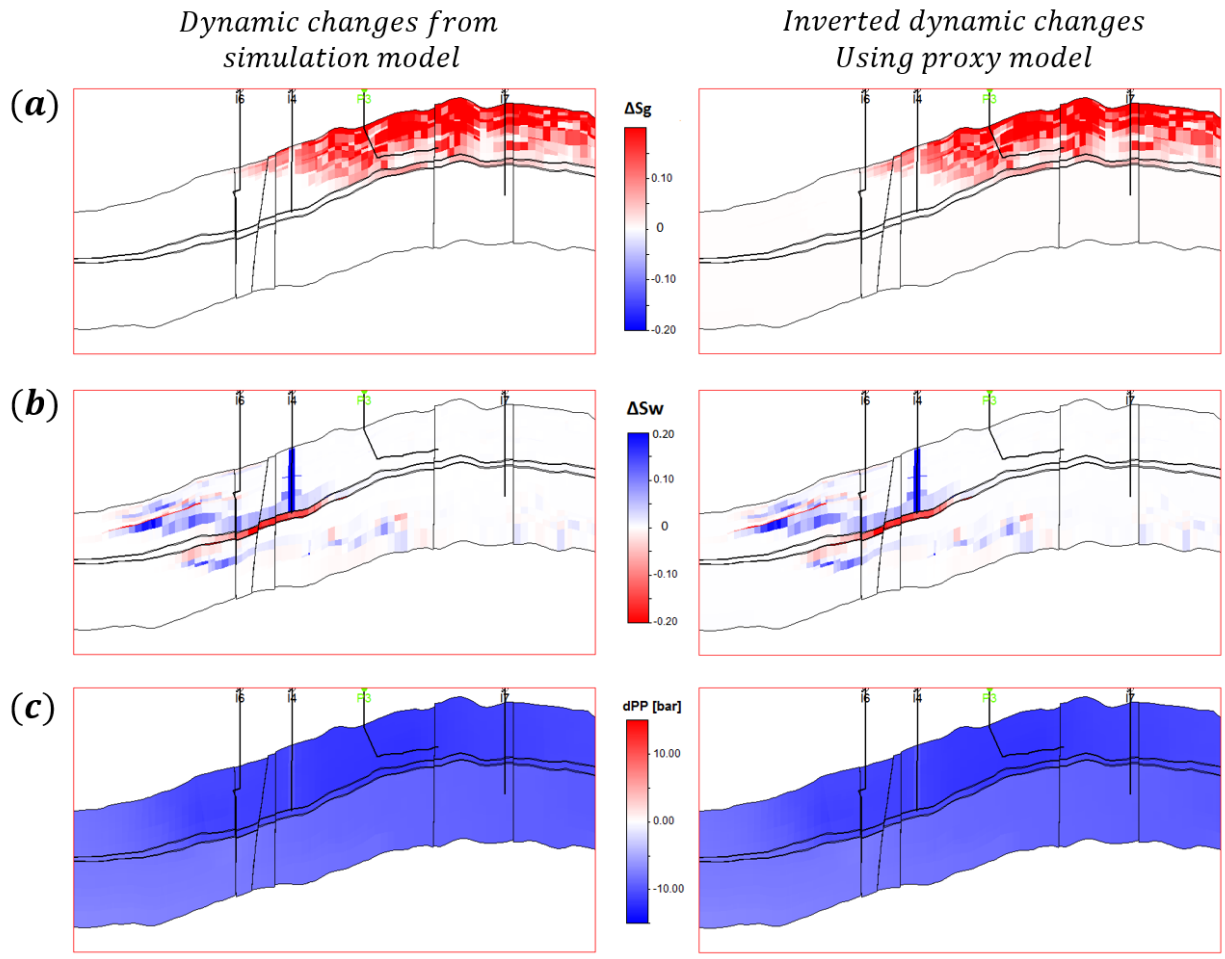

Figure 4.24: Cross-sections showing (left) dynamic changes generated from simulation model compared to (right) inversion results using proxy model for (a) gas, (b) water saturation and (c) pressure change. The input data for the inversion are generated from the proxy model equation.

Inversion results from the second route are displayed in Figure 4.25(a, b, and c). In general, the inversion results shows greater discrepancy between the inverted model parameters and with those simulated from ECLIPSE, as compared to the results shown in Figure 4.24(a, b, and c). This is particularly apparent in places where there are overlaps between pressure and saturation changes, such as the gas cap, and around the injector well I4. However, on a positive note, overall the polarities of the inverted dynamic changes are comparable to those simulated from ECLIPSE, which is essential for interpretation. These discrepancies are expected, since a different data kernel is used in forward and backward modelling.

The residuals and the convergence criteria are assessed in this section. The residual error is the value of the objective function at solution, which can be calculated for the independent observed data ($\delta I_P, \delta I_S, \delta V_P, \delta V_S, \delta \rho$). On the other hand, the exit criteria show the reason for the solver to stop the calculation. These exit criteria are unique in the MATLAB optimisation package. When the optimisation solver completes, it sets an exit criterion. The exit criterion is an integer that describes the reason the solver has halted its iterations. In general, positive criteria corresponds to successful solutions and negative ones are not. The zero exit criterion represents a solution that is computed by exceeding an iteration limit or limit on the number of function evaluations (MATLAB documentation). The exit criteria are colour-coded from -2 to 4 and explained in Table 4.3.

Exit Criterion	Colour	Description
1		The function converged to a solution
2		Change in solution was less than the specified tolerance
3		Change in the residual was less than the specified tolerance
4		Magnitude of search direction was smaller than specified tolerance
0		Number of iterations exceeded predefined value
-1		Stopped by output function
-2		Bounds are inconsistent and the problem is infeasible.

Table 4.3: The exit criteria and their description for the non-linear optimisation solver (MATLAB documentation).

Figure 4.26(a) to (e) shows the residual error (in route 2) for each of the predicted elastic properties at the objective function when a solution is found, and Figure 4.26(f) represents the exit criteria for each cell in the model. I observed that the residual errors for the different elastic properties are generally small, with higher residuals in composite elastic properties such as P and S-impedance. Because these result from the multiplication between P, S-wave velocity and density, the residual error is also amplified in these elastic properties. The residual errors are expected because the coefficients derived for the proxy model are calculated by linear regression between elastic properties from the sim2imp and simulation estimated dynamic properties, which might not be able to capture all the scatter in this approach. However, this regression is considered a robust

calibration, as in the derivation of the proxy model and its coefficients, all data points were used in the regression exercise.

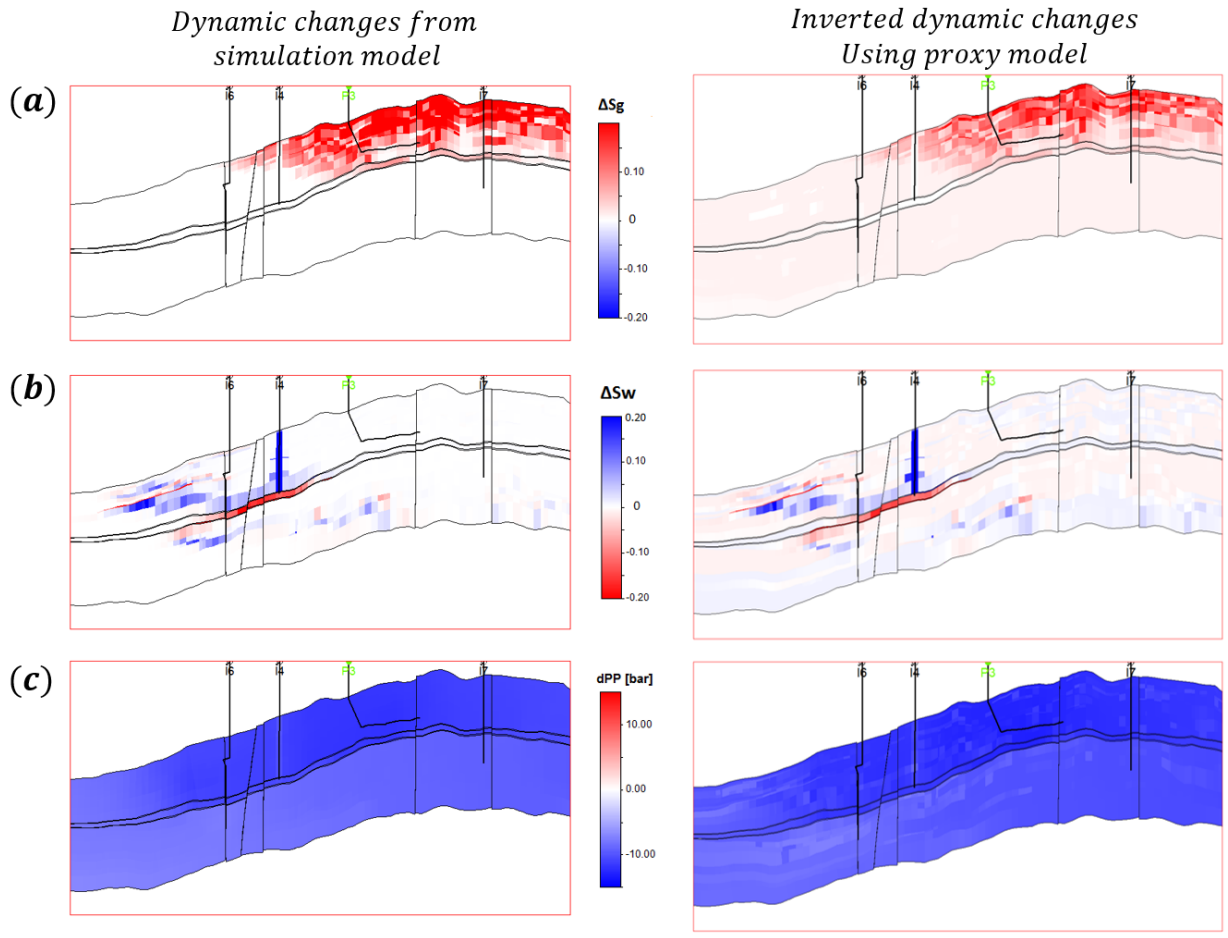

Figure 4.25: Cross-sections showing (left) dynamic changes generated from simulation model compared to (right) inversion results using proxy model for (a) gas, (b) water saturation and (c) pressure change. The input data for the inversion are generated from the sim2imp procedure.

The exit criterion show mostly '1', which informs us that the solver stopped because it has converged to a solution. In some cells, where the exit criterion is numbered as '3', this shows the change in the residual norm is very small; hence the solution is accepted. Given this is a non-linear problem, this could suggest that there could be multiple local minima. Thus, a different solution can be applied, such that one could make inferences from a range of models and search in many

directions. This brings us to the next section, where I suggest an alternative solution, although the current solution shown in Figure 4.26 has already yielded minor discrepancies compared to the true model parameters.

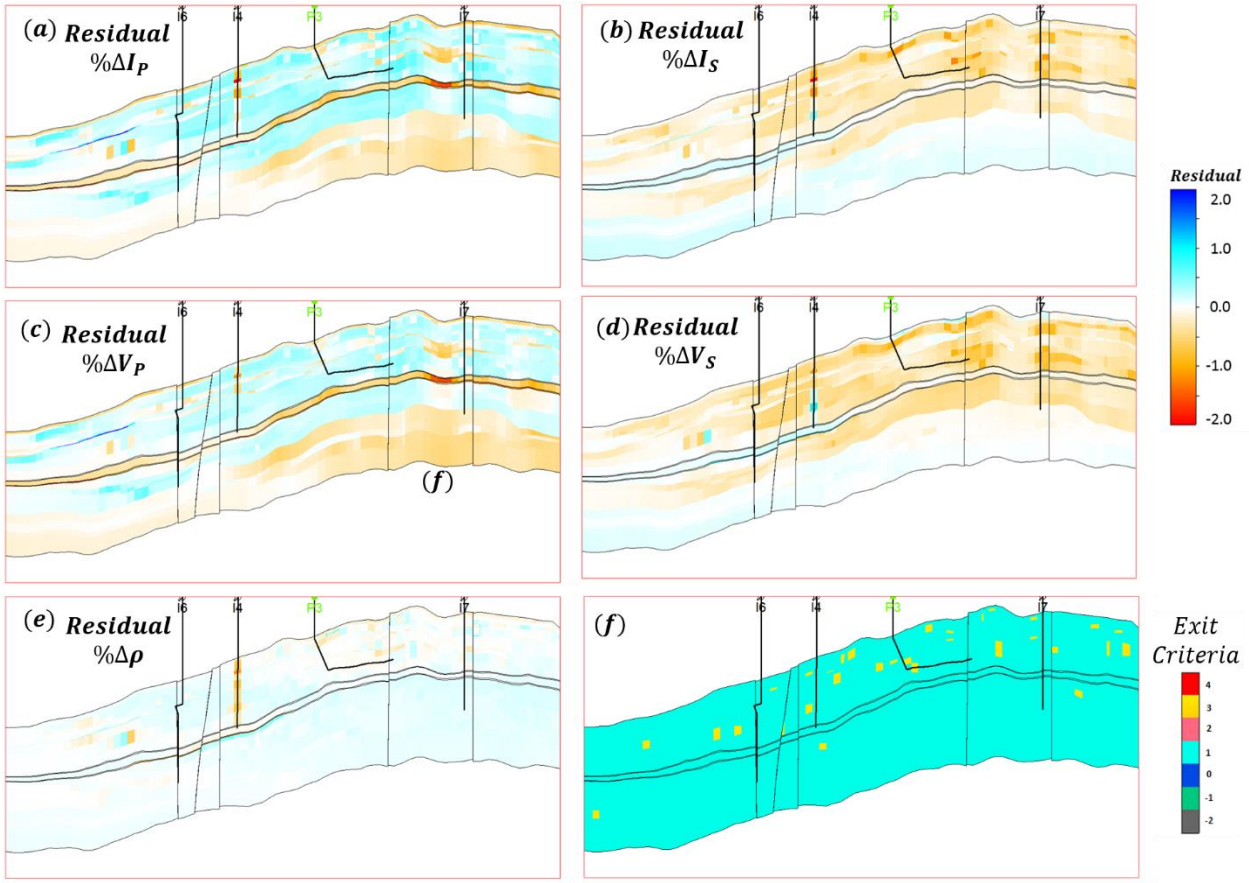

Figure 4.26: Cross-sections showing the residual error for percentage change in (a) P-impedance, (b) S-impedance, (c) P-wave velocity, (d) S-wave velocity and (e) density for the inversion (route 2) that uses input data from the sim2imp procedure. (f) shows the exit criteria colour coded from -2 to 4, described in Table 4.3.

4.8.1 Generation of populations that fit the data

An alternative approach is to compute the misfit for a very large class of models and to use the data fit, possibly in combination with Bayesian statistics, to make inferences about the range of models that explain the data in a certain sense (e.g. Mosegaard and Tarantola, 1995, Gouveia and Scales, 1997, 1998, Mosegaard 1998). Obviously, this approach requires a numerical approach to create such ensembles, but if the forward modelling can be easily computed, like the proxy model, computation time can be greatly reduced. An important concept in the generation of ensembles of models is the randomness in the search method that one employs. This stochastic approach will be applied to the actual data in Chapter 5.

4.9 Summary

This chapter first addressed the need for a proxy model to invert for pressure and saturation changes in the impedance domain. Pressure and saturation changes are more easily decomposed from the elastic properties rather than from seismic amplitude differences. The aim of the remainder of the chapter was to show the derivation and the validation of the proxy model on a set of synthetic data.

The proxy model derived in this chapter is set to achieve the aforementioned goals, which are to provide a fast-track method to both forward model elastic properties and invert for pressure and saturation changes in a compacting chalk reservoir. The analysis reported in this chapter has validated the competence of the proxy model approach for both forward and backward modelling, by comparing the discrepancy in estimated elastic properties with the true model, which is the sim2imp procedure. Marginal differences were observed between the predicted elastic properties between the proxy model and those calculated by sim2imp. Similarly, the porosity reduction calculated using the proxy model was also comparable to those predicted from the ECLIPSE simulation model. This confirms that the compaction behaviours can be simplified into analytical equations and be embedded in the proxy model.

The inversion problem is cast as an optimisation problem, where for each cell, multiple forward modelling is allowed, to minimize the misfit between the predicted data and the observed data.

Crucially, by including constraints such as bounding values and statistical information from the simulation model, the optimisation process to solve for pressure and saturation changes is expedited. I have kept the use of prior information to the minimum. In practice, the selection of bounding constraints and prior information depends on data availability. For the actual data I will also explore possible a priori information from a well history-matched simulation model and engineering concepts. The inversion using the proxy model equation shows promise, and the inverted solutions are also considered stable. The residual errors are less than ±2% for all estimated data.

CHAPTER FIVE

INVERSION FOR PRESSURE AND SATURATION CHANGES: APPLICATION TO THE EKOFISK FIELD

This chapter is dedicated to a real data application by using the proxy model derived in Chapter 4 to invert for changes in pressure and saturation. First, I will describe the seismic data that will be use as inputs into the inversion engine. Next, I will introduce the engineering consistent constraints and additional information that will help stabilize the inversion solution. Finally, the results from a stochastic approach via Bayesian McMC is presented showing the estimates of changes in pressure and saturation. The interpretation of the result is aimed to provide insights into well performance and pressure distribution inside the reservoir. Quantitative interpretation on this field using the inversion results shows good agreement with well production data and helps to explain strong localized anomalies in both the Ekofisk and Tor formations.

5.1 Introduction

This chapter will bring together the material presented thus far in Chapter 4 and perform the inversion on the 4D geophysical parameters: relative changes in elastic properties and time-shift measurements, into variations in pressure and saturation in the Ekofisk field. The 43 years of production history of Ekofisk is well documented in the literature. I have given a brief description of the field and the production mechanisms associated with the field in Chapter 2. Next, I present some description on the area of interest, the type of seismic data made available such as the relative change in V_P, V_S, ρ and time-shifts.

5.2 Area and Time period of Interest

Ekofisk is a large reservoir with a coverage area of 49 km^2. In order to make the study manageable, I will focus on a sub-area of the field to perform the inversion. Figure 5.1 shows a map of the reservoir time-shifts across the entire field and the area of interest is delineated in the black box. The northern part of the area of interest intersects the central region which is notorious for overburden gas cloud, also known as the seismic obscured area (SOA) delineated by the yellow polygon. Inside the SOA, the gas cloud prevents optimal imaging and the seismic data quality greatly deteriorates, in this area I will show how engineering constraints are useful to make educated inferences. Outside the SOA, clean and well-delineated 4D signals can be observed at injector and producer wells operating between the LoFS (Life of Field Seismic) surveys. The SOA is smaller in the LoFS surveys compared to the towed streamer due to better repeatability and the installation of permanent seabed seismic system, acquisition of wide-azimuth, long-offset multicomponent data for powerful imaging and processing techniques. Velocity model building workflow using FWI and joint PP-PS tomography applied in combination with wide-azimuth multicomponent processing has reduced the extent of the SOA for both PP and PS data (Bertrand et al., 2013b).

The inversion is applied to the second and the sixth of the LoFS surveys acquired two and a half years apart. The study is restricted to LoFS 2 and LoFS 6 because the historic production data from

wells shows sufficient fluctuations between this time period. The wells also operate long enough to create significant 4D seismic anomalies on the data. The area of interest (AOI) is 4.32 x 5.17km.

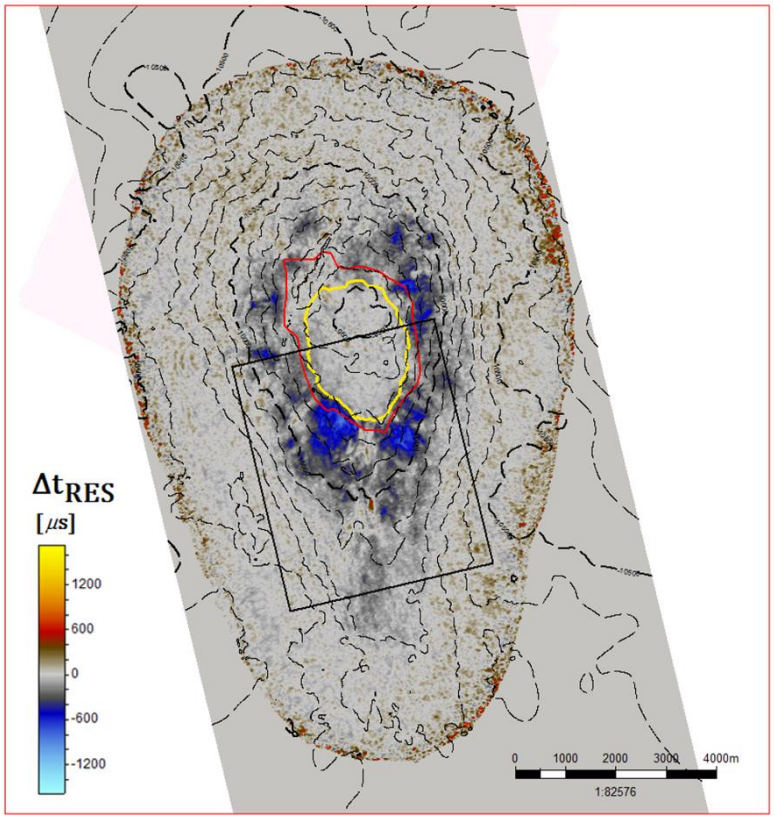

	No. of Lines	Spacing
Inline	330	12.5 m
Crossline	400	12.5 m

Figure 5.1: The subarea selected for the study is shown in the black rectangle. The map shows the reservoir time-shifts between Lofs 2 and Lofs 6. The area consists of 330 x 400 seismic bins, with a spacing of 12.5m in both inline and crossline directions.

5.3 Data Description: Time-lapse Time-shifts and Time strain

In this section the geophysical data and parameters that are used for characterization of pressure and saturation changes in the reservoir are described. The data contains time-shifts and time-strains obtained from analysis of baseline and monitor seismic data as well as corresponding elastic parameters obtained from 4D pre-stack inversion. Both of these attributes have been obtained from previous data analyses by the ConocoPhillips Geophysical Implementation Team, and inversion results by Lafet et al. (2009). Time-lapse time-shifts are not only used to time-align different

vintages of time-lapse seismic surveys, but also have a diagnostic value in monitoring reservoir compaction. The dominant 4D seismic effects are strongly represented in the time-shifts and time strain in both maps and sections. In highly porous chalk fields such as Ekofisk, 4D changes are not limited to the reservoir but are also transmitted into the overburden due to reservoir compaction. The compaction-induced geomechanical changes in the overburden result in large 4D effects, measured as changes in two-way travel-time between surface and top reservoir. The overburden time-shifts is defined as the cumulative time-shifts measured at top reservoir. Joint interpretation of the five Ekofisk 3D seismic streamer surveys (1989, 1999, 2003, 2006 and 2008) has revealed overburden travel time differences as large as 20ms. This is contributed by various production mechanisms inside the reservoir such as a pressure depletion event from 1971-1989 causing substantial subsidence. From 1989-1999, a full field water injection program caused field scale geomechanical responses such as water weakening and other dynamic changes such as gas going back into solution due to re-pressurisation.

In the LoFS surveys with high signal to noise ratio and low NRMS, detectable travel-time differences as small as $200\mu s$ are observed at wells which have been active for less than a year. Previously in the streamer data at Ekofisk, the NRMS was about 12% (Haugvaldstad et al., 2011) whereas in the LoFS data the recorded NRMS is as low as 5% (Bertrand et al., 2014). The $NRMSD$ is often used as a quality control for 4D seismic data and to assess noise levels above the zone of interest. The calculation of $NRMSD$ is given below:

$$NRMSD = \frac{RMS(D)}{\frac{1}{2}\left(RMS(B)+RMS(M)\right)} \tag{5.1}$$

where B and M are the baseline and monitor volumes respectively. The use of the RMS operation on the difference cube (D) means that this is an absolute measurement only and that the polarity of the difference is not preserved by this attribute.

The time-shift measurements were made using the non-linear inversion method by Rickett (2007). In this technique, time-shift traces between the base traces and the monitor traces are calculated by solving a nonlinear system based on 4D differences and Tikhonov regularization. It used a Gauss-Newton algorithm which optimises the NRMS value calculated between the base and the

monitor data after the estimated time-shift has been applied back to the monitor data. The strength of the method also lies in maximizing the smoothness of the time-shift function as part of the objective function and as a result produces a more stable estimate of the time-strain. Another objective of the 4D time-shift estimation is to align the monitor to the base survey before 4D amplitude inversion, in order to remove very low frequency time-lapse effects linked to the geomechanics that subsequent impedance inversion will not take into account. Time-shift maps between LoFS 2 and LoFS 6 for intra Ekofisk and Balder formations are presented in Figures 5.2 (a) and (b).

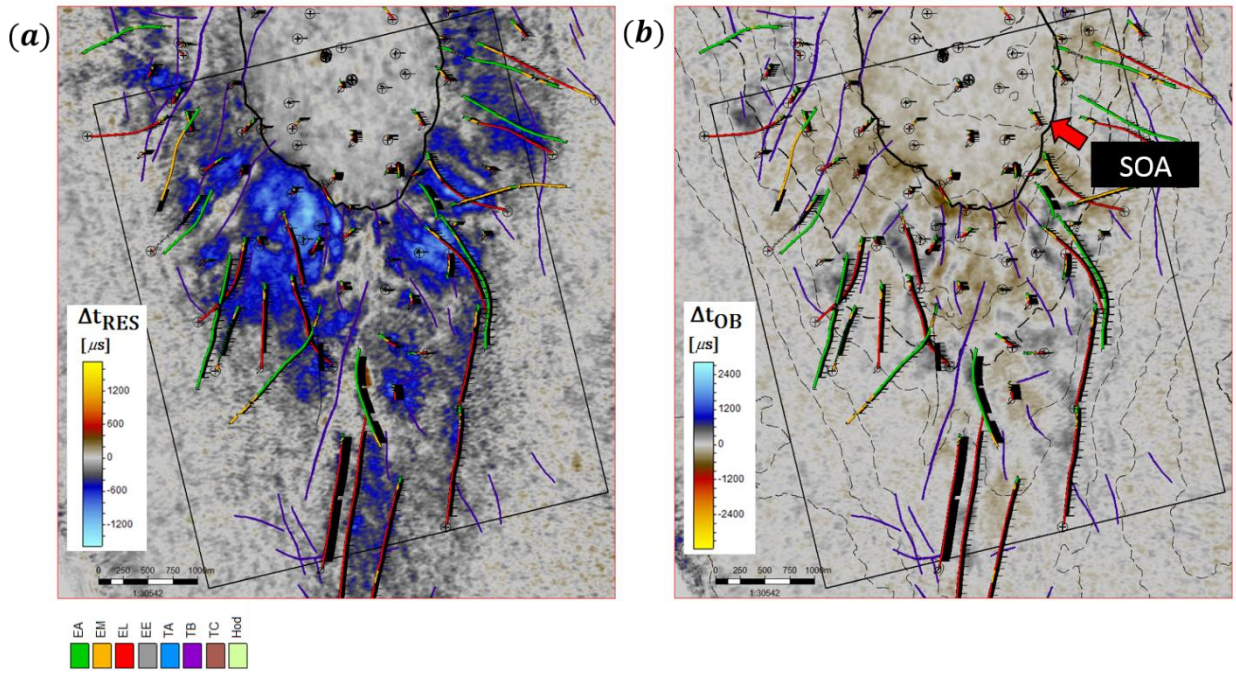

Figure 5.2: Maps showing (a) reservoir time-shifts and (b) overburden interval-Balder time-shifts. Balder is the overlying overburden shale adjacent to the reservoir. The SOA is pointed out by the red arrow, showing poor seismic quality.

5.4 Data Description: Amplitude changes and Relative change in V_P, V_S and ρ

A second and subtler component of the 4D signal is an amplitude difference caused by impedance changes occurring as the reservoir responds to water injection and pressure depletion. Although noisy on streamer seismic data, this 4D signal is important in planning new wells that are targeting specific intra-reservoir zones (Folstad 2010). Furthermore, the reservoir is relatively thick, and the

seismic suffers from interference of side lobes and tuning. This is also one motivation to carry out impedance inversion for more direct interpretation. Another motivation is that amplitudes have been used with success elsewhere - for example, the successful case study on South Arne (Herwanger et al., 2010) shows that time-lapse AVO (amplitude versus offset) inversion and rock-physics analysis can be employed to accurately monitor preferred fluid pathways inside the reservoir.

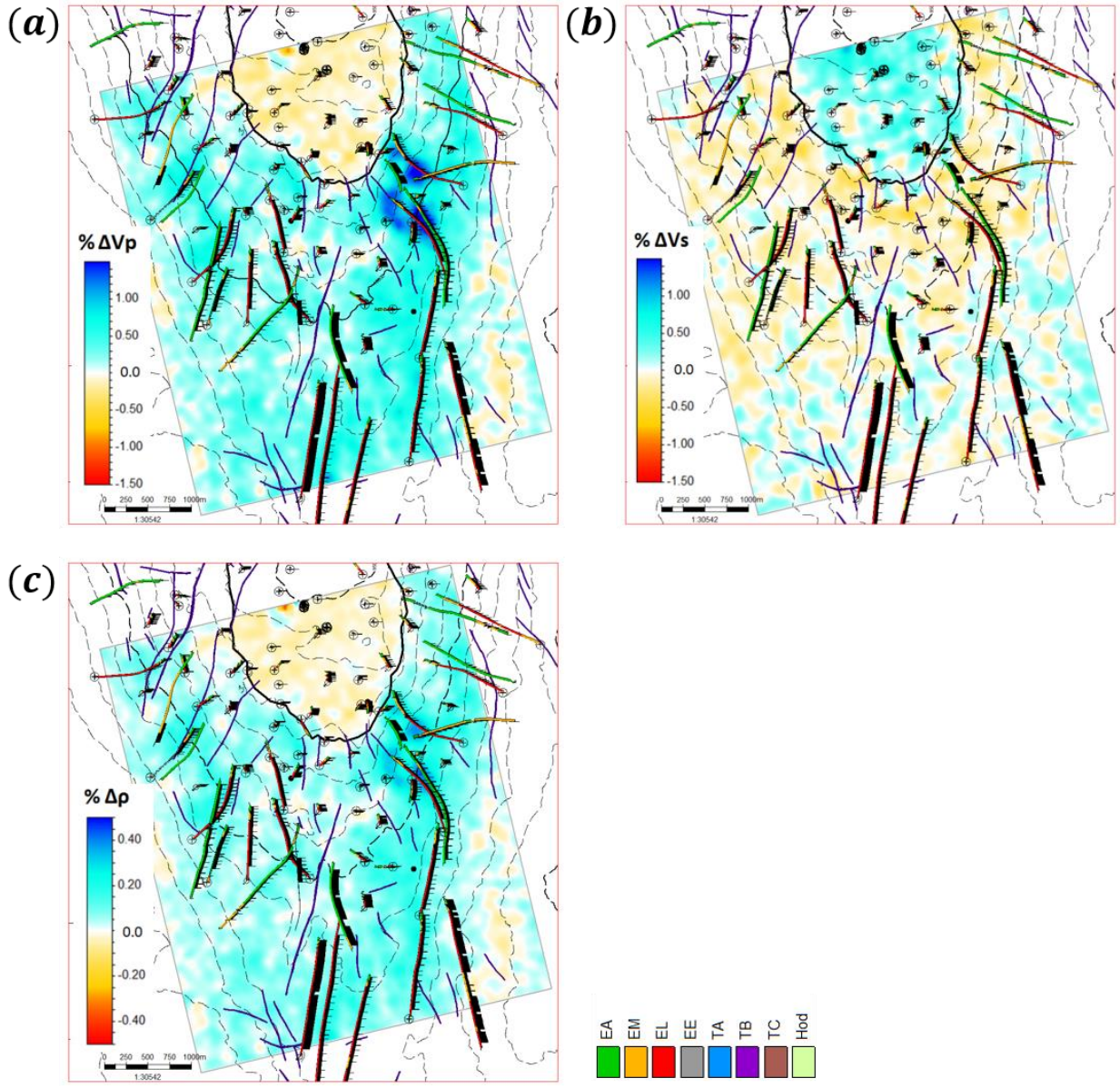

Figure 5.3: Maps of percentage change of (a) V_P, (b) V_S, and (c) ρ averaged across the Ekofisk formation. These products are generated via a 4D simultaneous pre-stack elastic inversion.

The pre-stack elastic properties are obtained from the joint multi-vintage inversion provided for Ekofisk by Lafet et al. (2009). Their inversion of the LoFS data incorporates all angle stacks from the baseline and monitor surveys, and deploys a convolutional model and the full Zoeppritz equation. The multi-vintage, global inversion starts by building an initial layered model using a stratigraphic grid framework defined in two-way time and common to all surveys. It is populated by different distributions of P-wave velocity,V_P, S-wave velocity, V_S and density, ρ, at each survey time. During the inversion, the model properties are iteratively perturbed to find a global solution that simultaneously optimises the match between the input angle stacks and the corresponding synthetics for all seismic vintages. In the inversion procedure, the model building process also included low frequencies from both the well logs and a high quality migration velocity model. The accuracy of this low frequency model was confirmed by running localised-inversions at the location of blind-wells. This also provides us with a confidence measure in the quality of elastic inversion results not only at the well locations but also away from the wells. Access is given to these results, and we use the percentage changes of $\Delta V_P/V_P$, $\Delta V_S/V_S$ and $\Delta\rho/\rho$ output from this inversion procedure (see Figure 5.3) as input data into our method for estimating pressure and saturation changes.

5.5 Assumptions

Three assumptions are implicit in this technique. Firstly, creep behaviour is not taken into account. Creep in chalk weakens the rock without any drop in pressure following the invasion of water. The rock will thus have a greater compaction later in time when pressure eventually drops (Barkved et al., 2003). Secondly, gas saturation changes is excluded as a model parameter. There are several points that we consider why gas saturation is not prominent in our inversion scheme and these are presented below. Our observations from the predictions of the coupled fluid-flow and geomechanical simulator shows gas saturation changes accumulate around producers only, and is negligible away from the locality of the wells. This suggests that effect of compaction compensates for the original pressure drop due to oil production, and gas is not liberated from solution in the inter-well space. Secondly, evidence from recorded gas-oil ratio (GOR) during the LoFS period shows minimal fluctuations, suggesting little changes in free gas volume.

Furthermore, time-shifts and impedance changes due to gas saturation increases are not predicted to be as influential as those changes induced by compaction alone. The observed data shows a net hardening in the seismic time-shifts and P-wave velocity maps around these producers. This is also because the initial gas saturation in our baseline (LoFS 2) is already quite high at 10%, and the non-linear portion of the property versus saturation behaviour is not accessed. The synthetic impedance and time-shifts modelling in Section 4.5 also supports this argument. It is widely known that the abrupt reduction in V_P with the first few percent of gas dominates the P-wave seismic response, as illustrated in Figure 5.4. A small amount of gas increase typically less than 5% saturation from 0% cause a significant drop in the effective fluid modulus, and consequently a significant drop in the saturated bulk modulus of the rock. A clear departure from non-linear behaviour is observed between the gas saturation with V_P after 10% gas saturation, any increase of gas saturation from 10% gas is less apparent from V_P. Therefore it is a challenge to detect gas saturation changes with P-wave seismic or time-shifts in the reservoir in the presence of compaction.

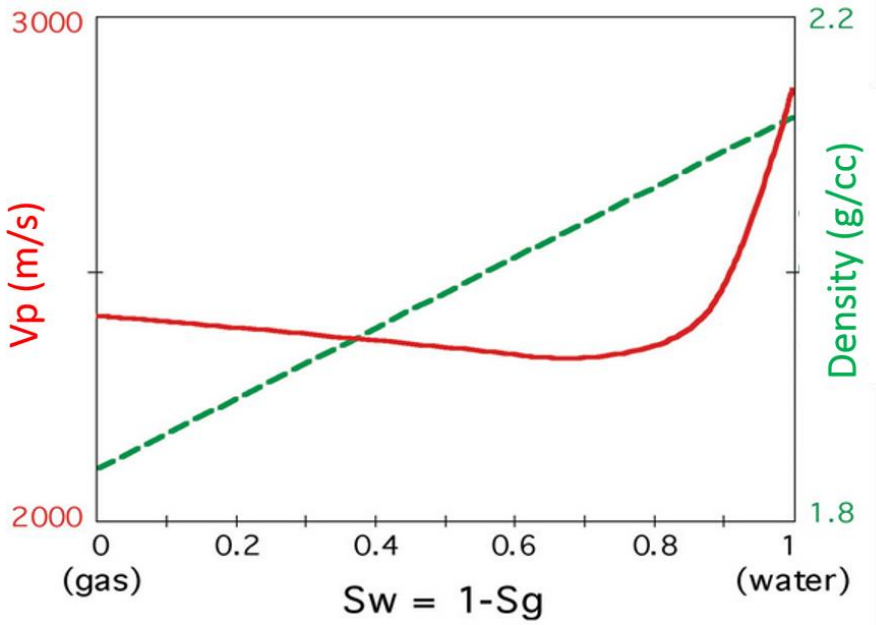

Figure 5.4: Change in V_P and density with change in gas saturation for a gas-brine mixture. The curve for V_P is calculated using the Gassmann fluid substitution recipe.

Similar observations were also documented in nearby chalk field Valhall, where at some of the well perforations, gas comes out of solution due to localized pore-pressure decline below bubble point, causing a reduction in impedance. The exact position of these regions is difficult to detect in the acoustic impedance attribute due to the masking effect of compaction and inter-well interference (Huang et al. 2011), shown in Figure 5.5. Historically in Valhall, rock compaction was recorded as the main driver in contributing to the total cumulative oil compared to other drive mechanisms. Although producers have produced excess gas however the recorded GOR development has been otherwise small. It was also shown that contribution to oil produced from gas influx mechanism flattens out when rock compaction becomes abnormally high (Cook et al. 1996). Also, this is similarly inferred in the deep water BC-10 Brazilian field (Galarraga et al. 2015). At some producers, absence of gas was observed when the pressure is very low (below bubble point) with high cumulative oil production. This absentee in gas is attributed to increase in compressibility of the rock.

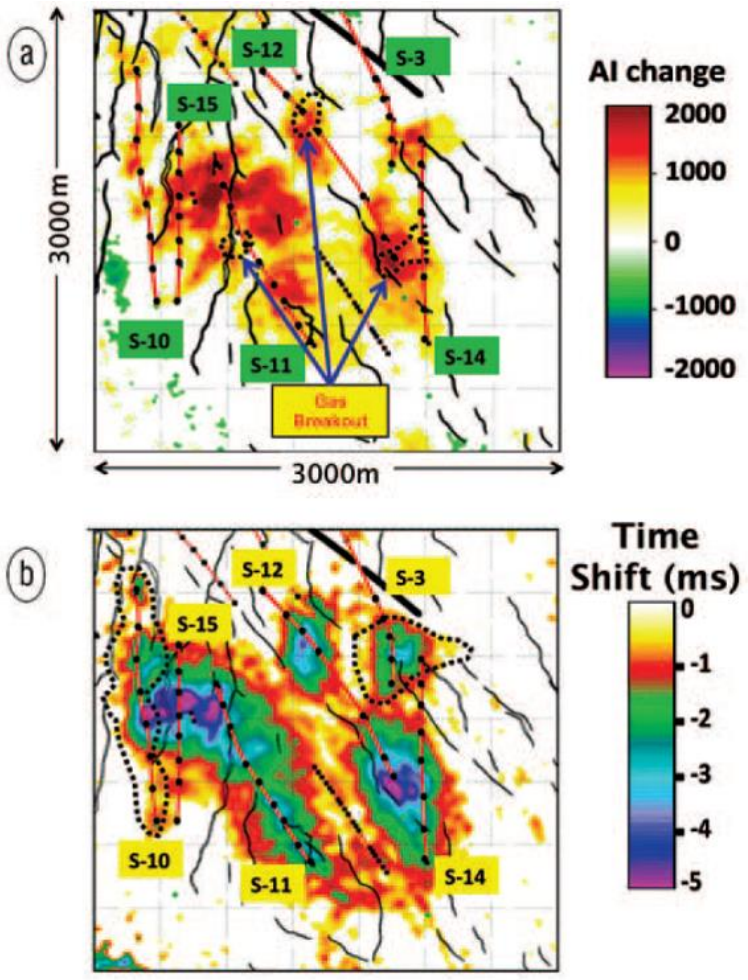

Figure 5.5: Maps showing production wells on the south flank of Valhall overlaid on (a) mapped AI change between monitor Lofs10 and baseline and (b) time-shift attribute. The positive AI change and negative time-shifts points towards a hardening response due to compaction resulted from pressure depletion. The dotted circular areas in (a) is inferred as zones of gas evolution from the technique well2seis. However, the gas signals are masked by the geomechanical response (Huang et al., 2011)..

Thirdly, since we are inverting the LoFS survey data and there is no pre-production PRM seismic, it is difficult to know the initial stress state of the rock. Compaction due to depletion from a specific initial porosity and effective stress state cannot be directly mapped onto depletion at the same initial porosity. An approximation is simply to use the curves as they are, assuming independence from the initial stress state. I find that this assumption creates minor errors (less than 5% error) in the modelling of the compaction. It is true that the use of compaction curve irrespective of initial

stress state is precarious since inverting pressure from an initial stress state of high effective stress (low pore pressure) will be different from low effective stress (high pore pressure), whereby the former has a higher compaction gradient than the latter. The average pore pressure in the LoFS period is approximately 5500-6000psi. The pressure change in the LoFS period is within +/- 1500 psi resulting in an effective pressure of 4500-5000psi, this falls within the linear part of the compaction curves, hence the compaction gradient is not largely dependent on the initial state and the linearization of the compaction curves hold true. If the pressure change is enormous like those in the earlier days of Ekofisk (1971-1989, 1989-1999), this assumption will be quite flawed as the initial state takes a major role in deciding the amount of compaction in the chalk. The present study on the LoFS period has strain rates that are small and the average field effective stress is lower compared to the streamer period.

5.6 Inversion Workflow

In this section, the process of an inversion for reservoir pressure and saturation change is described. The workflow is summarized in Figure 5.6. The workflow starts with using inputs of the relative change of V_P, V_S, and ρ inverted from the observed amplitude difference after time-shifts correction. However, this step could create errors after time-shifts correction, as the waveform re-construction only takes into account of the kinematics and not changes in amplitude. This remains a challenging issue in both computing and correcting for time-shifts. In the subsequent step, based on knowledge from 4D seismic interpretation around wells and from prominent 4D seismic signals, I get a better understanding on how pressure and saturation affects the 4D seismic anomalies for both the relative change of petro-elastic parameters and time strain. I then map the elastic properties and time-strain onto the reservoir grid. The pressure-saturation change inversion starting model is the history matched pressure and saturation change results from the simulation model, these changes are inherently smooth in nature. I also carefully designed some engineering consistent constraints to stabilize the inversion. Apart from using the elastic properties as input, time strain is also included to yield constraint. The first stage of the inversion is to assess how additional information like time strain and EC constraints make a difference to the pressure and saturation change. The next step is to perform the inversion via a stochastic approach to provide

some measure of uncertainty. Results from both deterministic and stochastic approach is step 1 and 2 are shown in subsequent sections.

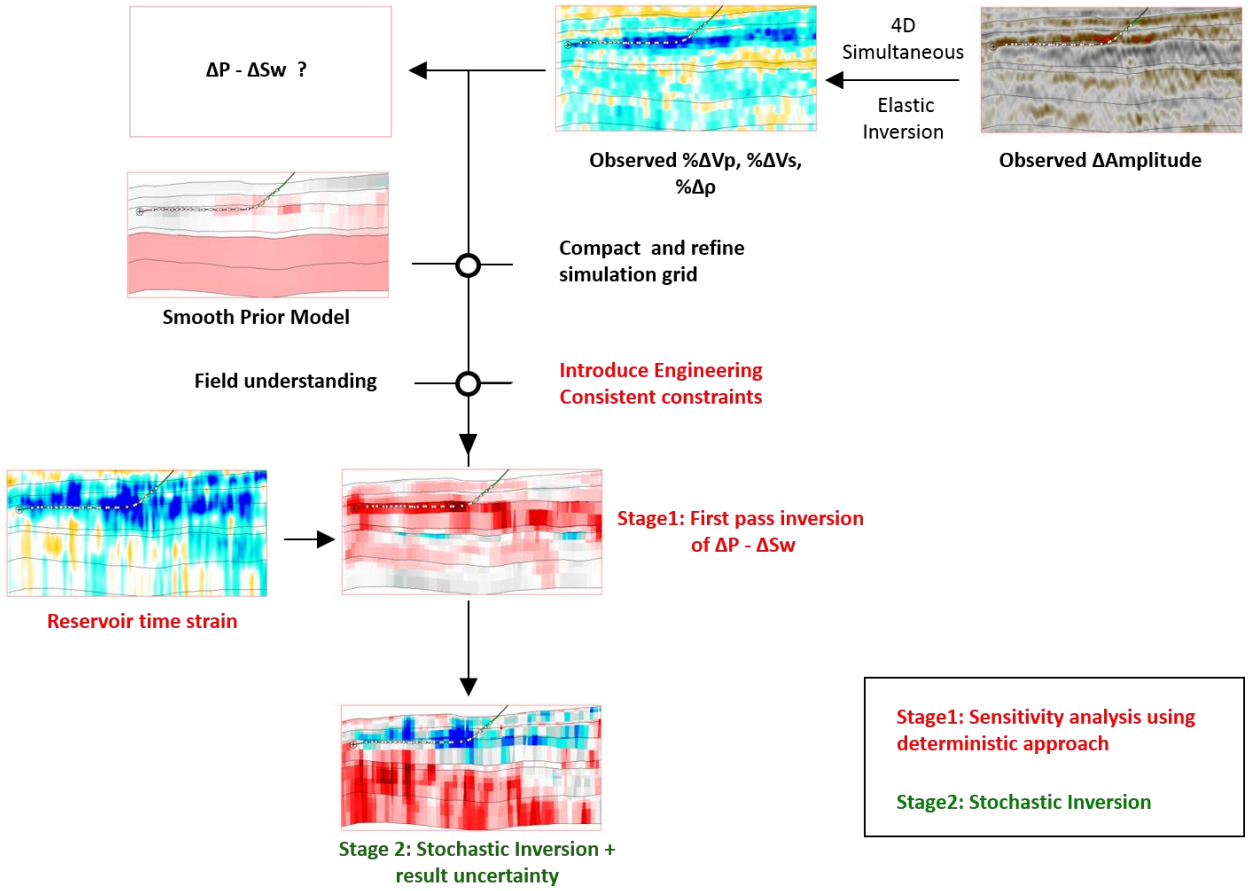

Figure 5.6: The hierarchal workflow proposed to invert for changes in pressure and saturation as outlined in this thesis.

5.7 Inversion Implementation

The formulation of an inference problem can be split into two components. One component is the identification of a suitable, accurate forward operator that can adequately describe the physics that represents the observed relative change in different elastic properties as a function of the reservoir dynamic properties. This is explicitly described in the previous section as a proxy model. The second component is how the problem is being posed and how the inversion problem can be solved effectively for example by including constraints to expedite the convergence of a solution.

I first describe how the input seismic data are treated. Firstly, the observed change in amplitude after time-shift removal is inverted to relative changes in the elastic properties such as: $\%\frac{\Delta V_P}{V_P}, \%\frac{\Delta V_S}{V_S}, \%\frac{\Delta \rho}{\rho}$. Then, data from both seismic: $(\%\frac{\Delta V_P}{V_P}, \%\frac{\Delta V_S}{V_S}, \%\frac{\Delta \rho}{\rho})$ and from engineering domains and the flow-simulation model $(\Delta P,\ \Delta S_w, \varphi_i)$ were registered into a common grid in depth. Because the simulation model is built with reference to pre-production in 1976, the grid is retained in pre-production depth. Due to chalk compaction, normal static parameters like porosity are dynamic in the Ekofisk field, and over time the reservoir has compacted considerably. In order to accurately map seismic properties into the simulation grid, the simulation model grid was compacted to fit the seismic horizons in depth (Reidar Midtun, personal communication). Figure 5.7 shows the grid (a) before and (b) after compacting the cells, the later version shows the grid now conforms with the newly picked horizons in the monitor time after compaction. The simulation predictions are also used to build a prior model in the inversion.

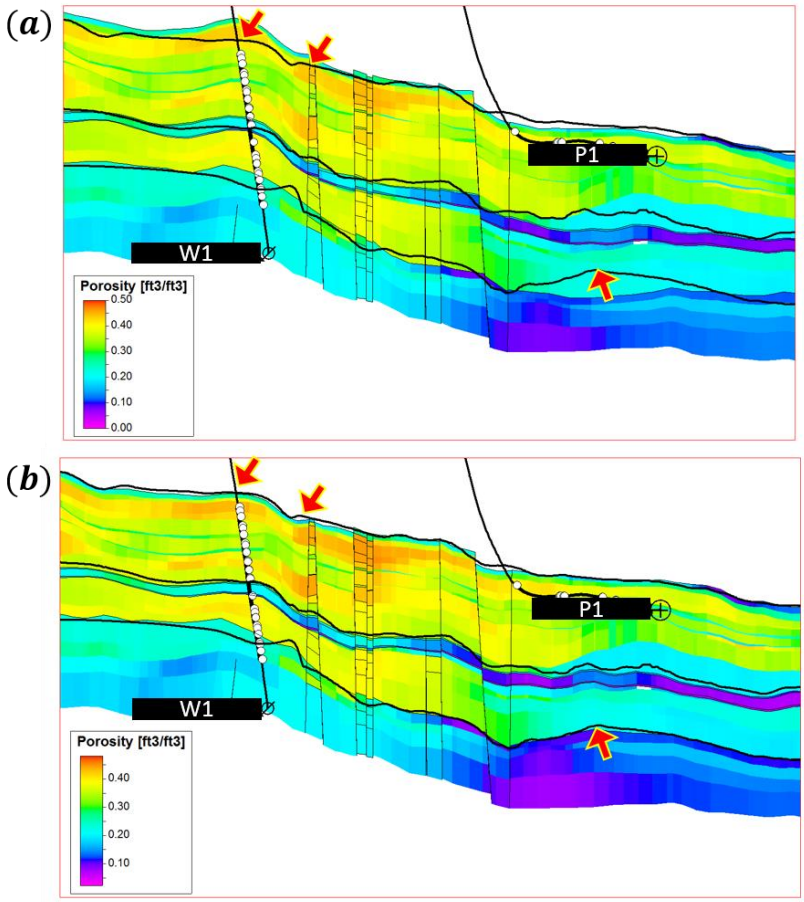

Figure5.7: (a) shows mapping of the reservoir property such as porosity into the reservoir, the results seems far from satisfactory. In order to accurately map seismic properties into the simulation grid, the simulation model grid was compacted to fit the seismic horizons in depth as shown in (b).

5.7.1 Engineering consistent constraints

There are many ways to incorporate a priori information into the inverse problem. In this section, I will present some engineering consistent constraints to condition the prior model. It is generally understood that 4D seismic signatures are sensitive to changes in reservoir pressure, water and gas saturation caused by fluid extraction or injection from wells. Therefore, 4D seismic data cannot be unambiguously interpreted without a clear understanding of the production and injection history. However there are several unknown parameters such as pressure, saturation, porosity, and compaction that can be calibrated by only a small amount of spatially coarse data from wells. In practice, useful information from well logging and well tests are called "ground truths" and could be included. However, there will be limitations in terms of the number of sample points in time

and space. One source of information to tap into is the simulation model prediction and engineering concepts that are valid in specific fields. The simulation model is capable of providing spatial constraints in a three dimensional sense, which is helpful in significantly reducing the number of possible solutions for a non-unique problem for each spatial location, and retains the most plausible ones.

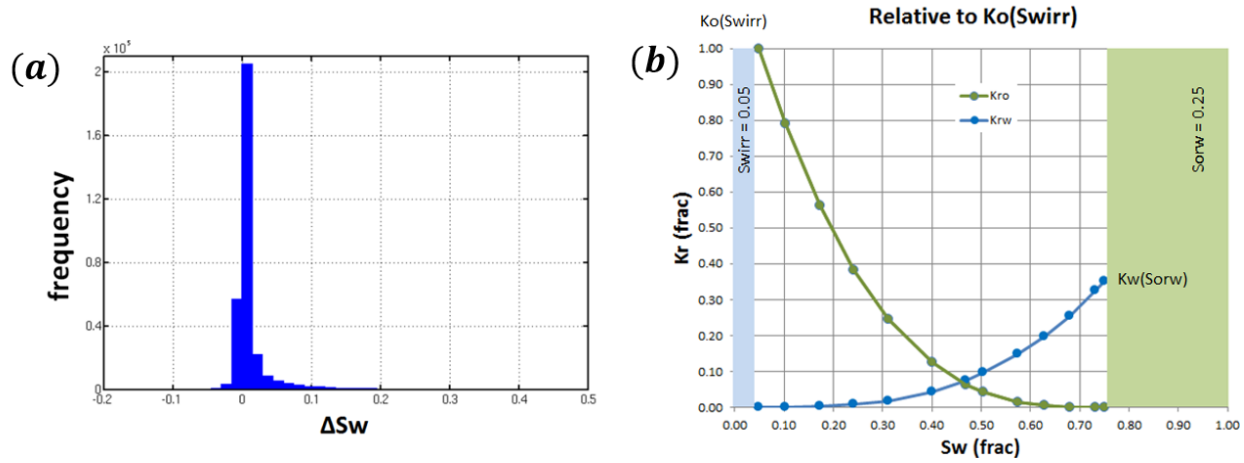

Figure 5.8: An inequality constraint is applied to the non-water leg regions, where the change in water saturation should follow a statistical expression (min and max) retrieved from the reservoir simulation post-history matched result, shown as a histogram in (a). Figure 5.8(b) shows this constraint is reasonable as it falls within the range of $1 - S_{or} - S_{wirr}$.

The first engineering consistent (EC) constraint imposed is in the water leg. No change is expected in saturation in the water leg from pre-production to current state hence it is only logical to impose $\Delta S_w = 0$ as the water saturation is always unity. However, it is permissible to have pressure signals within the water leg, so the constraint on pressure is not imposed in the water leg. In other words, the assumption is that above the oil water contact, changes in saturation are allowed, hence an inequality constraint above the water-leg of -0.10≤ ΔS_w ≤0.5 was applied to this section of the solution space. The upper and lower boundaries are extracted from simulation model statistics (minimum and maximum values) and shown in Figure 5.8(a). Figure 5.8(b) shows that this is engineering consistent as it falls within the range of $1 - S_{or} - S_{wirr}$. The S_{wirr}, irreducible water saturation is defined as the minimum water saturation obtainable or the fraction of the effective porosity that contains water that will not flow out of the rock. The S_{or}, residual oil saturation is

described as the remaining oil saturation after the reservoir has been fully flooded. It is evident that all or most North Sea Chalk fields have difficulty in identifying transition zone, tilted or blurry oil-water contact (Megson and Hardman 2001) such as in the Tyra, South Arne, Joanne, Halfdan field and so on, thus the constraint impose on the water leg has to be carried out in a conservative manner. In this field, the engineering consistent constraint is implemented based on the original oil water contact (OOWC) defined in 1971 (pre-production) using the reservoir simulation model which was built by integrating petrophysical well logs and well tests information. I only impose $\Delta S_w = 0$ below the OOWC at pre-production by giving a flag value of '0', as shown in Figure 5.9(a). Above the OOWC, the flag is '1' and the changes in water saturation is free to fall within the range of $1 - S_{or} - S_{wirr}$. Figure 5.9(b) shows the location of the water leg in the cross-section of the model after the applying this constraint on the inversion.

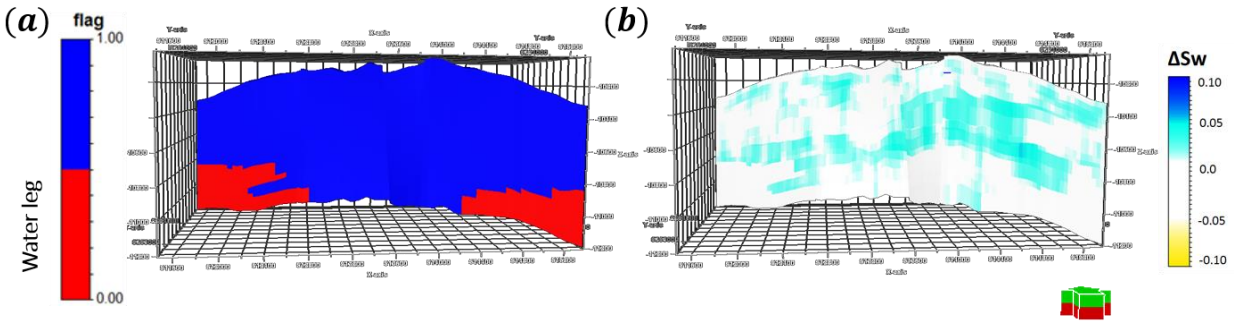

Figure 5.9: (a) The location of the water leg is flagged in red colour. The result from inversion shows that the water leg region will not have changes in water saturation as a result of the constraint, shown in (b).

For the second EC constraint, I create a spatially-varying upper and lower bound for the prior model in each grid cell. I first evaluate on a well-by-well basis the relative misfit between the historic bottom hole pressure (BHPH) and the simulated bottom hole pressure (BHP), and the historic water injection rate (HWIR) and the simulated water injection rate (WIR). Apart from 4D seismic history matching, other data such as static pressure recorded during field shut downs, Repeat formation testers (RFT), Production logging tools (PLT), well interference tests, well production or injection tests and tracer data are also frequently used to match the dynamic changes recorded at the wells. Usually the well pressures have to match the HBHP within the range of 300psi. If the relative misfit is within this margin of error, the statistical measure of pressure and

saturation changes close to well perforations was extracted from the simulation model using a Gaussian window. This in turn imposed a tight upper and lower bound for changes in pressure and saturation as estimated from the reservoir simulation predictions displayed in Figure 5.10 (a) and (b). Instead of extracting a single value of pressure or saturation changes between each time step on the historic production plot, I extract the upper and lower bound of pressure or saturation changes in cells around the wells from the simulation model. These constraints are realistic given that the simulation model is relatively well history matched. If the well performs badly in terms of its relative misfit, the prediction around the well is excluded. Although one might question the reliability of the model compared to observed data from seismic, the application here does not disregard the seismic, but in turn allows some statistical control on possible ballpark values of changes of both pressure and saturation. For example, in the case of the inter-well space, the prior model is heavily reliant on the seismic instead of the simulation model prediction.

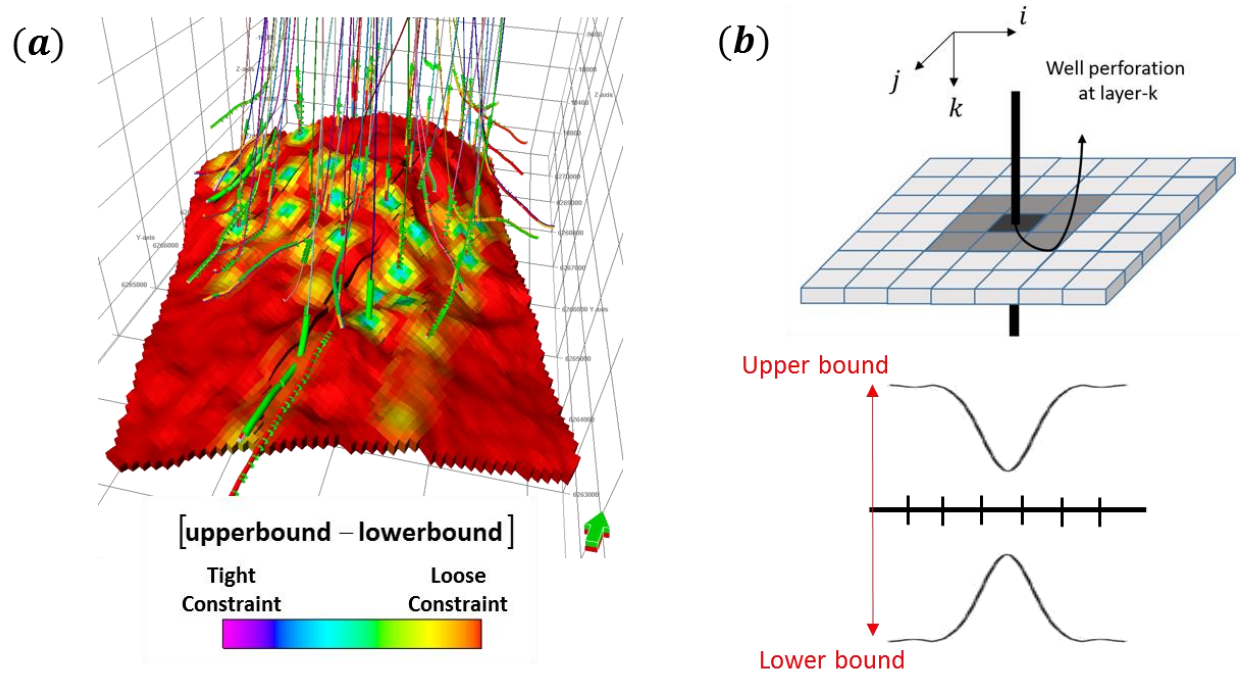

Figure 5.10: (a) The Gaussian window is drawn around each of the well perforations that were active during LoFS 2 - LoFS 6. (b) The constraints are only applied to a well with an excellent history matched profile of the production data, with a tighter bound at the well perforation and a wider bound away from the well.

5.7.2 Additional Information: time strain

Additional information for the inversion, apart from the proxy model, is the use of the time-strain. Since the elastic properties such as V_P and ρ are relatively correlated, reservoir time-strain is also included as a separate observation. For example, a well which is a controlled injector with sound history-matched pressure and saturation shows a good match between the measured time-strain versus the computed time-strain. Figure 11 (a) shows the good match between the observed and computed time strain using inputs from the well history match simulation model. Figure 11(b) shows the empirically derived correlation between time strain and the changes on the dynamic properties. This strong correlation was added to the joint objective function of the inversion.

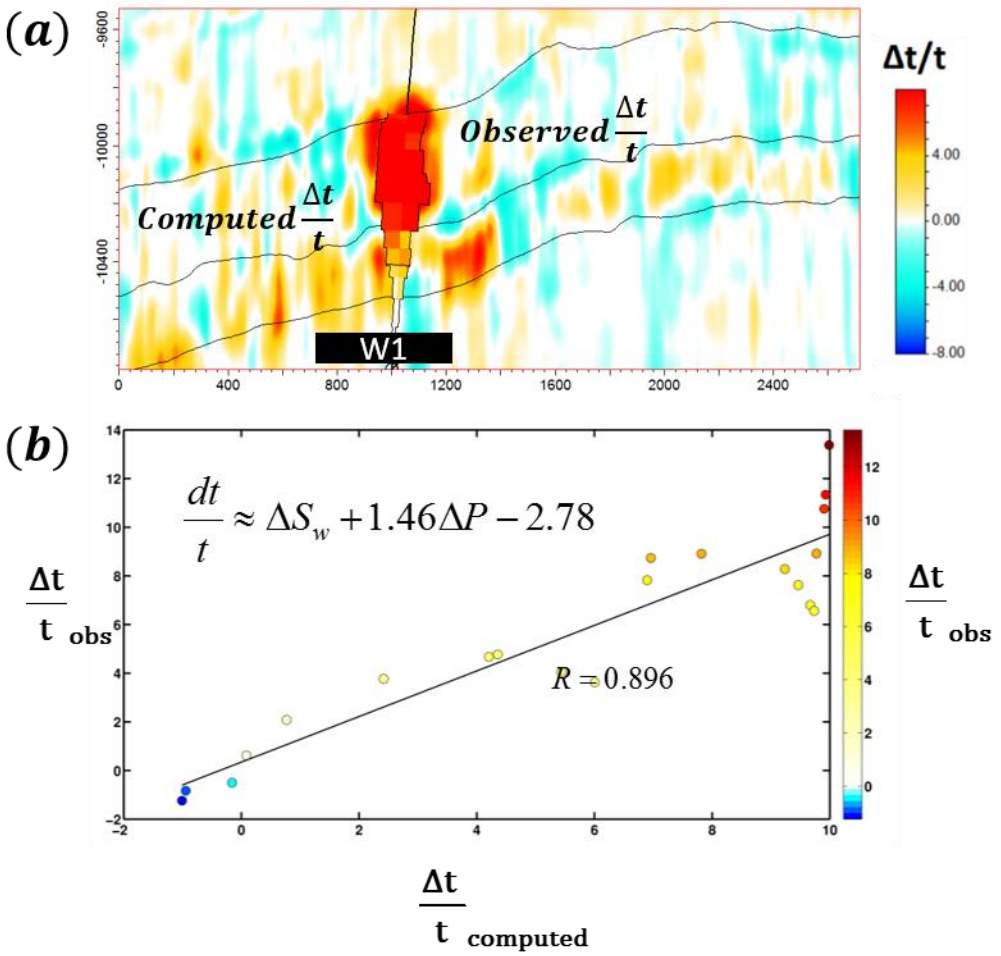

Figure 5.11: A good fit is found between the (a) computed time strain and the observed time strain at well W1. (b) The relationship of the observed time strain with water saturation and pressure changes is linear and is given in the equation.

5.7.3 Inversion using deterministic gradient-based optimisation

I first invert for the dynamic changes using a deterministic gradient-based optimisation, proposed in Chapter 4. The objective function of the problem is solved on a cell-by-cell basis and the joint objective function using the relative change in elastic properties and time-shifts is written as:

$$minimize\ f(\Delta P, \Delta S_w)$$

$$f(\Delta P, \Delta S_w) = w_1\left[\%\Delta V_P - G_{Vp}(\Delta P, \Delta S_w)\right]^2 + w_2[\%\Delta V_S - G_{Vs}(\Delta P, \Delta S_w)]^2 + w_3\left[\%\Delta\rho - G_\rho(\Delta P, \Delta S_w)\right]^2 + w_4\left[\frac{\Delta t}{t} - G_{\frac{\Delta t}{t}}(\Delta P, \Delta S_w)\right]^2 \quad (5.2)$$

where w_1, w_2, w_3 and w_4 are the weight factors. The weight factors are computed from the standard deviation of the data (Drahos 2008) as:

$$w_1 = \frac{1}{2\sigma_1^2},\ w_2 = \frac{1}{2\sigma_2^2},\ w_3 = \frac{1}{2\sigma_3^2},\ \text{and}\ w_4 = \frac{1}{2\sigma_4^2} \quad (5.3)$$

where σ is the standard deviation of the data. The intention is to weight each measurement in proportion to its error, for example there is more uncertainty in the density estimate output from the pre-stack elastic inversion compared to P and S-wave velocities. The task of inverting for density values from seismic data has remained an elusive task. In general, P- and S-impedance or P- and S-wave velocity can be reasonably estimated from P-P and P-S seismic inversion (Downton, 2005, Mahmoudian, 2006). Reliable determination of density from seismic data requires long offsets, or it can be determined from measured converted waves; and long offset data are notoriously noisy. In the deterministic approach, a lower weighting factor is prescribed to the objective function component of density since there is less reliability on this data.

5.7.4 Bayesian Framework

Inversion being a highly non-unique problem, a wide range of models can satisfy the data and a single model will lack predictive power. This is where the stochastic approach will facilitate more

reliable dynamic properties. In this Bayesian inversion, a stochastic approach is pursued. Bayes theorem (Bayes, 1763) provides a robust framework to address the uncertainties in the data and assimilate the prior information into the inversion problem. In this framework the solution to the inverse problem is represented by a posterior probability density function (PDF) for the model parameters (Tarantola, 2005). This requires prior knowledge of the range of uncertainty in the model parameters, and outputs in turn a posterior probability of the model parameters conditioned to the measured data. The final goal is therefore to estimate the posterior distribution

$$p(\Delta P, \Delta S_w | D) = p(\Delta P, \Delta S_w, H | x) p(D | \Delta P, \Delta S_w, H) \tag{5.4}$$

Where $p(\Delta P, \Delta S_w, H | x)$ represents the prior PDF and $p(D | \Delta P, \Delta S_w, H)$ is the likelihood. Data here is represented by the multiple time-lapse seismic data (D) with different levels of uncertainties. The hyper-parameters (H) are parameters of the prior distribution.

As described previously, I incorporate the prior information (x) into the inversion problem through EC constraints and information given from the history matched simulation model. Upper and lower bounds were created using the spatial constraints and feasible values from the history-matched simulation prediction. These bounds are prior information fed into the inversion procedure**.** Incorporating prior information can speed up the convergence of the inversion process towards the most probable solution. A multivariable Gaussian pdf is used to describe the likelihood, $p(D_i | \Delta P, \Delta S_w, H)$:

$$p(D_i | \Delta P, \Delta S_w, H) = \frac{1}{\sqrt{2\pi |\varepsilon_i|}} exp\left\{ -\frac{1}{2} [D_i - f_i(\Delta P, \Delta S_w)]^T \varepsilon_i^{-1} [D_i - f_i(\Delta P, \Delta S_w)] \right\} \tag{5.5}$$

Where ε_i represent the uncertainties in the i^{th} data with a diagonal covariance function, ε, f_i is the forward modelling procedure represented by the proxy model equation. The posterior PDF is two-dimensional, representing the pressure and saturation changes. The posterior PDF is simulated via the Metropolis method (Metropolis et al., 1953) which is a Markov-chain Monte Carlo (McMC) algorithm. More information on Metropolis method is described in Appendix A. The algorithm is set up in a way similar to JafarGandomi and Curtis (2012).

The mechanics of the Metropolis-Hastings algorithm starts with the initial values for $m_i\ (\Delta P,\ \Delta S_w)$ and calculates corresponding time-lapse seismic data $D(m_i)$ by modelling via the proxy model equation. A new candidate parameter vector m_{i+1} is proposed by randomly selecting a candidate of the dynamic properties from the prior distributions using a proposed Gaussian distribution. The corresponding time-lapse seismic parameter $D(m_{i+1})$ and the likelihood $L(m_{i+1})$ are subsequently calculated. A proposal Gaussian distribution is suggested since it resembles the actual posterior distribution of the dynamic parameters, similar to the time-lapse seismic data. The Metropolis rule is used to accept or reject the new candidate model by the acceptance probability of,

$$P = min\left[1, \frac{L(m_{i+1})}{L(m_i)}\right] \tag{5.6}$$

Where $L(m_{i+1})/L(m_i)$ indicates the ratio of the current and candidate likelihood. If the candidate model configuration is rejected, the current model remains for the next iteration, otherwise, m_{i+1} is accepted as the next model sample. These steps are repeated until the required number of samples in the set $S = \{m_1, m_2, \dots, m_N\}$ are obtained. The set S contains a set of samples that approximately samples the posterior PDF. By calculating the sample density in S, an estimate of the posterior distribution is obtained. More information on the convergence test can be found in Gelman et al. (1996) for Efficient Metropolis jumping rules.

Data uncertainties quantification are essential in the inversion procedure where they act as regularisation term or weights in the objective function. Here I assume that the accuracy of the time-lapse seismic data is correlated with survey repeatability, hence I apply less confidence to the data if it is associated with a higher $NRMSD$. $NRMSD$ refers to the energy in the difference cube. I construct a spatially varying uncertainty estimate for each measured data, D_{obs} from the non-repeatability of the overburden at the same vertical location, assuming vertical stationarity of the 4D noise level. The seismic data used in this analysis are acquired with a highly repeatable Permeant Reservoir Monitoring (PRM) system and have been processed with a mature processing flow optimized through several vintage processing. In particular the data has gone through an effective de-multiple flow which minimized the presence of non-stationary coherent noise with depth. This is confirmed by very high-repeatability (less than 5% $NRMSD$). Therefore, these

seismic data do not show noticeable non-stationary noise with depth. Additionally, using a window close to the target, whilst avoiding the target formation itself, this ensures the estimated uncertainty for geophysical parameters are fit for the purpose.

I account for the uncertainties in the elastic properties by calculating the standard deviation of those elastic properties based on the $NRMSD$ from a 1s gate in the overburden. Having identified an area (X) with very low $NRMSD$, we calculate the mean of the standard deviation ($\bar{\sigma}_{NRMSD}$) in this area, which is then used to calibrate the uncertainty values for $\%\frac{\Delta V_P}{V_P}$, $\%\frac{\Delta V_S}{V_S}$ and $\frac{\Delta t}{t}$ spatially. In Equation (5.7), we calculate the standard deviation of the noise level ($NRMSD$) in X, annotated as σ_{NRMSD}, and the standard deviation of the geophysical attribute in the same area X is annotated as σ_p (shown in Figure 5.12). Using the ratio of these quantities, we can calculate a spatially varying standard deviation for any given geophysical attribute:

$$\sigma_{p(x,y,z)} = \frac{\sigma_p}{\sigma_{NRMSD}} NRMSD(x,y,z) \tag{5.7}$$

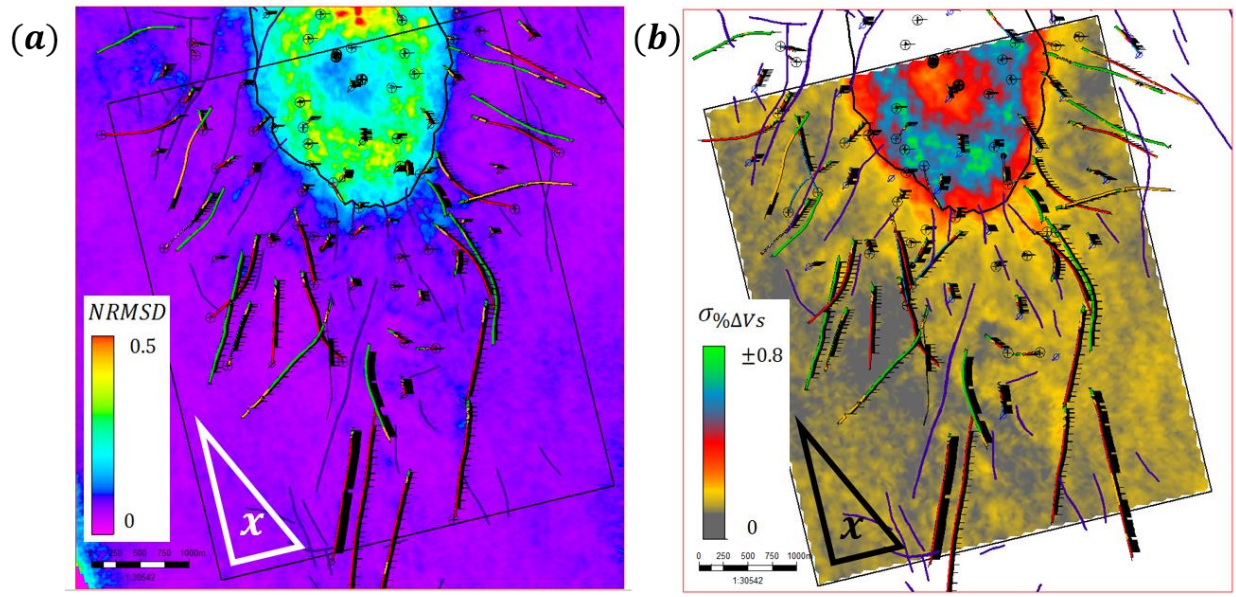

Figure 5.12: LoFS2/LoFS6 NRMSD map (a) computed in a 1s gate at 2500-3500ms window in the overburden. The area in bright colour with high NRMSD values is seismically obscured because of an overburden gas cloud. The standard deviation map (b) computed for the relative change of S-velocity is computed spatially by using area 'X' to calibrate the uncertainty values to the NRMSD.

The convergence of the McMC sampling depends on the prior range and the width of the Gaussian proposal distribution. If one is very close to the solution, then a wider proposal of perturbation will delay the convergence. However if one is far from the solution then a wider proposal will accelerate the convergence. The estimated uncertainties for V_P, V_S and time-strain are projected to the estimated pressure and saturation changes through the McMC inversion engine using the diagonal covariance function. These uncertainty bounds were relatively wide which helped the inversion engine to search for optimal solutions. Figures 5.13 (a) and (b) show examples of search chains where the posterior distribution is explored by 15,000 iterations with a Metropolis algorithm with a "burn-in" period of 5000 iterations for both pressure and water saturation change. It was observed that the parameters start to converge at around 5000 iterations for several runs across different cells inside the model. I decided to run 15000 iterations since the McMC samples converge to a stationary distribution at this number of iterations. I choose to calculate the mean, median and mode of the posterior distribution, which may be used to represent the best model estimate. Associated uncertainties with each estimated model parameter are represented by the standard deviation of the posterior distribution.

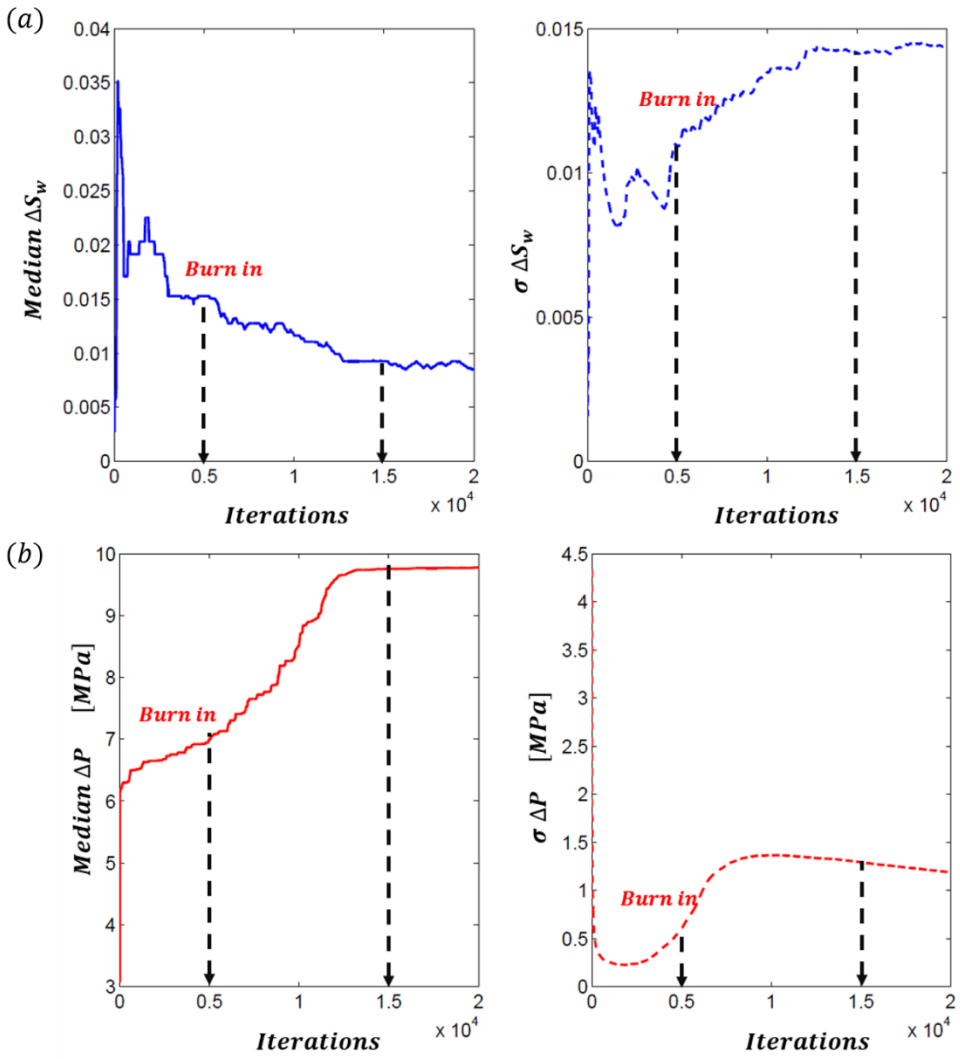

Figure 5.13: Statistical behaviour of the McMC chains for one sample point for both changes in saturation (a) and pressure (b). The burn in occurs at 5000 iterations, in which the parameters become stable and starts to converge.

5.8 Results and Discussion

Here I describe the key results of the inversion and will associate them with qualitative and quantitative interpretations. A fast track deterministic inversion described in Section 5.7.3 is performed to understand the contributions of both EC constraints and time strain information in the inversion results. Figure 5.14 shows clear evidence of the progressive improvements in the results by including constraints and subsequently adding additional data such as time strain. Figure 5.14 (a - left) depicts the estimated pressure and saturation changes from inversion of elastic parameters without using EC constraints. In the constrained scenario (Figure 5.14a - middle), I apply spatial constraints and extracted the upper and lower bounds on the potential range of unknowns $(\Delta P, \Delta S_w)$ with greater confidence around the well perforations. In Figure 5.14 (a - right), after including time-strain as additional independent information, a clearer delineation in pressure and saturation around the wells is observed. The result shows that the polarity of pressure change from the inversion results is consistent with well locations. Results show pressure build-up is found around the injectors and majority of the producers show pressure depletion. Although there is arguably less improvement in the prediction of the water saturation changes after adding constraints into the inversion process (Figure 5.14 b from left to right), the magnitude of the saturation changes are more balanced and considered to be of the same approximate magnitude.

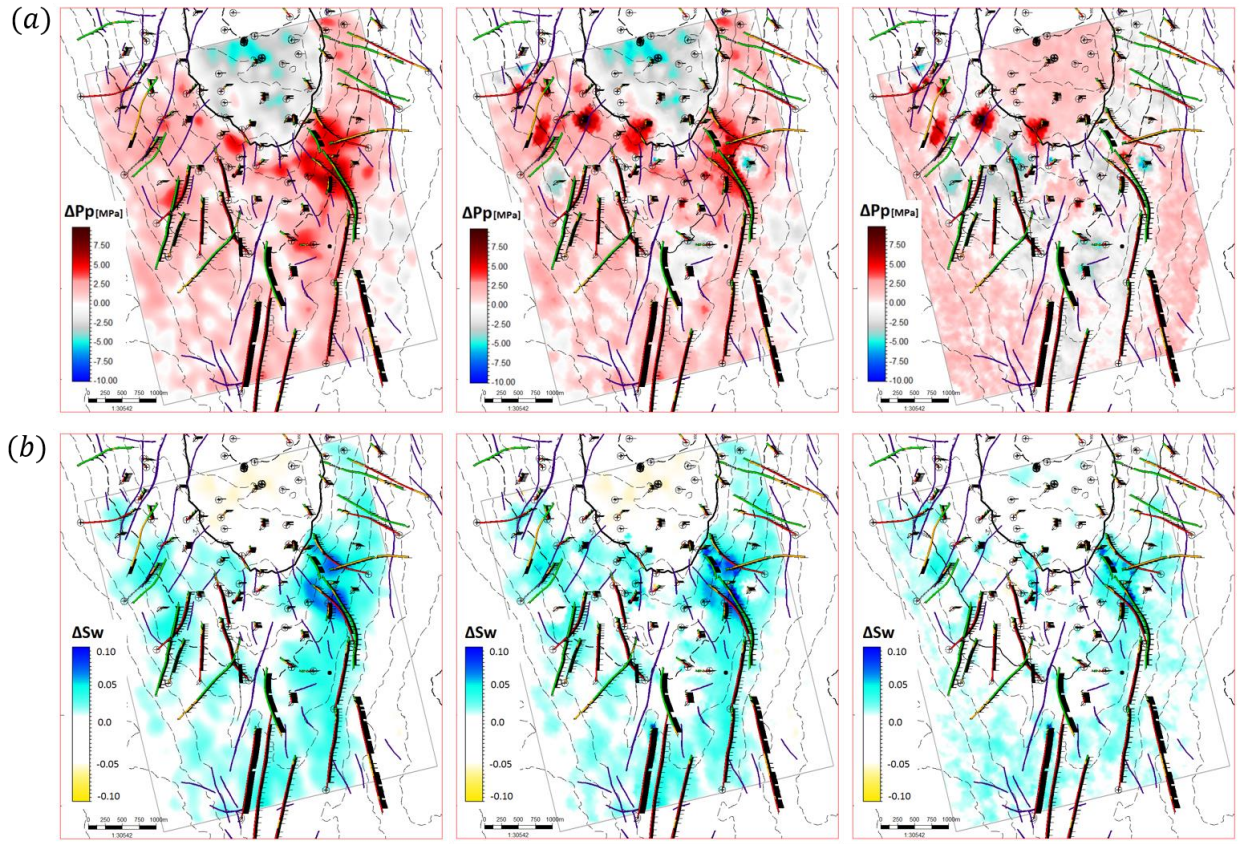

Figure 5.14: Above, the progressive improvement on the results for (a) pressure change and (b) water saturation in an unconstrained situation, followed by adding EC constraints and additional information such as time strain.

Having carried out this sensitivity study, I proceed to run the inversion in a stochastic manner, taking into account of the uncertainties in the data. The stochastic results (Figures 5.15a and b) are computed by taking the posterior median solution obtained from the simulations after a period of burn-in for both changes in pressure and saturation. In Figures 5.16(a) and (b) shows the posterior uncertainty is represented by one standard deviation - around 2MPa for pressure and a fraction of 0.05 for water saturation. Large uncertainties are estimated at regions where there is a considerable misfit between seismic observation and the simulation model prediction. These regions also indicated a lower level of confidence in the estimates.

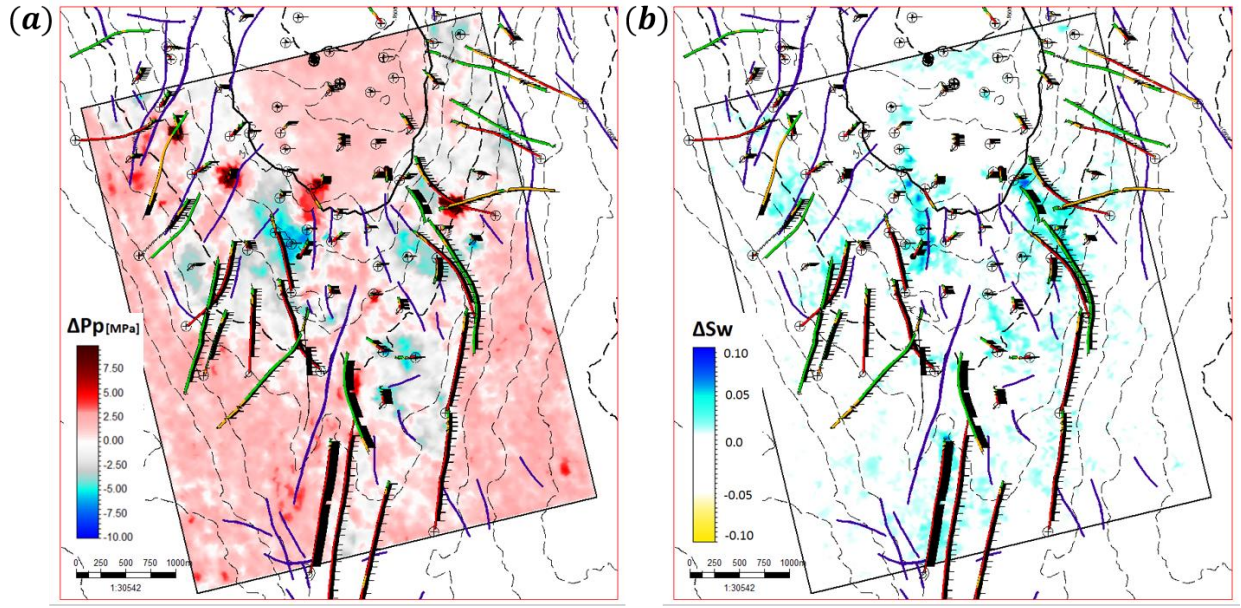

Figure 5.15: The stochastic result for changes in (a) pressure and (b) water saturation.

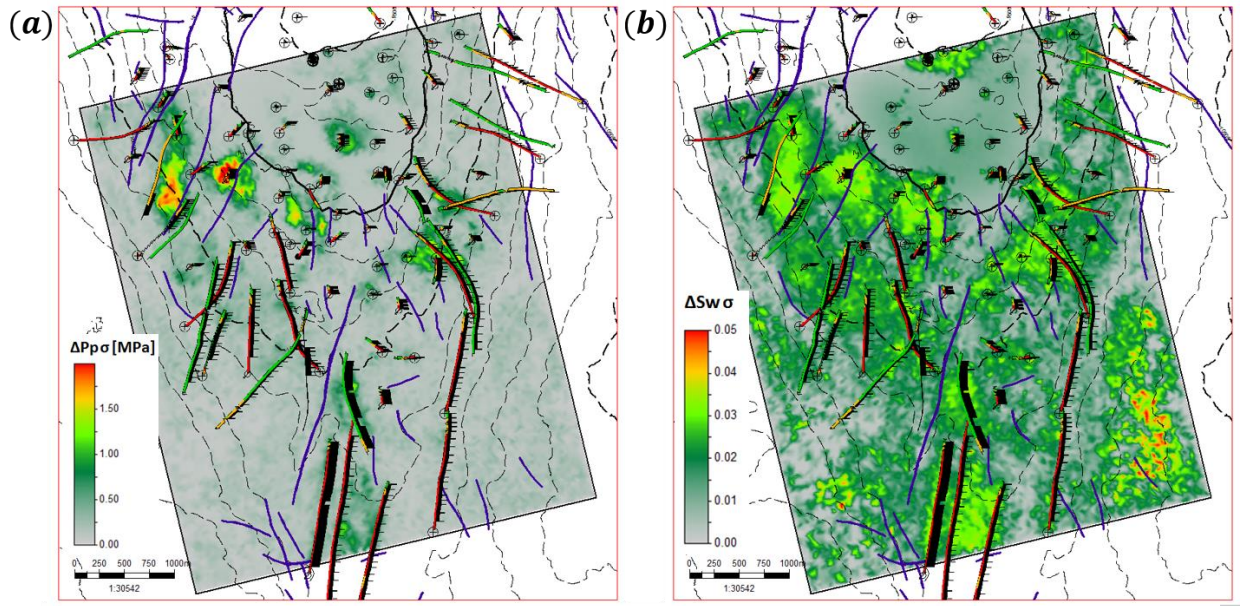

Figure 5.16: Posterior standard deviation after stochastic inversion for (a) changes in pressure and (b) changes in water saturation. Areas with bright colours correspond to lower confidence in the inversion result.

The validity of the inversion can also be checked by using the inverted pressure and saturation changes to compute changes in reservoir thickness (dz) via the fast proxy model equation derived in Chapter 4. The changes in thickness can be expressed as:

$$dz = \frac{\left[F_p + \left(\frac{\Delta S_w}{\Delta S_{wmax}}\right)(F_{ww} - F_p)\right] \cdot \Delta P}{(1-\varphi_1)} \cdot z_1 \tag{5.8}$$

The full derivation of Equation 5.8 is provided in the Appendix E. Having inverted pressure and saturation changes from 4D seismic attributes, I can use the proxy model to calculate changes in reservoir thickness using Equation (5.8). I then compare the modelled change in reservoir thickness with the interval-reservoir time-shift maps. The comparison is shown in Figure 5.17 and Figure 5.18 for Ekofisk and Tor formations respectively. Maps in Figure 5.17 and Figure 5.18 illustrate that comparable trends with compaction are expected in some of the major producers and injectors situated in oil producing areas in both formations. However, a closer look also reveals differences, partly due to the timing of pressure and saturation changes. The comparison reveals stronger compaction in the time-shift data – this could arise if water intrusion occurs before pressure build-up due to fracture flow. Other possible explanations are that the static parameters are not adequately captured in the original reservoir model or that there are other physical processes affecting changes in compaction such as creep.

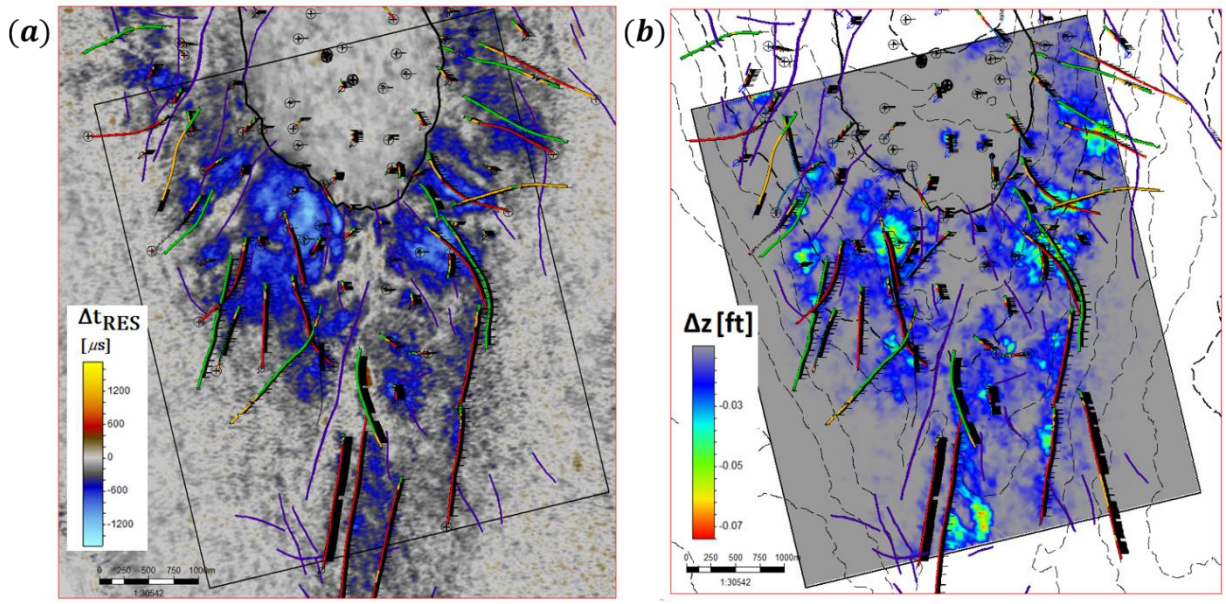

Figure 5.17: Computed changes in thickness (feet) for Ekofisk formation (right) using the proxy model equation and inputs from the inverted results, compared against the measured interval Ekofisk formation time-shifts (left).

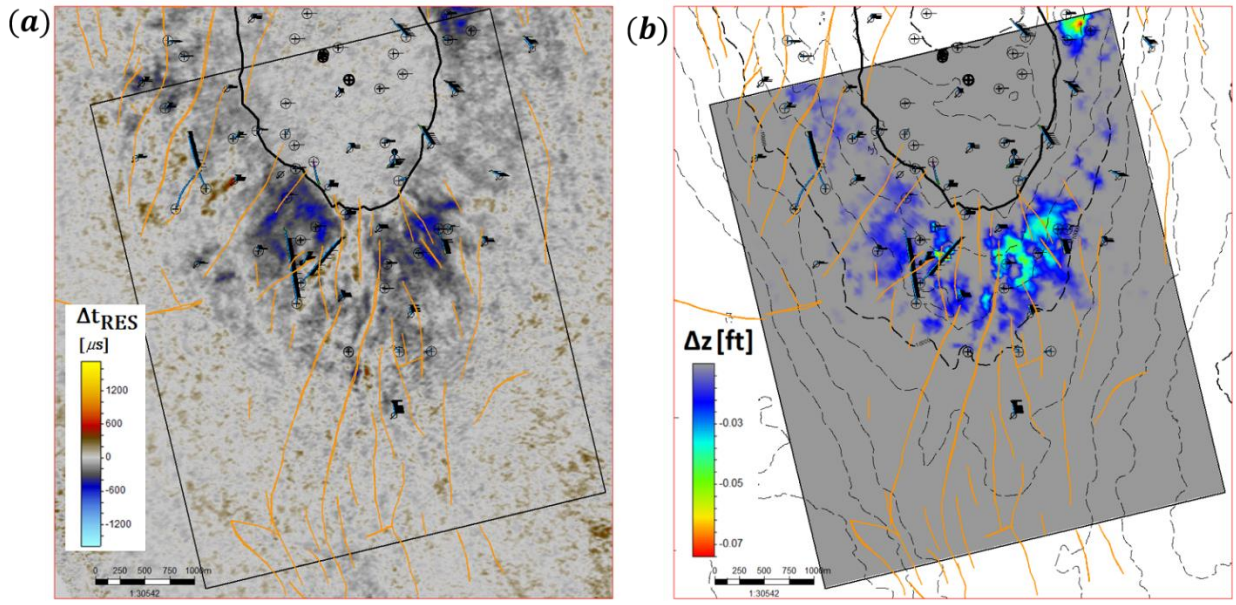

Figure 5.18: Computed changes in thickness (feet) for Tor formation (right) using the proxy model equation and inputs from the inverted results, compared against the measured interval Tor formation time-shifts (left).

Using the inverted results, some observations close to wells in an area of the field with strong 4D seismic signals is explained as shown in Figure 5.19. Here, I describe three cases (amongst many) that the inversion results are in good agreement with the measured data from production. Firstly, a potential pressure sink is observed around producers P1, P2 and P3, which is also measured in both reservoir and overburden time-shifts as hardening signals in Figures 5.19(a –left and right). In terms of the magnitude shown in Figure 5.19(b - left), the pressure drawdown predicted from this inversion is close to 4MPa. Based on field records, the absolute formation pressure from the downhole pressure gauge at baseline and monitor time period are consistent with this understanding. Secondly, large softening anomalies from strong pressure increases around the injectors I1 and I2 are observed. Lastly, there is a sweep pattern visible as water encroachment towards the producer P2 and P3 from the injector I2, shown as a blue line in Figure 5.19(b –right). Most of the interpretations are supported by repeat formation tester (RFT) and downhole pressure gauge measurements acquired every 6 months at the wells.

The RFT data in Figure 5.20(b) shows that both injectors I1 and I2 were originally water flooded, hence the 4D signal is predominantly pressure-related. The water saturation log for both injector wells I1 and I2 show highly water saturated with S_{wi} close to 1 – S_{or}. The S_{or} is given as 0.275 in this field, hence the maximum water that can displace oil is given as 0.725. It is engineering consistent not to expect any change in water saturation as the wells are already nearing the maximum water flooded state. The production data in Figure 5.20(a) also demonstrated that the injectors I1 and I2 are put on stream after LoFS2, and inject at a high constant rate. As a consequence, I expect a large pressure increase which is also shown in the inversion, whereby an increase in pressure greater than 10MPa was recorded. The producers P2 and P3 intersected an oil filled zone in both Ekofisk and Tor formations. The production data for P2 in Figure 5.20(c) reveals a steady increase in water cut and potentially an increase in gas production rate. These infer a drop in pressure and that water from the nearby injectors could have invaded the producers and raised the water cut.

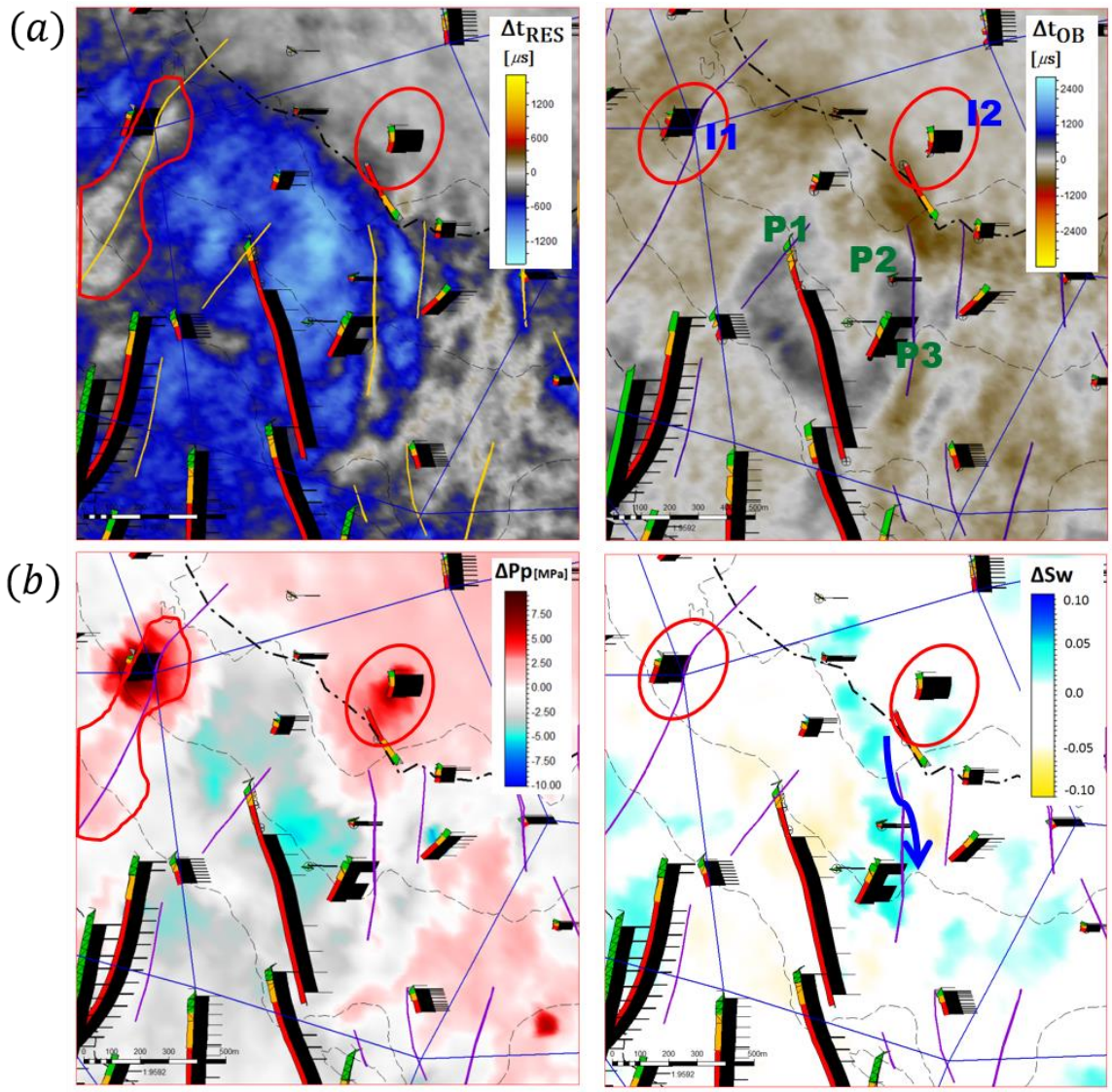

Figure 5.19: (a) A display of the time-shift maps of interval Ekofisk formation (left) and interval Balder formation (right). Wells labelled as 'I' are injectors and 'P' are producers. (b) The inverted changes in pressure (left) and water saturation (right) are also displayed. The red circles represent pressure anomalies from the inversion and have a good match with the observed time-shifts in both reservoir and overburden. The blue arrow represents a sweep pattern from the injector I2 to P2.

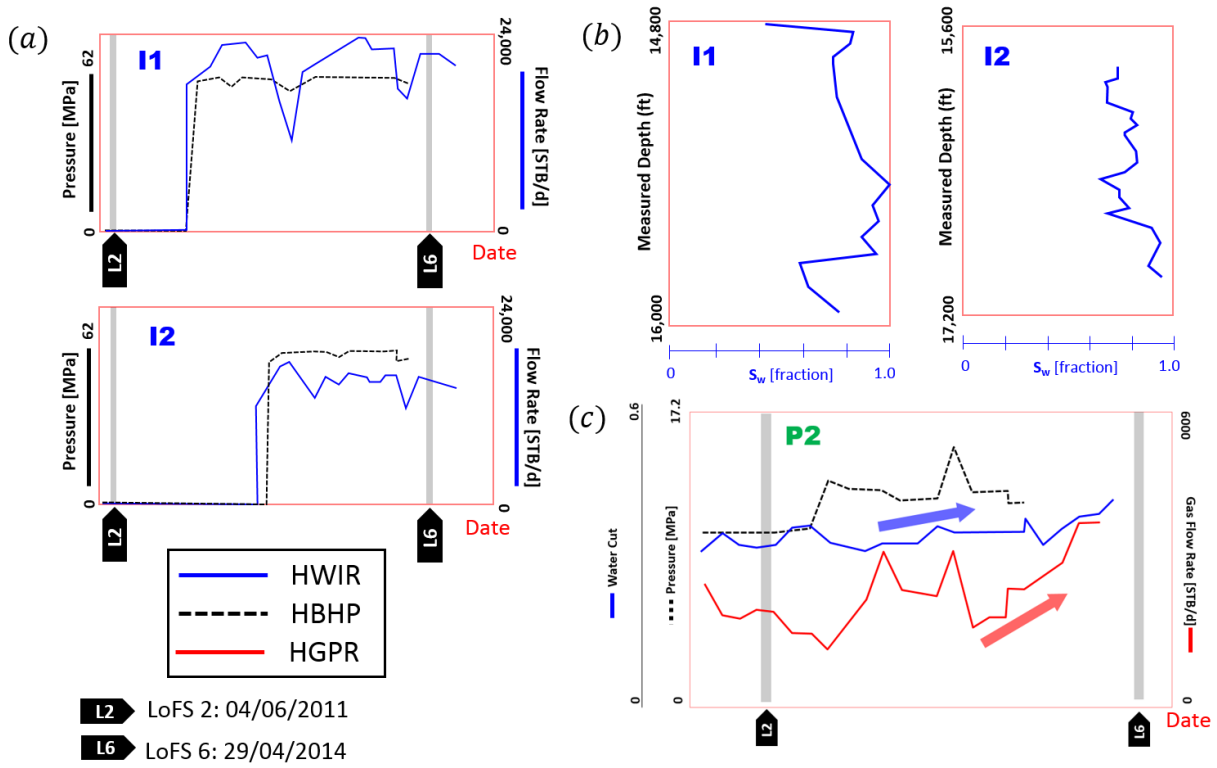

Figure 5.20: HWIR is the historic water injection rate, HBHP is the historic bottom hole pressure and HGPR represents the historic gas production rate. (a) Downhole pressure gauges and production data between LoFS 2 and LoFS 6 show both I1 and I2 recorded a large increase in HWIR and HBHP. (b) The RFT data for both of these injectors also shows along the trajectory of the wells, it is originally water flooded so 4D signals are predominantly pressure driven. (c) In the well P2, production data shows an increase in gas production rate which is indicative of a drop in pressure, and the recorded increase in water cut could point towards water coming from the nearby injector.

Figure 5.21 depicts a cross-section through 4 wells (I2, P1, P2 and P3) for (a - left) time-strain, (a – right) changes in amplitude, (b) percentage changes in elastic properties, (c) simulated prediction from fluid flow simulator, (d and e) inverted pressure and saturation changes from deterministic and stochastic approaches and (f) the associated uncertainties. The inversion results suggest an anomalous pressure increase along the injector I2 and slight pressure drop along producer P2. Water was also shown to be encroaching towards P2 from the injector. Production data indicated a steady increase in water cut, and an increase in gas production rate in P2, supporting the claim that water from the nearby injectors could have invaded the producer, which is consistent with the

inversion results. The water cut in P2 is also shown in production logging tool (PLTs) acquired in 2006, showing a 55% contribution from TA (first reservoir unit within the Tor formation) in Figure 5.21 (top right table). Whilst agreement between the simulator and the 4D seismic data is not necessarily expected, as the model may not be correct - the water sweep pathway is shown in the inversion result but not in the simulation model. This connectivity between injector and producer was not predicted by the simulator but was shown in the seismic data. This result supports the water breakthrough of 55% detected in the TA formation by the PLT. This shows that seismic data helps support well data in suggesting a potential area for model updating, such as including a preferred fluid pathway between both wells.

Areas located inside the seismic obscured area (SOA) has no signal recorded in the observed data because the signals are erroneous and was removed during processing, therefore the inversion solutions in those areas are biased towards the prediction of the simulation model. The EC constraint is applied to the entire trajectory of this well, hence this shows a prediction inside the SOA when there is actually no reliable seismic data. At the toe of the injector I2, a pressure increase signal was found to be consistent with the measured time-shifts and changes in amplitude. This anomaly is not predicted by the simulation model, but is in visual agreement with the seismic data. This reveals a spread of the injection response into the tighter and lower permeability chalk sediments in TB and TC formations. Water injection in an area of low permeability will result in a relatively strong pressure signal, this is also supported by Darcy's law where that a lower permeability results in a higher pressure for the same input flow rate. Also, depending on the matrix permeability of the rock and the fracture gradient, such injection could also develop fractures. In which both cases of injecting into a low permeability rock in water leg that could potentially create permeability corridors point towards a softening signals. Furthermore, it is originally water flooded hence the 4D signal is very likely to be pressure driven

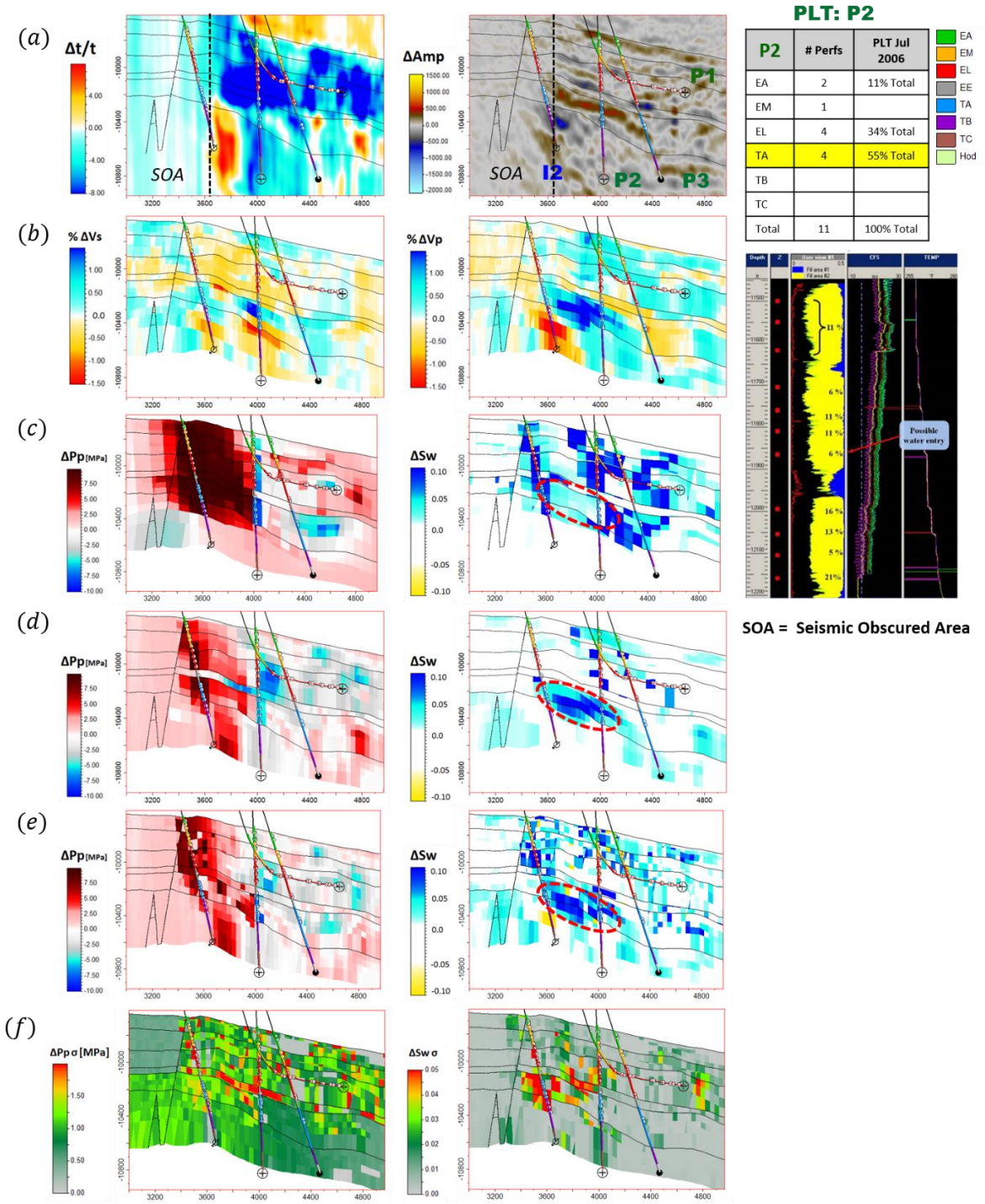

Figure 5.21: (a) Time-strain (left) and amplitude difference after time-shift correction (right). (b) Inverted fractional changes in S-velocity (left) and P-velocity (right). (c) Changes in pressure (left) and water saturation (right) from simulation model. (d) Stochastic results for changes in pressure (left) and water saturation (right). (e) Posterior uncertainty for changes in pressure (left) and water saturation (right) with one standard deviation in (f). In top right, the table shows the individual contribution of water saturation in the PLT perforation in P2.

Lastly, I would like to demonstrate the impact of the EC constraints in Figures 5.22(a) and (b). Figure 5.22(a) evaluates the objective function at the solution; the map shows small values of the objective function when the solution is found indicating first-order optimality was fulfilled. The first-order optimality is a measure of how close the solution is to optimal. At the location(x, y, z), the objective function is calculated for a range of solutions reported in Figure 5.22(b), the initial guess is given as the red point, and the final solution that converged at global minimum is given as the cyan point. The EC constraint is represented by the black dotted line box, which firstly constrained the solution space and secondly guided the initial solution to the global minimum. Figure 5.22(b) also shows the limit of the deterministic solution such that it has a narrow sampling path in the solution space. Secondly, in either the proxy model or full physics model there could be regions in the solution space that is highly non-unique (i.e. a flat global minimum), a stochastic solution will ensure an exhaustive search and that the best estimate of the solution and the corresponding uncertainty will be extracted.

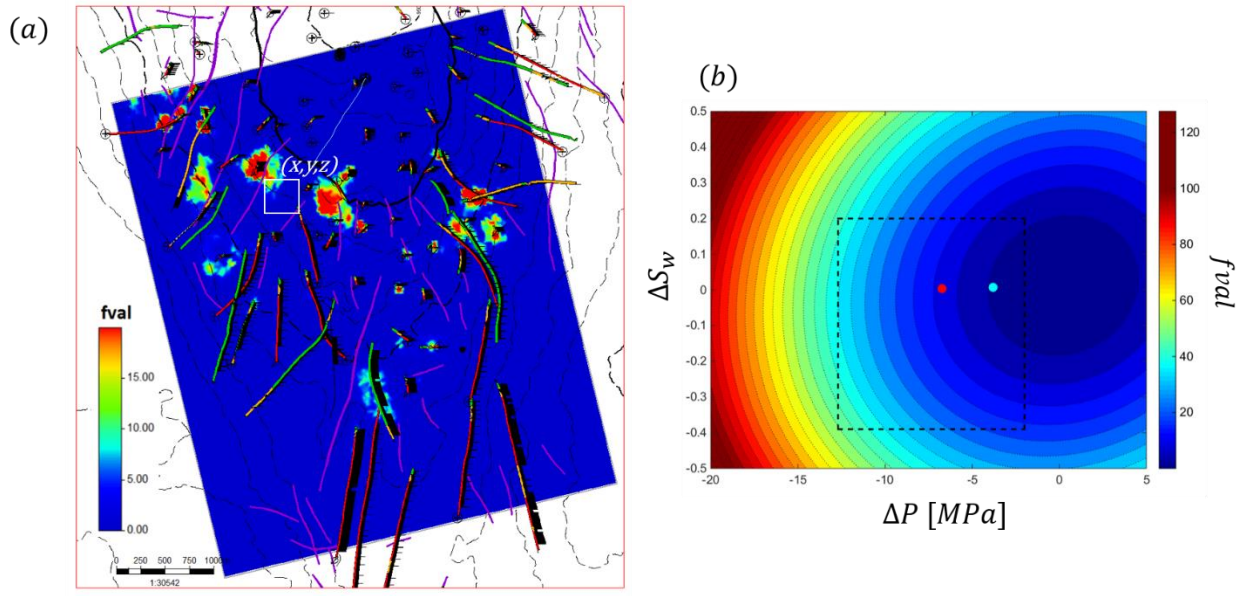

Figure 5.22: (a) The objective function values at the solution for the deterministic inversion results of the Ekofisk formation and (b) represents the initial and final solution bounded by EC constraints at location (x,y,z).

5.9 Conclusions

The engineering-constrained inversion method developed in a Bayesian framework shows considerable promise. The goal of this chapter was to verify that the theoretical basis for the inversion pressure and saturation changes using the proxy model described in Chapter 4 produced reasonable results when used with real data. Uncertainties from the seismic and from the engineering domain are included in the Bayesian framework thus giving an additional robustness to the technique, providing a measure of the uncertainty related to the inverted pressure and saturation changes. Quantifying these uncertainties is an important factor for further quantitative interpretation of the results. The data uncertainties and constraints are of special interest since they both influence the convergence and outcome of the inversion process. The resulting changes of dynamic properties from probabilistic inversion show an improvement from the history matched flow-simulation model. Although the stochastic method required higher computational effort, it has the added advantage of capturing uncertainties in its predictions, and is not sensitive with respect to local minima.

Application of this inversion workflow to the Ekofisk field has revealed encouraging results suggesting potential areas for model updating. Inconsistency with current interpreted conductive pathways between well I2 and P2 has suggested a different perspective in current understanding of reservoir dynamics. The inverted attributes provide the critical lateral information away from the wells where the confidence in the reservoir model properties is lower. The result also has a good match with well production data, which explains strong localized pressure, saturation and compaction anomalies. By transforming the 4D seismic data into the engineering domain, quantitative maps of pressure and saturation may be used to update the simulation model, or as a direct aid for making more informed reservoir management decisions. One of the greater implications is also to use these estimates of pressure and saturation to update the simulation model to reduce the misfit between 4D seismic and the prediction of the simulation model, or as additional constraints in history matching. The inverted dynamic properties from 4D seismic have good spatial coverage and resolution compared to the well data. This provides a pragmatic way to close the loop between reservoir dynamic properties and 4D seismic data.

Application of the method in a volumetric 3D manner has proven that this technique can effectively help to detect preferential conduits between producers and injectors, weakened zones in the producing formations due to pressure draw-down and invasion of water and determine the efficiency of well injections. These effects are paramount in 3D interpretation especially if the reservoir is thick such as in the case of Ekofisk. Previous methods that work effectively on maps lacked the vertical resolution for both pressure and saturation analysis. Working in 3D volumes also shows the greater possibility of understanding communication between different stratigraphic layers in the reservoirs and gives greater confidence in the selection of well paths for more effective well planning.

Lastly, I would like to highlight the advantage of the proxy model in providing a fast-track computation for the relative changes in elastic properties by honouring the physical relationship. The computing costs for the forward method are linearly proportional to the number of model parameters, and in this case, it only depends on the distribution of the changes of pressure, saturation, and the individual coefficients that weight the relative contribution of each term in the proxy model equation. The strength of this workflow lies in its ease of parameterization and fast run time, making it amenable to exhaustive sampling methods like McMC.

CHAPTER

SIX

PRESSURE INVERSION USING OVERBURDEN STRAIN:

A SYNTHETIC EXAMPLE

Here, I will demonstrate how time-lapse information outside the reservoir can be employed to estimate vertical strain, and subsequently infer pressure changes inside the reservoir. The Geertsma's pressure inversion method (Hodgson et al., 2007) provides the basis for a linear inversion to both pressure changes and also the Hatchell-Bourne-Røste R-factor. I will demonstrate two synthetic studies, first to infer which data should be extracted in the overburden for Geertsma's solution and secondly to validate Geerstma's solution with numerical modelling. The remainder of the chapter focuses on a proposed method to invert for the R-factor apart from pressure changes, by calibrating the results with pressure information from a well-history matched simulation model.

6.1 Introduction

In Chapter 4 and 5, I demonstrated the use of reservoir time-lapse information such as time-shifts and the relative change of elastic properties to characterise reservoir dynamic properties. In this chapter, I will shift my focus to using information from the rocks surrounding the reservoir under production. Production or injection of fluid volumes in a hydrocarbon reservoir leads to subsurface deformation and changes in the strain state not only of the reservoir, but also the surrounding rocks. It has been demonstrated in several field studies that summation schemes based on Geertsma's analytical solution are capable of modelling this strain distribution (e.g. Toomey et al., 2015), and also inverting for changes in reservoir pressure from time-shifts measured by time-lapse seismic data (Hodgson et al., 2007). These schemes provide a simple yet effective approach for tackling the small to moderate magnitude strains detected in many applications of time-lapse seismic data. In this chapter, I will extend the work of Hodgson et al. (2007) to infer reservoir dynamic changes with the aid of reservoir engineering concepts. However, before embarking on the extension of the current theory, I will first call attention to a compilation of work in the literature, specifically those involving non-reservoir time-lapse information in compacting reservoirs.

6.2 Summary on Overburden Time lapse information for Reservoir Characterisation

Some of the key publications on using overburden seismic data for reservoir characterization are highlighted in Figure 6.1. The pioneering work of Geertsma (1966, 1973) shows the relationship between stress and strain of permeable fluid-saturated materials, assuming linear-poroelastic behaviour of the solid skeleton. It was pointed out by Lubinski (1954), that similar stress-strain relations in thermoelasticity exist that provide the effect of changes in pore pressure on the bulk stress-strain system. This popular formulation from the work of Geertsma (1966, 1973) who developed an analytical solution for surface and subsurface displacements for a compacting reservoir was then widely adapted. Segall (1992, 1994) extended Geertsma's method for arbitrarily shaped reservoir in computing poroelastic stress changes due to fluid extraction. His application

on the deep Lacq gas field in southwestern France shows good agreement between the predicted vertical displacements with the subsidence observed from leveling data.

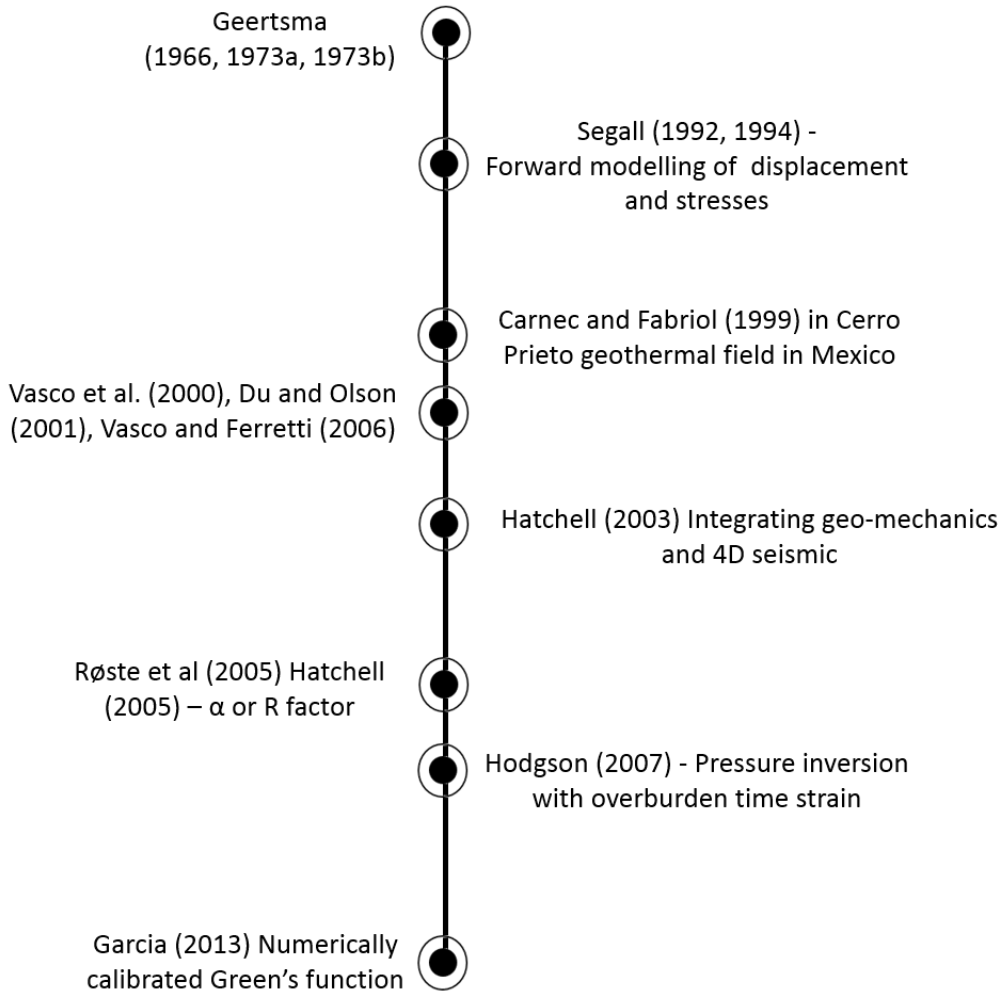

Figure 6.1: The timeline of the literature using overburden information for reservoir characterisation, specifically in the pursuit of pressure, permeability distribution and velocity sensitivity to stress of the reservoir.

The solution from Segall (1992) was also used by Carnec and Fabriol (1999) in Cerro Prieto geothermal field in Mexico. Apart from forward modelling of strain and displacement, Du and Olson (2001) developed an inverse procedure to relate surface subsidence to reservoir pressure change in a synthetic study. Work from Vasco and Ferretti (2006) shows a method for inferring reservoir volume change and flow properties, such as permeability, using subsidence and satellite-

derived InSAR observation from Wilmington field, California. This study serves as an early attempt in reconciling reservoir production and surface deformation data for real data. In 2005, the dilation factor or the R-factor was determined by both Røste et al., 2005 and Hatchell and Bourne 2005 independently. The R-factor is a constant used in relating strain to the fractional change in vertical P-wave velocities. It provides a link between time-lapse seismic and geomechanics, where one can easily relate the vertical strain component, ε_{zz} to changes in vertical P-wave velocity and time-shifts. The strain model proposed by Hatchell and Bourne (2005) consider the changes in travel time due to small changes in layer thickness and velocity as:

$$\Delta t = \left(\frac{\partial t}{\partial z}\right)\Delta z + \left(\frac{\partial t}{\partial z}\right)\Delta v \tag{6.1}$$

with z representing thickness and v, P-wave velocity and the travel time for a normal incidence P-wave as t. Evaluating the partial derivatives for $t = z/v$ leads to:

$$\frac{\Delta t}{t} = \frac{\Delta z}{z} - \frac{\Delta v}{v} \tag{6.2}$$

In the case of normal incidence P-wave, the fractional changes in velocity is proposed to occur in propotion to fractional change sin path length, such that $\frac{\Delta v}{v} = -R\varepsilon_{zz}$. The model now relates time strain to vertical strain using the R-factor:

$$\frac{\Delta t}{t} = (1 + R)\varepsilon_{zz} \tag{6.3}$$

This provided Hodgson (2009) with the foundation to invert for reservoir dynamic property such as pressure change, ΔP using time strain, $\frac{\Delta t}{t}$ information – by firstly using the R-factor to convert time strain measurements to vertical strain, this is shown in section 6.4.1. Equation 6.4 shows the forward modelling equation, where the operator G is given as the Geertsma Green's function to estimate time strain from the changes in pore pressure. Results are presented from application of the method to Genesis field in the Gulf of Mexico in Figure 6.2. The pressure changes inverted from time strain information compares favourably to those from the reservoir simulator predictions (Hodgson et al., 2007).

$$\left(\frac{\Delta t}{t}\right)_M = (1+R)\sum_{n=1}^{N}\Delta p_n G_{n,m}^{\varepsilon_{zz}} \tag{6.4}$$

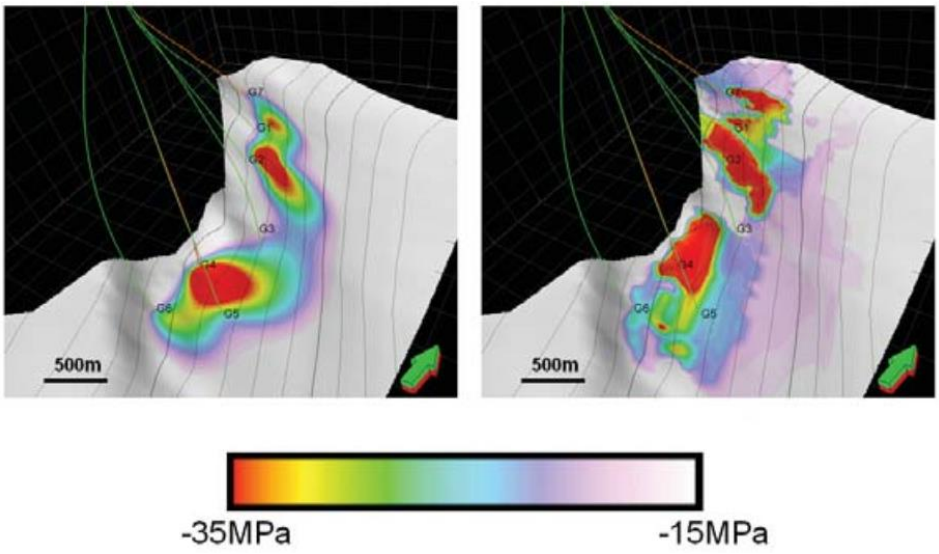

Figure 6.2: (right) Pressure change inverted from Geertsma and (left) pressure change predicted from a fluid flow simulator (Hodgson et al., 2007).

An adaptation to this solution was suggested by Garcia and MacBeth (2013) where instead of using an analytical equation to capture the complicated geology of the subsurface, a method based on transfer functions is propose in which the function itself is calibrated using numerically generated overburden strain deformation using a selected number of reference sources. This was applied in the South Arne field where the reservoir strain using the transfer function which is a Wiener operator shows higher definition compared to the Geertsma's solution.

6.3 Theory

The Geerstma's solution (1966, 1973) that is employed in this chapter is based on the theory of poroelasticity (Biot, 1941, Rice and Cleary, 1976), where the equations are listed in Appendix F. The simple geomechanical model employed by Geertsma assumes a linear poroelastic medium and material isotropy. In the pure compliance formulation (in which strain is one dependent variable), the sum of the mean normal stresses is: $\sigma_{kk} = (\sigma_{xx} + \sigma_{yy} + \sigma_{zz})/3$. In an isotropic poroelastic medium, the solid volume strain, ε_{kk} as a function of σ_{kk} and pore pressure, p can be written as:

$$\varepsilon_{kk} = \frac{\sigma_{kk}}{3K} + \frac{\alpha p}{K} \tag{6.5}$$

Where K is the bulk modulus and α is the Biot's coefficient, ranges between 0 and 1, and is generally an increasing function of porosity. Equation 6.5 reveals that if the rock is free from constraints ($\sigma_{kk} = 0$) it will tend to contract by an amount of $\alpha p/K$ in a pore pressure draw-down scenario. On the other hand, if the reservoir is completely constrained volumetrically ($\varepsilon_{kk} = 0$) then it will be driven into extension by $\sigma_{kk} = -3\alpha p$ (Segall 1992). In reality what we expect is the rocks surrounding a reservoir to provide an incomplete constraint, when the rock is restrained from its reference stress state or pre-stress state, it contracts by less than $\alpha p/K$ and its surrounding is put under extension. The common approach used in the industry is to assume uniaxial compaction, when the lateral extent of a reservoir is much larger than thickness. Thus, lateral strain can be neglected $(\varepsilon_{xx} = \varepsilon_{yy} = 0)$, and the reservoir deforms only in the vertical direction. The second assumption is that the total vertical stress acting on the reservoir remains constant during production. In this condition, the constitutive equation can be expressed using stress components as the dependent variables and solved for the vertical stress as:

$$\sigma_{zz} = \frac{2\mu(1-v)}{1-v}\varepsilon_{zz} - \alpha p \tag{6.6}$$

Solving for the vertical strain gives:

$$\varepsilon_{zz} = \frac{\sigma_{zz}}{K_v} + \frac{\alpha p}{K_v} \tag{6.7}$$

where K_v is called the drained vertical incompressibility. The deformation and pore pressure field are coupled through the equilibrium equations for the solid and the equation governing pore fluid flow. Generally, the pressure change can be generated from a fluid flow simulator and for most consolidated clastic reservoirs. Although the equations in Appendix F show the changes in fluid mass and displacements are coupled in a linear poroelastic medium; in practice the flow equation is solved independently from the stress equation in the fluid flow simulator, or in other words, there is no coupling between these two sets of equations, and information is passed in only one direction. A full coupling approach is preferred but is often challenging because a large system of nonlinear coupled partial differential equations incorporating all the relevant physics need to be derived (Minkoff et al., 2003). In strongly compacting reservoirs, a loosely coupled or fully coupled approach should be taken, as the stress changes are generally non-negligible and the changes in effective stress alters the static properties of the reservoir, such as porosity and permeability.

In my work, I assume deformations due to reservoir pressure change as quasi-static, which means a steady state has been achieved. The time period that I will investigate is between LoFS 2 and LoFS 6, which is 18 months apart; this is sufficient for pressure to equilibrate inside the reservoir - of course the pressure diffusion ultimately depends on the permeability and porosity of the reservoir. Between the LoFS surveys, the pressure perturbations are small, therefore the strain in the reservoir and the surrounding rocks is also small; hence, linearity could be assumed between pressure change and strain. In addition, due to short acquisition period in the LoFS period, we can assume that any change in applied stress is followed instantaneously by the corresponding deformation and stress is imaged. This will be further discussed in the application on the Ekofisk data in Chapter 7. However, in the streamer period, where large pressure changes and compaction events took place (observed time-shifts as large as 15ms), the relationship between strain and pore pressure is more likely to be non-linear. In addition, the time period between baseline and subsequent monitor or between monitor pairs in the streamer data has a time gap of several years, which means time-dependent effects such as creep could have taken place. This means the pressure inverted using time-shift measurements affected by creep could be overestimated.

6.4 A Green's Function Solution

In this section, I attempt to use the observed quasi-static displacements to infer the distribution of pressure change within the reservoir. The approach of using time strain information from time-lapse seismic was first applied by Hodgson et al. (2007) and Hodgson (2009). Geertsma (1966, 1973) and Segall (1992) show the displacement in a poroelastic medium can be generated by a distribution of centres of dilation with a magnitude proportional to $\alpha\Delta p(\zeta, t)$; the volumetric strain in the reservoir can be estimated using Equation (6.8). Segall (1992) shows that displacement tensor of i^{th}, at an observation point x in the subsurface at time t, given by a centre of dilation located at ζ is:

$$u_i(x,t) = \frac{\alpha}{\mu}\int_v \Delta p(\zeta,t) g_i(x,\zeta) dV_\zeta \tag{6.8}$$

where $g_i(x,\zeta)$ can be thought of as the displacement at x resulting from a unit pressure at ζ in volume element dV, which is also the Green's function for the displacement. This is solved by Geertsma (1966), who provided an analytical Green's function for a nucleus of strain in a homogeneous linear poroelastic half space. The half space is represented as $x > 0, -\infty < y < \infty$. A depletion of the pore pressure causes the stresses and strains both inside and outside the reservoir to be changed. Linear elastic properties are assigned to both reservoir and surroundings, provided there is no material contrast. The displacements caused by a bounded volume of reduced pore pressure using the nucleus concept in a half-space with a traction-free surface was solved independently by Mindlin and Cheng (1950) and Sen (1943). Combinations of point forces are known generally as nuclei of strain (Love, 1944). The Green's function for the displacement field due to a point source of pressure change of fluid volume is identical to the displacement field due to a centre of dilatation.

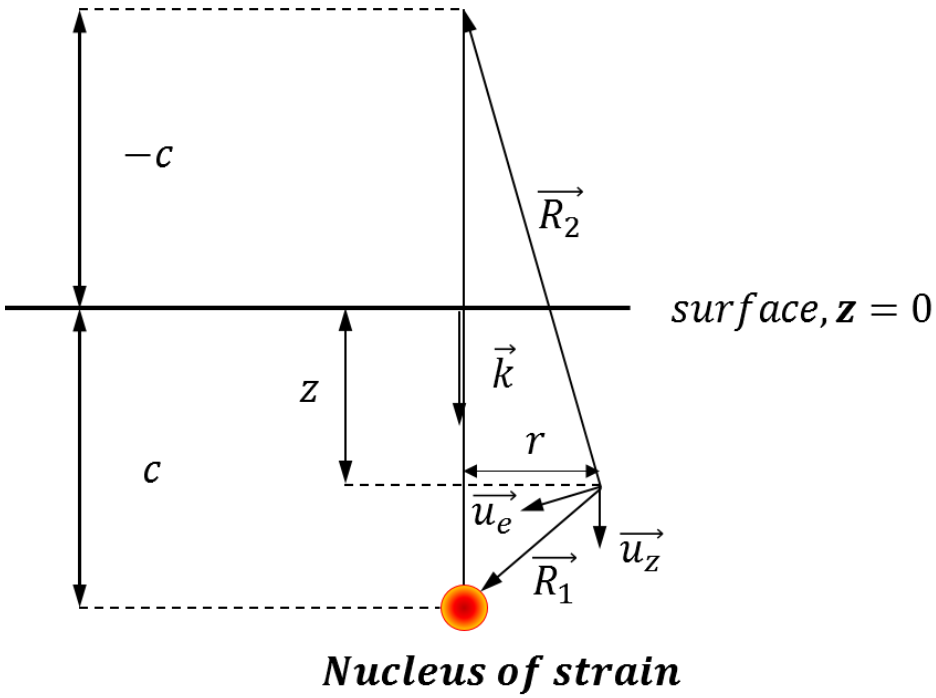

Figure 6.3: Geometry for the Geertsma solution. $\vec{k}$ is the unit vector in the z-direction. If z=0, $\vec{u}$ and $\overrightarrow{R_1}$ are codirectional (modified after Fjær, 1992).

The boundary condition is that the surface at $z = 0$ is a traction free surface which means that vertical stress must be zero. As illustrated in Figure 6.3, outside a nucleus at depth of burial $z = c$, the displacement $\overrightarrow{u_e}$ at a radial distance r from the nucleus amounts to:

$$\overrightarrow{u_e} = \frac{c_m}{4\pi}\left[\frac{\overrightarrow{R_1}}{R_1^3} + \frac{(3-4v)\overrightarrow{R_2}}{R_2^3} - \frac{6z(z+c)\overrightarrow{R_2}}{R_2^5} - \frac{2\vec{k}}{R_2}\{(3-4v)(z+c) - z\}\right] \tag{6.9}$$

where Δp is the volume of pressure change, $R_1^2 = r^2 + (z-c)^2$, $R_2^2 = r^2 + (z+c)^2$ and $\vec{k}$ is the unit vector in z-direction and r is the distance from the volume element to the observation point. c_m is the uniaxial compaction coefficient, which is given by Wang (2000) as:

$$c_m = \frac{\alpha(1-2v)}{2\mu(1-v)} \tag{6.10}$$

The vertical displacement, $\overrightarrow{u_z}$ is:

$$\overrightarrow{u_z} = \frac{c_m}{4\pi}\left[\frac{z-c}{R_1^3} - \frac{4v(z+c)-(z+3c)}{R_2^3} - \frac{6z(z+c)^2}{R_2^5}\right] \tag{6.11}$$

The components of the strain tensor are found by taking the derivative of the displacement Green's function. For example, the vertical component of strain is the vertical derivative for the vertical displacement, given as:

$$\frac{\partial u_z}{\partial z} = \varepsilon_{zz} = \frac{c_m}{4\pi}\left[\begin{array}{c}\frac{1}{R_1^3} - \frac{3(z-c)^2}{R_1^5} + \frac{4v-1}{R_2^3} + \frac{3(z+c)\left(4v(z+c)-(z+3c)\right)}{R_2^5} \\ -6\left\{\frac{(z+c)^2}{R_2^5} + \frac{2z(z+c)}{R_2^5} - \frac{5z(z+c)^3}{R_2^7}\right\}\end{array}\right] \tag{6.12}$$

These are the basic equations of the nucleus of strain method, a full derivation can be found in Geertsma (1966, 1973). The displacements at the surface can be determined numerically by adding up the contribution from the different elements of the reservoir. Hypothetically, if the reservoir takes the form of a contracting sphere within an infinite medium, the displacement field around the reservoir will be spherically symmetric and given by:

$$u = \frac{u_0 R_o^2}{r^2} \tag{6.13}$$

Here, r is the radial distance from the centre of the sphere (reservoir), u is the radial displacement, u_0 is the displacement at the surface of the sphere, and R_0 is the radius of the sphere (reservoir). What we observe from this equation is that as we move away from the source, the displacement field disappears, with one over radius squared ($1/r^2$), as mentioned in Fjær et al. (2008).

Using the approach in Hodgson (2009), which accounts for arbitrarily shaped reservoirs. The analogy of non-overlapping cuboids to cells in a reservoir model grid is used. The equation can be written as a summation over N cuboids as:

$$u_i = \frac{\alpha}{\mu}\sum_{n=1}^{N} \Delta p_n \int_{V_n} G_i(x,\zeta)\, dV_n \tag{6.14}$$

where G_i represents the Green function for displacement at x resulting from a unit pressure at ζ in volume element dV_n. The volume integral is achieved by using a numerical method provided by

Stroud (1971). Assuming the volume integral has been performed as part of the Green's function calculation, the vertical strain can be expressed as a linear system of equations:

$$\varepsilon_{zz,M} = \sum_{n=1}^{N} \Delta p_n G_{n,M}^{\varepsilon_{zz}} \tag{6.15}$$

where $\varepsilon_{zz,M}$ is the M^{th} observation, and Δp is the reservoir pressure changes. In a forward modelling procedure to calculate strain, the change in pressure is the average pressure change over each cuboid discretized in the simulation model. Equation (6.14) can be applied to any component of displacement, stress and strain if the Green's functions for these components are available. The diagram in Figure 6.4 shows how a rectangular reservoir is divided into four equal cuboids. At each observation point, the strain is summed over the four cuboids.

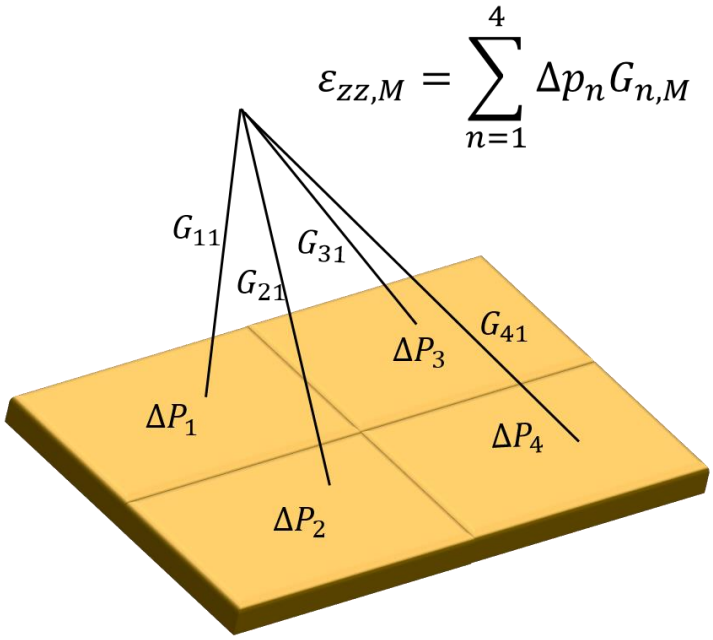

Figure 6.4 shows the representation of a reservoir as four non-overlapping cuboids. The pressure change in each cube is summed over to yield the observed strain. (Redrawn after Hodgson 2009).

6.4.1 Using overburden deformation to infer reservoir pressure change

In the inversion procedure outlined by Hodgson (2009) and Hodgson et al., (2007), additional constraints are also added into the inversion, such as using engineering data (well-based pressure

measurements) and a regularisation term to ensure the solution is smooth. Equation (6.15) is solved using a least squares objective function with a smoothing constraint, which employs a Laplacian finite-difference operator.

$$E = \|G\Delta p - d\|^2 + \alpha^2\|L\Delta p\|^2 \tag{6.16}$$

G is the forward operator that relates the data d, given as time strain, to the model parameter, Δp. The second term is the regularisation term; having this in the objective function means minimizing $\alpha^2\|L\Delta p\|^2$ penalises pressure change distributions that are rough in the second derivative and requires the solution to be smoothly varying.

The input data for this inversion engine is time strain and, hence a conversion has to take place to relate time-strain to physical strain. The simplest relation is the linear relationship between fractional change in time-lapse time strain and the physical strain, with a constant factor known as the R-factor, proposed by Hatchell and Bourne (2005). Equation (6.15) can be rewritten as Equation (6.18) by substituting the vertical strain with the relationship given in Equation (6.17).

$$\frac{\Delta t}{t} \approx (1 + R)\varepsilon_{zz} \tag{6.17}$$

$$\left(\frac{\Delta t}{t}\right)_M = (1 + R)\sum_{n=1}^{N} \Delta p_n G_{n,m}^{\varepsilon_{zz}} \tag{6.18}$$

In Hodgson's (2009) work, the value of R is assumed to be 5, as proposed by Hatchell and Bourne (2005) for most non-reservoir rocks. A constant R is assumed throughout the overburden. This is a huge uncertainty, as in more recent work R is found to be not only a function of lithology but also initial stress state and strain polarity, meaning that R values can be different for the same rock undergoing loading (compaction) versus unloading (extension). Another method to obtain R is to compare modelled strain values from the geomechanical simulator to observed time strain value. The ratio of the observed physical strain to the time strain gives the R-factor. However, this requires good estimates of pressure information from the simulator and good calibration for the geomechanical properties in the reservoir model.

6.5 Velocity Stress/Strain Relationship

It is established from laboratory observations that a change in the stress state of a rock will cause a change in elastic velocity. Laboratory data also shows that velocities initially increase rapidly at low effective stresses, but that this increase will gradually reach a plateau at higher stresses before sample destruction. Many rock models exist to describe the variation of various rock properties under a host of different conditions, however, many of these models require the parametrization of a large number of unknowns. The complexity and uncertainty of rock models is one explanation for the prevalence of empirical relationships in the oil industry.

The observed mechanical properties of a rock such as strength and elastic wave velocities depend largely on the rock heterogeneity. Rocks have heterogeneities on many different length scales. For example, layering and faulting exist on macroscopic scales, while micro cracks, mineralogy and porosity exist on the microscopic scale. For seismic properties we are interested in length scales on the order of tens of metres which are generally described in terms of continuum mechanics, i.e. the rock is described as a homogeneous elastic material. The aim of microscopic rock models is to describe the macroscopic properties based on the microscopic behaviour. The observed stress dependency of acoustic wave velocities implies a non-linear stress-strain relationship, because for a linear material the acoustic velocity would be constant. Holt et al. (2005) give an overview of the sources of non-linearity in sedimentary rocks: Change in porosity with stress, the existence of sharp grain contacts and the presence of cracks and fractures. These nonlinearities can be incorporated in macroscopic models, that use the framework of continuum mechanics, or microscopic models which deal with nonlinearities on the scale of particles or microscopic inclusions.

6.5.1 Rock physics: Third order elasticity

One approach to link stress and strain tensor to anisotropic velocity is using the third order elasticity. The model developed by Prioul et al. (2004) includes the effects of triaxial stress changes on the full anisotropic stiffness tensor. The added advantage is that the effects of stress-induced anisotropy and variations in larger offset time-shifts can be incorporated in this model. This

mathematical model however does not directly address the microstructural properties of the rock. The model fits two linear trends for both low and high stress regions between the non-linear stress versus velocity relationship, shown in Figures 6.5 (a) and (b). Furthermore, the model can only be parameterised with triaxial stress velocity measurements whereby such experiments are limited in the literature and makes it hard to parameterize. Since these data are scarce and empirical, it has little use for application. Also, the cut-off for low and high stress regions is arbitrary and varies for different rock types (Verdon, 2012). These factors limit the general applicability of the model.

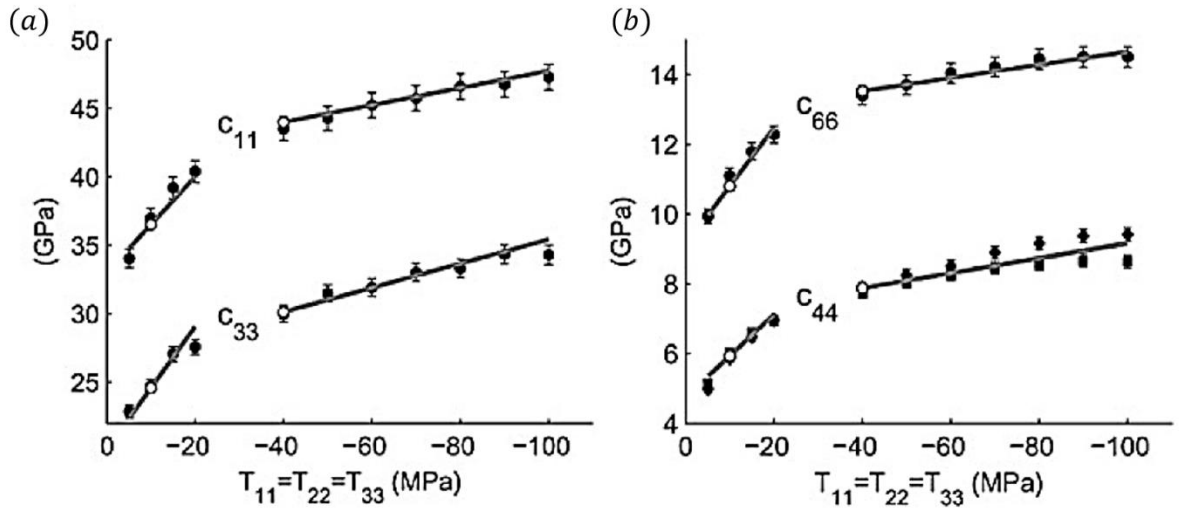

Figure 6.5: 3rd order elasticity is employed to model the nonlinear elasticity of a North Sea shale. Two linear fits are given, divided by low and high stress regions (from Prioul et al. 2004).

In the work of Herwanger (2008), it was concluded that production induced horizontal stress and strain changes have a marked influence on vertical velocity. It was concluded that the overburden deforms under a zero volumetric strain condition ($\varepsilon_{11} = \varepsilon_{22} > 0, \varepsilon_{33} < 0$), which yields a higher change in vertical velocity for the same amount of vertical stress change compared to the reservoir under uniaxial compression ($\varepsilon_{11} = \varepsilon_{22} = 0, \varepsilon_{33} < 0$). His work also goes to show that there are repercussions when neglecting the influence of horizontal strains on the vertical velocity.

6.5.2 R-factor

The most commonly used approach in relating stress or strain to velocities is the R-factor. The model assumes proportionality between the fractional changes in vertical P-wave velocity and the vertical strain. The vertical P-wave velocities are the most commonly measured property in conventional seismic surveys; and often the characteristic feature of the compaction process is that it is more or less uniaxial, therefore the changes in vertical stress and strain will be the largest geomechanical effects for a compacting reservoir. The coupling of geomechanics and time-lapse seismic by Hatchell and Bourne (2005) shows the problem in a new light. If the R-factors can be obtained independently whether by theory or experiment, the vertical strain can be determined from zero offset time-shifts and vice versa. The collective work by Hatchell and Bourne (2005) on various types reservoirs shows consistent R-factors (1-3 for reservoir rock, 4-6 for non-reservoir rock), although the R-factors varied for rocks experiencing compressive strain and extensional strain, with the former being 5 times smaller. Some recent work show that R-factor is also a function of lithology (Staples et al., 2007, De Gennaro et al., 2008). Also, the R-factors have been found to be dependent on stress path (Holt et al., 2008), types of deformation and on the magnitude of applied stress (Pal-Bathija and Batzle, 2007). Despite the ease of use of the R-factor, different R-factors are required for extension and compaction, for different applied stress magnitudes, and different triaxial stress state. This means that this approach does not lend itself to model scenarios where the stress changes during production are not known in advance. The R-factor model does not adequately describe the full, triaxial, anisotropic, non-linear response from seismic velocities as the model is only limited to both vertical P-wave velocity and vertical strain.

The R-factor bypassed a complicated system to relate key 4D seismic parameters to geomechanical via one parameter. However, experimental evidence shows that the propagation velocity of compressional waves (and shear waves) is dependent on changes in the triaxial stress state (or in an alternative formulation, change in strain) of the rock (Mavko et al., 1998). Additionally, we know from geomechanical modeling that stress and strain changes in the subsurface during reservoir production are triaxial, and cannot be adequately described using “mean” stress (Herwanger and Horne, 2005). It must, therefore, be instructional to investigate the effect of horizontal stress and strain changes on vertical velocity. We will show the comparison of the Geertsma strain prediction and a numerical geomechanical modelling, to demonstrate that if the

horizontal strains and stresses are small, the influence on vertical strain is negligible (shown in Section 6.5.2).

Extending the work by Fuck and Tvanskin (2011) and Herwanger and Koutsabeloulis (2011) that introduced a two parameter R-factor model, with a formulation based on independent contributions from volumetric and deviatoric components of the strain tensor, Rodriguez-Herrera et al. (2015) presents a more generalised velocity-strain relationship. To calculate the time-shifts, one would require the initial P-wave velocity, V_p^0, velocity sensitivity parameters R_1 and R_2, volumetric (ε_{vol}) and vertical (ε_{33}) strain estimates from a coupled geomechanical model.

$$\Delta t|_{(z_1,z_2)} \approx \int_{z_1}^{z_2} \frac{\varepsilon_{33}}{V_p^0} \partial z + \int_{z_1}^{z_2} \frac{1}{V_p^0} (R_1 \varepsilon_{33} + R_2(\varepsilon_{vol} - \varepsilon_{33})) \partial z \tag{6.19}$$

The velocity sensitivity parameters R_1 and R_2 in Equation (6.19) are taken from a first order approximation of the "third-order" elastic constants, resolving into the strains acting parallel (R_1) and perpendicular (R_2) to the wave propagation direction.

$$R_1 = -\frac{1}{2c_{33}^0} c_{111} \tag{6.20}$$

$$R_2 = -\frac{1}{2c_{33}^0} c_{112} \tag{6.21}$$

The axial, c_{111} and orthogonal, c_{112} third order elasticity constants have to be derived empirically. This was applied to the Dalia field, offshore West Africa, where the predicted time-shifts compares well with the observed time-shifts.

Table 5.1 shows a compilation of R-factors from various methods. The different methods are colour coded different in the table. It is clear that there is an apparent discrepancy between laboratories derived versus field measured R-factors. In Section 6.6, I will describe the proposed method by Wong and MacBeth (2016), and the full application of the method on the Ekofisk field is provided in Chapter 7.

Dilation R+	Compressive R-	Data	Stress (MPa)	Method	Lithology	Reference
4 – 6		4D seismic	In situ	Scaling between 4D seismic and geomechanical model	Shale	Hatchell and Bourne (2005)
1 – 3			In situ		Sandstone or carbonate	
1 – 5		4D seismic	In situ	4D seismic (Valhall field)	Chalk	Røste et al. (2005)
2 – 6					Shale	
2		4D seismic, compaction logs, bathymetry	In situ	Scaling 4D seismic between estimates of overburden strain from compaction logs and repeat bathymetry (Ekofisk field)	Chalk	Janssen et al. (2006)
4 – 6					Shale	
20		4D seismic		Scaling of velocity changes between 4D seismic and geomechanical model (Snorre field)	Shale	Røste et al.(2015)
1 – 3				Velocity-porosity model	various	Hatchell and Bourne (2005)
2 – 10				Microcrack model		
4.4 – 5.4			5 – 40 (differential)	Asperity-deformation model	Shale	Carcione et al. (2007)
2 – 2.3			5 – 40	Hertz-Mindlin Model	Shale	
4.25 – 5			5 – 40	Hertz-Mindlin Model	Sand	
304		Velocity, strain	2.4 – 8.2 (vertical compressive)	Laboratory uniaxial strain	Finest-grained sand	Vega (2003)
283			4.3 – 10.3		Fine-grained	
147			2.6 – 8.1		Coarse-grained	
729		Velocity	0.7 (uniaxial)	Laboratory uniaxial stress	Dry Berea sandstone block	Sarkar et al. (2003)
40 – 45		Velocity	7 – 14 (differential)	Laboratory hydrostatic stress (North Sea)	Brine-saturated shale cores	Wang (2002)
	10 – 30	Chalk cores	Various	Laboratory (Ekofisk field)	Chalk	Janssen et al. (2006)

6 – 91		Cores	63 – 7 (differential), 7 – 56 (uniaxial)	Laboratory ultrasonic and deformation	Sandstones	Bathija et al. (2009)
6.3 – 10.6		Cores	49 – 7 (differential), 3.5 – 7 (uniaxial)	Laboratory ultrasonic and deformation	Shale	
13	6	North Sea shale core		Laboratory ultrasonic and deformation	Shale	Holt (2008)
16		4D seismic	In situ	Scaling between Geertsma's inversion pressure change and pressure from well history-matched fluid flow simulator (Ekofisk field)	A half space of average material of shale and chalk	Wong and MacBeth (2016)
207.5, 31.2, 35.7, 11.6	68.8, 10.0, 11.5, 3.4				End members of shallow shale, soft chalk, compacted shale and stiff chalk	

Table 6.1 Summary of R-factor values taken from various methods, colour-coded in yellow (scaling between time lapse seismic and geomechanical model), green (rock physics model), blue (laboratory) and red (Scaling the pressure from Geertsma's inversion and a well history matched flow simulator).

6.6 Synthetic Studies

In this section, two separate synthetic examples are given to investigate different components of the Geertsma method. The first study is a resolution test to decide which horizon in the overburden should be incorporated in the inversion procedure to yield the most accurate pressure change response. I will use the mechanical properties and reservoir geometry of the Ekofisk field. The synthetic model is made up of many cuboids and has an anticlinal structure, with an elevation of 100m (shown in Figure 6.6). A pressure source is located in the centre of the reservoir to model the strain response at difference distances away from the reservoir. Three scenarios are tested, where observations were generated at reflectors at 500m, 1000m and 2000m away from the pressure source.

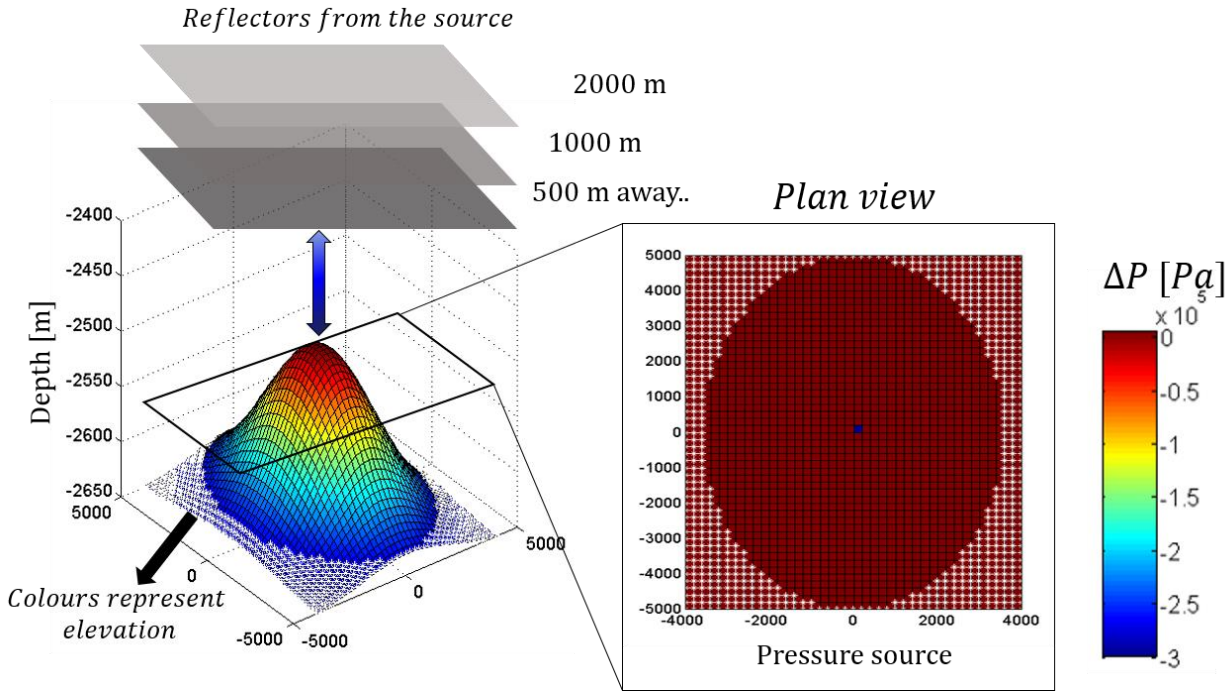

Figure 6.6: (Left) the synthetic model with an anticlinal structure and the location of the reflectors at different distances away from the pressure source, (right) plan view of the pressure sources with the coloured bar for pressure difference.

6.6.1 A resolution experiment

I have also considered different shapes for the pressure source, apart from a unit impulse, such as four impulses and a line. Figures 6.7, 6.8 and 6.9 show that in all the tests the strain response is

progressively blurred out as the observation is made further from the source. The observed strain measurements at different distances away from the source are used to invert for the pressure change inside the reservoir. The pressure change inverted using observation points furthest away from the reservoir shows that the inverted result is most diffused and with the highest error. This synthetic modelling demonstrates that a deeper horizon or a horizon that is closer to the reservoir helps to recover higher resolution pressure change.

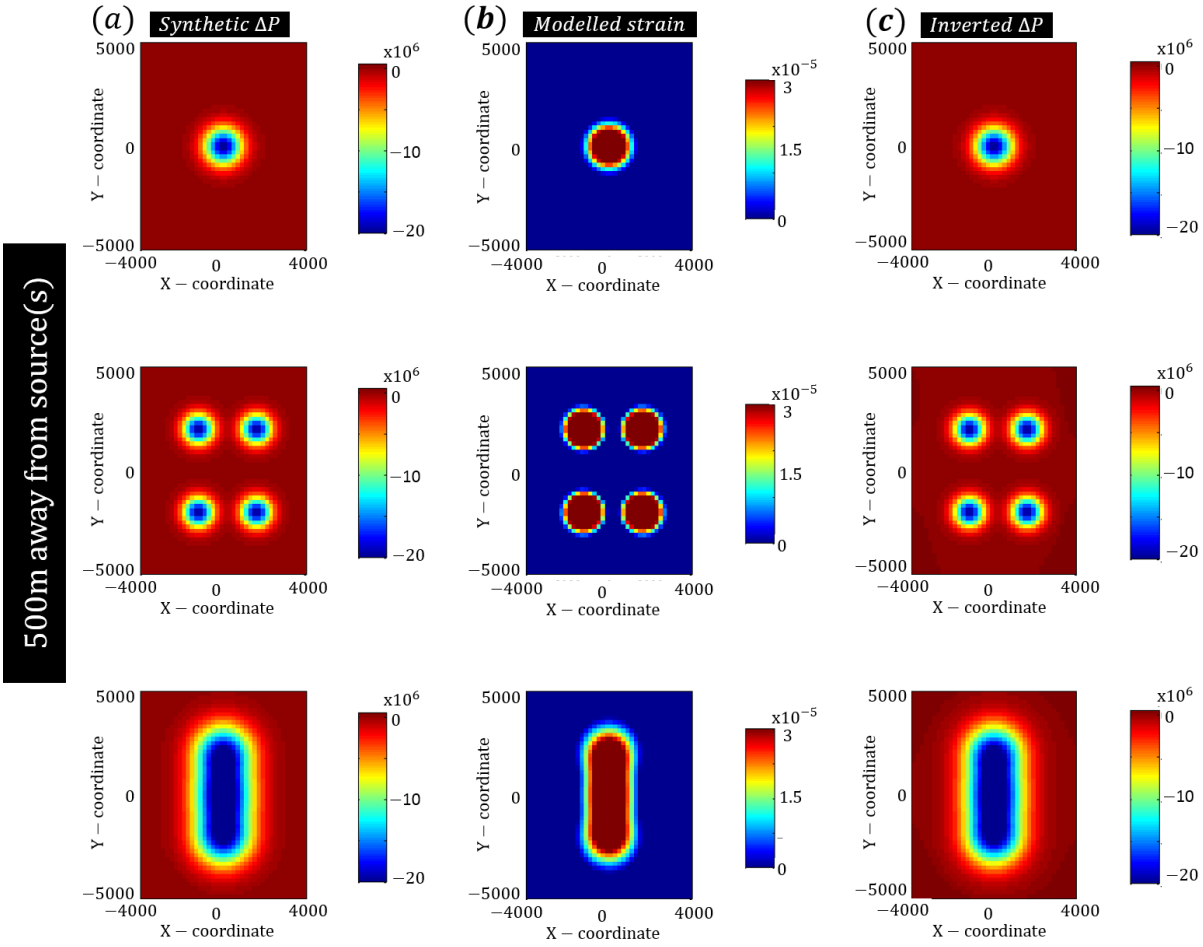

Figure 6.7: (a) The input pressure and (b) the modelled strain at reflector 500m away from the source and (c) the inverted pressure using the strain information.

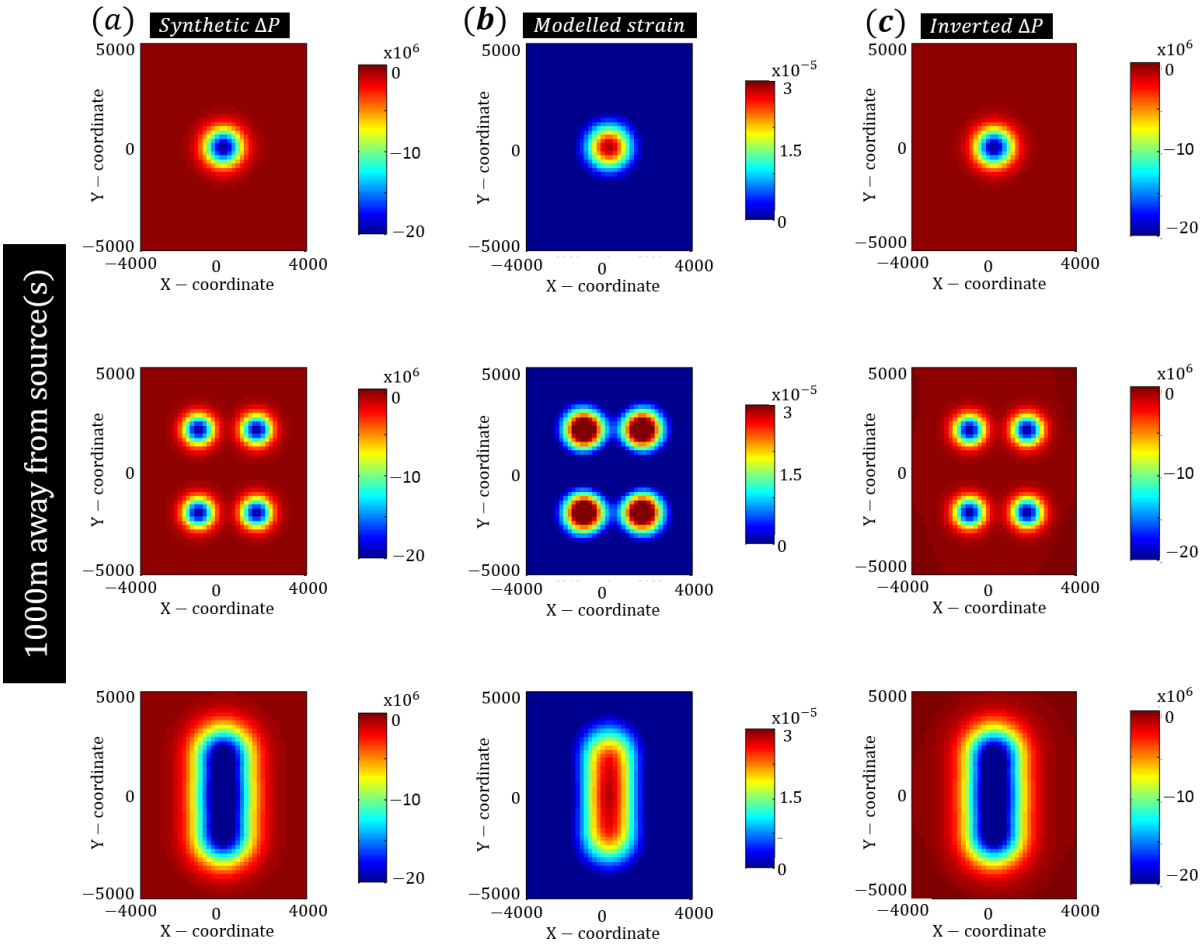

Figure 6.8: (a) The input pressure and (b) the modelled strain at reflector 1000m away from the source and (c) the inverted pressure using the strain information.

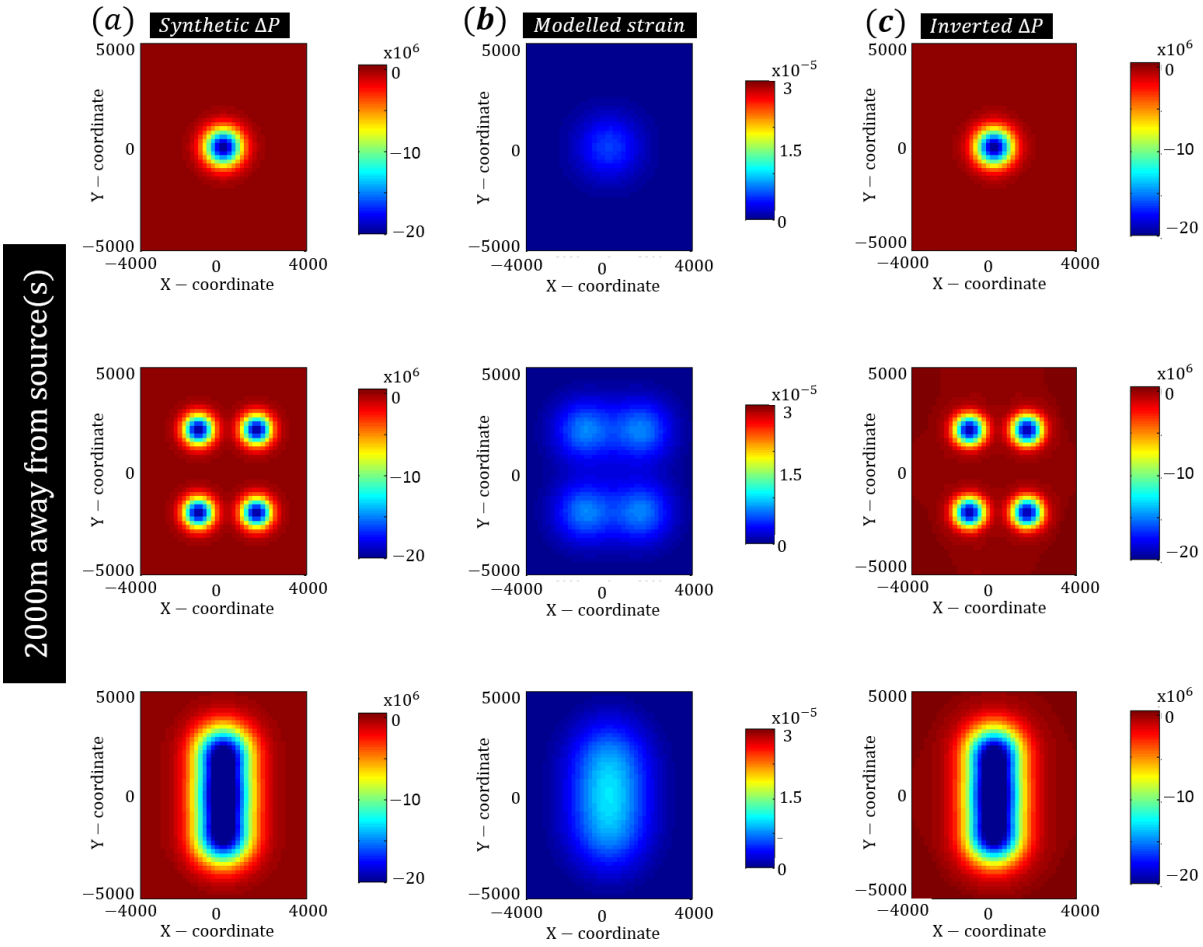

Figure 6.9: (a) The input pressure and (b) the modelled strain at reflector 2000m away from the source and (c) the inverted pressure using the strain information.

6.6.2 Validating Geertsma's solution with the numerical approach

I showed in the previous section on using the Green's function method, the calculation of strain and recovery back to pressure change for a homogeneous elastic half-space. For a general heterogeneous poroelastic medium, analytical solutions are not available and one must then resort to numerical methods. In the next synthetic example, I will show a different method, which is purely numerical, by finite element to compare results from two different solutions. The general method for solving the governing equations is based on the numerical solution using finite differences or finite elements (Mitchell and Griffiths, 1980). Here, I will compare the results of

small displacements calculated from a finite element simulator (VISAGE) to the analytical Geertsma's solution, and assess the error between them.

I employed two different constitutive models in VISAGE. For the chalk, the constitutive model is the ISAMGEO chalk model, which provides different criteria for failure in shear, compression or tension, as determined by the local stress state induced by depletion and injection. The constitutive model of chalk is a proprietary model developed by the German company ISAMGEO, which is also available in the VISAGE geomechanical simulator. The yield surface is a combination of the Mohr-Coulomb criterion with a pressure cap proposed by Papamichos et al. (1997). A full description of the constitutive model for the partially saturated collapsible chalk is beyond the scope of the thesis, and I refer to Papamichos et al. (1997) for details. The yield surface used in this current work is shown in Figure 6.10. The original Mohr-Coulomb and the Mohr-Coulomb with pressure cap is shown in a plane of isotropic mean effective stress, p versus the shear stress intensity, τ. The surrounding shale is simulated as elastic material. In this modelling exercise, all parameters for the ISAMGEO model are taken as default values from the simulator since triaxial/uniaxial compressive or hydrostatic compression laboratory tests are not available.

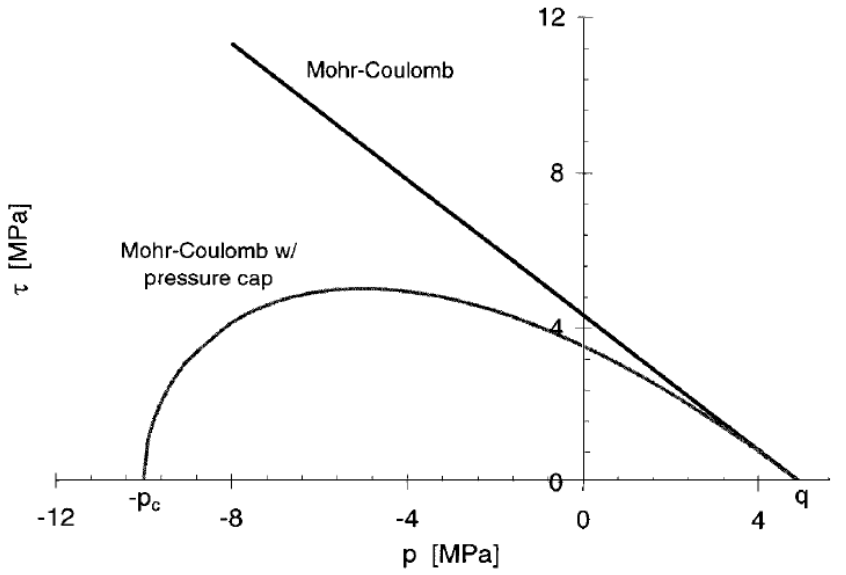

Figure 6.10: Illustration in the $\tau - p$ plane of the original Mohr-Coulomb and the Mohr-Coulomb with a pressure cap yield surface (Papamichos et al., 1997). The parameters q and p_c represent the size of the yield surface, and are also identified as the intercepts of the yield surface with a positive (tension) and negative (pressure-cap) p-axis, respectively.

This synthetic study is designed using a sector model from the Ekofisk field fluid flow simulation model. The porosity variation in this sector model is modified such that the lateral and vertical porosities are smoothly varying, so that the similar assumption of a homogeneous medium is also applied in this method. Three wells (2 vertical and 1 horizontal) were simulated to show three different pressure patterns within 1.5 years, which is similar to the time difference between LoFS 2 and LoFS 6. Different pressure change patterns are modelled by controlling the trajectories and the injection timing and rate of the wells. Figure 6.11(a) shows different pressure patterns at the locations of both injectors, where the producer has an elongated pressure change pattern (similarly to those created by long, horizontal producers in the field data). This is achieved by imposing a longer production and injection rate at I1 and P0 to generate a widespread pressure change pattern; whilst injector I2 was turned on a few months before monitor time to create an impulse response. The production and injection profile as a function of time provided from the fluid flow simulator is shown in Figure 6.11(d).

Overburden horizons, as shown in Figure 6.11(b), are used to build the structural frame of the overburden, whilst the underburden horizon was graded to match that of the bottom reservoir horizon shape. The model is populated with rock mechanical properties from Table 6.2 for reservoir, overburden, and sideburden, that are isotropic elastic materials. The reservoir is populated with chalk mechanical properties whilst the overburden, sideburden, and underburden are populated with shale mechanical properties; this is illustrated by the geomechanical model in Figure 6.11(c). Five layers are used to construct the overburden, and the underburden is made from one single layer. To reduce the impact of boundary constraints, the overburden was extended to the seafloor and the base of the model was extended to 24,000ft (approximately 7.3km). Five rows of elements are added on each side of the original reservoir grid to construct the sideburden. In Geertsma's method, which assumes no material contrast in the reservoir and the surroundings, an average is taken from chalk and shale in this modelling procedure.

The model is then initialised with the initial pore pressure and the initial stress state as boundary conditions. The next step is to predict the deformation changes in the reservoir and surroundings at the monitor time. This is done by using pore pressure and saturation information from the reservoir flow model prediction. The finite element model then calculates the changes in stress and resulting strain and displacements.

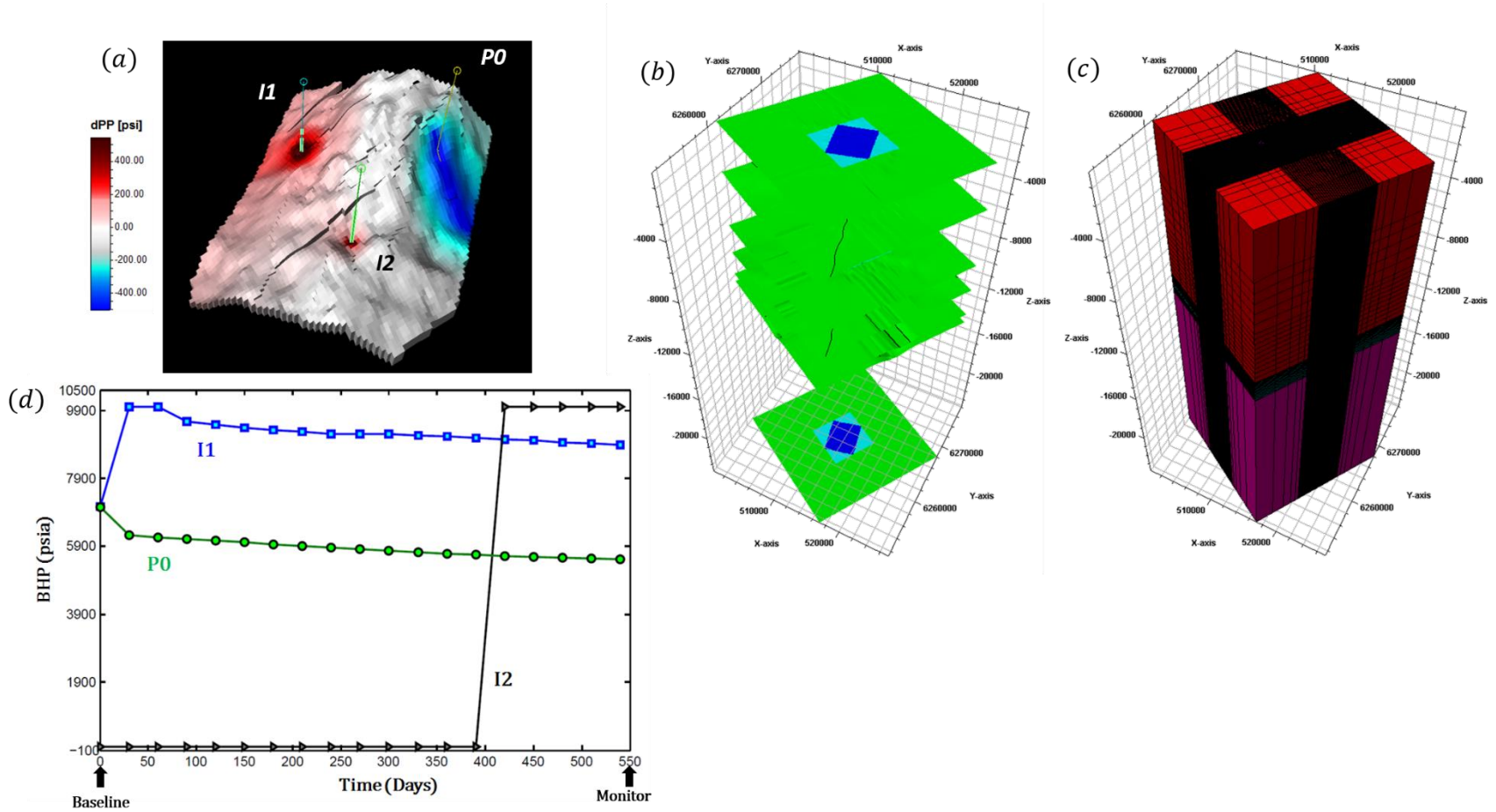

Figure 6.11 (a) One layer of the sector model and the modelled pressure change. (b) Shows the horizons used in construction of the geomechanical model. (c) Shows the cells inside the geomechanical model (red-overburden, cyan-reservoir, and pink-underburden). (d) Displays the bottom-hole pressure of the injectors (I1 and I2) and producer (P0).

	Reservoir	Overburden, sideburden and underburden
Number of Layer(s)	22	5, 1
Young's Modulus (MPa)	224800*exp(-11.2φ)	270
Shear Modulus (MPa)	1301.1 - 73348	108
Poisson's ratio	0.26-0.19φ	0.2
Porosity	0.1-0.46	0
Biot-Willis parameter	1	1

Table 6.2 Mechanical properties of the reservoir, overburden, underburden and sideburden used in my model.

Figure 6.12 shows the estimation of strain from the finite element model – VISAGE, where Figure 6.12(a) shows the plan view of the pressure change information. Two vertical cross-sections are constructed along the reservoir, given as A to A' and B to B'. Figures 6.12(b) and (c) show the predicted strains. Negative strain change is observed inside the reservoir at the injection location, which corresponds to dilation, whereas the immediate overburden and underburden at the locations of injection (I1, I2) show positive strain, which corresponds to compaction. The opposite effect is observed at the location of producer P0, the strain estimation shows that, due to pressure drawdown, the reservoir compacts and the surrounding rocks dilate. Figure 6.12(c) shows the flip of polarity between the top reservoir and top Balder (overburden) at the locations of the injectors (I1, I2) and the producer (P0).

The comparison between the strain estimates from VISAGE and Geertsma is given in Figures 6.13 (a and b), where the latter shows higher estimates at the well locations. There is overall good agreement, and the errors between both modelling approaches are small. This agreement is attributed to the fact that pressure changes are small, therefore the deformations themselves are small, and likely to be within the elastic region. Subsequently, the strain information from both methods are then used as input into Geertsma' pressure inversion. Figures 6.13 (c and d) shows the inversion results from using strain estimates calculated from Geertsma and VISAGE; the recovered maps for pressure change between the two methods are agreeable. The different pressure change patterns are equally well-resolved. Thus, Geertsma's modelling result is comparable to those from the numerical simulator - it also has the advantage of requiring less computational time and effort for parameterisation. Similar work was also presented by Toomey et al. (2015), as shown

in Figure 6.14, demonstrating the overburden displacement modelled using the Geertsma approach and that using FEM are comparable.

Unlike the FEM which requires vast amount of data, Geertsma's modelling is easy to parameterize and to implement for forward and backward modelling. Although core data are now more widely available, high-quality core from above a reservoir is rare, and cores from beyond the flanks or beneath a reservoir are never obtained. Thus, no matter how good the models are, there is a fundamental level of uncertainty that makes the forward prediction challenging. Thus, Geertsma is a good choice if the forward modelling needs to be tied regularly to real data, such as time-lapse seismic data of high spatial resolution.

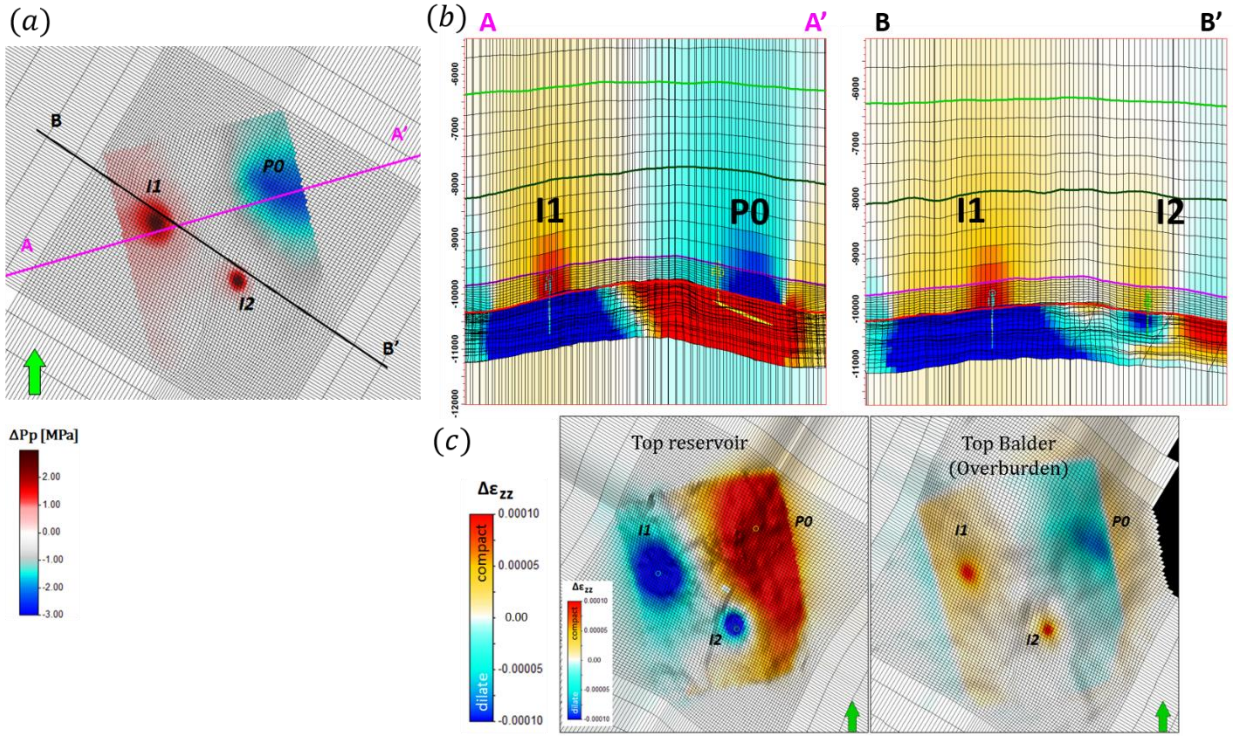

Figure 6.12: (a) Plan view of the geomechanical model with pressure change information. (b) Shows the two cross-section A-A' and B-B'. (c) Displays the strain prediction at top reservoir horizon and top Balder horizon.

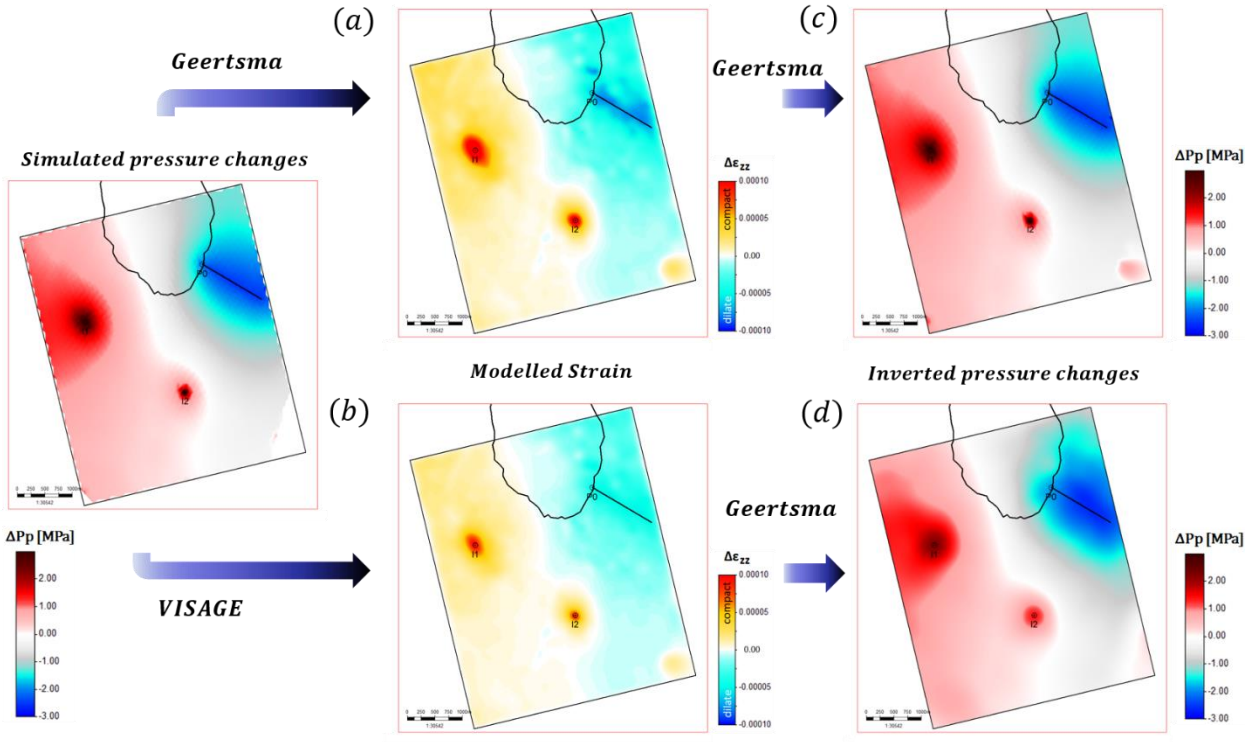

Figure 6.13: Strain prediction from (a) Geertsma's method and (b) VISAGE. Pressure change inverted from Geertsma's method using strain input from (c) Geertsma and (d) VISAGE.

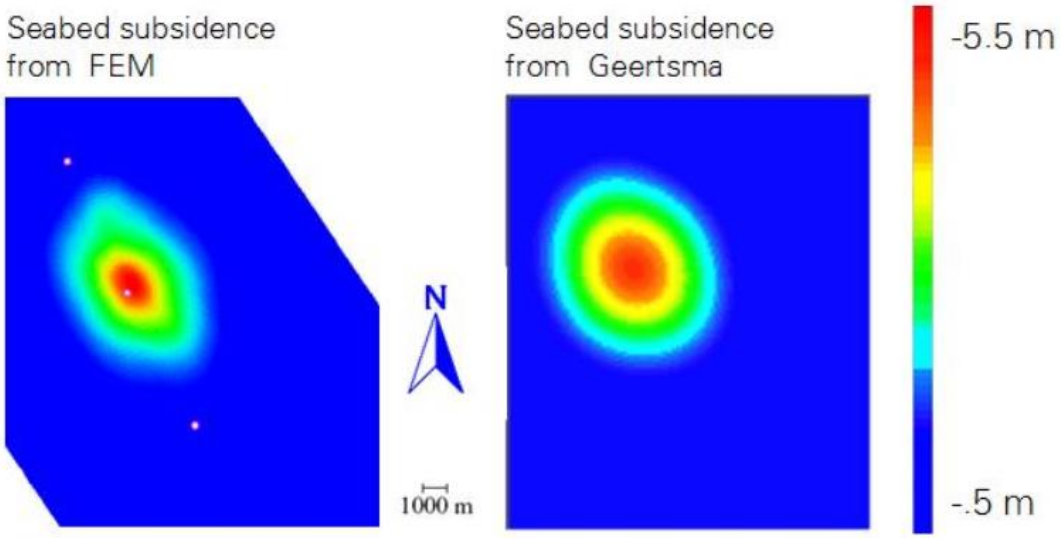

Figure 6.14: (left) Subsidence prediction for 2005 from a FEM (Kristiansen and Plischke, 2010) and (right) the subsidence prediction using Geertsma's analytical approach.

6.7 Proposed Method for R-factor Estimation

In the previous section, the inversion was carried out using strain estimates from two different methods: Geertsma and VISAGE. However, in real data, strain estimation is not acquired and is often predicted from a numerical simulator which requires calibration with data. As proposed by Hatchell and Bourne in 2005, R-factors can be used to convert time strain measurements from time-lapse seismic to vertical strain. This provides Hodgson (2009) the foundation to invert for pressure change using time strain information. The R-factors can be measured directly in the laboratory (Holt and Stenebråten, 2013) or inferred by comparing measurements from observed 4D seismic data to modelled geomechanical deformations (Hatchell et al. 2003), but consensus on the exact values to use has not yet been reached and they may still be considered uncertain. Unlike previous work which requires calibrated R-factors from matching geomechanical responses to time-shifts data. I propose a Geertsma-based inversion with prior constraints from a history matched simulation model. Compared to the geomechanical model, there are more data employed to calibrate and construct the fluid flow simulation model.

Unlike full geomechanical simulation, the formulation in Equation (6.18) provides an opportunity to close the loop between the measured time-shifts and pressure changes in a quick modelling and inversion study. It is then possible to build up statistics to quantify the R-factors by using knowledge of the pressure changes from a well-conditioned simulation model as a constraint, combined with a range of subsurface mechanical properties. The simulator honours material balance in the reservoir and is adequately matched to the historical well data via history matching. Therefore, it is assumed that the resultant pressure predictions are at least statistically accurate, and should possess more accuracy than an R-factor guess for a particular field. The R-factors are determined by scaling the pressure change solution such that the histograms of pressure estimated from the inversion scheme and the predictions from the simulator coincide. This process is depicted by the schematic diagrams in Figure 6.15. The blue histogram represents the inversion solution from Geertsma's method, by scaling the method of the blue histogram to the red, which correspond to pressure change information from a well history match model, one can calculate the R-factor. In the subsequent section, I will demonstrate the proof of concept for the proposed method.

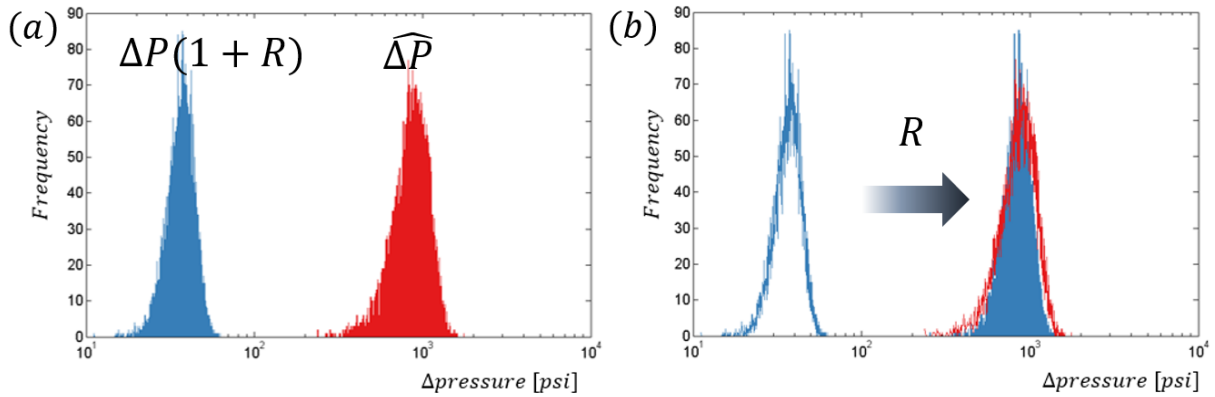

Figure 6.15: (a) Inversion solution from Geertsma's solution in blue and the pressure change from a well history matched simulator in red. (b) By scaling of the mean values of both histograms, the R-factor can be obtained.

6.8 Proof of Concept and Results

It is commonly known that a well history match simulation model gives a good estimate of field pressure. The question I try to answer is whether the mean pressure change from the well history matched simulation model is the best engineering metric to scale the histogram or is there another parameter more suitable for this purpose? The engineering metric will be assess by observing how stable is the mean pressure change in a range of models which are fairly history matched to the base case by still having an appropriate degree of statistical diversity in the models. I will generate a series of synthetic models with varying reservoir properties, but still honour material balance and maintain a low history matching misfit. I then study the stability of the mean of pressure change compared to the base case. The base case here is defined as the actual well history matched Ekofisk model.

The notion is to replicate several history matched models with small differences in local geology and then study the behaviour of the mean pressure change during a certain period of the field cycle. In most history matching procedures, multiple history matched reservoir models are often generated with the inclusion of both geological uncertainty and varying levels of trust in the production data. Subsequently, the geology of the mean of all these models will be used as the base case.

In the Ekofisk model, there is a correlation between porosity and permeability. The model is described by a classification of six porosity and permeability rock types, with their respective saturation regions and relative permeability tables, as detailed in Chapter 4, Section 4.2.1. Porosity and initial water saturation are kept constant in order not to affect the reserve of the reservoir. Since the rock types also correspond to different saturation regions and their respective relative permeability tables, this perturbation also re-distributes this information in the model. Each rock type is associated with a different colour, this is shown in Table 6.3.

Rock Type	**Effective permeability**		**Colour**	**Porosity Description**	
16	>15mD	Fractures		>32%	High porosity
15				<32%	Low porosity
14	5mD> & <15mD	Intermediate		>32%	High porosity
13				<32%	Low porosity
12	<5mD	Matrix		>32%	High porosity
11				<32%	Low porosity

Table 6.3 Rock types in the Ekofisk field are divided based on the effective permeability and porosity.

In this experimental design, I perturb the permeability of the base model in three separate ways: enhance the matrix permeability of the chalk matrix, change the effective permeability of the 'fracture' rock type, and lastly perturb the effective permeability at both high and low porosity regions. The amount of perturbation is given in Table 6.4. Figure 6.16 (a) shows the porosity-permeability cross-plot of the base case, whilst Figures 6.16 (b and c) demonstrate the changes in the saturation region as the permeability is changed in the model for cases 4 and 6. Figure 6.17 shows the distribution of permeability of all the models (1 – 6) compared to the base case. Subsequently, the dynamic changes such as pressure and saturation of the models with varying permeability are generated from the reservoir fluid flow simulator.

Rock type	Case number	Case colour	Perturbation
	Base case		No perturbation
Chalk matrix (<5mD)	**1**		+ 0.1 mD
	2		+ 1.0 mD
Fractures (>15mD)	**3**		+ 10 mD
	4		+ 100 mD
High porosity regions (Porosity> 35%)	**5**		+10 mD
Low porosity regions (Porosity<35%)	**6**		+10 mD

Table 6.4: Perturbation of permeability for the different rock types corresponding to different case numbers.

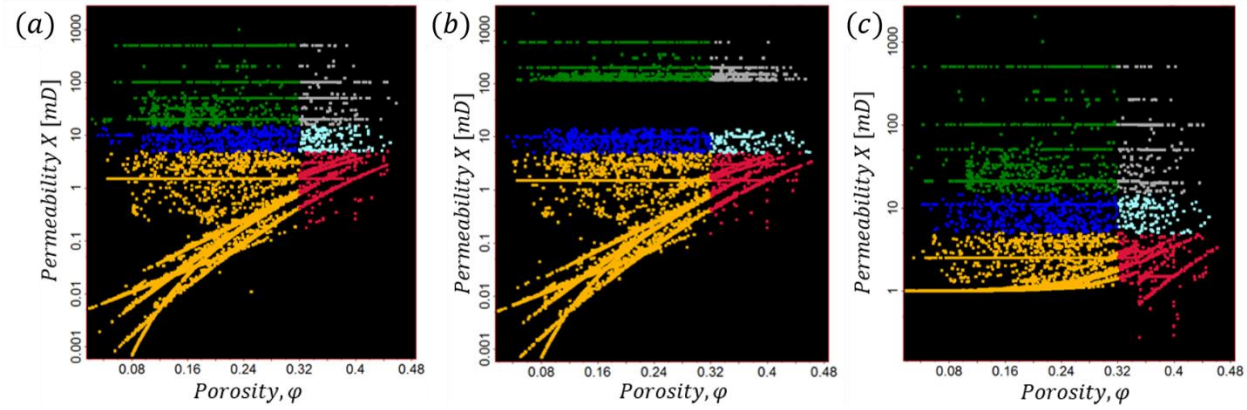

Figure 6.16: Permeability versus porosity cross-plot for (a) base case, (b) case 4 and (c) case 6. The colours in the cross-plots correspond to rock types described in Table 6.3.

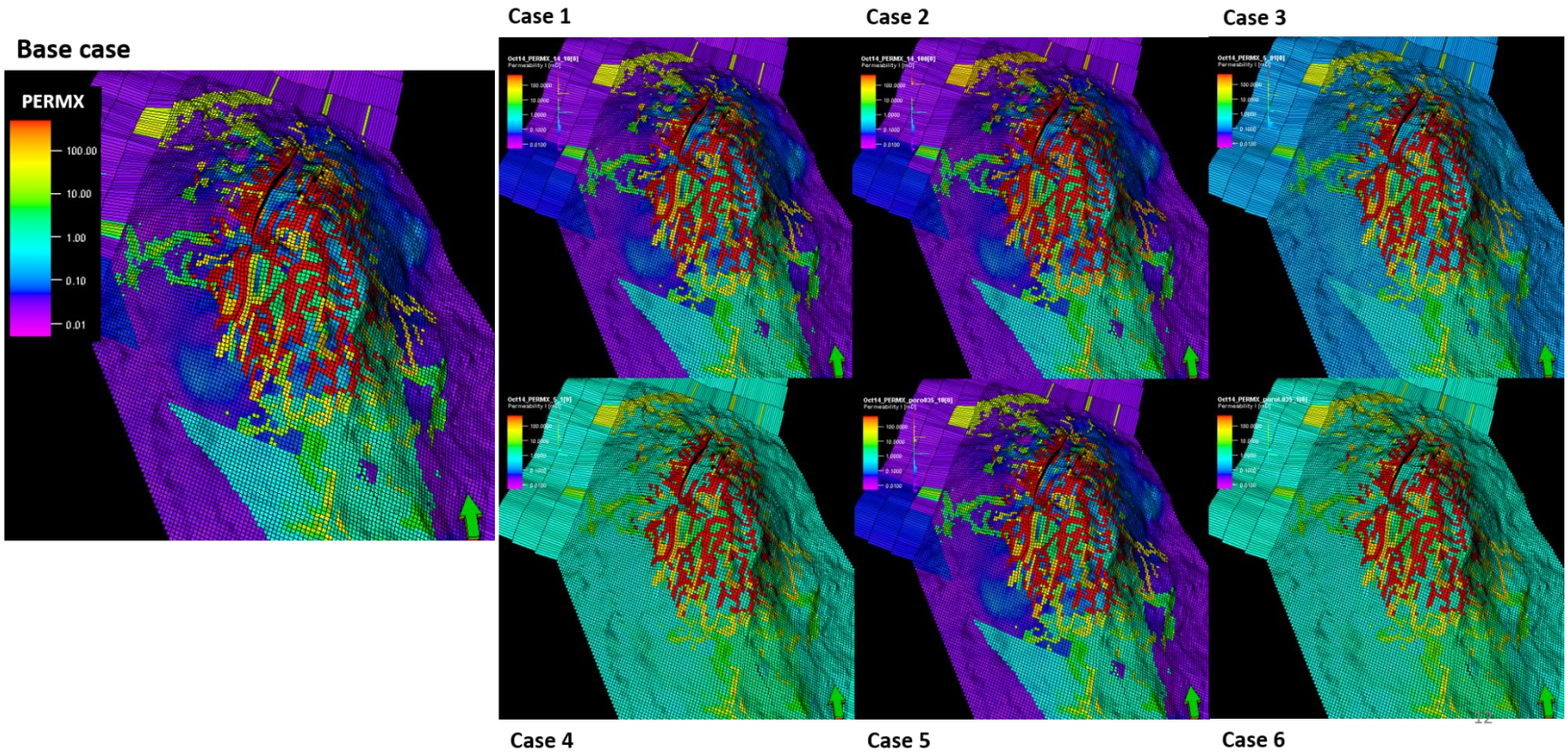

Figure 6.17: Permeability maps for the base case and the perturbed cases of 1 to 6.

Assessing the history matching quality of the different models to the base case

No real rules of thumb are in place for determining the quality of a model history match, but the duration of a history match period is important (Rietz and Palke, 2001). There are also other guidelines to determine the quality of match, such as global reservoir pressure and saturation. I will assess the models by inspecting the length of the history matched period and the global match in reservoir pore pressure, field oil production rate, field water production rate and the material-balance match. The principle of material balance is based on simple mass balance of the fluids in the reservoir. Figure 6.18 describes in words the material balance equation first presented in 1941 by Schilthuis:

$$\left\{\begin{matrix} Amount\ of\ fluids \\ in\ reservoir\ initially \\ (reservoir\ vol.) \end{matrix}\right\} - \left\{\begin{matrix} Amount\ of\ fluids \\ produced\ at\ time = t \\ (reservoir\ vol.) \end{matrix}\right\} = \left\{\begin{matrix} Amount\ of\ fluids \\ remaining\ in\ reservoir \\ at\ time = t \\ (reservoir\ vol.) \end{matrix}\right\}$$

Figure 6.18: The principle of the material balance equation.

The material balance calculation can be performed provided the oil and gas formation volume factors and gas solubility as a function of the reservoir pressure at initial and at $time = t$ are available. The pressure used is the volumetric average pressure of the entire reservoir. In all the models, the amount of fluid initially is the summation of the fluid produced and the fluid remaining at $time = t$. In this work, the predictions of the base case are treated as historic data, and the different models are perturbed to match the base case. In terms of the duration of the history match period, I will be mainly focused on the quality of the history match of all models with reference to the base case during LoFS2 – LoFS6. Figure 6.19 shows the field reservoir pressure of the base case superimposed with all other cases. Generally, I observed a reasonable match of the field pressure throughout the duration of the field production, with increasing discrepancies from the year 2000 onwards. Apart from case number 5 (pink curve), all cases are considered having a reasonable match to the field reservoir pressure, following a similar trend in pressure change compared to the base case.

Next, I evaluate the match to water production rate for all cases (Figure 6.20). A large increase in water production is observed for case number 4 (blue curve), due to the enhanced permeability of the fractures; this resulted in greater mobility of water. This is also reflected in Figure 6.21 for oil production rate, where again case number 4 (blue curve) shows a reduction in oil production at later stages of the field production. The chalk is water wet and in a fracture system, the relative permeability of water and oil is different. Water cannot progress in the fractures before the spontaneous imbibition of the matrix is fulfilled. In fractures, the S*orw* is also higher compared to the matrix. Therefore, if floods are carried out at too high a flow rate on water-wet cores, the trapping mechanisms present in the reservoir are not allowed to occur. Instead of entering small pores preferentially by capillary forces, the water flows at a relatively higher velocity through larger pores, thus tending to bypass 'groups' of smaller pores containing oil. This is essentially what happens in case number 4, where enhanced permeability in the fractures promoted earlier water breakthroughs in the wells and resulted in lower field oil production rate.

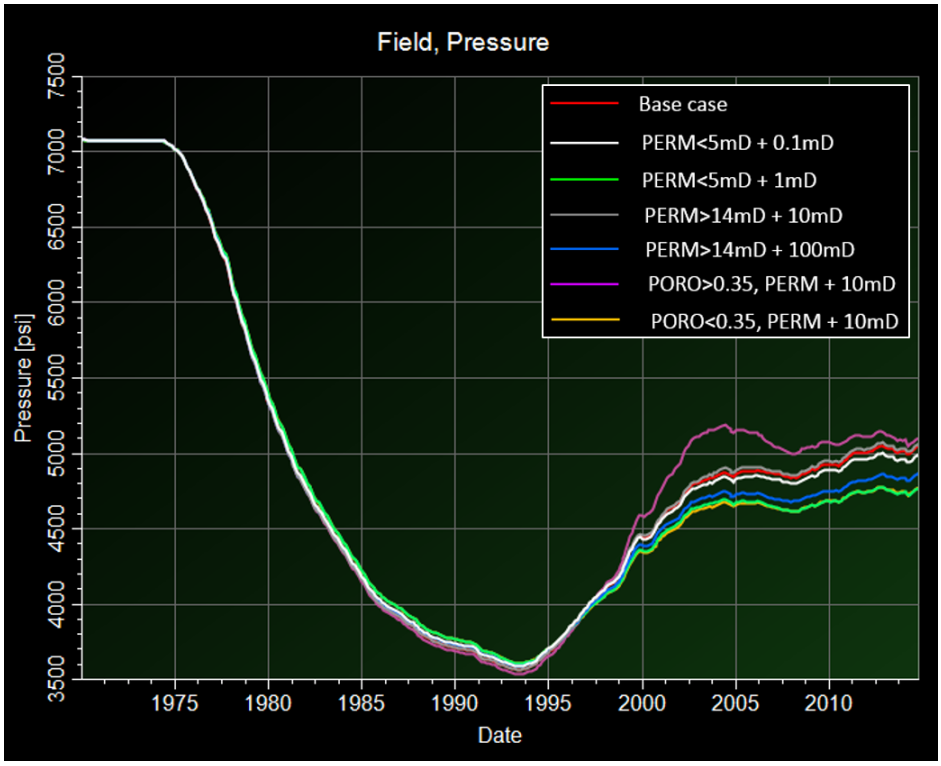

Figure 6.19: The field reservoir pressure of all cases compared to base case (in red).

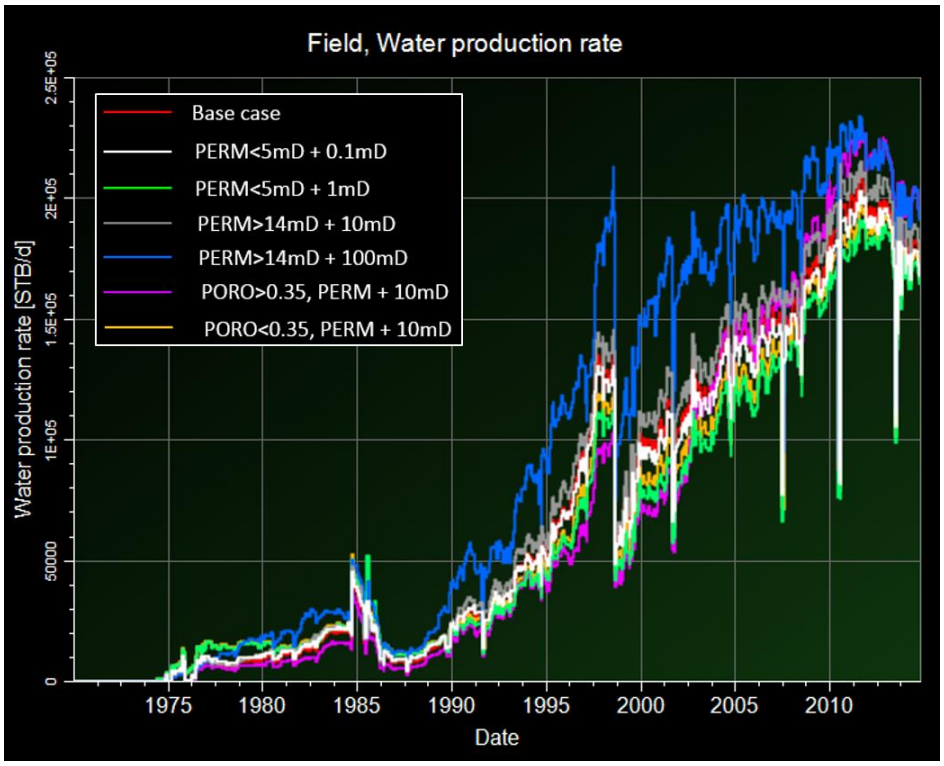

Figure 6.20: The field water production rate of all cases compared to base case (in red).

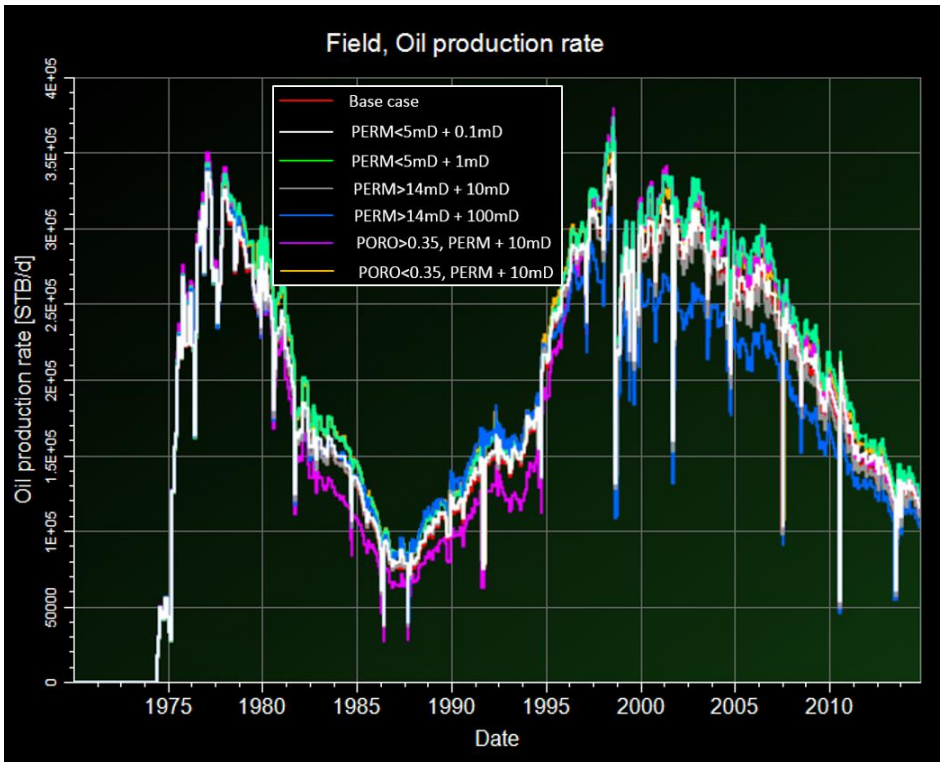

Figure 6.21: The field oil production rate of all cases compared to base case (in red).

In general, all cases show a high degree of conformance to the base case (in red) in terms of reservoir pressure profile for the period of Lofs2 to Lofs6, with the exception of case number 5 (in pink). However, it is the mean value of the pressure change from the simulation predictions that is used in comparing the mean of the pressure change solution inverted from Geertsma's method, not the absolute pressure. Figure 6.22(a) displays the histogram of the pressure difference between Lofs2 and Lofs6, Figure 6.22(b) shows the mean values of all cases compared to the base case (in red). Apart from case number 5 (pink histogram), all other cases are in agreement with the base case. Therefore, in practice, if the history matching of the pressure profile of the model is good, the mean of the pressure change from the model is a stable metric to use in scaling the histograms. This shows the proposed method has a stable metric and remains a reliable approach if more than one history matched model is present.

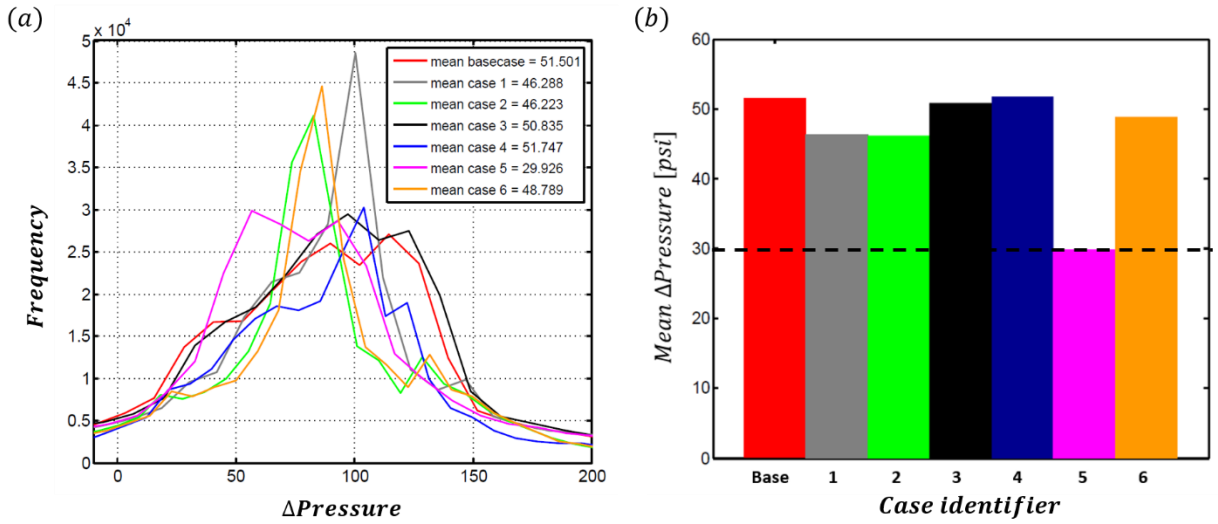

Figure 6.22: (a) Shows all the histograms from all cases compared to the base case. (b) Compares the mean value of the pressure change of the respective case to the base case, in red.

6.9 Summary

This chapter began with the summary of work found in the literature using overburden time-lapse information for reservoir characterisation. The remainder of the chapter focused on a link between strain and pressure change, using a simple, computationally inexpensive geomechanical model and the recovery of the R-factor, using some engineering constraints. The mathematical description of the displacement due to a nucleus of strain under pore-pressure reduction for a homogeneous

poroelastic medium has been published by Geertsma (1966, 1973) and various other authors. I have demonstrated, using a synthetic model, that the resolving power of the inversion lies in the distance between the source (pressure change in the reservoir) and the observation (reflector from which the measurement is taken). A synthetic study was also carried out to validate the results of Geertsma by comparing it to those modelled by a heterogeneous, iteratively coupled, finite element model. The strain estimations from these two methods are comparable. The semi-analytical formulation, when compared to finite element modeling, makes the modelling simple, fast and computationally cheap for both forward modeling and inversion.

Geertsma's method for pressure changes was applied by Hodgson (2009) for reservoirs of arbitrary shapes by the superposition of many cuboids. However, this approach requires prior knowledge of the R-factor to convert time strain to physical strain, which will be used as input into the inversion procedure. In this chapter, I have proposed an alternative method that utilises overburden time strain to estimate vertical strain and thus invert for reservoir pressure changes of the reservoir, and in that process quantify the R-factors by seeking agreement with the solution and prior constraints obtained from a well history matched simulation model. Since the simulator honours material balance in the reservoir and is adequately matched to the historical well data via history matching, it is therefore assumed that the resultant pressure predictions are at least statistically accurate, and should possess more accuracy than an R-factor guess for a particular field. In order to determine which statistical metric is best suited to scale the pressure estimates from the inversion procedure to those predicted from the history matched model, I carried out a study to examine the stability of the mean pressure of different history matched models. Multiple reservoir models with a small degree of variation in the permeability were generated with adequate well history matched quality to the pressure profile of the base case. The study shows that the mean pressure is a stable metric, and if the models are well history matched, the mean pressure values remain close to the base case, yet exhibits an appropriate degree of statistical diversity. In the next chapter, the Geertsma pressure inversion will be carried out for the Ekofisk field to estimate both pressure change in the reservoir and the field average R-factor.

CHAPTER SEVEN

PRESSURE INVERSION USING OVERBURDEN STRAIN: APPLICATION TO THE EKOFISK FIELD

The inversion approach introduced in Chapter 6 is applied to the Ekofisk field to estimate pressure change and the Hatchell-Bourne-Røste R-factor using a reservoir engineering constraint. The uncertainty on the R values is captured by running the inversion multiple times using a range of mechanical properties for the field of interest. In the Ekofisk field, the average R for the reservoir and overburden appears to be in the range 7 to 22. R-factors are also calculated for regions of pressure build-up and relaxation identified in the field, and the results confirm the current understanding determined by laboratory experiments and previous studies that the magnitude varies as a function of strain polarity, with the asymmetry being at most a factor of three. These results are validated with full geomechanical modelling followed by time-shifts modelling.

7.1 Introduction

I apply the technique proposed in Chapter 6 on the Ekofisk field by utilising time-lapse seismic signals in the overburden to estimate vertical strain, and thus invert for reservoir pressure changes. The benefit of using a Geertsma-based inversion is that the R-factors can be quantified when prior constraints are available from a well history matched simulation model, and their uncertainty defined. My results indicate that the magnitude of R is a function of strain change polarity, and that this is indeed necessary to simulate the observed time-shifts.

Is this applicable in the Ekofisk field?

This method is proposed on the Ekofisk field because of the geology of the overburden and the time scale within which the data is acquired. The overburden velocity is relatively constant with little varying geology. The mean velocity in the overburden is around 2000m/s. The overburden is described by Ottemöller et al., (2005) as mainly under-compacted, weak shale and mud rock with low shear strength ($\mu < 1$ GPa). Although the contrast between reservoir and overburden still exists, the R-factor that I intend to recover is an average R-factor for both reservoir and overburden. In the LoFS surveys, I observed time strain magnitudes that are small ($\pm 1000 psi$), and thus can assume the strain-pressure relationship to be linear between small time steps. The time strain measurements are robust due to the data acquired by a permanent reservoir monitoring system with high signal-to-noise ratio.

7.2 Data Description

To carry out the inversion, the following data are required: overburden time strain, pressure changes predicted from a well history matched simulation model, top reservoir horizon, reservoir thickness and the mechanical properties of both reservoir and overburden for the field of interest. The inversion is applied to the second and the sixth of the LoFS surveys acquired two and a half years apart.

7.2.1 Overburden time strain computed from 4D seismic

The overburden time-shifts are computed using the non-linear inversion method proposed by Rickett et al. (2007). The time strain is the derivative of time-shifts, and is an interval property that is easier to interpret in comparison to time-shifts. The inversion method outlined in Chapter 6 relates time-lapse time strain to vertical strain via the equation from Hatchell and Bourne (2005):

$$\frac{\Delta t}{t} = (1 + R)\varepsilon_{zz} \tag{7.1}$$

This provides a linear relationship between the input data (overburden time strain, $\frac{\Delta t}{t}$) and the desired transformation to vertical strain, ε_{zz}. Given time strain is the derivative and is prone to noise, I prefer to work with time-shifts measurements, which, in this case, can be calculated by integrating the time strain over a specific interval in the overburden. The time-shifts of a given interval in depth $\widetilde{\Delta t}(z)$ can be computed by integration of the previous equation as follows:

$$\widetilde{\Delta t}(z) = \frac{2(1+R)}{V} \int_{\frac{t_0 V}{2}}^{\frac{t' V}{2}} \varepsilon_{zz} \left(\frac{2z}{V}\right) dz \tag{7.2}$$

where $\widetilde{\Delta t}(z)$ is the time-shifts in the depth domain. The transformation for time, t, to depth, z, is given as:

$$z = \frac{tV}{2} \tag{7.3}$$

which is also expressed in the upper and lower limits of the integral. Equation (7.2), with the new limits can be written as:

$$\widetilde{\Delta t}(z) = \frac{2(1+R)}{V} \int_{z_o}^{z} \varepsilon_{zz} \left(\frac{2z}{V}\right) dz \tag{7.4}$$

The geology of the overburden is rather homogeneous, therefore the velocity, V is approximately constant with depth. The above equations will not hold true if the velocity varies greatly as depth increases. The time-shifts of a specific overburden layer are integrated over a 50ms window above and below a picked horizon. The summation over a 100ms window ensures enhancement of signal-

to-noise ratio. In this work, the integration of time strain over a small interval of the overburden will be referred to as the interval overburden time-shifts (IOT). The maps calculated for four horizons in the overburden are illustrated in Figure 7.1. The horizons chosen, in the order from closest to furthest from the reservoir are: Balder, Eocene, Top Eocene and Upper Oligocene 4. It is apparent that, for information observed away from the source (reservoir), the signal becomes more diffused and the magnitude reduces. The magnitude of the IOT diminishes from Balder to the surface furthest from the pressure source shown in Figure 7.1. This implies that as the IOT becomes negative (overburden compacts), it is likely that the underlying reservoir undergoes dilation, due to pressure increase. The horizons employed to create such IOT maps are shown in Figure 7.2.

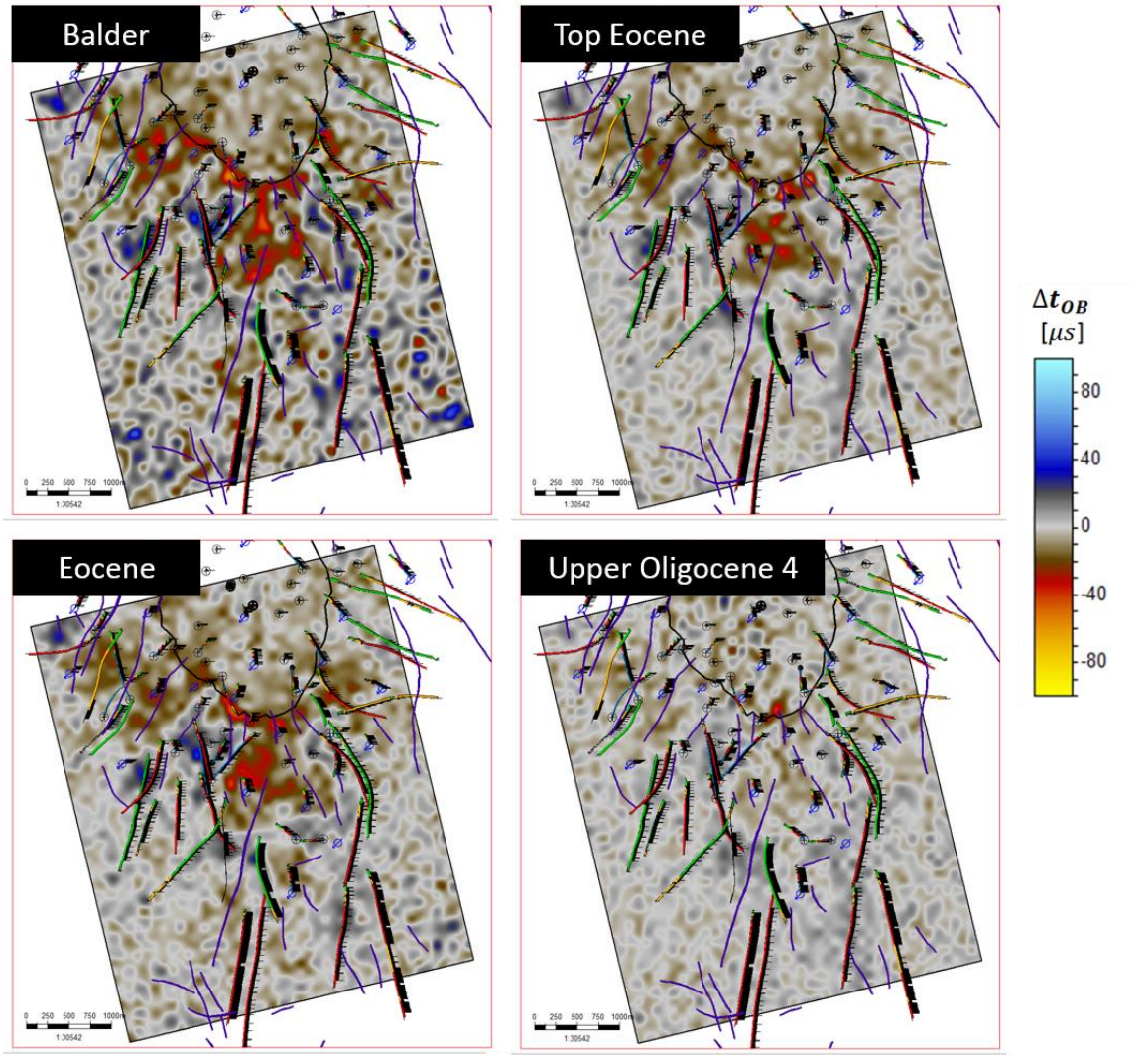

Figure 7.1: Interval overburden time-shifts (IOT) maps calculated for Balder, Top Eocene, Eocene and Upper Oligocene 4. The colour bar shows a reduction in IOT as red and an increase in IOT as blue.

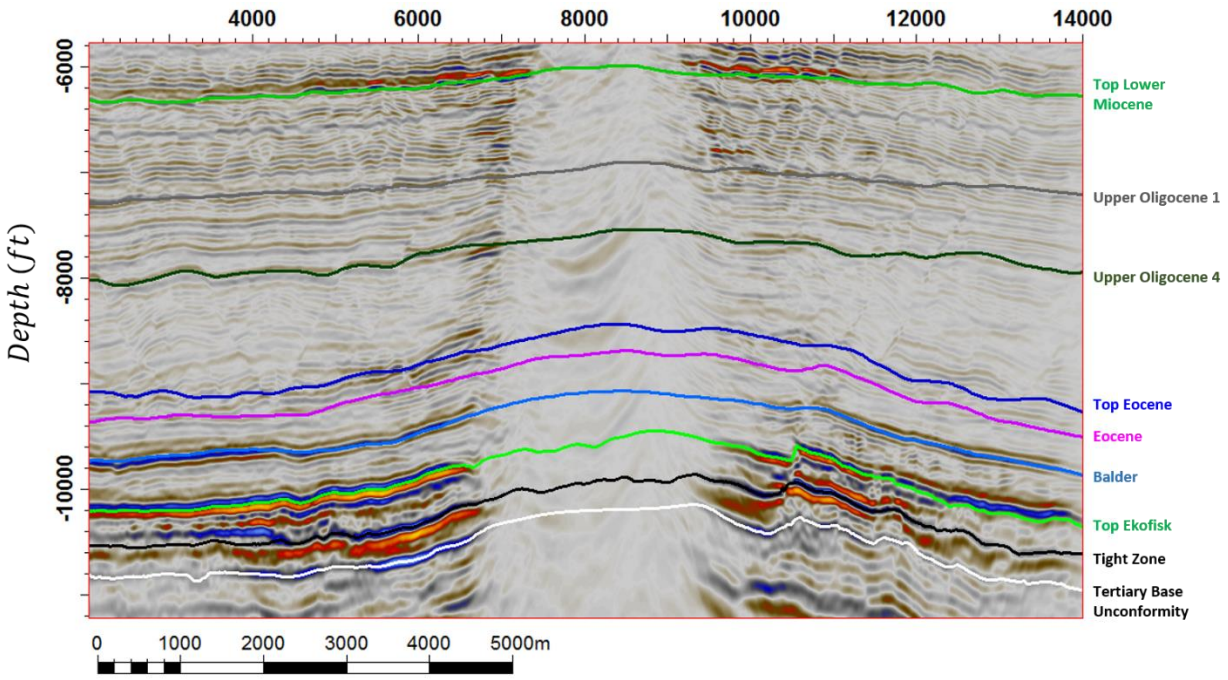

Figure 7.2: Overburden horizons in depth domain provided by ConocoPhillips. The gas cloud over the crest of the reservoir creates poor imaging of the data (this area is known as the seismic obscured area).

7.2.2 Top reservoir horizon and reservoir thickness

In order to compute the Green's functions, which requires the distance between observation points in the overburden and the pressure sources (reservoir), the top reservoir depth map is required. The depth map of the top of the reservoir is extracted along the Top Ekofisk horizon shown in Figure 7.2. In this inversion approach, the reservoir is laterally subdivided into equally spaced cuboids, but the cuboids vary in thickness. The variations in the integrated volume come from cells of different thicknesses, where the reservoir thickness is obtained by calculating the difference between the depth horizons of Top Ekofisk and the Tertiary Base Unconformity (Base reservoir). The reservoir thickness will yield the information regarding the thickness of each cuboid. The reservoir thickness map and the top reservoir depth map used as input data are depicted in Figures 7.3 (a) and (b). The volumes of individual cuboids of the reservoir are computed to perform the numerical integration of the cells inside the reservoir. If there are errors in the interpretation of the top and base of the reservoir, this could propagate errors into the volume integration. However,

given the overburden deformation at any given observation point is the sum of the contributions of all cuboids, the error can be distributed over the other cuboids in the reservoir. This hypothesis was tested by Hodgson (2009), where small errors in the reservoir thickness had a negligible effect on the overall inverted results.

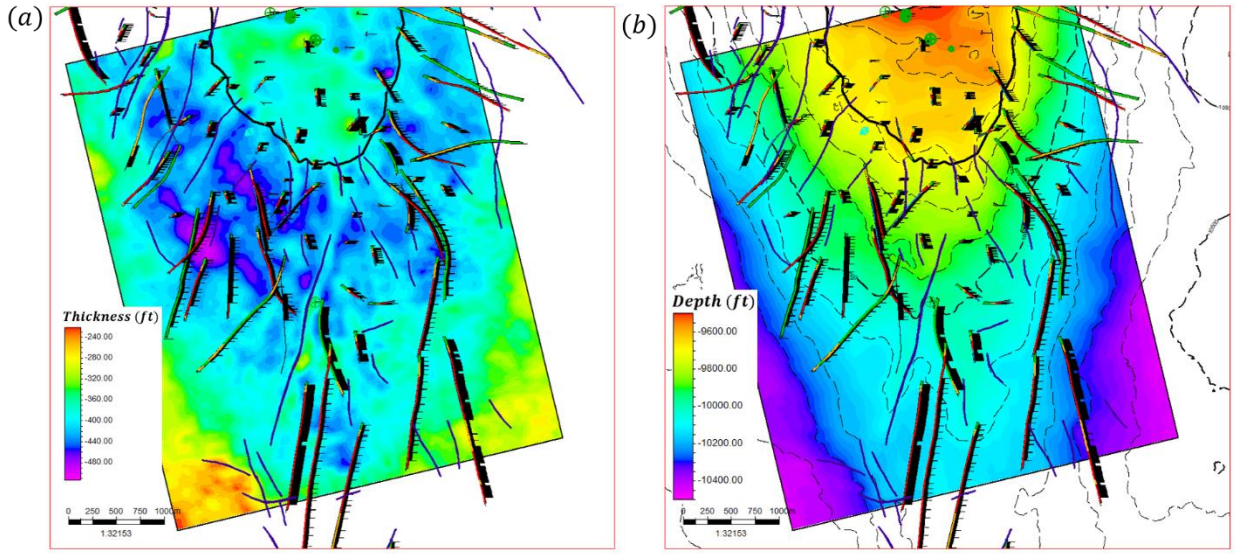

Figure 7.3: (a) The reservoir thickness between Top Ekofisk and the Tertiary Base Unconformity (TBU), whilst (b) shows the top reservoir depth.

7.2.3 Static moduli of rock types in reservoir and overburden

The mechanical moduli for both reservoir and overburden are required in order to describe the poro-elastic medium of the half space. Given the assumption that there is no material contrast between the different layer properties between overburden and reservoir in Geerstma's inversion scheme, an average will be taken using the values from both reservoir and overburden provided in Table 7.1. I calculated the Young's Modulus and Poisson's ratio for chalk using the porosity-dependent correlations, whilst properties for the shales were computed based on the stratigraphic age, using the relations proposed by Zhang et al., (2011). The younger shales are characterised by lower Young's modulus and Poisson's ratio, due to higher ductility, and vice versa for the deeper shales.

Mechanical properties	**Correlation**	**Chalk φ: 0.35 – 0.46**	**Shale (Miocene – Paleocene)**
Young's Modulus (MPa), E	224800*exp(-11.2φ)	4460 – 1310	270 – 1500
Poisson's ratio, v	0.26 – 0.19 φ	0.17 – 0.19	0.20 – 0.25
Shear Modulus (MPa), μ	$\frac{E}{2(1+v)}$	1874 – 559.8	108 – 577

Table 7.1: Mechanical properties of the end members: chalk and shale (Zhang et al., 2011).

In this study, the rocks are characterised using static mechanical properties, the reason being that the static counterpart is more representative of in-situ stress states. In the next section, I will discuss further the importance of static and dynamic moduli, and the causes for discrepancy between the two.

7.2.4 Static and dynamic moduli

If we measure the compressional and shear wave velocities of a rock from well logs or seismic data, along with the density, we can calculate the elastic modulus of the rocks as experienced by the elastic wave. This is the dynamic modulus which differs from the static elastic modulus calculated from stress and strain measurements in rock mechanics tests. Moduli obtained from rock mechanical tests, which are responding to the static, slowly varying stresses with larger amplitude, are often found to be substantially lower than those obtained by acoustic measurements (dynamic moduli). The origins of this difference are likely to be differences in strain amplitude and the heterogeneity of the rock microstructure, as discussed in Fjær et al. (2008). The strain amplitudes for seismic waves are of the order of 10^{-6} to 10^{-7}, while in a rock mechanical test they are typically 10^{-2} to 10^{-3} (Fjær et al., 2008).

Tests have shown that when the rock mechanical tests are conducted in such a way that strain amplitudes are lowered, by performing a short unloading-reloading cycle, then static moduli measured under these conditions tend towards the dynamic moduli (Fjær et al., 2008). There are several reasons proposed in the literature as to why such a difference exists between static and

dynamic moduli, these are summarised in Table 7.2. Causes of discrepancy also include cracks and heterogeneous microstructure. For example, a homogeneous elastic material such as steel has no difference between the dynamic and static moduli (Ledbetter, 1993). It is thought that the cracks in the rocks created these discrepancies, such that, during loading, crack surfaces slide past each other but the amplitudes of sound waves are not capable of creating frictional sliding; this theory is supported by Ide (1936), Walsh (1965), King (1983), Van Heerden (1987), Eissa and Kazi (1988), and Tutuncu et al. (1998).

The aim here is to report some correlations between static and dynamic moduli for sedimentary rocks, which will be useful for the Ekofisk field. Most if not all of the relations in the literature are derived empirically. The general trend shows that the dynamic Young's modulus calculated from acoustic velocity and density is higher than those computed from static tests. I compiled some conversion factors between static and dynamic Young moduli (E_{st} and E_{dyn}) for both carbonate and clastic rocks. These are reported in Figure7.4, which shows a cross-plot comparing static and dynamic Young's moduli for carbonate and chalk samples only. Yale and Jamieson (1994) reported the saturated dynamic Young's modulus can be 15-70% or 1.15 to 1.7 higher than the static counterpart. This is also in agreement with Olsen et al. (2008), where the saturated chalk samples from the Stevn outcrop in Denmark showed a dynamic to static conversion of 1.2 to 1.5. Henriksen et al. (1999) show a much larger conversion factor for dynamic to static at 2 to 4, for a water saturated North Sea chalk. Gommensen and Fabricius (2001) also reported a similar conclusion that the static bulk modulus is significantly lower than the corresponding dynamic modulus for water saturated chalk, although no conversion factor was proposed in that article. Figure 7.5 compares the dynamic-static conversion factors of chalk and carbonates to other rock types, such as clastics, igneous and metamorphic rocks. The dynamic-static conversion factors of clastic rocks are in agreement with those from Yale and Jamieson (1994) and Olsen et al. (2008). This study shows igneous and metamorphic rocks have higher dynamic to static conversion factors in comparison to sedimentary rocks, which is comparable to the findings of Henriksen et al. (1999). Therefore, the bounds estimated for Young modulus from Yale and Jamieson (1994) and Olsen et al., (2008) should be more relevant to the Ekofisk field.

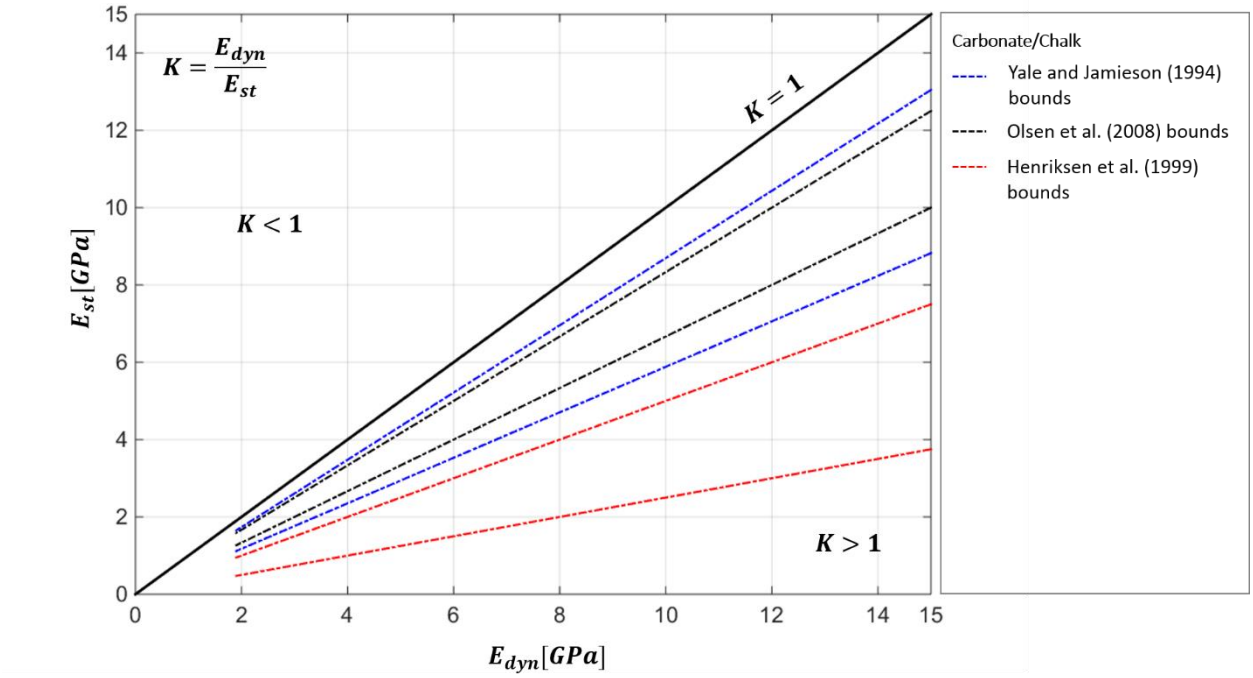

Figure 7.4: Plot of the relationship between static and dynamic Young's moduli for carbonate and chalk rocks.

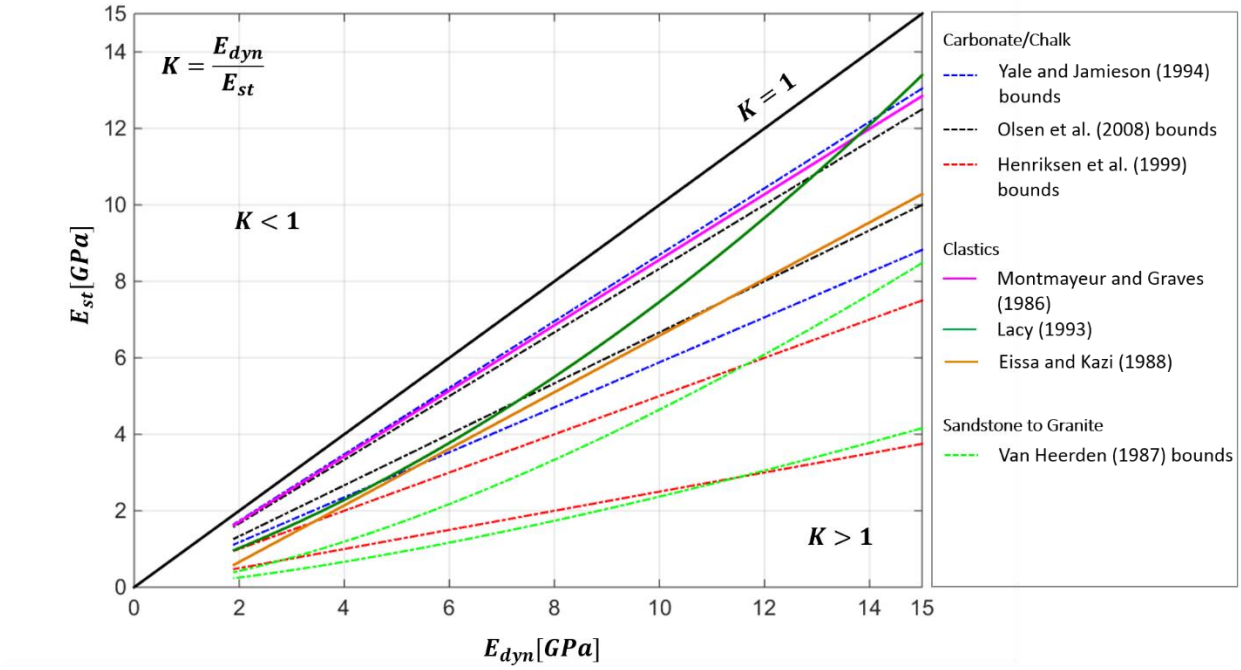

Figure 7.5: Plot of the relationship between static and dynamic Young's moduli for both sedimentary and non-sedimentary rocks.

Causes of discrepancy	Description	Sources
Cracks	• Granular microstructure causes nonlinear response • During loading, crack surfaces slide past each other, frictional resistance occurs, energy is lost and hysteresis is observed in stress-strain curve • Amplitude of sound wave is not sufficient to cause frictional sliding	Tutuncu et al., 1998, Van Heerden, 1987, Ide, 1936, King, 1983, Eissa and Kazi, 1988, Walsh, 1965
Presence and type of cementation	• Dynamic to static ratio is lower for samples with high quartz overgrowth cementation and high degree of grain suturing and embedment	Yale et al., 1995
Strain amplitude	• Most popular hypothesis • Dynamic measurements are made in the order of 10^{-8} to 10^{-6} and static test is made in the order of 10^{-4} to 10^{-2} • Displacement across crack surfaces are of the order of inter-atomic spacing and no frictional sliding occurs in strain amplitude less than 10^{-6} • Young's modulus decreases with increased strain amplitude	Winkler et al., 1979, Tutuncu et al., 1994, Sharma and Tutuncu, 1994, Tutuncu, 1998, Hilbert et al., 1994
Definition of static	• A need to emphasize a clearer definition of static. The consistent definition of static modulus should be the one calculated from the minor cycles where the loading and unloading portions of the cycle trace each other	Plona and Cook, 1995
Frequency	• In fluid-saturated samples, frequency dependence of the wave velocities and attenuation are observed at much lower frequency • An increase in moduli from seismic to ultrasonic frequencies accounts for the relative motion of fluid with respect to the solid skeleton and squirt flow • The frequency differences between dynamic (10^4 to 10^5 Hz) and static (10^4 to 10^2 Hz) are large enough to allow significant viscoelastic deformation in static tests and not in the deformation time frames of acoustic wave passage.	Spencer, 1981, Winkler, 1983, Tutuncu et al., 1998, Winkler, 1979, Biot, 1956, Mavko and Nur, 1979, Murphy et al., 1986

Table 7.2: Summary of the causes of discrepancy between static and dynamic moduli.

7.2.5 Inversion Workflow

The proposed method is Chapter 6 is carried out on the Ekofisk field data. Figure 7.6 shows a flow chart of the different forward and inversion routes typically performed in the industry. To model physical strains and stresses, Geertsma's method or FEM/FDM are routinely carried out, however the complexity of FEM/FDM models caused an increase in the time needed for the construction and the computation. The R-factor is then used to convert physical strain to time strain by assuming a linear relationship between velocity and strain. In the inversion route, Geertsma's method is favoured due to its efficiency to perform multiple forward modelling. The method that I will use to invert for pore pressure changes do not require an initial guess of the R-factor. Defining R-factor values for a specific field from other 4D seismic analysis could be erroneous. The R-factor estimated via this method is a by-product of the pressure inversion and it is lithology and strain polarity dependent.

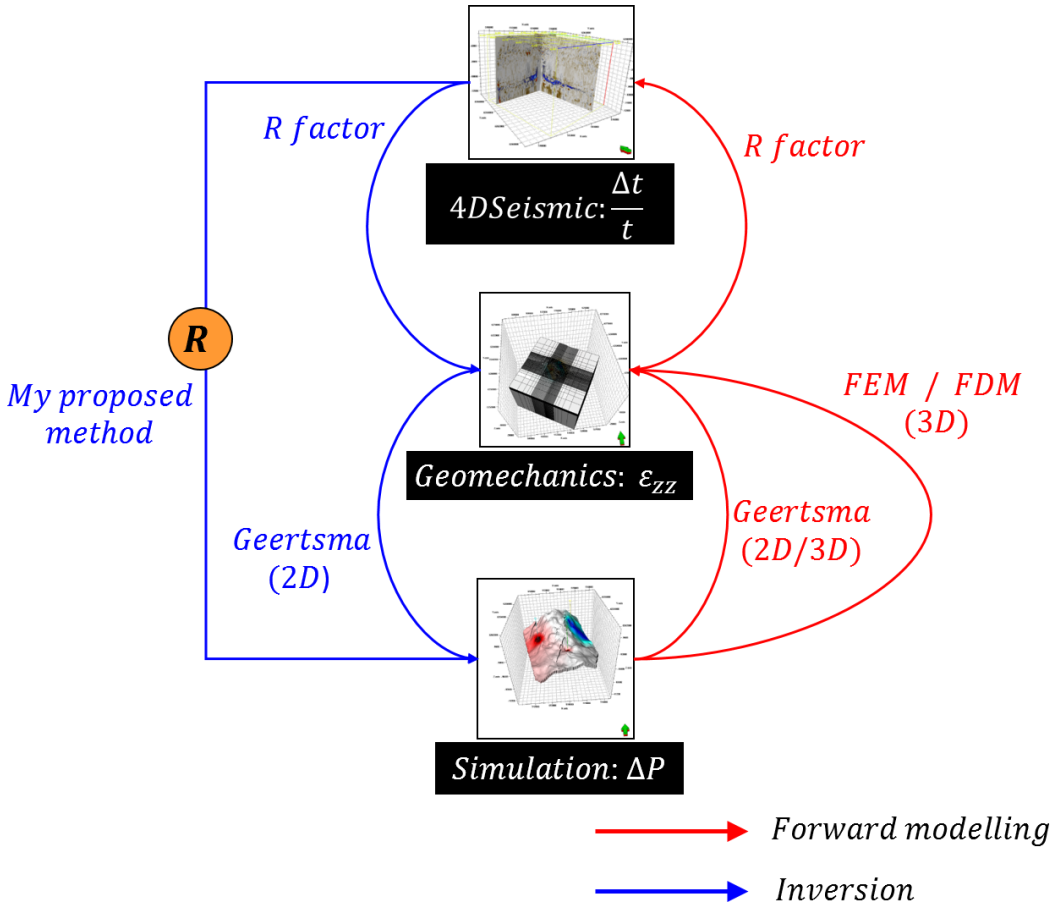

Figure 7.6: Flow chart shows the forward and inversion route typically carried out in the industry, my proposed method inverts for pore pressure changes directly from time strain without guessing the R-factor. The R-factor is a by-product of the pressure inversion.

This section describes the inversion workflow to extract both pressure changes and the R-factor. The workflow of the inversion is described in Figure 7.7. The input data for the inversion are IOT surfaces from the overburden, and maps of top reservoir and reservoir thickness. Having defined the static mechanical properties of the end-member rocks in both the reservoir and overburden, in Section 7.2.3, multiple Geertsma inversions are carried out using different combinations of the end-members' mechanical properties. The end-members are defined as: soft or porous chalk (μ=0.56GPa and ν=0.17), stiff chalk (μ=1.86GPa and ν=0.19), shallow shale (μ=0.10GPa and ν=0.20) and deep and compacted shale (μ=0.58GPa and ν=0.25). From each of the Geertsma inversions, an R-factor is calculated by scaling the inversion result to the pressure changes

estimated from a well history matched model. This allows us to build statistics on the R-factor as a function of different rock mechanical properties. I then compute the average R which is an equal weighting of all four end members. Subsequently, the average R is applied as a rock physics transform to convert the overburden time strain to physical strain, and invert the physical strain to changes in pressure, using the same Geertsma's inversion procedure. Both smoothing and well measurements were used as constraints were applied to stabilise the results of the inversion.

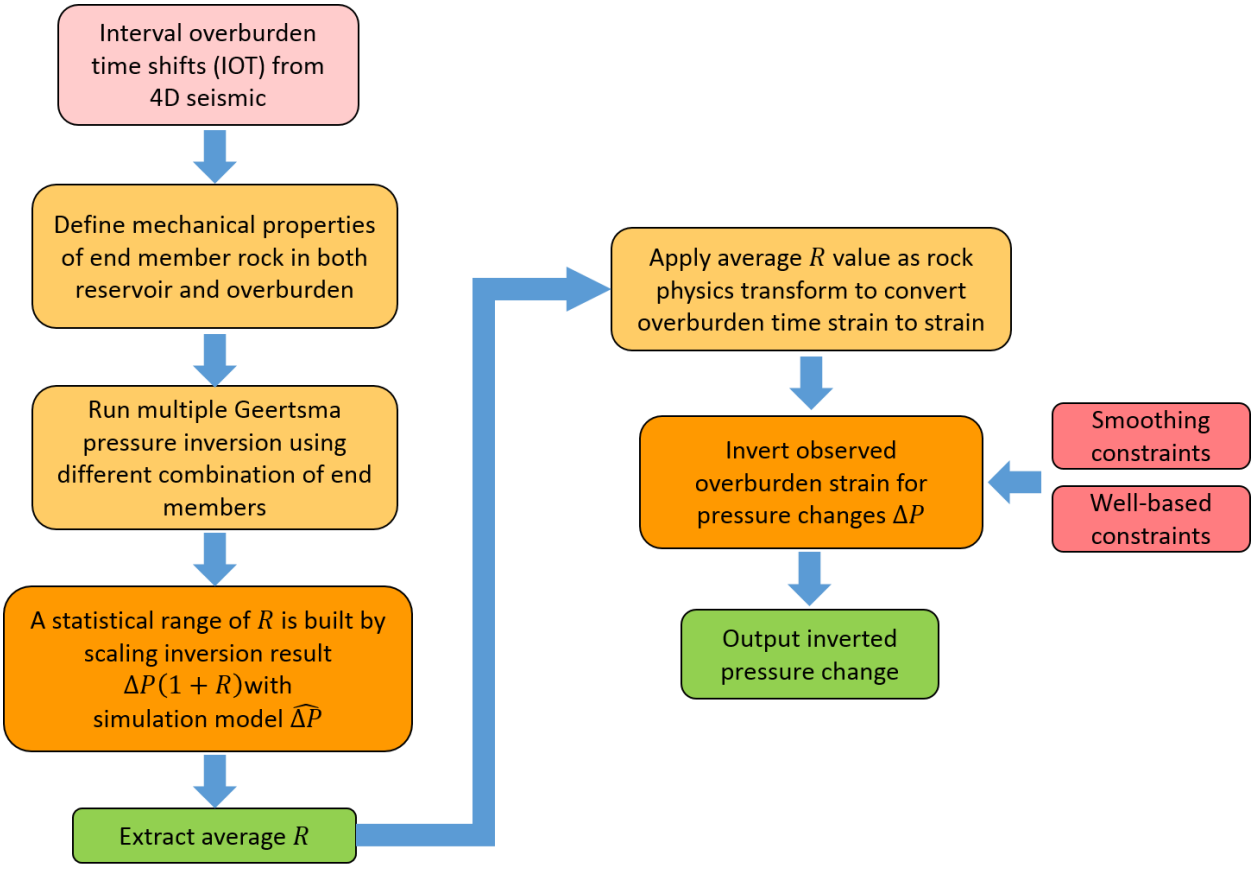

Figure 7.7: Workflow for Geertsma's pressure and R-factor inversion (Modified after Hodgson, 2009).

7.2.6 Constraints from history matched well predictions

The inversion procedure outlined by Hodgson (2009) and Hodgson et al. (2007) shows how constraints are added into the objective function. The objective function is given as:

$$E = \|G\Delta p - d\|_2^2 + \alpha^2\|L\Delta p\|_2^2 + \beta\|\delta_i\Delta p_i - d_i\|_2^2 \quad (7.5)$$

where E is the objective function, α is the weighting coefficient for the smoothness constraint whilst β is the weighting coefficient for the prior data d_i. d is given as data, L is the Laplacian operator, p is pressure changes and δ represent certain cells with known pressure change, p_i. The first term represents the smoothness constraint. The solution's smoothness can be implemented by quantifying the roughness by the second derivative. Minimising the first term penalizes the pressure changes that are rough in the second derivative sense, meaning the expected solution is smoothly varying and not flat (Menke, 2012). The second term is a 'hard data' constraint, which includes known pressure information (prior data) in certain regions in the reservoir. The prior data is defined as a pressure difference map, with regions of known or reliable data from the simulation model. My prior data is calculated by extracting pressure change information from the simulation model in regions with good history match quality. For each well, a measure of misfit is computed between the measured and predicted production data. Since we are only interested in the pressure change, I calculated the misfit between the simulated Bottom Hole Pressure (BHP_{sim}) and historic Bottom Hole Pressure ($HBHP$) at each well. The misfit is given as:

$$misfit = \frac{HBHP - BHP_{sim}}{HBHP} \tag{7.6}$$

Subsequently, wells with poor misfit are discarded and will not be included in the prior data.

7.3 Results

The pressure inversion is applied to two seismic vintages acquired two and a half years apart. According to the Geertsma formulation, the inverted pressure change also scales with the choice of the shear modulus and Poisson's ratio assigned to the average half-space representing the reservoir and overburden. This, therefore, poses an interesting possibility: the best choice R-factor can be found by performing many inversions for different combinations of shear modulus (μ) and Poisson's ratio (υ), and then finding the R that matches the estimates to the simulator predictions (matching the means of the histograms).

In the case of Ekofisk, a range of lithology dependent mechanical properties are available. Initially, a half-space consisting of 100% shallow shale (μ=0.10GPa and υ=0.20), soft chalk (μ=0.56GPa, υ=0.17), compacted shale (μ=0.58GPa, υ=0.25), and stiff chalk (μ=1.86GPa, υ=0.19) are all considered, together with a range of properties between these end points. The inversion with scaling adjustment gives R-factors of 127, 19, 22 and 7 for the four end member property, as shown in Figure 7.8. The R-factor recovered for chalk and shale is consistent with Janssen et al. (2006), where a smaller R-factor for chalk under compaction is recovered compared to a larger R-factor value for the overburden shale under dilation. However, a half-space composed completely of shallow shale is considered unlikely. The spread of R-factors recovered for different material properties helps define a range of possible uncertainty, as shown in Figure 7.9. All possible combinations of shear modulus (0.1 – 2GPa) and Poisson's ratio (0.15 – 0.25) is employed to calculate the R-factors. The final result in Figure 7.9 is determined by using a property average that is an equal weighting of all four end-points (μ=0.78, υ=0.20), for which a R-factor of 16 is recovered.

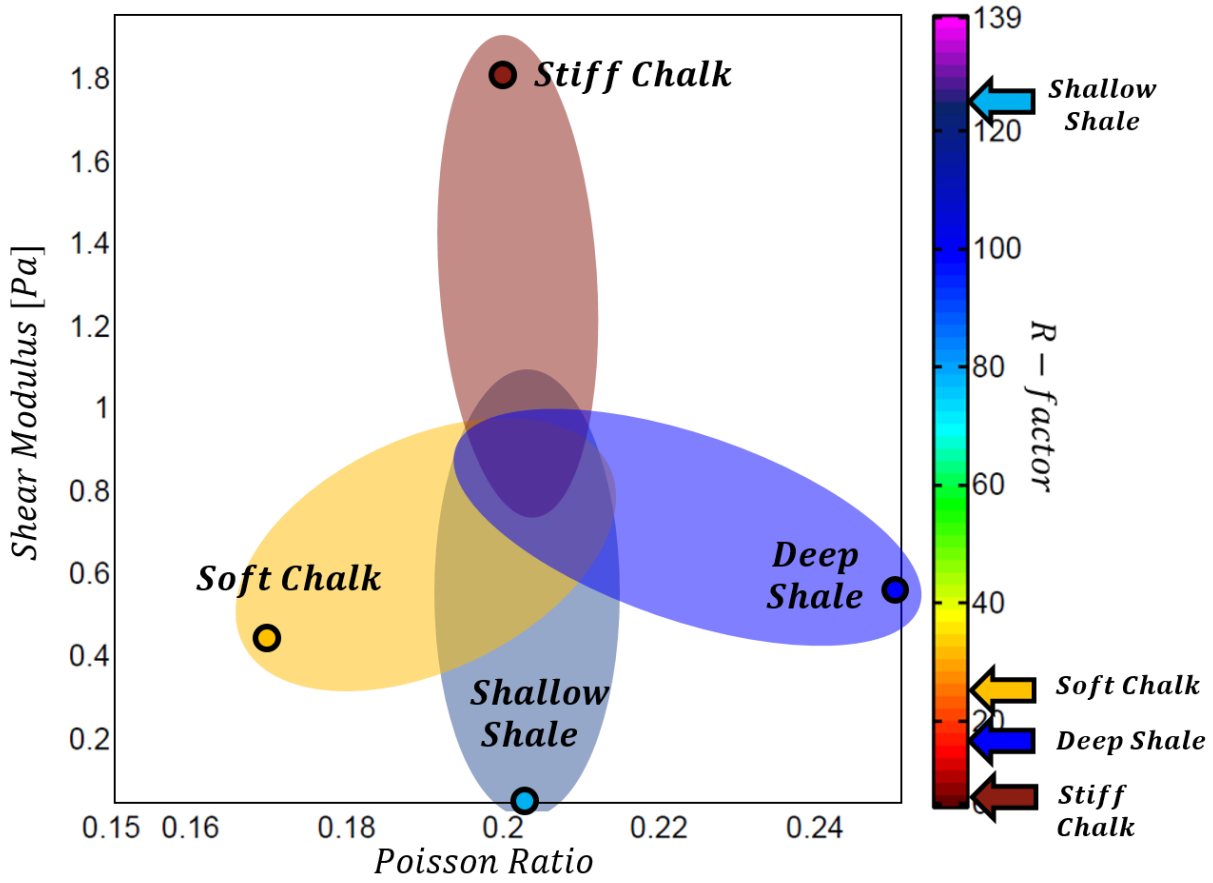

Figure 7.8: End members (stiff chalk, soft chalk, shallow and deep shale) and the distribution of these members in the space of shear modulus and Poisson's ratio.

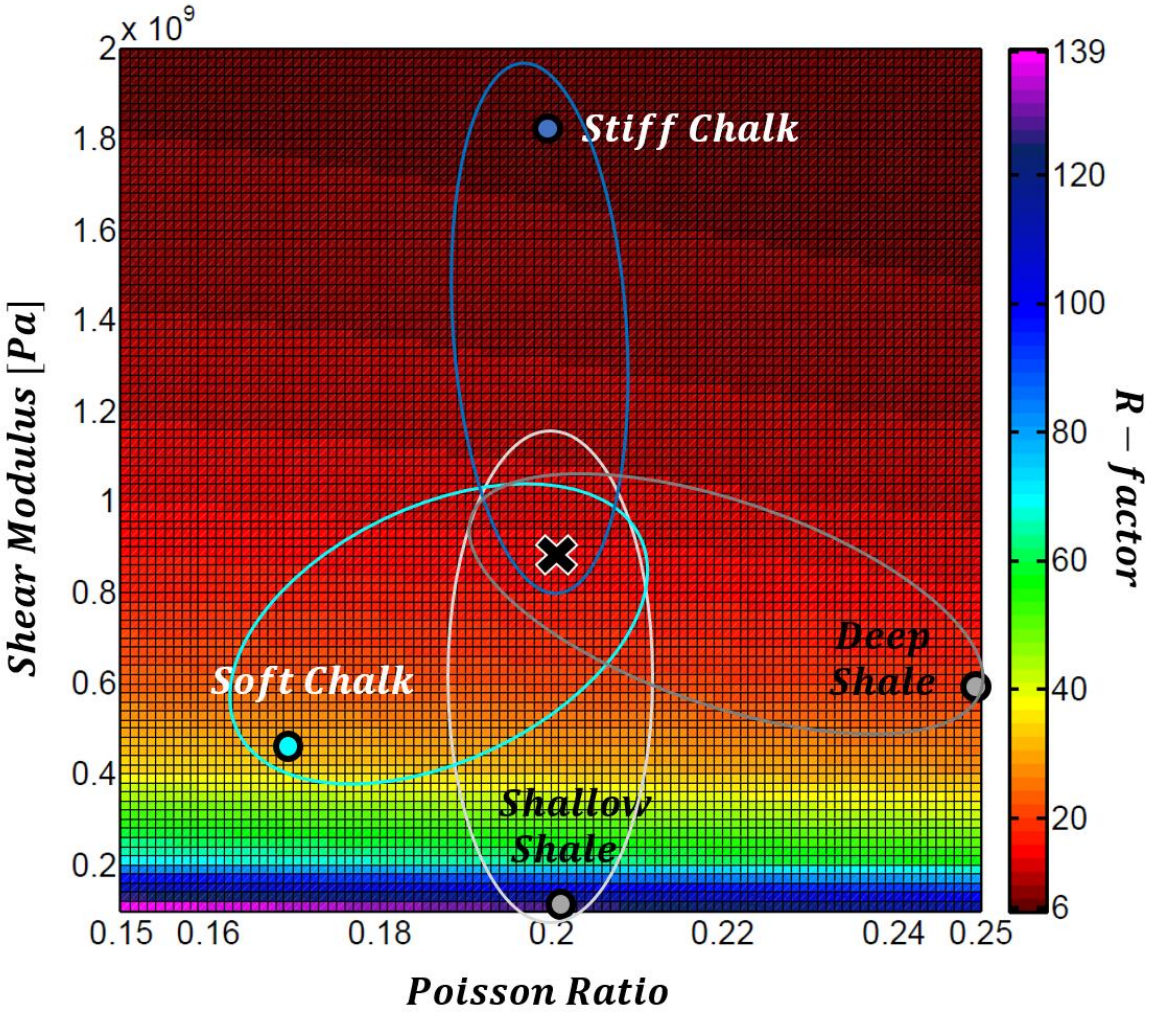

Figure 7.9: The average R is extracted by equal weighting of all four end points; at μ=0.78 and ν=0.2, the average R-factor is 16. All combinations between shear modulus of 0.1 to 2.0 GPa and Poisson's ratio of 0.15 to 0.25 are generated to build statistics on the R-factor.

Having recovered the average R that is representative of the half space medium, the average R-factor is then used to convert the time strain into physical strain:

$$\varepsilon_{zz}\left(\frac{2z}{V}\right) = \frac{V}{2(1+R)}\frac{d\Delta t(z)}{dz} \tag{7.7}$$

The Geertsma inversion is then carried out using the physical strain to invert for changes in pore pressure. The pressure change, inverted without and with a smoothing constraint, is shown in

Figures 7.10(a) and (b). Figure 7.10(b) shows a more realistic estimation of pressure change since pressure change has inherent smoothness characteristics.

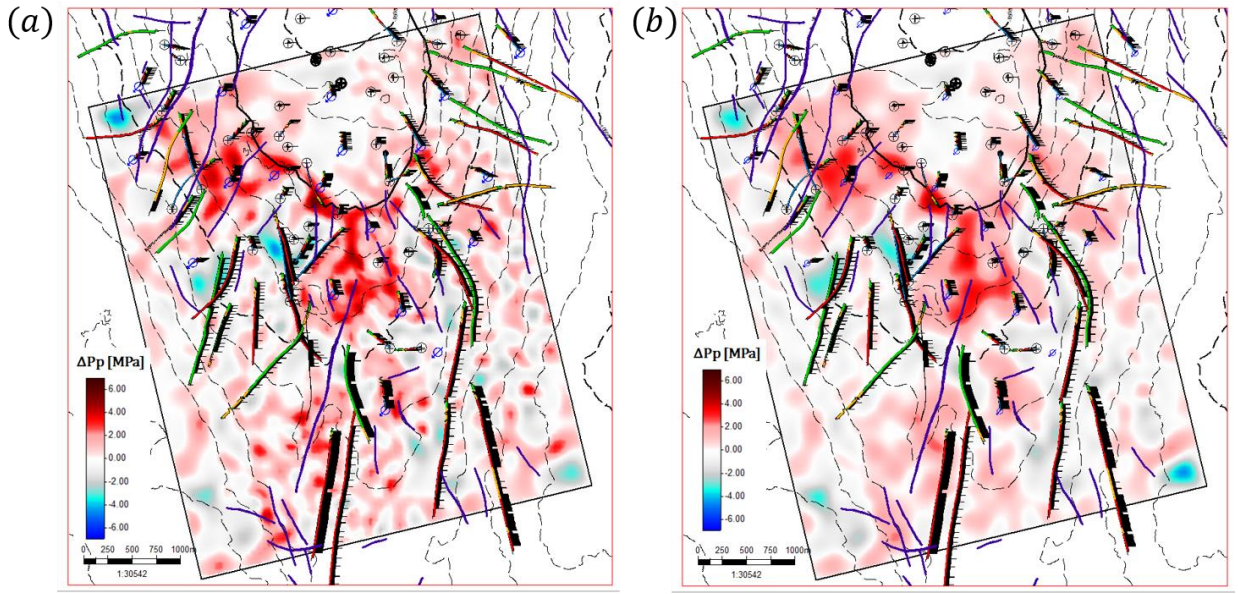

Figure 7.10: (a) Showing inversion result without smoothing constraint and (b) after applying smoothing constraint in the objective function, the latter is more realistic.

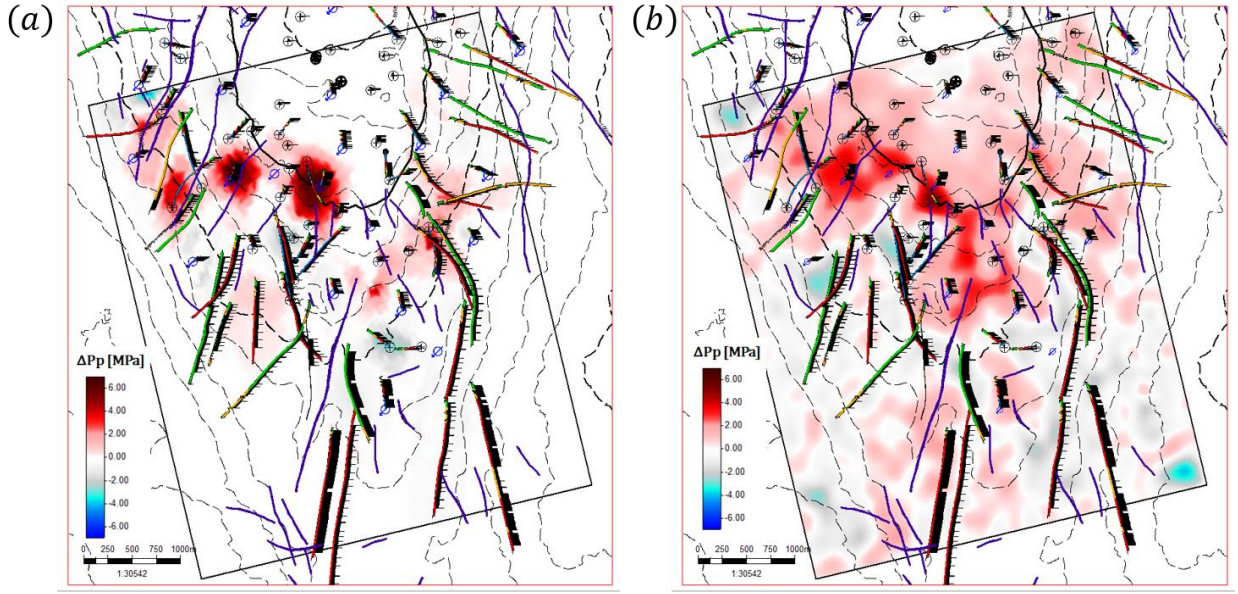

Figure 7.11: (a) Showing prior information extracted from a well history matched simulation model and (b) inversion result after incorporating the prior information.

The prior information from the well history matched simulation model is shown in Figure 7.11(a) and the inverted pressure change incorporating this prior information is reported in Figure 7.11(b). Comparing the result in Figure 7.11(b) to Figure 7.10(b), the former has a stronger pressure difference around wells compared to areas with no 4D seismic changes. As mentioned in the previous section, four horizons were chosen to compute the IOT. These horizons were chosen based on their distance from the reservoir, the need to include as much data as possible, and the signal-to-noise ratio at each. In Figure 7.12, (a) and (b) demonstrate the difference between using a single horizon versus using all the horizons which gives a higher signal-to-noise ratio, and more robust estimates of the pressure change. The inversion results presented in Figure 7.12(b) show good agreement between the polarity of the pressure change anomalies and the location of the producers and injectors. As expected, a large pressure response pattern is inverted for where several injector wells have been put in place.

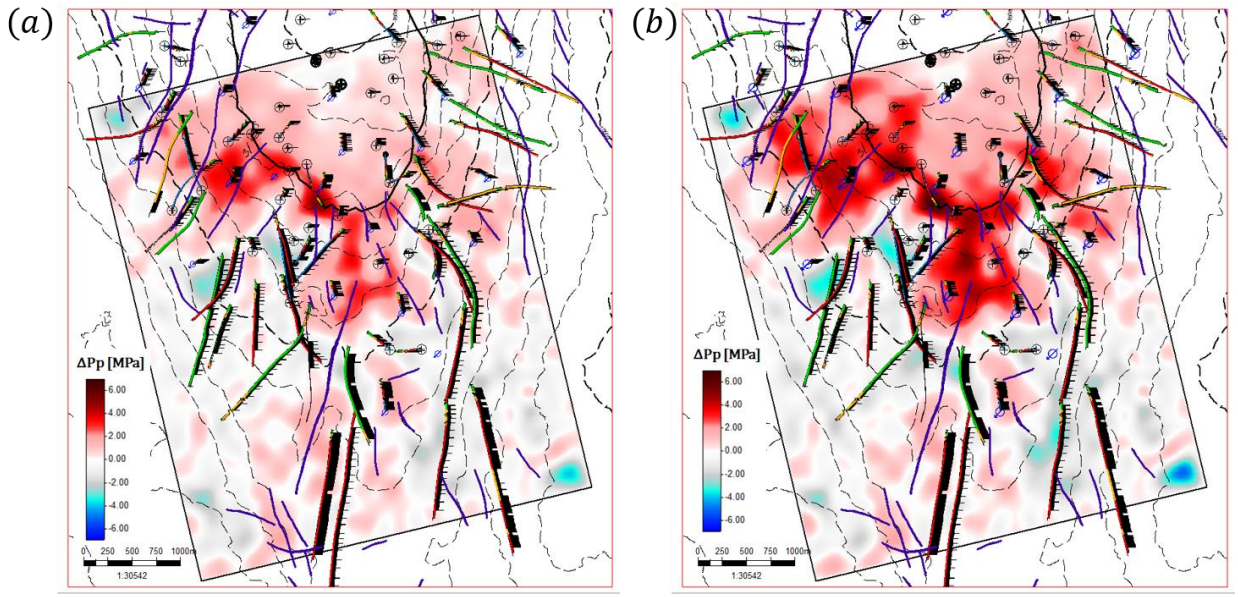

Figure 7.12: (a) Inverted pressure change using a single IOT (Balder) and (b) pressure change inverted using all four IOT maps from the overburden.

7.4 The Asymmetry R-factor and its Implication on Time-shifts

Due to the non-linear behaviour of the grain boundary stiffness with compressive stress, the seismic response to variations in the reservoir pressure is not symmetric: such that the response to

an increase in pore pressure differs from that for depletion. The nonlinear velocity behaviour of rocks as a function of stress is observed in laboratory measurements, and this behaviour is generally attributed to the deformation of micro cracks and pores, grain boundary contacts, and fractures with changing the confining stress (e.g. Rutqvist, 1995, Herwanger and Horne, 2009). At low effective pressures, seismic velocities are dominated by the changes in number density of small cracks or discontinuities between grain boundaries; whilst at higher effective pressures, these cracks close and velocities increase. Another explanation is stress hysteresis, which is also evident in rock properties, as mentioned in Helbig and Rasolofosaon (2000), Hueckel et al. (2001) and Ferronato et al. (2013).

In the work of Hatchell and Bourne (2005), an asymmetric R, as a function of strain polarity, is proposed as a way of interpreting the magnitude of the observed time-shifts with different observed strain deformations. Rocks that are undergoing an extensional strain change (often in overburden rocks) show larger fractional velocity changes in comparison to regions undergoing compressive strain changes (often, but not exclusively, in the reservoir). This behaviour is also similar to that observed in laboratory measurements (Holt et al., 2008, Holt and Stenebråten, 2013). In Holt and Stenebråten (2013), it was reported that the R-factor of a rock that has gone through an initial cycle of depletion followed by re-pressurisation is different compared to the same rock undergoing only injection; suggesting possible excess deformation due to internal defects from the first process. This understanding can be tested in this dataset by selecting two regions with different production/recovery mechanisms, predominantly influenced by either (a) reservoir depletion or pressure relaxation and (b) pressurisation.

A similar procedure was performed, but the inversion was limited to only areas with pressure increase and pressure depletion. R-factors were calculated by independent inversion of each region, using the average mechanical properties from the previous study. In order to ensure minimal overlap between these areas of pressure increase and decrease, the regions were selected around wells. This was also guided by the historic production data of the well, to avoid ambiguity. The results of this process are shown in Figure 7.13, indicating that the R for expansion (R+) is 3 times larger than that for compression (R-) – a similar asymmetry to that quoted in the previous publications (Holt et al., 2008 and Hatchell et al., 2003). Figure 7.13 shows as the R-factors

recovered for different rock types for the entire field, as the dotted black line, whilst the blue and red bold lines represent the compression (R-) and expansion (R+). Figure 7.14 summarised the R-factors calculated using this approach and compared with other methods, it is clear that the major inconsistencies in R-factor values from 4D seismic studies, theoretical modelling, and core analysis are apparent. The average R-factor recovered is 16, which is a reasonable estimate since it is found within the ballpark values from other R-factors estimated using 4D seismic data.

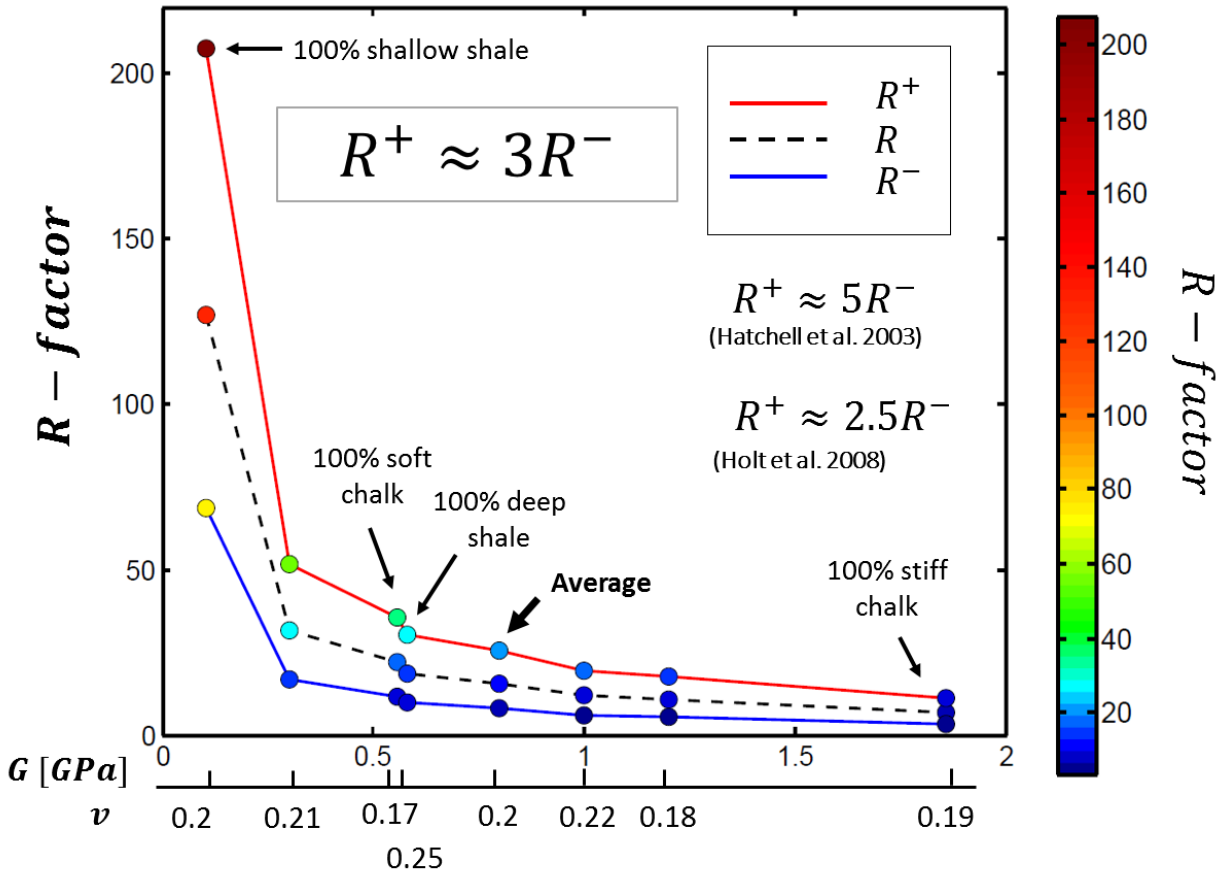

Figure 7.13: R-factor results corresponding to the different lithologies and strain polarities (+ is dilation and – is compressive) in the field study.

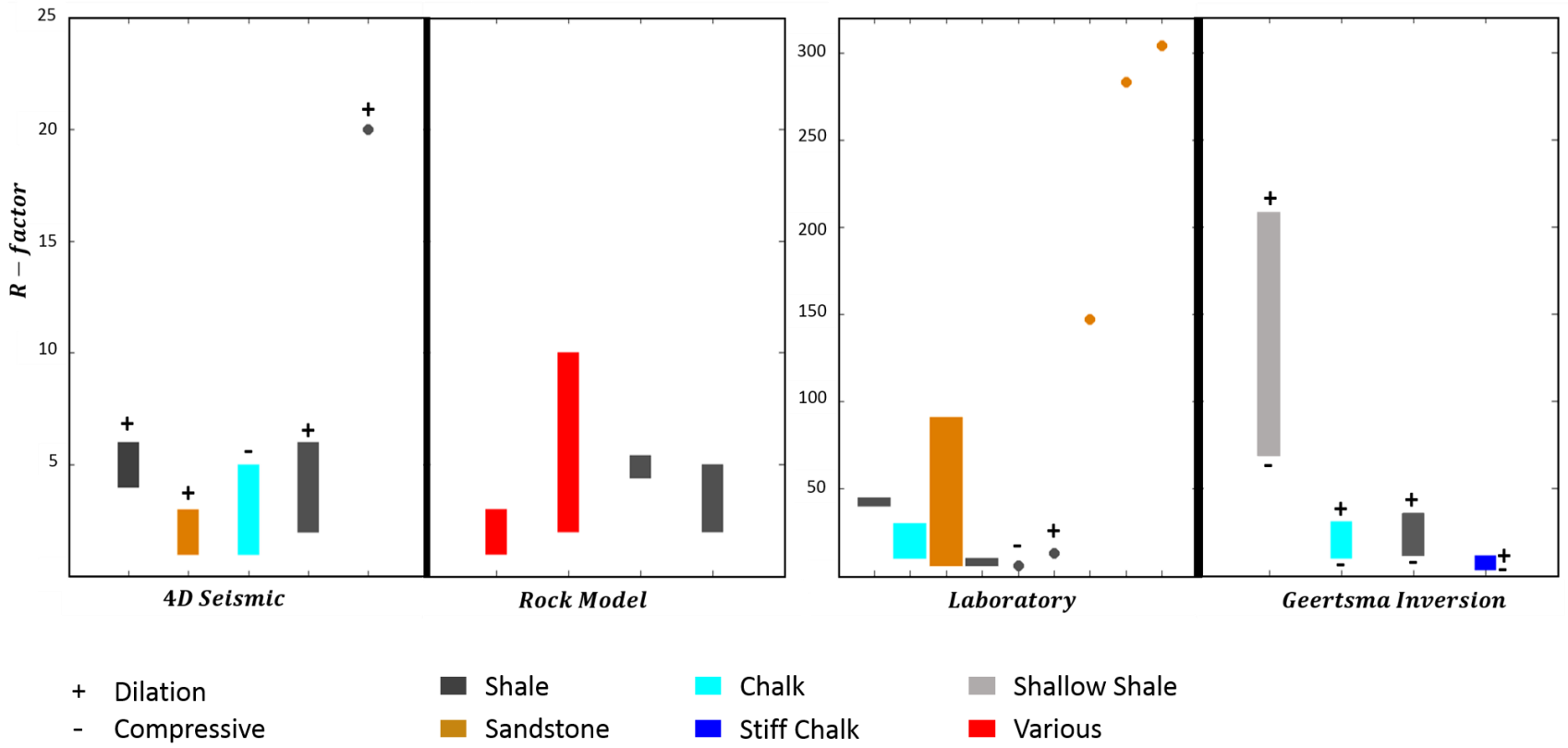

Figure 7.14: A compilation of R-factors from various methods. Refer to Table 6.1 in Chapter 6 for references.

To validate this finding for this particular field, time-shifts modelling was performed using a synthetic fluid flow simulation and a full geomechanical model with similar properties to the field. The flow simulation model consisted of two injectors and one producer with similar production history to the actual wells. For the geomechanics, the reservoir model was fully encased in a shale overburden, sideburden and underburden. Mechanical properties were assigned according to Zhang et al. (2011). This geomechanical model is described in Chapter 6 (Section 6.5.2). The time-shifts were calculated by firstly converting physical strain to time strain and subsequently computing the cumulative time strain; assuming both symmetric and asymmetric R-factors. The symmetric R is a function of lithology. Different R-factor values are applied to the reservoir, and the surrounding rocks. The asymmetric R is not only a function of lithology but also strain polarity, which means the same rock will be assigned different R-factors based on whether it is undergoing compression or dilation.

The R-factors required to populate the model in Figures 7.15 and 7. 16 were taken from the cross-plot in Figure 7.13. In Figure 7.15(b) the model is strictly dependent on lithology; the R-factors required for shale are higher than for chalk. In Figure 7.16(b), the R-factors are not only a function of lithology but also depend on strain change polarity. The overburden shallow shales have the lowest mechanical properties, hence a large R is assigned. The shale layer (Balder) adjacent to the reservoir is stiffer, hence a smaller R is assigned compared to that for the shallower shale. The Balder shale is also divided into compressive and dilating regions, where a larger R is assigned for expansion above the producer and a smaller R for the injector. The chalk in the reservoir is the stiffest material, and it has the smallest R-factor. The chalk undergoing compaction around the producer has a smaller R-factor than the chalk under dilation around the injector. Figure 7.15 gives the results for R+ = R-, and Figure 7.16 for the case of R+ = 3R, determined from previous findings. The asymmetric R-factors produce time-shifts that appear more consistent with the real field observations. A positive time-shifts is generated below the reservoir, implying a strong accumulation of time-shifts in the overburden relative to that in the compacting reservoir. This would not be the case unless the R-factor is asymmetric.

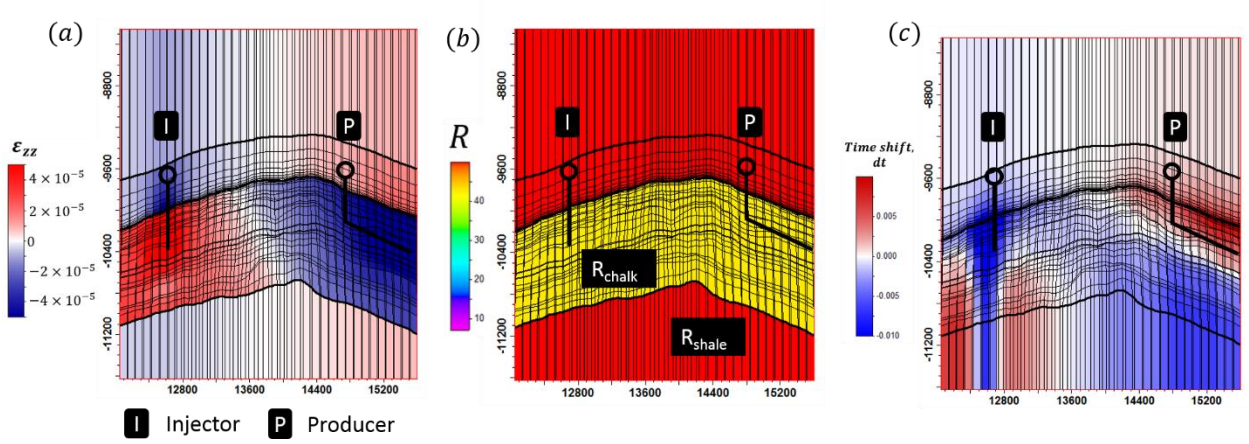

Figure 7.15: (a) Physical strain from geomechanical simulation (b) lithology dependent R and (c) modelled time-shifts.

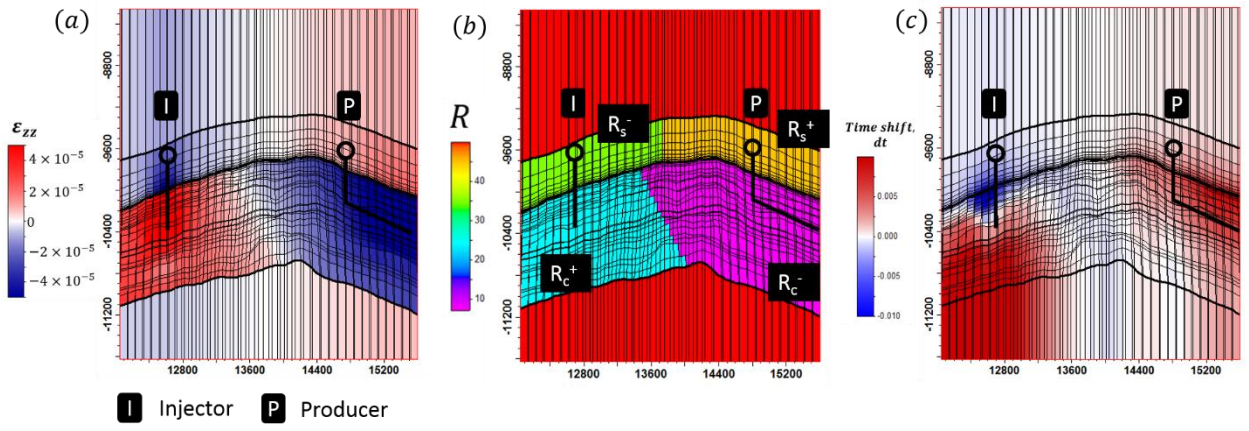

Figure 7.16: (a) Physical strain from geomechanical simulation (b) lithology and strain polarity dependent R and (c) modelled time-shifts.

Restricting the time-shifts analysis to the top of the reservoir in both Figure 7.15(c) and Figure 7.16(c) avoids this complexity. The positive time-shifts at the base reservoir event implies that velocity response to strain in the reservoir is smaller than in the overburden; if not we would expect zero or negative time-shifts at the base of the reservoir; hence, asymmetric R should be taken into account – this is evident by looking at time-shift characteristics below the base of the reservoir in real field examples. Field examples published in Hatchell and Bourne (2005) and Hatchell et al., (2007) reported a North Sea HTHP clastic, a Malaysia carbonate field, a North Sea chalk field

(Valhall) and a Danian chalk field, with the computed and modelled time-shifts are shown in Figure 7.17. All cases demonstrated a positive time-shifts or slow-down at the base of the reservoir to the underburden in the presence of field pressure depletion. The convention of the polarity for time-shifts in Figure 7.17 is counter-intuitive, where the slow-down response is represented in blue whilst speed-up is in red. The observed time-shifts cannot be created unless an asymmetry in the R-factor is present.

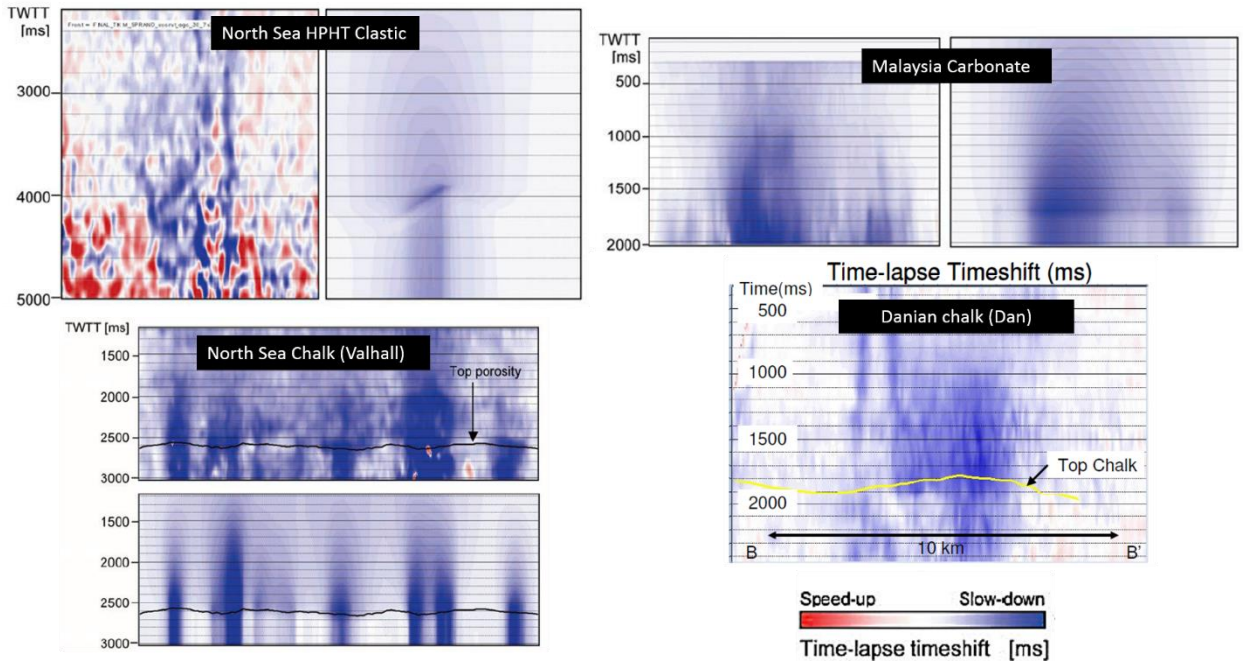

Figure 7.17: Observed time-shifts from various fields. Most depleting fields show a slow-down response in overburden, reservoir and underburden, suggesting the dilation mechanism in the overburden has far greater effect on the velocties than the compression mechanism in the reservoir (Hatchell and Bourne, 2005, Hatchell et al., 2007).

7.5 Time Dependent R-factor

Using a similar procedure to that outlined in Section 7.2.5, R-factors are also recovered for the streamer data for the periods of 1989-1999, 1999-2003, 2003-2006 and 2006-2008. The seismic data acquired in 2003, 2006, and 2008 were co-processed, using a similar processing workflow and cross-equalised (personal comm. Alex Bertrand). The results for the R-factor were calculated

as an equal weighting of all the end member rock types for all streamer data (see Figure 7.18). A trend is observed from 1989 to 2008, showing a decrease in the R-factor as a function of time. This can be explained by two processes: firstly that the pressure maintenance in the reservoir has improved over time, resulting in less strain and fewer velocity changes in the reservoir and overburden, therefore a smaller R-factor has been recovered; secondly, as compaction accumulates with time, the chalk becomes stiffer and less porous, and as a result, the rock becomes less sensitive to velocity changes, and a smaller R-factor has been estimated.

The recovery of the R-factor on the streamer data was carried out assuming that the mechanical properties of both chalk and shale remained constant throughout time. Of course, this is not true, especially in the early period of field production, where large compaction events take place. Therefore, the Poisson's ratio and the shear modulus of the chalk will increase with time, as the rock undergoes compaction. Using available core data provided from the operator, the shear modulus and Poisson's ratio of the chalk were calculated as a function of increasing effective stress. I observed a consistent increase in the shear modulus for the chalk with porosity from 32% to 37%, as shown in Figure 7.19(a). As the effective stress increases, the porosity of the chalk reduces, due to dry compaction. These samples did not undergo any changes in fluid type during laboratory testing. In contrast, Figure 7.19(b) shows the Poisson's ratio behaviour of the chalk from the same porosity group. Overall there is an increasing trend, but there are also conflicting results, showing a reduction in Poisson's ratio. This is due to a faster varying S-wave velocity compared to P-wave velocity during the stressing process. Most laboratory derived Poisson's ratios are subject to error, as core plugs undergoing de-stressing and re-stressing procedures results in hysteresis, suggesting that some grain bounds are broken by coring and subsequent testing.

In my work, I assume Poisson's ratio of the chalk increases with an increase in effective stress, as proposed by Zhang et al. (2011) in Valhall. If this is the case, it is assumed that the Poisson's ratio and the Shear modulus should have been lower during the streamer period than in the LoFS period. The supposedly lower R-factor is annotated as black arrows in Figure 7.18. The effective stress was lower in the beginning, therefore the R-factor will yield larger values than those, represented as a black cross in Figure 7.18. Since no pre-production seismic or cores are available, the initial

stress state is not known in this reservoir. Thus, it is not possible to extrapolate to the initial Poisson's ratio and shear modulus of the rock at pre-production time.

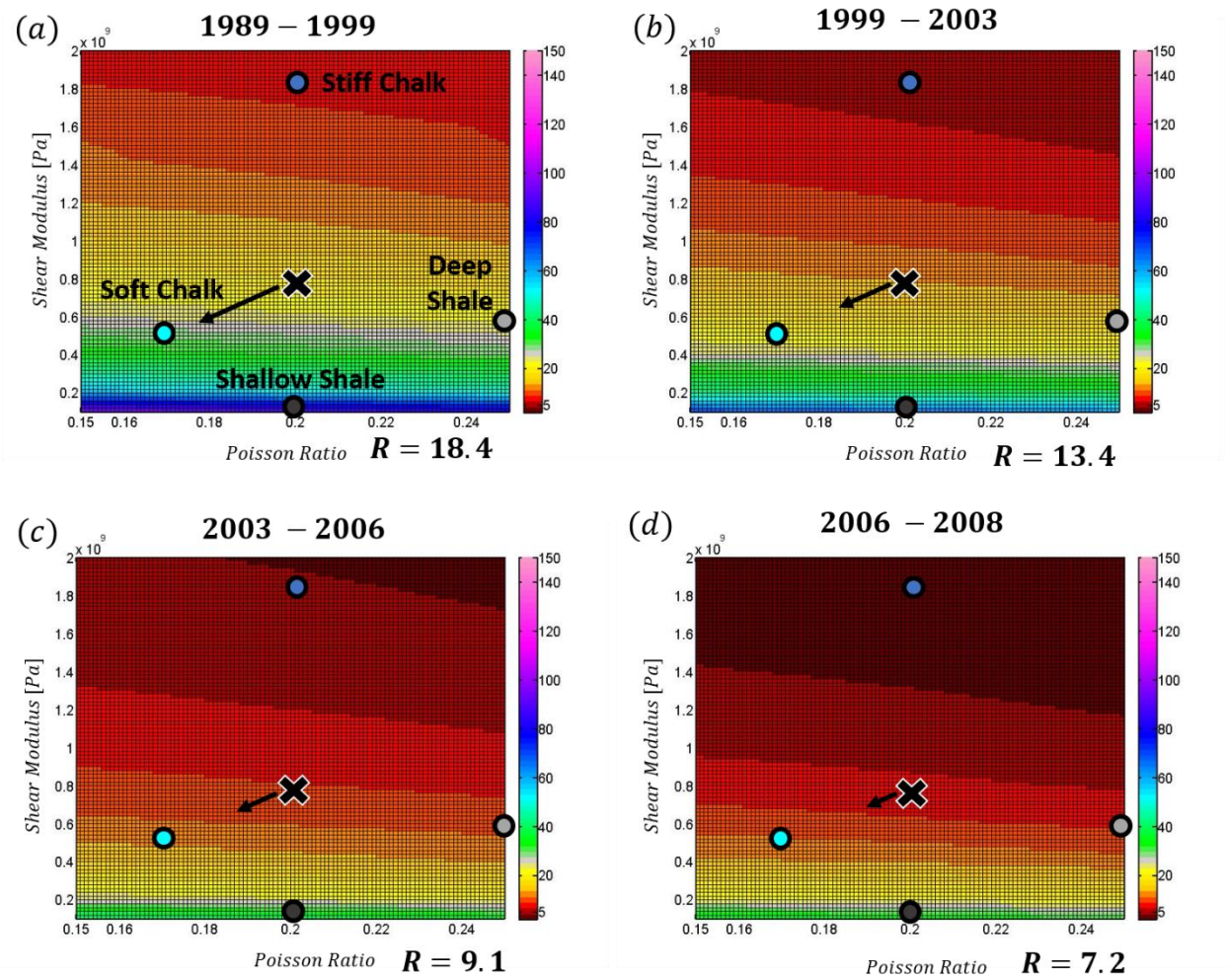

Figure 7.18: R-factors recovered for different vintages of the streamer data from (a) 1989 – 1999, (b) 1999 – 2003, (c) 2003 – 2006, and (d) 2006 – 2008.

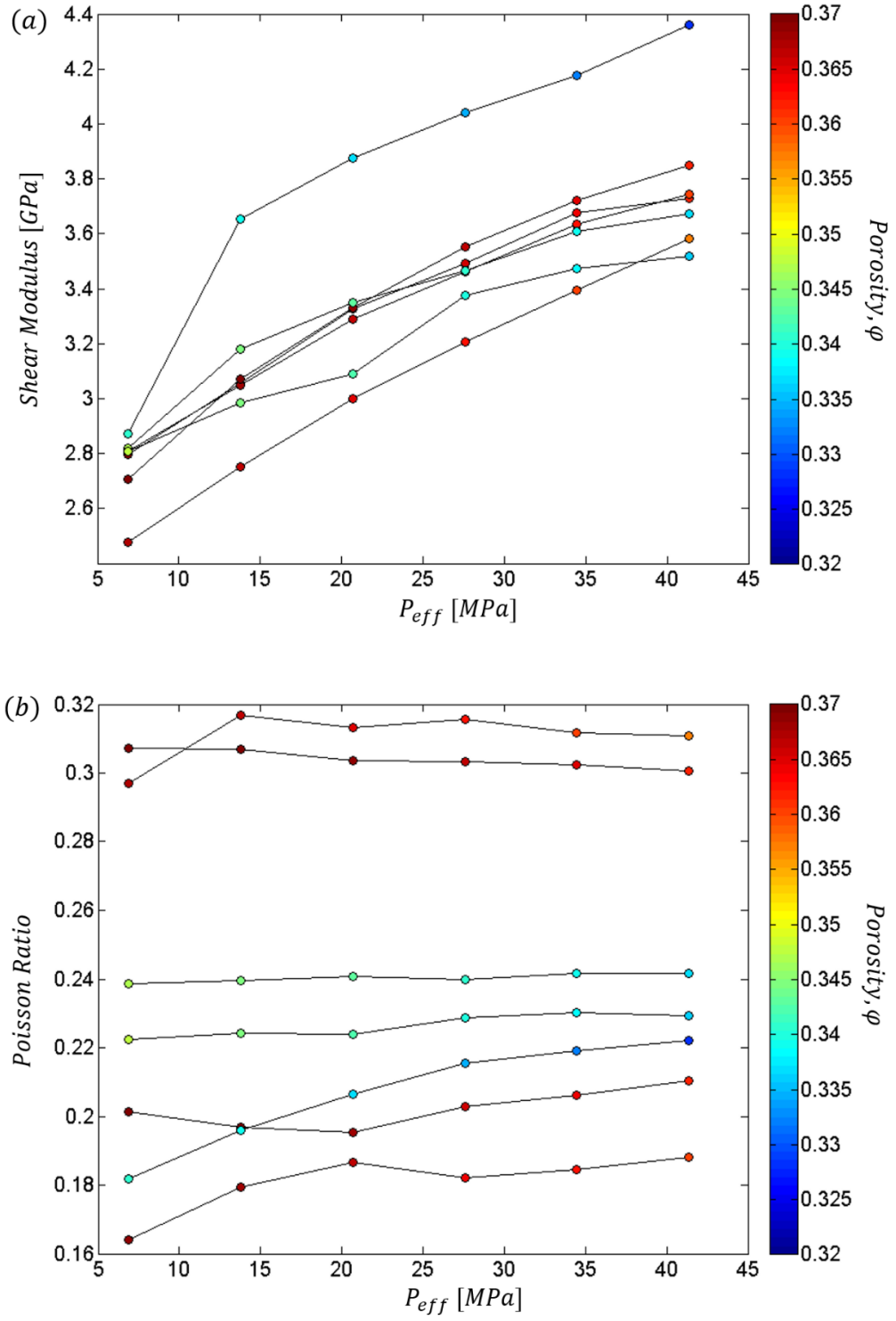

Figure 7.19: (a) Shear Modulus behaviour of Ekofisk chalk within 32% to 37% porosity as a function of increasing effective stress and (b) showing the corresponding behaviour of Poisson's ratio. These values are derived from laboratory measurements.

7.6 Discussion

The Ekofisk field was a challenging field in which to test this inversion scheme. This is due to the complex relationship between pressure and strain, porosity reduction, and chemical weakening of the rock. However, the results of the Ekofisk inversion are promising. There are similarities compared to the pressure change inverted in Chapter 5 and the magnitude of the results is also in agreement. Below I discuss several reasons for the limitations to this method.

Results for pressure depletion could be inaccurate

The relationship between pressure and strain is assumed to be linear in this inversion scheme. This could be assumed in the LoFS surveys due to the small changes in pressure and strain, but this assumption will breakdown for the streamer surveys where large variation of pressure has been recorded. Although suitable constitutive models exist to capture the non-linear relationship between pressure and strain, the parameterisation of such models is highly uncertain, due to limited measurements. The inversion result is reliable in pressure build-up regions, but uncertainties remain for the inverted pressure depletion due to the water weakening phenomenon. This is because, with the same amount of pressure decrease, with and without the intrusion of water, the strain at the reservoir will be vastly different, resulting in non-uniqueness in the inversion results in areas of pressure drawdown. The relationship between pressure and strain in this scheme does not include the water weakening dependence on changes in water saturation. For example, the pressure decrease inverted from the Geertsma's procedure might have been overestimated if water weakening is present, and this is not accounted for in the inversion procedure. This creates uncertainties in the pressure depletion zones from the inversion. This uncertainty can be minimized by cross-checking with the location of injector wells and predictions from the simulation model to deduce areas with possible water saturation changes. It is suggested that interpretations using pressure changes in those regions should be treated with caution.

Faults and changes in stress regime

The Ekofisk field is a highly faulted reservoir, with some faults extending to the overburden. The presence of faults is not considered in the model or inversion. Stress effects on faults will affect

the distribution of stress and strain in both reservoir and overburden. Discontinuity modelling involves introducing existing fault and discrete fracture network models into the geomechanical model, which is not accounted for in the current inversion scheme. Parameterising constitutive mechanical models for discontinuity objects is highly uncertain. These problems are also faced by geomechanicists conducting finite element (FE) or finite difference (FD) modelling to forward predict deformation and stresses in both reservoir and the surrounding medium. At present, I can only speculate that some of the disagreement between the inverted results and reality results from transference of stress to the overburden, due to faults.

Accuracy of time strain from NLI method

As mentioned in Chapter 3, there is a tradeoff between the accuracy of the time strain in the reservoir and resolution of the time strain result in the overburden, based on the weighting coefficient. Since this technique is applied to actual data, it is not possible to truly evaluate the optimum weighting coefficient to satisfy both a good resolution in the reservoir and an accurate time strain in the overburden. This creates uncertainties in the time strain result in the overburden, which is used as an input into the inversion scheme to produce pressure changes. However, by integrating the time strain over a specific interval in the overburden, as demonstrated in Equation (7.4), this could reduce the errors and reduce small jitters in the overburden time strains calculated from the Rickett et al. (2007) Non-Linear Inversion method.

7.7 Summary

The technique applied in the Ekofisk field not only inverts for pressure changes but also estimates the field dependent Hatchell-Bourne-Røste R-factors. This is achieved by constraining the inversion result by pressure change estimates from a well history matched simulation model. This method was carried out multiple times in order to build statistics regarding the R values, given the mechanical properties of the rocks in reservoir and overburden. The average R-factor recovered in the Ekofisk field was 16. R-factors were also calculated for regions of pressure build-up and drawdown/relaxation identified in the field, and the results confirm the current understanding determined by laboratory experiments and previous studies that the magnitude varies as a function of strain polarity, with the asymmetry being at most a factor of three. These results were validated with synthetic modelling of strain and time-shifts, showing that the observed time-shifts cannot be created unless this asymmetry is present. Comparisons with time-shifts from other fields show that a positive time-shifts or slow-down at the base of the reservoir to the underburden is often found in the presence of field pressure depletion, and the same response can only be replicated if an asymmetric R is accounted for in forward modelling.

I also extended the inversion to streamer data, where one would expect a larger R-factor during pre-production time, since the effective stress is lower. This is assuming the relationship between pressure and strain is still linear in streamer surveys, which is not likely to be true. There are many constitutive models that can describe non-linear deformation; however, parameterizations of these models remain sparsely constrained. Several reasons have been provided in the discussion to highlight drawbacks and uncertainties in the inversion results.

CHAPTER

EIGHT

CONCLUSIONS AND RECOMMENDATIONS

FOR FUTURE RESEARCH

8.1 Conclusions

The motivation of this research is to use numerical modelling and field data (time-lapse seismic data and production data) calibration to estimate dynamic changes of pressure and saturation in a compacting chalk reservoir. The data-driven methods implemented in this thesis and a summary of the different subjects of this research are presented in this chapter. The technical findings can be categorized into information from the reservoir and overburden:

Reservoir: As presented in Chapter 4 and 5, the inversion and analysis employed reservoir time-lapse seismic signals such as the percentage change in elastic properties and time strain to infer pressure and saturation changes. The inversion workflow not only combined elastic properties and time strain information but also constrained the results using engineering concepts and production data. Instead of performing cross-domain comparisons which are widely performed in qualitative model-based 4D seismic interpretation, I compared the inverted changes in pressure and saturation directly with those predicted from the simulation model. This provides the opportunity to perform detailed quantitative assessments; such comparison can also be fed into the seismic history matching workflows, which allows repetitive assessment and update of the simulation model based on 4D seismic data in a semi-automated manner. The inversion carried out on the Ekofisk field also provided insights into well performance and pressure distribution.

Overburden: Chapter 6 and 7 focused on the approach from Hodgson et al. (2007) and Hodgson (2009), which uses a simple geomechanical model: Geerstma's nucleus of strain to relate pressure change to overburden deformation. The departure from this method involves calibrating the inversion result with reliable pressure change information from the engineering domain to estimate an average R-factor for the assumed homogeneous, elastic half space. This is an innovation from the existing method since the R-factor recovered is field dependent, and is more accuracy than an R factor guess for a particular field

The proxy model formulated in Chapter 4 bypassed the rock physics model which requires extensive calibration and exhaustive modeling of various data to describe the rock and fluid properties. It was derived analytically through modelling and reverse engineering of synthetic data. The proxy model has three separate terms: a pressure term, a saturation term and a cross term

between pressure and saturation that describes the water weakening behaviour of the compacting chalk. The strength of the proxy model leads to an accelerated estimation of the percentage change in elastic properties. Most importantly, it is amenable to inversion.

The pressure-saturation decomposition method using the proxy model presented in Chapter 5 employs a stochastic approach via Bayesian McMC. This is because uncertainty of such predictions is usually high; henceforth the solution of such an inverse problem is not limited to a single set of predicted parameters but represented by a probability density function in model space. The application in Chapter 5 demonstrated that the Bayesian framework provides a suitable platform to incorporate data uncertainties and prior information. The stochastic results were compared with those derived from a deterministic approach using least-square optimization. The changes of dynamic properties from both deterministic and Bayesian inversion methods are in agreement, and both results show discrepancies compared to the predictions from the history matched fluid flow simulation model. Areas of discrepancy between the inverted (deterministic and stochastic) and predicted dynamic properties (from simulation model) provides an opportunity to update the static properties of the reservoir model. Quantitative interpretation of this field using the inversion results have good agreement with well production data, and help explain strong localized anomalies in both the Ekofisk and Tor formations.

In Chapter 6 and 7, I draw on the work from Hodgson et al. (2007), Hodgson (2009), and Hatchell and Bourne (2005) to invert for not only reservoir pore pressure change but also the average R-factor between reservoir and overburden. This approach also demonstrated a new way of defining the uncertainty on the R-values, by defining the range of mechanical properties and the region of different production mechanisms. The R-factors calculated for regions of pressure build up and drawdown/relaxation identified in the field, confirm the current hypothesis (supported in the literature by laboratory experiment and previous studies) that the magnitude varies as a function of strain polarity and lithology. My calculation of R-factors in different pressure regimes shows the R-factors in areas of extension are three times larger than R-factors in compression. Unlike full geomechanical simulation, the new formulation in Chapter 6 and 7 provides an opportunity to close the loop between the measured time-shifts and pressure changes in a quick modelling and inversion study. Of course, there are limitations with this method, such as not allowing mechanical

stratigraphy, which limits its application to a reservoir with a complex overburden and reservoir geometry. Suggestions on further research are provided in Section 8.3.

8.2 Novel Contributions

This thesis contributes several novel ideas to the estimation of pressure and saturation change in geomechanically active chalk reservoirs. In particular, the integration of engineering data to expedite the inversion process. This includes the incorporation of prior data into the inversion problem using constraints such as the water leg, predictions from the history matched simulation model, and linearization of the compaction curves into the forward modelling equation.

8.2.1 EC (Engineering-consistent) constraints

In the inversion scheme introduced in Chapter 4, and subsequently applied in the Ekofisk field in Chapter 5, the prior information are incorporated into the inversion problem through EC constraints. The source of prior information is given from the history matched simulation model and through reservoir engineering concepts. The first EC constraint imposed is in the water leg. It is assumed that no changes in saturation are possible in the water leg, and only a pressure signal could occur in the water leg. An inequality constraint (above water-leg, $-0.10 \leq Sw \leq 0.5$) was applied, with the upper and lower boundaries extracted from simulation model statistics. For the second EC constraint, the solution space close to well perforations was constrained using a 3D Gaussian window; imposing tight upper and lower bounds for changes in pressure and saturation as estimated from the reservoir simulation. These constraints are realistic given that the model is relatively well history matched. The impact of these constraints in expediting the solution is demonstrated in Section 5.8.

8.2.2 Linearization of compaction curves

Another use of the engineering data is the compaction curves derived from laboratory data, subsequently calibrated with well data, radioactive marker bullets and repeated logging measurements (Sylte et al., 1999, Janssen, Smith and Byerley, 2006). The derived proxy model is based on the basic form of the rock physics trends expected from the reservoir. Generally, changes in water saturation and in some instances pressure (if small changes from initial pressure is expect) can be linearly related to the relative change in impedance. However compaction behaviour such as water weakening shows a clear departure from linearity. Henceforth a cross term between pressure and saturation change is required to capture this geomechanical effect. The novel idea is the incorporation of the compaction curves into the proxy model equation. Two separate functions, F_P and F_{WW} were created from the compaction curves for dry compaction and water weakening. Figure 8.1 shows how F_P and F_{WW} captures the behaviour of the chalk under separate conditions of dry compaction and water weakening. A higher initial porosity will have a higher compaction gradient for both dry compaction and water weakening, as illustrated in Figure 8.1.The advantage of this integration is to allow the compaction component to be part of the analytical equation, instead of relying on numerical calculation from the simulation model.

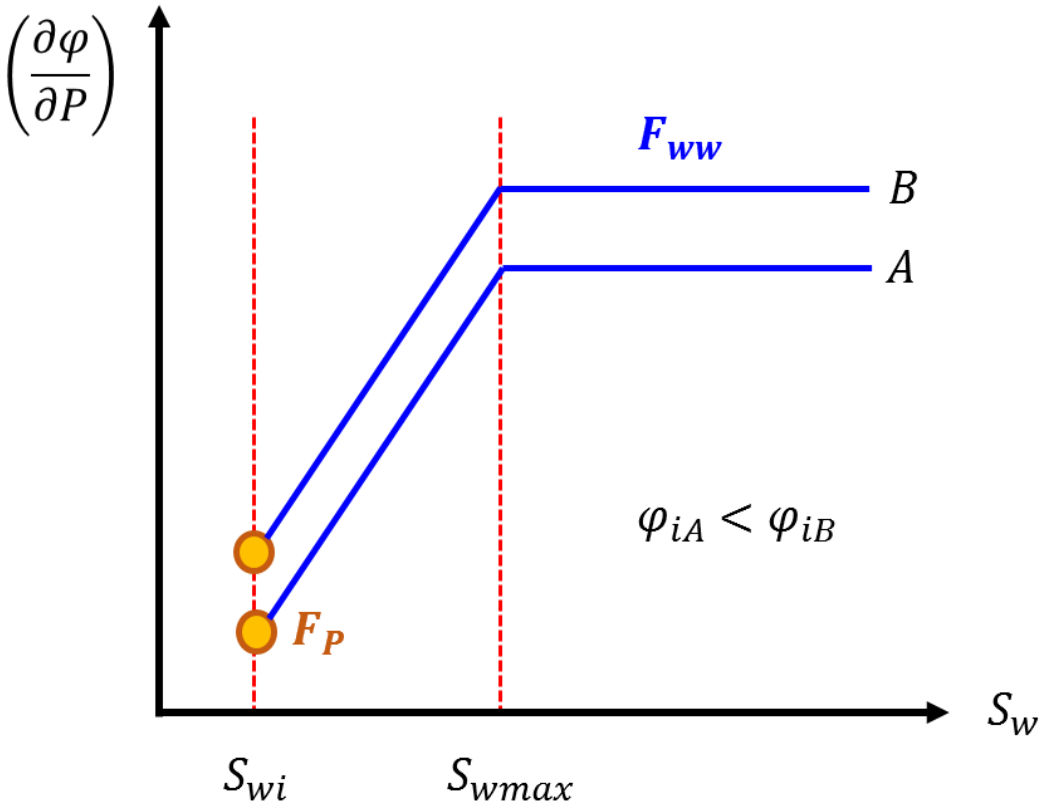

Figure 8.1: The compaction functions are showed as a function of water saturation and compaction gradient. The compaction gradient of these functions increase with an increase in initial porosity.

8.2.3 R-factor recovery by scaling with engineering constraint - Material balance

The single parameter R-factor reported in Hatchell and Bourne (2005) varies by only a narrow range for a wide variety of lithologies and basins around the world. These characteristics make the R-factor popular and widely used in the industry. However, this is not always supported in experimental measurements (for example Bathija et al., 2009, Janssen et al., 2006). My work of estimating the R-factor from Geertsma's pressure inversion also shows the R-factor has a much wider range of magnitude for different lithologies. The extension R-factors recovered for individual lithologies of different mechanical properties vary from 11.6 to 207.5; and a narrower range is recovered for the compressive R-factors: 3.4 to 68.8. This scatter for individual lithologies can be explained by the varying burial history and heterogeneity. The novelty of this approach is that the inversion result from Geerstma's relations was constrained using pressure change

information from the simulation model, and the R that matches the estimates to the simulator predictions is calculated. The simulator honours material balance in the reservoir and is adequately matched to the historical well data via history matching. It is assumed that the resultant pressure predictions from the simulator are at least statistically accurate, and should possess more accuracy than an R-factor guess for a particular field. This not only provides us a method to estimate R-factor values for an average mechanical property of the subsurface but also for a range of different lithologies. It is shown in Chapter 7 that different lithologies have a range of sensitivity to stresses and strains, reflected in the R-factor ranges.

Hard data such as bottom-hole pressure, downhole deformation measurements, time-lapse production logging tool, seafloor subsidence and tilt measurements can also be integrated into the objective function of the inversion, as additional constraints, in order to estimate a better pressure change solution. As opposed to R-factors that are derived from time-shifts to strain predictions predicted from an often poorly calibrated geomechanical model, the new method has the added advantage of using various available hard data to calibrate the output of the simulation model and, in turn, lend more confidence to the pressure information and the R-factor estimated from it. However, it is not explicitly proven in this thesis that the R-factors estimated using the newly derived method are more accurate than the conventional R-factors from matching geomechanical simulated predictions. Despite its minimal constraints and computationally fast and straightforward implementation, this method is, however, limited to reservoirs with homogeneous overburden and with the availability of a well history matched simulation model, calibrated with pressure information from wells.

8.3 Suggestions for Further Research

The methodology presented in this thesis were tested on both synthetic and real field data. However, further research and investigation are required to better define the cases where the assumptions for these methods are no longer adequate; and to refine the workflow of these methods. This further research could be addressed under the following categories:

8.3.1 A complete Seis2sim workflow for compacting reservoirs

The 4D seismic inversion research is a class of its own, as some of the existing 4D global or simultaneous inversion schemes include El Ouair and Stronen, 2006, Haaland et al., 2008, Lafet et al., 2009 and Tian, 2014 invert for multiple offsets and vintages simultaneously. Most of these methods invert for absolute and/or the difference in elastic parameters; and subsequently a rock physics transform is required to translate these parameters into reservoir dynamic properties. If we were to implement these inversion schemes on a compacting reservoir, it will be further complicated by the geomechanical component inside the reservoir and the reservoir response to the deformation in the overburden, which creates further non-uniqueness in the inversion problem. The pressure-saturation inversion workflow presented in Chapter 4 and 5 only focused on the reservoir. The inversion requires interval parameters such as relative change in elastic properties and time strain as inputs in the proxy model. The challenge here is to directly use time-lapse pre-stack or post-stack seismic data to invert for dynamic properties of the reservoir for a thick, multi-cycle, geomechanically active reservoir instead of the hierarchical approach that I have adopted. A complete Seis2sim workflow for this type of the reservoir needs to take full numerical geomechanical modelling into account in the forward modelling process for completeness, and be solved iteratively in a model-based inversion process. In a compacting reservoir, it is necessary to couple traditional reservoir simulation with a geomechanical simulation. The Sim2seis workflow for compacting reservoir estimates deformation and time-lapse seismic changes not only in the reservoir but also in the overburden (Herwanger and Horne, 2009), shown in Figure 8.2. However, calibration and parameterisation of the geomechanical model has always been challenging due to limited data and expensive computational time. Also, in a model-based inversion workflow the forward modelling should be quick to compute, because at every update of the reservoir strain, a new geomechanical model has to be run and from this the pressure change is inverted. The current run time of a geomechanical simulation is still not sufficiently quick to be considered for inversion. In addition, it has to be investigated whether a combined inversion of time-shifts and amplitude changes improves the pressure and saturation change estimation. Apparent lateral shifts induced by overburden deformation and velocity change (Cox and Hatchell, 2008), might be an additional constraint when interpreting the reservoir changes.

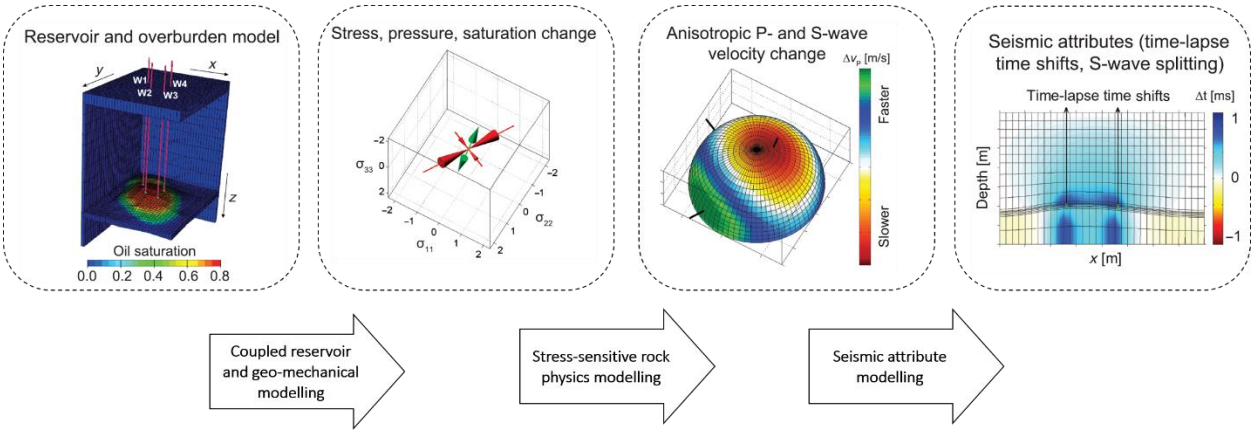

Figure 8.2: Workflow proposed by Herwanger and Horne (2009) to predict anisotropic seismic velocity changes and time-lapse seismic attributes.

8.3.2 Data and modelling uncertainties

The proxy model requires a set of calibrated coefficients (a, b,and c) from the petro-elastic model, changes in pressure (ΔP) and saturation (ΔS_w), and compaction curves expressed as functions (F_{ww} and F_p) of initial porosity (φ_i). However, uncertainties in the petro-elastic model (i.e. stress sensitivity parameters, mineral moduli, mixing law), and the petrophysical parameters (i.e. porosity) will impact the 4D pressure-saturation inversion result. This was addressed in Veire et al. (2006), Chu and Gist (2010), Trani et al. (2011) and Shahraeeni (2012). It was reported that an accurate petrophysical forward function is required for pressure-saturation change inversion; any error in the petrophysical forward function can result in large uncertainties in the estimated parameters. I suggest we should first understand how big these uncertainties are, and secondly investigate the propagation of these uncertainties into the inversion results. In addition to noise in the data, data uncertainties here also refer to input data such as the initial porosity estimated in the simulation model, either through kriging or cokriging between well-derived porosity logs, post-stack seismic inversion and other geostatistical techniques. One method of capturing the uncertainty of the initial porosity is to use the mean and standard deviation of the initial porosity extracted from multiple history matched models. The modelling uncertainties are represented by different rock physics models, and the discrepancy between using a full simulator to impedance workflow versus a proxy model. All these uncertainties could be characterised under a Bayesian scheme.

8.3.3 Correlated noise and uncertainties

The inversion scheme implemented in Chapter 5 assumes the noise and the data (seismic inverted parameters) are uncorrelated in space and have a normal distribution with a standard deviation of σ. This is because the inversion was carried out on a point-wise manner to reduce computational time, and the uncertainties of the seismic inverted data was not provided by the seismic inversion practitioner for this particular data set. The noise is taken as uncorrelated Gaussian noise with different standard deviations for each seismic inverted parameter. In reality, the errors in the seismic inverted parameters and the data itself are likely to be correlated, the objective function would then require application of the full data error covariance matrix, C_w.

$$f = (d_{obs} - d_{mod})^T C_w^{-1} (d_{obs} - d_{mod}) \tag{8.1}$$

The inverted seismic parameters are correlated because the inversion procedure that estimated these parameters has a high degree of coupling in the forward modelling. Both correlated and uncorrelated noise (such as ambient noise) exist in seismic data. Some larger correlation noise due to multiples, ground roll and other physical phenomenon can be filtered out in processing workflows, but most uncorrelated, random noise will persist in the data. It is however difficult to estimate the correlated noise in the data; we can estimate C_w by assuming a functional form of C_w and allow the parameters that define this function to vary, such that certain point is going to be influenced by points that are very close to it. Accounting for correlated noise in the data and propagating this error into the objective function will yield more realistic estimates of the model parameters and not under-estimate our uncertainties.

8.3.4 Limitations of the simple geomechanical model / Improvement to Geertsma's solution

The geomechanical model adopted in Chapter 6 and 7 is the simple, semi-analytical Geertsma's relation (1966, 1973), which assumes linearity between pressure and strain in a homogeneous, poroelastic half space. These assumptions are not valid for a wider application such as in heavily faulted reservoirs and reservoirs with complex overburden. The calculation of the Green's function

for a fully heterogeneous medium would require computation using a numerical method such as finite elements. More work is required to better define the cases where the assumption of a homogeneous medium is no longer sufficient.

The analytical model by Rudnicki (1999) uses the Eshelby (1957) solution to calculate the stress and strain changes inside an ellipsoidal inhomogeneity, due to imposed far-field changes such as pressure within the inhomogeneity. The material of the inhomogeneity is, however, assumed to be a linear, isotropic poro-thermo-elastic solid, such as in the case of Geertsma's model, which is very much idealised. However, this inhomogeneity can be a more representative model for a reservoir, aquifer or even a fault zone compared to Geertsma's homogeneous half space. The inclusion of Rudnicki's (1999) model is in an infinite medium, therefore we are restricted to reservoirs whose depth is much greater than their width, so that the effect of the free surface is negligible. His work shows an ellipsoidal inclusion or inclusions in an infinite elastic body; by manipulating the size and shape of the inclusion, the stress and strain in the inclusion changes, but only the deformation of the inclusion (i.e. reservoir) can be calculated. The conceptual model by Eshelby (1957) is shown in Figure 8.3. This method is useful to study how the reservoir geometry and the contrast between the reservoir and the surroundings affect the reservoir strain, but does not allow the investigation of how material contrasts, mechanical stratigraphy and geometrical effects affect the overburden deformation.

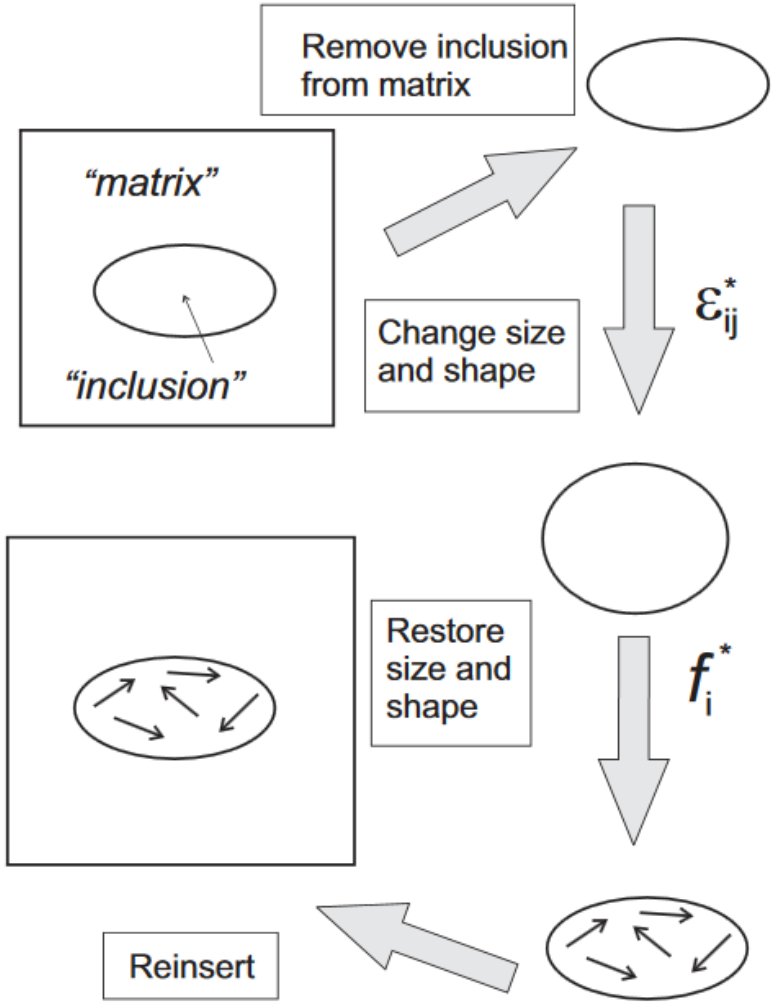

Figure 8.3: A sequence of cutting and welding operations used by Eshelby (1957) to determine the elastic field of an inclusion.

The work from Tempone et al., 2010 extends Geertsma's solution for a rigid layer in the basement. The rigid basement could be represented by crystalline basement rocks underlying a sedimentary basin or a stiff carbonate sequence under the reservoir interval. According to Tempone et al. (2010), modelling of the rigid layer in the underburden causes an increase in subsidence and vertical displacement above the reservoir, since the the rigid basement will act as force keeping all movements downwards, shown in Figure 8.4 . The rigid basement causes a decrease in time-shifts under the reservoir. This hypothesis could be one of the potential explanations for the over or

underestimation of time-shifts in some case studies. This work could potentially be extended to capture heterogeneity or to aid interpretation in the overburden such as in the Shearwater field, where stiffer chalk materials were found above the reservoir interval.

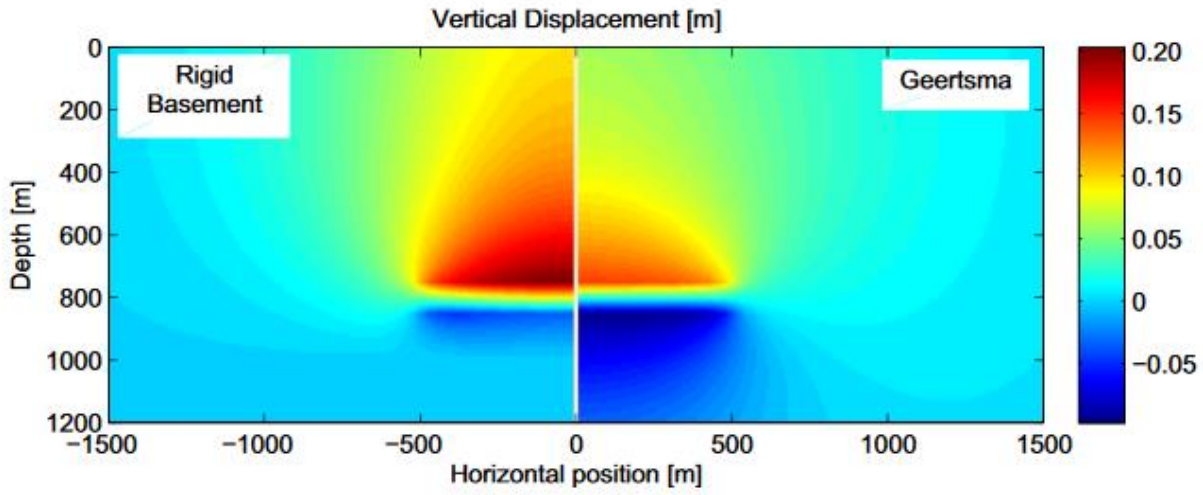

Figure 8.4: Vertical displacement calculated using (left) rigid basement and (right) Geertsma model (Tempone et al., 2010).

8.3.5 Interval R-factor

The technique developed for the Ekofisk field to estimate R-factor using a reservoir engineering constraint can also be extended to estimate interval R-factors. Reservoirs with heterogeneous overburden such as Shearwater (van Bergen et al., 2013), Elgin, and Franklin (Hawkins, 2008) have vertically varying lithology with chalk formations (Ekofisk, Hod, Tor and Herring) of interbedded argillaceous materials and clay formations (Kimmeridge Clay and Heather). In order to estimate the interval R-factors, in the same data-driven inversion procedure, the inversion is carried out using the interval overburden time-shifts (IOT) computed at different sections of the overburden, to compute a range of average R ($R_{avg1,}$ R_{avg2}, $R_{avg3\ldots}$) between the reservoir and overburden medium. Subsequently, the interval R-factors for individual layers can be computed using some form of averaging method such as harmonic, distance, arithmetic and so on from the range of average R-factors. The research problem here is what type of averaging function or relation accurately captures the relationship between the interval R-factors and the average R-factors. The proposed method shown in Figure 8.5 is similar to that of layer stripping in velocity

estimation, such that each time one layer is analyzed for its accurate velocity, starting from the top layer, down to the deeper layers. In contrast, to recover the interval R, we start from the deepest layer closest to the source (reservoir).

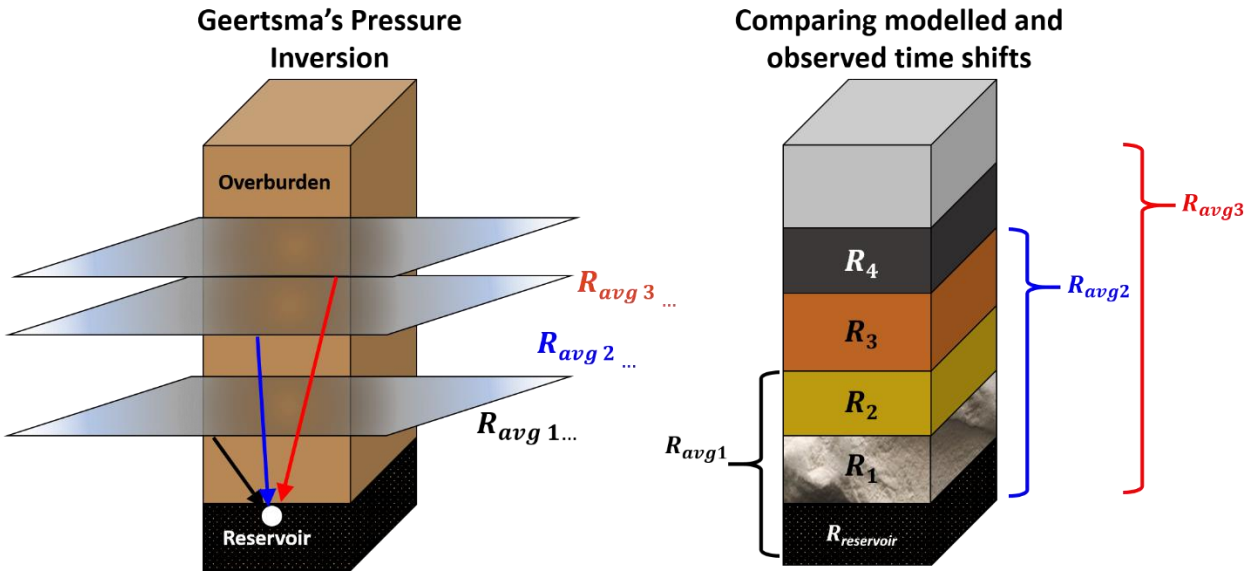

Figure 8.5: (left) Geertsma's pressure inversion is carried out to recover the average R in the homogeneous elastic half space. (b) While comparing the modelled time-shifts using the average R to the observed time-shifts, the interval R can be estimated separately.

8.3.6 Effects of horizontal stress and strain on R-factor

The current model of relating vertical strain to the fractional change in P-wave velocity assumes a linear relationship (Hatchell and Bourne, 2005). However, laboratory measurements show that the propagation velocity of compressional waves (and shear waves) is dependent on changes in the triaxial stress state of the rock (Mavko et al., 1998). Additionally, geomechanical modelling shows that stress and strain changes in the subsurface during reservoir production are triaxial, and cannot be adequately described using "mean" stress (Herwanger and Horne, 2005). In addition, Herwanger (2008) predicted that for the same amount of vertical stress change, the change in vertical velocity under zero volumetric strain conditions is found to be markedly higher than under uniaxial compression. A similar conclusion was presented by Sayers (2006). This might explain

why the R-factor observed in the overburden is at least twice the R-factor observed in the reservoir. Therefore, it is necessary to investigate the effect of horizontal stress and strain changes on vertical velocity. The R-factor approach is only valid if the changes in vertical stress and strain are the most dominant effect, and horizontal stresses and strains are negligible. This approach is only relevant to a subset of geomechanical scenarios; and further investigation should be carried out to understand the limits of this application. Reservoirs of a more complex geometry such as dipping layers has more significant later shifts induced by production. From the work of Cox and Hatchell, 2008 ignoring the horizontal shift will introduce systematic errors in the measurement of vertical time-shifts. In the Shearwater field, it can be observed that on the downdip side of the reservoir that the estimated vertical time-shifts are smaller than they should be, while on the updip side the vertical time-shifts are larger; this effect also increases in depth. The question is then on how to accurately estimate vertical and lateral shifts and that whether these changes are anisotropic and/or offset dependent and lastly, how will it affect the R-factors.

8.4 Final Remarks

The purpose of this research was to generate a pragmatic, integrated and data-driven approach to estimate pressure and saturation change for a compacting chalk reservoir. Information measured from dedicated PRM data provides an important contribution in the realms of reservoir characterisation, inversion and even history matching. The increased 4D repeatability and higher detectability of time-lapse seismic anomalies of the LoFS creates the opportunity to apply the fast-track pressure and saturation prediction methods proposed in this thesis. Besides, the higher frequency of the acquired seismic monitors will be beneficial, as the relationship between pore pressure change and strain can be assumed to be approximately linear. This work constitutes just another step towards understanding the pressure, saturation and geomechanical interplay in challenging fields such as Ekofisk, which will hopefully lead to further quantitative studies in 4D seismic interpretation and analysis.

APPENDIX A

BAYESIAN MCMC FORMULATION FOR PRESSURE AND SATURATION INVERSION

The Bayesian formulation for the inversion of pressure and saturation changes using time-lapse seismic data is described in this appendix. The "Bayesian approach" to inverse problems, describes the unknown model, m_{true} that we would like to uncover as a random variable, and the solution takes the form of a probability distribution for the model parameters called the posterior distribution. In a Bayesian approach, the prior information about the solution is incorporated into the data; this prior information can range from hard additional constraints to experience-based intuition. This is expressed mathematically as a prior distribution of the model. The posterior probability distribution of the model parameters is given as $q(m|d)$:

$$q(m|d) = \frac{f(d|m)p(m)}{c} \tag{A1}$$

where the data, d in our inversion scheme are represented by the inverted relative change in P-wave velocity, S-wave velocity and time strain. The model parameters, m are the change in pressure (ΔP), and saturation (ΔS_w). The prior distribution is denoted as $p(m)$, and the conditional probability distribution expressed as $f(d|m)$. c simply normalizes $q(m|d)$ so that its integral in model space is one. One simplification is to assume the prior distribution is uninformative. This indicates a prior distribution where all model parameter values have equal likelihood. In which case, Equation (A1) is simplified to:

$$q(m|d) \propto f(d|m) \tag{A2}$$

and the posterior distribution is precisely the likelihood function, $L(m|d)$. Under the maximum likelihood principle, the model, m_{ML} that maximizes $L(m|d)$ will be selected. In the application reported in Chapter 5, the data noise are independent and normally distributed, since data errors are independent, the likelihood functions can be written as:

$$L(m|d) = f(d|m) = f(d_1|m) \cdot f(d_2|m) \dots f(d_n|m) \tag{A3}$$

The likelihood function, $f(d|m)$ is presented as:

$$p(D_i|\Delta P, \Delta S_w, H) = \frac{1}{\sqrt{2\pi|\varepsilon_i|}} exp\left\{-\frac{1}{2}[D_i - f_i(\Delta P, \Delta S_w)]^T \varepsilon_i^{-1}[D_i - f_i(\Delta P, \Delta S_w)]\right\} \tag{A4}$$

The data here are represented by the multiple time-lapse seismic data (*D*) with different levels of uncertainties. The hyper-parameters (*H*) are parameters necessary to arrive at a solution but are of no direct interest to the inference problem, such as the coefficients in the proxy model and the linearised compaction functions. The ε_i represent diagonal covariance of the uncertainties in the i^{th} dataset, whereas f_i is the forward modelling procedure represented by the proxy model equation. Uncertainties in the data are provided from the NRMSD (for definition refer to Appendix C) calculated in the overburden using a 1s gate. The NRMSD map is then used to calculate the uncertainties for each data type spatially, assuming vertical stationarity of the 4D noise level. The prior distribution is represented as $p(\Delta P, \Delta S_w, H|x)$ and the prior information is x (shown in Equation A5). The prior distribution is represented by the engineering constraints (EC) described in Chapter 5. Upper and lower bounds were created using the spatial constraints and feasible values from the history-matched simulation prediction. These bounds are prior information fed into the inversion procedure**.** Incorporating prior information can speed up the convergence of the inversion process towards the most probable solution. The final goal is to draw samples from the posterior distribution represented as:

$$p(\Delta P, \Delta S_w|D) = p(\Delta P, \Delta S_w, H|x)p(D|\Delta P, \Delta S_w, H) \tag{A5}$$

In this approach, we draw samples from the posterior distribution using a McMC algorithm. At the end of 1990s, Monte Carlo integration and sampling have become firmly established as the technique of choice for Bayesian inversions for non-linear problems (Sambridge and Mosegaard,

2002). The McMC method depends only on the forward model and the associated likelihood calculations, making it easy for implementation. The Markov chain Monte Carlo methods can be used to directly simulate the posterior PDF (probability density function), which is, draw random samples distributed according to the posterior PDF, and from these calculate Bayesian estimates of constraint and resolution. For this implementation, the Metropolis-Hastings sampler (Metropolis et al., 1953) is used. There are three parts to this technique:

1. Monte Carlo
2. Markov Chains
3. Metropolis-Hastings

The Monte Carlo represents the method that generates random numbers. A Markov chain is a sequence of numbers where the current number depends on the previous number in the sequence. This refers to the number generated from a proposed distribution. Whereas, the Metropolis-Hastings algorithm is used to decide which proposed value to accept or reject from the proposal distribution.

$$r(k_{new}, k_{t-1}) = \frac{Posterior\ probability\ of\ k_{new}}{Posterior\ probability\ of\ k_{t-1}} \tag{A6}$$

The posterior probability distribution is calculated by multiplying the likelihood function and prior distribution. If the posterior probability of the new value, ($Posterior\ probability\ of\ k_{new}$) is greater, the ratio of the probability will be greater than 1, and the new value of k will be accepted. If the posterior probability of the previous value ($Posterior\ probability\ of\ k_{t-1}$) is greater, the new value might not necessarily be discarded. Ratios that are less than one will be treated as an acceptance probability. The acceptance probability is given as:

$$acceptance\ probability = \alpha(k_{new}, k_{t-1}) = \min[r(k_{new}, k_{t-1}), 1] \tag{A7}$$

In the case where the ratio is less than 1, then a uniform random number is drawn, and the new value of k will be kept if the random number is less than the acceptance probability. This procedure is described as:

$$Draw\ u \sim Uniform(0,1) \tag{A8}$$

$$If\ u < \alpha(k_{new}, k_{t-1}) \quad then\ k_t = k_{new}$$

$$If\ u > \alpha(k_{new}, k_{t-1}) \quad then\ k_t = k_{t-1}$$

The McMC Metropolis-Hastings method depends on the starting values, and the number of iterations can be reduced by discarding the burn-in period. The burn-in period is the time taken for the chain to stabilize. The values of k are correlated because they are generated from Mavko process. Excessive autocorrelation may indicate problems with model specification, but a thinning process is useful in reducing the autocorrelation. The thinning process refers to increasing the McMC sample size, and drawing samples at regular intervals.

APPENDIX B

A SENSITIVITY ANALYSIS FOR FRACTURE GRADIENT ESTIMATION AND UNCERTAINTIES

This appendix presents a sensitivity study for fracture gradient and the changes due to different production mechanisms for a clastic reservoir. The issue of drilling into depleted areas is increasing in importance as more wells are drilled in mature or brown fields. A knowledge of fracture gradient prediction methods is also useful in everyday operations such as cementing, sand consolidation, matrix and fracture acidizing, and hydraulic fracturing. Another important application is in secondary recovery. In most injection operations, it is desirable to stay below the fracture pressure, to prevent channeling from injector to producer. Different lithologies will have a different pore pressure and fracture pressure due to the variation in Poisson's ratio and permeability. The initial safety drilling window during the pre-drill condition is between the fracture gradient of the reservoir and the pore-pressure of the overburden to avoid blow out from the shales and mud losses in the reservoir. After pressure declines in the reservoir, the pore pressure and fracture gradients in both reservoir and overburden reduces, this subsequently narrows the safety drilling window after production, shown in Figure B1. Therefore, it is crucial to predict the changes of fracture gradient in reservoir after production. The prize includes establishing better safety drilling margin, ensuring the license to operate, managing the risk of the drilling opportunity and reducing rig operational costs.

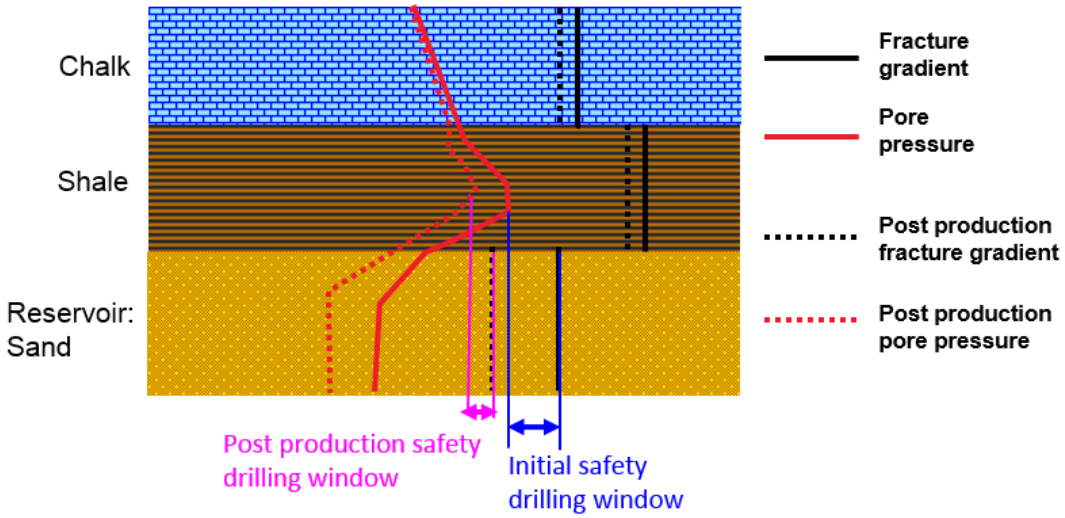

Figure B1: Conceptual diagram showing fracture gradient and pore pressure gradient before and after production.

The commonly used model is the elastic uniaxial strain model developed by Eaton (1969) to predict minimum stress as a function of depth and rock lithology. The dependence of the horizontal stress, σ_{Hmin} on rock lithology results from the dependence of Poisson's ratio, ν on rock lithology, as shown below:

$$\sigma_{Hmin} = \frac{\nu}{1-\nu}\left(\sigma_V - \alpha P_p\right) + \alpha P_p + \sigma_{tec} \quad \text{(B1)}$$

where σ_V is the vertical stress, which is dependent on bulk density logs, and in most cases we assumed the vertical stress to remain constant throughout the period of production. The Biot's coefficient,α, is assumed to be unity for mostly porous, permeable rocks. The pore pressure, P_p, can be obtained from seismic velocity via different routes, including tomography and full waveform inversion. The third term, σ_{tec} is the tectonic stress, which could be zero in tectonically relaxed areas, but can be important in tectonically active areas. A fracture will take the path of least resistance and open up against the least horizontal stress; hence the fracture gradient can be equivalent to the minimum horizontal stress.

We can envisage how the minimum horizontal stress changes as a function of production, as the pore pressure and the fluid type changes in the reservoir. The changes in the minimum horizontal stress can be estimated using the equation:

$$\Delta\sigma_{Hmin} = \frac{\Delta\nu}{1-\Delta\nu}\left(\sigma_V - \alpha\Delta P_p\right) + \alpha\Delta P_p + \sigma_{tec} \quad \text{(B2)}$$

by assuming there are no significant changes to the vertical stress, Biot's coefficient and the tectonic stresses. This assumption will not hold true if fault reactivation, reservoir compaction, and other geomechanical effects are expected. In order to quantify the uncertainties associated with the model and input variables. This sensitivity analysis was carried out using a generic petro-elastic model representing a typical North Sea clastic reservoir. The sensitivity analysis in Figure B2 shows the percentage change in the minimum horizontal stress and other elastic properties, such as P-impedance, S-impedance and Poisson's ratio, as a function of pore pressure, water saturation, Biot's coefficient, depth and lithology. The base value of each modelling case is highlighted in blue. The model shows high sensitivity towards Biot's coefficient. In most reservoirs, the Biot's coeiffient can be assumed to be one. However, in low permeability and shaly rocks, the value of Biot's coefficient is rarely equal to unity, and has to be calibrated. Water saturation, variation in lithology and pore pressure also show considerable influence on the fracture pressure. A low side estimate of fracture gradient can be defined as an oil-saturated, clean, porous sandstone, which will derive the lowest minimum horizontal stress.

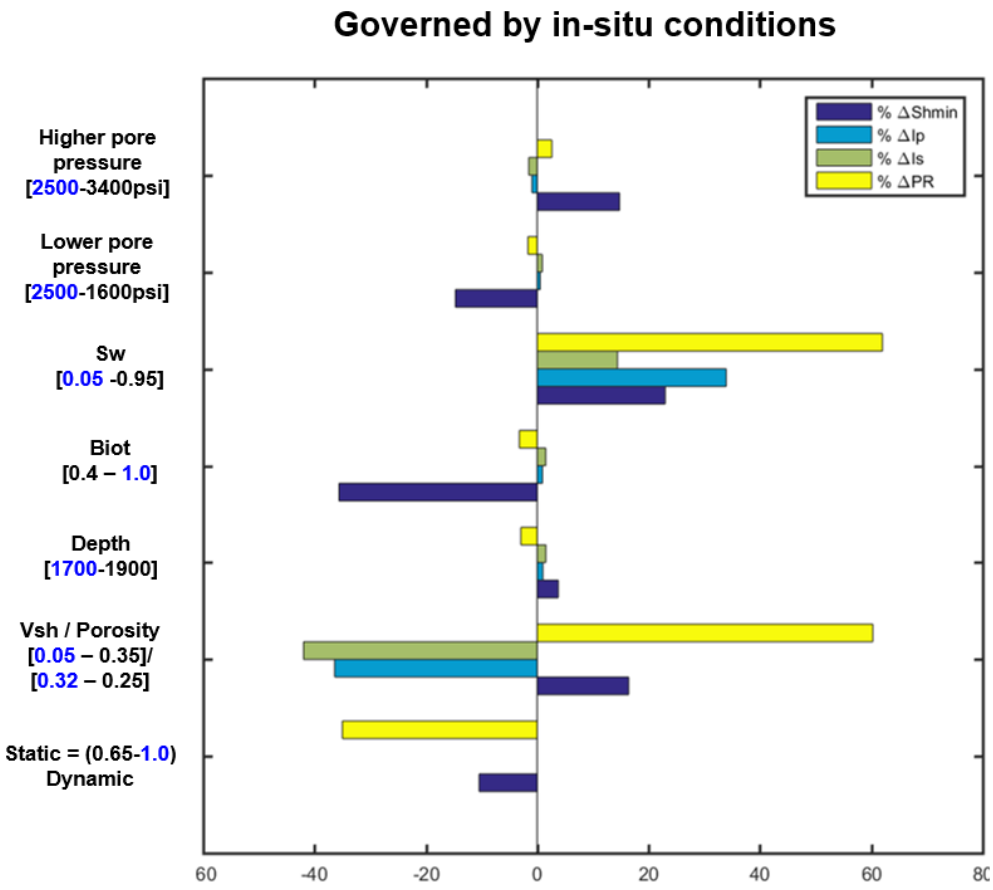

Figure B2: The percentage change in minimum horizontal stress due to different in-situ conditions.

Having assessed the influence of geology, pressure and saturation on the horizontal stress, I evaluate how the minimum horizontal stress changes as a function of production, shown in Figure B3. An injection event into the water leg that resulted in only pore pressure increase will subsequently increase the relative change in minimum horizon stress, this is vice versa for a depletion event without any changes in fluid type. A water flood scenario will also increase the minimum horizontal stress, which will stiffen the rock frame, and the rock is less likely to fracture. When there are coupled effects from both pressure and saturation changes, the changes in minimum horizontal stress is further complicated. For example, an injection into oil leg, not only results in increase in pore pressure but also water saturation, which means the increase in minimum horizontal stress will be twofold.

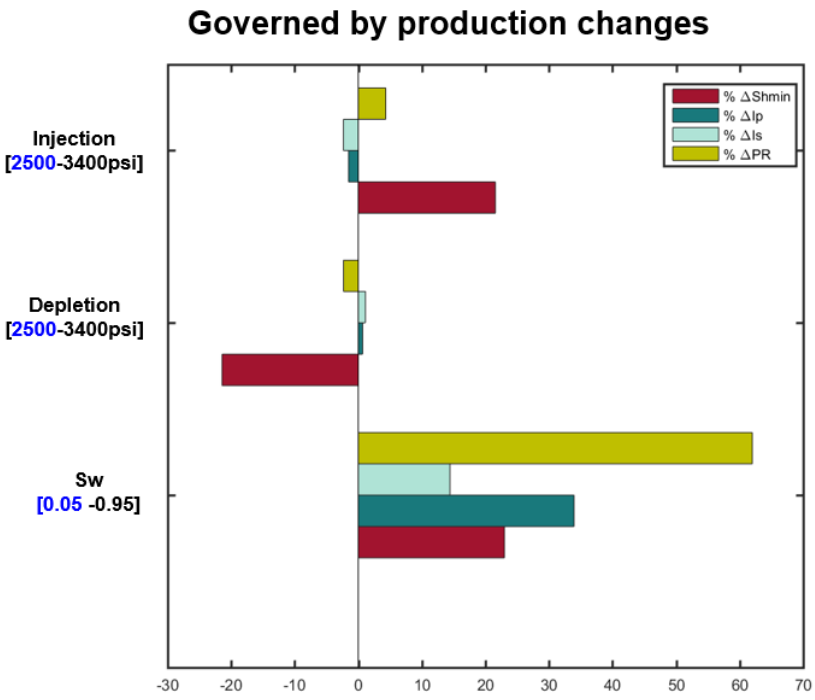

Figure B3: The percentage change in minimum horizontal stress due to production changes.

APPENDIX C

MODELLING TIME-SHIFTS WITH NOISE

This appendix investigate in detail the influence of noise on time-shift measurements using three separate methods: Rickett's Non-linear inversion (2007), Correlated Leakage method (Whitcombe et al., 2010), and cross correlation (Hale, 2006). We first examine the definition and relationship between percentage of noise, energy in the difference cube (NRMSD) and signal to noise ratio (SNR). Despite some limitations as reported in Kragh and Christie, (2002), the NRMSD is a widely used attribute to assess noise levels in seismic data. The NRMSD is defined as:

$$NRMSD = \frac{RMS(D)}{\frac{1}{2}(RMS(B)+RMS(M))} \tag{C1}$$

RMS is the root mean square, B and M are baseline and monitor seismic data. The signal to noise ratio is calculated as:

$$SNR = 10log_{10}\left(\frac{RMS(signal)}{RMS(noise)}\right) \tag{C2}$$

The percentage of noise is the normalized random noise scaled by the maximum value of the seismic trace. The relationship between these definitions are reported in Figure C1. The equivalent of SNR and NRMSD for different percentage of noise is provided in Table C1.

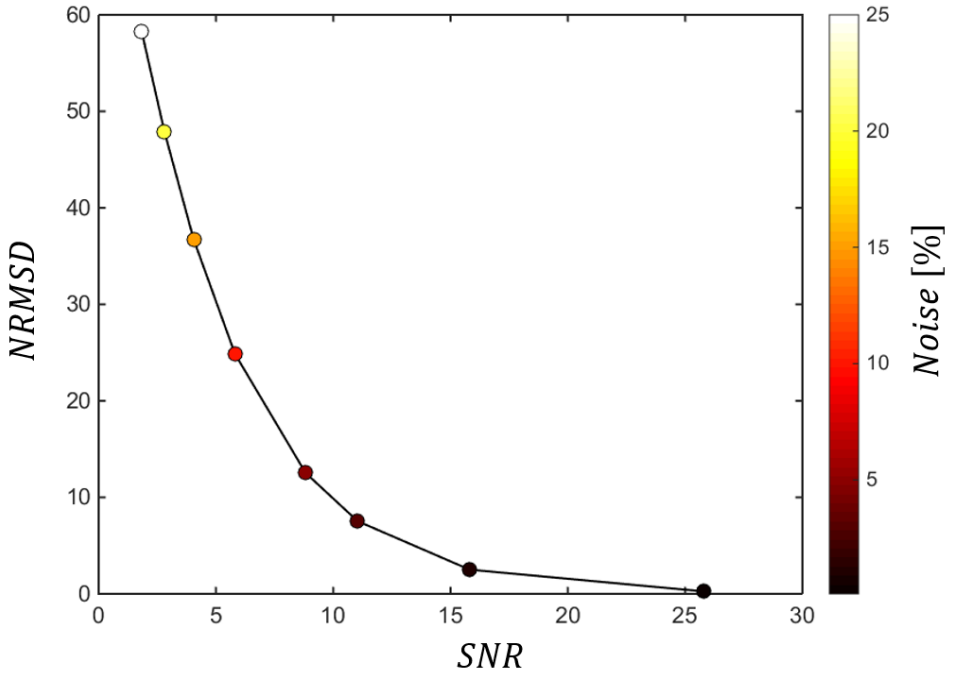

Figure C1: The relationship between NRMSD, SNR and percentage in noise.

Percentage of noise (%)	SNR	NRMSD
0.1	25.8	0.25
1	15.8	2.5
3	11.0	7.5
5	8.8	12.5
10	5.8	24.9
15	4.1	36.7
20	2.8	48.0
25	1.8	58.3

Table C1: The equivalent of SNR and NRMSD to the percentage of noise.

The focus is to understand the expected noise level in the LoFS surveys and how does it affect the time-shift measurement. As the survey interval is decreased such as in the LoFS, reservoir changes will become smaller and more difficult to detect. Baseline synthetic seismic traces are generated at a well location using well logs and the chalk petro-elastic model described in Chapter 2. For the monitor trace, a similar workflow is undertaken, after increasing the pore pressure in the monitor

‘scenario’ by 300pis. The expected background noise level is generated using the NRMS noise level (Kragh and Christie 2002), where we assumed the signal to noise ratios of the base and monitor traces to be equal and band-limited random noise is added to the synthetic seismograms. This yields baseline and monitor pairs with the desired NRMSD levels. Since we are only looking at a single trace, correlated noise is not accounted for. Figure C2 shows the results of the modelling for NRMSD of 5% or SNR of 13.2. Baseline and monitor traces are showed in column ‘1’, the baseline and monitor pair after added noise is reported in column ‘2’. Column ‘3’ shows the theoretical time-shifts calculated from the changes in velocity. There is no travel time difference above ‘top reservoir’ but an increase in time-delay is observed below ‘top reservoir’ due to the increase in pore pressure. Subsequently, the time-shifts are calculated using three separate methods from the seismic traces without noise, this is shown in column ‘4’. The equivalent time-shifts calculated from noise added seismic traces are reported in column ‘5’.

The NLI method shows the most accurate results as it replicates the theoretical time-shifts. Less confidence is placed on methods such as the correlated leakage method and cross-correlation. As the noise in the seismic waveform increases, the departure from the theoretical time-shifts also increases for all three methods. Figure C3 shows the comparison of the three methods to the theoretical measurement as a function of the NRMSD. A NRMSD of 5% is representative of the repeatability expected from a permanent OBC system. Figure C3 shows that at NRMSD of 5%, the measured time-shifts using NLI is around 0.35ms, whereas the actual time-shifts is 0.45ms. Therefore, any signal below 0.35ms will not be treated as signal. This is in agreement with the noise floor chosen at ±0.08ms in Chapter 3 for the LoFS surveys - any data points that fall within this range will not be treated as signal and will be excluded in all analyses. The information in Figure C3 can also be used as a guide for designing noise floors for a range of different NRMSD and SNR such as for streamer data. This also demonstrates the advantage of PRM system, with low non-repeatability and an increase in signal detectability, as demonstrated in Janssen et al., 2006, showed in Figure C4.

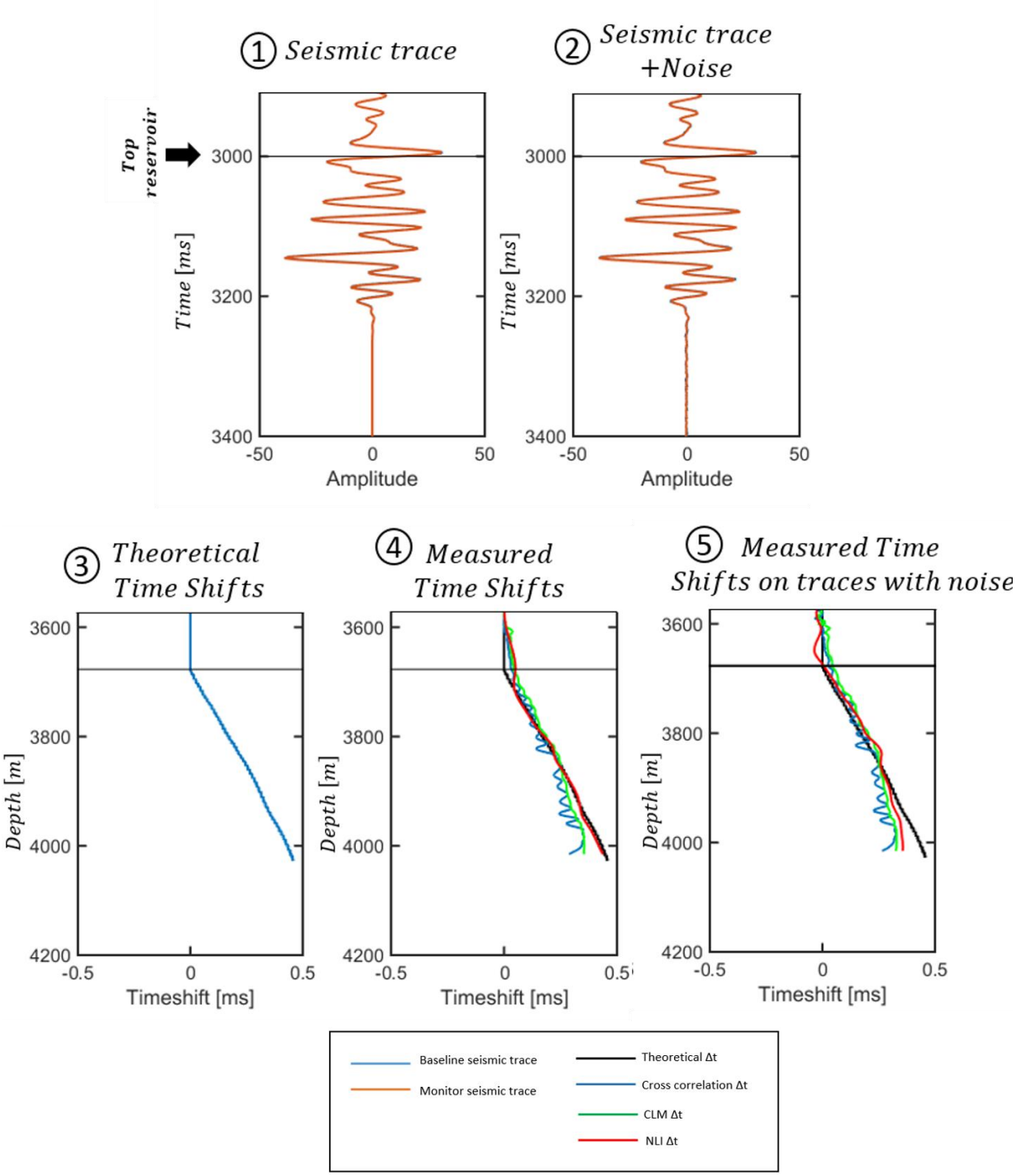

Figure C2: (1) Seismic trace of baseline-monitor, (2) Seismic trace of baseline-monitor with noise, (3) Time-shifts calculated from changes in velocity, (4) Measured time-shifts from seismic trace of baseline-monitor without noise and (5) Measured time-shifts from waveform with added noise.

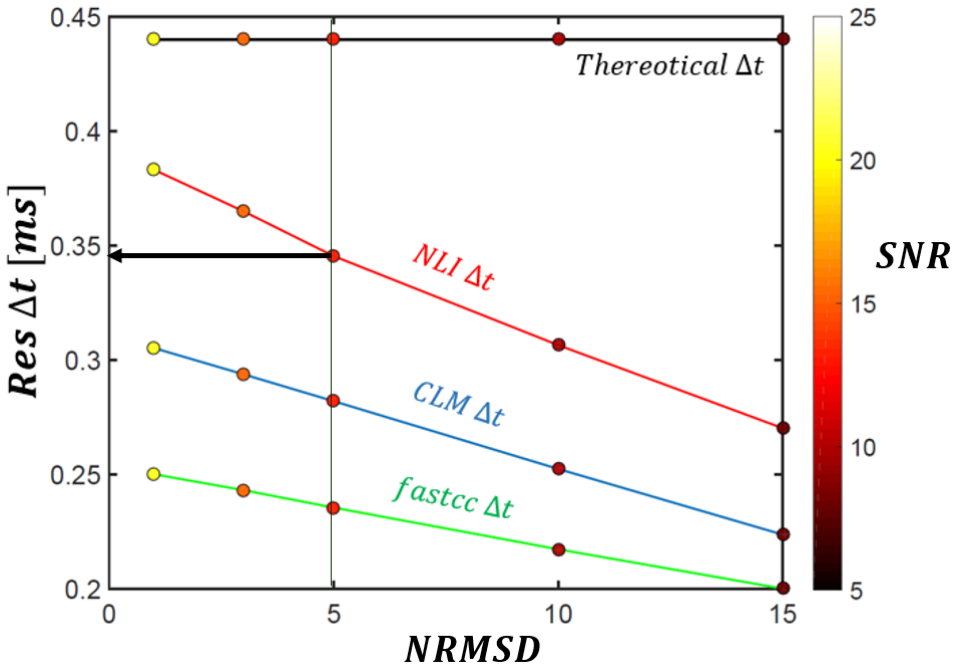

Figure C3: Reservoir time-shifts as a function of NRMSD.

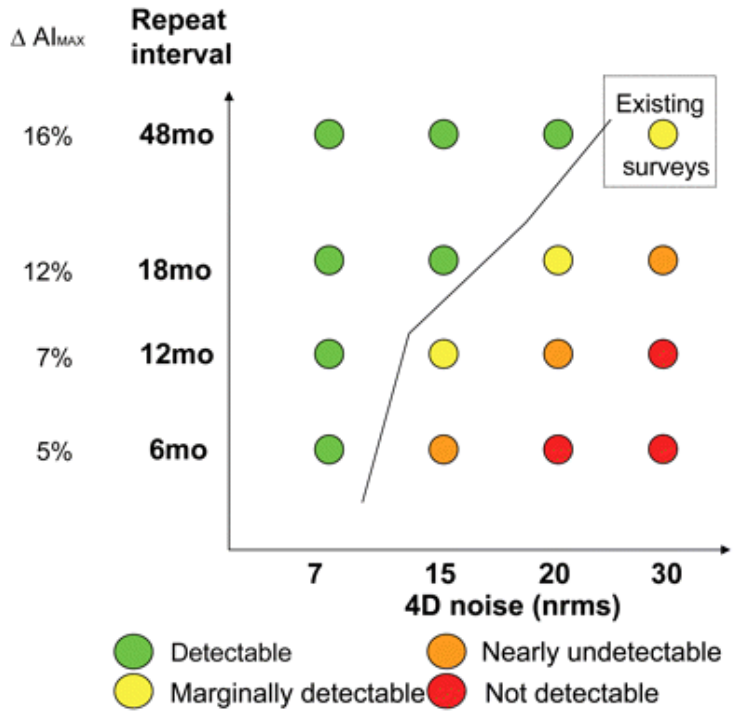

Figure C4: The results of detectability modelling from for the Ekofisk field (Janssen et al., 2006), any signals within 6 months require a NRMS of 7% for detection.

APPENDIX D

ANALYSIS OF THE OVERBURDEN TIME-LAPSE RESPONSE USING SEIS2SEIS

The work in Chapter 6 and 7 resulted in two major implications: firstly, the R-factor is recoverable using Geertsma inversion and prior constraint from the engineering; provided a fairly well history matched model is available. Secondly, although the technique appears to work with the real data, there are scenarios where the technique has failed due to unexpected overburden signal. These anomalous signals indicate that the overburden compacts and extends together with the reservoir contrary to normal geomechanical expectations. These anomalies together with some early hypotheses are presented in this appendix.

The method I used to examine the relative time-lapse seismic behaviour of the overburden to the reservoir is Seis2Seis, which is correlating seismic attributes from different parts of the field (overburden versus reservoir) at each spatial location. The workflow that demonstrates this technique is shown in Figure D1. Firstly, time-shift maps of the reservoir and a specific interval of the overburden are computed across all seismic baseline-monitor and monitor-monitor pairs. At each spatial location (i, j), the normalized cross correlation between the reservoir and overburden map is calculated - this attribute is known as 'NCC'. This procedure is repeated for different horizons in the overburden, starting from the overburden interval closest to the reservoir to the furthest. By analysing the NCC maps, it gives a vertical description of how the time-shifts in the overburden change relative to the time-shifts in the reservoir.

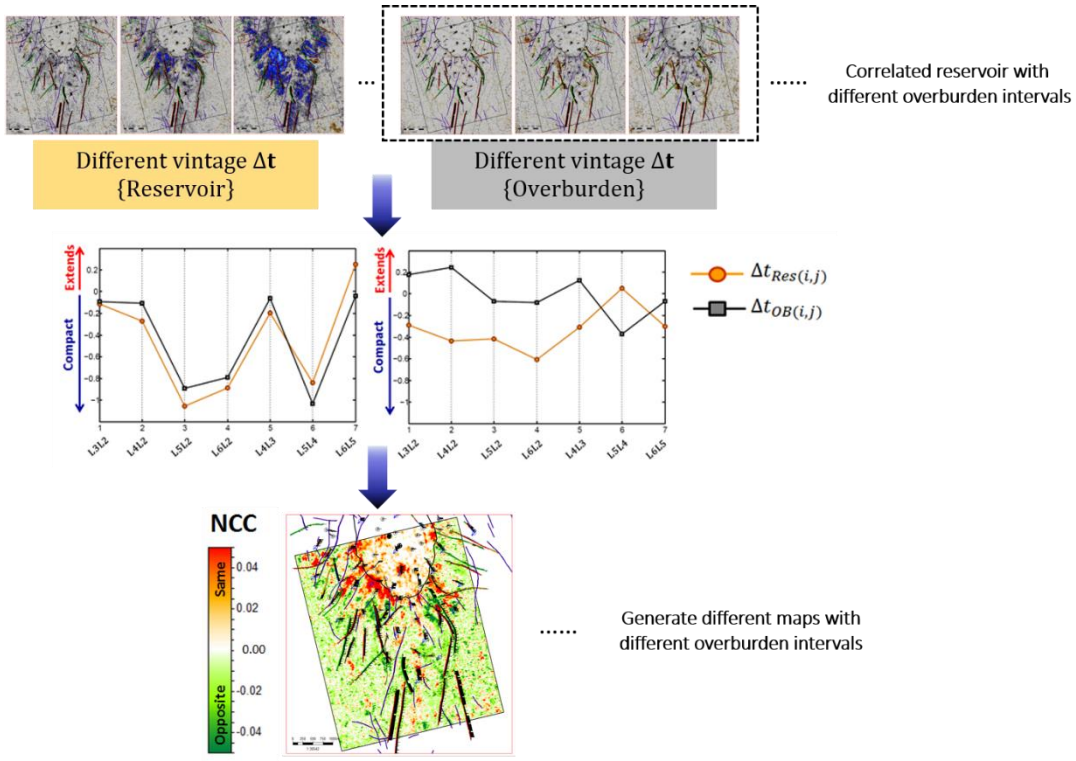

Figure D1: Workflow of Seis2Seis to investigate the relationship between reservoir and overburden time-shifts across different seismic vintages.

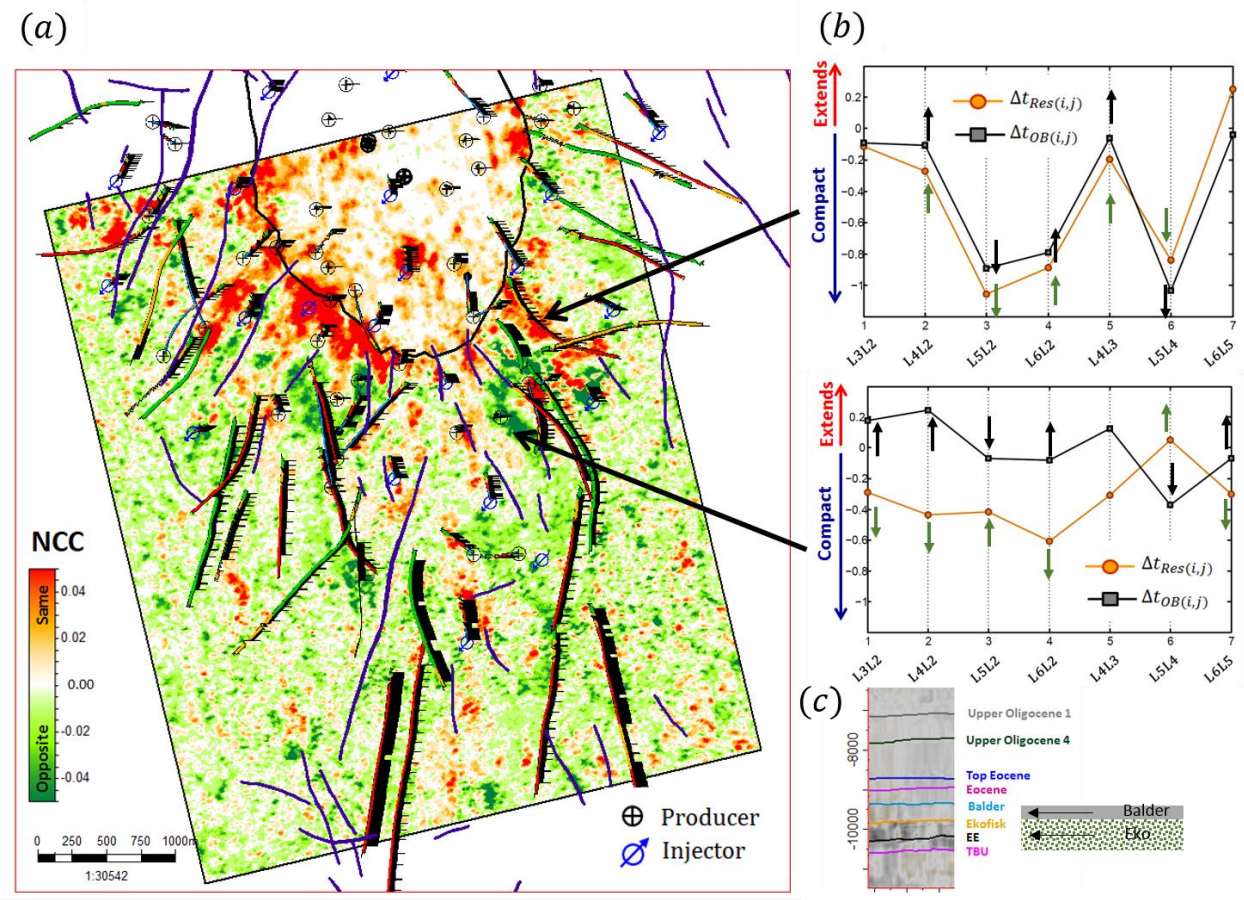

Figure D2: (a) NCC map generated for Balder-Ekofisk, (b) plots showing a positively and negatively correlated area and (c) horizons of Balder and Ekofisk in depth (ft).

Figure D2(a) shows the NCC map generated using time-shifts maps from Ekofisk (reservoir) and Balder (overburden interval closest to the reservoir). A positive NCC represents positive correlation, this is shown in Figure D2(b) where the time-shifts value at the spatial location increases and decreases consistently for both reservoir and overburden across all seismic pairs. The contrary is observed when the NCC shows a negative value, indicating negative correlation. Figure D2(c) shows the respective horizons. The positive correlation is counter intuitive to the expected geomechanical behavior. It is expected that as the reservoir undergoes compaction, the adjacent overburden extends. To monitor this behavior, NCC maps for all overburden intervals were computed from the order of deepest to shallowest overburden layer (shown in Figure D3).

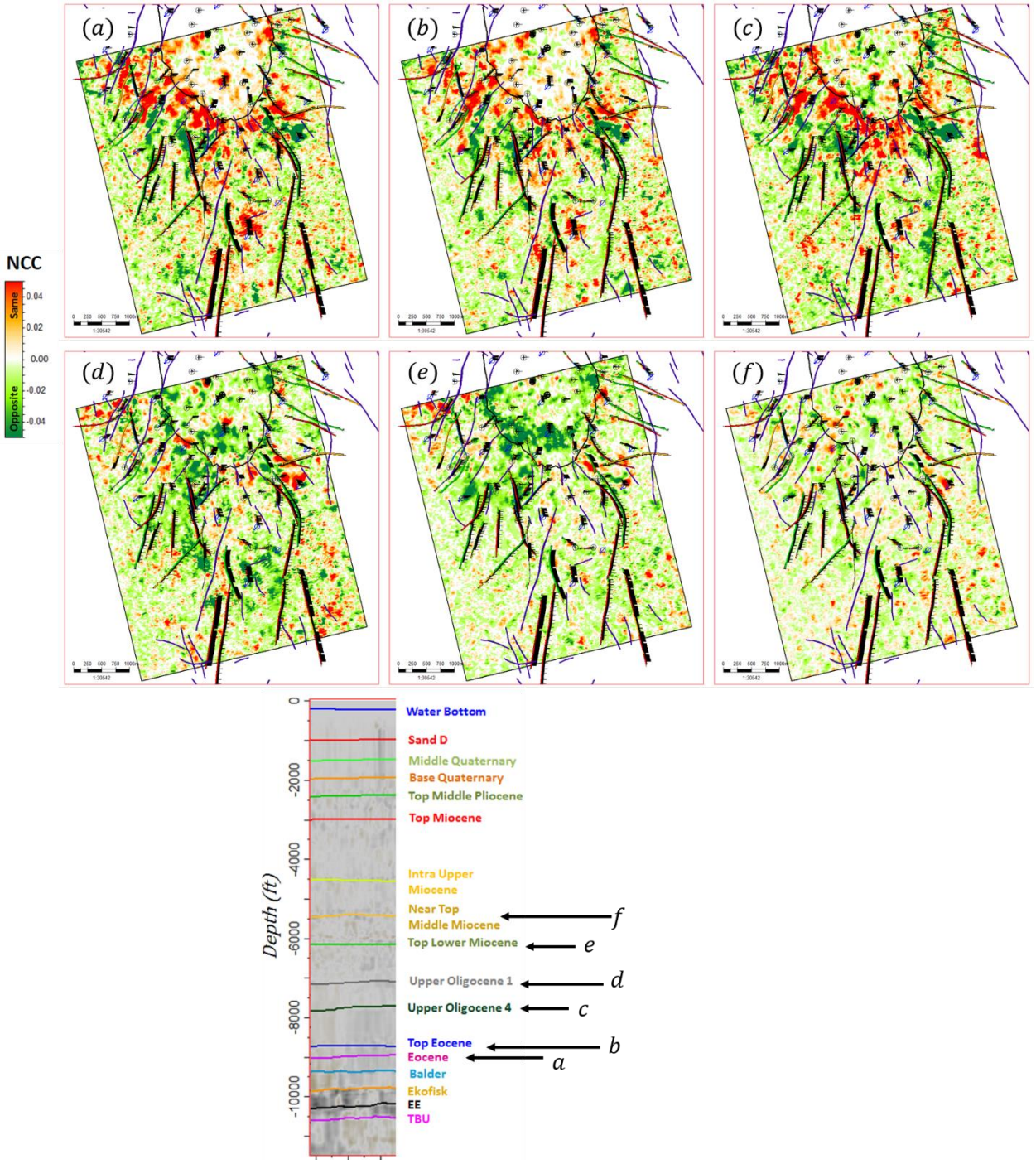

Figure D3: Maps of NCC calculated for the pairs of (a) Eocene-Ekofisk, (b) Top Eocene-Ekofisk, (c) Upper Oligocene 4-Ekofisk, (d) Upper Oligocene 1-Ekofisk, (e) Top Lower Miocene-Ekofisk and (f) Near Top Middle Miocene-Ekofisk.

Figures D3(a) to (c) show maps with positive and negative NCC, these maps are generated using time-shifts information closer to the reservoir. The positive NCC anomalies are found to be concentrated around the crest. Whilst Figure D3 (d) to (f) shows only negative NCC, where a reversal of polarities is observed in the shallower overburden.

Assuming these measurements are accurate and not biased due to the parameterization of time-shifts calculation method; the observations presented have a variety of geomechanical hypotheses: firstly the chalk could be a very stress and strain sensitive material, and can change the orientation and magnitude of the principal stresses, which in turn cause a change in the overburden velocity. This offers an explanation for the apparent difference in P-wave velocity stress-sensitivity between overburden and reservoir. The difference in stress sensitivity is caused by the influence of stress path such as the opening and closing of both horizontal and vertical fractures on vertical velocity. From the work of van Bergen et al. (2013), it was demonstrated that the fractures in the overburden chalk has caused changes in the azimuth and magnitude of the principal stresses. The stiff chalk material in the Shearwater field overburden for example, compacts instead of expands due to the closing and opening of fractures at different orientations.

In Valhall, pressure depletion acoustically hardens the reservoir and the stress and velocity in the overburden is reduced immediately above the strongly compacting parts of the reservoirs. In areas with much less compaction, however, vertical and lateral stress redistribution in the overburden can result in opposite effect (Jack et al., 2010). Figure D4 by Kristiansen et al., 2005 shows the development of stress arching around a horizontal well in the Valhall field. This creates compressive stresses at the above and below the reservoir highlighted by arrow 1 and 3, which could be another contender for the anomalous reservoir-overburden behaviour estimated using Seis2Seis. Other supporting reasons include the anomalies concentrated around the crest which are highly stressed during the doming process suggesting that the anomalies could be related to the fracture network. Creep could be another explanation, due to the very complicated microstructure, chalk is a very strain-rate sensitive material, laboratory data has shown that even at constant stress or increased in pressure with the invasion of water, there could still be deformation occurring.

Fractures and faults could have propagated upwards into the overburden, thus causing pressure communication between both intervals. This means pockets of large fractures or production

reactivated faults allowing pressure communication with the overburden. Hence the same polarity is observed in both the overburden and reservoir. Another explanation is the nature of how chalk compacts: forming concentrated stress regions and resulting in an 'isolated' arching effect similar to that observed in the Valhall field. These hypotheses will have to be developed further to unveil the likely contenders.

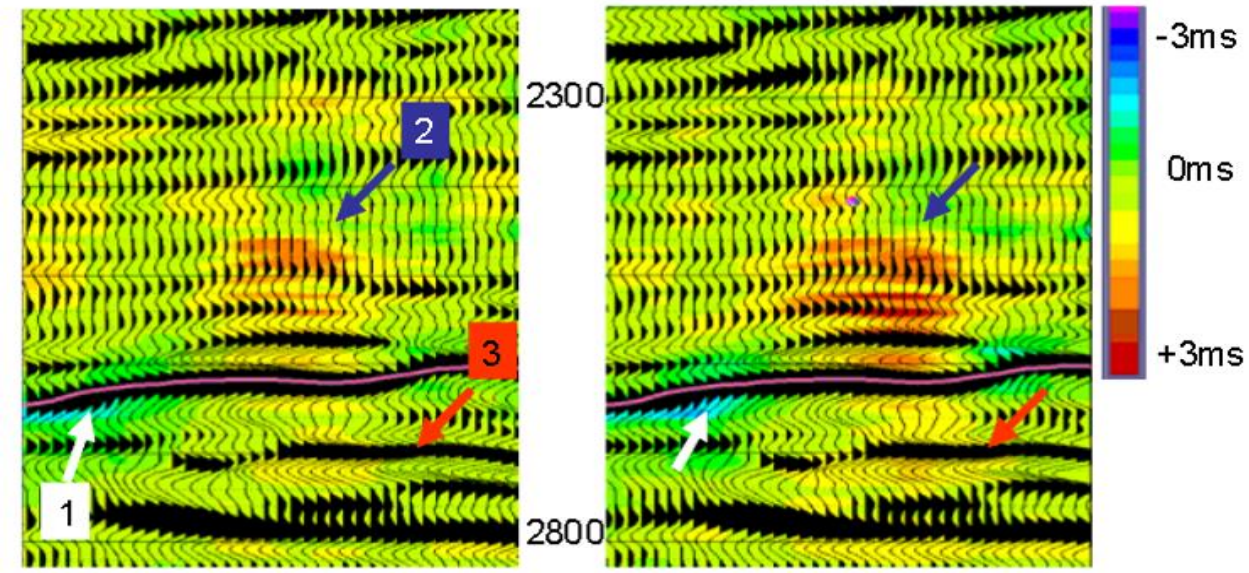

Figure D4: A cross section at a horizontal between two LoFS surveys showing how a stress arch is developing above the compacting chalk, the green colour (speed up) increase in intensity over time. This could be on explanation for the unexpected overburden-reservoir geomechanical behaviour (Kristiansen et al., 2005).

APPENDIX E

COMPACTION COMPUTATION

In order to verify the accuracy of our inversion result, we can also back-calculate the amount of compaction that has occurred in the reservoir by simply using the inversion results as inputs into the proxy model equation. Assuming the volume of the rock's skeletal frame, V does not change between time steps or in time, and that V is made up of the area, A and height, z:

$$V(1-\varphi) = constant \tag{E1}$$

$$A \cdot z(1-\varphi) = constant \tag{E2}$$

$$A \cdot z_1(1-\varphi_1) = A \cdot z_2(1-\varphi_2) \tag{E3}$$

The porosity, φ between time steps changes as a function of the changes of pressure and saturation, we can substitute the porosity and thickness in the second time step as:

$$z_1(1-\varphi_1) = (z_1 - dz)[1-(\varphi_1 - d\varphi)] \tag{E4}$$

If we simplify the equation:

$$dz(1-\varphi_1) = d\varphi(z_1 - dz) \tag{E5}$$

$$\frac{dz}{(z_1 - dz)} = \frac{d\varphi}{(1-\varphi_1)} \tag{E6}$$

Since the seismic data were acquired every six months through a PRM system, we can assume small changes in the thickness due to production related changes, we can further simplify it as:

$$\frac{dz}{z_1} = \frac{d\varphi}{(1-\varphi_1)} \tag{E7}$$

As described in Chapter 4, Section 4.6.3, change in porosity is captured as functions of dry and wet compaction curves for each porosity class, we can substitute the equation with:

$$dz = \frac{\left[F_p + \left(\frac{\Delta S_w}{\Delta S_{wmax}}\right)(F_{ww} - F_p)\right] \cdot \Delta P}{(1-\varphi_1)} \cdot z_1 \tag{E8}$$

This allows us to quantify the change in thickness between time step 1 (baseline) and time step 2 (monitor).

APPENDIX F

DEFORMATION IN POROELASTIC MEDIUM

The simple geomechanical model employed by Geertsma (1966, 1973) assumes a linear poroelastic medium and material isotropy. The constitutive equations for this model presented by Biot (1941) and Rice and Cleary (1976) are as follows:

$$2\mu\varepsilon_{ij} = \sigma_{ij} - \frac{v}{1+v}\sigma_{kk}\delta_{ij} + \frac{(1-2v)\alpha}{1+v}p\delta_{ij} \quad \text{(F1)}$$

$$\Delta m = \frac{(1-v)\alpha\rho_0}{2\mu(1+v)}\left[\sigma_{kk} + \frac{3}{B}p\right] \quad \text{(F2)}$$

where Equation (F1) relates strain ε_{ij}, to stress σ_{ij}, acting on the material element and the pore pressure, p. Equation (F2) relates the changes in fluid mass per unit volume, Δm to the mean normal stress, σ_{kk} and pore pressure, p. Other variables in the equations are shear modulus, μ, Biot's coefficient, α, Skempton's coefficient, B and Poisson's ratio, v. Biot's coefficient can be thought of as the ratio of increment of fluid content to change in bulk volume when pore fluid remains at constant pressure (drained condition), shown in Equation F3. Biot's coefficient is exactly one if all the bulk strain were due to pore volume change (i.e., the solid phase is incompressible). It is less than one for a compressible solid phase, because the change in bulk volume is greater than the change in pore volume by the amount of change in the solid volume (Biot and Willis, 1957, Nur and Byerlee, 1971). The Biot's coefficient varies between 0 and 1. The equation for Biot's coefficient can be derived:

$$\alpha = 1 - \frac{K}{K_g} \quad \text{(F3)}$$

where is K is the frame bulk modulus and K_g is the bulk modulus of the solid grain. It is also important to understand how pore pressure responds to a change in the mean stress under undrained conditions, which is introduced as Skempton's coefficient. In the undrained condition, fluid is constrained from flowing in and out of the material during deformation. Skempton's coefficient is nearly zero if gas fills the pores, as the load is supported by the frame; if water fills the pores, the coefficient is typically between 0.5 and 1.0, and 1.0 for fluid saturated soil and the load is supported by the fluid.

Using these constitutive relationships we can derive the equations that give the displacements induced in a poroelastic medium by a change in pore-fluid mass due to extraction or injection of fluid. Assuming the material can be treated as continuum and neglecting inertial forces, then conservation of linear momentum leads to the equilibrium equation of:

$$\frac{\partial \sigma_{ij}}{\partial x_j} - b_i = 0 \tag{F4}$$

where b_i is the external body forces, such as gravity. The kinematic relation between strain and displacement is:

$$\varepsilon_{ij} = \frac{1}{2}\left(\frac{\partial u_i}{\partial x_j} + \frac{\partial u_j}{\partial x_i}\right) \tag{F5}$$

The volumetric strain, ε_{kk} as a function σ_{kk} of can be written as:

$$\varepsilon_{kk} = \frac{\sigma_{kk}}{3K} + \frac{\alpha p}{K} \tag{F6}$$

By substituting Equations F6 and F5 to Equation F1, we can rewrite stress as a function of strain and pore pressure as:

$$\sigma_{ij} = \mu\left(\frac{\partial u_i}{\partial x_j} + \frac{\partial u_j}{\partial x_i}\right) + \frac{2\mu v}{(1-2v)}\frac{\partial u_k}{\partial x_k}\delta_{ij} - \delta_{ij}\alpha p \tag{F7}$$

The undrained Lamé parameter, λ_u can be related to Poisson's ratio, v and shear modulus, μ as:

$$\lambda_u = \frac{2\mu v}{(1-2v)} \tag{F8}$$

The equilibrium equation of F4 can be rewritten in terms of stress and strain by using the strain and displacement relation (F5) and the transformation in Equation F8, together with the constitutive equation (F1) to give the governing equation:

$$\frac{\partial}{\partial x_j}\left[\mu\left(\frac{\partial u_i}{\partial x_j}+\frac{\partial u_j}{\partial x_i}\right)\right]+\frac{\partial}{\partial x_j}\left[\lambda_u \frac{\partial u_k}{\partial x_k}\right]\delta_{ij}-\alpha\frac{\partial p}{\partial x_i}-b_i=0 \tag{F9}$$

Solving the forward problem in Equation (F9) requires finding the pore pressure distribution on the left hand side of the equation. This is achievable by combining Darcy's law with the conservation of fluid mass. For an isotropic material, ignoring body forces acting on the fluid, Darcy's law shows the fluid mass flux is a function of:

$$q_i = -\frac{\rho_0 k}{\eta}\frac{\partial p}{\partial x_i} \tag{F10}$$

where q_i is the fluid mass flux, k is the permeability, ρ_0 is the fluid density and η fluid viscosity. Conservation of fluid mass requires:

$$\frac{\partial q_i}{\partial x_i}+\frac{\partial m}{\partial t}=0 \tag{F11}$$

Combining these equations with a compatibility condition,

$$\nabla^2\sigma_{kk}+\frac{2\alpha(1-2v)}{(1-v)}\nabla^2 p=0 \tag{F12}$$

(Rice and Cleary 1973) yields a diffusion equation in fluid mass content as:

$$c\nabla^2 m=\frac{\partial m}{\partial t} \tag{F13}$$

where c is the hydraulic diffusivity which is a spatially variable function of porosity, permeability, fluid compressibility and fluid viscosity. As given in Rice and Cleary (1976), Equation F13 can be written to a diffusion equation in a linear combination of pore pressure and mean normal stress as:

$$c\nabla^2\left(\sigma_{kk}+\frac{3}{B}p\right)=\frac{\partial}{\partial t}\left(\sigma_{kk}+\frac{3}{B}p\right) \tag{F14}$$

These equations show the interaction between pore-pressure field and the strain field. A more comprehensive derivation of these equations can be found in Geertsma (1966) and Rice and Cleary (1976).

APPENDIX G

PUBLICATIONS

Wong M. Y., MacBeth, C., and Amini, H. (2017). Time-shifts Interpretation of legacy and frequent repeat seismic data in a compacting chalk reservoir. *79th EAGE Conference and Exhibition.*

Wong, M.Y., and MacBeth, C. (2016). R-factor Recovery via Geertsma's Pressure Inversion Assisted by Engineering Concepts. *EAGE Geophysics and Geomechanics, Jointly Applied to Subsurface Characterisation workshop.*

Wong, M.Y., JafarGandomi, A., MacBeth C., and Bertrand, A. (2015). Pressure and saturation change inversion using 4D seismic: Application to a chalk reservoir in North Sea, *SEG International Exposition and Annual Meeting.*

Wong, M.Y., MacBeth, C., and Bertrand, A. (2015). Engineering Consistent Constraints for the Inversion of Changes in Pressure and Saturation on Ekofisk. *77th EAGE Conference and Exhibition.*

Wong, M.Y., MacBeth, C., and Bertrand, A. (2015). Engineering Consistent Constraints for the Inversion of Changes in Pressure and Saturation on Ekofisk. *EAGE 4D Workshop: Getting the most out of 4D - from reservoir to surface*

Introduction

Time lapse seismic has over the last few years become a common practice in the reservoir management cycle. Benefits achieved by practical reservoir monitoring include reservoir model updating, drilling infill wells, and optimising production workflows. We will demonstrate some of the benefits of the extensive use of 4D seismic data in the development and characterisation of a chalk field; where 4D results add information key to characterisation of the rock physics model.

Our field of interest is a chalk field with reservoir rocks having high porosity, often exceeding more than 40% but with a low permeability rarely reaching more than 5 mD. Production is therefore enhanced through a system of natural and induced fractures allowing commercial production from the field. The field was originally developed by pressure depletion; and as a result of compaction the water bottom has subsided. Due to the strong geomechanical behaviour of the chalk, the time shift measurement is central to the field's 4D seismic interpretation. Both conventional legacy and 4D dedicated surveys were acquired in the field of interest, throughout the field's production period. The high repeatability surveys were acquired at least once a year, where the data shows high correlation with well activities. In comparison to the legacy data, the 3D seismic using modern frequent repeat survey shows clear signals with a side lobe reduction, and faults in the overburden that are better defined. Due to the short turn-around in acquisition and processing coupled with frequent monitoring, production changes are more evident from time-lapse signals and thus easier to be interpreted in the frequent repeat surveys. The value of information from frequent repeat surveys includes optimizing well locations and trajectories, suggesting well intervention, diagnosing mechanical issues and monitoring production impact such as injection, compaction, and overburden subsidence. Prior to quantitative interpretation of the data, we compared the noise floor for both legacy and frequent repeat data, where the noise floor from both data type are taken by the mean of all the surveys in an area in which it is relatively quiet from well activities. The noise floor in the legacy survey is expectedly higher than the modern frequent repeat data due to higher non-repeatability, by almost a factor of three. This helps to place higher uncertainties on the interpretation using legacy data.

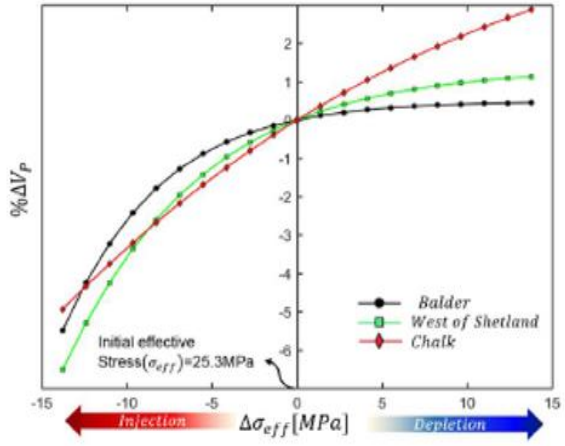

***Figure 1** P-wave velocity percentage change as a function of effective stress for chalk, West of Shetland and Balder sandstone.*

Stress Sensitivity

To estimate the pressure compliance of the dry rock frame, a pressure model from MacBeth (2004) is employed. Depending on the rock properties, each field has a very different stress sensitivity characteristics (Figure 1). For example, our field of interest which is a chalk is more stress sensitive than the West of Shetland sandstone. And in comparison, the West of Shetland sandstone is relatively

than the West of Shetland sandstone. And in comparison, the West of Shetland sandstone is relatively more stress sensitive than the Balder sands. The stress sensitivity is also dependent on the loading (depletion, pressure relaxation) and unloading (injection, shut in of a producer well) mechanisms and the initial effective stress. The rock is usually more stress sensitive at low effective stress and also in an unloading events such as injection compared to depletion. By calibrating these characteristics via rock mechanic testing, we can quantify how stress sensitive is the rock due to production changes and what percentage change will that manifest in P-wave or even S-wave velocities.

Reservoir Time Shift between legacy data vs. modern frequent repeat survey data

The attribute we will employ in our analysis is the reservoir time-shift, defined as the difference of top and base reservoir time shift. This was first analyzed in the Valhall field by Corzo (2012), with proven success. A positive reservoir time-shift is a speed-up attributed to compaction or impedance hardening. A negative reservoir time-shift is a slow-down due to dilation or impedance softening. The time-shift magnitude estimated from legacy and frequent repeat survey varies in both resolution and magnitude, with the legacy data recording a maximum of 20ms between the baseline and the first monitor acquired a decade later. This is due to significant geomechanical changes in the overburden resulting from pore collapse and chemical weakening of the chalk. The frequent repeat surveys recorded a high resolution time-shift with a maximum of +/- 1.5ms between surveys. A general understanding of the relationship between reservoir time-shift and various production mechanisms in our chalk field is depicted in Figure 2(a). The first quadrant is attributed to a hardening signal resulting from pressure increase and a change in saturation: water replacing oil, gas going back into solution or a combination of both. In the second quadrant the time-shift signal shows hardening corresponding to a decrease in pressure, which could be a result of pressure relaxation such as a reduction in injection activities, shutting in of an injector or a pressure depletion, which might occur when producing oil from the reservoir. This effect, coupled with water invasion, leads to water weakening which often creates enhanced compaction of the chalk. The third quadrant shows slowdown in time-shifts due to pressure reduction as a result of pressure falling below bubble point and gas being liberated from solution. Fluid replacement of an incompressible oil with highly compressible gas creates significant softening. In the fourth quadrant, a pressure increase, such as when injecting into the water leg, creates a softening signal, but at a lower magnitude compared to gas exsolution signals. If 4D responses are expected but none is recorded in the presence of production changes, this could be attributed to a cancellation between pressure and saturation changes. Our analysis of the data will be based on this conceptual model.

Figure 2(a) shows cross-plotting of the frequent repeat time shift data of the field and it can be observed that most of the points lie in the second and fourth quadrants, which are pressure driven. The time-shift data are derived from polygons around wells with strong 4D seismic anomalies. The data points on the cross plots are the mean 4D signal and the standard deviation of the reservoir time-shift. The large pressure variation from the injectors show a relaxation trend and a pressure build-up trend. Circled in black is a cluster of points that show small hardening signals due to pressure depletion from producer wells; this agrees with the general observations that a pressure depletion signal strength is often more difficult to detect than pressure build-up. The legacy reservoir time-shift data tells a very different story. With most data points plotted in the first quadrant, the 4D seismic signals from the legacy data period are mostly saturation dominated.

Updating stress sensitivity with 4D seismic data

Our aim is to reconstruct the observed time-shift signals in Figure 2 for both (a) frequent repeat data and (b) legacy data with a rock physics model. The rock physics model consists of a compaction model (Sylte et al., 1999), and a calibrated pressure model using data from rock mechanics measurements. We suspected hysteresis in the stress sensitivity curves, as we failed to reconcile our modelled time-shifts with the observed legacy data. In addition, a significant loading event prior to an unloading event suggested different stress sensitivity should be applied to the model. From production start up to the baseline, we have 18 years of primary depletion, which resulted in compaction of the

chalk. This essentially moves the stress sensitivity curve of the rock to a lower porosity curve. During the injection period that lasted 10 years after depletion (between baseline and monitor), pore pressure in the reservoir was expected to increase by about 5000 psi and more. A rock that has gone through an initial cycle of depletion followed by re-pressurisation becomes less stress sensitive compared to the same rock undergoing only injection, suggesting possible excess deformation due to internal defects from the first process (Holt, 2013). It was found that stress sensitivity was larger during the first unloading phase than the second unloading phase and post loading. This is possibly due to irreversible closing of cracks and mesoscale fractures. This understanding is tested in our rock physics modelling.

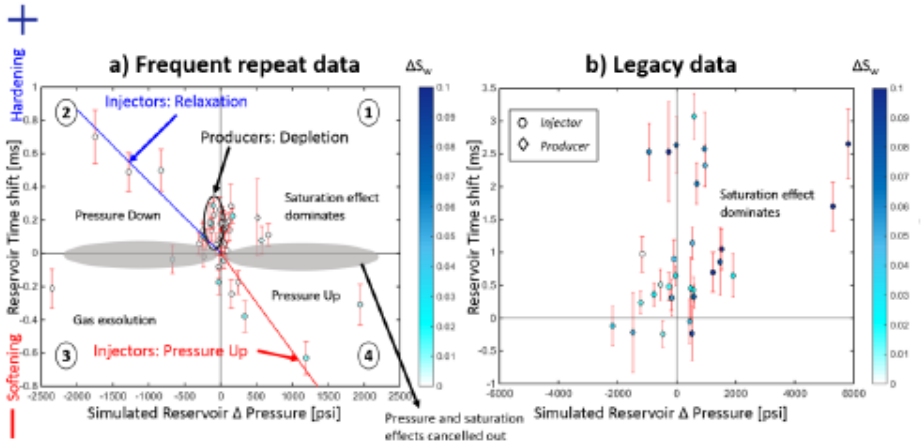

Figure 2 a) Cross-plotting of reservoir time-shift for frequent repeat data with reservoir pressure change overlaid with conceptual model predictions. b) Legacy data reservoir time-shifts versus reservoir pressure change.

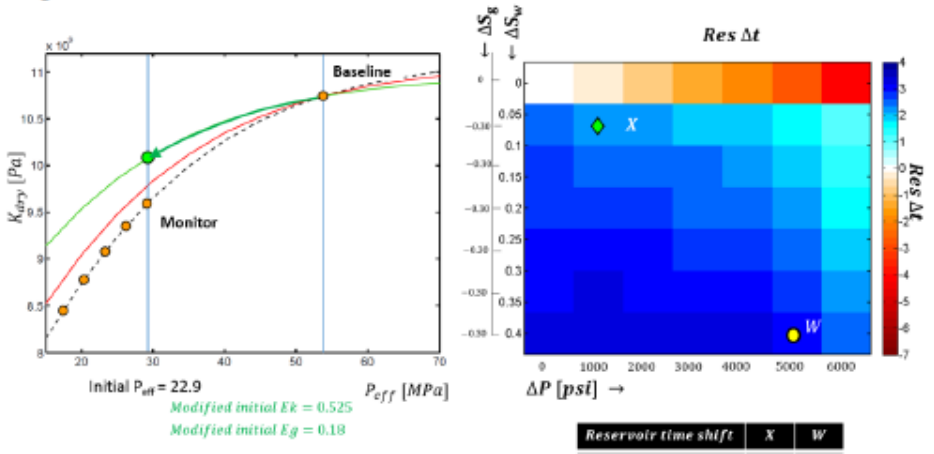

Reservoir time shift	X	W
Δt_{data} (ms)	2.5	2.65
Δt_{model} (ms)	2.33	2.95

Figure 3 (Left) Evolution of dry frame as a function of decrease in effective stress using modified stress sensitivity parameters. (Right) Reservoir time shifts modelling for well X and W. Bottom right table shows comparison between observed and modelled reservoir time shifts for well X and W.

We first implemented Holt's (2013) observations into our modelling, by lowering the stress sensitivity parameters in the MacBeth 2004 pressure model in an unloading scenario. This resulted in a marginal improvement in our modelled reservoir time-shift. However, since these parameters from Holt (2013)

were derived from experiments carried out on synthetic high porosity sandstone (mechanically similar to shallow, poorly cemented high porosity reservoir sand), we decided to modify the stress sensitivity unloading parameters further to match our observed reservoir time-shift. As a result of reducing the unloading parameters by 40% from their initial values (Figure 3 left – represented by green curve), our rock-physics modelling result shows a better agreement with the observed reservoir time shifts, showed in Figure 3(right). For the frequent repeat data, our modelling results are consistent with the observed reservoir time-shift recorded at the wells, in which the unloading (pressure increase) effect caused a stronger 4D reservoir time shift signal compared to loading (pressure relaxation). The 4D seismic data acquired after different production mechanisms provided us with a way to update the stress sensitivity parameters to accurately capture the loading and unloading characteristics of the chalk.

Conclusions

There is a strong correlation between time-lapse time-shift and the different production mechanisms in the field. The pursuit of understanding the reservoir level signature is an important one, in order to achieve that, we need to have a good handle on the different parameters that can affect the predictions of the reservoir signals via a rock physics model. Of all the parameters of the petro-elastic model, the rock stress sensitivity is the one which carries the highest uncertainty: the main reason for this is the difficulty of measuring this parameter using core samples. Core damage, frequency dispersion, geomechanical effects and the selection the effective stress coefficient could lead to underestimation of the rock stress sensitivity, whereas the rock drying processes, the presence of shales, imperfect stress recovery and stress asymmetry could lead to overestimating it. In the work, we showed how hysteresis or imperfect stress recovery could lead to overestimation of the unloading behavior of the rock, resulting in a lower speed up estimation for the reservoir time shifts attribute.

Acknowledgements

The authors would like to thank the sponsors of the Edinburgh Time-Lapse Project Phase V and VI (BG, BP, CGG, Chevron, ConocoPhillips, ENI, ExxonMobil, Hess, Ikon Science, Landmark, Maersk, Nexen, Norsar, OMV, Petoro, Petrobras, RSI, Shell, Statoil, Suncor, Taqa, TGS and Total) for supporting this research.

References

Corzo, M., MacBeth, C. and Barkved, O. [2012]. Estimation of pressure change in a compacting reservoir from time-lapse seismic data, *Geophysical Prospecting*. **61**(5), 1022-1034.

Holt, R. M. and Stenebråten, J. F. [2013] Controlled laboratory experiments to assess the geomechanical influence of subsurface injection and depletion processes on 4D seismic responses. Geophysical Prospecting, **61**. 476–488.

MacBeth, C., 2004. A classification for the pressure-sensitivity properties of a sandstone rock frame. *Geophysics*, 69(2), pp. 497-510.

Sylte, J.E., Thomas, L.K., Rhett, D.W. et al. [1999] Water Induced Compaction in the Ekofisk Field. *SPE Annual Technical Conference and Exhibition*, Houston, Texas, 3–6 October. SPE-56426-MS.

VIENNA 2016
30 May - 2 June 2016 | Messe Wien

WS14 B02

R-factor Recovery via Geertsma's Pressure Inversion Assisted by Engineering Concepts

M.Y. Wong* (Heriot-Watt University) & C. MacBeth (Heriot-Watt University)

SUMMARY

A technique is developed for a North Sea chalk reservoir to estimate the Hatchell-RØste R factors using a reservoir engineering constraint. This provides a way of defining the uncertainty on the R values, given the range of mechanical properties for the field of interest.
In our case study the average R for the reservoir and overburden appears to be in the range 7 to 22. R factors are also calculated for regions of pressure relaxation and drawdown identified in the field, and the results confirm the current understanding determined by laboratory experiment and previous studies that the magnitude varies as a function of strain polarity, with the asymmetry being at most a factor of three. These results are validated with full geomechanical modelling followed by time shift modelling, showing that the observed time shifts cannot be created unless this asymmetry is present

Introduction

Production or injection of fluid volumes in a hydrocarbon reservoir leads to subsurface deformation and changes in the strain state not only of the reservoir, but also the surrounding rocks. It has been demonstrated in several field studies that summation schemes based on Geertsma's analytical solution are capable of modelling this strain distribution (e.g. Toomey et al. 2015), and also inverting for changes in reservoir pressure from time-shifts measured by time-lapse seismic data (Hodgson et al. 2007). These schemes provide a simple yet effective approach for tackling the small to moderate magnitude strains detected in many applications of time-lapse seismic data. Following this approach, this current study utilises time-lapse seismic signals in the overburden to estimate vertical strain, and thus invert for reservoir pressure changes at a chalk field in the Norwegian Sea. We find that one benefit of using the Geertsma based inversion is that R-factors can be quantified when prior constraints are available from a well history matched simulation model, and their uncertainty defined. Our results indicate that the magnitude of R is a function of strain change polarity, and that this is indeed necessary to simulate the observed time shifts.

Theory and method

Our starting point is the work of Hodgson et al. (2007) and Garcia and MacBeth (2013), who developed a method for estimating reservoir pressure changes ΔP from measured volumes of seismic time-shifts in the overburden. Central to these methods is the Geertsma (1973) nucleus of strain model that is used to calculate total subsurface displacement by superimposing the influence of many such pressure contributions (see for example Segall 1992). This problem is solved numerically as a system of linear equations by summing contributions from pressure sources on a grid weighted according to a known set of Green's functions, G_{ij}, dependent on the location of the individual sources, and also on the average shear modulus and Poisson's ratio of the subsurface. The equation (1) links each estimated vertical strain $\varepsilon_{zz,i}$ in a cellular volume of M cells to the reservoir changes ΔP_j in a grid of N cells

$$\varepsilon_{zz,i} = \sum_{j=1}^{M} G_{ij} \Delta P_j . \qquad (1)$$

To relate vertical strain changes to the fractional velocity changes, and hence measured time-shifts, the R factor model of Hatchell and Bourne (2005) is now commonly employed. These factors can be measured directly in the laboratory (Holt et al. 2013) or inferred by comparing measurements from observed 4D seismic data to modelled geomechanical deformations (Hatchell et al. 2003), but consensus on the exact values to use has not yet been reached and they may still be considered uncertain. Unlike full geomechanical simulation, the formulation in (1) provides an opportunity to close the loop between the measured time shifts and pressure changes in a quick modelling and inversion study. It is then possible to build up statistics to quantify the R factors by using some knowledge of the pressure changes from a well-conditioned simulation model as a constraint, combined with a range of subsurface mechanical properties. The simulator honours material balance in the reservoir and is adequately matched to the historical well data via history matching. Therefore it is assumed that the resultant pressure predictions are at least statistically accurate, and should possess more accuracy than an R factor guess for a particular field. The R factors are determined by scaling the pressure change solution such that the histograms of pressure estimated from the inversion scheme and the predictions from the simulator coincide.

Application to a chalk field

The above methodology is applied to a geomechanically active chalk reservoir. During the seismic monitoring period, injection is carried out for pressure maintenance and an understanding of pressure changes will help to understand the overall performance of the wells. The pressure inversion is

applied to both seismic vintages acquired two and a half years apart. For input into the inversion, time-shifts are selected at four horizons in the overburden. Figure 1(a) shows the time shifts in the overburden interval above the reservoir. These horizons are chosen based their distance from the reservoir, the need to include as much data as possible, and the signal to noise ratio at each. As in previous implementations, the inversion is solved using a standard least squares objective function with a smoothing constraint (but no constraint from the simulation model predictions) – the typical

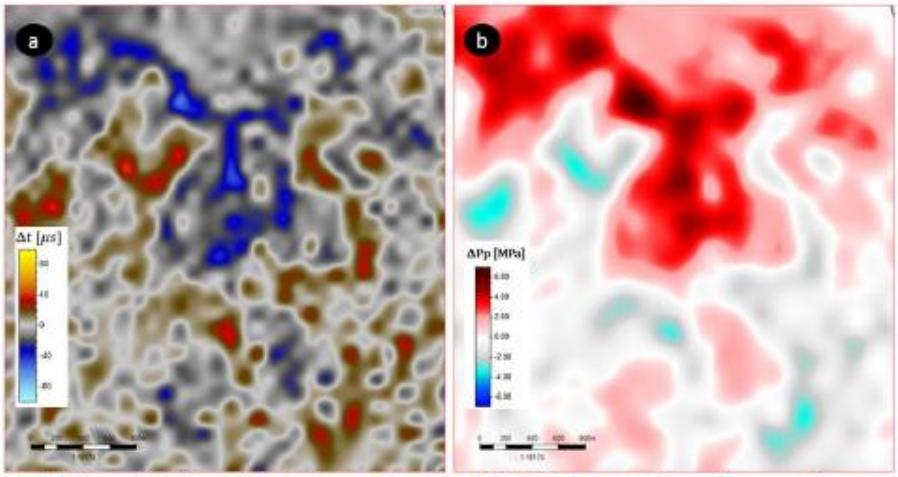

Figure 1 Maps of (a) time shifts in the overburden and (b) the Geertsma inverted reservoir pressure change. In (a), red signals signify an increase in travel time, or expansion, whilst the blue signals indicate a decrease in travel time, or compaction.

result for an average R-factor is displayed in Figure 1(b). According to the Geertsma formulation, the inverted pressure change also scales with the choice of the shear modulus and Poisson's ratio assigned to the average half-space representing the reservoir and overburden. This therefore poses an interesting possibility: the best choice R factor can be found by performing many inversions for different combinations of shear modulus (μ) and Poisson's ratio (υ), and then finding the R that matches the estimates to the simulator predictions (matching the means of the histograms). In this case study a range of lithology dependent mechanical properties are available from the Valhall field (Zhang et al. 2011). A half-space consisting of 100% shallow shale (μ=0.10GPa and ν=0.20), soft chalk (μ=0.56GPa, υ=0.17), compacted shale (μ=0.58GPa, υ=0.25), and stiff chalk (μ=1.86GPa, υ=0.19) are all considered initially, together with a range of properties between these end points. The inversion with scaling adjustment gives R factors of 127, 19, 22 and 7 for the four end member property pairs however a half-space of all shallow shale is considered unlikely. The spread of R factors recovered for different material properties helps define a range of possible uncertainty (see dotted black line in Figure 2). The final result in Figure 1(b) is determined by using a property average that is an equal weighting of all four end-points (G=0.78, υ=0.20), for which an R factor of 16 is recovered.

Hatchell and Bourne (2005) proposed an asymmetric R as a function of strain polarity as a way of interpreting the magnitude of the observed time shifts with different observed strain deformations. Rocks that are undergoing an extensional strain change (often in overburden rocks) show larger fractional velocity changes in comparison to regions with those undergoing compressive strain changes (often, but not exclusively, in the reservoir). This behaviour is also similar to that observed in laboratory measurement. For example Holt et al. (2013) find that the R factor of a rock that has gone through an initial cycle of depletion followed by re-pressurisation is different compared to the same

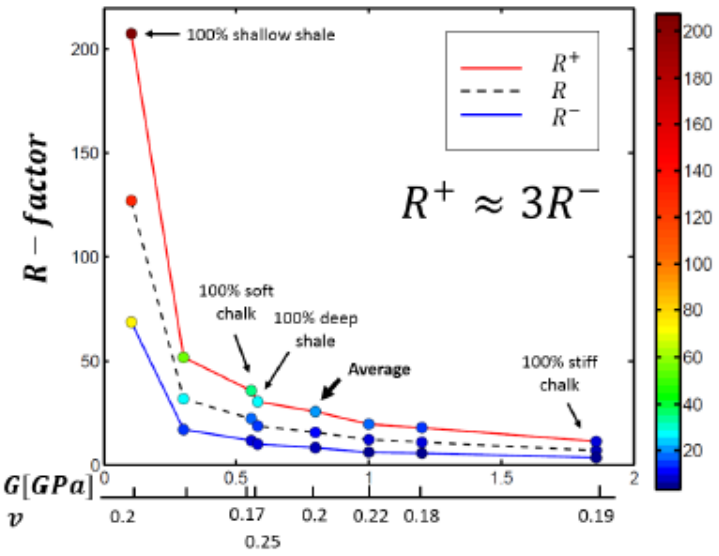

Figure 2 R factor results corresponding to the different lithologies in our field study.

rock undergoing only injection; suggesting possible excess deformation due to internal defects from the first process. This understanding can be tested in our current dataset by selecting two regions with different production/recovery mechanisms, predominantly influenced by either reservoir depletion or pressurisation. R factors are calculated by independent inversion of each region, using the average mechanical properties from the previous study. In order to ensure minimal overlap between these areas of pressure up and down, the regions are selected around wells. The results of this process are also shown in Figure 2, these indicating that the R for expansion (R+) is 3 times larger than that for compression (R-) – a similar asymmetry to that quoted in the previous publications. To validate this finding for our particular field, time shift modelling is performed using a synthetic fluid flow simulation and a full geomechanical model with similar properties to the field. The flow simulation model consists of two injectors and one producer with similar production history to the actual wells. For the geomechanics, the reservoir model is fully encased in a shale overburden, sideburden and underburden. Mechanical properties are assigned according to Zhang et al. (2011). The time-shifts are calculated by converting physical strain to velocity change, assuming both symmetric and asymmetric R factors. Figure 3(a) gives the results for R+ = R-, and Figure 3(b) for the case of R+=3R determined from our previous findings. The asymmetric R factors produce time shifts that appear more consistent with the real field observations. A positive time shift is generated below the reservoir, implying a strong accumulation of time shift in the overburden relative to that in the compacting reservoir. This would not be the case unless the R factor is asymmetric.

Conclusions

A technique is developed for estimating R factors using a reservoir engineering constraint. This provides a way of defining the uncertainty in the R factor, given a range of mechanical properties for the field of interest. Based on the mechanical stratigraphy in our field case, R may lie in the range 22 to 7. Application to selected regions of our field with predominantly expansion or compression in the overburden provides a measure of the R factor asymmetry and confirms that R+ is greater than R-, in agreement with both previous laboratory and seismic data analyses.

Acknowledgements

The authors thank the sponsors of the Edinburgh Time-Lapse Project Phase V and VI (BG, BP, CGG, Chevron, ConocoPhillips, ENI, ExxonMobil, Hess, Ikon Science, Landmark, Maersk, Nexen, Norsar, Petoro, Petrobras, RSI, Shell, Statoil, Suncor, Taqa, TGS and Total) for supporting this research.

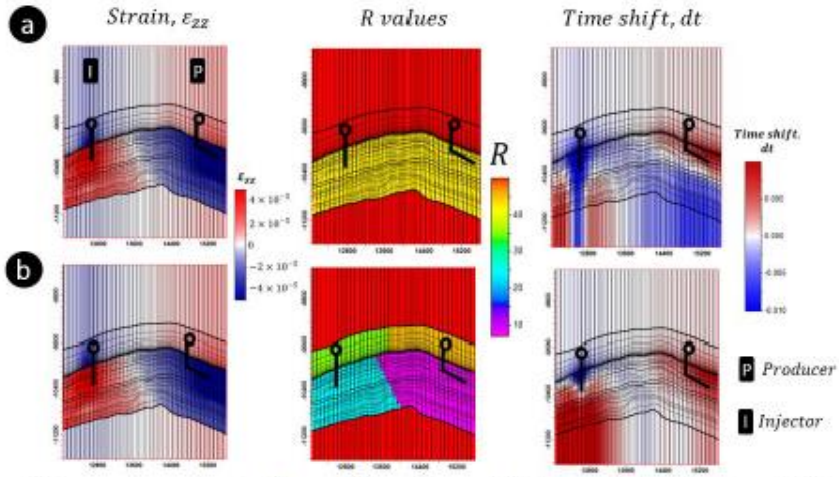

Figure 3 Cross sections showing the modelling of time shift from vertical strain extracted from a synthetic geomechanical model using (a) R+ = R- and (b) R+=3R-.

References

Garcia, A. and MacBeth, C. [2013] An estimation method for effective stress changes in a reservoir from 4D seismics data. Geophysical Prospecting, **61**. 803–816.

Geertsma, J. [1973] Land subsidence above compacting oil and gas reservoirs: Journal of Petroleum Technology 25, no. 06, 734–744.

Hatchell, P, van den Beukel, A., Molenaar, M. M., Maron, K. P., Kenter, C. J., Stammeijer, J. G. F., Sayers, C. M. [2003] Whole Earth 4D: Reservoir Monitoring Geomechanics. *73rd SEG Annual International Meeting*, Expanded Abstracts

Hatchell, P. and Bourne, S. [2005] Measuring reservoir compaction using time-lapse timeshifts, *75th SEG Annual International Meeting*, Expanded Abstracts

Hodgson, N., MacBeth, C., Duranti, L., Rickett, J., and Nihei, K. [2007] Inverting for reservoir pressure change using time-lapse time strain Application to Genesis Field Gulf of Mexico. The Leading Edge, 26:649.

Holt, R. M. and Stenebråten, J. F. [2013] Controlled laboratory experiments to assess the geomechanical influence of subsurface injection and depletion processes on 4D seismic responses. Geophysical Prospecting, **61**. 476–488.

Segall, P. [1992] Induced stresses due to fluid extraction from axisymmetric reservoirs. Pure and Applied Geophysics, 139(3):535–560.

Toomey, A., Robinson, N., and Kristiansen, T. G. [2015] A workflow for rapid modelling of production-related geomechanical changes and 4D time-shifts. *85th SEG Annual International Meeting*, Expanded Abstracts

Zhang, X., Koutsabeloulis, N. C., Kristiansen, T. G., Heffer, K. J., Main, I., Greenhough, J., and Hussein, A. M. [2011] Modeling Of Depletion Induced Micro-Seismic By Coupled Reservoir Simulation - Application To Valhall Field. SPE 143378

Pressure and saturation change inversion using 4D seismic: Application to a chalk reservoir in North Sea.

Ming Yi Wong, Heriot-Watt University, Arash JafarGandomi, CGG, Colin MacBeth, Heriot-Watt University, Alex Bertrand, ConocoPhillips Skandinavia AS, Henning Hoeber, CGG*

Summary

A comparative study is carried out between a deterministic and a stochastic approach via Bayesian McMC to obtain estimates of changes in pressure and saturation. The aim is to provide insights into well performance and pressure distribution within a geo-mechanically active chalk reservoir (Ekofisk). Uncertainty of such predictions is usually high; henceforth the solution of such an inverse problem is not limited to a single set of predicted parameters but represented by a probability density function on the model space. Both inversion approaches are similarly constrained by reservoir engineering concepts and predictions. We show that the Bayesian framework provides a suitable platform to incorporate data uncertainties and prior information. Quantitative interpretation on this field using the inversion results shows good agreement with well production data and helps to explain strong localized anomalies in both the Ekofisk and Tor formations.

Introduction

Time-lapse (4D) seismic has now become commonplace in oil and gas field development. One branch of active research is the evolution of quantitative estimation of pressure and saturation changes from 4D seismic signals. Such dynamic properties have important implications in reservoir characterization such as optimizing well production and injection rate, placement of new wells, and the prevention of mechanical failures. The method presented here not only yields such properties but can also assist applications such as seismic history matching and model updating. However, one needs to ensure that a forward model can adequately describe time lapse elastic properties as a function of the dynamic reservoir parameters, and that the inverted dynamic properties are realistic and engineering consistent (EC).

In this study, an inversion was performed on the 4D geophysical parameters: relative changes in elastic properties and time shift measurements, into variations in pressure and saturation. The key difference between this inversion scheme and existing inversion methods lies in the characteristics of the reservoir itself. Ekofisk is a compacted chalk reservoir, which is not only subject to dry compaction but also water weakening; this behavior is taken into account in our forward model. Most importantly, the inversion is constrained with reservoir engineering predictions, which helps reduce the non-uniqueness involved and maintains consistency with the physics of flow.

The Ekofisk field is a remarkable example of compacted chalk field. It is a four way dip anticline and produces oil and gas from naturally fractured chalk reservoirs of the Maastrichtian (Tor) and Danian (Ekofisk) Formations. The reservoir thickness, which is around 300m on average is more prominent in the crestal area and thins towards the flanks. The reservoir has high porosity and low matrix permeability. As captured in Figure 1, during early production by pressure depletion, pressure was close to bubble point; gas exsolution and compaction of the reservoir were extensive. As part of the effort to increase productivity, a full field water injection programme was put on stream which increased oil production rate, stabilized field pressure; but also resulted in the water weakening of chalk. The permanent reservoir monitoring system initiated in 2010 was an effort to allow 4D seismic data for reservoir surveillance to optimize new well locations and trajectories, priorities well interventions, as well as update the reservoir model and monitor the overburden (Bertrand et al. 2013). The inversion is applied to the second and the sixth of the LoFS (Life of Field Seismic) surveys acquired two and a half years apart.

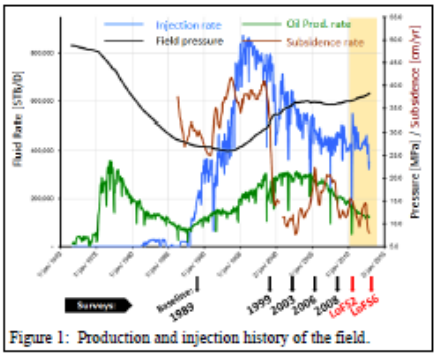

Figure 1: Production and injection history of the field.

Methodology

This is a continued effort from Corzo et al. (2013) where initial porosity was considered as an important factor in inverting for pressure depletion in the Valhall field. In the

DOI http://dx.doi.org/10.1190/segam2015-5813716.1

usual way, impedances are modelled by a petro-elastic model to convert dynamic parameters from the simulation model. The modelled impedance is thereafter compared to the observed impedance. This rock physics model requires extensive calibration and also the exhaustive modelling of various data to describe the rock and fluid properties. To overcome this, a fast-track forward modelling equation (proxy model) is proposed to capture the relationship between the percentage change in impedance and dynamic changes (Wong et al., 2015). The proxy model is derived analytically through modelling and reverse engineering of synthetic data. To compute the percentage changes in impedance, the proxy model requires a set of calibrated coefficients from the petro-elastic model (coefficients a_1, b_1 and c_1), changes in pressure and saturation (ΔP and ΔSw) and compaction curves from the laboratory expressed as a functions of initial porosity (F_{ww} and F_p). Sw_{max} is the maximum attainable water saturation before the chalk is consider fully wet. The proxy model is comprised of three distinct terms: a pressure term, a saturation term and a cross term between pressure and saturation that describes the water weakening behavior of the chalk. The equation of the proxy model is given in equation [1]:

$$\%\frac{\Delta Ip}{Ip} = a_1\Delta P - b_1\left[F_p + \left(\frac{\Delta S_w}{\Delta S_{w\max}}\right)(F_{ww} - F_p)\right]\Delta P + c_1\Delta S_w \qquad [1]$$

The strength of this equation is that it leads to an accelerated estimation of the impedances. Most importantly, it is now amenable to linearized inversion, and as a consequence the inversion has a less complicated solution space. Finally, it also provides an intuitive relationship between data and model, essential to quality control the results.

Bayesian inversion strategy

The problem under investigation is to make inference about changes in pressure and saturation at each spatial location, using multiple time-lapse geophysical data (D) with different levels of uncertainties. The hyper-parameters are parameters necessary to arrive at a solution but are of no direct interest to the inference problem, such as the coefficients in the proxy model and compaction curves; these are denoted as H.

Bayes theorem (Bayes, 1763) provides a robust framework to address the uncertainties in the data and assimilate the prior information into the inversion problem. In this framework the solution to the inverse problem is represented by a posterior probability density function (pdf), over the model parameters (Tarantola, 2005),

$$p(\Delta P, \Delta S_w|D) = \frac{p(\Delta P, \Delta S_w, H|x)p(D|\Delta P, \Delta S_w, H)}{p(D|x)} \qquad [2]$$

where $p(\Delta P,Sw,H|x)$ indicates prior pdf. Incorporating prior information (x) can significantly expedite the convergence of inversion process towards the most probable solution in the model space. Here we incorporate the prior information into the inversion problem through EC constraints. The source of prior information is given from the history matched simulation model.

The first EC constraint imposed is in the water leg. No change was observed in saturation in the water leg from pre-production to current state; hence it is only logical to assume no changes in saturation, and a possible presence of subtle pressure signal in the water leg. An inequality constraint (above water-leg, $-0.10 \leq S_w \leq 0.5$) was applied, with the upper and lower boundaries extracted from simulation model statistics. For the second EC constraint, the solution space close to well perforations was constrained using a 3D Gaussian kernel; imposing tight upper and lower bounds for changes in pressure and saturation as estimated from the reservoir simulation. These constraints are realistic given that the model is relatively well history matched.

We use a multivariable Gaussian pdf to describe the likelihood $p(D|\Delta P,Sw,H)$,

$$p(D|\Delta P, \Delta S_w, H) = \frac{1}{\sqrt{2\pi|\Sigma_i|}}\exp\left\{-\frac{1}{2}[D_i - f_i(\Delta P, \Delta S_w)]^T \Sigma_i^{-1}[D_i - f_i(\Delta P, \Delta S_w)]\right\} \qquad [3]$$

where $\sum_i$ represent the uncertainties in the i^{th} data with a diagonal covariance function $\sum$, f_i is the forward modelling procedure represented by our proxy model equation. We account for the uncertainties in the geophysical data by calculating the standard deviation of the geophysical data based on the NRMSD or energy in the difference cube from a 1s gate in the overburden. The NRMSD is often used as a quality control of seismic data and to assess noise levels. Data uncertainties are essential in the inversion procedure whereby they act also as regularisation term in the objective function.The posterior pdf is a two-dimensional pdf for pressure and saturation changes generated using a Markov-chain Monte Carlo method. We sample the posterior pdf via the Metropolis method which is a McMC algorithm. A description of the algorithm can be found in (JafarGandomi & Curtis, 2012).

Implementation of Bayesian inversion

Firstly, data across domains were reconciled into a common grid. The starting model is from the smooth history matched simulation prediction. We also set up the

DOI http://dx.doi.org/10.1190/segam2015-5813716.1

EC constraints as spatial bounds in the inversion workflow to yield realistic estimates of changes in pressure and saturation. The deterministic approach is carried out by assigning constant weights on different geophysical parameters that carry information on uncertainties in the data, which also determines the relative contributions of each individual dataset to the joint objective function.

The stochastic approach involves a spatially varying uncertainty estimated from the non-repeatability of the overburden. The posterior distribution is explored by 15,000 iterations with a Metropolis algorithm with a burn-in period of 5000 iterations. Both methods yield volumetric pressure and saturation changes. The first pass results informed us that the misfit is high for some wells due to slightly poorer match between the production data and the simulated prediction, and could bias the solution. Hence we loosen the EC constraints around such wells for both pressure and saturation respectively as a hierarchical updating approach to reduce the misfit.

Results and Interpretation

In this section, we compare and contrast between the stochastic and deterministic approach. In Figure 2 the comparison for changes in pressure and saturation were highlighted; the stochastic result shows the posterior median solution obtained from the simulations after a period of burn-in. Both methods consistently estimated similar anomalies across the Ekofisk formation, with marginal differences. The posterior uncertainty is represented by one standard deviation around 2MPa for pressure and a fraction of 0.05 for water saturation. Large uncertainties are estimated at regions where there is a considerable misfit between seismic observation and the simulation model prediction. These regions also indicated a lower level of confidence in the estimates.

The next focus is to use the inverted results to explain some of observations close to wells on an area of the field with very interesting 4D seismic signals. Figure 3 depicts a cross section along 4 wells (I2, P1, P2 and P3) for time strain, changes in amplitude, percentage changes in elastic properties, inverted pressure and saturation changes and the associated standard deviation. The inversion informed us of an anomalous pressure increase along the injector I2 and slight pressure drop along producer P2. Water was shown to be encroaching towards P2. Production data indicated a steady increase in water cut, and an increase in gas production rate in P2, inferring a drop in pressure and that water from the nearby injectors could have invaded the producer, which is consistent with the inversion results. The water cut in P2 is also shown in PLTs acquired in 2006, showing a good 55% contribution from TA (first reservoir unit within the Tor formation). This connectivity between injector and producer was not predicted by the simulator but shown in the seismic data. We support our arguments by cross checking with the production data made available such as RFT and downhole pressure gauge measurements acquired every six months. The RFT data shows that injector I2 was originally water flooded; hence the 4D signals are predominantly pressure driven. Production data also demonstrated that the injectors were put on stream after LoFS2, and injected at a high constant rate; the inversion shows an increase in pressure greater than 10MPa.

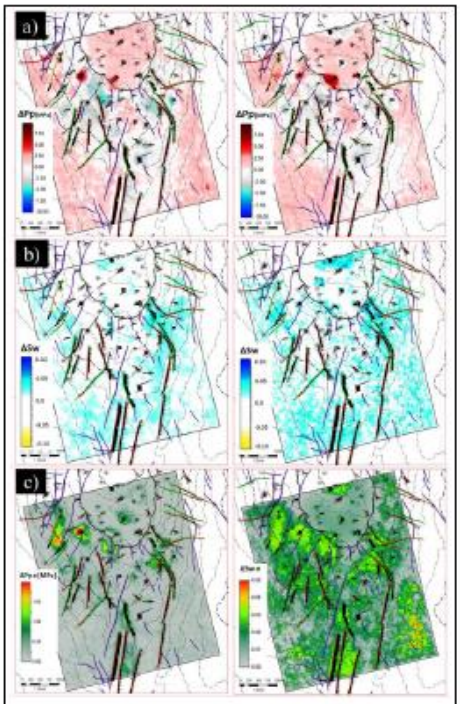

Figure 2: Comparison between deterministic (left) and stochastic (right) results for both changes in pressure (a) and saturation (b). 2(c) shows the posterior standard deviation after stochastic inversion, which also coincides with areas of the largest misfit.

Conclusions

The decomposition of pressure and saturation changes is crucial to explain different physical variables that contributed to similar 4D seismic differences.

DOI http://dx.doi.org/10.1190/segam2015-5813716.1

The inversion process is notorious for being non-unique and by employing a stochastic approach; it provides us with a measure of uncertainty. The data uncertainties and constraints are of special interest since they both influence the convergence and outcome of the inversion process. The resulting changes of dynamic properties from both deterministic and Bayesian inversion methods are similar and both show improvement from the history matched flow-simulation model. Quantitative interpretation of this field using the inversion results have good agreement with well production data, and help explain strong localized anomalies in both the Ekofisk and Tor formations

Acknowledgement: The authors would like to thank the sponsors of the Edinburgh Time-Lapse Project Phase V (BG, BP, CGG, Chevron, ConocoPhillips, ENI, ExxonMobil, Hess, Ikon Science, Landmark, Maersk, Nexen, Norsar, Petoro, Petrobras, RSI, Shell, Statoil, Suncor, Taqa, TGS and Total) for supporting this research. Special thanks to ConocoPhillips Skandinavia AS and the PL018 Partnership (Total E&P Norge AS, ENI Norge AS, Statoil Petroleum AS and Petoro AS) for their permission to publish this work. Special gratitude goes to Carlos Pacheco, Jean De Lanlay, Evgeny Tolstukhin and Reidar Midtun. Appreciation also goes out to Ilya Fursov for useful discussions.

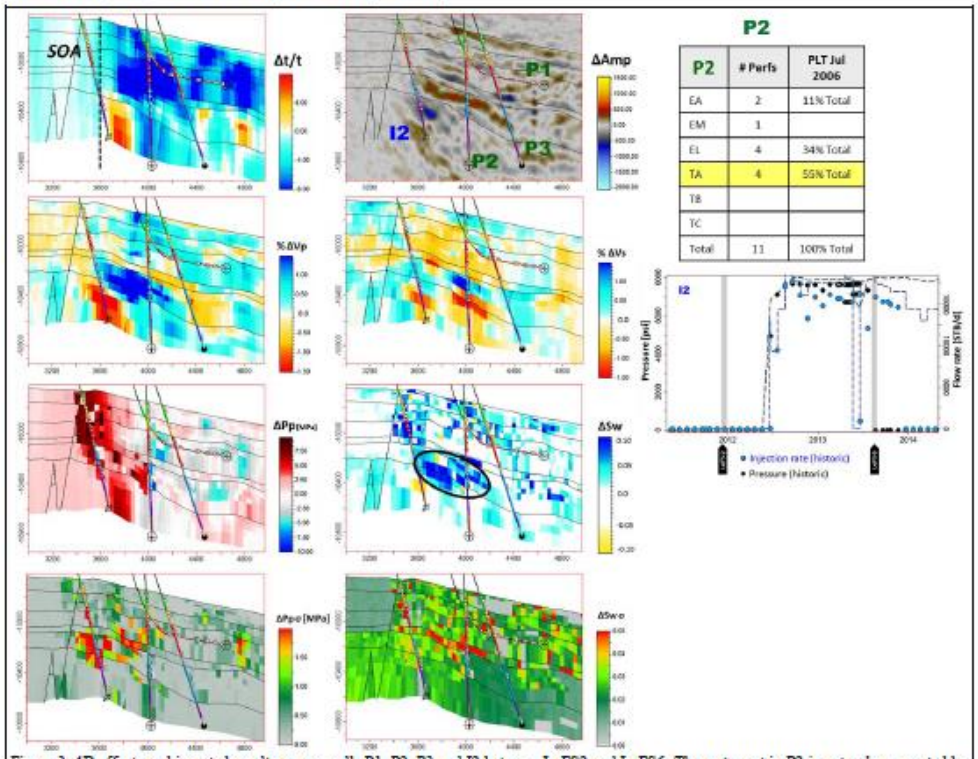

P2	# Perfs	PLT Jul 2006
EA	2	11% Total
EM	1	
EL	4	34% Total
TA	4	55% Total
TB		
TC		
Total	11	100% Total

Figure 3: 4D effects and inverted results across wells P1, P2, P3 and I2 between LoFS2 and LoFS6. The water cut in P2 is not only supported by production data but also in the PLT acquired in 2006. The increased in water saturation (circled in black) is also shown in the TA perforation. The number of perforations and the individual contributions at each interval is given in the table located at the top right. Production data for I2 between LoFS2 and LoFS6 shows the injection and pressure rate history; this is consistent with the pressure anomaly around I2.

DOI http://dx.doi.org/10.1190/segam2015-5813716.1

EDITED REFERENCES

Note: This reference list is a copyedited version of the reference list submitted by the author. Reference lists for the 2015 SEG Technical Program Expanded Abstracts have been copyedited so that references provided with the online metadata for each paper will achieve a high degree of linking to cited sources that appear on the Web.

REFERENCES

Bayes, T., and M. Price, 1763, An essay towards solving a problem in the Doctrine of Chances. By the late Rev. Mr. Bayes, F.R.S. communicated by Mr. Price, in a letter to John Canton, A.M.F.R.S: Philosophical Transactions, **53**, 370–418, http://dx.doi.org/10.1098/rstl.1763.0053.

Bertrand, A., P. G. Folstad, A. Grandi, G. Jeangeot, H. Haugvaldstad, B. Lyngnes, R. Midtun, and N. Haller, 2013, The Ekofisk Life of Field seismic (LoFS) system — Experiences and results after two years in operation: 75th Conference & Exhibition, EAGE, Extended Abstracts, doi:10.3997/2214-4609.20130424.

Corzo, M., C. MacBeth, and O. Barkved, 2013, Estimation of pore-pressure change in a compacting reservoir from time-lapse seismic data: Geophysical Prospecting, **61**, no. 5, 1022–1034, http://dx.doi.org/10.1111/1365-2478.12037.

JafarGandomi, A., and A. Curtis, 2012, Assessing the monitorability of CO_2 saturation in subsurface saline aquifers: International Journal of Greenhouse Gas Control, **7**, 244–260, http://dx.doi.org/10.1016/j.ijggc.2011.10.015.

Tarantola, A., 2005, Inverse problem theory and methods for model parameter estimation: Society for Industrial and Applied Mathematics, http://dx.doi.org/10.1137/1.9780898717921.

Wong, M. Y., C. MacBeth, and A. Bertrand, 2015, Engineering consistent constraints for the inversion of changes in pressure and saturation on Ekofisk: 77th Conference & Exhibition, EAGE, Extended Abstracts, WS02, http://dx.doi.org/10.3997/2214-4609.201413464.

DOI http://dx.doi.org/10.1190/segam2015-5813716.1

MADRID 2015
1-4 June 2015 | IFEMA Madrid

Th N101 03

Engineering Consistent Constraints for the Inversion of Changes in Pressure and Saturation on Ekofisk

M.Y. Wong* (Heriot-Watt University), C. MacBeth (Heriot-Watt University) & A. Bertrand (ConocoPhillips Norge)

SUMMARY

A high resolution, time lapse seismic inversion into pressure and saturation changes is performed. This provides insights into well performance and pressure distribution within a geo-mechanically active chalk reservoir (Ekofisk). The inversion is constrained by reservoir engineering concepts and predictions to reduce the non-uniqueness involved, and to maintain consistency with the physics of flow. At the heart of this inversion scheme is the effective union of engineering data and different seismic products such as reservoir time strain, percentage changes in elastic properties to influence the inversion. Quantitative interpretation on this field using the inversion results shows good agreement with well production data and helps to explain strong localised anomalies in both the Ekofisk and Tor formations. Analysis shows that the hardening signals around producers are due to lack of pressure support and reservoir compaction; whereas softening signals are attributed to high pressure flooding around injectors.

Introduction

Time-lapse (4-D) seismic has now become commonplace in oil and gas field development. One branch of active research is the evolution of quantitative evaluations and extraction of pressure and saturation changes from 4D seismic signals. Such dynamic properties have important implications in reservoir characterisation such as optimizing well production and injection rate, placement of new wells, and the prevention of mechanical failures. The method presented here not only yields such properties but can also assist applications such as seismic history matching and model updating. However, one needs to ensure that a forward model can adequately describe time lapse elastic properties as a function of the dynamic reservoir parameters, and that the inverted dynamic properties are realistic and engineering consistent (EC).

In this study, an inversion was performed on the 4D seismic data, in the form of percentage changes in elastic properties and time shift measurements, into variations in pressure and saturation for a geo-mechanically active chalk reservoir. The key difference between the recommended inversion scheme and existing inversion methods lies in the characteristics of the reservoir itself. Ekofisk is a compacted chalk reservoir, which is not only subject to dry compaction but also water weakening. The inversion is guided by a smooth starting model and associated weights from available seismic products. Most importantly, the inversion is also constrained with reservoir engineering predictions, which helps reduce the non-uniqueness involved and maintains consistency with the physics of flow.

The Ekofisk field is a remarkable example of compacted chalk field. It is a four way dip anticline and produces oil and gas from naturally fractured chalk reservoirs of the Masstrichtian (Tor) and Danian (Ekofisk) Formations. The reservoir thickness, which is around 300m on average is more prominent in the crestal area and thins towards the flanks. The reservoir has high porosity and low matrix permeability. During early production by pressure depletion, pressure was close to bubble point; gas exsolution and compaction of the reservoir were extensive. As part of the effort to increase productivity, a full field water injection programme was put on stream which increased oil production rate, stabilised field pressure; but also resulted in the water weakening of chalk. The permanent reservoir monitoring system initiated in 2010 was an effort to allow 4D seismic data for reservoir surveillance to optimise new well locations and trajectories, suggest and prioritise well interventions, as well as update the reservoir model and monitor the overburden (Bertrand et al. 2013). The inversion is applied to the second and the sixth of the LoFS (Life of Field Seismic) surveys acquired two and a half years apart. The main focus area is the south west part of the field.

Methodology and Inversion Workflow

This is a continued effort from Corzo et al. (2013) where initial porosity was considered as an important factor in inverting for pressure depletion in the Valhall field. In the usual way, impedances are modelled by a petro-elastic model to convert dynamic parameters from the simulation model. The modelled impedance is thereafter compared to the observed impedance. This rock physics model requires extensive calibration and also the exhaustive modelling of various data to describe the rock and fluid properties. To overcome this, a fast-track forward modelling equation (proxy model) is proposed to capture the relationship between the percentage change in impedance and dynamic changes. The proxy model is derived analytically through modelling of synthetic data. To compute the percentage changes in impedance, the proxy model requires a set of calibrated coefficients from the petro-elastic model (coefficients a_1, b_1 and c_1), changes in pressure and saturation (ΔP and ΔSw) and compaction curves from the laboratory expressed as a functions of initial porosity (F_{ww} and F_p). The proxy model is comprised of three distinct terms: a pressure term, a saturation term and a cross term between pressure and saturation that describes the water weakening behaviour of the chalk. The equation of the proxy model is given below:

$$\%\frac{\Delta Ip}{Ip} = a_1\Delta\mathbf{P} - b_1\left[F_p + \left(\frac{\Delta\mathbf{S_w}}{\Delta S_{wmax}}\right)\left(F_{ww} - F_p\right)\right]\Delta\mathbf{P} + c_1\Delta\mathbf{S_w} \qquad (1)$$

The proxy model can also be used for inversion to make inferences about the changes in pressure and saturation inside the reservoir. The strength of this equation is that it leads to an accelerated estimation of the impedances. Most importantly, it is now amenable to linearized inversion, and as a consequence the inversion has a less complicated solution space. Finally, it also provides an intuitive relationship between data and model, essential to quality control the results.

The first EC constraint imposed is in the water leg. No change was observed in saturation in the water leg from pre-production to current state; hence it is only logical to assume no changes in saturation, and a possible presence of subtle pressure signal in the water leg. An inequality constraint (above water-leg, $-0.10 \leq S_w \leq 0.5$) was applied, with the upper and lower boundaries extracted from simulation model statistics. For the second EC constraint, the solution space close to well perforations was constrained using a 3D Gaussian kernel; imposing tight upper and lower bounds for changes in pressure and saturation as estimated from the reservoir simulation. These constraints are realistic given that the model is history matched. Two assumptions are implicit in this technique:

- creep behaviour is not accounted for in this inversion; the creeping of chalk shows the rock weakens without any drop in pressure following the invasion of water; in which the rock will have a greater compaction later in time when pressure eventually drops (Barkved et al. 2003).
- gas exsolution is less detectable in seismic attributes; gas signals are transient and localised with weak signals. Gas is a second order effect; compaction could potentially mask the gas signal.

Inversion result using EC constraints

Firstly, data of across domains were reconciled into a common grid. The starting model is from the smooth simulation prediction. Figures 1a, 1b and 1c show the progressive improvement of the results by imposing constraints and adding more robust 4D signals such as the reservoir time strain onto inversion results. The results from the constrained inversion are far better than from the unconstrained solution; clearer delineation of pressure changes can be seen around wells. By adding the additional information from time strain, the objective function was modified by associating weights to the different data. The weights carry information on uncertainties and errors in the data; and show the relative contribution of each individual dataset to the joint objective function.

Hierarchical updating of inversion

The first pass inversion results informed us that some of the wells have a slightly poorer match between the production data and the simulated prediction, and could bias the solution. Hence the constraints around such wells were revised for both pressure and saturation respectively by relaxing the constraints. The end result of updating the misfit further improved the results.

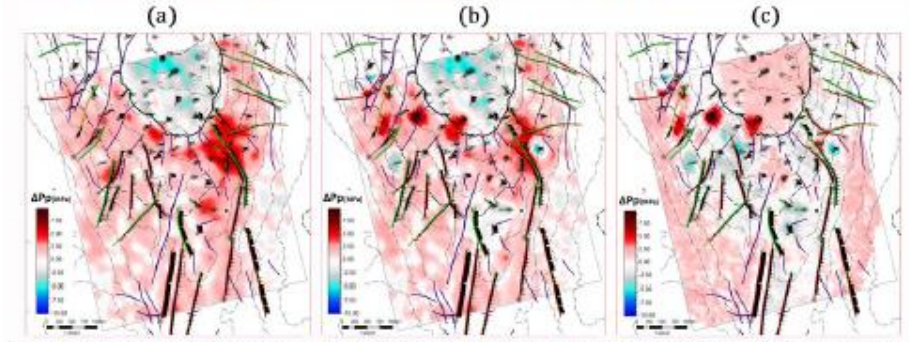

Figure 1 A display of the progressive improvement of inverted pressure changes from our inversion scheme. (a) unconstrained, (b) EC constraints imposed and (c) with the additional observations from reservoir time strain.

Interpretation

The next focus is to use the inverted results to explain some of observations close to wells on an area of the field with very interesting 4D seismic signals. The three major observations are shown in Figure 2. A potential pressure sink around the producers P1, P2 and P3 was identified, which is also correctly reflected in the inverted pressure change showing a pressure decrease close to 4MPa, and a strong pressure increase around injectors I1 and I2. Lastly, water encroaching towards the producers from the injectors was also observed. We support our arguments by cross checking with the production data made available such as RFT and downhole pressure gauge measurements acquired every six months. The RFT data shows that both injector I1 and I2 were originally water flooded, hence the 4D signals are predominantly pressure driven. The production data also demonstrated that the injectors were put on stream after LoFS2, and injected at a high constant rate; the inversion shows an increase in pressure greater than 10MPa. Production data indicated a steady increase in water cut, and an increase in gas production rate in P2, inferring a drop in pressure and that water from the nearby injectors could have invaded the producer, which is also consistent with the inversion results.

Figure 4 shows a cross section along these wells for time strain, changes in amplitude, elastic properties, pressure and saturation. Observation in section view agrees with the map description, such as the large pressure increase around injector I2, a higher pressure drop in the Ekofisk than in the Tor for P3, and the water invasion in P2 in the Tor interval but not in P3. The water cut in P2 is not only supported in the production data but also in PLTs acquired in 2006, showing a good 55% contribution from TA (first reservoir unit within the Tor formation).

Discussion and Conclusions

The decomposition of changes in pressure and saturation was successful by using an engineering based inversion approach. Application to the Ekofisk field revealed that over the course of two and a half years, the compaction effects due to pressure depletion and water flooding have dominated the 4D seismic signals. Quantitative interpretation on this field using the inversion results show good agreement with well production data, and help explained strong localised anomalies in both the Ekofisk and Tor formations. This work also shows the need to have a better understanding of the timing of the pressure and saturation changes. These in turn affect the magnitude and spatial distribution of compaction and help validate drainage and pressure support areas in the field.

Acknowledgements

The authors would like to thank the sponsors of the Edinburgh Time-Lapse Project Phase V (BG, BP, CGG, Chevron, ConocoPhillips, ENI, ExxonMobil, Hess, Ikon Science, Landmark, Maersk, Nexen, Norsar, Petoro, Petrobras, RSI, Shell, Statoil, Suncor, Taqa, TGS and Total) for supporting this research. Also special thanks to ConocoPhillips Skandinavia AS and the PL018 Partnership (Total E&P Norge AS, ENI Norge AS, Statoil Petroleum AS and Petoro AS) for their permission to publish this work. Special gratitude goes to Carlos Pacheco, Jean De Lanlay, Evgeny Tolstukhin and Reidar Midtun.

References

Barkved, O, Heavey, P, and Kjelstadli, R. [2003] Valhall Field – Still on plateau after 20 years of production. *SPE* 83957

Bertrand, A., Folstad, P.G., Grandi, A., Jeangeot, G., Haugvaldstad, H., Lyngnes, B., Midtun, R. and Haller, N. [2013] The Ekofisk Life of Field Seismic (LoFS) System: Experiences and results after two years in operation, 75th EAGE Conference, London.

Corzo, M., MacBeth, C. and Barkved, O. [2013] Estimation of pore-pressure change in a compacting reservoir from time-lapse seismic data. *Geophysical Prospecting* **61**, 1022-1034.

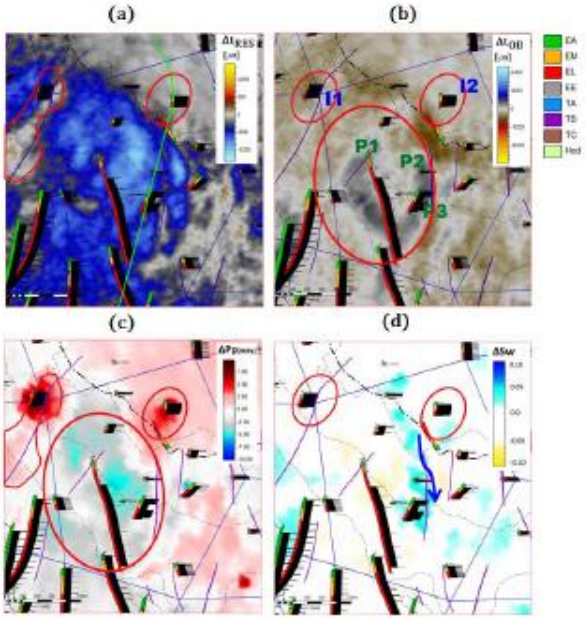

Figure 2 Map comparison of (a) reservoir time shift (b) overburden time shift (c, d) inverted pressure and saturation changes. Legend on the right represents stratigraphic units intersected by wells in Ekofisk (EA, EM, and EL), tight zone, Tor (TA, TB, and TC) and underburden (Hod). The cross section location in Figure 3 is represented as a green line along well I2 in Figure 2(a).

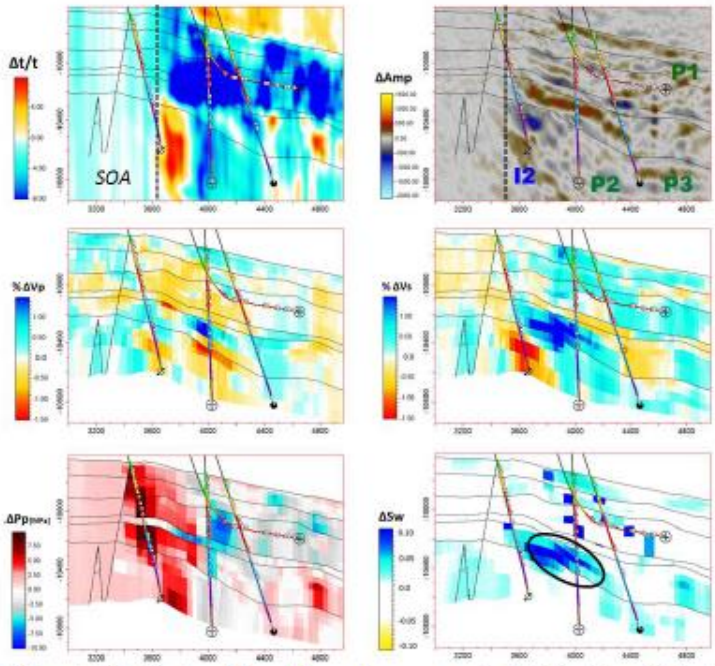

P2

P2	# Perfs	PLT Jul 2006
EA	2	11% Total
EM	1	
EL	4	34% Total
TA	4	55% Total
TB		
TC		
Total	11	100% Total

Figure 3 4D effects and inverted results across wells P1, P2, P3 and I2 between LoFS2 and LoFS6. The water cut in P2 is not only supported by production data but also in the PLT acquired in 2006. Our interpretation in the section is in good agreement with our map description.

MADRID 2015
1-4 June 2015 | IFEMA Madrid

WS02-C04

Engineering Consistent Constraints for the Inversion of Changes in Pressure and Saturation on Ekofisk

M.Y. Wong* (Heriot-Watt University), C. MacBeth (Heriot-Watt University) & A. Bertrand (ConocoPhillips Norge)

SUMMARY

A high resolution, time lapse seismic inversion into pressure and saturation changes is performed. This provides insights into well performance and pressure distribution within a geo-mechanically active chalk reservoir (Ekofisk). The inversion is constrained by reservoir engineering concepts and predictions to reduce the non-uniqueness involved, and to maintain consistency with the physics of flow. At the heart of this inversion scheme is the effective union of engineering data and different seismic products such as reservoir time strain, percentage changes in elastic properties to influence the inversion. Quantitative interpretation on this field using the inversion results shows good agreement with well production data and helps to explain strong localised anomalies in both the Ekofisk and Tor formations. Analysis shows that the hardening signals around producers are due to lack of pressure support and reservoir compaction; whereas softening signals are attributed to high pressure flooding around injectors.

Introduction

Time-lapse (4-D) seismic has now become commonplace in oil and gas field development. One branch of active research is the evolution of quantitative evaluations and extraction of pressure and saturation changes from 4D seismic signals. Such dynamic properties have important implications in reservoir characterisation such as optimizing well production and injection rate, placement of new wells, and the prevention of mechanical failures. The method presented here not only yields such properties but can also assist applications such as seismic history matching and model updating. However, one needs to ensure that a forward model can adequately describe time lapse elastic properties as a function of the dynamic reservoir parameters, and that the inverted dynamic properties are realistic and engineering consistent (EC).

In this study, an inversion was performed on the 4D seismic data, in the form of percentage changes in elastic properties and time shift measurements, into variations in pressure and saturation for a geo-mechanically active chalk reservoir. The key difference between the recommended inversion scheme and existing inversion methods lies in the characteristics of the reservoir itself. Ekofisk is a compacted chalk reservoir, which is not only subject to dry compaction but also water weakening. The inversion is guided by a smooth starting model and associated weights from available seismic products. Most importantly, the inversion is also constrained with reservoir engineering predictions, which helps reduce the non-uniqueness involved and maintains consistency with the physics of flow.

The Ekofisk field is a remarkable example of compacted chalk field. It is a four way dip anticline and produces oil and gas from naturally fractured chalk reservoirs of the Masstrichtian (Tor) and Danian (Ekofisk) Formations. The reservoir thickness, which is around 300m on average is more prominent in the crestal area and thins towards the flanks. The reservoir has high porosity and low matrix permeability. During early production by pressure depletion, pressure was close to bubble point; gas exsolution and compaction of the reservoir were extensive. As part of the effort to increase productivity, a full field water injection programme was put on stream which increased oil production rate, stabilised field pressure; but also resulted in the water weakening of chalk. The permanent reservoir monitoring system initiated in 2010 was an effort to allow 4D seismic data for reservoir surveillance to optimise new well locations and trajectories, suggest and prioritise well interventions, as well as update the reservoir model and monitor the overburden (Bertrand et al. 2013). The inversion is applied to the second and the sixth of the LoFS (Life of Field Seismic) surveys acquired two and a half years apart. The main focus area is the south west part of the field.

Methodology and Inversion Workflow

This is a continued effort from Corzo et al. (2013) where initial porosity was considered as an important factor in inverting for pressure depletion in the Valhall field. In the usual way, impedances are modelled by a petro-elastic model to convert dynamic parameters from the simulation model. The modelled impedance is thereafter compared to the observed impedance. This rock physics model requires extensive calibration and also the exhaustive modelling of various data to describe the rock and fluid properties. To overcome this, a fast-track forward modelling equation (proxy model) is proposed to capture the relationship between the percentage change in impedance and dynamic changes. The proxy model is derived analytically through modelling of synthetic data. To compute the percentage changes in impedance, the proxy model requires a set of calibrated coefficients from the petro-elastic model (coefficients a_1, b_1 and c_1), changes in pressure and saturation (ΔP and ΔSw) and compaction curves from the laboratory expressed as a functions of initial porosity (F_{ww} and F_p). The proxy model is comprised of three distinct terms: a pressure term, a saturation term and a cross term between pressure and saturation that describes the water weakening behaviour of the chalk. The equation of the proxy model is given below:

$$\%\frac{\Delta Ip}{Ip} = a_1\Delta\mathbf{P} - b_1\left[F_p + \left(\frac{\Delta\mathbf{S_w}}{\Delta S_{wmax}}\right)\left(F_{ww} - F_p\right)\right]\Delta\mathbf{P} + c_1\Delta\mathbf{S_w} \qquad (1)$$

The proxy model can also be used for inversion to make inferences about the changes in pressure and saturation inside the reservoir. The strength of this equation is that it leads to an accelerated estimation of the impedances. Most importantly, it is now amenable to linearized inversion, and as a consequence the inversion has a less complicated solution space. Finally, it also provides an intuitive relationship between data and model, essential to quality control the results.

The first EC constraint imposed is in the water leg. No change was observed in saturation in the water leg from pre-production to current state; hence it is only logical to assume no changes in saturation, and a possible presence of subtle pressure signal in the water leg. An inequality constraint (above water-leg, $-0.10 \leq S_w \leq 0.5$) was applied, with the upper and lower boundaries extracted from simulation model statistics. For the second EC constraint, the solution space close to well perforations was constrained using a 3D Gaussian kernel; imposing tight upper and lower bounds for changes in pressure and saturation as estimated from the reservoir simulation. These constraints are realistic given that the model is history matched. Two assumptions are implicit in this technique:

- creep behaviour is not accounted for in this inversion; the creeping of chalk shows the rock weakens without any drop in pressure following the invasion of water; in which the rock will have a greater compaction later in time when pressure eventually drops (Barkved et al. 2003).
- gas exsolution is less detectable in seismic attributes; gas signals are transient and localised with weak signals. Gas is a second order effect; compaction could potentially mask the gas signal.

Inversion result using EC constraints

Firstly, data of across domains were reconciled into a common grid. The starting model is from the smooth simulation prediction. Figures 1a, 1b and 1c show the progressive improvement of the results by imposing constraints and adding more robust 4D signals such as the reservoir time strain onto inversion results. The results from the constrained inversion are far better than from the unconstrained solution; clearer delineation of pressure changes can be seen around wells. By adding the additional information from time strain, the objective function was modified by associating weights to the different data. The weights carry information on uncertainties and errors in the data; and show the relative contribution of each individual dataset to the joint objective function.

Hierarchical updating of inversion

The first pass inversion results informed us that some of the wells have a slightly poorer match between the production data and the simulated prediction, and could bias the solution. Hence the constraints around such wells were revised for both pressure and saturation respectively by relaxing the constraints. The end result of updating the misfit further improved the results.

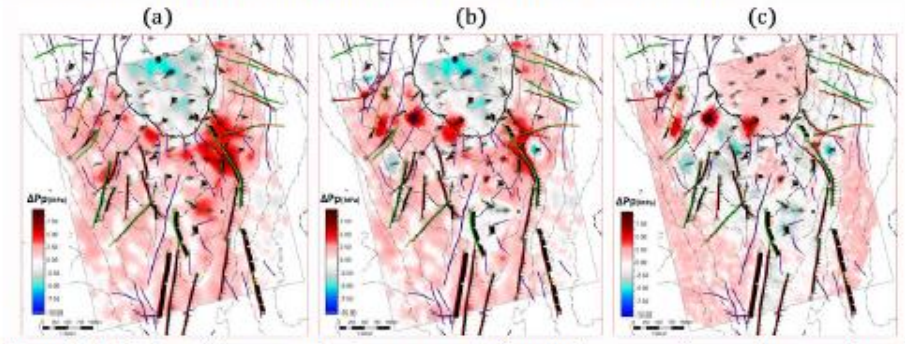

Figure 1 A display of the progressive improvement of inverted pressure changes from our inversion scheme. (a) unconstrained, (b) EC constraints imposed and (c) with the additional observations from reservoir time strain.

Interpretation

The next focus is to use the inverted results to explain some of observations close to wells on an area of the field with very interesting 4D seismic signals. The three major observations are shown in Figure 2. A potential pressure sink around the producers P1, P2 and P3 was identified, which is also correctly reflected in the inverted pressure change showing a pressure decrease close to 4MPa, and a strong pressure increase around injectors I1 and I2. Lastly, water encroaching towards the producers from the injectors was also observed. We support our arguments by cross checking with the production data made available such as RFT and downhole pressure gauge measurements acquired every six months. The RFT data shows that both injector I1 and I2 were originally water flooded, hence the 4D signals are predominantly pressure driven. The production data also demonstrated that the injectors were put on stream after LoFS2, and injected at a high constant rate; the inversion shows an increase in pressure greater than 10MPa. Production data indicated a steady increase in water cut, and an increase in gas production rate in P2, inferring a drop in pressure and that water from the nearby injectors could have invaded the producer, which is also consistent with the inversion results.

Figure 4 shows a cross section along these wells for time strain, changes in amplitude, elastic properties, pressure and saturation. Observation in section view agrees with the map description, such as the large pressure increase around injector I2, a higher pressure drop in the Ekofisk than in the Tor for P3, and the water invasion in P2 in the Tor interval but not in P3. The water cut in P2 is not only supported in the production data but also in PLTs acquired in 2006, showing a good 55% contribution from TA (first reservoir unit within the Tor formation).

Discussion and Conclusions

The decomposition of changes in pressure and saturation was successful by using an engineering based inversion approach. Application to the Ekofisk field revealed that over the course of two and a half years, the compaction effects due to pressure depletion and water flooding have dominated the 4D seismic signals. Quantitative interpretation on this field using the inversion results show good agreement with well production data, and help explained strong localised anomalies in both the Ekofisk and Tor formations. This work also shows the need to have a better understanding of the timing of the pressure and saturation changes. These in turn affect the magnitude and spatial distribution of compaction and help validate drainage and pressure support areas in the field.

Acknowledgements

The authors would like to thank the sponsors of the Edinburgh Time-Lapse Project Phase V (BG, BP, CGG, Chevron, ConocoPhillips, ENI, ExxonMobil, Hess, Ikon Science, Landmark, Maersk, Nexen, Norsar, Petoro, Petrobras, RSI, Shell, Statoil, Suncor, Taqa, TGS and Total) for supporting this research. Also special thanks to ConocoPhillips Skandinavia AS and the PL018 Partnership (Total E&P Norge AS, ENI Norge AS, Statoil Petroleum AS and Petoro AS) for their permission to publish this work. Special gratitude goes to Carlos Pacheco, Jean De Lanlay, Evgeny Tolstukhin and Reidar Midtun.

References

Barkved, O, Heavey, P, and Kjelstadli, R. [2003] Valhall Field – Still on plateau after 20 years of production. *SPE* 83957

Bertrand, A., Folstad, P.G., Grandi, A., Jeangeot, G., Haugvaldstad, H., Lyngnes, B., Midtun, R. and Haller, N. [2013] The Ekofisk Life of Field Seismic (LoFS) System: Experiences and results after two years in operation, 75th EAGE Conference, London.

Corzo, M., MacBeth, C. and Barkved, O. [2013] Estimation of pore-pressure change in a compacting reservoir from time-lapse seismic data. *Geophysical Prospecting* **61**, 1022-1034.

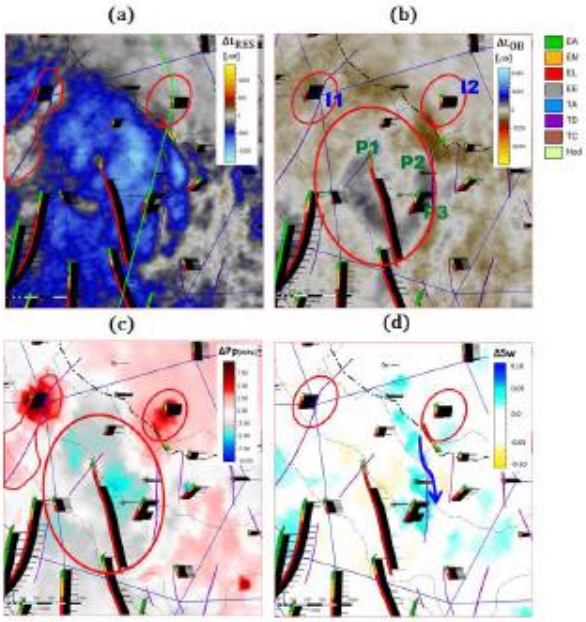

Figure 2 Map comparison of (a) reservoir time shift (b) overburden time shift (c, d) inverted pressure and saturation changes. Legend on the right represents stratigraphic units intersected by wells in Ekofisk (EA, EM, and EL), tight zone, Tor (TA, TB, and TC) and underburden (Hod). The cross section location in Figure 3 is represented as a green line along well I2 in Figure 2(a).

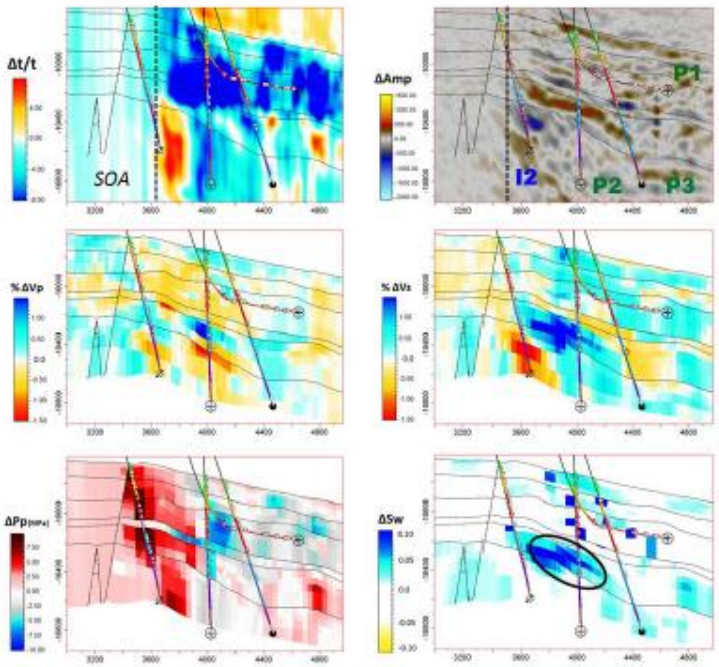

P2

P2	# Perfs	PLT Jul 2006
EA	2	11% Total
EM	1	
EL	4	34% Total
TA	4	55% Total
TB		
TC		
Total	11	100% Total

Figure 3 4D effects and inverted results across wells P1, P2, P3 and I2 between LoFS2 and LoFS6. The water cut in P2 is not only supported by production data but also in the PLT acquired in 2006. Our interpretation in the section is in good agreement with our map description.

REFERENCES

Adam, L., Batzle, M., and Brevik, I. (2005). Gassmann's fluid substitution paradox on carbonates: seismic and ultrasonic frequencies. *SEG International Exposition and Annual Meeting.*

Agarwal, B., Hermansen, H., Sylte, J. E., Thomas, L. K. (1999). Reservoir Characterization of Ekofisk Field: A Giant, Fractured Chalk Reservoir in the Norwegian North Sea – History Match. *Reservoir Simulation Symposium, Houston*.

Agarwal, B., Hermansen, H., Sylte, J.E. et al. (2000). Reservoir Characterization of Ekofisk Field: A Giant, Fractured Chalk Reservoir in the Norwegian North Sea—History Match. *SPE Res Eval & Eng*, 3 (6): 534-543.

Alam, M. M., Fabricius, I. L., and Christensen, H. F. (2012). Static and dynamic effective stress coefficient of chalk. *Geophysics*, 77(2), L1-L11.

Alerini, M., Ayzenberg, M.,Ek, T., Feng, T., Hustoft, L., Lie, E., Liu, S., and Skjervheim, N. S. a. J. A. (2014). Utilization of Time-lapse Seismic for Reservoir Model Conditioning. *76th EAGE Conference and Exhibition*.

Al-Najjar, N., Doyen, P., Brevik, I., Kvamme, L., and Psaila, D. (1999). Statfjord field- Time-lapse seismic interpretation using a 4D earth model. *SEG International Exposition and Annual Meeting, Houston, Texas.*

Alsos, T., Osdal B., and Høiås A. (2009). The many faces of pressure changes in 4D seismic at the Svale Field and its implication on reservoir management. *EAGE Conference & Exhibition*.

Alvarez, E. (2014). *Petroelastic Approximations for Quantitative 4D Seismic Interpretation*. PhD Thesis, Heriot-Watt University.

Alvarez, E., and MacBeth, C. (2014). An insightful parametrization for the flatlander's interpretation of time-lapsed seismic data. *Geophysical Prospecting*, 62 , 75–96.

Amini, H. (2014). *A pragmatic approach to simulator-to-seismic modelling for 4D seismic interpretation.* PhD Thesis, Heriot-Watt University.

Amini, H., MacBeth, C., and Shams, A. (2011). Calibration of Simulator to Seismic Modelling for Quantitative 4D Seismic Interpretation. *73rd EAGE Conference & Exhibition incorporating SPE EUROPEC.*

Anderson, R., Boulanger, A., He, W., Xu, L., Flemings, P., Burkhart, T., and Hoover, A. (1997). 4D time-lapse seismic monitoring in the South Timbalier 295 Field, Gulf of Mexico. *SEG International Exposition and Annual Meeting.*

Austad, T., Strand, S., Madland, M. V., Puntervold, T., and Korsnes, R. I. (2008). Seawater in chalk: An EOR and compaction fluid. *SPE Reservoir Evaluation & Engineering*, 11(4):648–654.

Ayzenberg, M., and Liu, S. (2014). Saturation and Pressure Inversion - From 4D Seismic to Reservoir Model Updating. *76th EAGE Conference and Exhibition*.

Ayzenberg, M., Hustoft, L., and Feng, N. S. a. T. (2013). Utilization of Time-lapse Seismic for Reservoir Model Conditioning. *75th EAGE Conference & Exhibition incorporating SPE EUROPEC.*

Barkved, O., Heavey, P., Kjelstadli, R., Kleppan, T., and Kristiansen, T. G. (2003). Valhall field – still on plateau after 20 years of production. *Proceedings of Offshore Europe*.

Barkved, O.I. (2012). *Seismic Surveillance for Reservoir Delivery*. EAGE Publications.

Batzle, M., and Wang, Z. (1992). Seismic properties of pore fluids. *Geophysics*, v. 57, no. 11, p. 1396–1408.

Bayes, T. (1763). An essay towards solving a problem in the Doctrine of Chances. *Philosophical Transactions,* 53:370–418.

Berryman, J.G. (1980). Long-wavelength propagation in composite elastic media II. Ellipsoidal inclusions. *Journal of Acoustic Society of America*, 68(6), 1820–1831.

Bertrand A., Folstad, P. G., Lyngnes, B., Buizard, S., Hoeber, H., Pham, N., de Pierrepont, S., Schultzen, J., and Grandi, A. (2014). Ekofisk life-of-field seismic: Operations and 4D processing. Ekofisk life-of-field seismic: Operations and 4D processing, *Leading Edge*, **33**, 142–148.

Bertrand, A., Folstad, P. G., Grandi, A., Jeangeot, G., Haugvaldstad, H., Lyngnes, B., Midtun, R. and Haller, N. (2013a). The Ekofisk Lifs of Field Seismic (LoFS) System: Experiences and results after two years in operation. *75th EAGE Conference and Exhibition.*

Bertrand, A., Hellmann, T., Henstock, C., Lyngnes, B., Buizard, S., Oexnevad, G. and Haller, N. (2013b). Wide-azimuth PP/PS Depth Imaging at Ekofisk Using Full Waveform Inversion. *75th EAGE Conference and Exhibition.*

Bhakta, T., and M. Landrø, (2013). Discrimination between pressure and fluid saturation changes in compacting reservoirs using both the time-lapse amplitudes and traveltime information. *75th EAGE Conferenc and Exhibition.*

Biot, M. (1941). General Theory of Three-Dimensional Consolidation. *Journal of Applied Physics,* 12:155–164.

Biot, M. A. (1956). Theory of propagation of elastic waves in a fluid saturated porous solid. I. Low-frequency range. *Journal of the Acoustical Society of America*, **28**, 168–178.

Biot, M. A., and Willis, D. G., (1957). The elastic coefficients of the theory of consolidation. *J. Appl. Mech*., 24,594-601.

Borre, M. (1998). Ultrasonic velocity of North Sea Chalk – predicting saturated from dry. *Nordic Petroleum Technology Series: IV, Research in Petroleum Technology* (ed. M. F. Middleton), pp. 71-98.

Borre, M. K., and Fabricius, I. L. (2001). Ultrasonic velocities of water saturated chalk from the Gorm field, Danish North Sea: Sensitivity to stress and applicability of Gassmann's equation. In I. L. Fabricius (Ed.), *Research in petroleum technology: Nordic Petroleum Technology Series V*. Vol. 1-2, pp. 1-18.

Brain, J. (2017). Results from a 4D Seismic Campaign to Unlock the Remaining Potential from the Rotliegend Gas Fields of the Southern North Sea. *First EAGE Workshop on Practical Reservoir Monitoring.*

Brown, S. R. (1987). Fluid flow through rock joints: The effects of surface roughness. *J. Geophys. Res*., 92, 1337-1347.

Bruno, M. (2002). Geomechanical and decision analyses for mitigating compaction related casing damage. *SPE drilling & completion*, 17(3):179–188.

Calvert, M. A., Vagg, L. D., Lafond, K. B., Hoover, A. R., Ooi, K. C., and Herbert, I. H. (2014). Insights into sweep efficiency using 4D seismic at Halfdan field in the North Sea. *The Leading Edge*, 33(2), 182–187.

Caldwell, J., Koudelka, E., Nesteroff, K., Price, R. and Zhang, P. (2015). Seismic permanent reservoir monitoring (PRM)–A growing market. *First Break*, 33, 65-73.

Calvert, M.A., Roende, H. H., Herbert, I. H., and Zaske, J. (2013). Quick Impact of New 4D over the Halfdan Field, Danish North Sea, *EAGE Conference & Exhibition.*

Carcione, J., M. Landrø , A. Gangi, and F. Cavallini, (2007). Determining the dilation factor in 4D monitoring of compacting reservoirs by rock-physics models. *Geophysical Prospecting*, 55, no. 6, 793 – 804.

Carnec, C. and Fabriol, H. (1999). Monitoring and modeling land subsidence at the Cerro Prieto geothermal field, Baja California, Mexico, using SAR interferometry, *Geophys. Res. Lett*., 26, 1211–1214.

Castellini, A., Yeten, B., Singh, U., Vahedi, A., and Sawiris, R. (2006). History matching and uncertainty quantification assisted by global optimization techniques. *In 10th European Conference on the Mathematics of Oil Recovery.*

Chin, L. Y., and Nagel, N. B. (2004). Modeling of subsidence and reservoir compaction under waterflood operation. *Int. J. Geomech*., 4, 28–34.

Chu, D., and Gist, G. A. (2010). Inversion of 4D seismic data: U.S. Patent 2010/0142323 A1.

Cole, S., Lumley, D. Meadows, M. and Tura, A. (2002). Pressure and saturation inversion of 4D seismic data by rock physics forward modelling. *SEG International Exposition and Annual Meeting.*

Coleman, T.F. and Y. Li. (1994). On the Convergence of Reflective Newton Methods for Large-Scale Nonlinear Minimization Subject to Bounds. *Mathematical Programming*, Vol. 67, No. 2, 1994, pp. 189–224.

Coleman, T.F. and Y. Li. (1996). An Interior, Trust Region Approach for Nonlinear Minimization Subject to Bounds. *SIAM Journal on Optimization*, Vol. 6, pp. 418–445.

Cook, C. C., and Jewell, S. (1996). Reservoir Simulation in a North Sea Reservoir Experiencing Significant Compaction Drive. *SPE*.

Corzo, M. (2009). *Quantitative analysis of a dynamically compacting reservoir*. Ph.D. thesis, Heriot-Watt University.

Corzo, M., MacBeth, C., and Barkved, O. (2013). Estimation of pore-pressure change in a compacting reservoir from time-lapse seismic data: *Geophysical Prospecting*, 61, 1022-1034.

Cox, B. and Hatchell, P. (2008). Straightening out lateral shifts in time-lapse seismic. *First Break*, 26.

Das, A., Roy, B., Folstad, P. G., Lyngnes, B., Smith, B., and Grandi, A. (2013). Dynamic rock physics modelling for compacting chalk reservoirs. *SEG International Exposition and Annual Meeting*.

Das, A., Roy, B., Folstad, P.G., Lyngnes, B., Smith, B., and Grandi, A. (2016). Modeling dynamic elastic properties of compacting chalk reservoirs using an integrated rock-physics workflow: A case study in the Ekofisk Field, Norway. *The Leading Edge*, 35 (6), 516-522.

Davies, D. M. D., Mannaerts, H. C., McGarrity, J., Ibram, M., McKenzie, C., Campbell, S., Alexander, G., Lozano, A., Kommendal, J. H., Barkved, O. O., and Van Gestel, J.-P. (2011). High-Density OBC-A Step Change in Reservoir Imaging-A BP North Sea View. *SPE*.

Davolio, A., Maschio, C. and Schiozer, D. J. (2011). Incorporating 4D seismic attributes into history matching process through an inversion scheme. *SPE 62577*.

De Gennaro, S., Onaisi, A., Grandi, A., Ben-Brahim, L., and Neillo, V. (2008). 4D reservoir geo-mechanics: a case study from the HP/HT reservoirs of the Elgin and Franklin fields. *First Break*, 26.

de Waal, H., and Calvert, R. (2003). Overview of global 4D seismic implementation strategy. *Petroleum Geoscience*, 9:1–6.

Deb, K. (1995). *Optimization for engineering design: algorithms and examples*. Prentice-Hall.

Deb, K., and Goyal, M., (1998). A robust optimization procedure for mechanical component design based on genetic adaptive search. Trans ASME. *J Mech Des*. 120(2): 162–164.

Delage, P., Schroeder, C., and Cui, Y.J., (1996). Subsidence and Capillary Effects in Chalks. *Proc.*, Eurock, 1291–1298

Dons, T., Jørgensen, O., and Gommesen, L. (2007). Observations and quantitative analyses of waterflood patterns in a chalk reservoir using seismic data, Halfdan field, Danish North Sea. *Offshore Europe, SPE 108531*.

Downton, J. (2005). *Seismic parameter estimation from AVO inversion*. PhD Thesis, University of Calgary.

Drahos, D. (2008). Determining the Objective Function for Geophyical Joint Inversion. *Geophyical Transaction*, Vol. 45 No.3. pp. 105-121.

Du, J., and Olson, J. E. (2001). A poroelastic reservoir model for predicting subsidence and mapping subsurface pressure fronts. *Journal of Petroleum Science and Engineering*, 30, 181-197.

Dusseault, M. B. (2011). Geomechanical Challenges in Petroleum Reservoir Exploitation. *Korean Journal of Civil Engineering*, Special issue on Energy Geomechanics.

Eaton, B. A. (1969). Fracture Gradient Prediction and Its Application in Oilfield Operations. *Society of Petroleum Engineer*.

Eissa, E., and Kazi, A. (1988). Relation between static and dynamic Young's moduli of rocks. *Int. J. Rock Mech. Min. Sci. & Geomech*, 25: 479-482.

El Ouair, Y., and Strønen, L. (2006). Value creation from 4D seismic at the Gullfaks Field: achievements and new challenges. *SEG International Exposition and Annual Meeting*.

Eshelby, J.D. (1957).The determination of the elastic field of an ellipsoidal inclusion, and related problems. *Proceedings of the Royal Society A*, 241 (1226): 376–396.

Fabricius, I. (2007). Chalk: composition, diagenesis and physical properties. *Geological Society of Denmark. Bulletin*.

Falahat, R., Shams A., and MacBeth, C. (2013). Adaptive scaling for an enhanced dynamic interpretation of 4D seismic data. *Geophysical Prospecting*, 61, 231-247.

Feazel, C. T., Keany, J., and Peterson, R. M. (1985). Cretaceous and Tertiary Chalk of the Ekofisk Field Area, Central North Sea. *Carbonate Petroleum Reservoirs*, 495-507.

Ferronato, M., Castelletto, N., Gambolati, G., Janna, C. and Teatini, P. (2013). II cycle compressibility from satellite measurements. *Geotechnique*, 63(6), 479-486.

Fjær, E. and Holt, R. (1999). Stress and stress release effects on acoustic velocities from cores, logs and seismics. *In SPWLA 40th Annual Logging Symposium.*

Fjær, E., Holt, R., Horsrud, P., Raaen, A., and Risnes, R. (2008). Petroleum related rock mechanics. 53.

Fjær, E., Holt, R.M., Horsrud, P., Raaen, A.M., Risnes, R., 1992. *Petroleum Related Rock Mechanics*. Elsevier.

Floricich M., MacBeth C., Stammeijer J., Staples R., Evans A. and Dijksman C. (2006). A New Technique for Pressure – Saturation Separation from Time-Lapse Seismic. Schiehallion Case Study, *68th EAGE Conference & Exhibition.*

Floricich, M., (2006). *An engineering-consistent approach for pressure and saturation estimation from time-lapse seismic data.* PhD thesis, Heriot Watt University.

Folstad, P. G. (2010). Monitoring of the Ekofisk Field. *GEOExPro,* Vol. 7, No. 3.

Folstad, P. G., Haugvalstad, H., and Jeangeot, G. (2011). Ekofisk PRM —The technical case for this brand new installation. *EAGE Workshop on Permanent Reservoir Monitoring (PRM)—Using Seismic Data*.

Friedmann, F., Chawathe, A., and Larue, D. K. (2003). Assessing uncertainty in channelized reservoirs using experimental designs. *S'PE Reservoir Evaluation & Engineering,* 6(04):264 –274.

Fuck, R. F., Tsvankin, I., and Bakulin, A. (2011). Influence of background heterogeneity on traveltime-shifts for compacting reservoirs: *Geophysical Prospecting*, 59, 78-89.

Fursov, I. (2015). *Quantitative application of 4D seismic data for updating thin-reservoir models.* PhD Thesis, Heriot-Watt University.

Galarraga. M. A., Wang, K., and Farmer, H. G. (2015). First Results of 4D Monitoring from the Deepwater BC-10 Life of Field Seismic (LoFS), Brasil. *77th EAGE Conference and Exhibition.*

Garcia, A., and MacBeth, C. (2013). An estimation method for effective stress changes in the reservoir from 4D seismic data. *Geophysical Prospecting,* 61:803-816.

Gassmann, F. (1951). Elastic waves through a packing of spheres. *Geophysics,* 16(4):673-685.

Geertsma, J. (1966). Problems of rock mechanics in petroleum production engineering. *In Proceedings of 1st Congress on International Society of Rock.*

Geertsma, J. (1973). A basic theory of subsidence due to reservoir compaction: the homogeneous case. *Trans. Royal Dutch Soc. Geol. & Mining Eng*, 22:43–62.

Gelman, A., Roberts, G.O., Gilks, W.R. (1996). Efficient Metropolis jumping rules. In: Bernardo, J.M., Berger, J.O., Dawid, A.P., Smith, A.F.M. (Eds.), *Bayesian Statistics*, 5.Oxford University Press, 599-607.

Gennaro, M. (2011). *3D seismic stratigraphy and reservoir characterization of the Chalk Group in the Norwegian Central Graben, North Sea*. PhD thesis, University of Bergen.

Gennaro, M., Wonham, J. P., Sælen, G., Walgenwitz, F., Caline, B., and Faÿ-Gomord, O. (2013). Characterization of dense zones within the Danian chalks of the Ekofisk Field, Norwegian North Sea. *Petroleum Geoscience*, 19, 39-64.

Gommesen, L., and Fabricius, I. L. (2001). Dynamic and static elastic moduli of North Sea and deep sea chalk. *Physics and Chemistry of the Earth Part A-Solid Earth and Geodesy*, 26, 63–68.

Gommesen, L., Fabricius, I. L., Mukerji, T., Mavko, G., and Pedersen, J. M. (2007). Elastic behaviour of North Sea chalk : A well-log study. *Geophysical Prospecting*, v. 55, p. 307–322.

Gommesen, L., Mavko, G., Mukerji, T., and Fabricus, I. (2002). Fluid substitution studies for North Sea chalk logging data. *SEG International Exposition and Annual Meeting*.

Goodwin, N. (2015). Bridging the Gap Between Deterministic and Probabilistic Uncertainty Quantification Using Advanced Proxy Based Methods. *SPE Reservoir Simulation Symposium*.

Gosselin, O., Aanonsen, S., Asvatsmark, A., Cominelli, A., Gonard, R., Kolasinski, M., Ferdinandi, F., Kovaic, L., and Neylon, K. (2003). History matching using time-lapse seismic. *In SPE Annual Technical Conference and Exhibition*.

Gouveia, W. P., and Scales, J. A. (1998). Bayesian seismic waveform inversion: parameter estimation and uncertainty Analysis. *J. Geophys. Res*.103 2759–79.

Guilbot, J., and Smith, B. (2002). 4-D constrained depth conversion for reservoir compaction estimation: Application to Ekofisk field. *The Leading Edge.*

Guilbot, J., Smith, B., and Pirera, F. (2002). Interpretation tools and methods for chalk reservoir characterisation. *64th EAGE Annual International Meeting*.

Håkansson, E., Bromley, R.G., and Perch-Nielsen, K. (1974). Maastrichtian chalk of north-west Europe: a pelagic shelf sediment. In: Pelagic Shelf Sediments: On Land and under the Sea (Eds

Hale, D. (2006). Fast local cross-correlations of images. *SEG International Exposition and Annual Meeting*.

Han, D., and Batzle, M. (2000). Velocity, Density and Modulus of Hydrocarbon Fluids: (1) Data Measurement, (2) Empirical Modeling. *SEG International Exposition and Annual Meeting*.

Hancock, J.M. (1975). The petrology of the chalk. *Proceedings of the Geologists' Association*, 86, 499– 535.

Hatchell, P., and Bourne, S. (2005). Rocks under strain: Strain-induced time-lapse. *The Leading Edge*, 24(23): 1222–1225.

Hatchell, P., Jorgensen, O., Gommesen, L., and Stammeijer, J. (2007). Monitoring reservoir compaction from subsidence and time-lapse time-shifts in the Dan field. *SEG International Exposition and Annual Meeting*.

Hatchell, P., van den Beukel, A., Molenaar, M., Maron, K., Kenter, C., Stammeijer, J., van der Velde, J., and Sayers, C. (2003). Whole earth 4D: Reservoir monitoring geomechanics. *SEG International Exposition and Annual Meeting*.

Haugvaldstad, H., Lyngnes, B., Smith, P., and Thompson, A. (2011). Ekofisk time-lapse seismic – a continuous process of improvement. *First Break*, 29. 113-120.

Hawkins, K., Howe, S., Hollingworth, S., Conroy, G., Ben-Brahim, L., Tindle, C., Taylor, N., Joffroy, G., and Onaisi, A. (2007). Production-induced stresses from time-lapse time-shifts: A geomechanics case study from Franklin and Elgin fields. *The Leading Edge*, 26:655.

He, W., Guerin, G., Anderson, R., and Mello, U. (1998). Time dependent reservoir characterization of the LF sand in the South Eugene Island 330 Field, Gulf of Mexico. *The Leading Edge*, 17(10):1434–1438.

Helbig, K. and Rasolofosaon, P. N. J. (2000). A theoretical paradigm for describing hysteresis and nonlinear elasticity in arbitrary anisotropic rocks. *Proceedings of the Ninth International Workshop on Seismic Anisotropy*.

Henriksen, A. D., Fabricius, I. L., Borre, M. K., Korsbech, U., Theilgaard, A. T., and Zandbergen, J. B. (1999). Core density scanning, degree of induration and dynamic elastic moduli of

Palaeogene limestone in the Copenhagen area. *Quarterly Journal of Engineering Geology*, 32, 107–117.

Herbert, I. H., Escobar, I., and Arnhild, M. (2013). Modelling Fluid Distribution in a Chalk Field Using Elastic Inversion. *EAGE Conference and Exhibition SPE EUROPE*.

Hermansen, H. (2008). The Ekofisk Field: Achieving Three Times the Original Value. *19th World Petroleum Congress*.

Hermansen, H., Thomas, L. K., Sylte, J. E., and Aasbøe. (1997).Twenty Five Years of Ekofisk Reservoir Management. *SPE Annual Technical Conference*.

Herwanger, J. (2008). R we there yet?. *70th EAGE Annual International Meeting*.

Herwanger, J. V, Schiøtt, C. R., Frederiksen, R., If, F., Vejbæk, O. V, et al. (2010). Applying time-lapse seismic methods to reservoir management and field development planning at South Arne, Danish North Sea. *Petroleum Geology Conference series*, v.7. p. 523-535.

Herwanger, J. V., and Horne, S. A. (2009). Linking reservoir geomechanics and time-lapse seismics: Predicting anisotropic velocity changes and seismic attributes. *GEOPHYSICS*, 74(4), W13-W33.

Herwanger, J. V., and Koutsabeloulis, N. (2011). *Seismic Geomechanics: How to Build and Calibrate Geomechanical Models using 3D and 4D Seismic Data*. EAGE Publications.

Hilbert, L. B., Hwong, T. K., Cook, N. G. W., Nihei, K. T., and Myer, L. R. (1994). Effects of Strain Amplitude on the Static and Dynamic Nonlinear Deformation of Berea Sandstone. *Rock Mechanics*, Nelson & Laubach (eds), Balkema, Rotterdam.

Hodgson, N., MacBeth, C., Duranti, L., Rickett, J., and Nihei, K. (2007). Inverting for reservoir pressure change using time-lapse time strain Application to Genesis Field Gulf of Mexico. *The Leading Edge*, 26:649.

Hodgson, N. (2009). *Inversion for reservoir pressure change using overburden strain measurements determined from 4D seismic*. PhD Thesis, Heriot-Watt University.

Holt, R. M., and Stenebråten, J. F. (2013). Controlled laboratory experiments to assess the geomechanical influence of subsurface injection and depletion processes on 4D seismic responses. *Geophysical Prospecting*, 61, 476-488.

Holt, R. M., Fjær, E., New, O. M., and Stenebråten, J. F. (2008). Strain Sensitivity of Wave Velocities in Sediments and Sedimentary rocks. *American Rock Mechanics Association.*

Holt, R. M., Nes, O-M., and Fjær, E. (2005). In-situ stress dependence of wave velocities in reservoir and overburden rocks. *The Leading Edge*, 24(12), 1268-1274.

Hjuler, M. L. (2007). *Diagenesis of Upper Cretaceous onshore and offshore chalk from the North Sea area*. PhD Thesis, Technical University of Denmark.

Huang, Y., MacBeth, C., Barkved, O., Gestel, J. P., and Dybvik, O. P. (2011). Enhanced dynamic Interpretation from correlating well activity to frequently acquired 4D seismic signatures. *The Leading Edge,* 30, 1042-1050.

Hueckel, T., Cassiani, G., Tao, F., Pellegrino, A., and Fioravante, V. (2001). Effect of aging on compressibility of gas/oil bearing sediments and their subsidence. *ASCE Journal of Geotechnical and Geoenvironmental Engineering*, 127(11), 926-938.

Ian, H., Barkved, O., and Kommedal, J.H. (2010). The Life-of-field Seismic System at Valhall, Norwegian North Sea. *Methods and Applications in Reservoir Geophysics*.

Ide, J. M. (1936). Comparison of statically and dynamically determined Young's modulus of rocks. *Proc. Nat. Acad. Sci.*, 22: 81-92.

Jack, I., Barkved, O., and Kommedal, J. H. 2010. The Life-of-field Seismic System at Valhall, Norwegian North Sea. Methods and Application in Reservoir Geophysics.

JafarGandomi, A., and Curtis, A. (2012). Assessing the monitorability of CO_2 saturation in subsurface aquifers. *International Journal of Greenhouse Gas Control*, **7**, 244-260.

Janssen, A. L., Smith, B. A., and Byerley, G. W. (2006). Measuring velocity sensitivity to production induced strain at the Ekofisk Field using time-lapse time-shifts and compaction logs. *SEG International Exposition and Annual Meeting.*

Japsen, P. et al., (2004). Influence of porosity and pore fluid on acoustic properties of chalk : AVO response from oil, South Arne Field, North Sea. *Petroleum Geoscience*, 10: 319-330.

Johnston, D. H. (2013). *Practical applications of time-lapse seismic data, Distinguished Instructor Short Course.* SEG.

Kanu, C., Toomey, A., Hodgson, L., Gherasim, M., L'Heureux, E., Du, B., and Zhang, Q. (2016). Evaluation of time-shift extraction methods on a synthetic model with 4D geomechanical changes. *The Leading Edge*, 35:10, 888-893.

Keszthelyi, D., Dysthe., D. K., and Jamtveit, B. (2016). Compaction of North Sea chalk by Pore-Failure and Pressure Solution in a Producing reservoir. *Frontiers in Physics*, 4.

King, M. (1983). Static and dynamic elastic properties of rocks from the Canadian Shield. *Int. J. Rock Mech. Min. Sci. & Geomech. Abstr*, 20: 237-241.

Kragh, E. and Christie, P. (2002). Seismic repeatability, normalized RMS, and predictability. *The Leading Edge*, 21(7):640–647.

Kristiansen, T. G., and Plischke, B. (2010). History Matched Full Field Geomechanics Model of the Valhall Field Including Water Weakening and Re-Pressurisation. *Society of Petroleum Engineers*.

Kristiansen, T.G., Barkved, O.I., Buer, K. and Bakke, R. (2005). Production Induced Deformations Outside the Reservoir and Their Impact on 4D Seisimic. *International Petroleum Technology Conference*.

Lafet, Y., Roure, B., Doyen, P.M., and Buran, H. (2009). Global 4D seismic inversion and time-lapse fluid classification. *SEG International Exposition and Annual Meeting*.

Landa, J. L., and Giiyagiiler, B. (2003). A methodology for history matching and the assessment of uncertainties associated with flow prediction. *In SPE Annual Technical Conference and Exhibition*.

Landa, J., and Kumar, D. (2011). Joint Inversion of 4D Seismic and Production Data. *SPE Annual Technical Conference and Exhibition*.

Landa, J., Meadows, M., Thacher, C., Waddle, R., and Williams, N. (2015). Map-Based Estimation of Reservoir Pressure and Saturation from 4D Seismic with a Data-Driven Procedure. *SPE Annual Technical Conference and Exhibition*.

Landrø, M. (2001). Discrimination between pressure and fluid saturation changes from time-lapse seismic data. *Geophysics*, 66, 836-844.

Landrø, M., Veire, H. H., Duffaut, K., and Najjar, N. (2003). Discrimination between pressure and fluid saturation changes from marine multicomponent time-lapse seismic data. *Geophysics*, 68, 1592-1599.

Ledbetter, H. (1993). Dynamic vs. static Young's moduli: A case study. *Materials Science and Engineering*, A165, L9–L10.

Loe, N., Mathiesen, E., Jones, M. E., and Leddra, M. (1992). The influences of changes in the pore fluid on the one-dimensional compaction behavior of chalk. *Proc. 4th North Sea Chalk Symposium.*

Love, A.E.H. (1944). *A Treatise on the Mathematical Theory of Elasticity*. 4th ed. Dover. New York.

Lubinski, A. (1954). Theory of elasticity for porous bodies displaying a strong pore structure. *Proc. Second U.S. Natl. Cong. Appl. Mech.*, p.247.

MacBeth, C. (2004). A classification for the pressure-sensitivity properties of a sandstone rock frame. *Geophysics*, 69(6):497–510.

MacBeth, C., Floricich, M., and Soldo, J. (2006). Going quantitative with 4D seismic analysis. *Geophysical Prospecting*, 54, 303-317.

MacBeth, C., Soldo, J., Floricich M. (2004). Going quantitative with 4D seismic. *SEG International Exposition and Annual Meeting.*

Madland, M. V., Omdal, E., Megawati, Hildebrand-Habel, T., Korsnes, R. I., Evje, S., Cathles, L. M., Hiorth, A. (2010). Chemical alterations induced by roc-fluid interactions when injecting brines in high porosity chalks. *Transp Porous Med*.

Mahmoudian, F. (2006). *Linear AVO inversion of multi-component surface seismic and VSP data*. M. Sc. Thesis, University of Calgary.

Marsh, M., Whitcombe, D., Raikes, S., Parr, R., and Nash, T. (2003). BP's increasing systematic use of time-lapse strategy. *Petroleum Geoscience*, 9:7–13.

Mavko, G., Mukerji, T., and Dvorkin, J. (2009). *The Rock Physics Handbook*. Cambridge University Press.

Mavko, G., and Nur, A. (1979). Wave attenuation in partially saturated rocks. *Geophysics*, 44, 161–178.

Megson, J., and Hardman, R. (2001). Exploration for and development of hydrocarbon in the Chalk of the North Sea: a low permeability system. *Petroleum Geoscience*, **7**, 3–12.

Menke, W. (1989). *Geophysical Data Analysis: Discrete Inverse Theory*. Academic Press.

Menke, W. (2012). *Geophysical Data Analysis: Discrete Inverse Theory*. Waltham, MA: Academic.

Metropolis, N., Rosenbluth, A.W., Rosenbluth, M.N., Teller, A.H., and Teller, E. (1953). Equations of State Calculations by Fast Computing Machines. *Journal of Chemical Physics,* 21 (6): 1087–1092.

Micksch, U., Herbert, I. H., Cherrett, A. J., Roende, H., Calvert, M. A., and Zaske, J. (2014). Integrated 4D Inversion Approach in Danish Chalk Fields. *EAGE Conference and Exhibition*.

Mindlin, R., and Cheng, D. (1950). Nuclei of Strain in the Semi-Infinite Solid. *Journal of Applied Physics*, 21:926.

Minkoff, S., Stone, C., Bryant, S., Peszynska, M., and Wheeler, M. (2003). Coupled Fluid Flow and Geomechanical Deformation Modeling. *J.of Petroleum Science and Eng*, 38, 37.

Misaghi, A., Negahban, S., Landrø, M., and Javaherian, A. (2010). A comparison of rock physics models for fluid substitution in carbonate rocks. *Exploration Geophysics*, v. 41, no. 2, p. 146.

Mitchell, A. R., and Griffiths, D. F. (1980). *The Finite Difference Method in Partial Differential Equations*. John Wiley and Sons.

Mohamed, S.E., and Samsudin, H. T. (2011) Application of 4D seismic for reservoir management in Carbonates. Does it work? *SPE*.

Mosegaard, K. (1998). Resolution analysis of general inverse problems through inverse Monte Carlo sampling, *Inverse Probl.*, 14, 405–426.

Mosegaard, K., and Tarantola, A. (1995). Monte Carlo sampling of solutions to inverse problems. *J. Geophys. Res.*, 100 12 431-47.

Murphy, W. F., Winkler, K. W., and Kleinberg, R. L. (1986). Acoustic relaxation in sedimentary rocks: Dependence on grain contacts and fluid saturation. *Geophysics*, 51, 757–766.

Nagel, N. B. (1998). Ekofisk Field Overburden Modelling. *SPE/ISRM Eurock*.

Nes, O., Holt, R., and Fjoer, E. (2002). The reliability of core data as input to seismic reservoir monitoring studies. *SPE Reservoir Evaluation & Engineering*, 5(1):79–86.

Newman, G. H. (1983). The effect of water chemistry on the laboratory compression and permeability characteristics of some North Sea chalks. *Jour. Petroleum Technology*.

Olsen, C., H. F. Christensen, and I. L. Fabricius, 2008a, Static and dynamic Young' s moduli of chalk from the North Sea: Geophysics, 73 , no. 2, E41 – E50

Ottemöller, L., Nielsen, H. H., Atakan, K., Braunmiller, J., and Havskov, J. (2005). The 7 May 2001 induced seismic event in the Ekofisk oil field, North Sea. *J. Geophys. Res.*, 110, B10301.

Pal-Bathija, A., and Batzle, M. (2007). An experimental study of the dilation factor in sandstone under anisotropic stress conditions. *SEG International Exposition and Annual Meeting*.

Papamichos, E., Brignoli, M., and Santarelli, F.J. (1997). An experimental and theoretical study of a partially saturated collapsible rock. *Mech. Cohes.-Frict. Mater*, 2, 251–278.

Plona, T. J., and J. Cook, M. (1995). Effects of stress cycles on static and dynamicYoung's moduli in Castlegate sandstone. *Proceedings of the 35th U. S. Symposium on Rock Mechanics*, 155–160.

Prioul, R., Bakulin, A., and Bakulin, V. (2004). Non-linear rock physics model for estimation of 3-D subsurface stress in anisotropic formations: Theory and laboratory verification. *Geophysics*, 69(2):415–425.

Reklaitis, G. V., Ravindran, A., and Ragsdell, K. M. (1983). *Engineering optimization methods and applications.* Wiley, New York.

Rice, J., and Cleary, M. (1976). Some Basic Stress Diffusion Solutions for Fluid Saturated Elastic Porous Media; With Compressible Constituents. *Reviews of Geophysics and Space Physics*, 14:227.

Rickett, J., Duranti, L., Hudson, T., Regel, B., and Hodgson, N. (2007). 4D time strain and the seismic signature of geomechanical compaction at Genesis. *The Leading Edge*, 26(5):644.

Rietz, D., and Palke, M. (2001). History matching helps validate reservoir simulation models. *Oil and Gas Journal*.

Risnes, R., and Flaageng, O. (1999). Mechanical properties of chalk with emphasis on chalk-fluid interactions and micromechanical aspects. *Oil & Gas Science and Technology – Rev. IFP*, 54(6):751–758.

Risnes, R., Madland, M.V., Hole, M., and Kwabiah, N.K. (2005). Water Weakening of Chalk-Mechanical Effects of Water–GlycolMixtures. *Journal of Petroleum Science and Engineering*, 48 (1–2): 21–36.

Rodriguez-Herrera, A., Koutsabeloulis, N., Onaisi, A., Fiore, J., and Selva, F. (2015). Stress-induced signatures in 4D seismic data: Evidence of overburden stress arching. *SEG International Exposition and Annual Meeting.*

Røgen, B., Fabricius, I. L., Japsen, P., Høier, C., Mavko, G., and Pedersen, J. M. (2005). Ultrasonic velocities of North Sea chalk samples : influence of porosity, fluid content and texture. *Geophysical Prospecting*, 53: 481–496.

Roggero, F., Ding, D. Y., Berthet, P., Lerat, O., Cap, J. and Schreiber, P.-E. (2007). Matching of Production History and 4D Seismic Data-Application to the Girassol Field, Offshore Angola. *SPE Annual Technical Conference and Exhibition*.

Roggero, F., Lerat, O., Ding, D. Y., Berthet, P., Bordenave, C., Lefeuvre F., and Perfetti, P. (2012). History Matching of Production and 4D Seismic Data: Application to the Girassol Field, Offshore Angola. *Oil & Gas Science and Technology – Rev. IFP Energies nouvelles.*

Røste, T., Stovas, A., and Landrø, M. (2005). Estimation of layer thickness and velocity changes using 4D prestack seismic data. *EAGE Conference and Exhibition.*

Rudnicki, J. (1999). Alteration of regional stress by reservoirs and other inhomogeneities: stabilizing or destabilizing? *Proc. 1999 Int. Cong. of Int. Soc.Rock Mechanics*, pages 25–28.

Rutqvist, J. (1995). Determination of hydraulic normal stiffness of fractures in hard rock from hydraulic well testing. *International Journal of Rock Mechanics, Mining Science & Geomechanics*, 32: 513-523.

Sambridge, M., and Mosegaard, K. (2002). Monte Carlo Methods in Geophysical Inverse Problems. *Review of Geophysics*, 40(3), 1009.

Sandø, I. A., Munkvold, O.-P., and Elde, R. (2009). Two decades of 4D geophysical developments–experiences, value creation and future trends. *71st EAGE Conference and Exhibition Incorporating SPE EUROPEC.*

Sarkar, D., Bakulin, A., and Kranz, R. (2003). Anisotropic inversion of seismic data for stressed media: Theory and a physical modeling study on Berea sandstone. *Geophysics*, 68 , no. 2, 690 – 704.

Sayers, C. (2006). Sensitivity of time-lapse seismic to reservoir stress path. *Geophysical prospecting*, 54(3):369–380.

Sayers, C. (2007). Asymmetry in the time-lapse seismic response to injection and depletion. *Geophysical Prospecting*, 55(5):699–705.

Schilthuis, R. J. (1936). Active Oil and Reservoir Energy. *Trans., AIME,* 118: 33-52.

Scholle, P.A. (1977). Chalk diagenesis and its relation to petroleum exploration: Oil from chalks, a modern miracle? *AAPG Bull.*, 61**,** 982–1009.

Schroeder, C., and Shao, J. (1996). Plastic Deformation and Capillary Effects in Chalks. *5th North Sea Chalk Symposium*.

Scott Jr, T. (2007). The effects of stress paths on acoustic velocities and 4D seismic imaging. *The Leading Edge*, 26:602.

Segall, P. (1992). Induced stresses due to fluid extraction from axisymmetric reservoirs. *Pure and Applied Geophysics*, 139(3):535–560.

Segall, P., Grasso, J., and Mossop, A. (1994). Poroelastic stressing and induced seismicity near the Lacq gas field, southwestern France. *Journal of Geophysical Research 99.*

Sen, B. (1943). Note on the stresses produced by nuclei of thermo-elastic strain in a semi-infinite elastic solid. *Quarterly of Applied Mathematics*.

Setarri, A. (2002). Reservoir compaction. *Journal of Petroleum Technology*, (8):62–69.

Shahraeeni, M. S., Chao, G. and Curtis, A. (2012). Fast probabilistic petrophysical mapping of reservoirs from 3D seismic data. *Geophysics*, vol 77, no. 3.

Sharma, M. M., and Tutuncu, A. N. (1994). Grain contact adhesion hysteresis: A mechanism for attenuation of seismic waves. *Geophysical Research Letters*, 21:21, 2323-2326.

Smith B. A., Sylte J. E., Clausen, C. K., and Guilbot J. (2002). Ekofisk 4D Seismic – Influence on Flow Simulation and Compaction Modelling. *Offshore Technology Conference*.

Smith, B., and Brown, L. (2005). Extrapolation to Critical Porosity with the Hashin-Shtrikman Lower Bound. *SEG International Exposition and Annual Meeting.*

Smith,T. M., Sondergeld, C. H., and Rai, C. S. (2003). Gassmann fluid substitutions: A tutorial. *Geophysics*, 68, 430-440.

Sønneland, L., Reymond, B., Thorsteinsen, H., Johansen, R., and Pedersen, L. (1996). Reservoir monitoring: fluid fronts classification from seismic and well log data. *SEG International Exposition and Annual Meeting.*

Sørnes, A. R., Brevik, I., Statoil, R., Ebbellsvei, A., and Trondheim, N. (2000). Fluid Substitution in Carbonate Rocks : Scattering vs Gassmann Theory. *SEG International Exposition and Annual Meeting*.

Spencer, J.W. (1981). Stress relaxations at low frequencies in fluid-saturated rocks: Attenuation and modulus dispersion. *Journal of Geophysical Research*, 86, 1803–1812.

Staples, R., Hague, P., Cooke, G., Ashton, P., Stammeijer, J., Jolley, S., Stevens, T., and Marshall, J. (2002). Integrating 4D seismic to optimize production. *SPE European Petroleum Conference*.

Staples, R., Ita, J., Burrell, R., and Nash, R. (2007). Monitoring pressure depletion and improving geomechanical models of the Shearwater Field using 4D seismic. *The Leading Edge*, 26:636.

Staples, R., Stammeijer, J., Jones , S., Brain, J., Smit, F., and Hatchell, P. (2006). Time-Lapse (4D) Seismic Monitoring - Expanding Applications. *CSPG-CSEG-CWLS Convention.*

Stephen, K. D., Soldo, J., MacBeth, C., and Christie, M. (2005). Multiple model seismic and production history matching: A case stud. *SPE 94173.*

Stroud, A. (1971). *Approximate calculation of multiple integrals*. Prentice Hall.

Sulak, A., and Danielsen, J. (1988). Reservoir aspects of Ekofisk subsidence. *Offshore Technology Conference*.

Sylte, J. E., Thomas, L. K., Rhett, D. W., Bruning, D. D., Nagel, N. B., and Company, P. P. (1999). Water Induced Compaction in the Ekofisk Field. *SPE Annual Technical Conference and Exhibition*.

Tarantola, A. (2005). *Inverse Problem Theory and Methods for Model Parameter Estimation*. Society for Industrial and Applied Mathematics.

Tarek, H. A. (2010) *Reservoir Engineering Handbook*. Elsevier/GPP, Gulf Professional Publ.

Tempone, P., Fjær, E., Landrø, M. (2010). Improved solution of displacements due to a compacting reservoir over a rigid basement. *Applied Mathematical Modelling*, 34(11): 3352-3362.

Terzaghi, K., and Peck, R.B. (1948). *Soil Mechanics in Engineering Practice*. 1st Edition, John Wiley and Sons, New York.

Terzaghi, K. (1923). Die berecbnung der durchlassigkeitsziffer des tones aus dem verlauf der hydrodynamischen spannungserscheinungen. Akademie der Wissenschaften in Wien. Sitzungsberichte. *Mathematisch-naturwissenschaftliche Klasse*, Part 11 a, Vol. 132, No. 3/4, 125-38.

Tian, S. (2014). *Closing the loop by enginering consisitent 4D seismic to simulator inverison*. PhD Thesis, Heriot Watt University.

Tolstukhin, E., Lyngnes, B., and Sudan, H. H. (2012). Ekofisk 4D Seismic - Seismic History Matching Workflow. *SPE Annual Technical Conference and Exhibition*.

Toomey, A., Robinson, N., and Kristiansen, T. G. (2015) A workflow for rapid modelling of production-related geomechanical changes and 4D time-shifts. *SEG International Exposition and Annual Meeting*.

Trani, M. Arts, R. Leeuwenburgh, O., and Brouwer, J. (2011). Estimation of changes in saturation and pressure from 4D seismic AVO and time-shift analysis. *Geophysics*, 76, no.2, C1-C17.

Trythall, R., Parr, R. S., Wreford , J., and Smout, A. (2003) Andrew Seismic Reservoir Surveillance. *65th EAGE Conference & Exhibition*.

Tura, A., and Lumley, D. E. (1999). Estimating pressure and saturation changes from time-lapse AVO data. *SEG International Exposition and Annual Meeting*.

Tutuncu, A. N., Podio, A. L., and Sharma, M. M. (1998). Nonlinear viscoelastic behavior of sedimentary rocks, Part I: Effect of frequency and strain amplitude. *Geophysics*, 63, 184–194.

Tyrell, T., and Merico, A. (2004). Emiliania huxleyi: Bloom observations and the conditions that induce them, p. 75–97. In H. R. Thiertein and J. R. Young [eds.], *Coccolithophores: from molecular processes to global impact*. Springer-Verlag.

Van Bergen, P., De Gennaro, S., Fairhurst, F., Hurry, R., Concho, M., Watson, J. Sturgess, L. and Bevaart, M. (2013). Shearwater - Securing the Chalk - Effects of Depletion of a HPHT Reservoir on Chalk Overburden. *Society of Petroleum Engineers*.

Van Heerden, W. L. (1987). General relations between static and dynamic moduli of rocks. *International Journal of RockMineral Science and GeomechanicalAbstracts*, 24, 381–385.

Vasco, D. and Ferretti, A. (2006). On the use of quasi-static deformation to understand reservoir fluid flow. *Geophysics*, 70(4):13–27.

Vega, S. (2003). *Intrinsic and stress-induced velocity anisotropy in unconsolidated sands*. Ph.D. thesis, Stanford University.

Veire, H., Borgos, H. and Landrø, M. (2006). Stochastic Inversion of Pressure and Saturation Changes from Time-Lapse AVO data. *Geophysics*, 71(5):C81–C92.

Verdon, J. P. (2012). *Microseismic monitoring and geomechanical modelling of CO2 storage in subsurface reservoirs.* Springer.

Waggoner, J. (2001). Integrating time-lapse 3D (4D) seismic data with reservoir simulators. *EAGE Conference and Technical Exhibition.*

Walls, J. D., Dvorkin, J., and Smith, B. A. (1998). Modelling Seismic Velocity in Ekofisk Chalk. *SEG International Exposition and Annual Meeting.*

Walsh, J. B. (1965). The effect of cracks on the uniaxial compression of rocks. *Journal of Geophysical Research*, 70, 399–411.

Wang, H. F. (2000). *Theory of Linear Poroelasticity with Applications to Geomechanics and Hydrogeology*, Princeton University Press.

Wang, Z. (2000). *Dynamic versus static elastic properties of reservoir rocks*, in Wang, Z., and Nur, A. eds., *Seismic and acoustic velocities in reservoir rocks*; Volume 3: Recent developments: Geophysics Reprint Series, 19, 531 – 539.

Wang, Z. (2002), Seismic anisotropy in sedimentary rocks, part 2: Laboratory data. *Geophysics*, 67, 1423 – 1440.

Warpinski, N., and Teufel, L. (1992). Determination of the effective stress law for permeability and deformation in low-permeability rocks. *SPE Form Eval*. (1992) **7**:123–31.

Watts, G. (2011). Permanent reservoir monitoring still facing challenges in bid for industry acceptance. *First Break*, 29, no.5, 13-15.

Wen, X.-H., Lee, S., and Yu, T. (2006). Simultaneous integration of pressure, water cut, 1 and 4-D seismic data in geostatistical reservoir modeling. *Mathematical geology*, 38 (3)**,** 301-325.

Whitcombe, D. N., Paramo, P., Philip, N., Toomey, A., Redshaw, T., and Linn, S. (2010). The correlated leakage method - It's application to better quantify timing shifts on 4D data. *72nd EAGE Conference & Exhibition incorporating SPE EUROPEC*.

Winkler, K., and A. Nur, (1979). Friction and seismic attenuation in rocks. *Nature,* Vol. 277.

Wirgin, A. (2004). The inverse crime. OR 12.

Wong, M. Y., and MacBeth, C. (2016). R-factor Recovery via Geertsma's Pressure Inversion Assisted by Engineering Concepts. *78th EAGE Conference and Exhibition 2016 - Workshops.*

Xu, S., Chen, G., Zhu, Y., Zhang, J., Payne, M., Deffenbaugh, M., Song, L., and, Dunsmuir, J. (2007). Carbonate Rock Physics: Analytical Models and Validations Using Computational Approaches and Lab/Log Measurements. *International Petroleum Technology Conference*.

Yale, D. P., and Jamieson Jr., W. H. (1994). Static and dynamic rock mechanical properties in the Hugoton and Panoma fields, Kansas. *SPE Mid-Continent Gas Symposium*.

Yale, D. R., Nieto, J. A., and Austin, S. P. (1995). The effect of cementation on the static and dynamic mechanical properties of the Rotliegendes sandstone. *35th U. S. Symposium on Rock Mechanics*.

Yin, Z., Ayzenberg, M., MacBeth, C., Feng, T., and Chassagne, R. (2015). Enhancement of dynamic reservoir interpretation by correlating multiple 4D seismic monitors to well behavior. *Interpretation*, 3, SP35-SP52.

Zhang, Q., and Du, B. (2016). Multiscale and iterative refinement optical flow (MSIROF) for seismic image registration and gather flattening using multidimensional shifts. *SEG International Exposition and Annual Meeting*.

Zhang, X., Koutsabeloulis, N. C., Kristiansen, T. G., Heffer, K. J., Main, I., Greenhough, J. and Hussein, A. M. (2011). Modeling Of Depletion Induced Micro-Seismic By Coupled Reservoir Simulation - Application To Valhall Field. *Society of Petroleum Engineers*.